Behaviour of Post-Tensioned Slab Bridges with FRP Reinforcement under Monotonic and Fatigue Loading

by

Martin Noël

A thesis
presented to the University of Waterloo
in fulfilment of the
thesis requirement for the degree of
Doctor of Philosophy
in
Civil Engineering

Waterloo, Ontario, Canada, 2013

Author's Declaration

I hereby declare that I am the sole author of this thesis. This is a true copy of the thesis, including any required final revisions, as accepted by my examiners.

I understand that my thesis may be made electronically available to the public.

Abstract

The introduction of fibre-reinforced polymers (FRPs) to the field of civil engineering has led to numerous research efforts focusing on a wide range of applications where properties such as high strength, light weight or corrosion resistance are desirable. In particular, FRP materials have been especially attractive for use as internal reinforcement in reinforced concrete (RC) structures exposed to aggressive environments due to the rapidly deteriorating infrastructure resulting from corrosion of conventional steel reinforcement. While FRPs have been successfully implemented in a variety of structural applications including bridges and parking garages, little research has been conducted on the use of FRP reinforcement for short span slab bridges. Furthermore, the behaviour of FRP-RC flexural members cast with self-consolidating concrete (SCC) is largely absent from the literature.

The present study investigates the behaviour of an all-FRP reinforcement system for slab bridges which combines lower cost glass FRP (GFRP) reinforcing bars with high performance carbon FRP (CFRP) prestressed tendons in SCC to produce a structure which is both cost-efficient and characterized by excellent structural performance at the serviceability, ultimate and fatigue limit states. An extensive experimental program comprised of 57 large or full-scale slab strips was conducted to investigate the effects of reinforcement type, reinforcement ratio, member depth, prestressing level and shear reinforcement type on the overall flexural performance of slab bridges under both monotonic and fatigue loading. The proposed reinforcement system was found to display excellent serviceability characteristics with reduced deflections and crack widths compared to the steel-reinforced control slab. The slabs also

displayed high load capacities as well as significant deformability to allow for sufficient warning prior to failure. Lastly, the use of post-tensioned CFRP tendons limited the stresses in the GFRP reinforcing bars leading to significantly longer fatigue lives and higher fatigue strengths compared to non-prestressed slabs.

To compliment the main experimental study, a series of ancillary tests were conducted to characterize the mechanical and fatigue properties of the reinforcing bars used. Both CFRP and GFRP bars were tested under uniaxial tension to measure their ultimate tensile strengths and moduli of elasticity. In addition, the fatigue behaviour of the GFRP bars was assessed through a series of axial bar tests as well as flexural beam-hinge tests conducted at various load ranges to determine the effect of concrete on the fatigue behaviour of the GFRP bars. It was found that the abrasion induced at the bar-concrete interface reduced the fatigue lives of the bars by a full order of magnitude and the beam-hinge specimens failed within one million cycles at load ranges as low as 20% of their measured static ultimate capacity.

Analytical models from current North American design codes were used to predict the behaviour of the slab bridge strips at service and at ultimate. Where these models failed to accurately represent the experimental findings, simple modifications were proposed. The results from the ancillary tests were also used to modify existing analytical models to predict the effects of fatigue loading on the deflection, crack width, shear resistance and flexural capacity of each of the tested slabs. A hypothetical two-lane slab bridge reinforced with the proposed FRP system was also evaluated according to the provisions of both major North American bridge design codes to highlight the viability of the proposed FRP reinforcement system for practical design applications.

Acknowledgements

To adequately thank everyone who contributed towards this thesis in one way or another would require a chapter of its own. I will always be grateful for the support I have received and the experiences I have had throughout my academic career.

I am sincerely thankful to have had the opportunity and pleasure of working with my supervisor, Professor Khaled Soudki, whose support and dedication has been exceptional throughout my tenure at the University of Waterloo. I hold him in the highest regard both personally and professionally and have had the privilege of considering him as both a mentor and a friend. Thanks also to my committee members, Professors Tim Topper and Jeff West for their helpful discussions and advice, and Professors Kaan Inal and Mark Green for reviewing my thesis.

I would also like to acknowledge the technical assistance of laboratory technicians Richard Morrison, Douglas Hirst, Rob Sluban and Ken Bowman. Their technical expertise was invaluable during the experimental phase of this study. The expertise and advice of Dr. Ahmed El-Sayed during the formative stages of this project is also gratefully acknowledged. I would also like to express my gratitude to the staff at Hanson Pipe and Precast who helped with the construction of the test specimens, and to the Natural Science and Engineering Research Council of Canada for their financial support.

I am particularly thankful for my colleagues who assisted me throughout various stages of this study and who enhanced my student experience. Special thanks to Adham El Menoufy, Rizwan Azam, Mohamed Yakhlaf, Mohammed Zawam, Daniel Baggio, Noran Abdel-Wahab, Rania Al-Hammoud, Abdulaziz Alaskar, Hesham Elhuni, Amr Abdel-Havez, Slamah Krem and Ayman Shihata for all of their help. Thanks also to Drs. Hugues Vogel and Dagmar Svecova from the University of Manitoba, who first introduced me to research in the field of structural engineering.

Lastly, I would like to express my deepest thanks to my friends and family who have supported me in this journey. Thank you to my parents who have always encouraged me and given me the confidence to reach my goals. Thank you to my wife, Lindsay, my greatest source of joy, whose love, patience and support has carried me through the ups and downs of the past few years and given me perspective of the important things in life; to her, this thesis is dedicated.

Table of Contents

List of Figures

List of Tables

List of Symbols

a	=	length of the shear spans
a	=	depth of the concrete rectangular stress block
A	=	area of the concrete section
A_{ct}	=	effective area of concrete in tension
A_{ducts}	=	area of the post-tensioning ducts
A_{frp}	=	cross-sectional area of the FRP reinforcement
A_{frpi}	=	cross-sectional area of FRP reinforcement layer *i*
a_g	=	nominal size of the coarse aggregate
A_r	=	area of the reinforcement
A_v	=	cross-sectional area of the shear reinforcement
$A_{v,min}$	=	minimum area of shear reinforcement
b	=	width of the beam
B	=	overall width of the bridge
B_e	=	effective width of the bridge
b_v, b_w	=	width of the concrete member
c	=	depth to the neutral axis

C = resultant compression force in the section

C_f = CHBDC correction factor

c_u = depth to neutral axis at failure

d = effective depth to the reinforcement

D = variable representing damage accumulation

$d_{c,}\ d_{cs}$ = thickness of the concrete cover to the centroid of the reinforcement

D_f = damage level causing failure

d_{frpi} = depth of reinforcement layer *i*

d_{long} = effective shear depth of the longitudinal reinforcement

d_p = effective depth to the prestressing tendons

d_s = diameter of the stirrups

d_v = effective shear depth of the section

e = eccentricity of the prestressing tendons

E = modulus of elasticity

E = width of the equivalent strip in inches

E_1 = first-cycle modulus of elasticity

E_c = modulus of elasticity of the concrete

E_{frp} = modulus of elasticity of the FRP reinforcement

$E_{frp,N}$ = fatigue modulus of elasticity of the FRP reinforcement

E_N = cyclic secant modulus of elasticity of the concrete

E_o = initial modulus of elasticity

E_p = modulus of elasticity of the prestressing tendons

E_s = elastic modulus of the steel reinforcement

E_r = modulus of elasticity of the reinforcement

E_{vFRP} = modulus of elasticity of the FRP stirrup

F = force in the reinforcement

F = width dimension characterizing load distribution

f_c = compressive stress in the concrete

f'_c = concrete compressive strength

f_{cm} = factor related to the concrete compressive strength

f_{cr} = cracking strength of concrete

f_{ct} = maximum stress in the concrete between cracks

F_f = fatigue modulus of elasticity at failure

f_{frp} = stress in the FRP reinforcement

$f_{FRPbend}$ = tensile capacity of the FRP stirrup

f_{frpi} = stress in FRP reinforcement layer *i*

f_{frpm} = mean stress in the FRP reinforcement between cracks

f_{frpu} = FRP ultimate tensile strength

f_{fs} = allowable fatigue stress range in FRP reinforcement

$f_{gfrp,dc}$ = stress in the GFRP reinforcing bars at the decompression moment

f_{min} = minimum applied stress

f_{max} = maximum applied stress

F_o = initial fatigue modulus of elasticity

f_p = stress in the FRP tendons at ultimate

F_p = statistical coefficient depending on the reliability level

f_{pe} = effective prestress in the FRP tendon

f_{po} = stress in the prestressed reinforcement when the stress in the surrounding concrete is zero

f_r = modulus of rupture of the concrete

$f_{r,eff}$ = effective modulus of rupture of the concrete

$f_{r,N}$ = cyclic modulus of rupture of the concrete

f_t = average tensile stress in the concrete

F_v = amplification factor to account for the transverse variation in maximum longitudinal vertical shear intensity

h = height of the section

h_1 = distance from the neutral axis to the centre of the FRP reinforcement

h_2 = distance from the neutral axis to the extreme tension fibre

l_1, l_2 = horizontal distances from the fictitious crack tip to each support

I_{cr} = cracked section moment of inertia

$I_{cr,N}$ = cracked section moment of inertia under fatigue loading

I_e = effective moment of inertia

$I_{e,N}$ = effective moment of inertia under fatigue loading

I_g = gross section moment of inertia

I_t = transformed section moment of inertia

J = CHBDC overall performance factor

jd = length of the internal lever arm

k = ratio of the neutral axis depth to the effective depth of the reinforcement

k_b = bond-dependent coefficient for calculating crack widths

k_n = cyclic curvature of a concrete section

k_o = initial curvature of a concrete section

k_p = coefficient to account for the tendon profile

k_s = coefficient to account for the loading configuration

K_{tr} = factor accounting for the presence of transverse reinforcement

K_{te} = effective fatigue stress factor

L = length of the clear span

ℓ_d = development length of the FRP bar

ℓ_e = embedment length of the FRP bar

L_g = uncracked length of the concrete member near the supports

L_1 = modified span length of the bridge

m = moment at a section due to virtual loads

m = maximum longitudinal moment per metre of width

M = moment at a section due to real loads

m_{avg} = average longitudinal moment per metre of width

M_f = factored moment

M_a = applied moment

M_c = applied moment at a service state corresponding to a maximum concrete strain of 0.001

M_{cr} = cracking moment of a concrete section

$M_{cr,N}$ = cyclic cracking moment of a concrete section

M_{dc} = decompression moment

m_i = number of fatigue specimens at a given stress level

M_r = moment resistance of the section

M_s = service load moment

M_T = maximum longitudinal moment for one lane width of truck or lane loading

M_{ult} = applied moment at ultimate

n = number of applied load cycles

n = number of surviving fibres in a fibre bundle

n = modular ratio of the reinforcement to the concrete

n = total number of fatigue specimens

n = number of design lanes on the bridge

N = number of applied load cycles

N = total number of fibres in a fibre bundle

N_f = factored axial force in the member

N_f = fatigue life corresponding to the applied stress level

N_L = number of design lanes on the bridge

N_{norm} = normalized fatigue life

P = applied load

P = probability of failure

P, P_e = effective prestressing force

Q_{ij} = normalized fatigue life of a specimen

r = radius of the bend of an FRP stirrup

R = ratio of minimum to maximum applied stress

R_{ki} = characteristic value of the fatigue life

R_L = modification factor for multi-lane loading

s = bar spacing

s = stirrup spacing

S = applied load range

S = distance between supports in feet

S_{min} = minimum applied stress

S_r = applied stress range

S_c = average crack spacing

s_z, s_{ze} = crack spacing parameters

t = time under cyclic loading in hours

T = resultant tension force in the section

T = number of seconds required to complete one cycle

v = maximum longitudinal vertical shear per metre width

v_{avg} = average longitudinal vertical shear per metre width

V_c = concrete contribution to shear resistance

$V_{c,N}$ = concrete contribution to shear capacity under fatigue loading

V_f = factored shear at the critical section

V_{frp} = contribution to shear resistance of the FRP stirrup

$V_{p,frp}$ = vertical component of the prestressing force in draped tendons

V_T = maximum longitudinal shear for one lane width of truck or lane loading

w = crack width at the tension face of the member

W = overall bridge width

w_c = maximum flexural crack width

w_{max} = initial flexural crack width

$w_{max,N}$ = cyclic flexural crack width

w_n = cyclic flexural crack width

w_o = initial flexural crack width

w_s = inclined width of the fictitious shear crack

W_1 = modified width of the bridge

x = ratio of applied load cycles to fatigue life

x = distance between two successive sections of a concrete member

y = height of the crack

Y = deflection or crack width during the first cycle

y_{cr} = centroid of the cracked section

y_e = effective section centroid

y_g = centroid of the gross section

y_t = depth to the centroid of the section from the extreme tension face

α = angle of inclination of the shear bar

α = Weibull shape parameter

α_1 = concrete stress block parameter

α_1 = coefficient accounting for the bond characteristics of the reinforcement

α_2 = coefficient accounting for the loading conditions

α_c = axial stiffness ratio of the CFRP tendons to the combined reinforcement stiffness

β = ratio of h_2 to h_1

β = factor used to account for the shear strength of cracked concrete

β = Weibull scale parameter

β_1 = concrete stress block parameter

β_d = modification factor to account for the reduced stiffness of the FRP reinforcement

β_{RH} = shrinkage factor to account for the effect of relative humidity

β_s = shrinkage factor to account for the effect of time

β_{sc} = shrinkage factor to account for the effect of cement type

γ_c = unit weight of concrete

δ, Δ = midspan deflection

Δ = stress range in the concrete expressed as a fraction of the compressive strength

Δ_i = relative displacements between the two FRP anchors after the initial cycle

Δ_n = cyclic deflection

Δ_N = relative displacements between the two FRP anchors under fatigue loading

Δ_o = initial deflection

δ_s = additional shear deformation due to unrestrained shear cracking

δY = change in deflection or crack width

ε_c = cyclic creep strain in the concrete

ε_c = average strain in the concrete between cracks

ε_c = compressive strain in the concrete

ε'_c = concrete strain corresponding to the peak stress

ε_{cs} = axial shrinkage strain

ε_{cu} = concrete crushing strain

ε_{frp} = strain in the FRP reinforcement

ε_{frps} = strain in the FRP reinforcement at service states

ε_{frpu} = FRP rupture strain

ε_i = strain at the critical section after the initial cycle

ε_m = mean reinforcement strain

ε_N = strain at the critical section under fatigue loading

ε_{pe} = effective prestrain in the tendons

ε_s = reinforcement strain at the crack

ε_{sh} = restrained shrinkage strain in the concrete

ε_t = average tensile strain in the concrete

ε_v = strain in the stirrup

ε_x = strain in the concrete section at mid-depth

η = correction factor relating I_{cr} and I_g

θ = deformability index

θ = angle of the shear crack

μ = lane width modification factor

$\hat{\mu}$ = variance

ξ = ratio of effective stress to ultimate strength of the prestressing tendons

ρ_{frpb} = balanced reinforcement ratio

ρ_i = reinforcement ratio of the reinforcement at level *i*

σ = stress in the composite

σ, σ_a = applied stress level

σ_e = equivalent static strength of the fatigue specimens

σ_f = tensile capacity of the fibres

σ_m = mean compressive stress in the concrete expressed as a fraction of the compressive strength

σ_{max} = maximum applied stress

σ_r = residual strength of the fatigue specimens

σ_u = ultimate strength of the FRP

σ_v = capacity of bent FRP stirrups

ϕ_c = material resistance factor for concrete

ϕ_{frp} = material resistance factor of the FRP

ψ = curvature at a section

ψ = factor accounting for the load level

ψ_c = curvature at a service state corresponding to a concrete strain of 0.001

ψ_{mid} = curvature at midspan

ψ_{ult} = curvature at ultimate

Ω_u = strain reduction coefficient

Chapter 1 - Introduction

1.1 General

The deterioration of reinforced concrete (RC) structures caused by corrosion of steel reinforcement is currently a major concern affecting the safety and functionality of our infrastructure. A large number of bridge structures are in need of repair or replacement, thus placing an enormous strain on the overall transportation network and requires large capital investments which ultimately affect all taxpayers. In order to ensure that new structures require less maintenance and have longer service lives than their predecessors, the cause of the problem, namely corrosion of steel reinforcement, must be addressed.

Fibre-reinforced polymer (FRP) materials have shown tremendous potential as an alternative reinforcement type for both RC and prestressed concrete (PC) structures. FRPs have been used in a wide variety of structural applications, from reinforced concrete deck slabs to post-tensioned parking garages. However, one promising application for FRP reinforcing bars in FRP-RC slab bridges has yet to be investigated thoroughly through extensive experimental and analytical programs.

Longitudinally-reinforced slabs are the simplest form of concrete bridge superstructure, while prestressed slabs can be used for greater span-to-depth ratios. Between 1950 and 1995, approximately 6000 prestressed concrete slab bridges were constructed, constituting more than 8 percent of the total number of bridges built during that period (Tabsh 1995). Slab bridges can be simply supported or continuous, cast-in-place or precast, with solid or void

sections. They differ from slab-on-girder superstructures in that the reinforcement is parallel to the direction of traffic and the slab spans can be much longer than the typical 2-3 m spacing of longitudinal girders. The relatively low stiffness of GFRP reinforcement has limited its use in longer spans due to poor serviceability performance, particular under traffic loading where heavy trucks can lead to large deflections and crack widths. The use of post-tensioned CFRP tendons to improve both the serviceability and ultimate flexural behaviour of GFRP-RC slabs has potential as a new corrosion-resistant reinforcement system for the effective design of slab bridges.

Similar advances in concrete materials technology have led to the development of self-consolidating concrete (SCC). Unlike conventional concrete, SCC does not require mechanical vibration in order to fully encapsulate the reinforcement and flow to all corners of the formwork. SCC is able to flow under its own weight to provide a uniform cross-section free from segregation of aggregates, while minimizing surface bleeding and eliminating the presence of internal voids or honeycombing. All of these advantages lead to improvements in concrete quality while reducing labour costs, construction time and noise related to consolidation.

A review of available literature has shown that studies are currently lacking on the behaviour of FRP-reinforced SCC members. It is likely that the use of both FRP materials and SCC will continue to increase both in scope and in quantity, and it is important that their use is supported by experimental research to ensure safety, functionality and efficiency in design.

Furthermore, there are currently no standard methods for predicting the fatigue life, residual stiffness or remaining life of GFRP-RC members. The issue of fatigue of FRP reinforcement is addressed implicitly in design codes by limiting the stress in the FRP bars due to live loads at service. Although the fatigue behaviour of FRP composites has been studied for aerospace and marine applications, these materials differ in type, composition and fabrication process compared with FRP reinforcing bars, and the load ranges and environmental exposure to which the materials are subjected vary greatly. Few experimental studies are available in the literature on the fatigue behaviour of FRP-RC or PC members, and—to the author's knowledge—no comprehensive attempts have been made to quantitatively predict the effect of cyclic loading on the long term behaviour of structural members with FRP reinforcement. This is likely partly due to the difficulty in gripping FRP reinforcing bars for testing, especially for fatigue, and the complex failure modes observed. Nevertheless, it is imperative that an understanding of the long-term effects of repeated loading on FRP-RC and PC structures is achieved, and preferably through a simple experimental process that can be replicated for various types of FRP bars.

1.2 Scope of Research

The research study presented herein focuses on refining an FRP reinforcing system for slab bridges that has good performance at service, ultimate and fatigue limit states. A total of 57 full-scale and reduced-length one-way SCC slab strips were tested in flexure under monotonic or fatigue loading to determine the effect of various parameters including reinforcement type, reinforcement ratio, post-tensioning force and various types of shear reinforcement on the overall performance of slab bridges. The ability of current North American design models to

predict the serviceability and ultimate capacity of the slabs containing both active and passive FRP reinforcement was also investigated.

In addition, ancillary studies were conducted to characterize the static and fatigue behaviour of the FRP reinforcing bars used in the main study. Both the CFRP and GFRP bars were tested in uniaxial tension to obtain their tensile mechanical properties. Two types of fatigue tests were also conducted on the GFRP reinforcing bars, namely bare bar axial tension tests and flexural hinged-beam tests. The results of these tests were used to calibrate analytical models to predict the fatigue life and residual stiffness of the GFRP reinforcing bars, and in turn, to predict the long-term serviceability and service lives of GFRP-RC members. The analytical models were used to accurately predict the fatigue behaviour of the slabs tested in the main experimental study.

1.3 Research Objectives

The primary goal of this study was to develop a reinforcing system for slab bridges which combines prestressed and non-prestressed FRP reinforcement to produce a structural member with excellent serviceability while also displaying high deformability at ultimate loads and good fatigue characteristics. In order to achieve this goal, the effects of various parameters on the overall flexural performance of the slabs were investigated. Specific objectives are summarized as follows:

1. To add to the currently limited body of work on the structural behaviour of FRP-RC and PC members made with SCC.

2. To develop and refine an all-FRP reinforcing system combining active and passive FRP reinforcement to allow for the efficient design of sustainable slab bridges with excellent performance characteristics.
3. To investigate the effects of reinforcement type, reinforcement ratio, cross-section depth, number of prestressing tendons, effective prestressing force and bond between the prestressing tendons and the concrete slab on the flexural performance of full-scale slab strips.
4. To investigate the effectiveness of CFRP post-tensioned tendons for increasing the shear resistance of slab bridges.
5. To investigate the effectiveness of various shear reinforcement types for slab bridges, including C-shaped stirrups, inverted U-shaped stirrups and shear bars with and without mechanical anchorage, to increase the shear resistance of concrete slab bridges under static and fatigue loading. The effect of fibre type (glass or carbon) and stirrup diameter were also investigated.
6. To study the effect of different reinforcement configurations on the serviceability, flexural and shear resistance of the slabs under cyclic loading.
7. To quantify the effects of cyclic loading on the fatigue life and residual stiffness of GFRP reinforcing bars for use in structural concrete members through a simple and repeatable test method.
8. To develop analytical models which will accurately predict the performance of the slabs at serviceability, ultimate and fatigue limit states.

1.4 Thesis Organization

Chapter 2 includes a detailed background and comprehensive review of available literature on the use of FRP reinforcement and SCC for structural applications, as well as research on the fatigue of FRP and concrete structures. A description of the main experimental program is provided in Chapter 3, including details of the test specimens, test setups and procedures; the results of the experimental program are discussed in Chapter 4 for each phase of the main experimental study.

Chapter 5 presents the details of an ancillary testing program which was conducted to investigate the mechanical properties of the FRP reinforcing bars under both static and fatigue loading conditions. Chapters 6 and 7 focus on an analytical investigation to predict the behaviour of the slabs under static and fatigue loading, respectively, and the proposed reinforcement system is evaluated using current North American bridge design codes in Chapter 8. Finally, Chapter 9 summarizes the conclusions drawn from the experimental and analytical investigations and provides recommendations for future work.

Chapter 2 - Background and Literature Review

2.1 Introduction

A large number of concrete bridge structures throughout North America are now being considered for repair or replacement. An estimated $74 billion is needed to repair deteriorated reinforced concrete (RC) structures in Canada (NSERC 2010). In particular, corrosion-induced deterioration has had a detrimental effect on the structural integrity of conventionally-reinforced concrete bridges. Fibre-reinforced polymer (FRP) materials have emerged as an alternative to steel for both reinforced and prestressed concrete (PC) structures (ACI Committee 440 2007) which can effectively double a structure's service life (NSERC 2010). FRPs are non-corrosive and have a high strength-to-weight ratio making them attractive for construction purposes; carbon and glass FRP (CFRP and GFRP, respectively) reinforcing bars have been successfully used in many structural concrete applications throughout North America and overseas and can result in significant savings over the service lives of bridge structures exposed to aggressive environments due to reduced maintenance and repair costs. In most cases these savings are realized within the first 20 years of service (Grace et al. 2012).

Short span bridges comprise a major portion of the national bridge inventory. Of the 163,000 single span concrete bridges in the United States, 23% are considered structurally deficient or functionally obsolete—the majority of these are less than 15 m in length (Mabsout et al. 2004). RC slab bridges are generally considered to be an efficient and economical solution for short span bridge structures between 3 and 16 m (Azizinamini et al. 1994). Some of the main advantages of cast-in-place concrete slab bridges include ease of construction, use of local

materials and the ability to provide a smooth finishing surface by field adjustment of the roadway profile during construction (Mabsout et al. 2004). Alternatively, slab bridges and box culverts can be constructed from precast segments to minimize construction time and ensure a quality concrete product.

Unlike slab-on-girder superstructures, RC slab bridges and box culverts are designed with the main reinforcement parallel to the direction of traffic, and behave like wide beams when subjected to multilane loading (Frederick 1997). For this reason, slab bridges are typically designed as a series of beam strips subjected to one-way bending; the effective strip method has been shown to provide conservative estimates of the load effects observed in existing RC slab bridges (Saraf 1998). Post-tensioning is often used in order to reduce member dimensions, create watertight sections, limit cracking and control deflection.

Recently, the use of FRP reinforcement in concrete slab bridges has been studied at the University of Missouri in Rolla and implemented in the widening and rehabilitation of the Southview Bridge (Galati et al. 2004, Fico et al. 2006). Slab strips with GFRP top and bottom reinforcing mats were constructed and tested in the laboratory. Post-tensioned CFRP tendons were used to increase the slab stiffness through prestressing action; in addition to improved serviceability, post-tensioning increased the design shear capacity by more than 70% (Fico et al. 2005). GFRP bars as passive and CFRP tendons as active internal reinforcement were found to be a feasible solution for replacing steel reinforcement in concrete slab bridges. Despite this, no comprehensive research program has been conducted to date to investigate the effect of various parameters on the performance of FRP-RC slab bridges in order to optimize an all-FRP

reinforcement system meeting structural requirements at serviceability, ultimate and fatigue limit states to produce an economical and sustainable alternative to conventional design.

Advanced materials technology has also led to the increased use of self-consolidating concrete (SCC) for various types of structural applications. While SCC was first developed in response to a lack of skilled workers for placing quality concrete and to accommodate increasingly congested rebar detailing, a growing number of precasters, ready-mix suppliers and contractors are recognizing the benefits of SCC for reducing construction time and labour costs. A significant amount of research is available on the physical properties of SCC; however, the cumulative body of work on the use of FRP reinforcement with SCC is currently limited. These types of studies are necessary to increase confidence for industry members to adopt these advanced material technologies. This study is not focused on comparing SCC with conventional concrete explicitly, as numerous studies are readily available in this respect; rather the combined behaviour of state-of-the-art sustainable materials (FRP and SCC) to produce structures with excellent performance characteristics is investigated to serve as a reference for design engineers for confident implementation in the field.

The following sections include a summary of the available literature on the behaviour of FRP materials and SCC, as well as FRP-RC and FRP-PC members, including the effects of flexure, shear and fatigue.

2.2 Fibre-Reinforced Polymers

Although originally manufactured for use in the aerospace industry, FRP materials were eventually developed for civil engineering applications and have been at the nexus of numerous

research efforts over the last two decades as reinforcement for new structures or for the rehabilitation of existing ones. FRP reinforcing bars are made of continuous longitudinal fibres impregnated in a resin matrix through a pultrusion process, bonding the fibres together to provide shape and load transfer capabilities. The specific composition of FRP bars varies between manufacturers and by fibre type.

Among the various types of FRP materials available, the two which are most commonly used as reinforcement in concrete structures are CFRP and GFRP, which are made from carbon and glass fibres, respectively. Since the fibres provide strength and stiffness to the composite bar in the longitudinal direction, the mechanical properties vary significantly between bar types; in particular, the ultimate tensile strength and modulus of elasticity are primarily governed by the type of fibre used. Out of the commercially available FRP products, CFRP displays the most desirable material properties for structural use in terms of high tensile strength and stiffness, good durability and fatigue characteristics, and low relaxation. GFRP—although lower in cost—is generally not desirable for prestressing due to its low transverse shear strength, a susceptibility to creep rupture and stress corrosion (Braimah 2000). Typical tensile stress-strain curves of CFRP and GFRP reinforcing bars are shown in Figure 2.1 (ISIS Canada 2008).

Governing standards for the production of FRP reinforcement have recently been developed (CSA S807-10 2010). However, mechanical properties vary between reinforcing bars produced by different manufacturers. A summary of these properties for commercially available CFRP bars in Canada is given in Table 2.1 (Pultrall 2007, Hughes Brothers 2011a). Table 2.2

summarizes the properties for GFRP bars (Pultrall 2011a,b,c, Hughes Brothers 2011b, Schoeck Canada 2011).

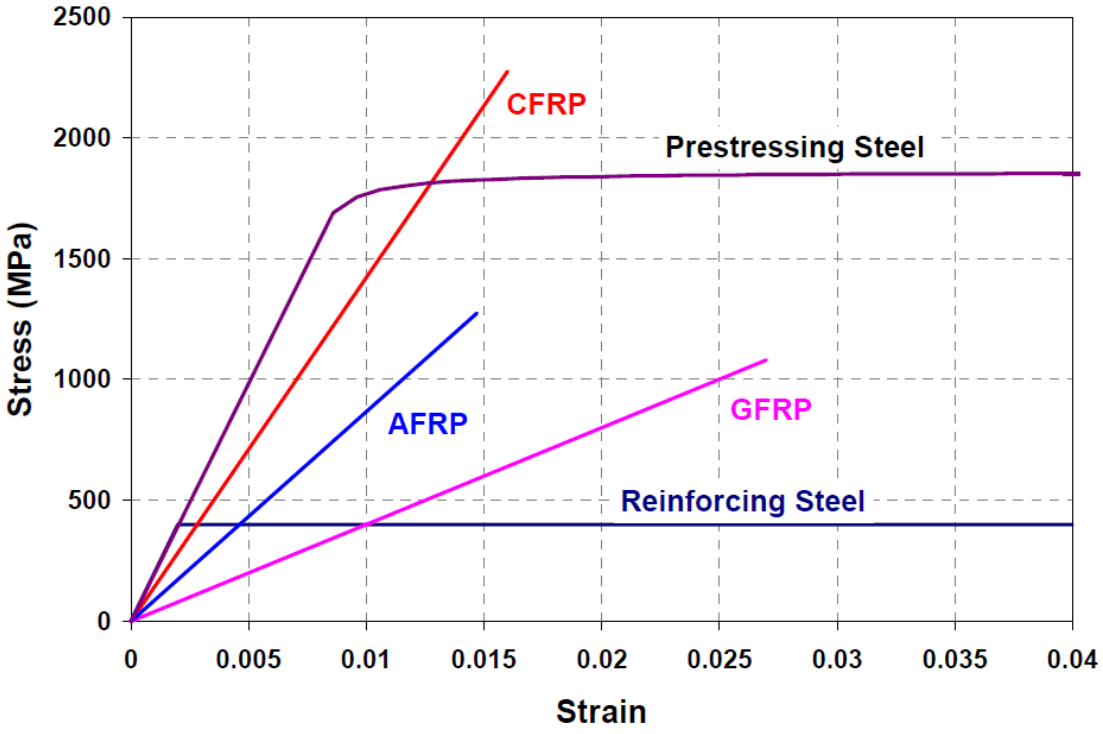

Figure 2.1 - Typical stress-strain curves for FRP and steel reinforcing bars (ISIS Canada 2008)

Table 2.1 - Material properties of commercially available CFRP reinforcing bars

Bar type	Bar size	Nominal bar diameter (mm)	Guaranteed tensile strength (MPa)	Tensile modulus of elasticity (GPa)	Ultimate strain (%)
V-Rod *(Pultrall 2007)*	#2	6.4	1356	127	1.22
	#3	9.5	1431	120	1.33
	#4	12.5	1765	144	1.32
Aslan 200 *(Hughes Brothers 2011a)*	#2	6	2241	124	1.81
	#3	10	2172	124	1.75
	#4	13	2068	124	1.67

Table 2.2 - Material properties of commercially available GFRP reinforcing bars

Bar type	Bar size	Nominal bar diameter (mm)	Guaranteed tensile strength (MPa)	Tensile modulus of elasticity (GPa)	Ultimate strain (%)
V-Rod (low modulus) *(Pultrall 2011a)*	#3	10	700	42.5	1.65
	#4	13	681	44.1	1.54
	#5	16	804	42.5	1.89
	#6	19	666	44.5	1.50
	#8	25	588	43.9	1.34
V-Rod (standard) *(Pultrall 2011b)*	#2	6	938	52.5	1.79
	#3	10	889	53.4	1.66
	#4	13	941	53.6	1.76
	#5	16	934	55.4	1.69
	#6	19	807	56.6	1.43
	#7	22	816	53.5	1.53
	#8	25	703	52.9	1.33
V-Rod (high modulus) *(Pultrall 2011c)*	#3	10	1372	65.1	2.11
	#4	13	1312	65.6	2.00
	#5	16	1184	62.6	1.89
	#6	19	1105	64.7	1.71
	#7	22	1059	62.6	1.69
	#8	25	1000	66.4	1.51
	#10	32	1093	65.1	1.68
Aslan 100 *(Hughes Brothers 2011b)*	#2	6	896	46	1.94
	#3	10	827	46	1.79
	#4	13	758	46	1.64
	#5	16	724	46	1.57
	#6	19	690	46	1.49
	#7	22	655	46	1.42
	#8	25	620	46	1.34
	#9	29	586	46	1.27
	#10	32	551	46	1.19
ComBAR *(Schoeck Canada 2011)*	--	8	1500	>60	--[a]
	--	12	1350	>60	--[a]
	--	16	>1200	>60	--[a]
	--	25	>1100	>60	--[a]
	--	32	>1000	>60	--[a]

a – Not reported

While the advantages of FRP materials—resistance to corrosion, high strength-to-weight ratio, good fatigue characteristics and electromagnetic neutrality—have become evident over the past twenty years, some drawbacks have prevented FRPs from being fully embraced by the construction industry. Among these is the high material cost of FRP reinforcement, although life-cycle cost analyses often show that the long-term cost of using FRP reinforcement can be

much lower than for similar structures reinforced with black or epoxy-coated steel (Grace et al. 2012). Other issues, including the relatively low axial stiffness and transverse strength of FRP materials can be overcome through a shift in design methodology by focusing on serviceability limits first and checking load capacity second.

Another concern for designers, however, is the lack of ductility of FRP bars. FRPs are linearly elastic to failure and do not deform plastically like steel. As a result, tensile failure of FRP-reinforced or prestressed concrete members is usually sudden and violent, with little or no warning. In order to induce a more gradual failure, members are usually over-reinforced such that concrete crushing occurs before rupture of the tensile FRP reinforcement, which is a rather inefficient use of the materials since the full strength of the FRP bars is not utilized. Alternatively, a reinforcement system consisting of multiple bar types or reinforcement layers at different strain levels can be used to induce a pseudo-ductile progressive failure mode.

2.3 Self-Consolidating Concrete

Normally-consolidated concrete (NCC) generally requires mechanical vibration in order to fully encapsulate internal reinforcement and spread to all corners of the formwork. Insufficient vibration can lead to voids within the concrete section or gaps along the surface which can undermine the structural integrity of the member while reducing the aesthetic quality of the concrete finish. On the other hand, excessive vibration can lead to segregation of aggregates and surface bleeding and can result in damage to the reinforcement or formwork. Placement of NCC therefore requires a certain level of skill and experience in order to produce a quality product.

Self-consolidating concrete (SCC) was first developed in Japan in the 1980s in response to the decreasing number of available skilled workers in the construction industry. SCC is highly flowable, non-segregating concrete that can spread into place, fill the formwork, and encapsulate the reinforcement without any mechanical consolidation (ACI Committee 237 2007). SCC is therefore an attractive alternative to NCC as a means to significantly reduce construction time while simultaneously decreasing labour and equipment costs. Other advantages include the ability to fill highly congested sections and complex formwork, reduce construction noise, decrease employee injuries, provide more flexibility for detailing reinforcing bars and creating smooth surfaces free from honeycombing, bleeding or discolouration (ACI Committee 237 2007).

2.3.1 Fresh Properties

The workability of SCC in the fresh state is usually defined in terms of filling ability, passing ability and stability. Filling ability describes the ability of the concrete to flow into and completely fill all spaces in the formwork under its own weight. Passing ability refers to how easily the concrete can pass through obstacles such as congested reinforcement without blockage. Lastly, stability describes the concrete's ability to maintain a homogeneous distribution of its constituents during flow and setting. The degree of stability, filling ability and passing ability required depends on the application (ACI Committee 237 2007). The self-compactibility of SCC is generally measured with a slump flow test. Typical slump flow values range from 600 mm to 750 mm (Domone 2006), although Hwang et al. (2006) recommend a slightly smaller range of 620 mm to 720 mm.

SCC mix designs must be carefully calibrated to balance deformability and stability (Khayat 1999). SCC mixes usually contain fine powders including cementitious materials such as silica fume and fillers such as limestone or fly ash. Increasing the water-powder ratio can ensure good deformability (filling ability) but can also reduce the cohesiveness of the paste leading to segregation of the fine and coarse aggregate particles. Using powder materials with different morphology and grain size distribution can improve particle packing density and reduce inter-particle friction thus improving deformability, self-compactibility and stability (Khayat 1999, Brouwers & Radix 2005, Sonebi et al. 2007). The coarse aggregate content and maximum aggregate size are typically lower than in conventional mixes to improve stability. The use of viscosity modifying admixtures (VMAs) and high range water reducers (HRWRs) can also improve deformability while maintaining adequate stability. Small dosages of VMA can improve the robustness of the SCC, making it less sensitive to changes in material properties and placement conditions (Khayat 1999).

2.3.2 Hardened Properties

The majority of available literature concerning SCC is focused on its fresh properties since they are very different from conventional concrete. It should be noted, however, that the mechanical properties of hardened SCC are not necessarily the same as those of NCC. Collepardi et al. (2005), for example, have reported a 20% increase in compressive strength compared to NCC with a similar water-cement ratio. Many of the findings from studies on the hardened properties of SCC report controversial results with respect to comparisons of mechanical properties with NCC, highlighting the significant effect of the mix design used; it is therefore difficult to draw general conclusions to describe all cases. SCC typically has high

powder volumes and low water-powder ratios in combination with superplasticizers to achieve the desired fluidity and stability; the mechanical properties of concrete are greatly influenced by the type and proportion of powder additions and do not depend solely on the water-powder ratio (Sonebi et al. 2003, Domone 2007).

Many SCC mixes contain a relatively low coarse aggregate volume and maximum aggregate size. This can result in smoother crack interfaces and hence, a reduction in aggregate interlock. For a similar concrete compressive strength, the shear strength between pre-fractured concrete surfaces has been observed to be approximately 10% lower than NCC for a given normal stress (Schiessl & Zilch 2001). The higher paste volume may affect other properties as well; the modulus of elasticity of low strength SCC mixes have been reported to be on average 40% lower than NCC mixes with the same compressive strength, although the difference is reduced to about 5% at higher strengths, and there is little difference in the relationship between compressive and tensile strength between NCC and SCC (Domone 2007). SCC also generally displays similar creep behaviour to conventional concrete (ACI Committee 237 2007).

Some SCC mixtures may be at risk of high autogenous shrinkage due to their low water-cementitious materials ratio, although drying shrinkage values are often similar or lower than for NCC with similar compressive strength (ACI Committee 237 2007). Schindler et al. (2007) conducted an experimental study on 21 different SCC mixtures and found that total shrinkage strains were similar or less than the control mixes after 112 days, concluding that excessive drying shrinkage is not expected for full-scale members made from SCC. Similarly, based on an experimental study, Turcry et al. (2006) concluded that SCC has the same risk of cracking due to shrinkage as NCC as long as the fresh SCC is sufficiently stable. Collepardi et al. (2005) reported

similar elastic and shrinkage strains but increased creep strains in SCC compared with similar NCC.

2.3.3 Structural Performance

Summarizing the findings of a number of studies on reinforced and prestressed SCC beams, Domone (2007) states that SCC beams displayed a similar flexural load capacity with a tendency for greater deflections and ultimate strains compared with NCC beams. Similarly, a report from the National Cooperative Highway Research Program (NCHRP) on SCC for precast, prestressed concrete bridge elements states that SCC girders displayed smaller cambers due to greater elastic shortening and long term prestressing losses arising from lower stiffness and greater drying shrinkage. Similar cracking moments, flexural stiffness (pre and post-cracking) and shear cracking strengths were observed between prestressed SCC and NCC girders (Khayat & Mitchell 2009). Lin & Chen (2012) observed smaller crack widths in SCC beams compared with NCC beams, and the stiffness of the SCC beams varied with coarse aggregate content.

Studies on the shear resistance of SCC beams have yielded controversial results. Lin & Chen (2012) observed similar shear capacities between SCC and NCC beams; Boel et al. (2010), meanwhile, have reported slightly lower shear strengths for SCC mixes, and Desnerck et al. (2009) found that the ultimate shear strength of SCC was higher than NCC despite having a lower coarse aggregate content which was attributed to the improved structure of the concrete matrix.

A number of research studies have also reported similar or better bond of SCC to steel reinforcement as compared to NCC, especially after 28 days (Chan et al. 2003, Zhu et al. 2004,

De Almeida Filho et al. 2005, Collepardi et al. 2005, Girgis & Tuan 2005, Boel et al. 2010, Kim et al. 2012). Daoud et al. (2003) found that SCC had a similar bond strength compared with NCC for deformed steel bars but different bond capacities for smooth bars which rely solely on adhesion and friction for force transfer.

It should be noted that while almost all of the available literature on the bond of reinforcement to SCC is related to steel-RC, the observed trends are not necessarily the same for FRP-RC members. Steel reinforcement relies primarily on mechanical bearing between the concrete and the lugs on the surface of the reinforcing bars for load transfer. While FRP bars generally do have some surface deformations to enhance bond characteristics, these differ in type, size and stiffness compared with steel rebar, and a relatively larger portion of the bond stress is transferred by friction and chemical adhesion. Therefore, the bond transfer mechanisms and failure modes may differ between FRP-reinforced and steel-reinforced SCC.

2.4 FRP-Reinforced Concrete Members

Steel-RC has been in use for over a century and its structural behaviour in common applications is fairly well understood. The main disadvantage of reinforced concrete has always been corrosion of internal steel reinforcement, especially in aggressive environments and where de-icing salts are used such as on bridges and in parking structures. With the development of FRP reinforcing bars, the potential of reinforced concrete unhindered by the risk of corrosion has resulted in numerous research efforts in an attempt to better understand the performance of this relatively new material for both short term and long term use.

Guidelines have recently been developed for the design of FRP-RC members (ACI Committee 440 2006, ISIS Canada 2007). These guidelines differ from conventional concrete design for flexural members for several reasons. First, the lower stiffness of FRP reinforcement compared to steel results in greater deflections and crack widths at service, such that serviceability criteria often governs the design. Secondly, the linear elastic nature of FRP materials implies that the mode of failure of under-reinforced members occurs suddenly by rupture of the reinforcement. In order to ensure some ductility, and therefore visual warning prior to failure, over-reinforced sections are generally more desirable since concrete crushing in the compressive zone of flexural members occurs more gradually than tension failures and do not result in immediate collapse. Thirdly, shear design models developed for steel-reinforced sections are not directly applicable to FRP-reinforced members. The primary mechanisms resisting the applied shear after cracking in slender concrete members without shear reinforcement include the uncracked concrete in the compression zone, aggregate interlock across the shear crack plane and dowel resistance of the longitudinal reinforcement. Due to the lower stiffness of FRP reinforcement, the neutral axis of cracked flexural members is closer to the compression face and cracks are wider than in a similar, conventionally reinforced member. In addition, FRPs are characterized by very low dowel resistance and hence shear strength is significantly reduced. Lastly, FRP reinforcing bars in the compression zone are usually neglected in design calculations due to their low compressive strength and relatively similar elastic moduli compared with concrete.

2.4.1 Serviceability

Although FRP-RC members often have an increased moment capacity compared with similarly under-reinforced steel-RC members, their low post-cracking stiffness often results in

serviceability of the member governing design. Serviceability criteria, as specified in the Canadian Highway Bridge Design Code (CSA 2010), include a crack width limit of 0.5 mm and FRP stress limits of $0.65f_{frpu}$ and $0.25f_{frpu}$ for carbon and glass FRP, respectively. El-Gamal & Benmokrane (2009) noted that FRP-RC slab designs were governed by crack width limits for all cases considered. The width of a crack at the surface of the reinforcement is equal to the sum of the relative slip of the reinforcement on either side of the crack; this is influenced both by the bond strength and stiffness of the reinforcement (Balazs 1993, Aiello & Ombres 2000). Due to the low elastic modulus of FRP, the slip of FRP reinforcing bars relative to concrete is greater than that of steel bars (Okelo & Yuan 2005). Michaluk et al. (1998) reported crack widths in GFRP-RC slabs of up to 19 times the width of cracks in similar steel-reinforced slabs. The wider cracks were accompanied by larger crack spacing, approximately 2.3 times that of the control slabs.

The cracking moment of FRP-RC sections is given by Equation 2.1. Since the stiffness of FRP materials is comparable to that of concrete, the CHBDC (CSA 2010) permits the use of gross section properties in place of transformed section properties when calculating the cracking moment.

Eq. 2.1 $$M_{cr} = \frac{f_r I_t}{y_t}$$

Where, M_{cr} is the cracking moment, f_r is the modulus of rupture of the concrete, I_t is the moment of inertia of the section and y_t is the depth to the centroid of the section from the extreme tension face.

Crack widths can be estimated using Equation 2.2 (ACI Committee 440 2006) or 2.3 (ISIS Canada 2007); reinforcement stress at a given value of applied moment can be estimated using Equation 2.4 (ISIS Canada 2007). Equation 2.2 is based on a physically derived model (Frosch 2009) that takes into account the mechanical and bond properties of the reinforcement, as well as the concrete cover and transverse spacing of longitudinal reinforcement. The bond coefficient, k_b, is used to account for the effect of the bond-slip characteristics of the type of reinforcement used.

Eq. 2.2 $$w = 2\frac{f_{frp}}{E_{frp}}\beta k_b\sqrt{\left(d_c^2 + (\frac{s}{2})^2\right)}$$

Eq. 2.3 $$w = 2.2k_b\frac{f_{frp}}{E_{frp}}\frac{h_2}{h_1}(d_cA)^{1/3}$$

Eq. 2.4 $$f_{frp} = \frac{M_s}{A_{frp}jd}$$

Where, w is the width of the crack at the tension face of the member, f_{frp} is the stress in the FRP reinforcement, E_{frp} and A_{frp} are the modulus of elasticity and cross-sectional area of the FRP reinforcement, respectively, h_1 and h_2 are the distance from the neutral axis to the centre of the FRP reinforcement and the distance from the neutral axis to the extreme tension fibre, respectively, β is the ratio of h_2 to h_1, k_b is a bond-dependent coefficient, d_c is the thickness of the concrete cover, s is the bar spacing, A is the effective tension area of concrete surrounding the tension reinforcement, M_s is the service load moment and jd is the length of the internal lever arm.

Load-deflection plots for FRP-RC members tend to be bilinear, with a significant reduction in flexural stiffness after cracking (Figure 2.2). The post-cracking flexural stiffness is governed by

the axial stiffness of the longitudinal reinforcement; El-Salakawy & Benmokrane (2004) noted that slabs reinforced with FRP bars having an axial stiffness ($E_{frp}A_{frp}$) close to that of the control slabs (E_sA_s) had very similar deflection behaviour prior to yielding of the steel reinforcement. Increasing the reinforcement ratio decreased crack spacing, crack width and crack penetration depth at service. In all cases the crack widths at service were well below the limit of 0.5 mm for exterior exposure.

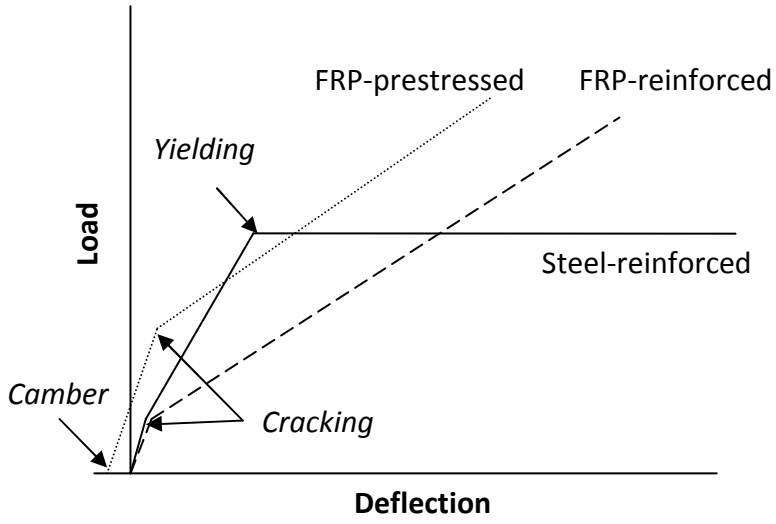

Figure 2.2 - Typical load-deflection response for reinforced and prestressed concrete members

A cracked member behaves as a member with a variable cross-section—the curvature at any given section depends on the bending moment and the cross-section properties. For instance, the curvature at a cracked section is much greater than at an uncracked section with similar internal forces. Between cracks, the concrete in tension contributes to the flexural stiffness and reduces the curvature of the section. Deflections of a cracked RC member are often calculated based on the assumption that a uniform effective moment of inertia can be

substituted for an actual variable moment of inertia (Razaqpur et al. 2000). However it is not possible to find a unique expression for an effective moment of inertia that is accurate for all beam loading and supporting conditions. As noted by Ghali (1993), the use of an empirical equation for an effective moment of inertia will be accurate for a particular moment diagram (load distribution) and will introduce errors for others. However this method is commonly accepted because of its simplicity and errors tend to be acceptably small.

The load-deflection response of a cracked RC member is traditionally estimated with the well-known Branson equation for the effective moment of inertia which was calibrated for steel-RC members (Equation 2.5). Bischoff (2005, 2007a, 2007b) noted that the Branson equation overestimated tension stiffening for high I_g/I_{cr} ratios which arise due to the low axial stiffness of FRP reinforcement; a modified form of the Branson equation for the effective moment of inertia has been adopted by ACI Committee 440 (2006) as given by Equation 2.6:

Eq. 2.5 $$I_e = I_{cr} + \left(I_g - I_{cr}\right)[\frac{M_{cr}}{M_a}]^3 \leq I_g$$

Eq. 2.6 $$I_e = (\frac{M_{cr}}{M_a})^3 \beta_d I_g + [1 - (\frac{M_{cr}}{M_a})^3] I_{cr} \leq I_g$$

Where, I_e, I_{cr} and I_g are the effective, cracked and gross moments of inertia, respectively, M_{cr} and M_a are the cracking and applied moments, respectively, and β_d is a modification factor to account for the reduced stiffness of the FRP reinforcement.

Due to the sharp increase in curvature after cracking, tension stiffening is relatively insignificant in FRP-RC beams. Therefore Razaqpur et al. (2000) proposed that the post-cracking moment of inertia can be taken as I_{cr} for the full length of the beam with a correction factor to account for

uncracked regions near the supports. Applying this approach to a beam under four-point bending, the deflection of the beam at midspan can be calculated using Equations 2.7 and 2.8.

Eq. 2.7 $$\delta = \frac{PL^3}{24E_cI_{cr}}[3\left(\frac{a}{L}\right) - 4\left(\frac{a}{L}\right)^3 - 8\eta(\frac{L_g}{L})^3]$$

Eq. 2.8 $$\eta = 1 - \frac{I_{cr}}{I_g}$$

Where, δ is the midspan deflection, P is the applied load, L and a are the clear and shear spans, respectively, L_g is the uncracked length of the member near the supports and η is a correction factor relating I_{cr} and I_g.

Deflection equations can sometimes underestimate overall deformation as a result of neglecting the additional imposed deformation resulting from diagonal cracking, which may be significant in some cases (Imjai et al. 2009).

2.4.2 Bond

Bond between reinforcing bars and concrete is a critical parameter affecting the structural performance of RC members including ultimate capacity, tension stiffening and deflection, crack widths and crack spacing, and deformability (Aiello et al. 2007). The bond strength of FRP bars to concrete is highly variable and depends on a large number of factors, but is generally less than for steel bars with reported values between 40% and 100% of the bond strength of deformed steel bars (Okelo & Yuan 2005). Bond-slip characteristics of FRP bars in concrete depend on bar diameter, surface roughness and strength of concrete (Tastani et al. 2005). Other factors include concrete cover and bar spacing (Fico et al. 2008).

The bond stress of GFRP reinforcing bars depends on chemical adhesion and mechanical interlock before bond slip occurs, and friction after the bar begins to slip prior to failure (Benmokrane et al. 1996). Chemical adhesion breaks down quickly once load is applied resulting in slip of the loaded end of the bar (Cosenza et al. 1997, Achillides & Pilakoutas 2004). This slip engages mechanical interlocking and friction force transfer mechanisms. Sand-coated FRP bars have been reported to display relatively small slip values at the peak bond stress and have little contribution from mechanical interlocking (Cosenza et al. 1997). While debonding typically starts at flexural crack locations, increasing or repeated loading may cause the maximum bond stress to move further and further down the free end leading to progressive bond failure.

There are four possible modes of bond failure between FRP and concrete (CEB-FIP 2000). The first is the shearing off of part or all of the surface deformations or sand coating of the bar; bond strength in this case is governed by the interlaminar shear strength between successive layers of fibres or the shear strength of the surface deformations. Secondly, bond failure can occur by concrete shear failure; this is similar to the bond failure mode observed with steel bars. A third possible failure mode is a combined mode with damage occurring in both the concrete and reinforcement. Lastly, the bar can "squeeze through" the concrete due to low radial stiffness, with bond resistance provided by the friction induced by wedging action of the bar deformations on the surrounding concrete.

For concrete compressive strengths greater than 30 MPa, the bond strength of FRP bars is not significantly affected by concrete strength as failure is generally governed by the interlaminar

shear strength of the FRP bar surface. Bond failure commonly occurs by abrasion or peeling off of the exterior shell from the bar core (Achillides & Pilakoutas 2004, Katz 2000). Following pullout failures, white powder consisting of crushed resin and chopped glass fibres has been observed on the concrete at the location of embedment; the bars were scratched and tiny fibres could be seen on the surface of the bar. Failure appeared to develop at a critical resin-rich interface between successive layers of fibres (Achillides & Pilakoutas 2004, Davalos et al. 2008).

2.4.3 Flexure

Flexural design of FRP-RC members is based on strain compatibility and depends on whether failure is governed by rupture of the tensile reinforcement or concrete crushing. To determine the mode of failure, the reinforcement ratio is compared to the balanced reinforcement ratio, given by Equation 2.9:

Eq. 2.9 $$\rho_{frpb} = \alpha_1 \beta_1 \frac{\Phi_c}{\Phi_f} \frac{f'_c}{f_{frpu}} \left(\frac{\varepsilon_{cu}}{\varepsilon_{cu} + \varepsilon_{frpu}}\right)$$

Where, ρ_{frpb} is the balanced reinforcement ratio, α_1 and β_1 are concrete stress block parameters, f'_c and f_{frpu} are the concrete compressive strength and FRP ultimate tensile strength, respectively, and ε_{cu} and ε_{frpu} are the concrete crushing strain and FRP rupture strain, respectively.

When the actual reinforcement ratio is greater than the balanced reinforcement ratio, the section is said to be over-reinforced and flexural failure is induced by concrete crushing. Equilibrium of tensile and compressive forces in the section is obtained by assuming that the

compression zone can be approximated by a rectangular stress block using the parameters α_1 and β_1, and that all tensile stresses are carried by the FRP reinforcement alone. When the actual reinforcement ratio is less than the balanced reinforcement ratio, the section is said to be under-reinforced and failure occurs by rupture of the FRP reinforcement. The design procedure is similar to over-reinforced sections except that α_1 and β_1 are replaced by α and β, respectively, which are functions of both the concrete compressive strength and the strain in the concrete at failure. Equilibrium of compressive and tensile forces is obtained by iteration, beginning with an assumed value for the depth to neutral axis, *c*. Equilibrium conditions are given by Equations 2.10 and 2.11:

Eq. 2.10 $$T = C$$

Eq. 2.11 $$M_r = T\left(d - \frac{\beta_1 c}{2}\right)$$

Where, M_r is the moment resistance of the section, *T* and *C* are the resultant tension and compression forces in the section, respectively, *d* is the effective depth to the reinforcement, β_1 is a stress block parameter and *c* is the depth to the neutral axis.

2.4.4 Shear

Unlike the flexural behaviour of reinforced concrete, shear strength models are still open to discussion although they have been studied for over 100 years. The lack of full understanding of the shear behaviour of reinforced concrete is apparent in the fact that shear strengths for concrete members predicted by various current design codes can vary by factors greater than 2, while flexural strength predictions vary by less than 10% (Bentz et al. 2006). As stated by the

joint ASCE-ACI Committee 445 on Shear and Torsion (1998), the five mechanisms that resist applied shear are shear stresses in the uncracked concrete, aggregate interlock across the shear crack plane, dowel action of the longitudinal reinforcing bars, arch action (primarily in deep members) and residual tensile stresses transmitted across cracks. Due to the low stiffness of FRP bars, FRP-RC members will develop deeper and wider cracks than conventionally-reinforced members—deeper penetrating cracks reduce the contribution of uncracked concrete in the compression zone while wider cracks limit the contribution of aggregate interlock and residual stresses—and the dowel strength of FRP bars is negligible due to the longitudinal orientation of the fibres, resulting in significantly reduced shear capacities of FRP-RC members without shear reinforcement (El-Sayed et al. 2005). Michaluk et al. (1998) estimated the dowel strength of GFRP reinforcement to be in the range of 7.5% to 13.8% of their ultimate tensile strength.

Studies on the effect of longitudinal reinforcement ratio on shear strength have yielded controversial results. Yost et al. (2001) reported that there was no significant relationship between the longitudinal reinforcement ratio and shear strength of GFRP-RC beams. On the other hand, several researchers (Alkhrdaji et al. 2001, El-Sayed et al. 2005, 2006, Lubell et al. 2009, Alam & Hussein 2011) found that increasing the amount of longitudinal reinforcement significantly increased the shear strength of GFRP-RC beams and slabs as the added stiffness reduced crack penetration depth and width, thus improving the effectiveness of shear transfer mechanisms while also increasing the dowel capacity of the reinforcement.

While FRP and steel-RC members exhibit fundamentally similar shear behaviour (Hoult et al. 2008), there is clearly a correlation between the axial stiffness of the reinforcement and the member's shear capacity. Due to the difference in material properties between steel and FRP, and specifically in the modulus of elasticity, design equations for the concrete contribution to shear strength in steel-RC members cannot be directly applied to FRP-RC specimens—doing so results in highly unconservative results.

Tureyen & Frosch (2002, 2003) developed a shear model for slender flexural members without transverse reinforcement having a span-to-depth ratio greater than 2.5. This model was developed based on the concept of an effective reinforcement ratio which is essentially the actual reinforcement ratio multiplied by the modular ratio of the reinforcement compared with steel. In this way, the shear capacities of steel-RC and FRP-RC members could be directly compared. Normalized shear strengths of concrete beams with steel and FRP reinforcement were plotted against their effective reinforcement ratio and were found to follow the same trend line, indicating that a unified calculation method was possible. The model was initially developed using imperial units but is given by Equation 2.12 for SI units:

Eq. 2.12 $$V_c = 0.42\sqrt{f'_c}\,bc$$

Where, V_c is the concrete contribution to shear resistance, f'_c is the concrete compressive strength, *b* is the width of the beam and *c* is the depth to the neutral axis.

This model was compared with test data from 370 test specimens with an average experimental-to-predicted strength ratio of 1.18, and a range of 0.88-1.72. El-Sayed et al.

(2005, 2006) found that the model given by Equation 2.12 was conservative for both slabs and beams with ratios of experimental-to-predicted shear strengths of 1.85 and 1.75, respectively. The Tureyen & Frosch model has since been adopted for use by ACI Committee 440 (2006) as well as the AASHTO LRFD Bridge Design Guide Specifications for GFRP-Reinforced Concrete Bridge Decks and Traffic Railings (2009).

The CHBDC (CSA 2010) provisions for the shear strength of FRP-RC members are based on the simplified modified compression field theory (Bentz et al. 2006) as given by Equations 2.13 through 2.16. The modified compression field theory (Vecchio & Collins 1986) is a theoretically derived model for determining the response of RC elements subjected to in-plane shear and axial stresses requiring the simultaneous solution of 15 nonlinear equations. This approach treats the cracked concrete as a new material with its own stress-strain characteristics and assumes that the critical crack direction is normal to the principal tensile strain direction. In order to make this approach practical for design, a number of simplifying assumptions were introduced to reduce the number of equations, including the assumption that the shear strength of members without stirrups is controlled by aggregate interlock. Aggregate interlock is highly dependent on the width of a shear crack and is thus influenced by the crack spacing (size effect) and axial stiffness of the reinforcement (strain effect). Both the size effect and strain effect are accounted for in the determination of β, given by Equation 2.14.

Eq. 2.13 $$V_c = 2.5\beta\phi_c f_{cr} b d_v$$

Eq. 2.14 $$\beta = \left(\frac{0.4}{1+1500\varepsilon_x}\right)\left(\frac{1300}{1000+s_{ze}}\right)$$

Eq. 2.15 $$\varepsilon_x = \frac{\frac{M_f}{d_v} + V_f}{2E_{frp}A_{frp}} \leq 0.003$$

Eq. 2.16 $$s_{ze} = \frac{35s_z}{15 + a_g} \geq 0.85s_z$$

Where, β is a factor used to account for the shear strength of cracked concrete, ϕ_c is the material resistance factor for concrete, f_{cr} is the cracking strength of concrete, d_v is the effective shear depth of the section, ε_x is the strain in the section at mid-depth, s_{ze} and s_z are crack spacing parameters, M_f and V_f are the factored moment and shear at the critical section, respectively, E_{frp} and A_{frp} are the modulus of elasticity and cross-sectional area of the FRP reinforcement, respectively, and a_g is the nominal size of the coarse aggregate. All other terms are as described previously.

Hoult et al. (2008) suggested that due to the increased strains likely to occur in FRP-RC members, a second order diagonal crack width approximation to the modified compression field theory provides greater accuracy. The following modified expression for β was proposed:

Eq. 2.17 $$\beta = \left(\frac{0.3}{0.5 + (1000\varepsilon_x + 0.15)^{0.7}}\right)\left(\frac{1300}{1000 + s_{ze}}\right)$$

2.5 FRP-Prestressed Concrete Members

As with reinforced concrete, corrosion of steel prestressing strands has become a growing concern in recent years and non-corrosive alternatives to steel such as FRPs have been extensively researched for prestressing applications. CFRP in particular is ideal for prestressing because of its very high strength and low relaxation and has been used successfully in

prestressed concrete bridges and parking structures (Abdelrahman et al. 1995, Fam et al. 1997, Amato 2009).

Post-tensioning is advantageous in that prestressing can be done on site for either cast-in-place or precast members. In addition, parabolic or other longitudinal profiles can be easily constructed for post-tensioning tendons and the tendons can be either bonded or unbonded. Prestressing losses are often lower than for pretensioned members due to reduced creep, shrinkage and elastic shortening as a result of higher concrete strength at the time of stressing.

In the past, post-tensioning of FRP tendons has been difficult due to a lack of effective anchorage systems. Unlike steel, FRP bars have a very low transverse strength perpendicular to the orientation of the fibres; gripping the bar places high lateral stresses on the bar which can damage the fibres and cause premature rupture. During fatigue testing of CFRP post-tensioned beams, Braimah et al. (2006) found that all but one tendon failed before reaching 2 million cycles, with failure usually initiating at the tendon-anchor junction.

Recently a new type of split-wedge anchor system for prestressing CFRP tendons has been developed at the University of Waterloo capable of carrying the full tensile capacity of the bars (Al-Mayah et al. 2006, 2007). These anchors are suitable for prestressed concrete applications due to their compactness, ease of use and reusability. The three-part anchor is shown in Figure 2.3; components include an exterior barrel, a three-piece wedge grip and a copper sleeve which is deformable and helps protect the fibres from damage. This system reduces stress concentrations through a circular profile along the contact surface of the wedges and barrel along the length of the anchor. Results from fatigue tests using these anchors revealed that all

specimens failed due to fracture of the CFRP bar with no indication of premature failure at the anchorage zone (Elrefai et al. 2007).

Figure 2.3 - CFRP split wedge anchor system

Similarly to reinforced concrete, guidelines have been developed specifically for use with FRP-PC members (ACI Committee 440 2004, ISIS Canada 2008). These guidelines reflect the properties of FRP prestressing strands including their lower stiffness compared to steel, linear-elastic behaviour, and in the case of GFRP, the risk of creep rupture. Stress limitations for CFRP and GFRP prestressing tendons as specified by the CHBDC (CSA 2010) are given in Table 2.3.

Table 2.3 - Allowable stresses in FRP prestressing tendons

Tendon type	At jacking	At transfer
CFRP	$0.70f_{frpu}$	$0.65f_{frpu}$
GFRP	$0.30f_{frpu}$	$0.25f_{frpu}$

Partial prestressing can be used to improve the deformability of concrete beams and reduce the cost compared with fully prestressed members (Abdelrahman & Rizkalla 1999). Partial

prestressing can be achieved either by adding non-prestressed reinforcement or by lowering the jacking stresses.

2.5.1 Flexure

Cracking moments of prestressed concrete members are governed by the initial prestress force and are not significantly affected by tendon type, bond or prestressing reinforcement ratio (Kato & Hayashida 1993). Post-cracking behaviour, however, is significantly affected by these factors. The flexural response of concrete beams partially prestressed by CFRP tendons was investigated by Abdelrahman & Rizkalla (1997). The load-deflection response was bilinear with a reduced stiffness after cracking, and the deflection of the beams at failure was similar to the steel-prestressed control beams when failure occurred by concrete crushing. When failure initiated by CFRP rupture, however, deflections at ultimate were considerably smaller than for the control beams. In addition, crack widths and crack spacing were larger at similar loads when compared to the control beams indicating lower flexural bond strength. Fam et al. (1997) also noted that the post-cracking stiffness of beams prestressed with CFRP was similar to beams prestressed with steel up to yielding of the steel strands.

The design of FRP-PC members for serviceability and moment resistance is similar to that of FRP-RC members except that the initial force in the concrete and tendons should be accounted for. Rupture of the FRP prestressing strands is permissible by the CHBDC (CSA 2010) as long as supplementary reinforcement is provided to carry the unfactored dead loads or alternative load paths exist such that failure of the member does not lead to the catastrophic collapse of the entire structure. The available strain capacity in the tendon after prestressing is the ultimate

tensile strain capacity of the bar less the effective prestressing strain, decompression strain and the strain due to sustained loads. Assuming the decompression strain and the strain resulting from sustained loads are negligible, the simplified expression for the balanced reinforcement ratio is given by Equation 2.18:

Eq. 2.18 $$\rho_{frpb} = \alpha_1 \beta_1 \frac{\phi_c f'_c}{\phi_{frp} f_{frpu}} \left(\frac{\varepsilon_{cu}}{\varepsilon_{cu} + \varepsilon_{frpu} - \varepsilon_{pe}}\right)$$

Where, ε_{pe} is the effective prestrain in the tendons and all other terms are as noted previously.

When the actual reinforcement ratio exceeds the balanced reinforcement ratio, failure initiates by concrete crushing. Since the stress in the FRP tendons is not known, an iterative process may be used beginning with an initial estimate of the depth of the neutral axis. Applying conditions of strain compatibility and assuming concrete crushes at a strain of 0.0035, the strain (and therefore stress) in the prestressing strands can be calculated. The calculated strain is added to the effective prestressing strain to give the total strain in the bar. This procedure is repeated until equilibrium is reached.

When the actual reinforcement ratio is less than the balanced reinforcement ratio, rupture of the tendons precedes concrete crushing. The design approach is similar to over-reinforced sections except that the stress in the tendons is known while the concrete compressive strain is unknown. The iterative procedure involves varying the assumed depth to the neutral axis and the corresponding rectangular concrete compression block parameters α and β, until equilibrium of forces is reached. When multiple layers of FRP reinforcement are provided, the strain in the outermost layer is the critical strain since it will be the first to reach rupture strain.

As with reinforced concrete, failure by rupture of FRP prestressing strands generally occurs suddenly with little warning. Providing non-prestressed reinforcement in addition to the prestressing strands can prevent sudden failure of the beam after rupture of the prestressing strands. Since FRP materials do not undergo plastic deformation, high levels of ductility (which is a measure of the energy absorbed by the flexural member) are difficult to obtain. Some methods which have been proposed to increase the ductility of FRP-PC members are confining the concrete in the compression zone, adding non-prestressed reinforcement or using partial bonding (ACI Committee 440 2004, ISIS Canada 2008). Failure by concrete crushing occurs more gradually and can result in greater ductility than tension-controlled failures (Grace & Sayed 1998, Grace & Singh 2003).

Deformability, on the other hand, is the ratio of deflection at ultimate to deflection at cracking or at service. Deformability is commonly used as a measure of the safety of FRP-RC and PC members since high deformability provides visual warning of failure. A deformability index was developed by Dolan & Burke (1996) using the curvatures at ultimate and at service which has since been adopted by ISIS Canada (2008) and ACI Committee 440 (2004) as given by Equation 2.19. An overall performance factor combining strength and deformability is used by the CHBDC (CSA 2010), given by Equation 2.20 for rectangular sections.

Eq. 2.19 $$\theta = \frac{(d-kd)\varepsilon_{frpu}}{(d-\frac{a}{\beta_1})\varepsilon_{frps}}$$

Eq. 2.20 $$J = \frac{M_{ult}\psi_{ult}}{M_c\psi_c} \geq 4.0$$

Where, θ and *J* are a deformability index and overall performance factor, respectively, *d* and *kd* are the effective depth and depth to neutral axis, respectively, ε_{frpu} and ε_{frps} are the strains in the FRP reinforcement at ultimate and service states, respectively, *a* is the depth of the equivalent stress block, β_1 is the stress block reduction factor for concrete, M_{ult} and M_c are the applied moment at ultimate and at a service state, respectively, and ψ_{ult} and ψ_c are the curvatures at ultimate and at a service state, respectively. The service state for Equation 2.20 is taken as the load causing a maximum compressive concrete strain of 0.001.

2.5.2 Shear

Prestressing can be a very effective way of increasing the shear strength of concrete beams with FRP reinforcement by reducing or eliminating cracking of the concrete. Yonekura et al. (1993) studied the flexural and shear behaviour of post-tensioned concrete beams with CFRP tendons; beams without any prestressing failed in shear, although both strength and stiffness were increased by increasing the prestressing force. The additional stiffness provided as a result of prestressing significantly increased the shear capacities of the beams and with sufficient prestressing force a flexural mode of failure was induced.

Park & Naaman (1999a) found that CFRP-PC beams had a lower shear capacity than similar steel-PC beams due to their lower post-cracking stiffness which resulted in wider shear cracks at ultimate. In another study, Park & Naaman (1999b) investigated the dowel behaviour of CFRP tendons under tension. While the dowel resistance of steel reinforcement is generally non-critical in conventionally-reinforced or prestressed members due to yielding of the longitudinal steel, FRP bars may rupture prematurely due to transverse shear stresses. The

ultimate dowel force and shear displacement of the CFRP tendons decreased with increasing tension ratio in the tendons. The CFRP tendons were found to have just 40-50% of the dowel resistance of steel bars, with approximately 15% of the ultimate displacement. When the shear plane was inclined, the shear strength was reduced by almost 40%.

Several important parameters influence the shear capacity of prestressed concrete members; among them are the reinforcement ratio and prestressing force. Axial tension decreases the shear capacity, while axial compression increases it (Vecchio & Collins 1986, ASCE-ACI Committee 445 1998). However, it is not well known just how much shear capacity is influenced by axial load. Saqan & Frosch (2009) constructed 9 large scale beams to investigate the influence of prestressing and mild reinforcement on the shear behaviour of concrete members. Each beam had the same prestressing force but contained varying amounts of prestressing and mild reinforcement. According to the ACI 318-08 (2008) design model, these beams should all have the same shear capacity; however the addition of mild reinforcement was found to increase the shear cracking strength while the addition of prestressing steel increased both the flexural stiffness and ultimate shear strength.

As with reinforced concrete, several design models exist for the concrete contribution to shear strength in FRP-prestressed members. ISIS Canada (2008) and the CHBDC (CSA 2010) have adopted the simplified modified compression field theory given by Equation 2.13 (Bentz et al. 2006); the effect of the level of prestressing force in the member is accounted for in the calculation of the mid-depth strain in the member, ε_x, given by Equation 2.21. Meanwhile, ACI Committee 440 (2004) uses Equation 2.22 to determine the shear capacity of FRP-prestressed

flexural members, which ignores the effect of prestressing force on the concrete contribution to shear resistance.

Eq. 2.21 $$\varepsilon_x = \frac{\frac{M_f}{d_v} + V_f - V_{p,frp} + 0.5N_f - A_{frp}f_{po}}{2(E_S A_S + E_{frp}A_{frp})} \leq 0.003$$

Eq. 2.22 $$V_c = 0.17\sqrt{f'_c}bd$$

Where, $V_{p,frp}$ is the vertical component of the prestressing force in draped tendons, N_f is the factored axial force in the member, f_{po} is the stress in the prestressed reinforcement when the stress in the surrounding concrete is zero and d is the effective depth of the reinforcement. All other terms are as previously noted.

Wolf & Frosch (2007) compared the test results from a database of 86 steel-PC members to the predicted shear strengths using the unified model developed by Tureyen & Frosch (2003), given by Equation 2.12. They found good correlation between the experimental results and analytical predictions, thus verifying that the Tureyen & Frosch model is also applicable to prestressed flexural members.

2.5.3 Unbonded Tendons

Most reinforced and prestressed concrete members generally rely on fully bonded reinforcement for the transfer of loads. For conventionally reinforced structures, this is useful to protect against corrosion and to take advantage of the large strain capacity of steel. FRP materials, however, do not yield and thus have a limited strain capacity. Burgoyne (1993) proposed that prestressed FRP reinforcement should not be bonded to concrete to eliminate

the effect of local strain increases at crack locations; essentially this means that while the concrete can have large strains at a few crack locations, the tendon has relatively low strain along its entire length (Lees & Burgoyne 1999). This is a particularly efficient alternative for prestressing applications as most of the strain capacity of the reinforcement is absorbed before the member is placed in service. Leaving FRP tendons unbonded also introduces savings in construction costs associated with grouting, facilitates the replacement of tendons in the case of strength inadequacy or future increases in design loads, and results in an increased deformability to provide sufficient warning of failure (Braimah et al. 2006). Grace & Singh (2003) noted that higher levels of unbonded prestressing force resulted in higher energy ratios, referring to the ratio of inelastic energy absorbed to the total energy of the beam, and hence greater ductility.

Since the strain, and therefore stress, in an unbonded tendon are lower than in a bonded tendon, the moment capacity of the beam is reduced with the final failure often caused by concrete crushing at the location of a crack (Lees & Burgoyne 1999). Maissen & De Smet (1995) found that post-tensioned T-beams with unbonded CFRP tendons exhibited considerably fewer cracks than similar beams with bonded tendons. Rotations were concentrated at the crack locations resulting in local increases in concrete compression and premature failure of the beam by concrete crushing. As a result, the full capacity of the CFRP strands was not reached.

As noted by Kordina et al. (1989), the behaviour of beams prestressed with unbonded tendons is most appropriately modelled using a tied arch or A-frame analogy. Despite this, existing equations based on the truss analogy were found to predict the load capacities well (better

than using a tied arch model). Ranasinghe et al. (2002) reported a 90% increase in shear capacity in an unbonded reinforced concrete beam compared to a fully bonded beam due to the development of arch action. The unbonded prestressed concrete beam reached a flexural mode of failure corresponding to a load capacity increase of 82% compared to the fully bonded beam which failed in shear. Unbonded beams, however, displayed a noticeable reduction in stiffness and lower flexural cracking loads compared to bonded specimens.

Evaluating the stresses in unbonded prestressing tendons is complicated by the fact that a strain compatibility approach is not applicable since the strain increase in unbonded tendons is member-dependent rather than section-dependent. The stress in an unbonded tendon depends on the deformation of the entire member and is generally assumed to be uniform throughout its length. Strain reduction coefficients can be used in a modified strain compatibility analysis to simplify the calculations (Naaman & Alkhairi 1991a, 1991b, Naaman et al. 2002). The stress in the unbonded tendon at ultimate, f_p, is given by Equation 2.23 (ISIS Canada 2008, ACI Committee 440 2004):

Eq. 2.23 $$f_p = f_{pe} + \Omega_u E_p \varepsilon_{cu}\left(\frac{d_p}{c_u} - 1\right) \leq 0.8 f_{frpu}$$

Where, f_p and f_{pe} are the stress at ultimate and effective prestress in the FRP tendon, respectively, Ω_u is a strain reduction coefficient, E_p is the modulus of elasticity of the prestressing tendon, ε_{cu} is the crushing strain of the concrete, d_p is the effective depth to the tendon, c_u is the depth to neutral axis at failure and f_{frpu} is the ultimate tensile strength of the FRP tendon.

2.6 FRP Shear Reinforcement

Shear reinforcement is often provided in reinforced and prestressed concrete in the form of steel stirrups. Stirrups are generally the outermost reinforcement in concrete members and therefore have a reduced concrete cover making them more susceptible to deterioration caused by corrosion. FRP stirrups, on the other hand, are resistant to corrosion but require special attention in the design of the bent portion.

The longitudinal orientation of individual fibres within FRP rods results in high uniaxial tensile strengths but very little resistance to transverse loading. A number of studies have reported a significant reduction in the tensile strength of bent FRP bars and stirrups at the location of the bend (Maruyama et al. 1993, Ehsani et al. 1993, Ishihara et al. 1997). Bend strength generally decreases with decreasing bend radius and can be as low as 35% of the tensile capacity of straight portions of the bar (Shehata et al. 2000). Morphy et al. (1997) recommended limiting the strength of CFRP stirrups to 50% of the ultimate straight bar capacity for design. Factors influencing bend capacity include the method of bending, radius of the bend, type of fibres and diameter of the bar (El-Sayed et al. 2007).

Ehsani et al. (1995) studied the effects of various parameters on the bond of hooked GFRP reinforcing bars embedded in concrete by conducting a series of pullout tests. When the ratio of bend radius to bar diameter was negligible, the bars failed in shear at the bend location under very low load. Increasing the bend radius to three times the bar diameter resulted in splitting of the concrete or fracture of the bar outside of the specimen, depending on the concrete cover and embedment length. Increasing the concrete compressive strength was

effective in increasing the initial stiffness and tensile stress in the bar while reducing slip. Similarly, increasing the bend radius increased both load capacity and initial stiffness. Morphy et al. (1997) have suggested that the bend radius be no less than 50 mm.

El-Sayed et al. (2007) reported that increasing the embedment length of CFRP stirrups from 5 to 20 times the bar diameter doubled the capacity of the stirrups, and at 20 times the bar diameter the full tensile strength of the longitudinal bar was reached. Similarly, increasing the tail length increased the stirrup capacity, and the authors suggested that a minimum tail length of 6 times the bar diameter should be provided. Ehsani et al. (1995) suggested using a tail length and development length of 12 and 16 times the bar diameter, respectively.

Ahmed et al. (2008) conducted a performance evaluation of beams containing CFRP stirrups for shear reinforcement. Although the stirrups ruptured at the bend location before reaching their full tensile capacity, they carried a higher load than similar steel stirrups which yielded, followed by concrete crushing. Even though the stiffness of CFRP is lower than steel, lower shear crack widths were observed at all stages of loading, which may be a result of improved bond characteristics. Serviceability limits including crack widths of less than 0.5 mm and stirrup strains less than 2500 $\mu\varepsilon$ (CSA 2006) were met, and the authors found the limit on the strain in the stirrups to be very conservative.

The capacity of FRP stirrups is given in the CHBDC as the smaller of Equations 2.24 and 2.25. The contribution to shear resistance provided by vertical FRP stirrups is given by Equation 2.26 (CSA 2010):

Eq. 2.24 $$\sigma_v = \frac{\left(0.05\frac{r}{d_s}+0.3\right)f_{FRPbend}}{1.5}$$

Eq. 2.25 $$\sigma_v = E_{vFRP}\varepsilon_v = 0.004E_{vFRP}$$

Eq. 2.26 $$V_{frp} = \frac{\phi_{frp}A_v\sigma_v d_{long}cot\theta}{s}$$

Where, σ_v is the tensile capacity of bent FRP stirrups, *r* is the radius of the bend, d_s and A_v are the diameter and cross-sectional area of the stirrup, respectively, $f_{FRPbend}$ is the tensile capacity of the straight portin of the FRP stirrup, E_{vFRP} and ε_v are the modulus of elasticity of the FRP stirrup and strain in the stirrup, respectively, V_{frp} is the contribution to shear resistance of the FRP stirrup, ϕ_{frp} is the material resistance factor of the FRP, d_{long} is the effective shear depth of the longitudinal reinforcement, θ is the angle of the shear crack and *s* is the stirrup spacing.

While the use of FRP stirrups is an attractive alternative to conventional steel stirrups for many applications, the use of any type of closed stirrup is generally undesirable for slab bridges. Another approach for introducing FRP shear reinforcement which is more conducive to slab applications from a constructability standpoint is through the use of straight shear bars. These can either be placed vertically or inclined to increase their embedment length and to efficiently intercept diagonal shear cracks. Stirrups lacking end anchorages can make a significant contribution to the shear capacity of reinforced concrete sections despite relying solely on the bond stress developed along the length of the bar (Varney et al. 2011). Regan & Kennedy-Reid (2004) observed that removing 65-75% of stirrup anchorages resulted in a reduction in shear capacity of only 14-33%. Steel stirrups without end anchorages reached their yield stress, and the ultimate shear capacities were well above theoretical predictions.

Shear bars can be easily inserted into the reinforcing cage prior to casting, reducing construction time and labour costs. Stress development at an inclined crack is limited by the lesser of the development lengths above and below the crack and by the bond strength of the reinforcement (Regan & Kennedy-Reid 2004). Due to the small embedment length available in slabs, the majority of studies on the effectiveness of straight or inclined shear bars have generally been limited to deep beams, wall beams, corbels or dapped-end beams (Kong et al. 1972, Zielinski & Rigotti 1995, Teng et al. 2000, Tan et al. 2004, Yang et al. 2007). However, the use of CFRP shear reinforcing bars was found to be an attractive alternative to closed stirrups in RC beams with a height of only 250 mm, reducing the time associated with fabricating and placing the transverse shear reinforcement (Kobraei et al. 2011). In general, inclined shear bars were found to be more effective in resisting diagonal splitting stresses, reducing crack widths and deflections and resisting fatigue loading.

Assuming a uniform bond stress distribution introduces a negligible error when the bonded length is small (Aiello et al. 2007). For a uniform bond stress distribution, the shear contribution of vertical FRP shear bars is given by Equation 2.26, with σ_v taken as the smaller of Equations 2.25 and 2.27. The shear contribution of inclined FRP shear bars is given by Equation 2.28:

Eq. 2.27 $$\sigma_v = \frac{\ell_e}{\ell_d} f_{frpu}$$

Eq. 2.28 $$V_{frp} = \frac{\phi_{frp} A_v \sigma_v d_{long} (cot\theta + cot\alpha) sin\alpha}{s}$$

Where, ℓ_e and ℓ_d are the available embedment length and development length of the FRP bar, respectively, and α is the angle of inclination of the shear bar. All other symbols are as noted previously.

With the recent development of straight FRP bars with headed anchorages, straight bars as shear reinforcement are an increasingly viable alternative to bent stirrups since force transfer is ensured by mechanical bearing rather than by bond stresses alone. Double-headed GFRP bars as shear reinforcement have compared favourably with bent stirrups in experimental studies (Johnson & Sheikh 2012).

2.7 Fatigue

Fatigue behaviour is an important limit state that must be considered by designers of concrete bridge decks, parking garages and other structures subjected to cyclic loading (Demers 1998a, Adimi et al 2000). A single lane of a Class A highway bridge experiences an average daily truck traffic of over 1000, or 27 million trucks over a 75 year design life (CSA 2010). Bridge deck slabs directly sustain these repeated moving wheel loads and may be susceptible to fatigue damage (El-Ragaby et al. 2007a). Fatigue life and fatigue strength of reinforced concrete elements are influenced by many factors including the material properties of the concrete and reinforcement, reinforcement ratio, transverse reinforcement, minimum and maximum values of repeated loading, range and rate of loading as well as environmental factors such as temperature and humidity (Chang & Kesler 1958). The response of a member subjected to fatigue loading is affected by both the strength of the materials and the interaction between the concrete and reinforcement (El-Ragaby et al. 2007b, Higgins et al. 2006). It is generally

agreed that the most important factor influencing fatigue behaviour is the applied load range, or rather the induced stress range in each component (ACI 215R-74 1997).

2.7.1 FRP

Fatigue of composite materials has been studied for many decades, although the majority of the work done has focused on aerospace, marine and transportation applications and is not generally applicable to the construction field. Only a limited number of studies are available on the fatigue behaviour of FRP reinforcement in concrete structures for civil engineering applications. In particular, there are significant differences in the magnitude of the deformations involved and the environment in which the materials are used (Adimi et al. 2000). There is also a difference in the composition and fabrication process of the composites in many cases, as FRP reinforcing bars are generally produced by pultrusion as opposed to laminates or moulded shapes. Nevertheless, there is something to be gained by reviewing the previous literature on the fatigue of FRP composites, as some of the general findings are transferable and provide a basis for further study.

2.7.1.1 General

The fatigue behaviour of FRP depends on many parameters, including the fibre and resin types comprising the composite as well as the configuration and geometry of the test specimens (Konur & Matthews 1989). Unlike metals, for which inelastic deformations are a manifestation of crystallographic slip, degradation of polymeric composites occurs in the form of localized microcracking leading to progressive debonding of the fibres and resin and can begin at relatively low loads (Carlson & Kardomateas 1996).

FRP composites are inherently heterogeneous and their fatigue failure mechanisms contrast those typically observed in metals. The fatigue failure sequence for homogeneous metals consists of initial crack nucleation and subsequent propagation in a single mode, whereas FRP materials can display a variety of failure modes including matrix cracking, fibre-matrix debonding, void growth and finally fibre rupture (El-Ragaby et al. 2007, Kim & Ebert 1978). Fatigue in metals is generally governed by fracture mechanics and demonstrates a stable crack growth rate until a critical crack length is reached leading to unstable crack growth and fracture. For inhomogeneous materials, fatigue failures are generally the result of damage accumulation rather than damage propagation (Reifsnider 1991). Damage mechanisms can be either progressive, such as matrix and interfacial damage, or non-progressive, such as fibre damage.

The predominant mechanisms leading to failure depend on the range of applied strain, dividing typical FRP fatigue life curves—commonly referred to as S-N curves—into 3 distinct stages as seen in Figure 2.4 (Talreja 1981a, Brondsted et al. 1997). At high strain values failure is dominated by fibre breakage and interfacial debonding; the S-N curve is nearly horizontal for this stage in a log-log diagram and the number of cycles to failure depends on the statistical strength distribution of the individual fibres. The horizontal fibre breakage band represents a non-progressive failure damage mode with fibre breaks occurring randomly. As the number of broken fibres increases, the probability of finding a cross-section with a stress high enough to break the remaining fibres also increases, and final failure may extend over more than one cross-section as individual fibre ruptures are joined by longitudinal matrix cracks. The second stage is more representative of classical fatigue behaviour where the S-N curve can be

described by a power law function. This inclined zone is dominated by progressive matrix cracking and interfacial shear failures. In this zone, damage accumulation is cycle dependent while the rate of damage accumulation is strain dependent. Finally, in the third stage, the slope tends to flatten out again at low stress levels; below a certain strain level, no propagating cracks are initiated in the matrix constituting a fatigue limit. For low stiffness composites, such as GFRP, this strain limit is usually much less than the strain capacity of the composite.

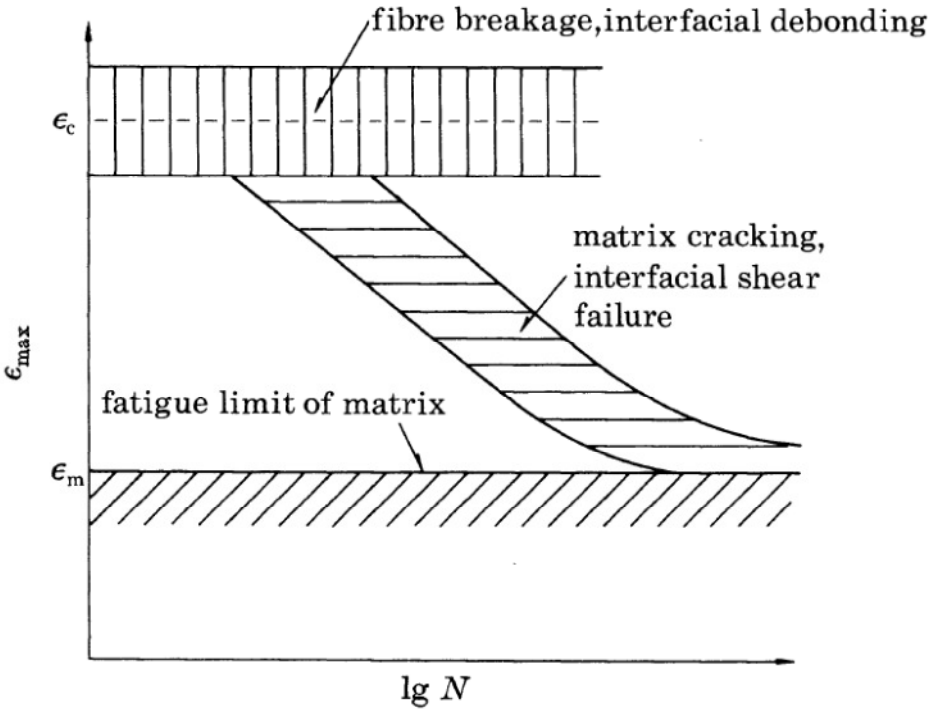

Figure 2.4 - Fatigue life diagram for unidirectional composites (Talreja 1981a)

For low modulus, high failure strain E-glass composites, all of the fatigue data may fit within the intermediate sloped progressive damage mechanisms band. Conversely, for high modulus, low failure strain CFRP, only the horizontal catastrophic damage band may be observed. The composite fatigue strain limit is a matrix-dominated property (Konur & Matthews 1989);

minimum fatigue strain limits (the strain below which the rate of matrix crack propagation becomes negligible) for matrix cracking and longitudinal splitting have been reported as 0.006 and 0.001, respectively, for epoxy matrix unidirectional composites (Talreja 1981a).

The first stage of deterioration by fatigue is the formation of "damage zones" containing microscopic cracks, fibre-matrix interface failures and pullout of fibres from the matrix. These begin very early in the fatigue process, usually in the first few cycles, and are characterized by a sharp initial decline in stiffness. The second stage is generally characterized by a very gradual deterioration and stiffness reduction, followed by a third stage of fibre fracture and unstable damage accumulation leading to failure (Van Paepegem & Degrieck 2002b).

The fatigue failure mechanism of FRP composites involves several steps. Fatigue damage is generally initiated by local stress concentrations arising from micro defects in the material. The high level of anisotropy in FRP materials creates local triaxial stress states within the composite during uniaxial loading due to differences in Poisson's ratio and elastic modulus values between the fibres and matrix (Kim & Ebert 1978). Weak fibres may fail early in the test resulting in stress concentrations at the broken fibre ends at the fibre/matrix interface. Shear strains are induced in the adjacent matrix causing cracks to grow through the resin parallel to the fibres. The debonded length depends on the shear strength of the interface and is usually on the order of a few fibre diameters. These matrix and interface cracks prevent the redistribution of load to other fibres as the damage progresses leading to more fibre breaks, further matrix and interface damage and eventually to ultimate rupture of the composite. The fatigue sensitivity of unidirectional composite materials depends on the susceptibility of the material to the

initiation and growth of longitudinal splits; interface bond is often the limiting factor in the mechanical properties of FRP materials. Even at low stress amplitudes debonding will often eventually occur (Dew-Hughes & Way 1973, Talreja 1981a, Curtis 1989, 1991, Dittenber & Hota 2010).

The stochastic nature of fatigue in composite materials has been widely observed (Talreja 1991, Demers 1998a, Liu & Mahadevan 2010). In fact the fatigue life of GFRP often scatters over one order of magnitude for a given set of parametric values (Kim & Ebert 1979). This large scatter stems mainly from the high anisotropy of the material, variation in fibre volume fraction, density of defects and the distribution and alignment of fibres (Kim & Ebert 1979) as well as competing damage and failure mechanisms (Nijssen 2010). There is also a large variation in the strengths of individual fibres, even under static loading (Curtis 1991, Mallick 2011). A number of statistical distributions have been used to describe the fatigue data of FRP composites including normal (Demers 1998a), log-normal (Kim & Ebert 1979) and Weibull (Sendeckyj 1981, Talreja 1991, Zhou & Mallick 2004), with distribution parameters calibrated experimentally.

2.7.1.2 CFRP

Typical S-N curves for CFRP show an average downward slope of about 5-8% of initial static strength per decade of logarithmic life, such that after one million cycles the fatigue strength of CFRP is in the range of 50 to 70 percent of its initial static strength; CFRP tests up to 10 million cycles indicate a continued trend of residual strength degradation of 5-8% (Curtis 1989). The endurance limit of CFRP bars is a function of both the mean stress and the ratio of maximum and minimum stresses (ACI Committee 440 2006).

2.7.1.3 GFRP

GFRP is much more sensitive to fatigue than CFRP due to its lower stiffness which causes the matrix to be worked at higher strains (Curtis 1989, 1991). GFRP data show shorter fatigue lives than CFRP for the same normalized maximum stress (Demers 1998a); as a result, S-N curves for GFRP are generally much steeper, while the S-N curves for CFRP materials are almost flat (Konur & Matthews 1989). ACI 440 (2006) limits the stress in FRP reinforcement subjected to fatigue to 20% and 55% of the ultimate static tensile strength for glass and carbon FRP, respectively.

Individual glass fibres are generally not prone to fatigue failure (ACI Committee 440 2006); however, when embedded into a matrix forming an FRP composite, a loss of 10% in initial static strength per decade of logarithmic life has been reported (Mandell 1982). This effect has been attributed to fibre-fibre interactions rather than the stress corrosion induced by the growth of flaws in individual fibres. Environmental factors also play a role in the fatigue behaviour of glass fibres due to their susceptibility to moisture, alkaline and acidic solutions (ACI Committee 440 2006).

E-glass fibres are the most widely used due to their good physical and electrical properties and reasonable weathering ability (Dew-Hughes & Way 1973). However E-glass is known to suffer from a loss of strength with time under load (Mandell 1982). S-glass composites have a higher modulus and better fatigue performance than E-glass (Konur & Matthews 1989) but are generally more expensive.

Both the strength and stiffness of GFRP degrade under fatigue loading. Fatigue modulus degradation can be a criterion for failure and provides an indirect assessment of damage growth in the FRP. Three regions of modulus degradation are typically observed, namely initial decay for the first 1000 cycles or less, gradual decay over the greater part of the fatigue life and finally rapid decay for the final cycles before failure (Demers 1998b).

2.7.1.4 Matrix

The fatigue behaviour of composites is also significantly affected by the type of matrix used, particularly at low stress levels. Polymer matrices deteriorate under fatigue loading, usually by fatigue crack growth, leading to a loss of stiffness and eventually failure (Mandell 1982). The fatigue behaviour of various resins have been observed to be cycle dependent rather than time dependent and their fatigue behaviour is similar to that of metals (Dew-Hughes & Way 1973). Interface bond between the resin and fibre is often the limiting factor in the mechanical properties of FRP. Debonding has been observed at cyclic loads less than 30% of the ultimate tensile strength of GFRP (Dew-Hughes & Way 1973).

Epoxy matrix composites generally have a superior fatigue performance due to their inherent toughness, durability and compatibility with glass fibres (Konur & Matthews 1989). Vinyl ester resins are commonly used in GFRP composites as they are stronger than polyester and cheaper than epoxy resins; vinyl ester is a hybrid form of polyester which has been toughened with epoxy molecules within its molecular structure. Although vinyl ester bonds well to glass fibres, it is not suitable with Kevlar or carbon fibres.

A study comparing the fatigue behaviour of E-glass/vinyl ester and E-glass/epoxy composites in deflection controlled bending tests found that the vinyl ester specimens displayed a more rapid stiffness loss than those with epoxy. Similarly, fibre-matrix debonding was more prevalent for a similar number of cycles and fatigue lives were reduced for specimens with vinyl ester resin (Newaz 1985). However, the fatigue behaviour of E-glass/vinyl ester specimens has been reported to be superior to that of E-glass/polyester (Dyer & Isaac 1998). Adimi et al. (1997) have suggested using vinyl ester or epoxy resin in place of polyester for GFRP reinforcing bars subjected to fatigue loading.

Polymer composites are also poor thermal conductors; a significant amount of heat may be generated when the cycling frequency is high, especially at high stress levels. This phenomenon is more severe with GFRP because the strain levels tend to be much higher than for high-modulus fibres (Mandell 1982). Frequencies less than 4-5 Hz produce negligible internal heating in GFRP composites (Demers 1998b).

2.7.1.5 Fatigue Modelling

The simplest way to present fatigue life data is often in the form of an S-N curve, where the applied stress range is plotted versus the number of cycles to failure in a semi-log or log-log plot. The data are commonly fitted with a regression following either a logarithmic (Equation 2.29) or power law function (Equation 2.30). Power law functions tend to be more accurate for extrapolation to high cycle fatigue for many composites (Nijssen 2010), although they generally do not describe low cycle fatigue data well. Although this relationship is sometimes treated as deterministic, the stochastic nature of the data often requires consideration of the probability

of failure for an assumed statistical distribution of data. This allows a family of S-N curves corresponding to different probabilities of failure to be constructed. The Weibull distribution has proved to be particularly well-suited for describing composite material strength and fatigue life data.

Eq. 2.29 $$S = AlnN + B$$

Eq. 2.30 $$S = AN^B$$

Where, *S* is the applied load range, *N* is the number of cycles to failure and *A* and *B* are experimentally calibrated fatigue coefficients.

Many of the fatigue models developed for composite materials are empirical in nature. It is difficult to move away from this empiricism for two main reasons (Talreja 1999); first, the mechanisms of fatigue damage are varied and complex owing to numerous factors, and second, the concepts and analyses developed for fatigue and fracture of metals have limited application to composites. In addition, macroscopic and phenomenological damage models are more practical than microscopic physical models as they require less data, are easier to measure and the interaction of different damage types can often be neglected (Yao & Himmel 2000). Phenomenological models are those which relate empirical observations of phenomena to each other in a way that is consistent with fundamental theory without being directly derived from theory.

Fatigue damage may be defined as any permanent change in a composite system due to fatigue loading (Kim & Zhang 2001). As fatigue loading affects both the strength and stiffness of

composite materials, most phenomenological models can be characterised either as residual stiffness models or residual strength models. The advantage of residual stiffness approaches is that the remaining life can be assessed using non-destructive methods and often requires less testing. A disadvantage of most residual stiffness models is that they are not valid for all 3 stages of stiffness degradation (Van Paepegem & Degrieck 2002b). Furthermore, failure criteria are not always well-defined.

Residual strength approaches, on the other hand, are simple and exhibit a clear explanation for failure in stress-controlled tests as failure occurs when the instantaneous value of strength is equal to the instantaneous value of applied stress (Post et al. 2010). Weaknesses of residual strength theories include the following: remaining life cannot be assessed non-destructively, it is not a sensitive measure of damage accumulation—as residual strength changes very slowly until close to failure—and it requires an extensive experimental characterization (Vassilopoulos & Keller 2011). In general, stiffness change is greater than changes in residual strength (Sendeckyj 1991) and displays less scatter (Vassilopoulos & Keller 2011). Residual strength models are not considered in detail in this study due to the extensive scope of the experimental testing required.

There is also a debate on whether data from static tests should be included together with fatigue data as the load corresponding to 1 cycle to failure (or 0.25 cycles, depending on the loading scheme). According to Nijssen (2006) neither inclusion nor exclusion of static data can be adequately justified. Despite this, several researchers recommend limiting regression to fatigue data since most expressions do not accurately describe fatigue behaviour in the low

cycle region outside of actual data (Nijssen 2010). Static tests are usually conducted at much lower strain rates, may have different failure modes and do not necessarily fit regression lines for fatigue data. However, including static results may improve predictions when the low-cycle behaviour is important (Vassilopoulos & Keller 2011).

2.7.1.5.1 Residual Stiffness Models

One commonly used damage metric is the degradation in stiffness in FRP composites caused by the repeated application of loads. This can be non-destructively monitored by measuring the change in deformation (strain, deflection, etc.) over time. This phenomenon can be described using Equation 2.31 or 2.32:

Eq. 2.31 $$\varepsilon_e = \frac{\sigma}{E_o(1-D)}$$

Eq. 2.32 $$D = 1 - \frac{E}{E_o}$$

Where, σ and ε_e are the stress and strain in the composite, respectively, E and E_o are the current and initial modulus of elasticity, respectively, and D is a variable describing the change in stiffness.

Although D is often referred to as a damage variable, it is not directly based on actual damage mechanisms (Van Paepegem 2010). Structural changes on a microscopic scale are characterized by a macroscopic reduction in stiffness (Van Paepegem & Degrieck 2002a); the use of the damage variable, D, allows one to model the composite as an undamaged homogeneous solid with degraded stiffness properties (Van Paepegem & Degrieck 2002b). This

is useful for monitoring damage in real structures during service, since the stiffness can be used as a measurable, non-destructive parameter.

A plot of the normalized residual stiffness versus number of cycles can typically be divided into 3 stages consisting of rapid initial stiffness degradation, a stable period of gradual stiffness degradation and finally rapid deterioration just prior to fatigue failure (Figure 2.5). The second stage can be represented as a linear function of the number of applied load cycles as given by Equation 2.33, resulting in a constant rate of stiffness degradation as given by Equation 2.34. Assuming that the fatigue life follows a power law function, the change in stiffness can then be related to the fatigue life by Equation 2.35 (Brondsted et al. 1997).

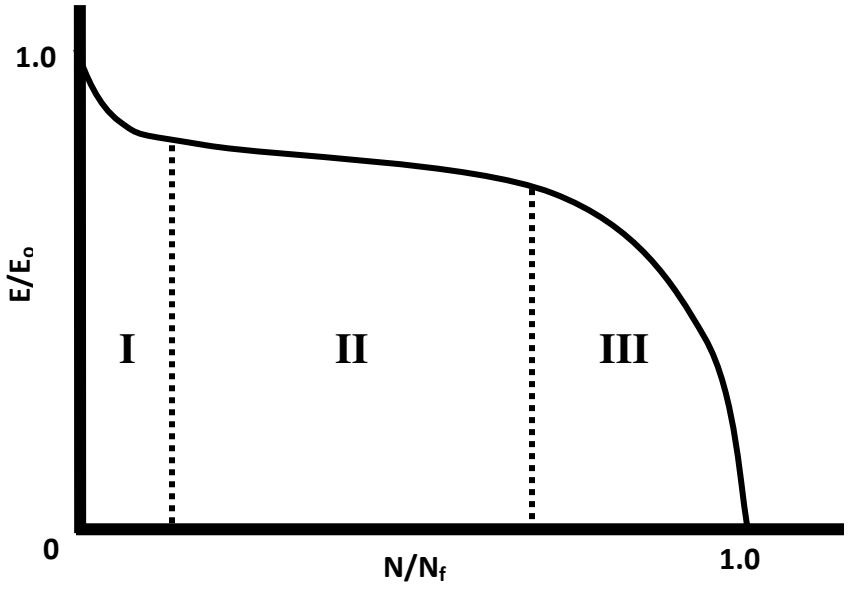

Figure 2.5 - The three stages of fatigue stiffness degradation

Eq. 2.33 $$\frac{E}{E_1} = AN + B$$

Eq. 2.34 $$\frac{d(E/E_1)}{dN} = A$$

Eq. 2.35 $$\frac{d(E/E_1)}{dN} = -K(\frac{\sigma}{E_o})^n$$

Where, E, E_o and E_1 are the current, initial and first-cycle modulus of elasticity, respectively, N is the number of applied cycles, A and B are calibration coefficients, σ is the applied stress level, and K and n are power law coefficients.

Integrating Equation 2.35 gives:

Eq. 2.36 $$\frac{E}{E_1} = 1 - K(\frac{\sigma}{E_o})^n N$$

By defining a stiffness degradation criterion, the number of cycles to a defined damage level can be determined. Similarly, the stiffness degradation at a given load level for a prescribed number of cycles can be predicted. A series of fatigue life curves defined by a certain stiffness or stiffness reduction can be used in place of a general failure criterion, although a fatigue failure criterion corresponding to the fatigue resultant strain reaching the static ultimate strain has been used by several researchers (Hwang & Han 1986, Whitworth 1998, Kim & Zhang 2001).

Hwang & Han (1986) have described the fatigue modulus degradation using a power law as given by Equations 2.37 and 2.38:

Eq. 2.37 $$\frac{dF}{dn} = -Acn^{c-1}$$

Eq. 2.38 $$F_f - F_o = -AN^c$$

Where, *dF/dn* is the fatigue modulus degradation rate, *n* and *N* are the number of applied cycles and fatigue life, respectively, *A* and *c* are power law coefficients, and F_o and F_f are the initial fatigue modulus and fatigue modulus at failure, respectively.

Kim and Zhang (2001) used a similar approach, except that the damage rate was described with a power law:

Eq. 2.39 $$\frac{dD_f}{dN} = \alpha {\sigma_{max}}^{\beta}$$

Eq. 2.40 $$N = \frac{{\sigma_u}^{-\beta}}{\alpha(\beta-1)}\left[\left(\frac{\sigma_{max}}{\sigma_u}\right)^{1-\beta} - 1\right]$$

Where, *dDf/dN* is the damage rate, σ_{max} and σ_u are the maximum applied stress and ultimate strength of the FRP, respectively, *N* is the fatigue life of the FRP and α and β are power law coefficients.

2.7.1.5.2 Other Models

A fibre bundle model was developed by Chi et al. (1984) to describe the fibre strength distributions of statically loaded fibre bundles using a 2-parameter Weibull distribution, which was later adapted by Zhou & Mallick (2004) for fatigue testing, as given by Equations 2.41 to 2.44. This model assumes that the tensile stress-strain curve for each fibre in a bundle is linear elastic to failure, the fatigue life of each fibre follows a power law, and the fatigue strength coefficient follows a Weibull distribution. It is also assumed that the applied load is shared equally among surviving fibres so that the probability of failure is proportional to the number of ruptured fibres. Implicit in this assumption is the idea that negligible interaction exists between fibres, a condition which is clearly violated once the fibres are impregnated in a polymer resin.

Nevertheless, it is a trivial process to remove this condition and replace the ratio of ruptured fibres with a different damage metric—such as stiffness—and calibrate accordingly.

Eq. 2.41 $$P = \exp\left[-\left(\frac{\sigma_f}{\sigma_o}\right)^{\beta}\right] = 1 - \frac{n}{N} = \frac{\sigma}{E\varepsilon}$$

Eq. 2.42 $$\sigma_{max} = \sigma_f (2N_f)^b$$

Eq. 2.43 $$P = \exp\left[-(\frac{\sigma_{max}}{\sigma_o})^{\beta}(2N)^{-b\beta}\right]$$

Eq. 2.44 $$\ln[-\ln(P)] = \beta \ln(\sigma_{max}) - \beta \ln(\sigma_o) - b\beta \ln(2N)$$

Where, P is the probability of failure, σ_f is the tensile capacity of the fibres, β and σ_o are calibration coefficients, n and N are the number of surviving fibres and total number of fibres, respectively, σ and ε are the average stress and strain in the fibres, respectively, E is the modulus of elasticity of the fibres, σ_{max} is the maximum applied stress level, N_f is the fatigue life corresponding to the applied stress level, and b is a power law coefficient.

Chou & Croman (1978) introduced a strength-life equal rank (SLER) assumption to relate the fatigue lives and static strengths of composites assuming that both followed the 2-parameter Weibull distribution, as given by Equations 2.45 to 2.47. SLER assumes that static strengths are uniquely related to the fatigue lives and residual strengths of fatigue specimens at runout; this procedure implies that the strongest specimen also has the longest fatigue life or the highest residual strength. While simple and intuitive, this assumption may not be necessarily valid if competing failure modes are observed during fatigue tests.

Eq. 2.45 $$F_{R(0),S}(x) = 1 - \exp(-x^{\alpha} + S^{\alpha})$$

Eq. 2.46 $$F_N(n) = 1 - \exp(-n^{\alpha 1})$$

Eq. 2.47 $$n_\gamma^{\alpha 1} = x_\gamma^\alpha - S^\alpha$$

Where, $F_{R(0),S}(x)$ is the conditional probability of failure at a normalized stress of *x* given that *x* is greater than the normalized applied stress, *S,* $F_N(n)$ is the probability that the actual fatigue life is less than the normalized fatigue life, *n*, $\alpha 1$ and α are Weibull shape parameters, and n_γ and x_γ are values that give a cumulative distribution of fatigue life or static strength, respectively, of $1 - \gamma$.

Sendeckyj (1981) also used the SLER assumption to develop a method capable of fitting various fatigue models to the experimental fatigue data of composite materials. This method simultaneously determines the fatigue model parameters and the Weibull distribution parameters describing the static strength by converting fatigue data to equivalent static strength values using the maximum likelihood estimate (MLE) method; this iterative process is optimized by maximizing the Weibull shape parameter for the equivalent static strength data (maximizing the shape parameter essentially corresponds to the distribution having the lowest scatter). While the approach proposed by Sendeckyj can be applied to various fatigue models, Equation 2.48 gives the equivalent static strength of specimens tested under fatigue loading based on the so-called wear-out model. The probability that the actual static strength is higher than the equivalent static strength is given by Equation 2.49:

Eq. 2.48 $$\sigma_e = \sigma_a[(\frac{\sigma_r}{\sigma_a})^{1/S} + (n-1)C]^S$$

Eq. 2.49 $$P(\sigma_e) = \exp[-(\frac{\sigma_e}{\beta})^\alpha]$$

Where, σ_e, $\sigma_a$and σ_r are the equivalent static strength, applied stress level and residual strength of the fatigue specimens, respectively, *n* is the number of applied cycles, *C* and *S* are model calibration coefficients, $P(\sigma_e)$ is the probability that the static strength is greater than the equivalent static strength, and α and β are Weibull distribution parameters.

For fatigue failure, the residual strength is equal to the applied stress level and the number of applied cycles is equal to the fatigue life, *N,* thus simplifying to Equation 2.50:

Eq. 2.50 $$\sigma_e = \sigma_a[1 - C + CN]^S$$

Where, *N* is the fatigue life of the specimen and all other symbols are as noted previously.

For *C* = 1, Equation 2.50 reduces to the classical power law fatigue failure criterion, whereas *C* < 1 results in an S-N curve that flattens out at low cycles on a log-log plot. Values of *C* > 1 result in a curve which steepens at low cycles; this phenomenon has not been observed in composites.

For a given number of cycles, the probability of failure can be given by Equation 2.51:

Eq. 2.51 $$P(N) = \exp\{-[\frac{(N-A)}{\beta_f}]^{\alpha_f}\}$$

Where, *P(N)* is the probability of survival after *N* cycles, and *A*, α_f and β_f are Weibull distribution parameters.

Equation 2.51 is a 3-parameter Weibull function; to eliminate the difficulty caused by a negative location parameter, *A*, conditional probabilities can be used:

Eq. 2.52 $$P(\sigma_e|\sigma_e > \sigma_a) = \exp[-(\frac{\sigma_e}{\beta})^{\alpha} + (\frac{\sigma_a}{\beta})^{\alpha}]$$

Eq. 2.53 $$P(N|\sigma_e > \sigma_a) = \exp\{-\left[\frac{(N-A)}{\beta_f}\right]^{\alpha_f} + \left[\frac{\sigma_a}{\beta}\right]^{\alpha}\}$$

Where, $P(\sigma_e|\sigma_e > \sigma_a)$ and $P(N|\sigma_e > \sigma_a)$ are the conditional probability that the actual static strength is greater than the equivalent static strength and the conditional probability of survival after *N* cycles, respectively, given that the equivalent static strength is greater than the applied stress level. All other terms are as noted previously.

2.7.2 Concrete

Concrete is susceptible to fatigue failure, especially as the repeated loading of flexural members causes cracks to penetrate deeper, thus shifting the neutral axis upwards and reducing the area of concrete in compression (Chang & Kesler 1958, Naaman 1982). Fatigue of concrete is a result of the accumulation of the irreversible energy of deformation manifested as inelastic strains in the form of cracks and creep (Heffernan & Erki 2004). The modulus of elasticity of concrete can also decrease significantly during a test due to crack formation at the microscopic level (Shah 1984). At high stresses the fatigue behaviour of concrete is influenced by the effects of creep, evidenced by a reduction in fatigue life for reduced load rates. Thus the damage caused by high repeated loads depends both on the number of applied cycles and the total time the concrete is sustaining high stresses (Award & Hilsdorf 1974). However, the rate of loading has little effect on fatigue strength when the maximum stress level is less than 75% of its static strength.

The fatigue strength of plain concrete is similar whether it is loaded in tension, compression or flexure (ACI 215R-74 1997). Concrete has no known fatigue limit up to 10 million cycles (Hsu

1981); the fatigue strength of concrete for a life of 10 million cycles for compression, tension or flexure is approximately 55% of its static strength (ACI 215R-74 1997). ACI 215R-74 (1997) recommends a stress range in concrete in compression of less than 40% of the ultimate static compressive strength when the minimum compressive stress is zero; the allowable stress range is linearly reduced to zero as the minimum compressive stress is increased to 75% of the ultimate static compressive strength.

Concrete is considered to be a notch-insensitive material (ACI 215R-74 1997) and the normalized fatigue curve, given by Equation 2.54, is independent of compressive strength, curing condition, age, moisture conditions, etc. (Hsu 1981):

Eq. 2.54 $$\frac{f_{max}}{f'_c} = 1 - \beta(1 - R)logN$$

Where, f_{max} is the maximum applied stress, f'_c is the concrete compressive strength, β is a calibration factor, *R* is the ratio of minimum to maximum applied stress and *N* is the fatigue life of the concrete.

The value of β in Equation 2.54 has been reported to be between 0.064 and 0.0685 (Hsu 1981). When time under load is a critical parameter, Equation 2.55 can be used to account for the strength reduction with time:

Eq. 2.55 $$\frac{f_{max}}{f'_c} = 1 - 0.0662(1 - 0.556R)logN - 0.0294logT$$

Where, *T* is the number of seconds required to complete one cycle.

Due to the high scatter present in the fatigue data of concrete, probabilistic concepts are often applied. Similar to FRP composites, the fatigue life of conventional concrete has been described by the 2-parameter Weibull distribution. Unlike the log-normal distribution—which shows a decreasing hazard function—the Weibull distribution gives an increasing hazard function with increase in life or time, which better describes the actual behaviour of engineering materials subjected to fatigue, as the failure rate is generally expected to increase with time (Oh 1986). In addition, it is easy to use, has well developed statistics, and has been used in a number of studies (Oh 1986, Goel et al. 2012).

2.7.3 Steel

Research on the fatigue of metals is well-developed and—for simple geometries—the mechanics are fairly well-understood. Metals are sensitive to stress concentrations at notch locations resulting in the formation of local plasticity zones. In conventional rebar, for example, fatigue cracks will typically form at the toe of lugs on the bar surface used to enhance bond with concrete. In general, the fatigue of steel occurs in three phases, namely crack initiation, steady crack propagation and brittle fracture (El-Ragaby et al. 2007). Fatigue crack growth in metals occurs in a stable fashion prior to reaching the critical length for fracture (Mandell 1982). Typically, fatigue strength decreases with an increase in bar diameter (Tilly 1979). ACI 215R-74 (1997) recommends a maximum stress range in reinforcing steel given by Equation 2.56, although it need not be less than 138 MPa; this value has been adopted as a practical fatigue limit since the lowest stress range known to have caused a fatigue failure of a deformed reinforcing bar embedded in a concrete beam was 145 MPa with a minimum stress of 121 MPa.

Fatigue of steel reinforcing bars has not been a significant factor in their application as reinforcement in concrete structures.

Eq. 2.56 $$S_r = 161 - 0.33S_{min}$$

Where, S_r and S_{min} are the applied stress range and minimum applied stress, respectively.

2.7.4 Reinforced Concrete

The application of repeated loads can significantly reduce the ability of a RC structural member to resist applied loads, as well as leading to increased deflections and crack widths due to creep and fatigue softening. Fatigue must be considered in design as it can lead to bond degradation, reduced shear and flexural capacities and reduced service lives; fatigue can be a governing limit state for partially prestressed members (Naaman 1982).

In most applications, fatigue failure due to concrete is not likely to occur (Naaman 1982). However, fatigue can be a contributing factor in the progressive deterioration of structures (Hordijk & Reinhardt 1993) and concrete softening due to repeated loads can lead to an increase in stresses in the tensile reinforcement (Heffernan & Erki 2004). Therefore the flexural fatigue performance of cracked RC and PC members is primarily influenced by the type of reinforcement that is used. The fatigue lives of flexural members are typically a function of the stress range induced in the reinforcement (Braimah et al. 2006). Local stress increases at crack locations increase the potential for fatigue-induced failures. The stronger the bond between the reinforcement and the surrounding concrete, the greater the local variation in reinforcement stress (ACI 215R-74 1997).

Bending fatigue tests on concrete beams simulate service conditions more closely than axial bar tests since the interactive effects at the reinforcement-to-concrete interface can be considered. Cyclic frequencies are generally limited by high ranges of deflection and the necessity to avoid local heating due to friction at crack locations in the concrete; high frequency testing can generate a significant amount of heat at the concrete-bar interface and increasing the cyclic frequency can decrease the observed fatigue life (Adimi et al. 2000). It is also necessary to make assumptions about the load carrying contribution of the concrete and the accuracy of the location of the reinforcement. Bending tests can give slightly longer lives than bare bar axial tests although the differences are small; the reason for this is that the likelihood of the highest stress concentrations (crack locations) coinciding with the worst defects in the bar is low (Tilly 1979).

Repeated loading can also have a detrimental effect on the bond between reinforcing bars and the surrounding concrete. Factors affecting bond strength under cyclic loads include the concrete compressive strength, cover, bar size, anchorage length, surface conditions, reinforcement properties, confinement, strain range and rate of loading. The primary mechanism governing bond failure in conventionally reinforced concrete members is the progressive crushing of the concrete in front of the lugs (ACI 408.2R-92 2005). This can result in increased displacement of the reinforcing bar relative to the concrete, known as slip (Rteil et al. 2011).

The fatigue behaviour of concrete beams is characterized by a continual change in stiffness due to cyclic creep of the concrete in compression, the development of vertical and diagonal cracks,

a reduction in the stiffness contribution of tension zone concrete due to crack formation and progressive bond degradation, as well as cyclic strain softening of the longitudinal reinforcement (Chang & Kesler 1958, Balaguru & Shah 1982). This change in stiffness is generally observed by pronounced increases in crack widths and deflections in the early stages of cyclic loading followed by a relatively stable period of gradual stiffness loss until failure is preceded by a period of rapid deterioration (Naaman 1982).

The increase in deflections or crack widths in conventional RC can be estimated using Equation 2.57 (Shah 1984):

Eq. 2.57 $$\frac{\delta Y}{Y} = e^{Bx} - 1$$

Where, δY is the change in deflection or crack width, Y is the corresponding deflection or crack width during the first cycle, B is a constant given as 0.667 for deflection calculations and 1.670 for crack widths, and x is the ratio of applied cycles to fatigue life.

Other models have also been developed by Balaguru & Shah (1982), given by Equations 2.58 to 2.60, and by Lovegrove & El Din (1982), given by Equations 2.61 to 2.63:

Eq. 2.58 $$E_N = \frac{\sigma_{max}}{\frac{\sigma_{max}}{E} + \varepsilon_c}$$

Eq. 2.59 $$f_{r,N} = f_r\left(1 - \frac{\log N}{10.954}\right)$$

Eq. 2.60 $$w_{max,N} = \frac{w_{max}(1.2)\left(\frac{h_2}{h_1}\right)_N \varepsilon_{s,N}\left[1+1.22\left(\frac{\log N}{7}\right)^2\right]}{\left(\frac{h_2}{h_1}\right)\varepsilon_s}$$

Eq. 2.61 $$\Delta_n = 0.225\Delta_o \log n$$

Eq. 2.62 $$k_n = 0.225k_o \log n$$

Eq. 2.63 $$w_n = w_o(0.382 - 0.0227 \log n) \log n$$

Where, E and E_N are the initial and cyclic secant modulus of elasticity of concrete in compression after N cycles, σ_{max} is the maximum compressive stress in the concrete, ε_c is the cyclic creep strain in the concrete, f_r and $f_{r,N}$ are the initial and cyclic modulus of rupture after N cycles, w_{max} and $w_{max,N}$ are the initial and cyclic flexural crack widths after N cycles, h_1 and h_2 are the distance from the reinforcement to the neutral axis and from the extreme tension fibre to the neutral axis, respectively, ε_s is the reinforcement strain at the crack, Δ_o and Δ_n are the initial and cyclic deflection after n cycles, k_o and k_n are the initial and cyclic curvature after n cycles, and w_o and w_n are the initial and cyclic flexural crack widths after n cycles.

2.7.4.1 FRP-Reinforced or Prestressed Concrete

A number of studies (Saadatmanesh & Tannous 1999, El-Ragaby et al. 2007a, Braimah 2000) have reported generally good fatigue performance of FRP bars compared to steel in the form of bare bars and as tensile reinforcement in RC or PC members. This is particularly the case for high modulus fibres such as carbon (ACI 440.1R-06). Unlike steel, however, the fatigue behaviour of FRP reinforcing bars is influenced by the presence of the concrete surrounding it (Rahman et al. 1996). Concrete affects the fatigue behaviour of FRP bars adversely due to its harsh alkaline environment and friction between the FRP bar and the concrete resulting in abrasion of the bar surface (Rahman et al. 1996, Adimi et al. 2000, El-Ragaby et al. 2007).

Failure of FRP in reinforced concrete may be initiated at the bar surface inside the concrete in the form of matrix cracks caused by friction with the concrete (Adimi et al. 2000). Friction fretting of the rod surface with successive destruction of the bar may take place close to flexure-induced cracks where the bond stresses are high and partial slip occurs (CEB-FIP 2000).

Katz (2000) examined the surfaces of FRP bars subjected to cyclic loads embedded in concrete and observed significant damage characterized by areas where the external layer of the bar was abraded and had sheared off, with most of the damage occurring in the initial cycles. Bars with an external sand coating developed small cracks around the sand particles reducing their bond to the polymer matrix. Katz (2000) also observed that FRP bars fabricated with a polymer having good mechanical properties at the surface showed mixed damage to the concrete and the reinforcing bar. Two deterioration mechanisms were reported to occur during cyclic loading, namely abrasion of the concrete layer near surface deformations or sand particles and loosening of the bond between the sand particles and the FRP surface polymer. When the surface polymer had poor mechanical properties, a gap formed between the FRP bar and the concrete and the external layer of polymer was sheared from the core. Conversely, damage during pullout of steel reinforcing bars was located solely in the concrete. Similar results were obtained by Lee et al. (2009).

Surface treatments such as helical wraps which are used to enhance bond with concrete can have a detrimental effect on fatigue performance (Katz 1998). Local stress concentrations due to surface features such as ribs, wraps or other deformations can degrade fatigue performance

by imposing multiaxial stresses that increase matrix-dominated damage mechanisms which are normally suppressed in fibre-dominated materials.

Bond degradation typically occurs near cracks and migrates away from the crack with increasing load (Sooriyaarachchi et al. 2005) or repeated loading. As the bond between the reinforcement and the surrounding concrete degrades with increasing number of cycles, an associated increase in slip and crack widths is observed (Balazs 1991).

The long term and fatigue behaviour of concrete beams prestressed with CFRP was investigated by Braimah (2000). CFRP-prestressed beams exhibited lower long term deflections than similar steel-prestressed beams. Fatigue testing consistently led to fractures at the junction of the CFRP bar and the anchorage system; when premature failure at the location of the anchors was prevented, the CFRP-prestressed beams performed well under fatigue loading.

2.7.4.2 Shear

Studies on the influence of fatigue on shear resistance have shown that repeated loading can cause diagonal cracks to become quite wide leading to a reduction in the concrete contribution to shear resistance (Higgins et al. 2006, 2007). This is due to a breakdown in aggregate interlock caused by abrasion along the crack interface, debonding of the longitudinal reinforcement along the crack interface and, if present, debonding of the stirrups near the diagonal crack (Kreger et al. 1989). If no shear reinforcement is provided, this can lead to shear failures at loads which are lower than predicted for members subjected to static loading. If transverse shear reinforcement is provided, the stress range in the stirrups will increase with additional load cycles which could lead to stirrup rupture. As noted by Teng et al. (2000),

repeated loading reduces the shear strength of RC beams although the effect of fatigue on shear capacity is less significant compared with that on flexural capacity. Fatigue considerations are more likely to be critical for short spans (Hawkins 1972). The shear fatigue strengths of steel-RC beams subjected to one million load cycles have been reported in the range of 50% - 70% of the ultimate static capacity (Chang & Kesler 1958, Teng, Ma & Weng 2000) although shear failures have been observed at loads as low as 25% of the expected shear capacity (Hawkins 1972).

Fatigue loading can also change the mode of failure of a member from flexure to shear or vice versa (Hawkins 1972, Ueda & Okamura 1983). Chang & Kesler (1958) state that a beam subjected to fatigue loading which is weaker in shear than in flexure could fail in one of five ways, namely destruction of the compression zone, splitting action along the reinforcement, diagonal cracking, bond failure or fatigue of the reinforcement. Essentially this means that the mode of fatigue failure cannot necessarily be determined by its static response.

2.8 Summary and Research Needs

The excellent mechanical properties of FRP materials coupled with the rate of deterioration of existing infrastructure due to corrosion of conventional steel reinforcement are leading to increased acceptance of FRP reinforcing bars for a wide range of structural applications. FRPs possess high strength, low weight and are resistant to corrosion and other forms of deterioration; in the past several decades, FRPs have been successfully implemented in a wide range of structural applications including parking garages and bridges. Similarly, the time and cost savings as well as the quality assurance provided by SCC are changing its perception as a

niche product as more industry members are employing it for common applications. Although SCC remains the product of choice for concrete sections having highly congested reinforcement details, it is now also being increasingly applied to almost all types of precast and cast-in-place applications. While both FRPs and SCC have been researched extensively in the past, experimental programs on their combined use are presently lacking in the literature.

Furthermore, the use of GFRP reinforcing bars in bridge applications has largely been limited to slab-on-girder construction where the spans range from 2-3 m. One of the main reasons for this is the relatively low axial stiffness of GFRP reinforcement which makes it impractical for longer spans where excessive reinforcement ratios are required to meet serviceability criteria. In addition, the shear resistance of GFRP-RC sections is a concern due to the formation of wide cracks that reduce the contribution of aggregate interlock. Thus, the use of GFRP reinforcing bars for the primary reinforcement of slab bridges has not been extensively studied despite the exposure of many slab bridges to aggressive environments and de-icing salts. The use of post-tensioned CFRP tendons shows promise for the implementation of a non-corroding all-FRP reinforcement system that addresses the serviceability issue while improving the behaviour at ultimate limit states by increasing the flexural and shear resistance, as well as allowing for a pseudo-ductile progressive failure mode.

A review of the currently available literature highlights the need for an extensive experimental program to investigate the flexural behaviour of full-scale one-way slabs having lengths greater than 3 m and the applicability of design code equations to predict the behaviour of flexural members combining passive and prestressed FRP reinforcement. The extent to which the

addition of post-tensioned CFRP tendons improves the overall behaviour of GFRP-RC members needs to be quantified, including the reduction in deflections, crack widths and GFRP reinforcement stresses at service, as well as load capacity and deformability.

The advantages of FRP shear reinforcement in corrosive environments have also been made evident in recent years, despite challenges related to bending the longitudinal fibres without significantly and detrimentally affecting the strength of the bar. Shear reinforcement in the form of closed stirrups is also impractical for slab bridge applications where simplicity is one of the key advantages allowing for reduced construction times and costs. Headed anchorages have recently been developed for FRP bars that may present an attractive alternative to bent FRP stirrups for shear reinforcement. Further research on their use and comparison with other alternatives, as well as consideration of the effects of cyclic loading, is needed to validate their use in field applications.

Surprisingly, the fatigue behaviour of FRP-RC is largely absent from published literature (although a number of studies are available on the fatigue behaviour of FRP-strengthened steel-RC members). While there have been some experimental studies on the fatigue behaviour of CFRP-prestressed girders (Braimah et al. 2006), GFRP-RC 2-way deck slabs (El-Ragaby et al. 2007) and FRP-RC tension members (Adimi et al. 2000)—among others—there has been no effort, to the author`s knowledge, to develop fatigue life models for FRP-RC members or to predict the effect of fatigue load cycles on deflections or crack widths, nor have there been any reported methods to predict the remaining life of existing structures non-destructively through consideration of the residual stiffness of the member. Investigations of the fatigue shear

behaviour of FRP-RC sections are also lacking. This may be partially attributable to the difficulty in testing FRP reinforcing bars in fatigue to calibrate empirical models as well as the complexity of developing rational models for the fatigue of FRP due to the many factors involved. Nevertheless, for the long term safety and longevity of the bridges being designed today, it is imperative that tools be developed to assist engineers in predicting their behaviour up to the end of their expected service lives. This has been one of the primary goals of the research project summarized in this thesis.

Chapter 3 - Experimental Program

3.1 Overview

The main experimental study was comprised of a total of 57 concrete slab strips tested to failure under monotonic or cyclic loading. These tests were divided into three phases as shown in Figure 3.1. Phase I consisted of sixteen full-scale slab strips with the objective of exploring the potential advantages and limitations of the proposed all-FRP reinforcement system for slab bridges under static loading. In particular, the effects of reinforcement type, reinforcement ratio, prestressed tendons (bonded or unbonded) and shear reinforcement type on the overall flexural performance of slab bridges were investigated. While the prestressed slabs tested in Phase I demonstrated excellent serviceability characteristics and ultimate load-carrying capacities (see Chapter 4), slabs without transverse shear reinforcement tended to exhibit brittle diagonal tension failure modes which are undesirable. Each of the prestressed slabs with transverse reinforcement showed nearly identical responses up to failure regardless of the shear reinforcement type. Consequently, the twenty-five slabs tested during Phase II were designed with a reduced shear span-to-depth ratio (and hence, moment-to-shear ratio) in order to induce shear failures even when transverse shear reinforcement was provided. These tests were intended to identify the effectiveness of various shear reinforcement types under static and fatigue loading conditions. Lastly, Phase III consisted of sixteen full-scale slab strips which were all tested under cyclic loading in order to quantify the effect of post-tensioning and shear reinforcement on the fatigue life of GFRP-RC slab bridges.

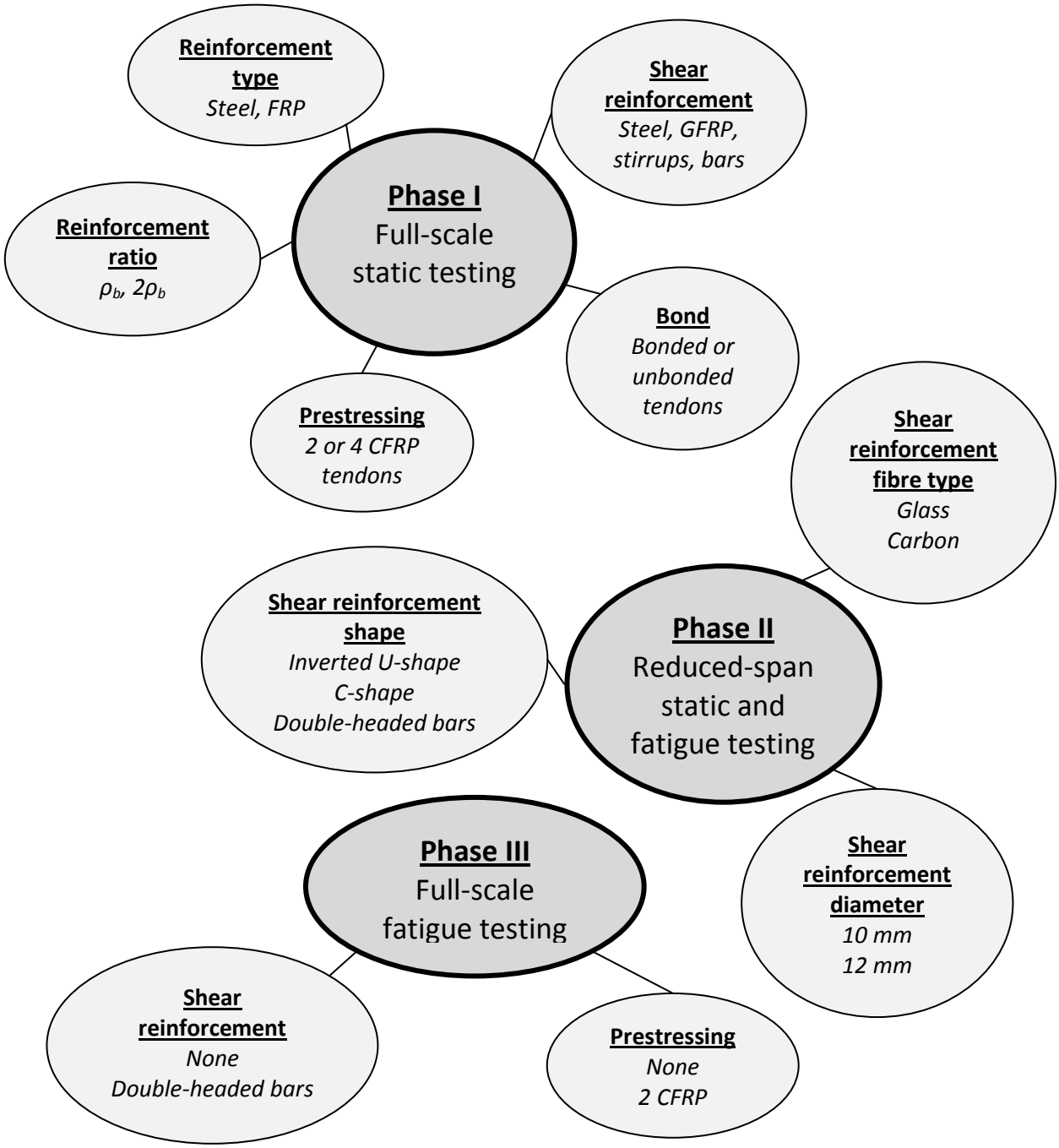

Figure 3.1 - Experimental test program

The full test matrix is summarized in Tables 3.1 and 3.2. The non-prestressed slabs include the steel-reinforced control slab, S, and all GFRP-reinforced slabs beginning with the letter 'G'; the number immediately following the letter 'G' indicates approximately which multiple of the

balanced reinforcement ratio is provided as tensile reinforcement (ie. specimen G1 has a reinforcement ratio approximately equal to the balanced condition, G2 is over-reinforced with a reinforcement ratio approximately equal to two times the balanced reinforcement ratio). The nomenclature for the remaining slabs is summarized as follows: a prefix of PT indicates that the slab was post-tensioned, followed by a 2 or 4 representing the number of prestressing tendons used. Various suffixes were appended to the specimen name to indicate an additional feature of the specimen, for example 'U' for unbonded tendons or 'G' for GFRP stirrups. Specimens tested in fatigue are numbered F1 to F4 for each group of identical slabs.

3.2 Test Specimen Details

While steel-RC flexural members are typically designed for strength, FRP-RC members are commonly designed to meet serviceability criteria first, with strength checked later. The control slab was designed to withstand the factored design load, which was obtained by placing the CHBDC design truck at critical locations along the length of a two-lane bridge having the same span as the test specimens (see Chapter 8). For most of the slabs tested in this study, the reinforcement ratio for the primary non-prestressed reinforcement was kept constant and equal to that of the steel-RC control slab. The higher tensile strength of the GFRP reinforcement compared with the steel resulted in an increase in moment capacity (thus meeting the strength criteria), although the post-cracking stiffness was significantly reduced. In order to produce an "equivalent" design, prestressed CFRP tendons were added to improve the serviceability and shear resistance of the slabs without excessively over-reinforcing the section; the results showed that the proposed reinforcement system presented a viable alternative to conventional steel reinforcement with improved serviceability and ultimate performance.

The reinforcement details of each slab are illustrated in Figure 3.2 and summarized in Tables 3.1 and 3.2. The guaranteed tensile mechanical properties of the reinforcing bars as provided by the manufacturers are provided in Table 3.3. The GFRP bars used in this study consisted of pultruded E-glass fibres impregnated with a modified vinyl ester resin with a minimum fibre volume fraction of 0.65.

Table 3.1 – Test matrix for full-scale specimens (Phase I and III)

Loading	Slab	Reinforcing bars	Shear reinforcement	Number of tendons	Effective prestress level (%)
Monotonic (Phase I)	S	6 15M Steel	--	--	--
	G1	6 #5 GFRP			
	G1-ST		10M Steel stirrups		
	G2	12 #5 GFRP	--		
	G2-ST		10M Steel stirrups		
	PT2a	5 #5 GFRP	--	2 B	46
	PT2	6 #5 GFRP			51
	PT2-ST		10M Steel stirrups		
	PT2-G		#3 GFRP C-shaped stirrups		55
	PT2-S		#4 GFRP vertical shear bars		
	PT2-S45		#4 GFRP inclined shear bars		
	PT2-U		--	2 UB	
	PT4			4 B	
	PT4-G		#3 GFRP C-shaped stirrups		
	PT4-U		--	4 UB	
	PT4-P			4 B	30
Fatigue (Phase III)	G1-F1	6 #5 GFRP	--	--	--
	G1-F2				
	G1-F3				
	G1-F4				
	G1S-F1		#5 GFRP headed shear bars		
	G1S-F2				
	G1S-F3				
	G1S-F4				
	PT2-F1		--	2 B	55
	PT2-F2				
	PT2-F3				
	PT2-F4				
	PT2S-F1		#5 GFRP headed shear bars		
	PT2S-F2				
	PT2S-F3				
	PT2S-F4				

Table 3.2 - Test matrix for reduced-length specimens (Phase II)

Loading	Slab	Reinforcing bars	Shear reinforcement	Number of tendons	Effective prestress level (%)
Monotonic	GU-10	6 #5 GFRP	#3 GFRP U-shaped stirrups	2 B	55
	GU-12		#4 GFRP U-shaped stirrups		
	CU-10		#3 CFRP U-shaped stirrups		
	GC-10		#3 GFRP C-shaped stirrups		
	GS-12		12 mm GFRP headed shear bars		
Fatigue	GU-10-F1	6 #5 GFRP	#3 GFRP U-shaped stirrups	2 B	55
	GU-10-F2				
	GU-10-F3				
	GU-10-F4				
	GU-12-F1		#4 GFRP U-shaped stirrups		
	GU-12-F2				
	GU-12-F3				
	GU-12-F4				
	CU-10-F1		#3 CFRP U-shaped stirrups		
	CU-10-F2				
	CU-10-F3				
	CU-10-F4				
	GC-10-F1		#3 GFRP C-shaped stirrups		
	GC-10-F2				
	GC-10-F3				
	GC-10-F4				
	GS-12-F1		12 mm GFRP headed shear bars		
	GS-12-F2				
	GS-12-F3				
	GS-12-F4				

Table 3.3 – Guaranteed properties of reinforcing bars as reported by the manufacturer

Material*	Nominal bar diameter (mm)	Nominal cross-sectional area (mm^2)	Tensile capacity (MPa)	Modulus of elasticity (GPa)	Yield strain (%)	Ultimate strain (%)
#3 GFRP RM1	9.5	71.3	765	45.4	--	1.69
#4 GFRP RM1	12.7	126.7	708	46.3	--	1.53
#4 GFRP RM2	12.7	126.7	941	53.6	--	1.76
#5 GFRP RM1	16	197.9	683	48.2	--	1.42
#5 GFRP RM2	16	197.9	934	55.4	--	1.69
#5 GFRP HM	16	197.9	1184	62.6	--	1.89
12 mm GFRP	12	113.1	1350	64.0	--	2.11
#3 CFRP	9.5	71.3	1431	120	--	1.19
#4 CFRP	12.5**	122.7	1765	144	--	1.23
15M Steel	16	200	400	200	0.2	>10

*RM1 – Regular modulus used in Phase I, II and a portion of Phase III; RM2 – Regular modulus used for most of Phase III; HM – High modulus used for Phase III shear reinforcement

**Measured

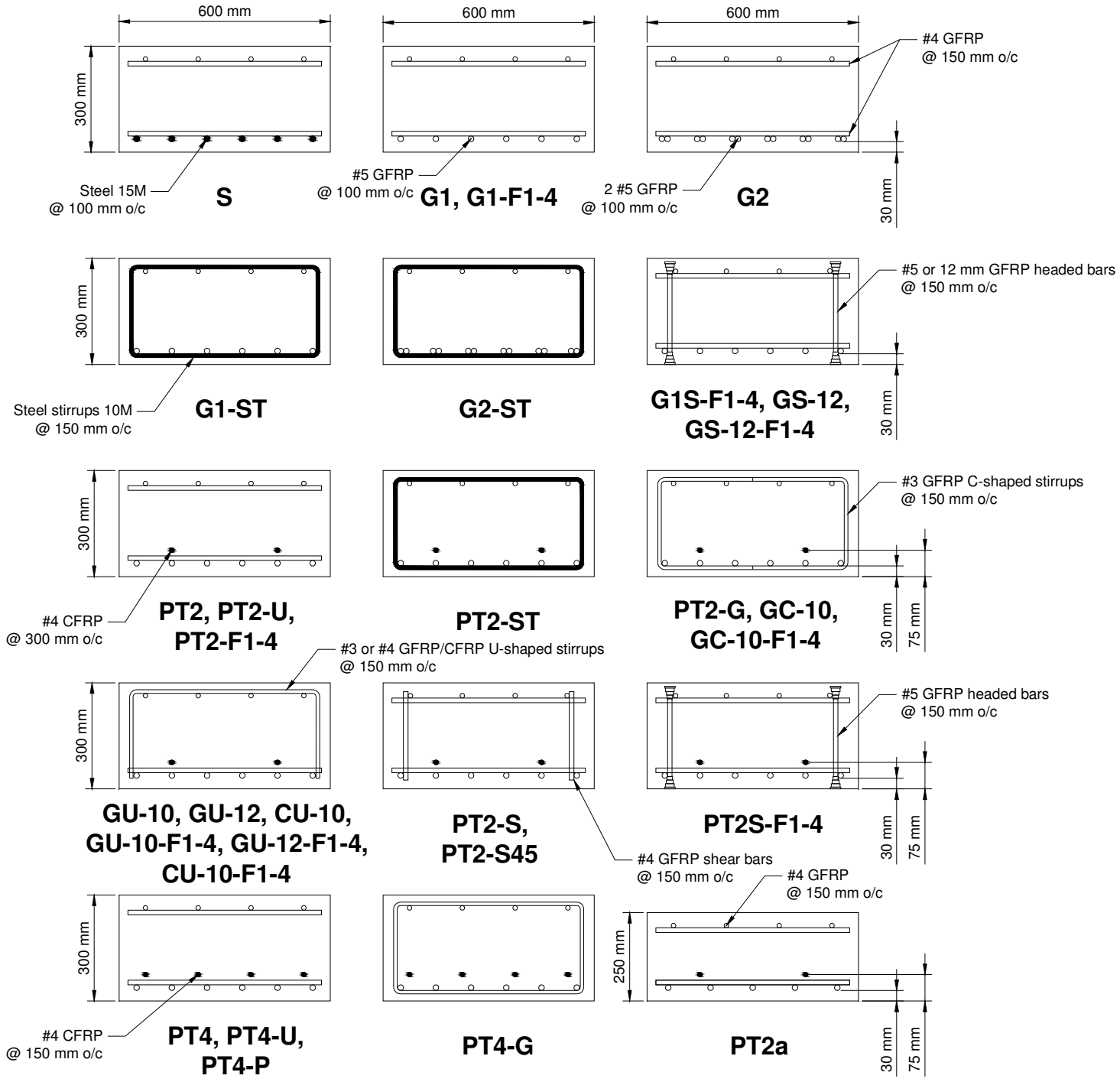

Figure 3.2 - Test specimen details

Each of the slabs had cross-section dimensions of 600 mm x 300 mm except for one slab, PT2a, which had a reduced depth of 250 mm to investigate the possibility of reducing the deck thickness through prestressing. The full-scale slab specimens tested in Phase I and Phase III had

lengths of 5 m, while the slabs in Phase II had lengths of only 2.5 m. Each of the 300 mm deep slabs contained either six or twelve #5 (16 mm diameter) GFRP bars in the bottom longitudinal direction, except for the control slab, S, which instead contained six 15M steel reinforcing bars. Slab PT2a, which had a reduced depth of 250 mm, was reinforced in the bottom longitudinal direction with five #5 GFRP reinforcing bars. These reinforcement configurations correspond to a reinforcement ratio just less than or approximately two times the balanced condition for the GFRP-reinforced slabs. Each slab also contained four #4 (13 mm diameter) GFRP reinforcing bars in the top longitudinal direction and spaced at every 150 mm in the transverse direction at the top and bottom of the slab serving as temperature and shrinkage reinforcement, except for slabs reinforced with stirrups. The top and bottom clear cover to the longitudinal reinforcement was kept constant at 30 mm.

Of the sixteen full-scale slabs tested in Phase I, five slabs were non-prestressed; these include the steel-reinforced control slab, S, and four GFRP-reinforced slabs. Specimens G1 and G2 contained approximately one and two times the balanced reinforcement ratio, respectively. Both of these slabs were expected to fail in shear before reaching their flexural design capacity, therefore specimens G1-ST and G2-ST contained 10M steel stirrups spaced at 150 mm on centre in order to increase the shear resistance of the section and induce flexural failure. The remaining eleven full-scale slab specimens contained either two or four #4 (13 mm diameter) CFRP prestressing tendons at a distance of 75 mm from the bottom concrete surface. Although the CHBDC allows effective prestress levels at transfer of up to 65% of the ultimate strength of the CFRP tendons, in practice prestress levels are usually limited to 40% to 60% of ultimate. For this study, a maximum prestress level of 55% of ultimate was selected to ensure good

serviceability while providing sufficient strain capacity to reach high loads at ultimate without rupturing. Three slabs (PT2a, PT2 and PT2-ST) had slightly lower effective prestressing levels due to relatively high prestressing losses, while one additional slab was post-tensioned with four CFRP tendons prestressed to only 30% of their ultimate strength to compare the behaviour of slabs having a similar prestressing force but a different number of tendons. Confinement was provided in the end regions of these slabs by placing 10M steel stirrups at a 50 mm spacing to resist the splitting stresses induced during prestressing. All of the post-tensioning ducts were filled with grout immediately after prestressing, with the exception of two slabs (PT2-U and PT4-U), for which the tendons were left unbonded. Six prestressed slabs did not contain any shear reinforcement within the main span, while five slabs contained various types of shear reinforcement at a spacing of 150 mm to compare their effect on the ultimate load-carrying capacity. The various types of shear reinforcement considered were steel stirrups, GFRP C-shaped stirrups, vertical GFRP shear bars and inclined GFRP shear bars.

In Phase II, the transverse shear reinforcement fibre type, shape and diameter were varied to study their effect on the static and fatigue shear behaviour of the prestressed slab bridge strips. Although conventional slab bridges typically do not include shear reinforcement, the lower shear strength of FRP-RC members may govern design in some cases. Since closed stirrups are not practical for slabs from a constructability standpoint, alternative shear reinforcement types which can be easily incorporated into a reinforcement grid were investigated. Five types of shear reinforcement were evaluated, namely #3 and #4 GFRP inverted U-shaped stirrups (series GU-10 and GU-12, respectively), #3 CFRP inverted U-shaped stirrups (series CU-10), #3 GFRP C-shaped stirrups (series GC-10) and 12 mm diameter GFRP double-headed shear bars (series GS-

12) as shown in Figure 3.3. The spacing of the shear reinforcement was kept constant at 150 mm, and the longitudinal reinforcement details were identical to slab PT2 from Phase I. For each shear reinforcement type studied, five identical specimens were prepared for a total of 25 specimens. In each group, one specimen was tested under monotonic loading and four specimens were tested under cyclic loading.

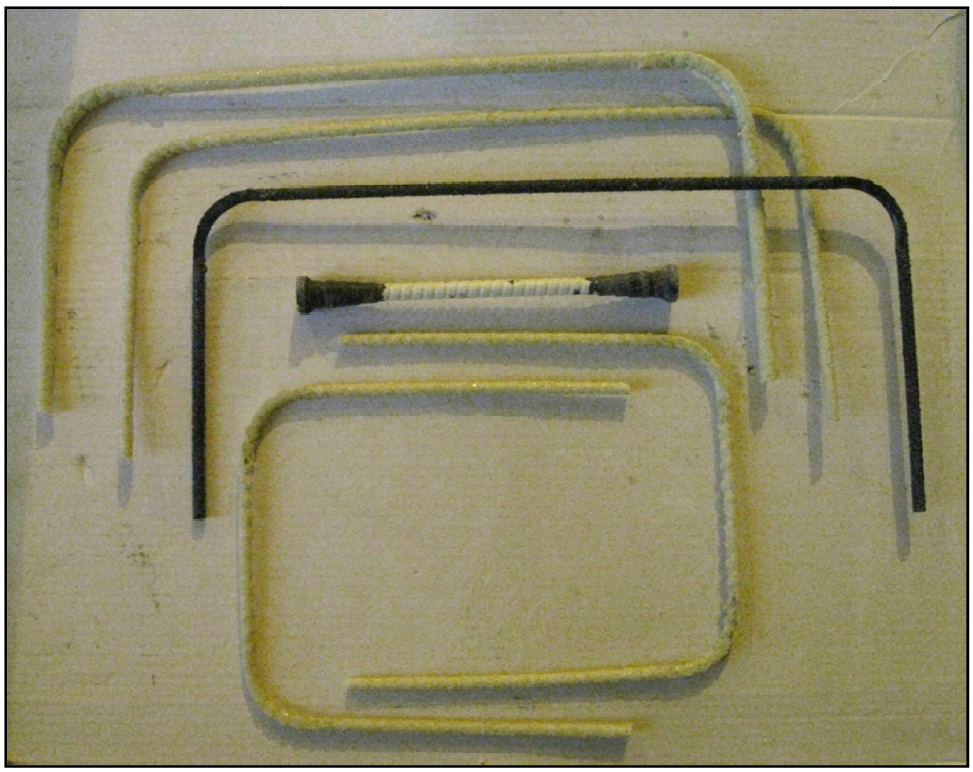

Figure 3.3 - Shear reinforcement types for Phase II

Phase III consisted of sixteen full-scale slabs tested under cyclic loading, eight of which were prestressed and eight slabs were non-prestressed. The longitudinal reinforcement details were identical to slabs G1 and PT2 from Phase I, with the exception that changes in the manufacturing process resulted in a slight change in the mechanical properties of the GFRP reinforcing bars (see Table 3.3). These changes apply to specimens G1-F1 to F4, G1S-F1 to F4

and PT2S-F1 to F4, which were the last twelve slabs to be constructed. Four prestressed slabs (PT2S-F1 to F4) and four non-prestressed slabs (G1S-F1 to F4) were reinforced in shear using double-headed shear bars; although similar in concept to the double-headed shear bars used in Phase II, the mechanical properties and bar diameter were changed. At the time of construction of the Phase II specimens, the FRP manufacturer supplying the longitudinal GFRP and CFRP reinforcement for this project did not have a comparable product design and therefore the double-headed shear bars used in Phase II were obtained from a different manufacturer. Prior to the construction of Phase III specimens, the original FRP manufacturer developed their own double-headed bars, although the minimum bar diameter was 16 mm compared to 12 mm for the bars used in Phase II. Since the use of a reinforcement system from a single manufacturer increases its practicality and hence the attractiveness and viability of a design concept, the shear bars used in Phase II were replaced with the larger bars for Phase III. Since all of the shear-reinforced slabs in Phase III had a flexural mode of failure, this change is believed to have a negligible effect on the results presented. The new shear bar is shown in Figure 3.4.

The double-headed anchor bars used in Phase III are comprised of high-modulus GFRP reinforcing bars with headed anchorages cast onto the ends of the bar and hardened at elevated temperatures. The maximum outer diameter of the anchor heads are 3 times the diameter of the GFRP bar with a head length of 100 mm. Grooves in the bar are used to enhance the mechanical interlock with the anchor heads (Figure 3.5) with reported average pullout strengths of 132.3 kN and 148.5 kN in confined concrete block specimens for concrete compressive strengths of 36 MPa and 47 MPa, respectively, corresponding to 57% and 64% of

their ultimate static tensile capacity. Specimens without spiral reinforcement for confinement of the anchor heads failed at lower loads (Mohamed & Benmokrane 2012).

Figure 3.4 – Double-headed shear bar used for Phase III

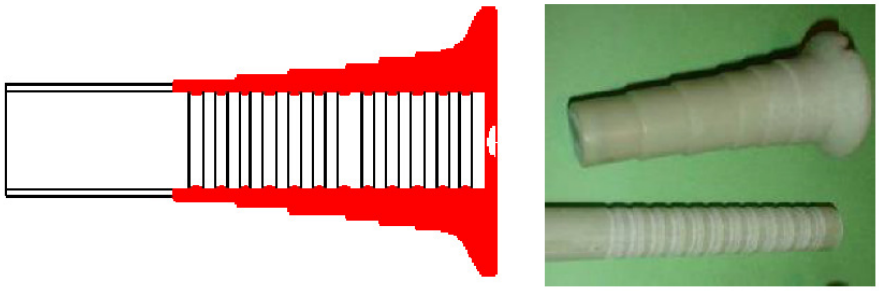

Figure 3.5 - Headed anchorage for shear bars (Mohamed & Benmokrane 2012)

3.3 Slab Fabrication

All of the slabs tested in this study were fabricated at a local precast plant using a proprietary SCC mix design with a maximum aggregate size of 13 mm, a water-cement ratio of approximately 0.4 and various chemical admixtures to produce a concrete with good flowability while ensuring consistent mechanical properties. An approximate mix design is given in Table 3.4. Slump flow tests were performed by quality control staff at the time of casting (Figure 3.6), and for each concrete pour a number of cylinders were cast in addition to the slabs for later testing of mechanical properties. Measured slump flow values ranged from 625 mm to 700

mm, and the average 28 day compressive strength was 54.1 MPa. Detailed concrete properties are summarized in Table 3.5.

Table 3.4 - Concrete mix design

Constituent	Quantity
Water	160 kg/m^3
Cement	360 kg/m^3
Coarse aggregate	860 kg/m^3
Fine aggregate	780 kg/m^3
High range water reducer	850 g/m^3
Air entrainment	85 g/m^3

Figure 3.6 - Slump flow test

Table 3.5 - Concrete properties

Specimens	Slump flow (mm)	28 day strength		Strength at time of testing	
		Average f'_c (MPa)	Average f_{sp} (MPa)	Average f'_c (MPa)	Average f_{sp} (MPa)
G1, G2	--	40.8	--	58.1	3.9
G1-ST, G2-ST	--	45.9	--	58.1	3.9
S, PT2	--	42.1	--	58.1	3.9
PT2-ST, PT2a	--	34.5	--	63.8	--
PT4, PT2-U, PT4-U	655	48.5	4.2	55.7	4.1
PT2-G, PT4-G, PT4-P	700	50.0	4.4	59.1	4.3
PT2-S, PT2-S45, PT2-F1	695	60.1	4.3	64.5	4.1
PT2-F2, PT2-F3, PT2-F4	625	58.3	4.3	64.7	4.1
CU-10, CU-10-F1	690	60.8	4.2	64.3	3.9
CU-10-F2, CU-10-F3	--	61.0	--	66.2	--
CU-10-F4, GU-10	635	58.9	4.1	67.9	4.3
GU-10-F1, GU-10-F2	--	57.8	--	63.7	--
GU-10-F3, GU-10-F4	--	57.5	--	61.0	--
GU-12, GU-12-F1	--	54.7	--	60.5	--
GU-12-F2, GU-12-F3	--	61.8	--	63.7	--
GU-12-F4, GC-10	--	60.0	--	63.9	--
GC-10-F1, GC-10-F2	--	57.7	4.2	63.1	4.1
GC-10-F3, GC-10-F4	--	59.4	--	66.3	--
GS-12, GS-12-F1	--	76.0	--	79.9	--
GS-12-F2, GS-12-F3	--	70.8	--	78.5	--
GS-12-F4	--	58.1	--	63.4	--
G1-F1, G1-F2, G1-F3	630	44.7	3.6	48.5	4.0
G1-F4, G1S-F1, G1S-F2	550	45.4	3.5	46.8	3.7
G1S-F3, G1S-F4, PT2S-F1	630	44.1	3.5	45.5	3.0
PT2S-F2, PT2S-F3, PT2S-F4	640	44.8	3.7	45.3	3.3

The concrete compressive strength, f'_c, and split cylinder tensile strength, f_{sp}, were measured at approximately 28 days and at the time of testing of the corresponding test slabs from the same concrete batch (Table 3.5). Tests were conducted in accordance with ASTM C39/C39M and C496/C496M, respectively. The results of the average concrete compressive tests for each batch with respect to the concrete age at the time of testing are given in Figure 3.7. Results from the concrete cylinder compressive strength tests were fairly consistent between batches, with the exception of a few outliers, and strengths were observed to remain fairly constant with time after 28 days, although a slight increase in strength was typical. At the time of testing, average concrete compressive strength values ranged from 45.3 MPa to 79.9 MPa, with

most of the values lying between 55 MPa and 65 MPa. The instances in which the concrete strength happened to be outside of this range could be attributed to the fact that, although the mix design was kept essentially the same using the proprietary mix design of the local precast plant, a new shipment of cement seemed to result in an unexpected change in compressive strength. The average strength at the time of testing was 61.5 MPa; for design purposes, a concrete strength of 60 MPa was assumed.

Splitting tensile test results are given in Figure 3.8 with respect to the age of the concrete at the time of testing; normalized tensile strength values (obtained by dividing the splitting tensile strength by the square root of the corresponding concrete compressive strength) are shown in Figure 3.9. A slight decrease in normalized tensile strength with time was observed, which is likely due to drying shrinkage of the concrete; in order to maintain compatibility with the slab test specimens, the concrete cylinders were not cured in a humidity controlled environment. At the time of testing the splitting tensile strength of the concrete ranged from $0.451\sqrt{f'_c}$ to $0.571\sqrt{f'_c}$. The splitting tensile strength is generally greater than the direct tensile strength and lower than the flexural strength, or modulus of rupture (ASTM 2011).

Randomly selected cylinders were cut in half longitudinally to examine the aggregate distribution inside the hardened concrete as a qualitative assessment of aggregate segregation. As shown in Figure 3.10, coarse aggregates were uniformly distributed throughout the depth of the cylinder indicating good stability of the concrete mix.

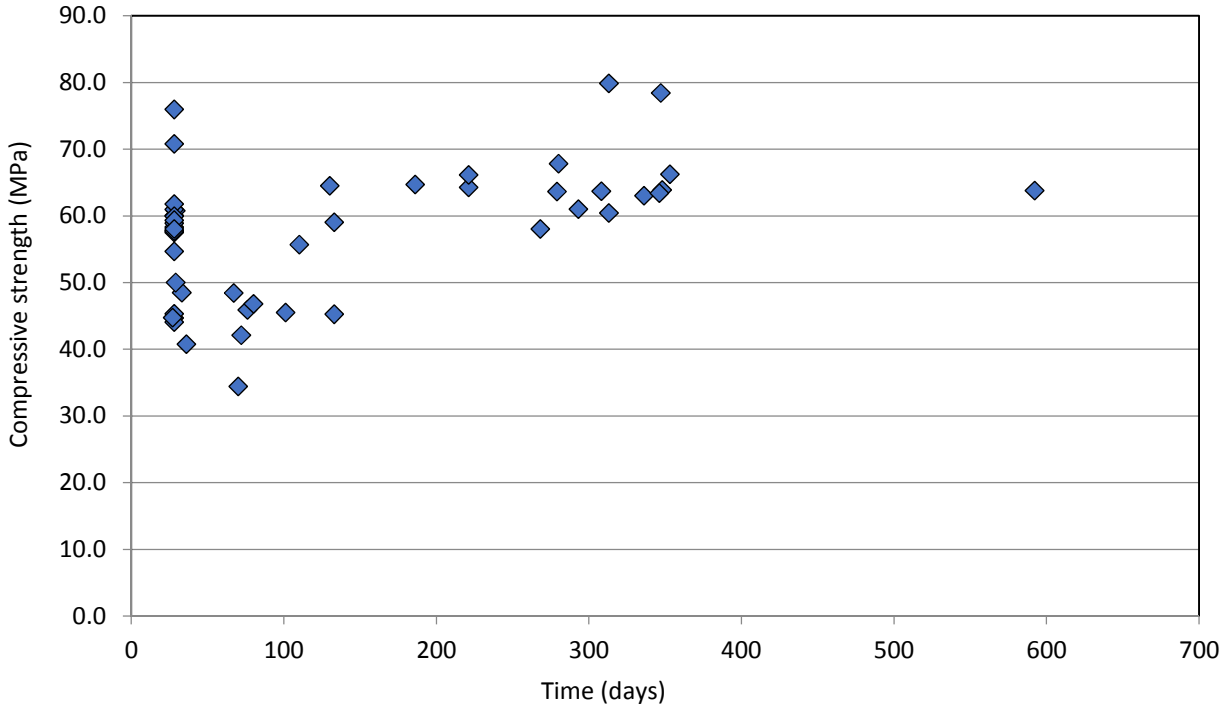

Figure 3.7 - Concrete compressive strength over time

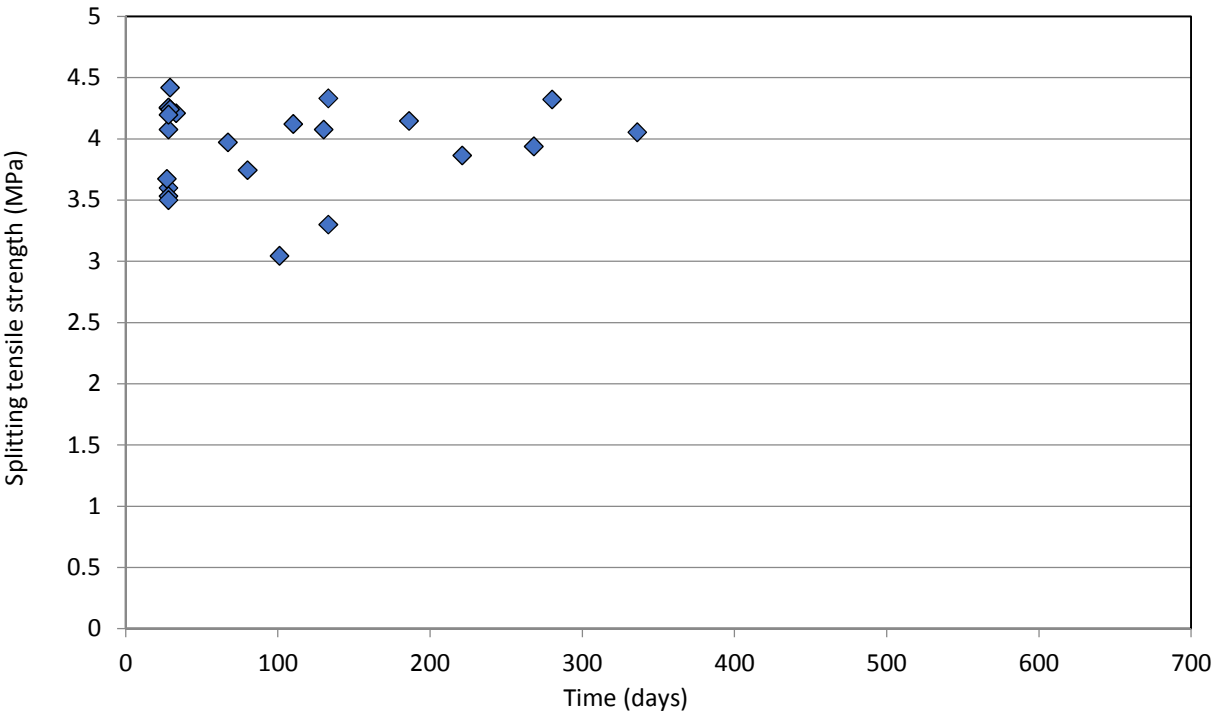

Figure 3.8 - Concrete splitting tensile strength over time

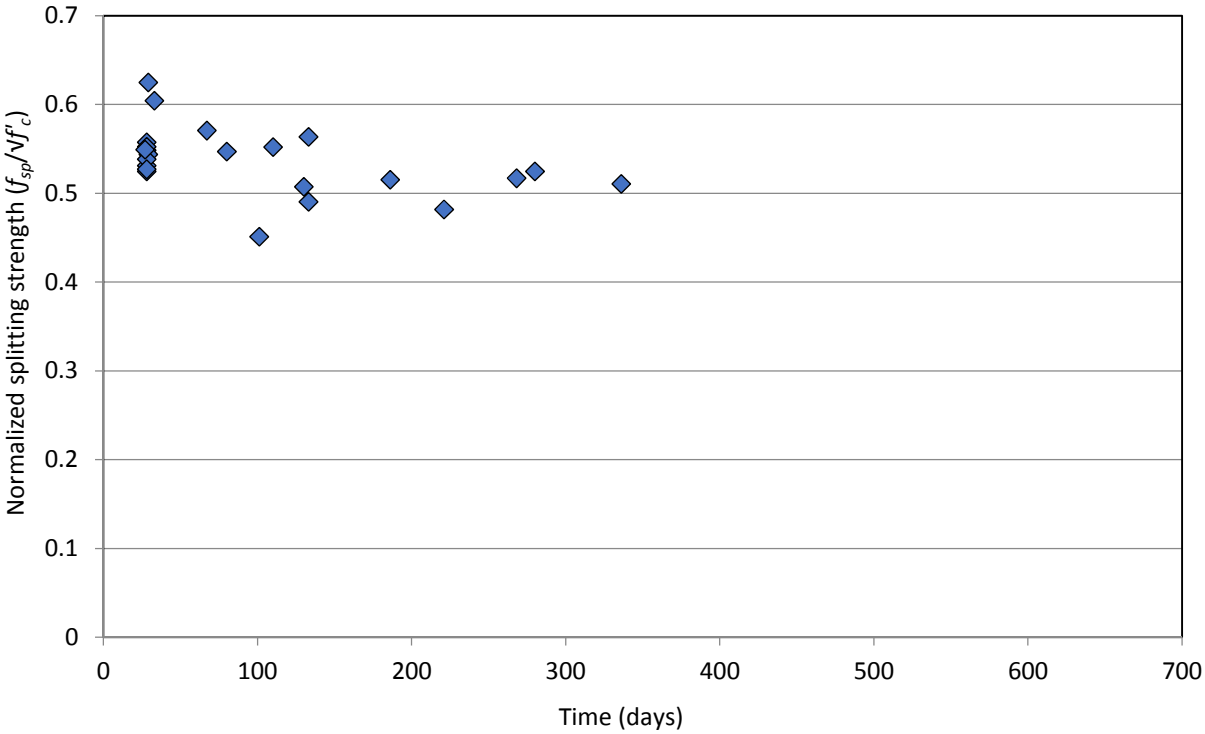

Figure 3.9 - Normalized splitting strength over time

Figure 3.10 - Segregation analysis of hardened concrete

Photographs of the fabrication process are given in Figures 3.11 to 3.13. Reinforcing cages were constructed and placed inside wooden forms on a steel casting bed; the concrete was poured from the centre of the slabs and allowed to flow to each end of the formwork.

Figure 3.11 - Construction of reinforcing cages with various types of shear reinforcement

Figure 3.12 - Completed reinforcing cages in wooden formwork

Figure 3.13 - Pouring concrete and completed specimens following formwork removal

3.4 Prestressing

The CFRP tendons were stressed one at a time using a two jack system and three wedge-type anchors developed at the University of Waterloo (Al-Mayah et al. 2006) as shown in Figure 3.14. One anchor was seated at the dead end and one at the live end, with the third anchor left unseated between the hydraulic cylinders and the concrete slab. The load was applied using the larger jack between the anchor and the steel post-tensioning setup; the smaller jack was then used to seat the third anchor which maintained the prestressing force in the concrete slab. Once the anchor was seated, the load in the hydraulic cylinder was released and the post-

tensioning setup was moved to the next bar. The initial applied load was recorded using a load cell between the live end anchor and the hydraulic jack. Losses within the slab were monitored using strain gauges mounted on the CFRP bars.

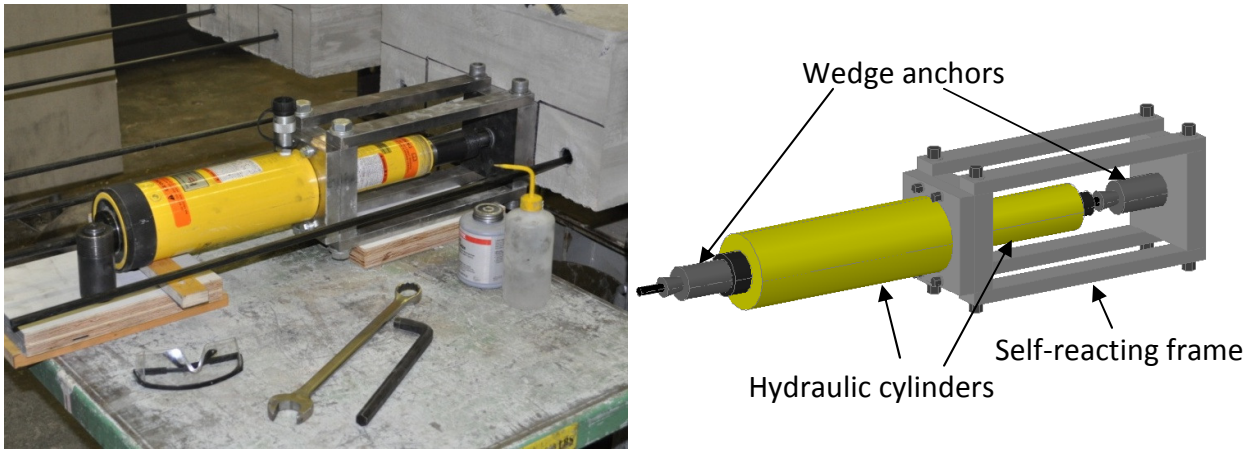

Figure 3.14 - Post-tensioning setup

For specimen PT2a, which was the first slab to be post-tensioned, each bar was tensioned to a jacking force of approximately 110 kN. The jacking force was later increased to 125 kN for the remaining prestressed slabs. The first three post-tensioned slabs, PT2a, PT2 and PT2-ST had the live end anchor oriented in the conventional manner such that during the seating of this anchor, the wedges were driven into the barrel by a hydraulic cylinder. As the wedges were driven inwards, they began to grip the bar and pulled the bar inwards as well. This resulted in rather significant seating losses (approximately 10%) with a final force in each bar of approximately 100 kN for PT2a and 110 kN for PT2 and PT2-ST, corresponding to 46 and 51% of the guaranteed capacity of the CFRP bar, respectively. Amato (2009) encountered a similar problem while post-tensioning a parking garage slab; by reversing the orientation of the anchor so that the barrel was pushed over the wedges, the anchorage losses were significantly

reduced. The remaining prestressed slabs used a reversed orientation for the live end anchor; this reduced seating losses to less than 4% in most cases such that the effective prestress force in each bar was approximately 120 kN, or 55% of the guaranteed tensile capacity of the CFRP bar. The reverse orientation of the anchors is shown in Figure 3.15. Slabs with a shorter length typically displayed slightly higher anchorage losses due to their shorter tendon length. Prestress losses due to elastic shortening and long term losses due to shrinkage and creep were negligible. A summary of the measured prestressing losses is given in Table 3.6 and photographs of the prestressing setup are given in Figure 3.16.

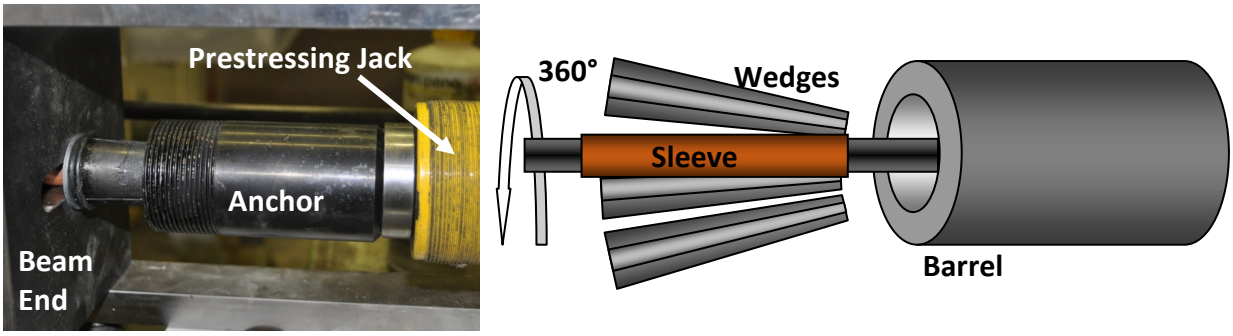

Figure 3.15 – Reverse orientation of live end anchor

After the bars were prestressed, the ducts were filled with post-tensioning grout to provide a bond transfer mechanism with the concrete slab (except for those which were to remain unbonded). Unfortunately, one of the anchors used for specimen PT4-G had been manufactured from a defective material, and the barrel cracked after the grout was beginning to set. Once the barrel cracked the anchor was no longer able to hold the force in the prestressing tendon, causing the tendon to slip and shoot out six inches from the live end. This sudden release of energy damaged the bar and the prestressing force was lost. Since the grout

was already partially set, there was no way to replace the damaged bar, therefore specimen PT4-G was tested with only 3 active tendons.

Table 3.6 - Prestressing losses

Slab	Jacking force per tendon (kN)	Average final force per tendon (kN)	Average prestress loss (%)
PT2a	110	97.2	11.7
PT2	125	109.3	12.5
PT2-ST	125	108.7	13.0
PT2-G	125	121.2	3.1
PT2-S	125	122.4	2.1
PT2-S45	125	123.0	1.6
PT2-U	125	123.8	1.0
PT4	125	122.2	2.3
PT4-G*	125	118.6	5.1
PT4-U	125	120.6	3.6
PT4-P	65	64.1	1.4
GU-10	125	116.6	6.7
GU-10-F1	125	118.4	5.2
GU-10-F2	125	120.9	3.3
GU-10-F3	125	118.5	5.2
GU-10-F4	125	117.4	6.1
GU-12	125	119.8	4.2
GU-12-F1	125	116.0	7.2
GU-12-F2	125	122.0	2.4
GU-12-F3	125	119.4	4.5
GU-12-F4	125	117.8	5.7
CU-10	125	112.1	10.3
CU-10-F1	125	119.0	4.8
CU-10-F2	125	118.1	5.5
CU-10-F3	125	122.4	2.1
CU-10-F4	125	117.9	5.7
GC-10	125	119.8	4.2
GC-10-F1	125	118.3	5.3
GC-10-F2	125	114.0	8.8
GC-10-F3	125	121.6	2.8
GC-10-F4	125	120.8	3.4
GS-12	125	124.5	0.4
GS-12-F1	125	115.5	7.6
GS-12-F2	125	113.9	8.9
GS-12-F3	125	119.7	4.3
GS-12-F4	125	118.8	5.0
PT2-F1	125	124.1	0.7
PT2-F2	125	122.3	2.2
PT2-F3	125	122.6	1.9
PT2-F4	125	120.7	3.4
PT2S-F1	125	122.7	1.8
PT2S-F2	125	119.8	4.1
PT2S-F3	125	120.4	3.7
PT2S-F4	125	123.6	1.1

*One tendon was lost after grouting

Figure 3.16 - Slabs before and after prestressing

The ducts in the prestressed slab specimens were filled using an unsanded, Portland cement-based, expanding shrinkage-compensated post-tensioning grout (KPM Industries 2011). The grout mix, which contains silica fume, is specified to have high early strength gain, high fluidity, excellent cohesive properties, low permeability and a net expansion of 3-5% to ensure

maximum bond. Due to the relatively small quantity of grout required, freshly mixed grout was gravity fed into the ducts using tubes rather than by pumping. The grout fluidity was measured using a flow cone test (ASTM C939) for three different water-cement ratios as shown in Figure 3.17. Increasing the water-cement ratio from 0.35 to 0.40 resulted in an average decrease in flow time of almost 50%. Further increasing the water content resulted in only a marginal decrease in flow time. The recommended flow time according to the Post-Tensioning Institute (PTI) is 11-30 seconds (Post-Tensioning Institute 2003); the efflux time of the grout with a water-cement ratio of 0.35 slightly exceeded this range, while both grout mixes with a water-cement ratio of at least 0.40 had satisfactory flow times.

Conversely, the compressive strength of the grout having a water-cement ratio of 0.40 was almost equal to the mix with a water-cement ratio of 0.35 after 14 days, and only slightly lower after 7 days, as determined by mortar cube tests (ASTM C942) and shown in Figure 3.18. Increasing the water content further resulted in a significant decrease in early strength gain.

Based on these tests, the grout used for the post-tensioned slabs was prepared with a water-cement ratio of 0.40 in order to ensure an optimal balance of good flowability without significantly affecting its hardened mechanical properties. The grouted prestressed slabs were allowed to cure for a minimum of 7 days before testing. In order to verify these results, sets of mortar cubes were twice cast in parallel with the grouting of prestressed slabs; after 7 days the average compressive strengths of the mortar cube sets were 48.9 MPa and 47.8 MPa; these values are well above the PTI specifications of 21 MPa and 35 MPa at 7 and 28 days, respectively.

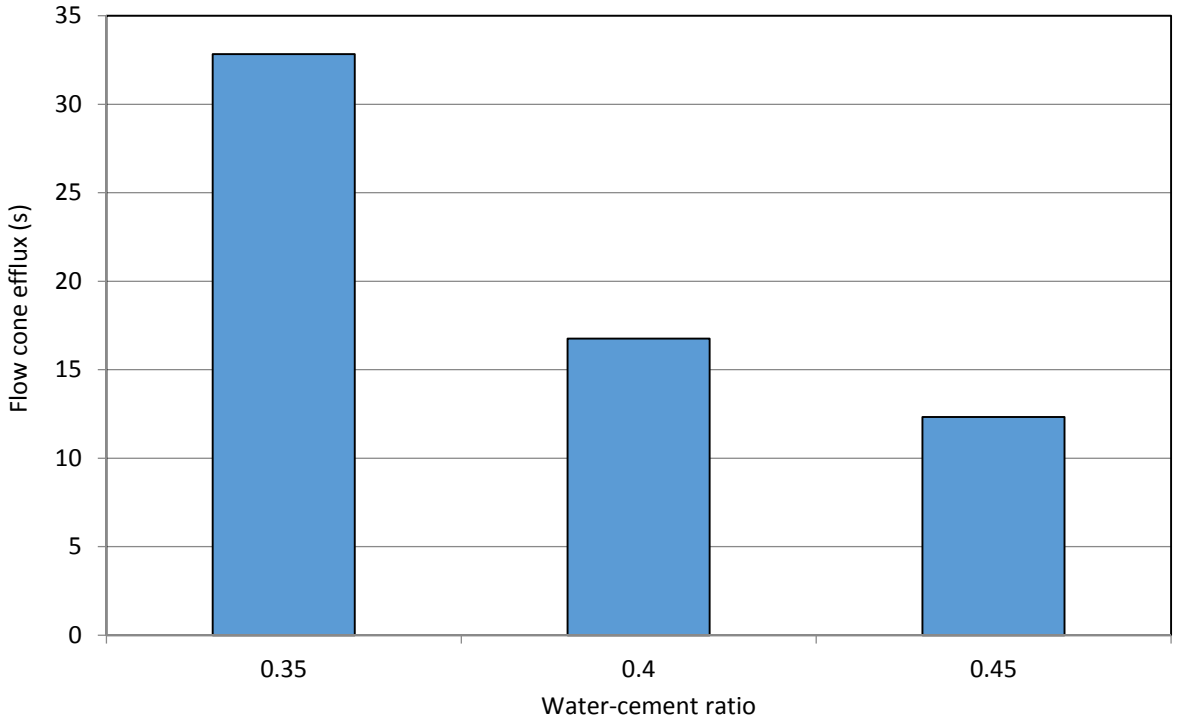

Figure 3.17 - Grout fluidity

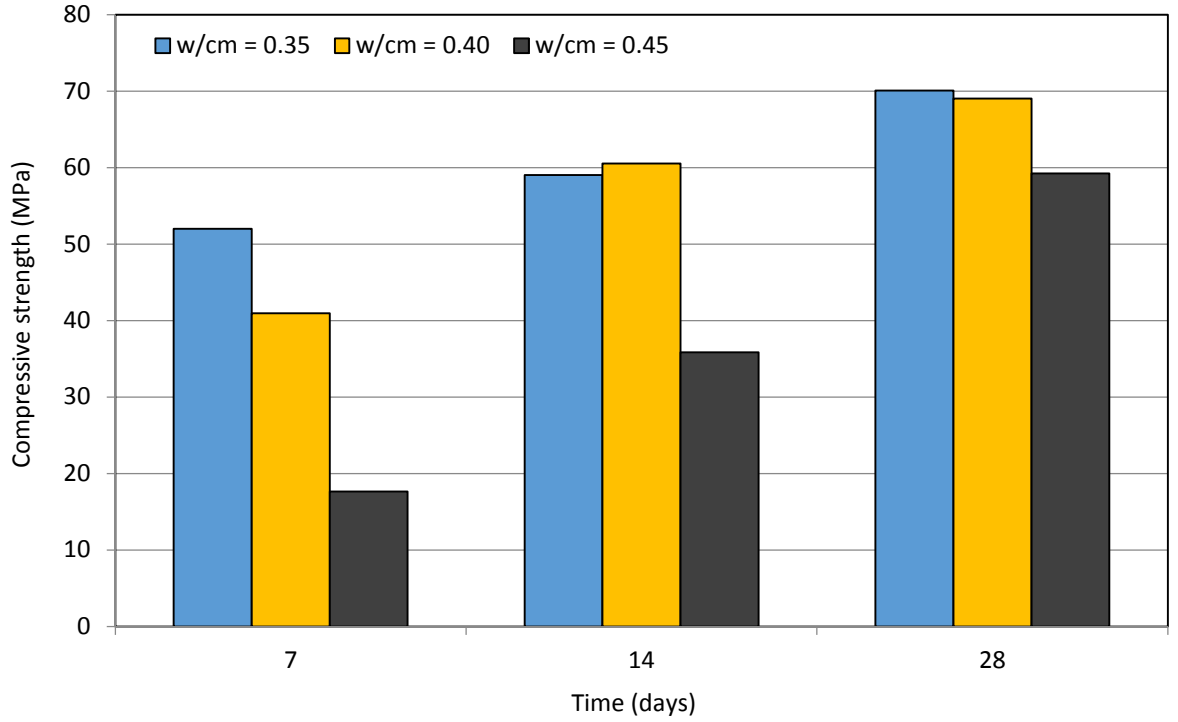

Figure 3.18 - Grout strength gain

3.5 Test Setup & Procedure

The full-scale slabs were tested under four-point bending on simple supports as shown in Figure 3.19. The centreline to centreline span between supports was 4500 mm with a shear span of 1750 mm. Meanwhile, the shorter slabs in Phase II were tested under three-point bending with a shear span of 1 m as shown in Figure 3.20. Instrumentation for each test setup is shown schematically in Figures 3.21 and 3.22.

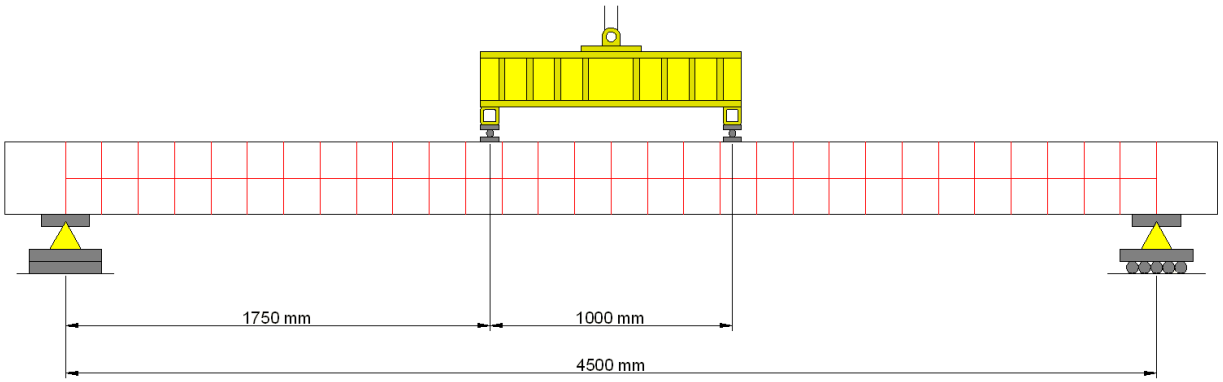

a)

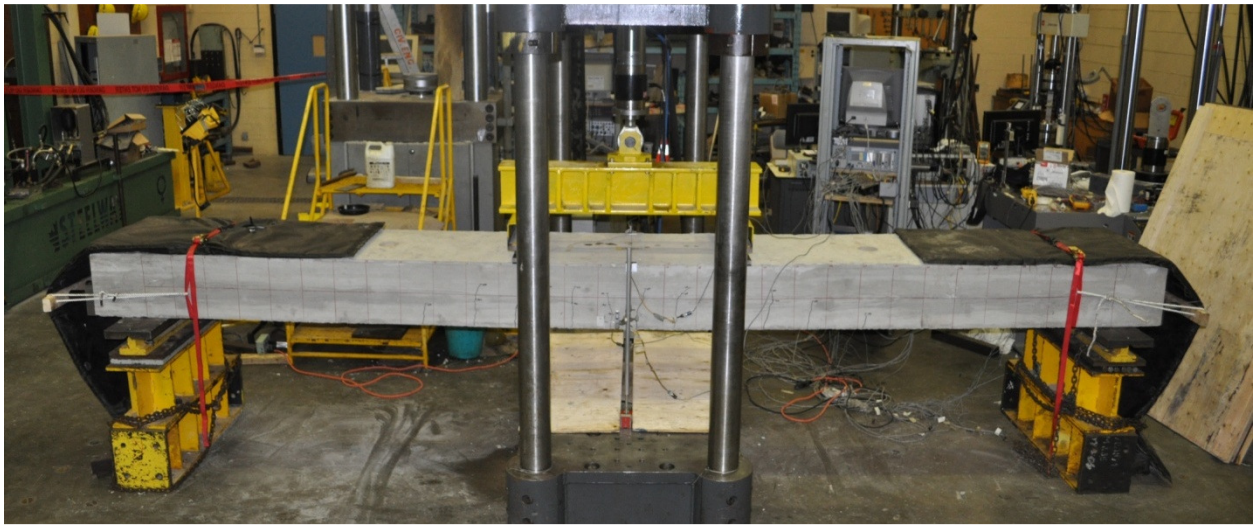

b)

Figure 3.19 - a) Test setup schematic and b) SCC slab strip in test frame

Figure 3.20 - Test setup for Phase II

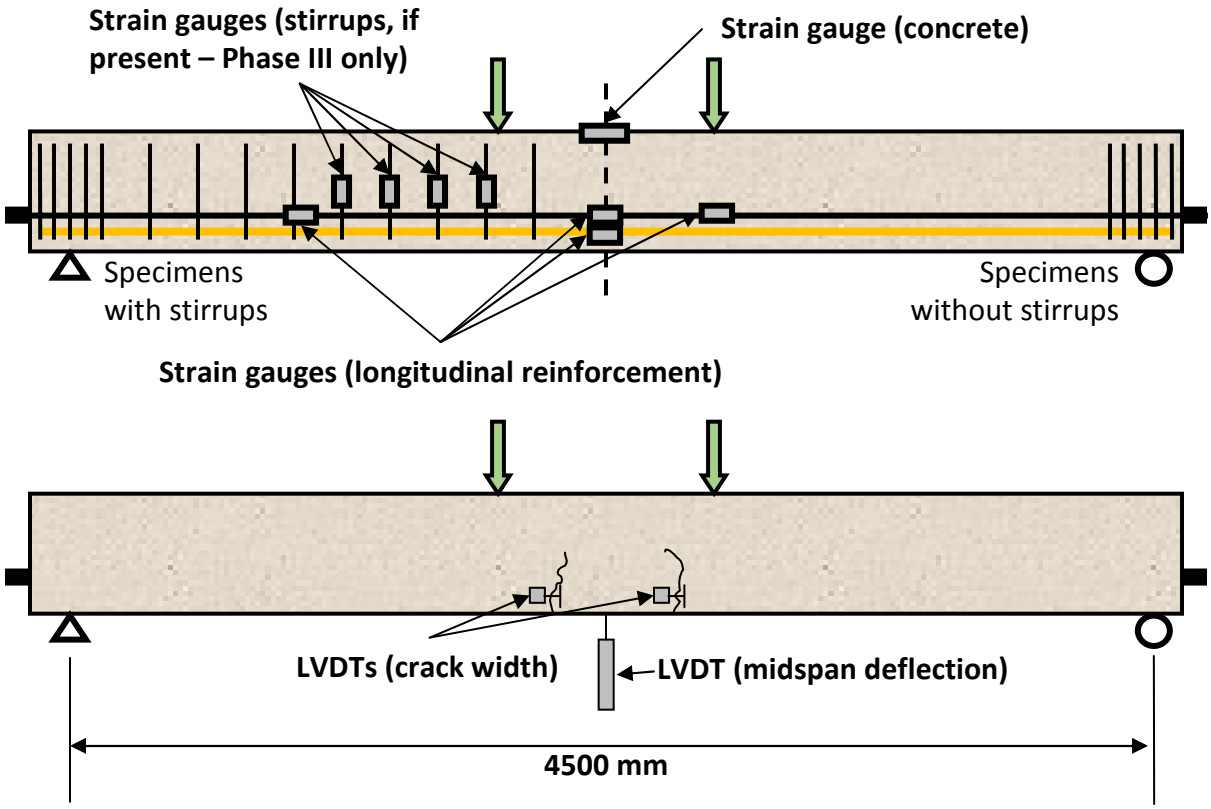

Figure 3.21 - Instrumentation for full-scale specimens

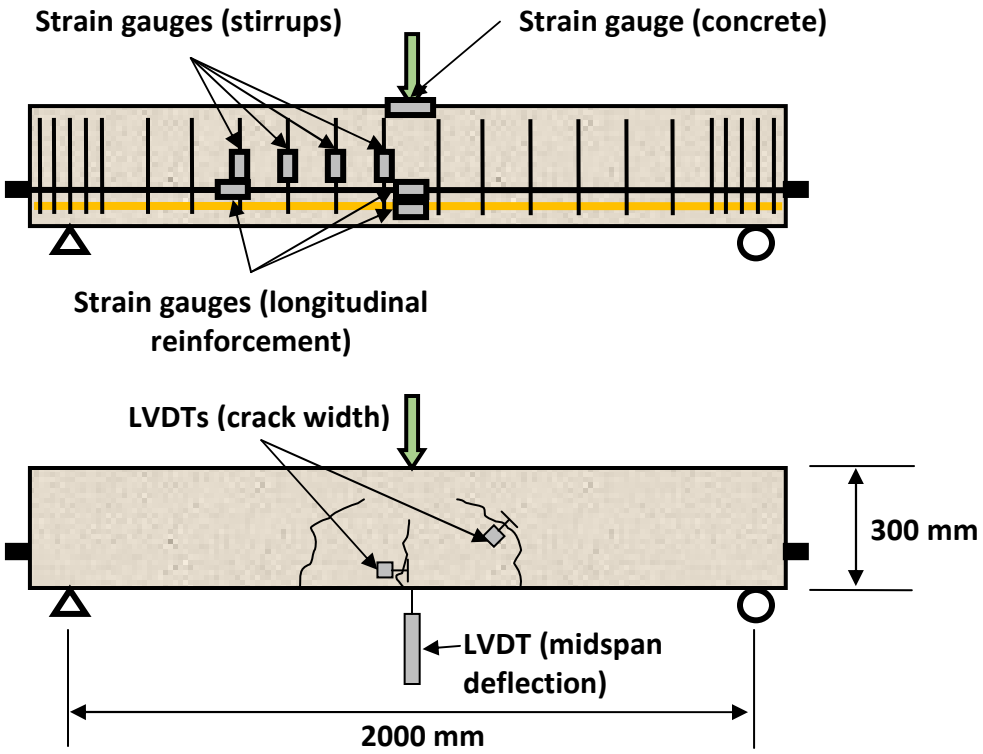

Figure 3.22 - Instrumentation for reduced-length specimens

Midspan deflection was measured with two linear variable displacement transducers (LVDTs) with a range of 150 mm on either side of the slab. Electrical resistance strain gauges made by Tokyo Sokki Kenkyujo Co., Ltd. were also bonded to the reinforcing bars and the top concrete surface at midspan. Strain gauges on the prestressing tendons measured strains at midspan, under one of the load points and at the center of one of the shear spans. For Phases II and III, strain gauges were also used to measure strains in the shear reinforcement at mid-depth for four consecutive stirrups near one of the loading points. Strain gauges having a length of 5 mm were mounted on the reinforcement and 60 mm long gauges were mounted on the concrete surface. The test was paused after the formation of flexural cracks, and initial crack width readings of the widest two cracks were taken using a handheld microscope while subsequent

crack width growth was measured using high accuracy LVDTs with a 5 mm range mounted across the crack; for Phase II slabs, one flexural crack and one shear crack were monitored using an LVDT mounted at an inclination of 45° to the horizontal at the mid-depth of the slab. The tests were paused periodically to mark the location of newly formed cracks.

The load was applied at a rate of 1.2 mm per minute until failure was reached under displacement control for the full-scale monotonic tests compared to 1.0 mm per minute for the shorter slabs, which displayed smaller deflections at ultimate. Cyclic loading was applied under load control at a frequency of 0.45-1.5 Hz, depending on the range of midspan deflection induced for the given load range; the slabs tested at high load ranges had to be tested at relatively low frequencies in order for the hydraulic actuator to accommodate the large deflections induced at the maximum load level. These constraints were exacerbated by a breakdown of the hydraulic pump during the testing program which limited oil flow through the hydraulic equipment; however, all of the testing rates are considered to be fairly low such that heat dissipation is not expected to be a concern and thus, the results are relatively insensitive to the test frequency used.

Fatigue load ranges were selected to cause failure within 1 million cycles in order to complete each test within a three week period, such that the experimental program could be completed within a reasonable time frame. Specimens which did not fail within 1 million cycles were subjected to additional cycles at a higher load range until fatigue failure occurred. The first cycle of each fatigue test was conducted at the same rate as the monotonic tests to assess the initial cycle response and to crack the specimen; after reaching the peak load, the slabs were unloaded and LVDTs were applied at the primary crack locations before beginning the fatigue

test. Load cycles were sinusoidal with a constant minimum load level of 10 kN and the maximum load selected to provide the desired load range. The applied cyclic load ranges and experimental results are discussed in Chapter 4.

Chapter 4 - Experimental Results

4.1 General

Fifty-seven full-scale and reduced-length slab strips were constructed and tested in four-point or three-point bending under monotonic and fatigue loading. The tests were divided into 3 phases as described in Chapter 3; Phase I and Phase III were comprised of full-scale specimens with various reinforcement configurations under static and fatigue loading, respectively, while Phase II consisted of 25 specimens having a reduced span length to investigate the contribution of various shear reinforcement types to the overall shear capacity under both static and cyclic loading conditions.

4.2 Phase I – Full-Scale Monotonic Testing

4.2.1 Test Results

The flexural performance of the 16 slabs tested under monotonic load in Phase I are summarized in Tables 4.1 and 4.2 for serviceability and ultimate limit states, respectively. The observed cracking loads for the various slabs are compared in Figure 4.1, while the midspan deflection, maximum crack width and maximum GFRP strain at the service load condition are shown in Figures 4.2 to 4.4. The service moment was taken as 41.6 kN·m, corresponding to the live load moment induced on a 600 mm wide strip by the CHBDC CL-625 design truck with dynamic load allowance for a 2-lane bridge having a span of 4.5 m and total width of 8 m (see Chapter 8).

Table 4.1 - Summary of test results at service loads

Slab	Cracking load (kN)	Midspan deflection (mm)	Maximum crack width (mm)	Midspan strain in primary reinforcement (με)	Midspan strain in primary reinforcement (%ε_y or %ε_{frpu})
S	25.2	6.0	0.11	950	47.5
G1	20.3	22.4	0.40	3656	25.8[a]
G1-ST	23.3	19.4	0.37	3358	23.7
G2	25.2	11.2	0.17	1559	11.0
G2-ST	31.8	7.9	0.18	1020	7.2
PT2a	34.8	12.5	0.12	2012	14.2
PT2	58.6	2.2	--[b]	128	0.9
PT2-ST	50.6	4.7	--[b]	694	4.9
PT2-G	59.9	2.0	--[b]	142	1.0
PT2-S	65.4	1.8	--[b]	99	0.7
PT2-S45	73.2	2.5	--[b]	142	1.0
PT2-U	60.1	2.4	--[b]	113	0.8
PT4	80.1	2.5	--[b]	128	0.9
PT4-G	82.1	2.1	--[b]	99	0.7[c]
PT4-U	98.9	1.7	--[b]	142	1.0
PT4-P	69.7	2.1	--[b]	113	0.8

a – Exceeds CHBDC limit

b – Uncracked at service

c – Interpolated from measured CFRP and top concrete strains, assuming linear strain variation

Table 4.2 - Summary of test results at ultimate loads

Slab	Peak load (kN)	Residual strength (kN)	Midspan deflection[a] (mm)	Δ_2/Δ_1[b]	Reinforcement strain at midspan[a] (με)	Reinforcement strain at midspan[a] (%ε_{frpu})	Concrete strain at midspan[a] (με)	Failure mode[c]
S	167	-	176	1.0	--[d]	--[d]	3644	FY → FC
G1	166	-	110	1.0	11563	81.6	2331	DT
G1-ST	213	-	122	1.0	14383	101.5	2286	FR
G2	220	-	74	1.0	7595	53.6	2027	DT
G2-ST	339	-	108	1.0	10032	70.8	2741	FC
PT2a	172	-	127	1.0	11605	81.9	2800	DT
PT2	206	-	71	1.0	7935	56.0	2041	DT
PT2-ST	285	246	115	1.1	13532	95.5	3325	FT → FR
PT2-G	249	212	86	1.5	9140	64.5	2636	FT → FR
PT2-S	248	206	89	1.5	9168	64.7	2391	FT → FR
PT2-S45	237	204	79	1.5	9891	69.8	2118	FT → FR
PT2-U	182	-	102	1.0	10018	70.7	2219	DT
PT-4	295	225	80	1.5	7992	56.4	2832	FT → DT
PT4-G	312	270	78	1.9	5980	42.2[e]	2832	FT → FC
PT4-U	242	166	100	1.2	10372	73.2	2597	FT → DT
PT4-P	255	-	69	1.0	7227	51.0	2149	DT

a - At peak load

b - Ratio of peak deflection to deflection at peak load

c - FY = Flexural failure induced by yielding of reinforcement; FC = Flexural failure induced by concrete crushing; DT = Diagonal tension failure; FT = Flexural failure induced by tendon rupture; FR = Flexural failure induced by rupture of reinforcing bars

d - Strain gauge malfunctioned

e - Calculated from measured CFRP and top concrete strains, assuming linear strain variation

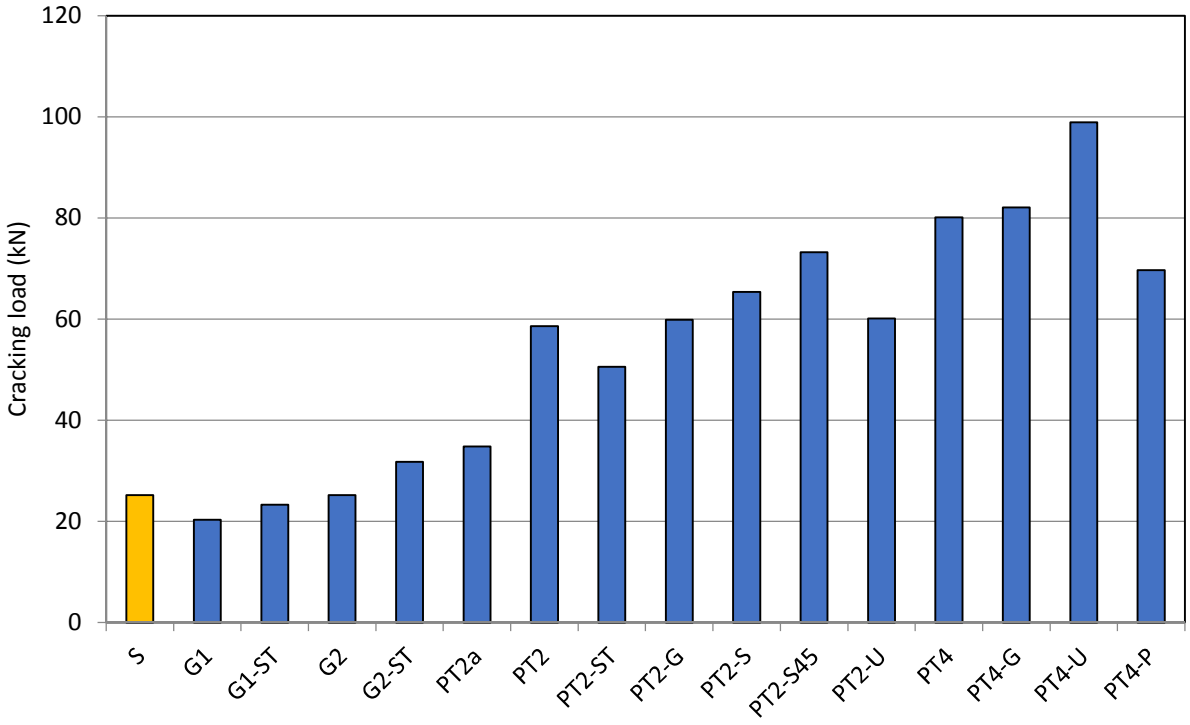

Figure 4.1 - Cracking loads of Phase I slabs

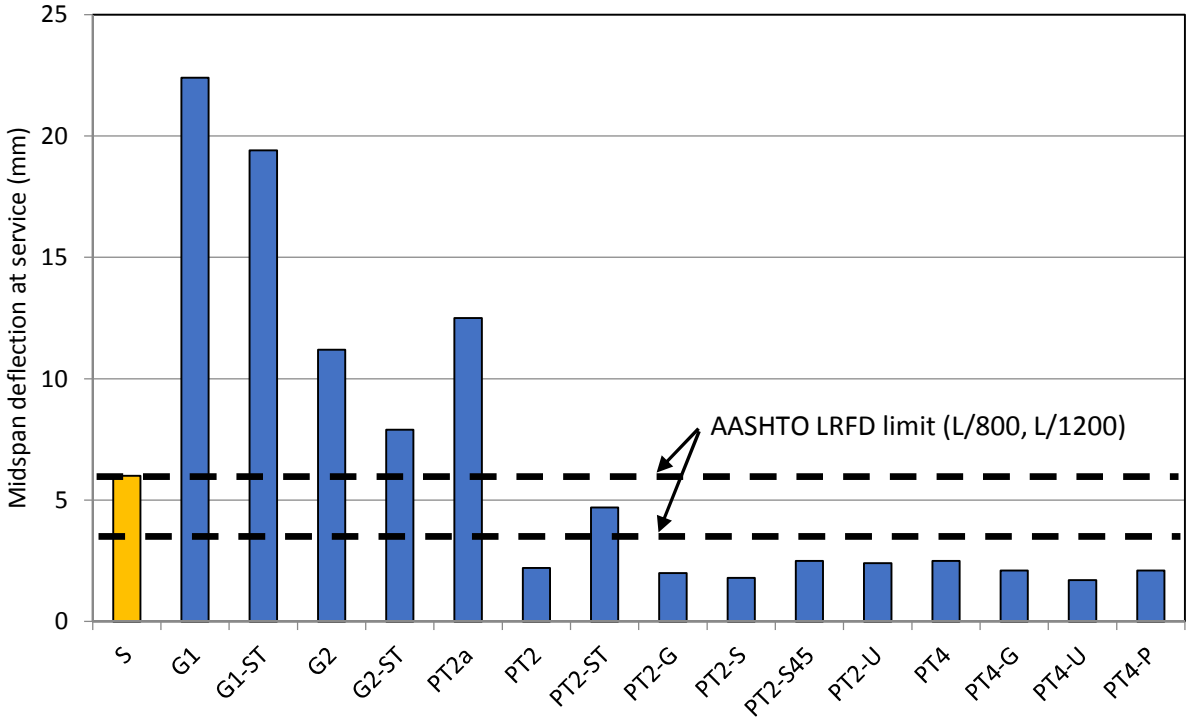

Figure 4.2 - Midspan deflection at service for Phase I slabs

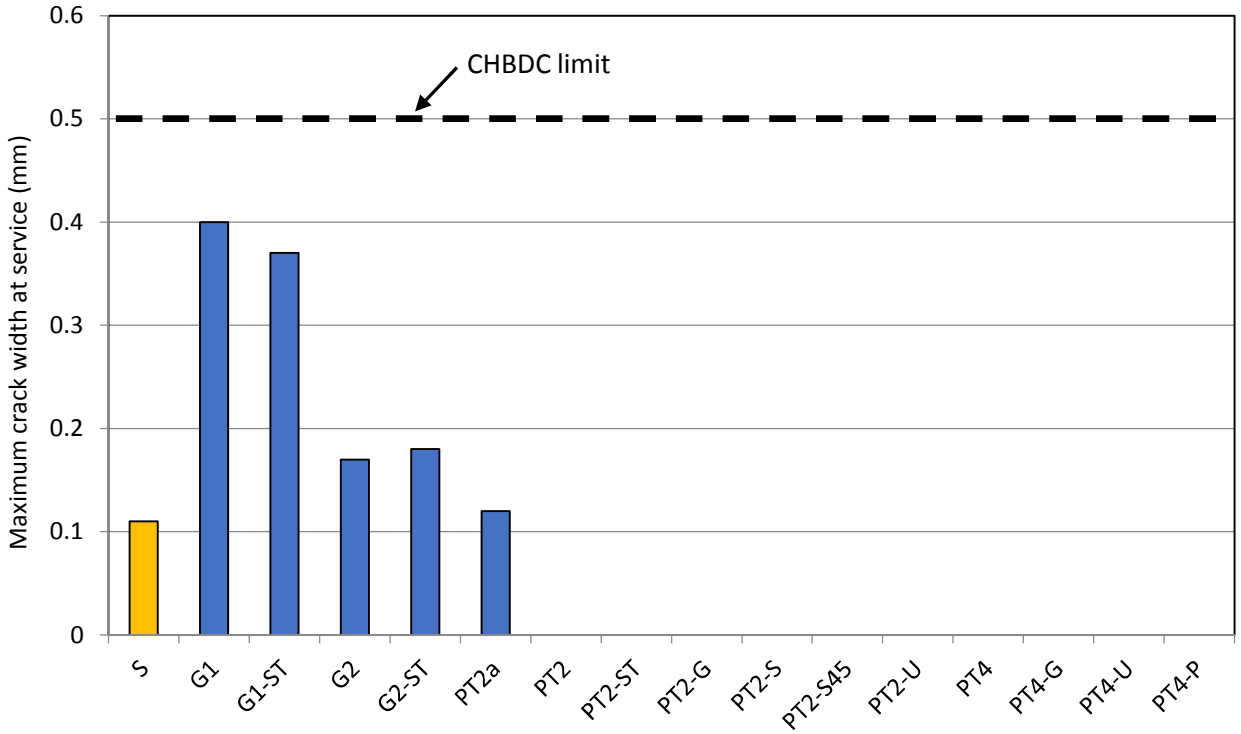

Figure 4.3 - Maximum crack widths at service for Phase I slabs

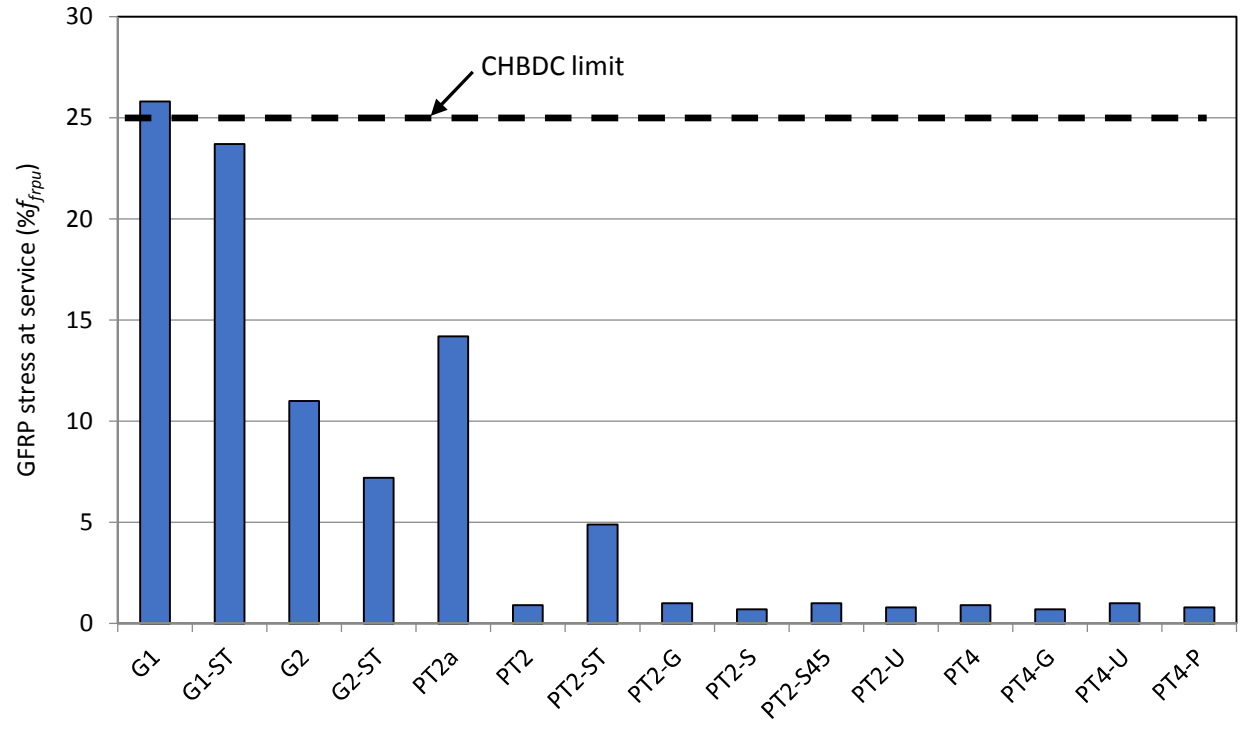

Figure 4.4 – Maximum GFRP stress at service for Phase I slabs

4.2.2 Serviceability Limit State

Several observations can be drawn from the observed flexural behaviour of the tested slabs. As shown in Figure 4.1, the cracking load increased with increasing prestressing level, as expected, and the deflections, crack widths and GFRP stresses at the service load each decreased with increasing prestressing force (Figures 4.2 to 4.4). The load-deflection responses of the slabs are shown in Figure 4.5, while the load-crack width responses and load-GFRP strain responses are shown in Appendix A and Appendix B, respectively.

The CHBDC does not specify a deflection limit for slab-type bridges; however the AASHTO LRFD Bridge Design Guide Specifications for GFRP-Reinforced Concrete Bridge Decks and Traffic Railings (AASHTO 2009) uses deflection limits ranging from $L/800$ to $L/1200$ depending on whether the bridge sustains vehicular traffic only or vehicular and pedestrian traffic. Although the service loads based on AASHTO LRFD design differ slightly from the CHBDC (refer to Chapter 8), the AASHTO LRFD limits are shown in Figure 4.2 for a relative comparison of the serviceability of the various tested slabs. None of the non-prestressed slabs met the AASHTO LRFD deflection limits, although all of the full-depth prestressed slabs had acceptable values of deflection at service. Crack widths were below the CHBDC limit of 0.5 mm for aggressive environments in all cases (Figure 4.3), although slab G1 slightly exceeded the GFRP service stress limit of $0.25f_{frpu}$ (Figure 4.4).

Figure 4.5a shows the effect of reinforcement type and reinforcement ratio on load-deflection response. As expected, the steel-reinforced control slab showed the highest post-cracking stiffness of the non-prestressed slabs. Although slabs G2 and G2-ST contained twice the area of

tensile reinforcement, the total axial stiffness ($A_{frp}E_{frp}$) of the reinforcement was still lower than for the steel-reinforced control slab (A_sE_s). This resulted in higher midspan deflections and crack widths at service compared to the control specimen (see Table 4.1). Slabs G1 and G1-ST showed the lowest post-cracking stiffness of the tested slabs, with more than three times the midspan deflection and crack widths at service as the control specimen.

Figure 4.5b shows the effect of increasing the number of prestressing tendons on the load-deflection response of the GFRP-reinforced slabs. Three distinct pairs of lines can be seen, corresponding to slabs with zero, two or four post-tensioned CFRP tendons. Prestressed slabs displayed both a higher cracking load and greater post-cracking stiffness than similar non-prestressed slabs. Slab PT4-G displayed the highest capacity of all the slabs (except for G2-ST) and the greatest post-cracking stiffness of the GFRP-reinforced slabs. Prestressed slabs displayed improved serviceability compared with the control slab, as very small deflections were observed at the given service load (typically about one-third those of the control slab). All of the prestressed slabs (except PT2a) were uncracked at service and easily met all serviceability criteria.

The effect of the prestressing force and the number of prestressing tendons on the load-deflection response is shown in Figure 4.5c. Specimen PT4-P had twice the number of CFRP tendons as slab PT2, but approximately the same total prestressing force. The cracking load of slab PT4-P was between that of slabs PT2 and PT4, with a similar post-cracking stiffness as slab PT4. Specimens PT4-P and PT2 both failed in shear at loads corresponding to approximately the same midspan deflection. Doubling the prestressing force per tendon (ie. slab PT4 vs. slab PT4-P) had almost no effect on the serviceability of the slabs, but changed the mode of failure from

shear to CFRP tendon rupture and displayed significant residual strength accompanied by additional post-peak deflection. The larger prestressing force did increase the cracking moment, but as the prestressed slabs were uncracked at service in all cases, the overall effect on serviceability was minimal.

As shown in Figure 4.5d, slab PT2a performed similarly to the non-prestressed slab G1 in terms of load-deflection behaviour, while showing reduced crack widths at service indicating that adding prestressed CFRP reinforcement can be used to efficiently increase the span-to-depth ratio of slab bridges reinforced with GFRP. Since many slab bridges have spans greater than 5 m, adding prestressed CFRP tendons becomes increasingly attractive for longer spans where GFRP reinforcement alone would lead to excessive deflections, crack widths and reinforcement strains.

Figures 4.5e and 4.5f show the effect of bond on the load-deflection response of the post-tensioned slabs. Unfortunately, both specimens prestressed with unbonded tendons, PT2-U and PT4-U, suffered the premature rupture of one tendon during loading. These occurrences are easily identified by the sharp load drops in Figures 4.5e and 4.5f; these premature ruptures are believed to be a result of stress concentrations induced by friction within the post-tensioning ducts (discussed in more detail later). Leaving the tendons unbonded had little effect on the serviceability performance of the prestressed slabs.

The load-deflection response of the post-tensioned slabs with various shear reinforcement types are compared in Figure 4.5g. All four slabs had a very similar response up to the initial

rupture of the CFRP tendons; the type of shear reinforcement used had no perceptible effect on serviceability.

Figure 4.6 shows typical plots of the increase in CFRP strain along the length of the member with increasing load. The strain values shown are the incremental values due to loading beyond the initial prestressing strain. Prior to the formation of the first flexural cracks between the load points, the incremental strain in the reinforcement was negligible. After the formation of flexural cracks within the constant moment region, the midspan strain increased rapidly, with similar increases observed under the loading points. The strains in the shear span remained small until flexural cracking extended into the shear span, thus transferring most of the internal tensile stresses to the reinforcement at crack locations. As the load was increased further, vertical cracks appeared along the entire length of the beam and the reinforcement strains showed a relatively linear variation between the supports and the loading points. Measured strains in the bonded reinforcement depend on the proximity of the strain gauges to cracks induced in the member; if a flexural crack passes near the strain gauge the recorded strains will be higher than if the crack is some distance away from the strain gauge where the surrounding concrete contributes to load resistance.

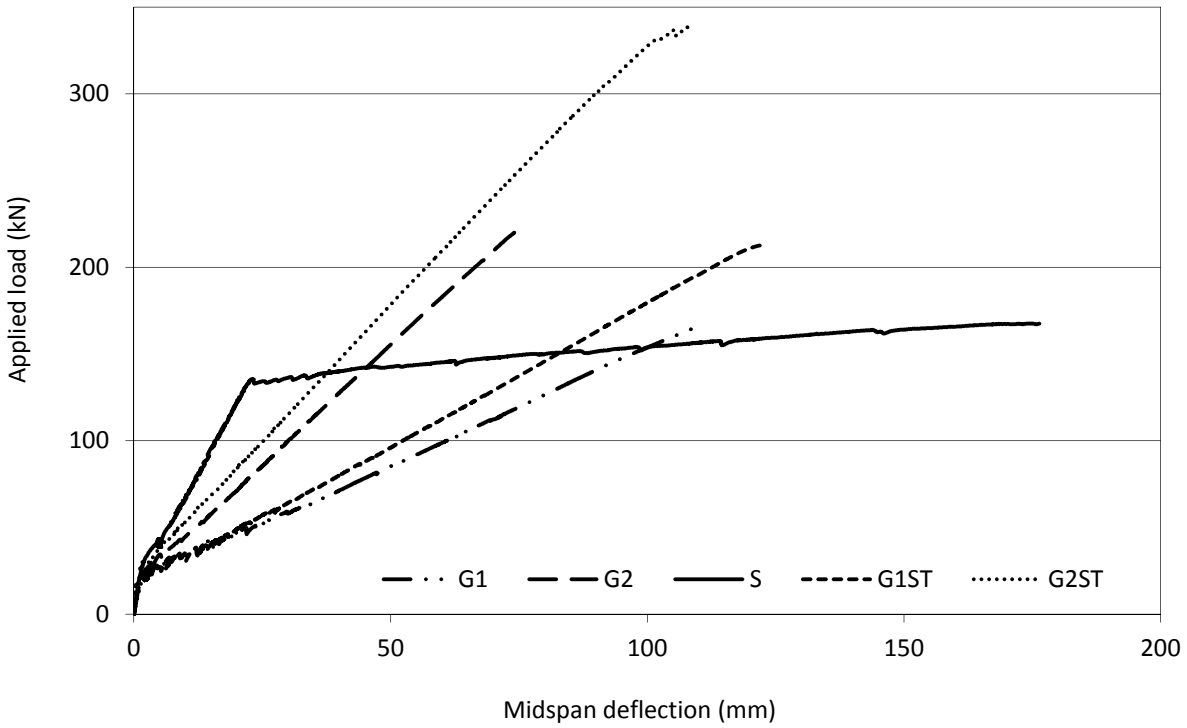

a) Effect of reinforcement type and ratio

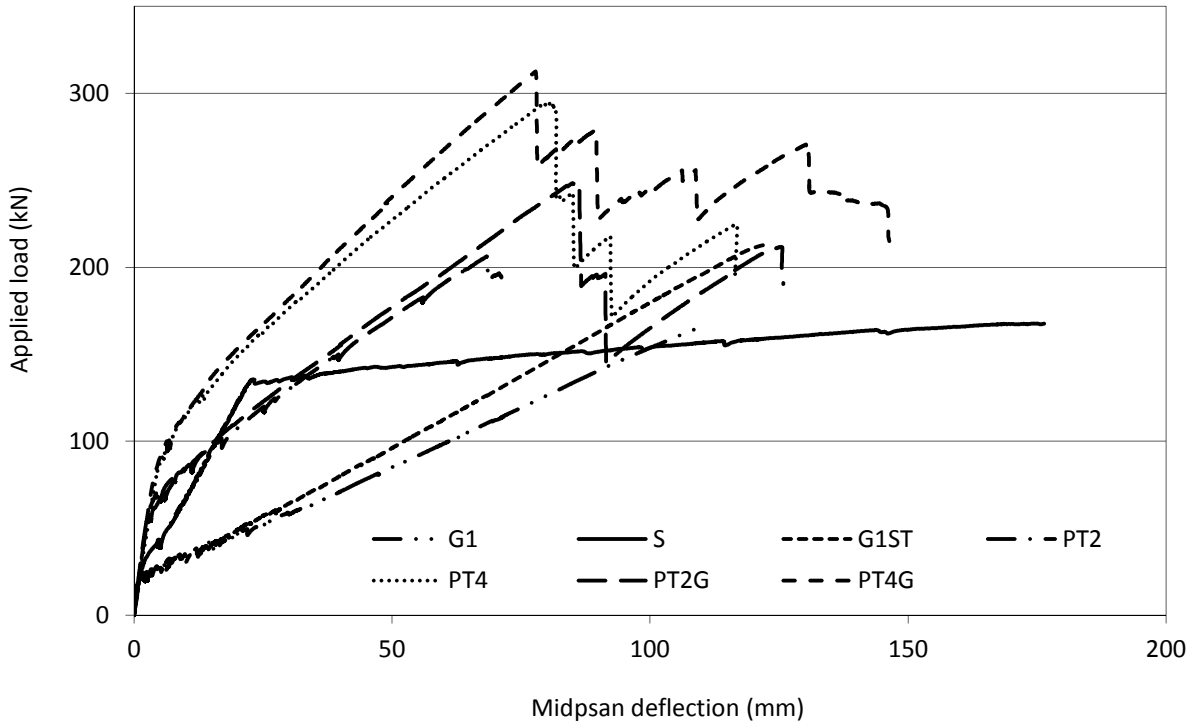

b) Effect of prestressing – 0, 2 or 4 post-tensioned tendons

Figure 4.5 – Load-deflection response

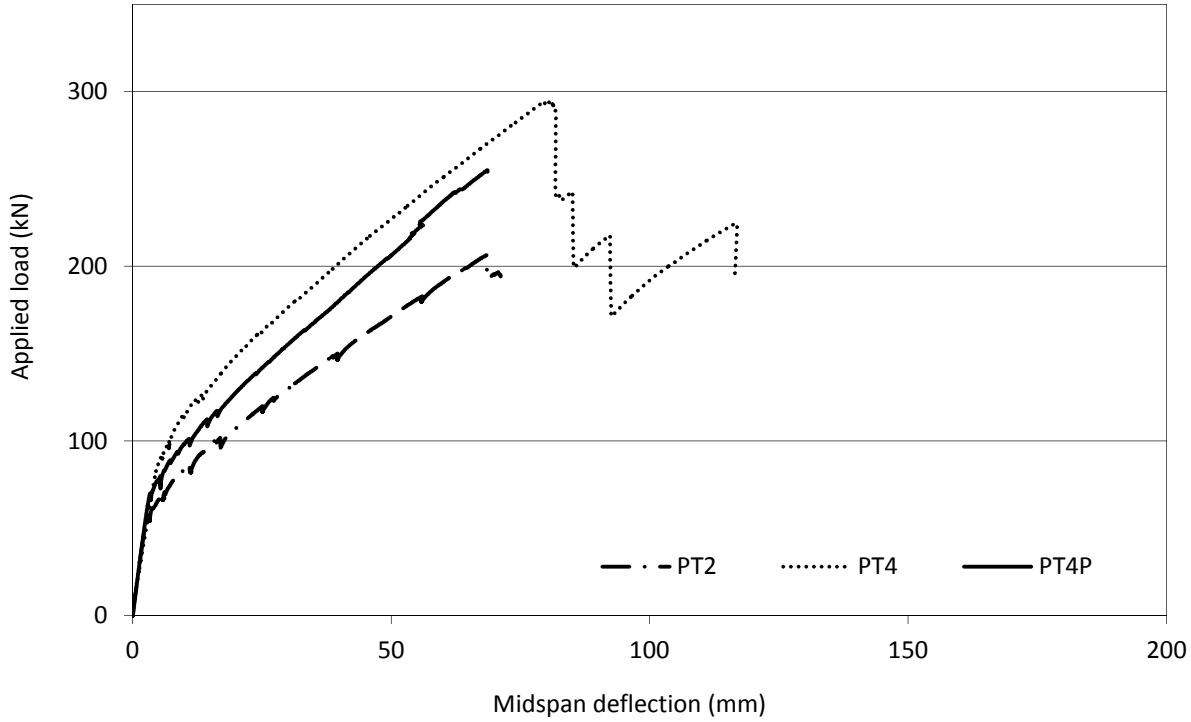

c) Effect of prestressing – 2 or 4 post-tensioned tendons with 30% or 55% prestress

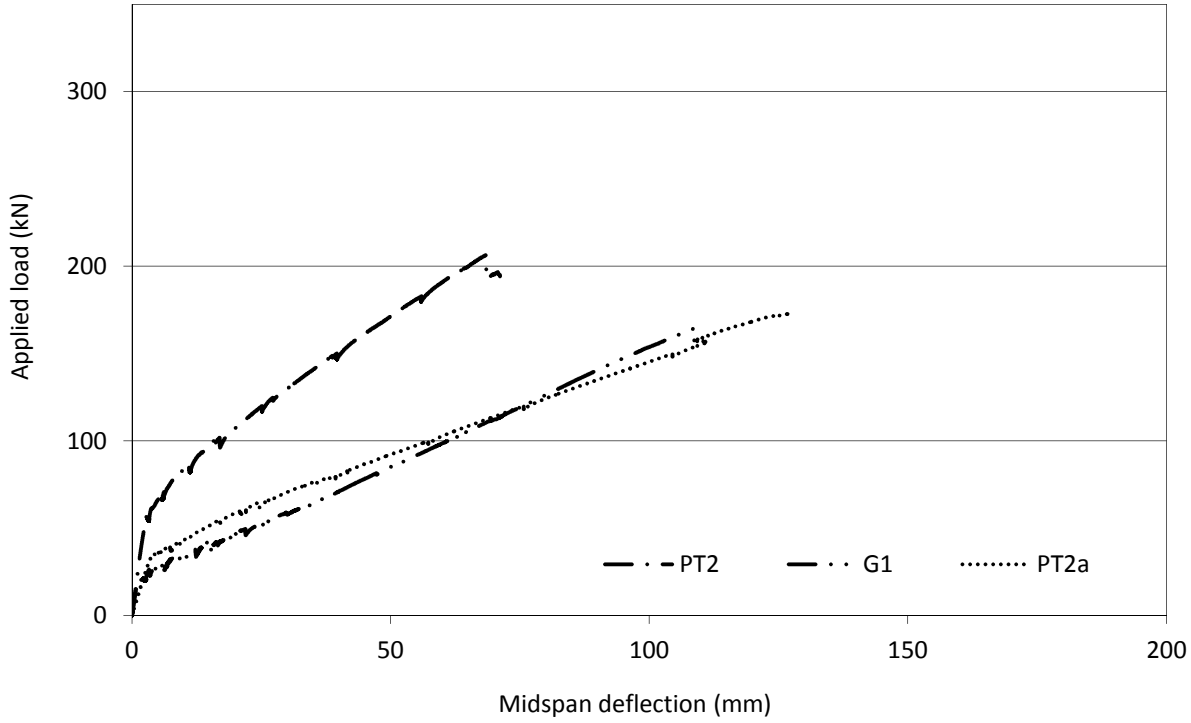

d) Effect of cross-section depth

Figure 4.5 – Load-deflection response (continued)

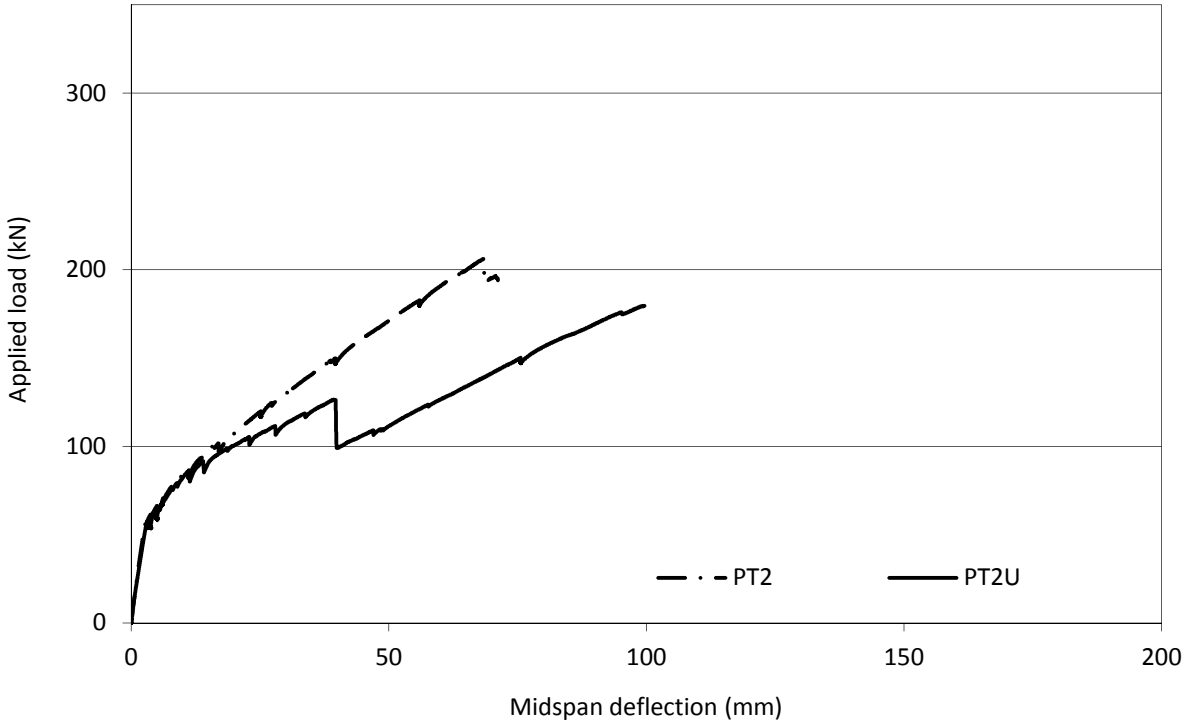

e) Bonded vs. unbonded – 2 post-tensioned tendons

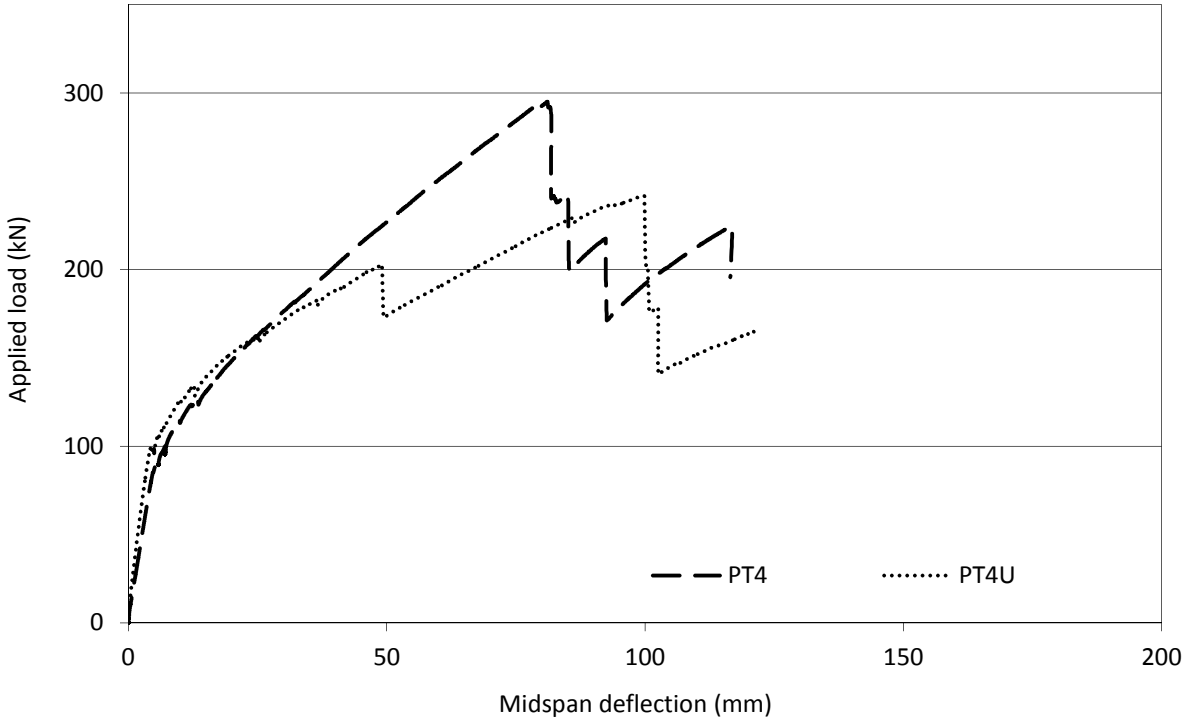

f) Bonded vs. unbonded – 4 post-tensioned tendons

Figure 4.5 – Load-deflection response (continued)

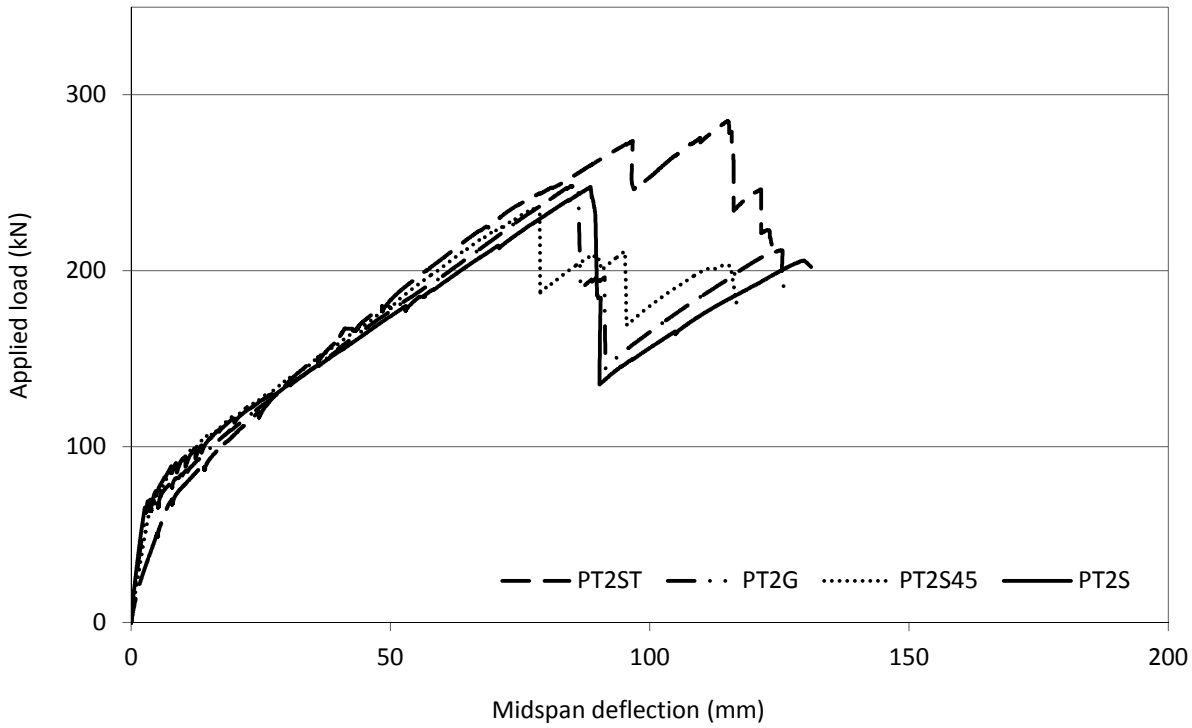

g) Shear-reinforced prestressed slabs

Figure 4.5 - Load-deflection response (continued)

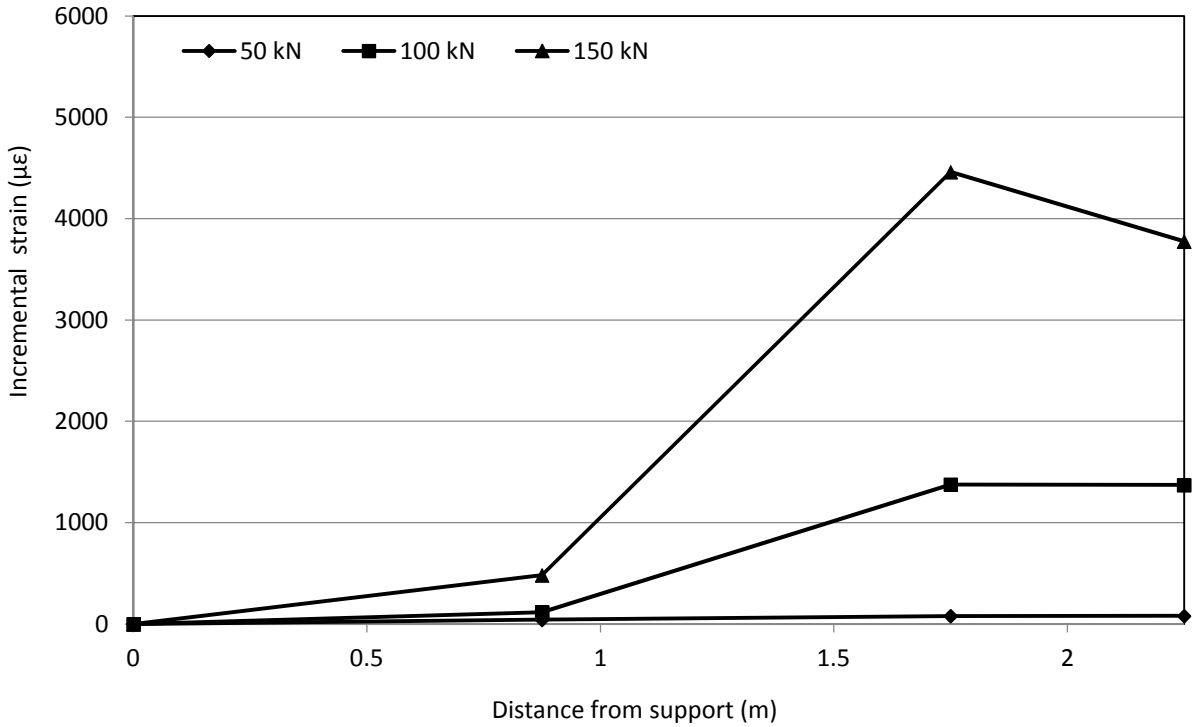

a) Slab PT2-G

Figure 4.6 – CFRP strain profiles

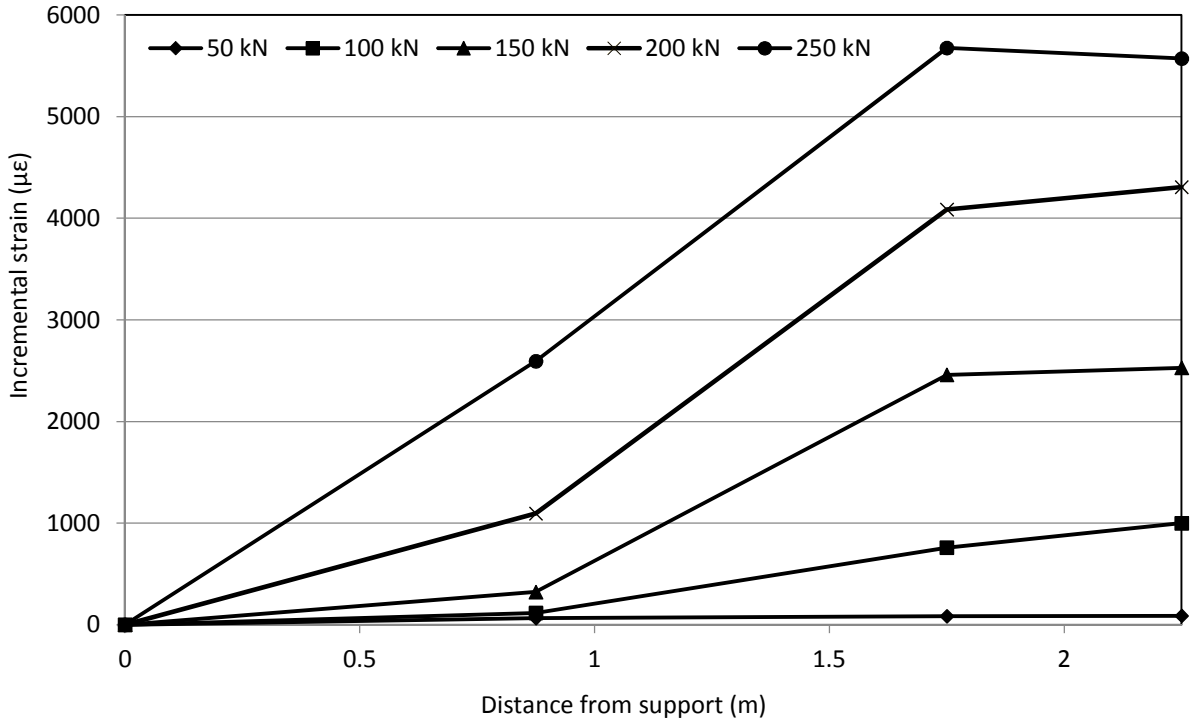

b) Slab PT4-P

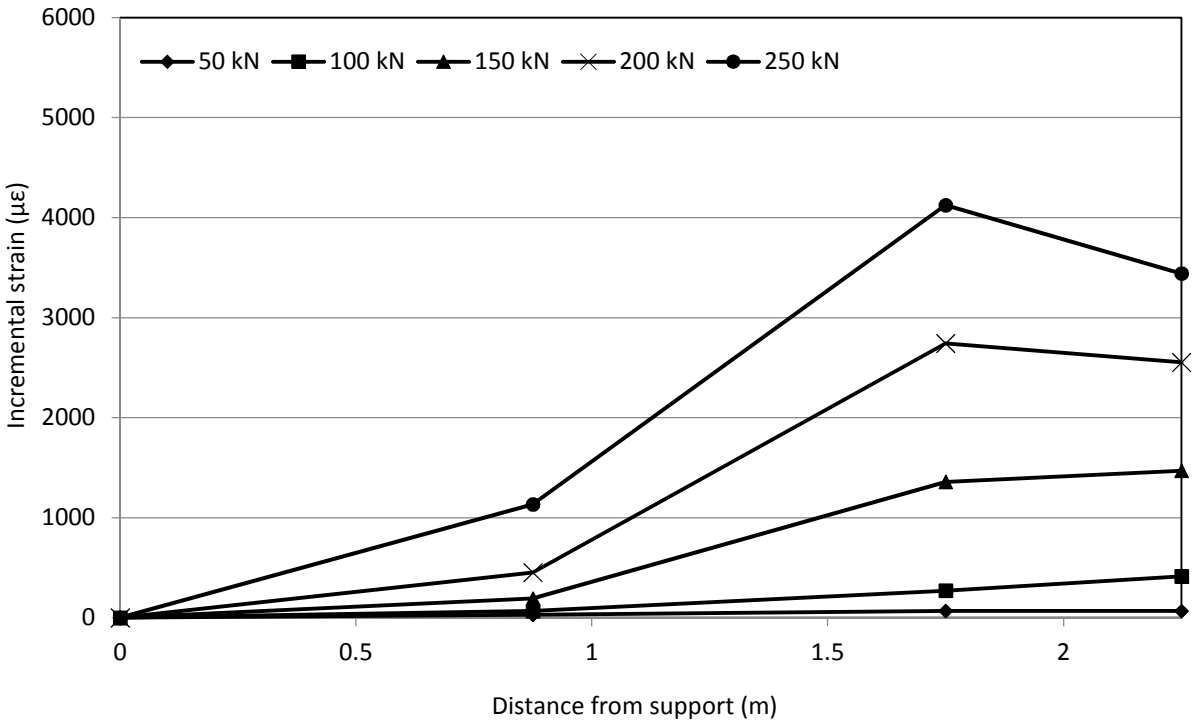

c) Slab PT4-G

Figure 4.6 - CFRP strain profiles (continued)

4.2.3 Ultimate Limit State

Failure loads for the tested slabs and the corresponding midspan deflections at ultimate are listed in Table 4.2 and compared in Figures 4.7 and 4.8. All of the GFRP-RC slabs easily surpassed the CHBDC factored design moment and shear values for a 600 mm wide strip of 70.7 kN·m and 92.3 kN, respectively (see Chapter 8), with the exception of slabs G1 and PT2a, which failed at applied shear values of 83 kN and 87 kN, respectively. It should be noted, however, that with the given test setup the critical location for shear occurs near one of the load points where both shear and moment are at their maximum values; conversely, in most cases, the critical section for shear in a real bridge will be near one of the supports where the moment is small and hence the shear resistance will be higher.

Some of the slabs continued to carry load following rupture of the CFRP tendons, as the passive GFRP reinforcement was still well below its ultimate strain capacity; therefore the residual strength (post-peak) values and corresponding maximum deflection values are also listed in Table 4.2 and shown in Figures 4.7 and 4.8. The strains in the GFRP reinforcement and top concrete fibre at midspan corresponding to the peak load are also listed in Table 4.2 as an indication of whether the specimens were nearing the capacity of the GFRP reinforcement or the concrete for the case of the slabs which failed in shear or by CFRP rupture. The complete load-strain responses of the slabs are shown in Appendix B.

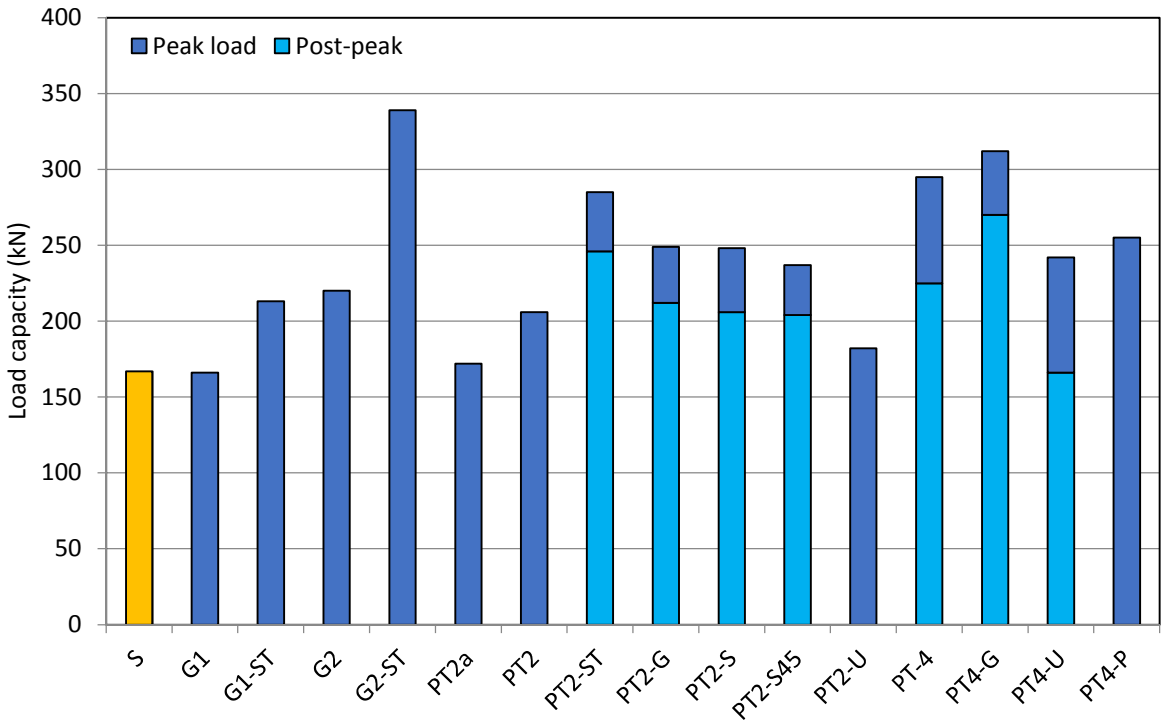

Figure 4.7 - Load capacities of Phase I slabs

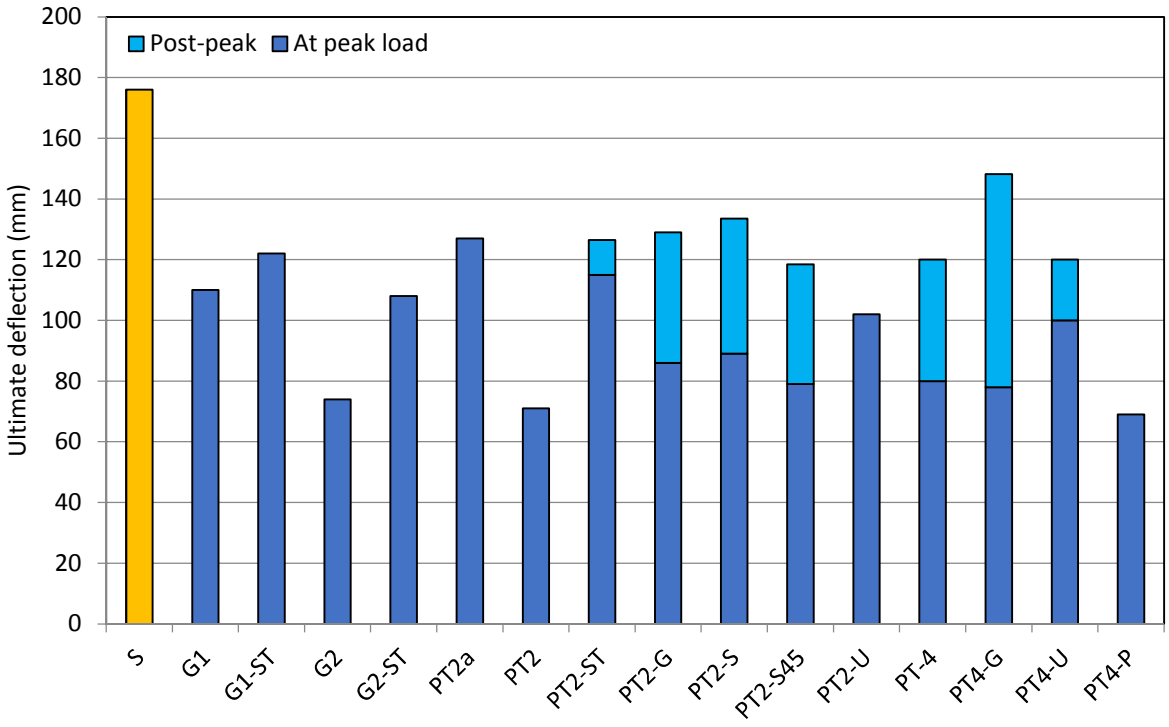

Figure 4.8 - Ultimate deflections for Phase I slabs

All of the tested slabs (except for slabs S and G1-ST) reached their peak loads prior to reaching the assumed rupture strain of the GFRP or crushing strain of the concrete. In most cases this was because the peak load corresponded either to shear failure or to the rupture of the CFRP bars. Slab G2-ST, however, failed due to crushing of the concrete in compression at a strain twenty percent lower than the assumed crushing strain of 0.0035. This can likely be attributed to the fact that the strain gauge was located at the midspan of the member, whereas crushing generally initiated at the location of the concentrated loads, namely the load points.

As expected, failure loads for the GFRP-reinforced slabs were equal to or higher than that of the steel-reinforced control slab. Doubling the reinforcement ratio significantly increased the ultimate capacity, especially when shear failure was precluded with the use of steel stirrups. Slab PT2a had a similar load capacity compared to the control slab despite the reduction in depth as a result of the addition of two CFRP post-tensioned tendons. All of the remaining prestressed slabs (except for slab PT2-U) showed significantly higher peak loads than the control slab, as the ultimate load-carrying capacity increased with an increasing number of CFRP tendons, particularly when shear failure was avoided. Slabs PT4 and PT4-G reached ultimate loads that were almost double that of the steel-reinforced control slab, S.

The addition of transverse shear reinforcement was effective in increasing the load capacities and ultimate deflections of the prestressed GFRP-RC slabs. Slab PT2-G, for example, had a load capacity approximately 25% higher than slab PT2 (which contained no shear reinforcement) and sustained almost twice the ultimate deflection. Prestressed slabs with shear reinforcement showed residual strengths after tendon rupture ranging from 83.1% to 86.5% of the observed

peak load. In some cases the post-peak deflection was significant, up to 190% of the deflection at the peak load (specimen PT4-G).

Slab PT2-U, on the other hand, failed in shear at a load which was only slightly higher than the peak load observed for the control slab, S. This is primarily due to the fact that one of the unbonded tendons failed prematurely such that only one active tendon was contributing to load resistance at ultimate. This is discussed further in the following section.

The safety of a conventionally reinforced section is often assessed in terms of its ductility, which is a measure of the energy that can be absorbed by a member through plastic deformation. Steel-reinforced sections typically display high ductility provided that the member is under-reinforced to allow yielding of the tensile reinforcement. Ductility is an important safety consideration for structural design because it provides visual warning prior to collapse, allowing users the chance to evacuate the structure. Due to the linear elastic nature of FRP materials, the concept of ductility is not valid for FRP-RC sections. Therefore, the safety of FRP-reinforced members must be assessed in other ways, such as deformability.

Deformability is a concept that is used to describe the degree of deformation that a flexural member can sustain prior to failure. A variety of deformability factors have been proposed which relate the deflection of a member at ultimate to the deflection at cracking or under service conditions. The CHBDC includes an overall performance factor, J, given by Equation 4.1, with the service condition taken as the point when the maximum concrete compressive strain reaches a value of 0.001. Rectangular sections are considered to have sufficient deformability when $J \geq 4.0$.

Eq. 4.1 $$J = \frac{M_{ult}\psi_{ult}}{M_c\psi_c}$$

Where, *J* is an overall performance factor, M_{ult} and M_c are the applied moment at ultimate and at service, respectively, and ψ_{ult} and ψ_c are the curvatures at ultimate and at service, respectively.

Table 4.3 and Figure 4.9 give the CHBDC overall performance factors for the 15 GFRP-reinforced slabs tested under monotonic load. In the cases where the maximum deformation did not correspond to the peak load, two deformability factors are given: *J* at the peak load and *J* at the maximum deflection. In all cases the deformability factors were satisfactory (except for specimen PT2-U which suffered a premature tendon rupture) and in some cases exceptional (especially specimen PT2a which had a reduced cross-section depth). In most cases, the overall performance factor at the maximum value of midspan deflection exceeded that at the peak load; this is expected as the additional deflection serves as a visual warning that failure is imminent and thus provides additional safety to the users. In general, the addition of shear reinforcement improved the deformability of the slabs, with the exception of specimen G1-ST; since the curvature values at ultimate and at service were calculated using measured strains, this unexpected result is likely attributed to lower-than-expected concrete strains measured in specimen G1-ST (ie. the moment and curvature corresponding to a concrete compressive strain of 0.001 were considerably higher for slab G1-ST than for slab G1).

Table 4.3 - CHBDC overall performance factors for GFRP-RC slabs

Slab	*J* at peak load	*J* at maximum deflection
G1	5.71	--
G1-ST	5.35	--
G2	4.07	--
G2-ST	6.40	--
PT2a	25.69	--
PT2	4.04	--
PT2-ST	12.74	11.56
PT2-G	6.24	7.13
PT2-S	5.74	7.01
PT2-S45	4.68	5.79
PT2-U	3.66	--
PT4	4.90	4.96
PT4-G	7.07	9.02
PT4-U	6.06	4.44
PT4-P	4.55	--

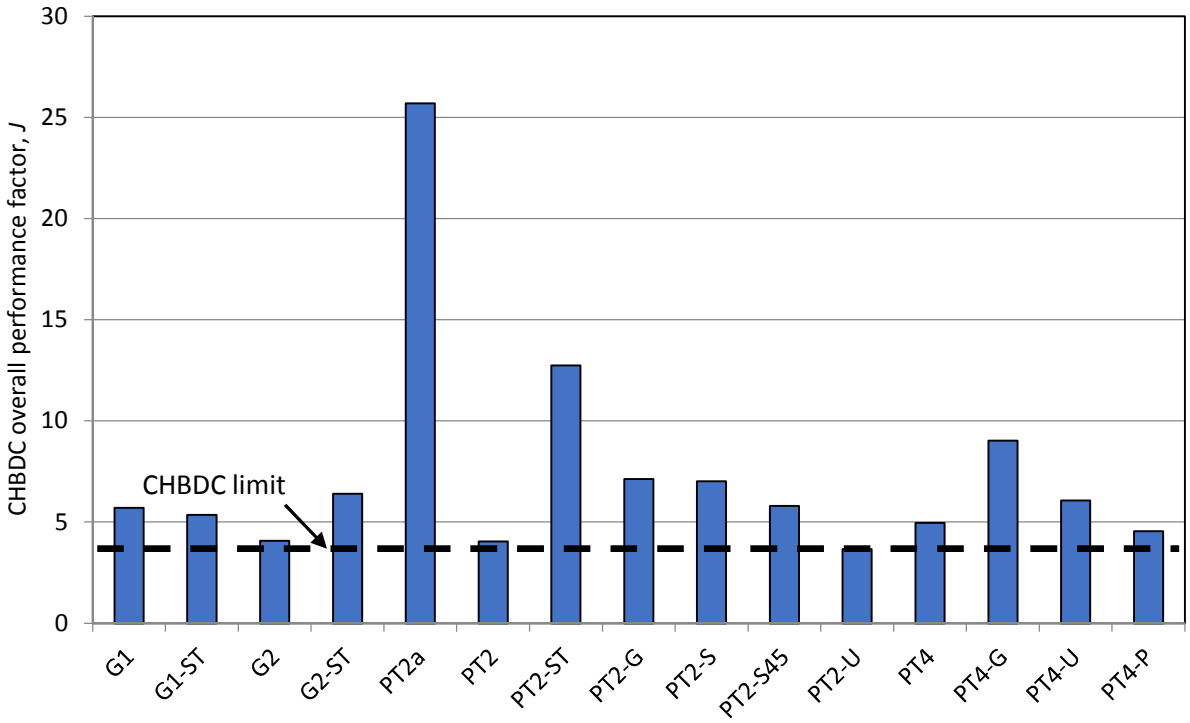

Figure 4.9 - CHBDC overall performance factors for Phase I slabs

4.2.4 Mode of Failure

Crack patterns at failure are shown in Figure 4.10. Initial cracks typically formed within the pure bending region between the load points. As the load was increased, vertical flexural cracking extended into the shear span and the slabs subsequently displayed inclined shear cracking upon further loading. The spacing of the primary cracks was similar for all slabs, corresponding to approximately half of the slab depth as expected, although some slabs showed a greater tendency for inclined cracking and secondary cracks than others. For example, slab PT2-S45 developed fewer inclined cracks than slab PT2-S which may be a result of an improved ability to arrest diagonal cracks due to the inclination of the shear reinforcement. On the other hand, slab PT2-S45 developed a large number of secondary flexural cracks. The prestressed slabs tended to develop flatter inclined cracks as a result of the change in the orientation of principal stresses caused by the axial compression introduced in the concrete section through prestressing.

The failure modes of the 16 slabs tested in Phase I are listed in Table 4.2. The steel-reinforced control specimen displayed significant ductility due to yielding of the tensile reinforcement prior to crushing of the concrete in the compression zone. Conversely, all GFRP-reinforced slabs containing zero or two prestressing tendons without transverse shear reinforcement failed in diagonal tension, a sudden and brittle failure mode which is undesirable and typically avoided whenever possible (Figure 4.11a). Specimen PT4-P, which had a similar total prestressing force as the specimens with two CFRP tendons also failed in brittle shear.

In the cases where shear reinforcement was provided, irrespective of the reinforcement type, the shear capacity of the member was sufficiently enhanced to induce a flexural mode of failure (Figure 4.11b). For the non-prestressed GFRP-reinforced slabs, flexural failure was induced by tensile rupture of the reinforcement or concrete crushing corresponding to the under-reinforced (G1-ST) and over-reinforced (G2-ST) sections, respectively. For the specimens post-tensioned with two CFRP tendons, flexural failure was initiated by CFRP tendon rupture, followed by additional deformation until the onset of GFRP rupture was reached at some residual strength level; following rupture of the prestressing tendons the slabs were essentially behaving as non-prestressed members with a reduced stiffness.

The remaining slabs post-tensioned with four CFRP tendons failed initially in flexure by tendon rupture, even those which did not contain any shear reinforcement. This behaviour confirmed the hypothesis that sufficient prestressing force could preclude shear failure of the GFRP-RC slabs. Specimens PT4 and PT4-U subsequently failed in diagonal tension following some post-peak deformation, while the shear-reinforced slab, PT4-G, ultimately failed by crushing of the concrete in the compression zone.

Both specimens containing unbonded tendons suffered the premature rupture of one CFRP tendon, evidenced by the sharp load drops in Figures 4.5e and 4.5f. Considering that at the peak load only three tendons were contributing to the load resistance for slab PT4-U, unbonding the tendons would seem to have only a small effect on the ultimate flexural capacity, provided premature tendon rupture could be avoided. However at both prestressing levels the peak load occurred at a greater corresponding deflection than for the case of bonded tendons, resulting in an improved deformability at the peak load.

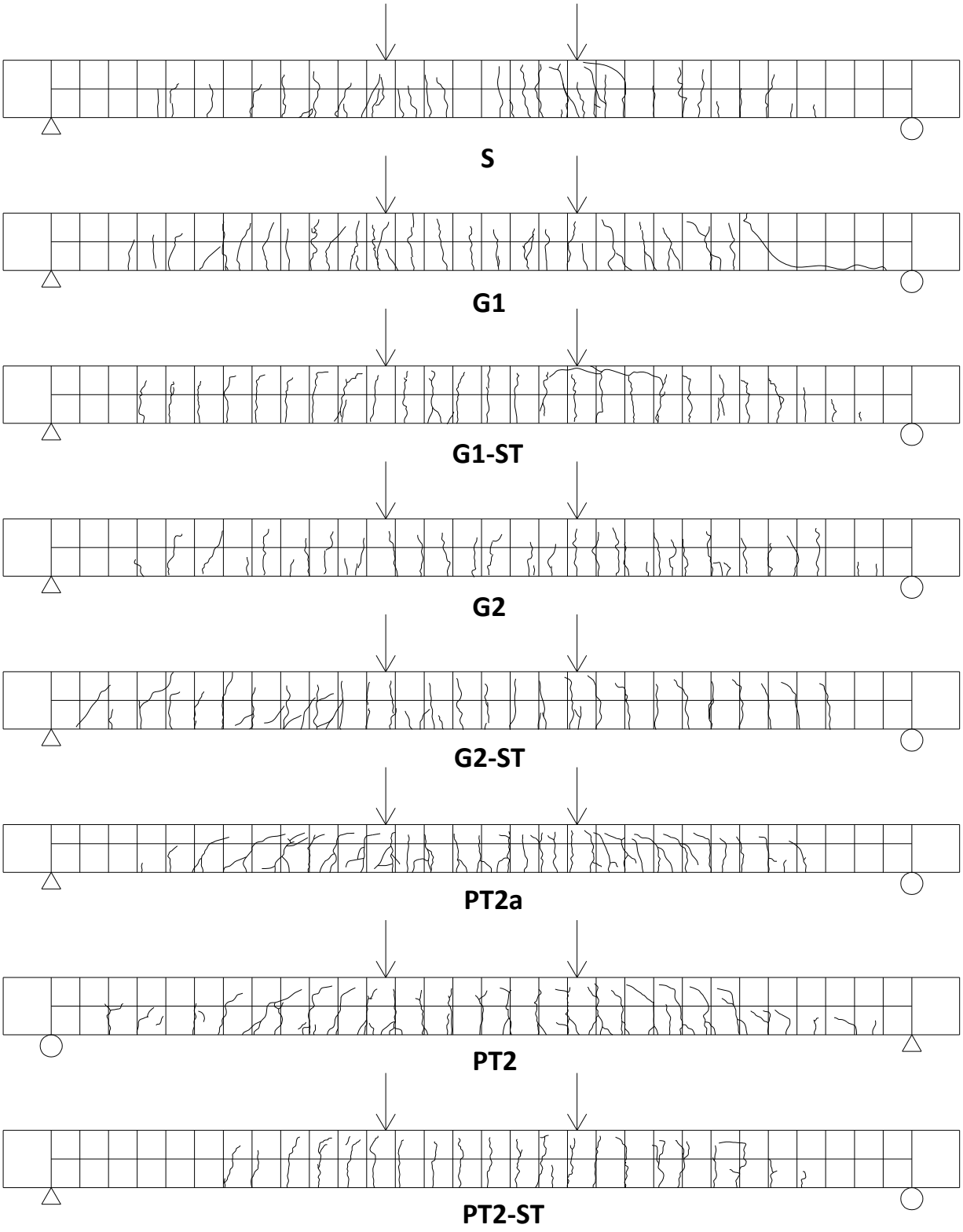

Figure 4.10 - Crack patterns at failure

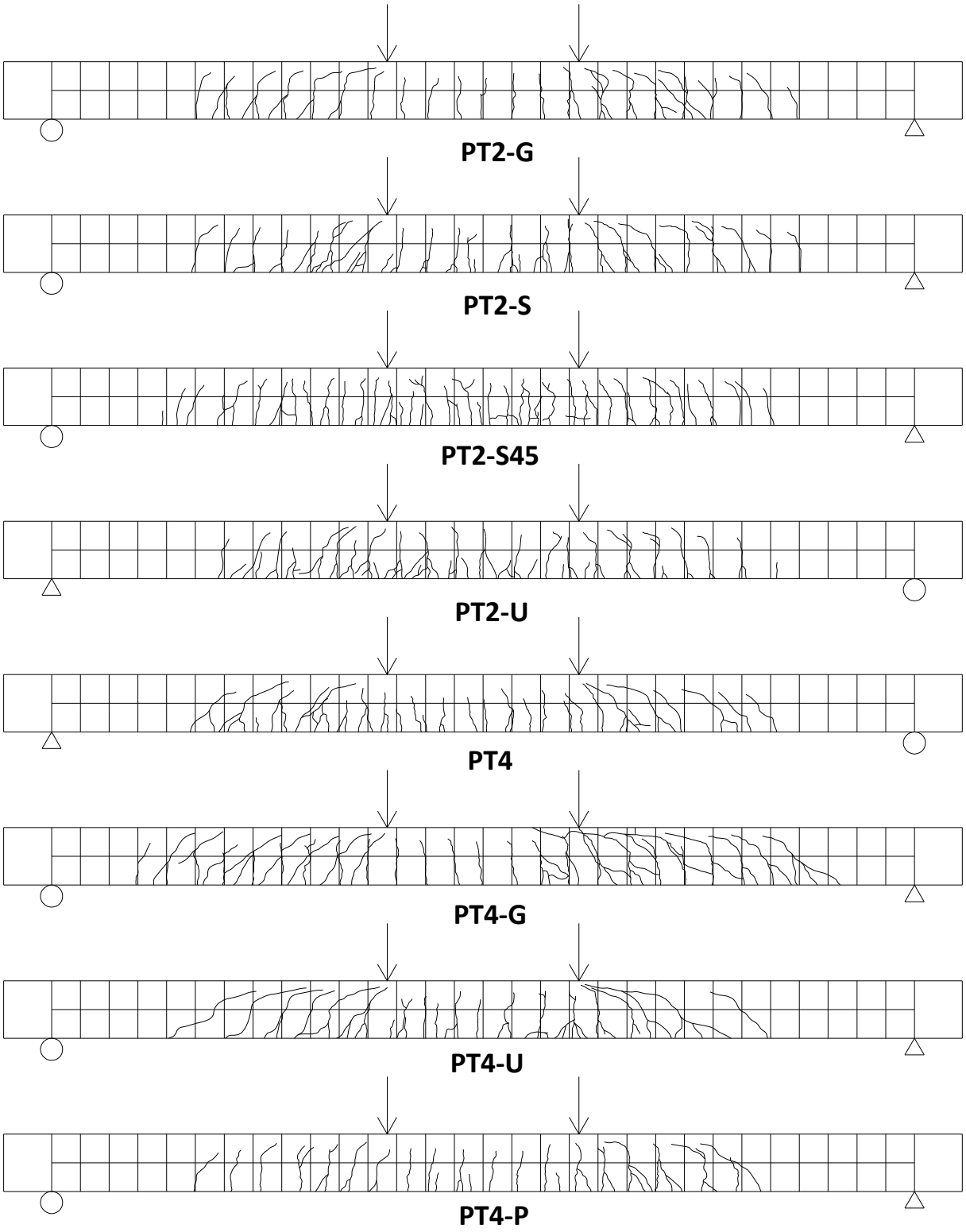

Figure 4.10 - Crack patterns at failure (continued)

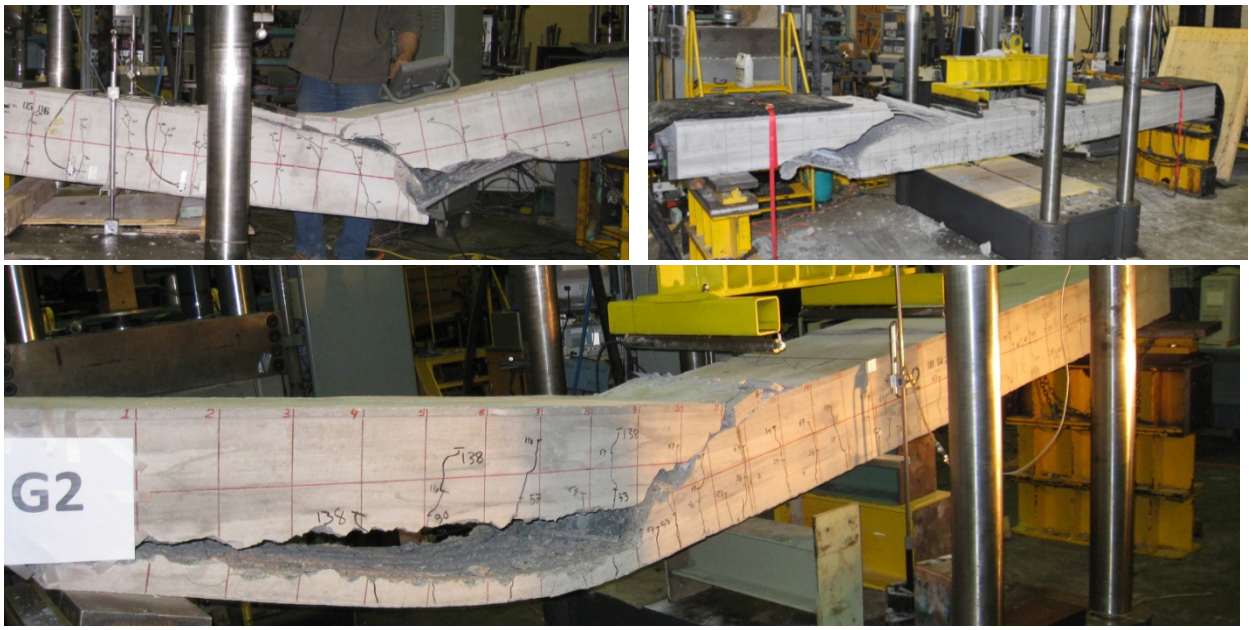

a)

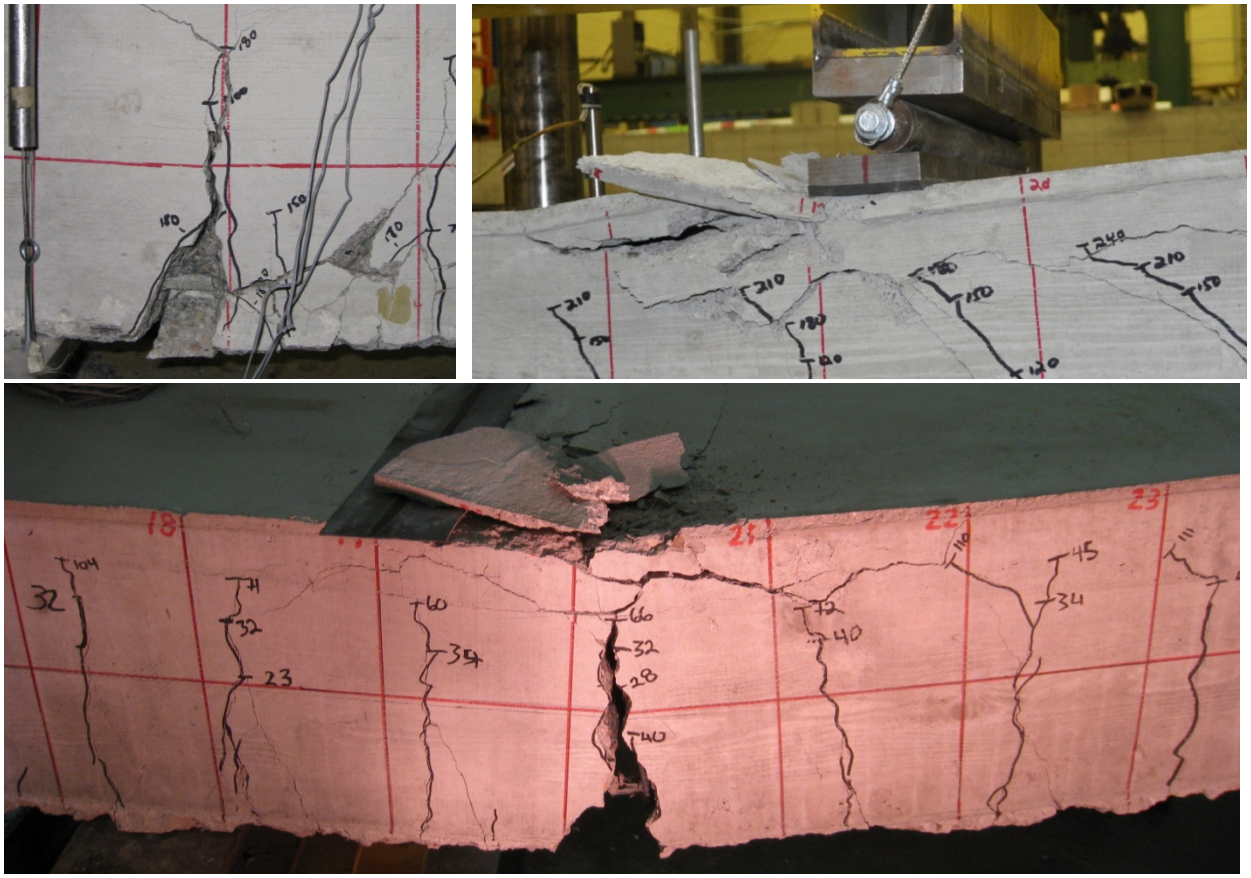

b)

Figure 4.11 - Examples of a) shear failure and b) flexural failure modes

While the actual location of the premature rupture was difficult to determine since the fractures tended to propagate along the length of the tendon, it appeared to initiate within the slab rather than at the tendon-anchor location. Premature rupture of the prestressing tendons is likely attributed to locally-induced transverse stresses and abrasion at the tendon-duct interface, which can significantly reduce the tensile stress that can be achieved; because FRP materials are incapable of plastic deformation, local stress concentrations may result in rupture of the bar. The post-tensioning ducts used in this study were corrugated galvanized steel with an internal diameter of 25.4 mm (1 in.), meeting the requirements of the Post-Tensioning Institute (PTI) for steel tendons (PTI 2003). The CFRP tendons had a nominal diameter of 12.5 mm plus an external sand coating; thus, for a perfectly concentric tendon, the clearance would be approximately 6 mm. However, some variation along the length is to be expected (ie. the "wobble effect") such that in some locations the tendon and duct may be touching or nearly touching prior to prestressing. As the tendon is prestressed, the corrugated sides of the duct are pressed into the side of the tensioned bar as it tries to straighten. Harping of CFRP tendons has been observed to significantly reduce their tensile capacity due to abrasion and induced bending and shear stresses (Noël & Soudki 2010). The sand particles used to coat the bar increase the friction between the two surfaces and may also cause some damage to the outer fibres of the bar as the relative displacement between the tendon and duct together with the transverse pressure applied at the points of contact cause the sand particles to dig into the fibres and abrade them. As bending moments are applied to the flexural member, the curvature of the ducts increases and can lead to increased contact between the tendon and the prestressing duct. Furthermore, the friction force induced at the points of contact result in

local variations in the normal stress in the bar; hence, the assumption of uniform stress along the length of the tendon may not be true and failure can occur at locations of high localized stress. Although it may be possible to employ a frictionless system comprised of a smooth or plastic duct and smooth tendon (no sand coating) with some type of sheathing, this has not been experimentally verified. For this reason, it is recommended to grout all tendons for field applications until a suitable solution for unbonded FRP tendons has been determined.

Each of the shear reinforcement techniques used was effective in increasing the shear capacity to induce flexural failure as expected. Specimens PT2-ST, PT2-G, PT2-S and PT2-S45 all had similar modes of failure. Pseudo-ductile progressive failure modes were observed as these slabs reached their flexural capacity since the GFRP bars remained intact after rupture of the CFRP tendons, allowing for further deformation. As a result, the slabs displayed high stiffness at service and high deformability at ultimate which is desirable for structural elements to provide sufficient warning prior to failure.

All of the slabs tested in Phase I, with the exception of slabs G2, PT2 and PT4-P, sustained ultimate deflections of more than 100 mm. Considering that most of the slabs had a significant margin of safety or overstrength with respect to the factored design load, the proposed reinforcement system has evidently displayed much potential for the design of safe and efficient bridge structures in aggressive environments with excellent performance at service loads and large deflections at ultimate. Phase II was developed to build upon the findings of Phase I to further refine the proposed FRP reinforcing system.

4.3 Phase II – Reduced-Length Slabs

Although the slabs tested in Phase I of the experimental program displayed good performance characteristics with respect to both serviceability and ultimate limit states, slabs without shear reinforcement ultimately exhibited shear failure modes which are brittle and undesirable for real structures. Phase II was conducted in order to further investigate the shear behaviour of concrete slabs with an all-FRP reinforcing system including a comparison of various types of FRP shear reinforcement and their behaviour under repeated loading. Twenty-five specimens were constructed with similar cross-section details as slab PT2 in Phase I, but with a reduced shear span to induce a shear failure mode even when transverse reinforcement was provided. Five types of shear reinforcement were considered, namely #3 GFRP U-shaped stirrups (series GU-10), #4 GFRP U-shaped stirrups (series GU-12), #3 CFRP U-shaped stirrups (series CU-10), #3 GFRP C-shaped stirrups (series GC-10) and 12 mm GFRP double-headed shear bars (series GS-12). For each shear reinforcement type, five identical specimens were constructed; one specimen from each group was tested monotonically to failure and four specimens were subjected to repeated loading at a given load range up to 1 million cycles, as described in the following sections.

4.3.1 Static Tests

All of the Phase II slabs that were tested monotonically failed in shear as expected. Their load-deflection responses were similar (Figure 4.12), although slab GC-10 had a slightly higher initial stiffness than the other slabs which may be partially attributable to greater confinement provided by the C-shaped stirrups. For each slab, four consecutive stirrups near the loading point were instrumented with strain gauges at the mid-depth of the slab. The maximum

measured stirrup strain versus applied load response is shown in Figure 4.13; depending on the inclined shear crack geometry, the maximum recorded strain corresponded to either the third or fourth stirrup away from the loading point, or a distance of 375 mm or 525 mm from the midspan.

Although the measured strains are highly dependent on the actual crack path geometry, several observations can be made. For each slab, the stirrups became engaged when inclined cracks began to widen at loads ranging from 290 kN to 330 kN. For slabs GC-10 and GU-10, which sustained the highest measured maximum stirrup strains prior to failure, the critical shear crack formed on the same side of the loading point as the strain gauges. The C-shaped stirrups reached maximum strains of 11400 με, corresponding to approximately 68% of the rupture strain of the straight portion of the bar as reported by the manufacturer (refer to Chapter 3), before failure occurred at the bent region of the stirrups. The U-shaped stirrups in slab GU-10—which were unanchored at one end—reached a maximum strain of 7200 με, or 43% of the rupture strain of the straight portion of the bar before pullout occurred. Conversely, the inverted U-shaped stirrups in slab GU-12 reached a maximum measured strain of only 3300 με, while the CFRP stirrups in slab CU-10 reached a maximum strain of 4100 με; however, since the critical crack did not form on the same side as the strain gauges, it is likely that the actual strain reached prior to pullout at the critical crack location was significantly higher than the measured values. Similarly, the double-headed GFRP bars in slab GS-12 reached a maximum measured strain value of 5500 με although the critical crack did not form on the same side as the strain gauges.

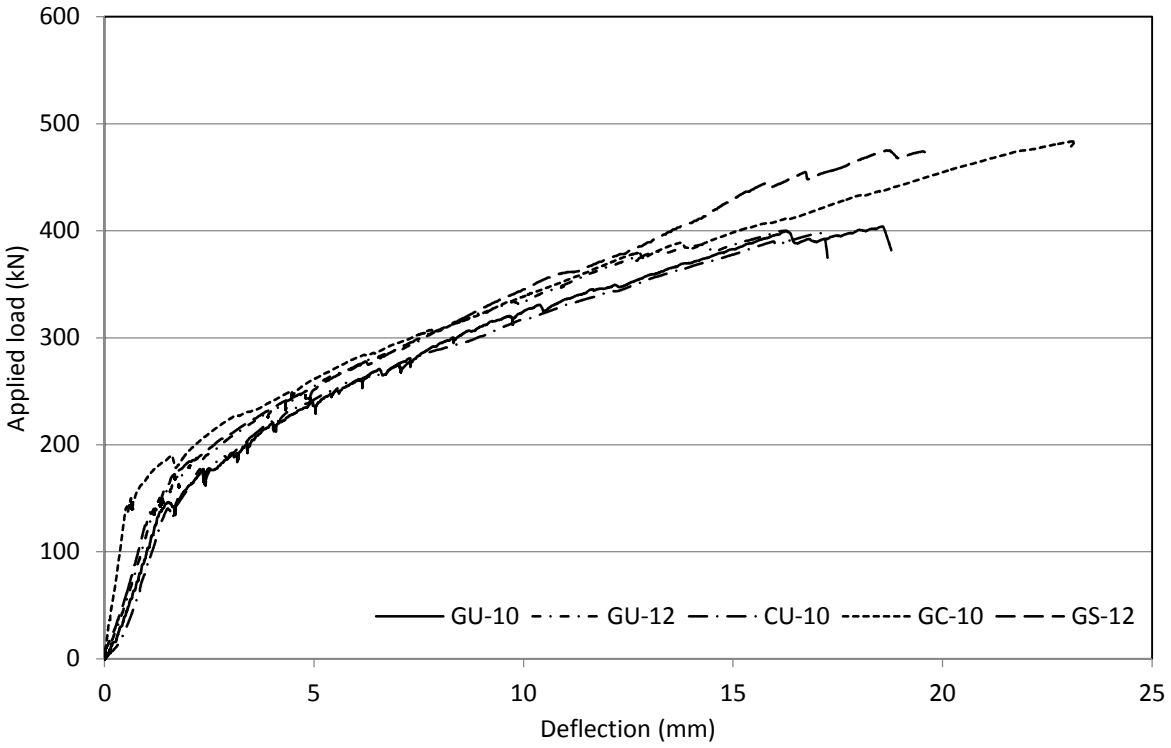

Figure 4.12 - Load-deflection response for Phase II monotonically tested slabs

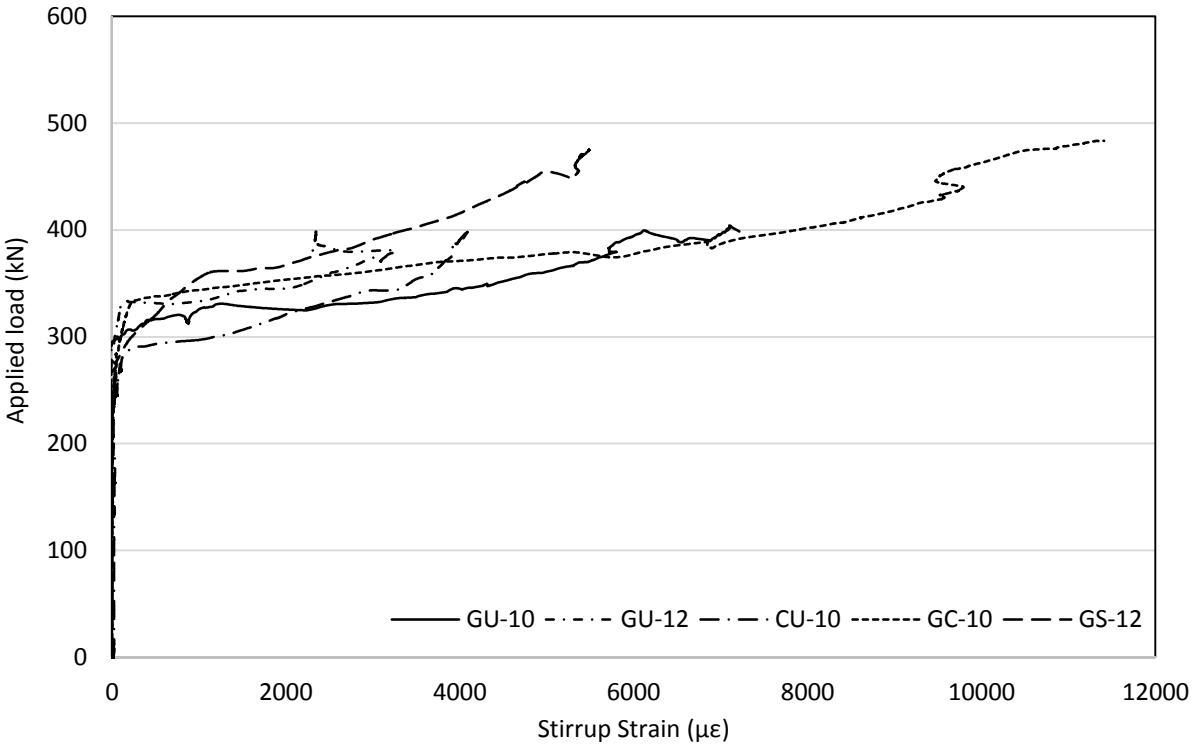

Figure 4.13 - Stirrup strains for Phase II monotonically tested slabs

Following the initiation of inclined cracking, short range LVDTs were used to monitor crack growth. Initial crack width readings were taken with a handheld microscope, after which the LVDTs were affixed to the concrete surface at the mid-depth of the slabs at an angle of 45° from horizontal such that they were approximately perpendicular to the crack orientation at mid-depth. Diagonal crack width is plotted versus applied load in Figure 4.14; although the most prominent inclined crack was initially chosen for monitoring crack width, the location of the critical crack which ultimately induced failure was impossible to predict and typically formed elsewhere. This resulted in some relatively narrow maximum recorded crack widths at ultimate as seen in Figure 4.14; nevertheless, several observations can be made. Hairline inclined cracks were first observed at loads ranging from approximately 200 kN to 250 kN, although they only reached widths of 0.5 mm at loads of more than 300 kN. Both slabs GC-10 and CU-10 sustained measured diagonal crack widths of more than 2 mm at ultimate, while slab GS-12 reached a measured diagonal crack width of about 1.2 mm at ultimate. The actual widths of the critical cracks at ultimate were larger than the recorded values in all cases; it is clear therefore that the shear reinforcement types considered were effective in preventing shear failure even when diagonal cracks became very wide.

Each of the three slabs reinforced with inverted U-shaped stirrups failed at a load of approximately 400 kN by pullout of the unanchored end of the stirrup and rupture at the bend location (depending on the depth at which each individual stirrup intercepted the shear crack), regardless of stirrup diameter or fibre type. Slabs with anchored shear reinforcement (GC-10 and GS-12) failed at higher loads at approximately 480 kN—slab GC-10 failed by rupture of the stirrups at the bend location while slab GS-12 failed by pullout of the GFRP shear bars from the

anchor head (Figure 4.15). All of the slabs failed at loads which were at least double the shear capacity of slab PT2 from Phase I, which had a similar longitudinal reinforcement configuration but no shear reinforcement; although some increase in the concrete contribution to shear resistance is expected due to the reduced moment-to-shear ratio of the shorter slabs, a large part of the overall increase in shear capacity is attributable to the presence of the shear reinforcement, thus highlighting their effectiveness. The failure loads are listed in Table 4.4.

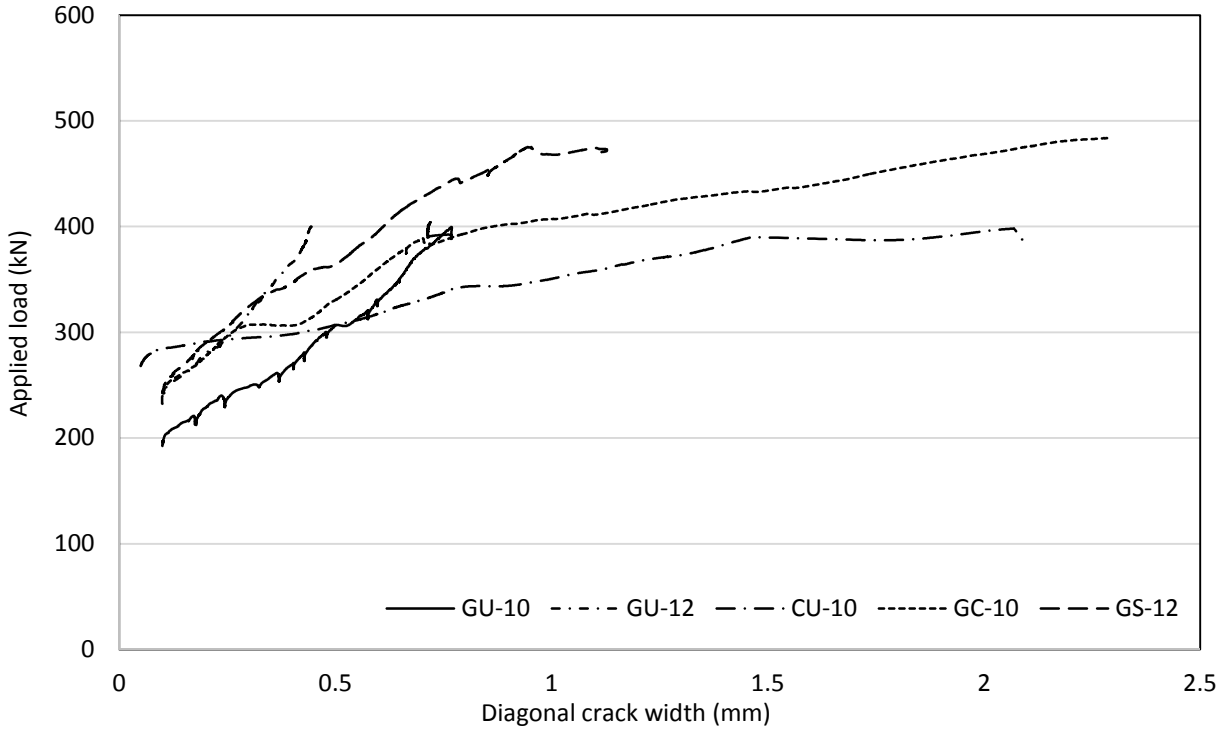

Figure 4.14 - Diagonal crack widths of Phase II monotonically tested slabs

Table 4.4 - Failure loads of Phase II monotonically tested slabs

Slab	Failure load (kN)
GU-10	404
GU-12	400
CU-10	398
GC-10	484
GS-12	475

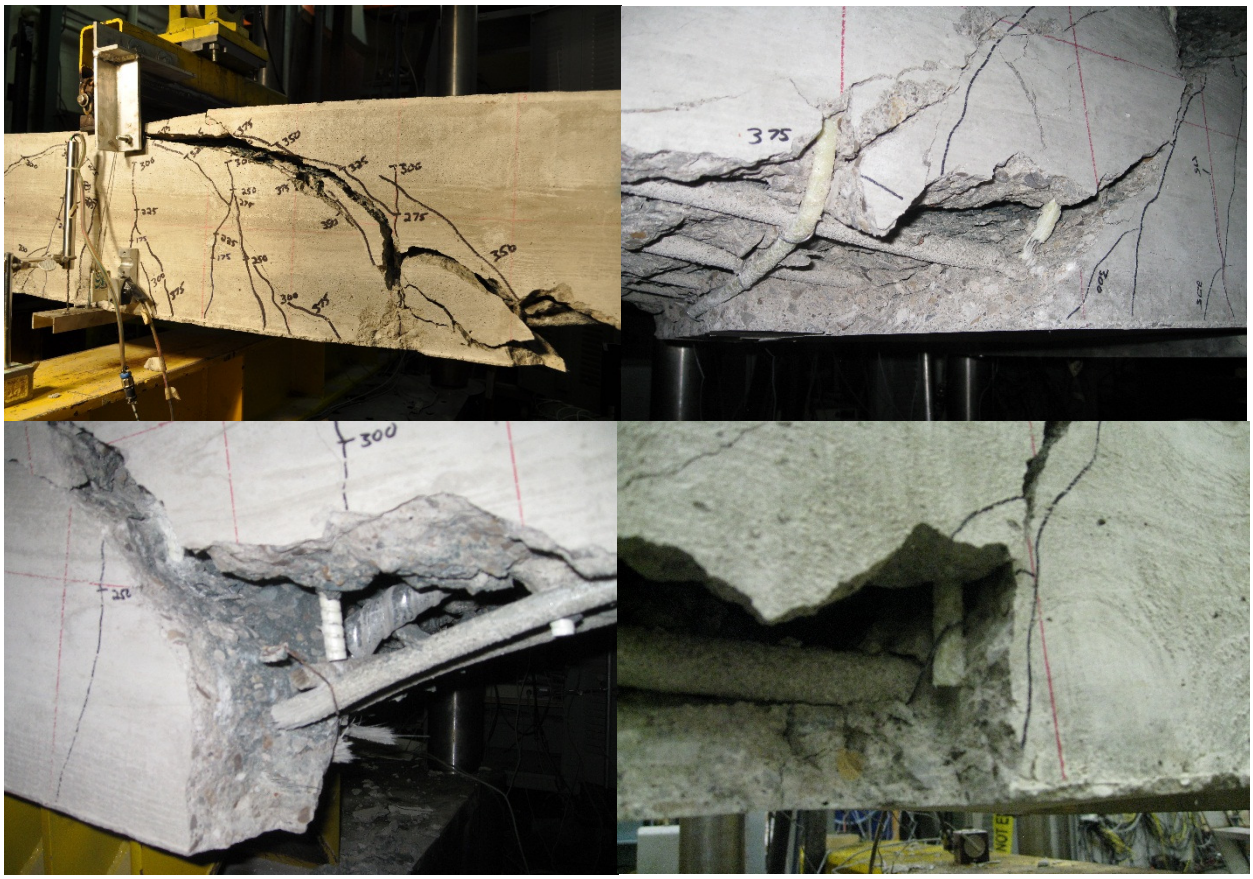

Figure 4.15 - Typical shear failures for Phase II slabs
(Clockwise from top left: critical shear crack; failure of C-shaped stirrup at bend location; U-shaped stirrup pullout failure; failure of anchor head)

4.3.2 Fatigue Tests

Four replicate specimens for each type of shear reinforcement considered were tested to failure under constant amplitude fatigue loading. The load range selected for the first slab in each series was selected to try to produce failure within 1 million cycles; slabs which did not fail within 1 million cycles were subjected to additional cycles at a higher load range until failure occurred. The load ranges selected for the subsequent slabs in each series were adjusted based on the results of the previous slabs to produce a range of fatigue lives between approximately 10000 cycles and 1000000 cycles to failure. The applied load ranges are summarized in Table

4.5 and shown in the form of an S-N curve in Figures 4.16 and 4.17. Specimens which reached 1 million cycles without failing are considered run-outs and are conservatively included in the S-N curves at a fatigue life of 1 million cycles.

Table 4.5 - Phase II fatigue test results

Slab	Description	Applied load range (kN)	Applied load range (% ultimate static strength)	Number of cycles to failure
GU-10-F1	#3 GFRP U-shaped stirrups	250	62	43273
GU-10-F2a		230	57	>1000000
GU-10-F2b		265	66	238788
GU-10-F3		255	63	30303
GU-10-F4a		240	59	>1000000
GU-10-F4b		280	69	297597
GU-12-F1	#4 GFRP U-shaped stirrups	250	63	39247
GU-12-F2a		230	58	>1000000
GU-12-F2b		270	68	34993
GU-12-F3		245	61	31936
GU-12-F4		240	60	514978
CU-10-F1	#3 CFRP U-shaped stirrups	260	65	463917
CU-10-F2		300	75	9531
CU-10-F3a		240	60	>1000000
CU-10-F3b		280	70	210205
CU-10-F4		255	64	54444
GC-10-F1	#3 GFRP C-shaped stirrups	260	54	176991
GC-10-F2a		240	50	>1000000
GC-10-F2b		270	56	45035
GC-10-F3		250	52	746650
GC-10-F4		255	53	325925
GS-12-F1a	12 mm GFRP double-headed shear bars	260	55	>1000000
GS-12-F1b		320	67	76156[a]
GS-12-F2		310	65	135271
GS-12-F3		290	61	136767
GS-12-F4		300	63	228922

a - Flexural failure

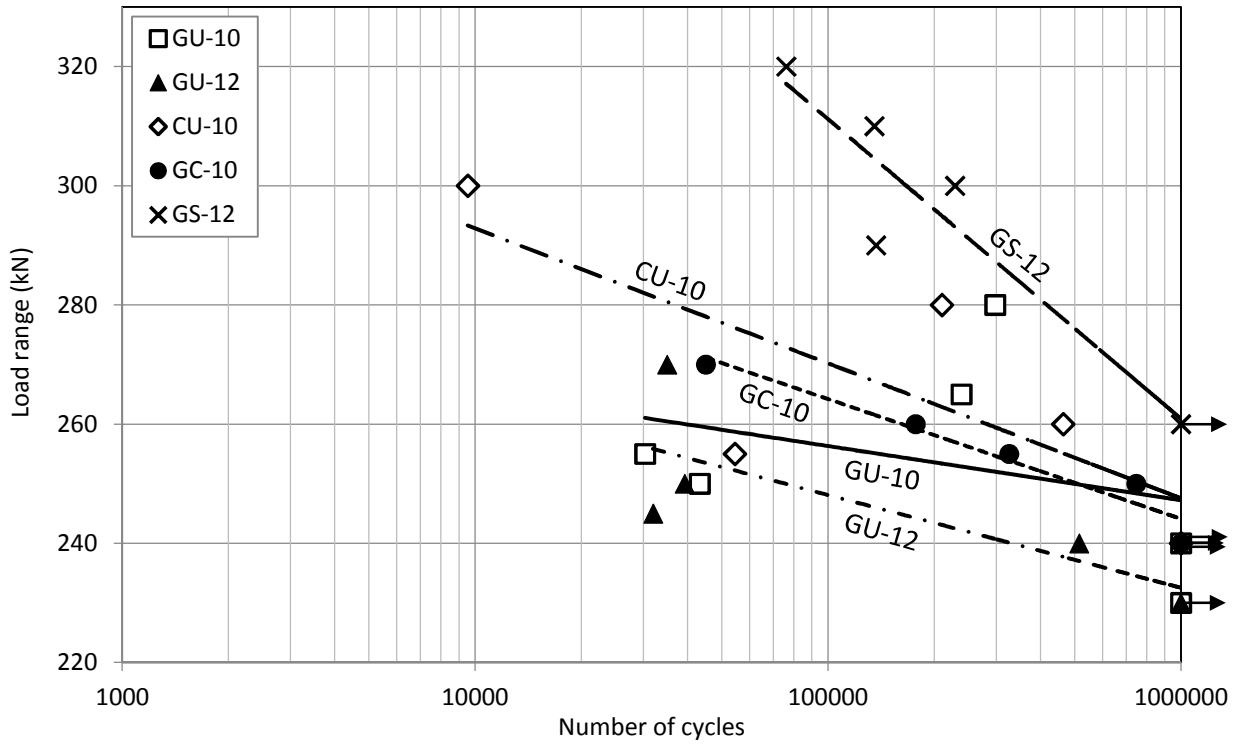

Figure 4.16 - Phase II fatigue test results

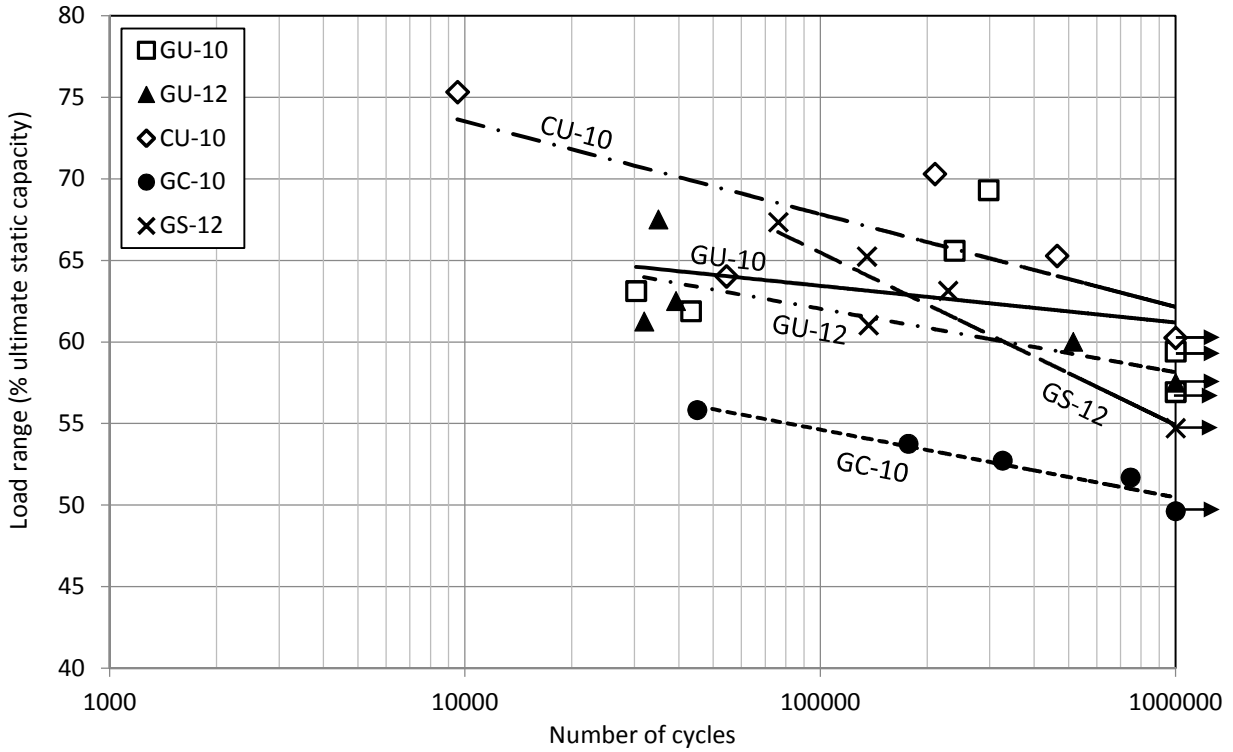

Figure 4.17 - Phase II fatigue test results

All of the slabs had a shear mode of failure, with the exception of slab GS-12-F1, which failed in flexure by rupture of the GFRP reinforcement after being subjected to 1 million cycles at a load range of 260 kN (55% of its ultimate static strength) followed by 76156 cycles at a load range of 320 kN (62% of its ultimate static strength); since the applied load range causing failure lies between the ultimate static shear capacity and the applied load range of the other fatigue specimens in this series (all of which failed in shear), this result is assumed to be an anomaly. It is possible that the first set of 1 million cycles resulted in significant damage to the longitudinal GFRP reinforcement causing premature failure; however, since the data point lies within a reasonable scatter band with relation to the other specimens in the series, and considering that wide diagonal cracks were evident at failure, it is assumed that shear failure was imminent. Therefore this result was not excluded from the analysis.

The S-N curves for each series are relatively flat, such that a small change in the load range results in a significant change in fatigue life. Hence, the range of applied load ranges for each slab type is not very wide, although the fatigue life values range from less than 10000 to more than 1000000. As expected, there is a significant amount of scatter among the shear fatigue results, particularly for the slabs which failed by pullout of the inverted U-shaped stirrups. Slabs containing C-shaped GFRP stirrups (series GC-10) displayed the highest correlation between load range and number of cycles to failure on a semi-log plot with a logarithmic regression R^2 value of 0.9375; on the other hand, slabs with inverted U-shaped #3 GFRP stirrups (series GU-10) showed no correlation with an R^2 value of 0.0001 which may be attributed to large variability in the fatigue bond strength of the GFRP-concrete interface. Series GS-12 displayed the highest fatigue strengths out of all of the tested slabs, although series CU-10 had

the highest ratio of fatigue strength to static strength for the load ranges considered. Series GU-12 had the lowest fatigue strengths out of all of the tested slabs while series GC-10 had the greatest reduction in strength with respect to ultimate static capacity. Fatigue strengths at 1 million cycles ranged from approximately 50% to 60% of the initial shear capacities of the slabs.

Maximum measured diagonal crack widths are plotted against the number of applied cycles at various load ranges in Figure 4.18. Asterisks are used in the legend to mark specimens which were tested at two different load ranges due to reaching 1 million cycles at a low load level; the first set of load cycles typically resulted in a greater initial crack width for the second set of cycles than might otherwise have been observed at the same load level. In general the results were as expected, as wider cracks were observed at higher load ranges, and cracks grew gradually with repeated loading until just prior to failure when crack widths grew rapidly. In some cases, however, the measured crack widths remained relatively small or decreased prior to failure; this occurred when a critical crack formed away from the crack which was being monitored.

The change in the maximum measured stirrup strains with increasing number of cycles is shown in Figure 4.19. Similar to diagonal crack width, stirrup strains tended to increase with increasing load range and increasing number of cycles, as expected. In most cases, stirrup strains were initially quite small; as noted for the statically tested specimens, stirrups only became engaged at loads of approximately 300 kN (Figure 4.13) which is higher than most of the fatigue load ranges considered, such that only hairline inclined cracks were observed after the initial cycle. Diagonal cracks typically became more prominent within the first 10000 cycles, after which the stirrups became engaged as evidenced by the sharp strain increases observed in

Figure 4.19. Once the stirrups were contributing to load resistance, strains increased gradually with additional cycles before a period of rapid strain increase prior to failure. In some cases, however, these trends were not observed due to the critical crack forming on the opposite side of the loading point than the stirrups which were instrumented with strain gauges; when this occurred strains tended to remain fairly constant or decrease as the critical crack grew in size, particularly just prior to failure.

The largest strains were generally observed in stirrups 3 or 4, at a distance of 375 mm and 525 mm from the load point, respectively, although in a few cases stirrup 2 (at a distance of 225 mm from the load point) had the highest measured strains depending on the crack path geometry. Measured stirrup strains were less than 3500 με in all cases for the load ranges considered until just prior to failure, when crack growth became unstable. Slabs with inverted U-shaped stirrups displayed a slightly erratic behaviour with respect to the change in strain with increasing number of cycles caused by the load redistribution resulting from progressive slip of individual stirrups. Thus, the rate of change of the stirrup strain was inconsistent compared to the slabs in series GC-10 and GS-12. The stirrup strains in series GC-10 did not increase until relatively late in their fatigue life followed by a fairly rapid increase in strain. Meanwhile, the double-headed shear bars in the slabs of series GS-12, which were tested at the highest load ranges, were engaged from the first cycle onwards and displayed a gradual strain increase over the fatigue life of the slabs.

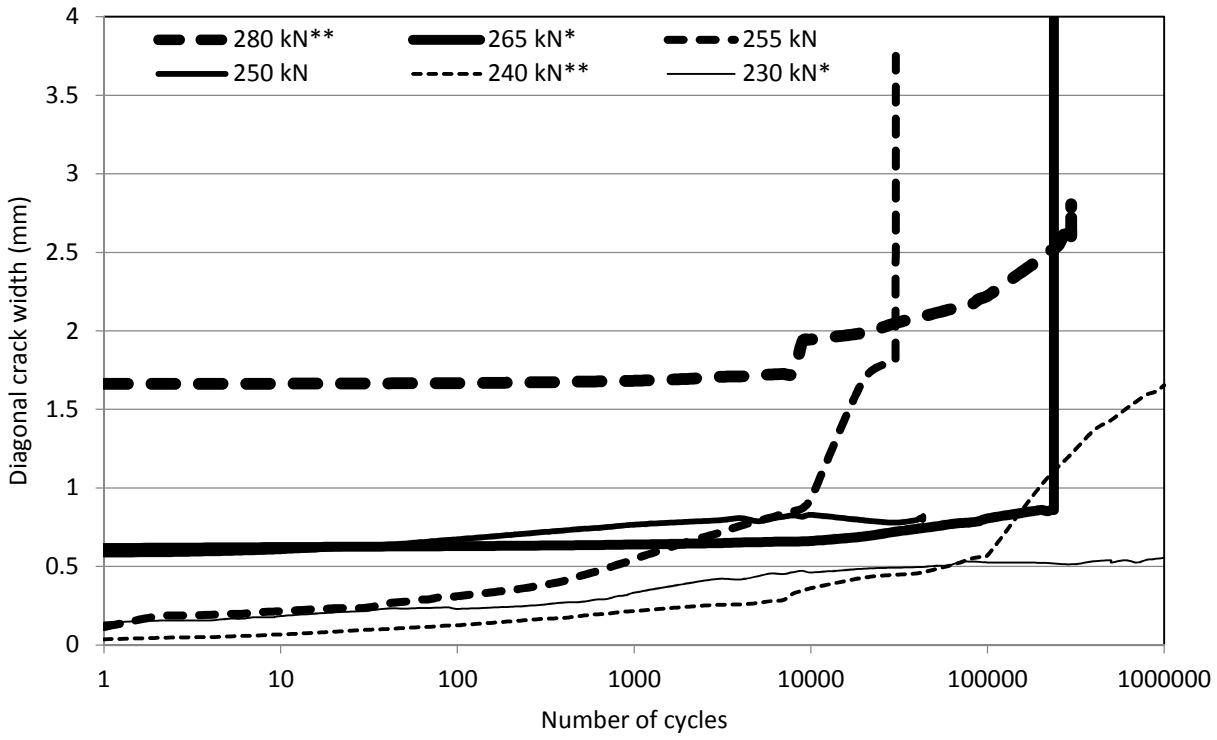

a) GU-10 series

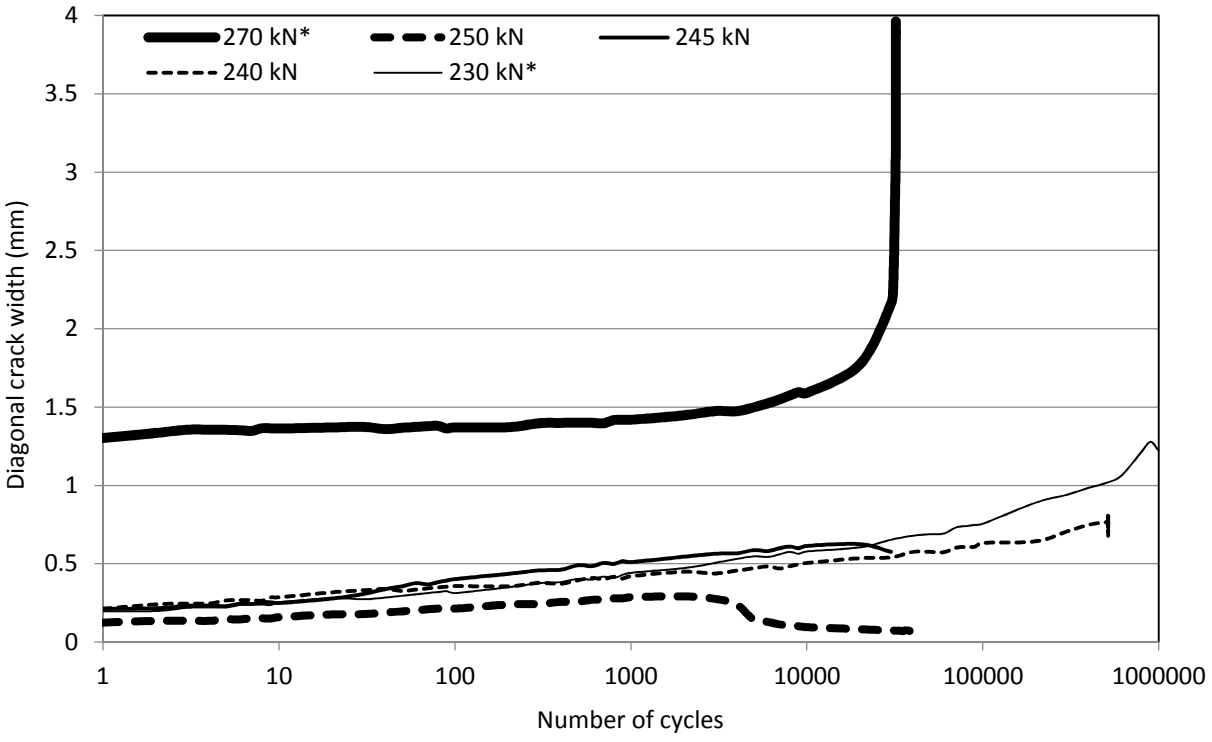

b) GU-12 series

Figure 4.18 – Diagonal crack width growth with repeated loading

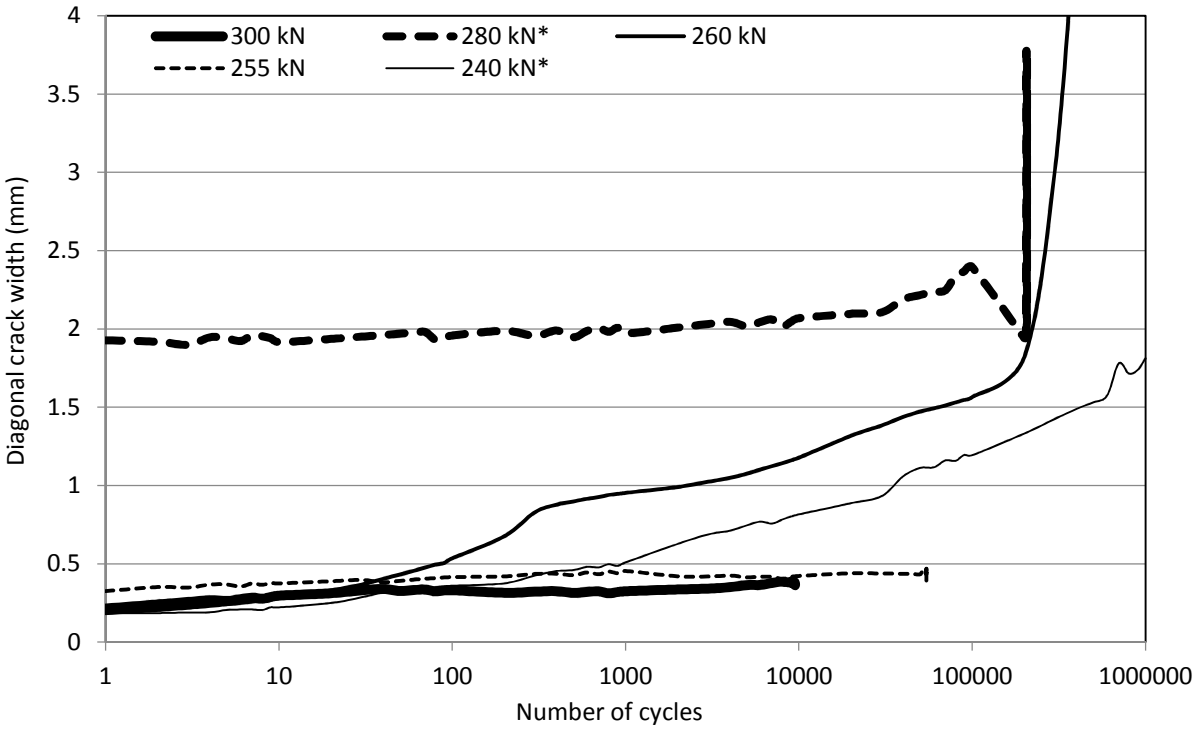

c) CU-10 series

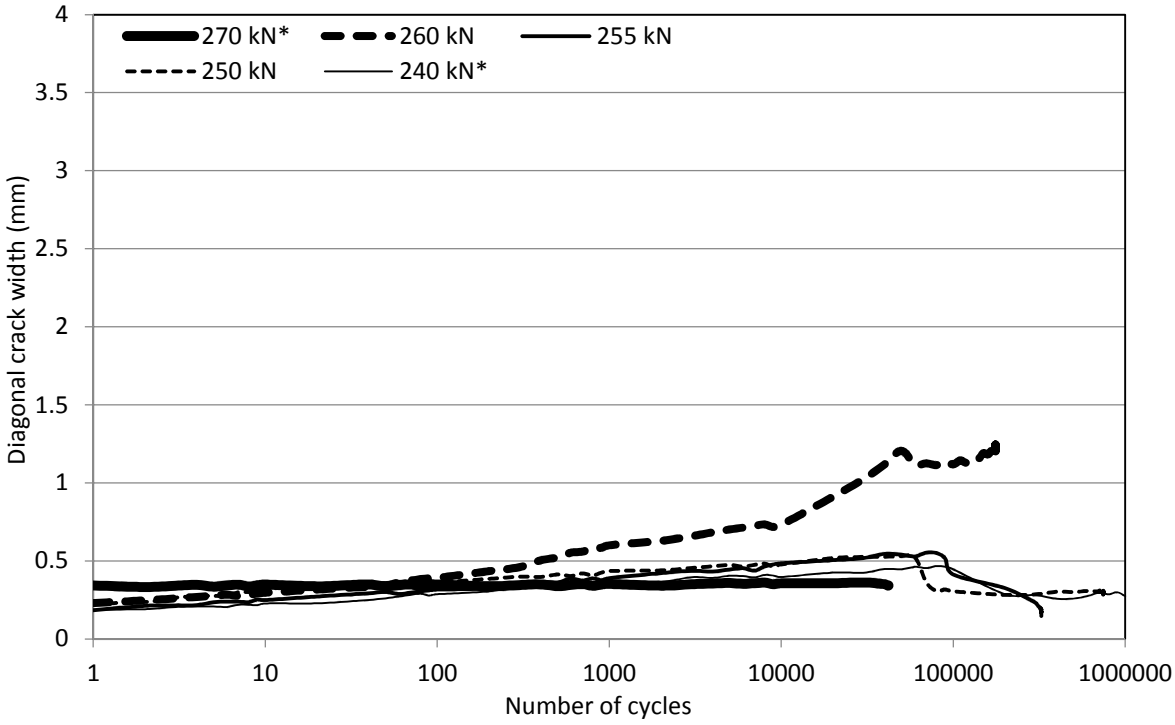

d) GC-10 series

Figure 4.18 – Diagonal crack width growth with repeated loading (continued)

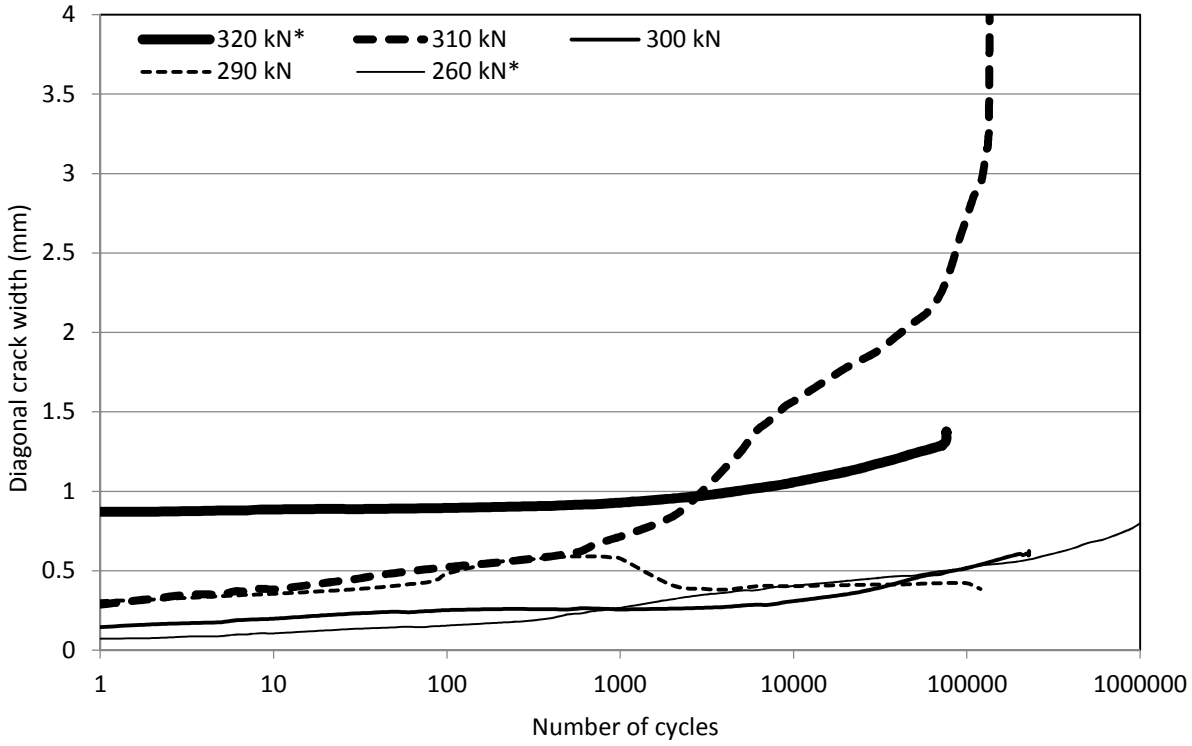

e) GS-12 series

Figure 4.18 - Diagonal crack width growth with repeated loading (continued)

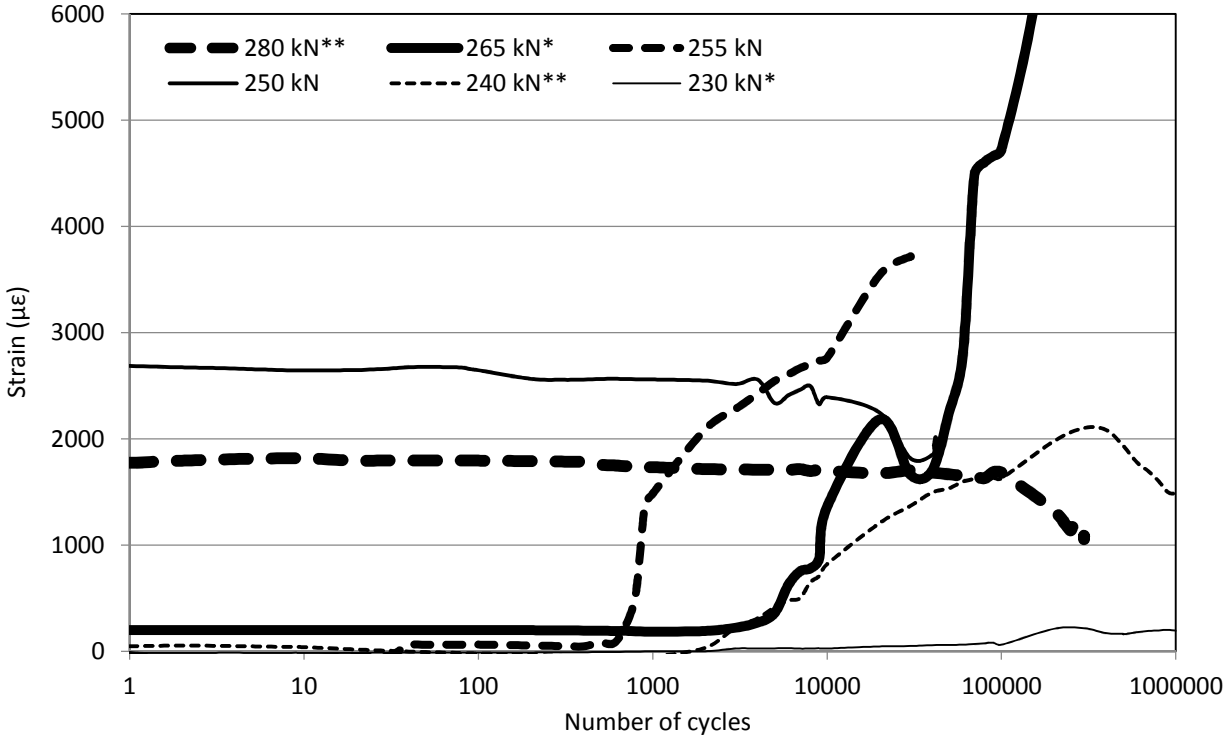

a) GU-10 series

Figure 4.19 – Maximum stirrup strain versus number of cycles

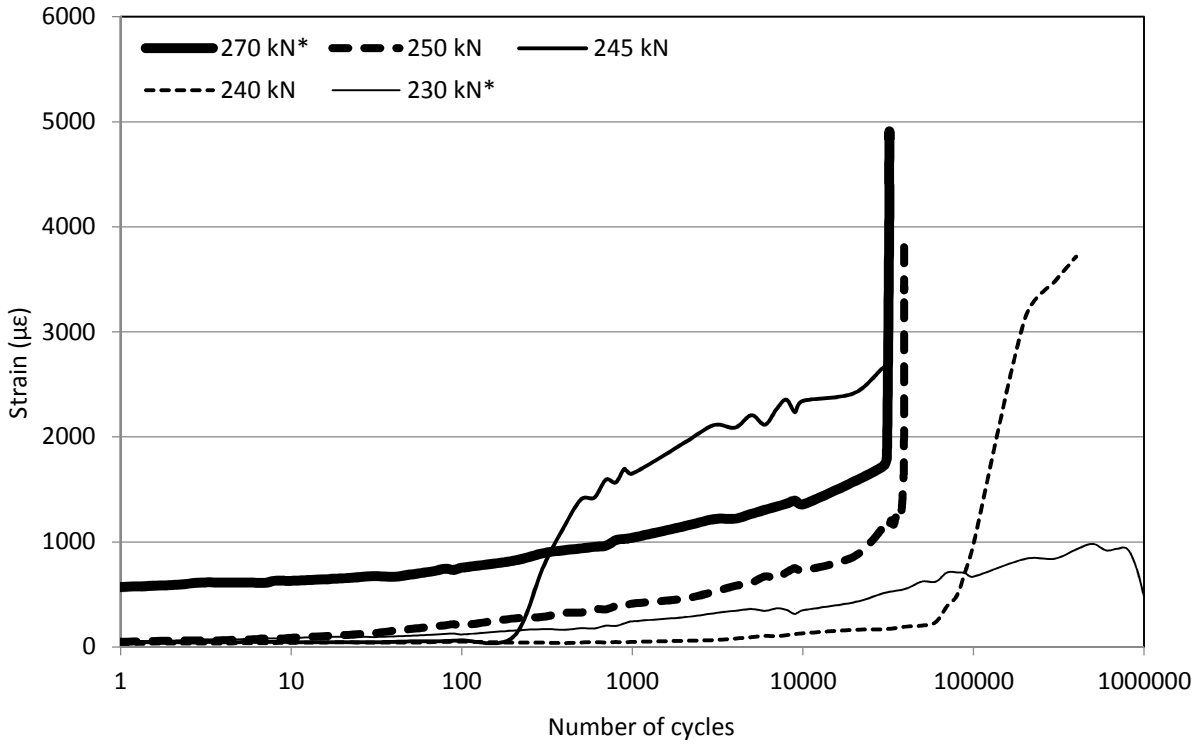

b) GU-12 series

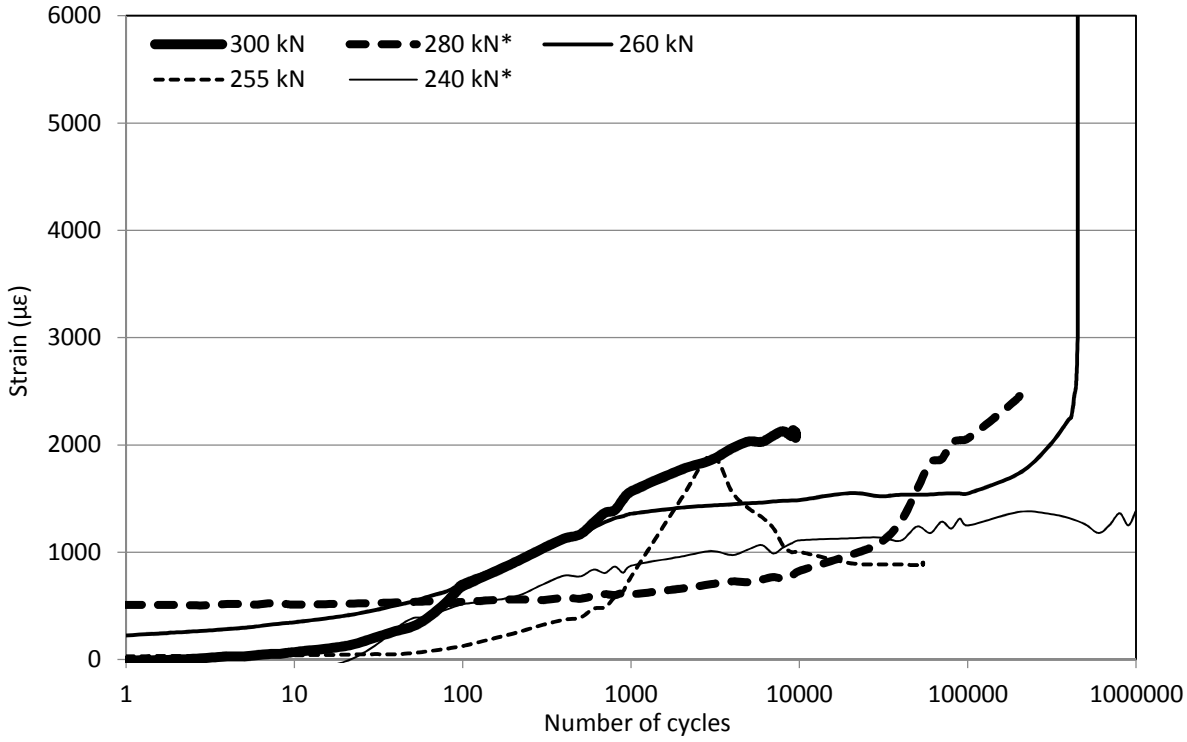

c) CU-10 series

Figure 4.19 – Maximum stirrup strain versus number of cycles (continued)

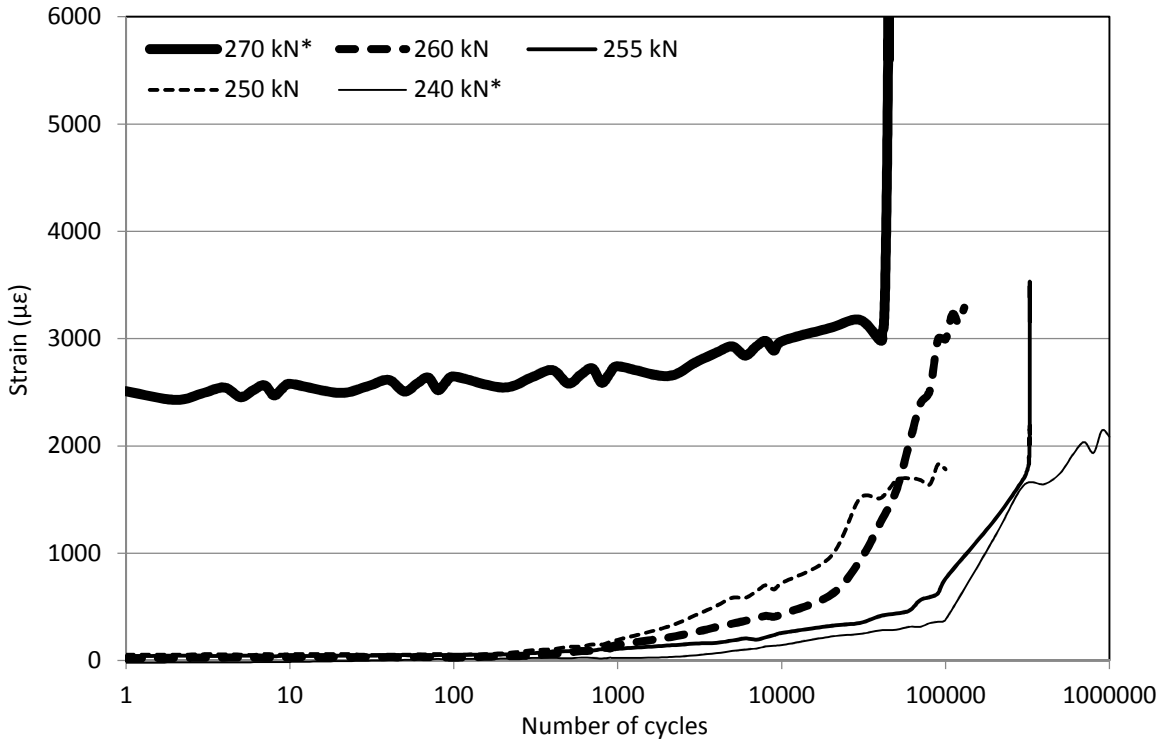

d) GC-10 series

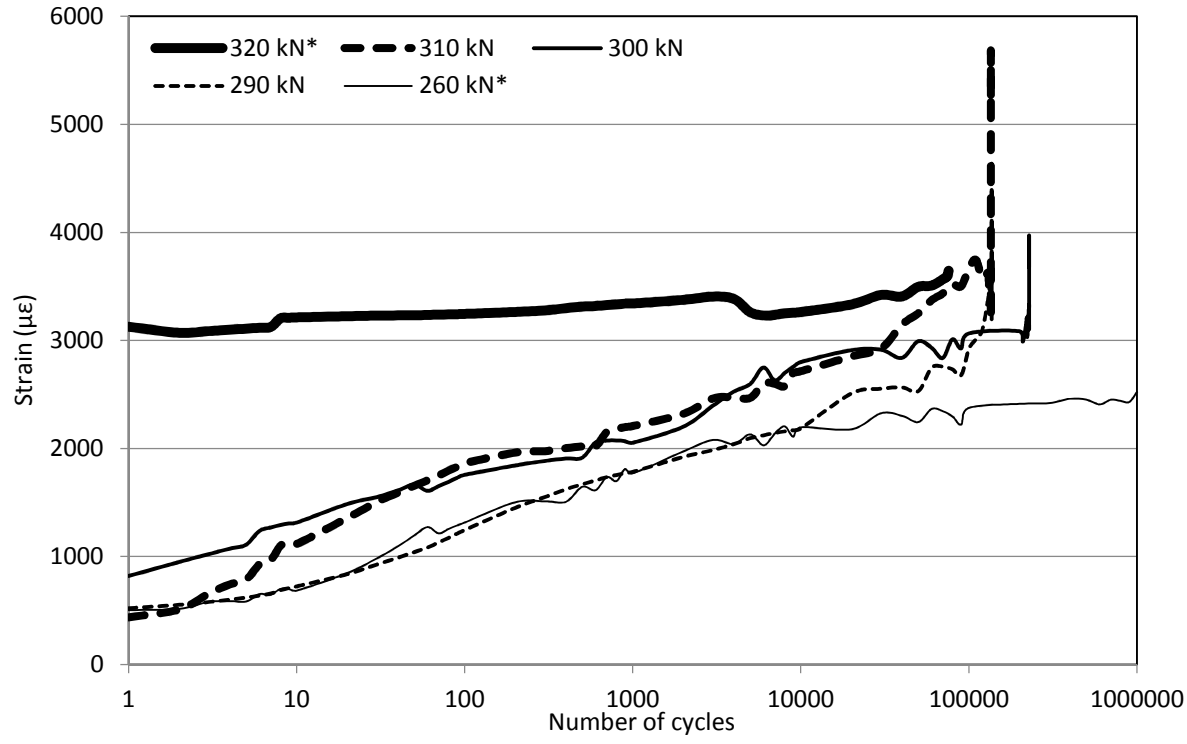

e) GS-12 series

Figure 4.19 - Maximum stirrup strain versus number of cycles (continued)

Typical stirrup strain distributions observed in the individual slabs throughout the fatigue tests are shown in Figure 4.20. These strain distributions can be categorized into five groups:

Type I distributions refer to cases when measured strains remained fairly constant over the life of the slab, with one or two stirrups engaged and the remaining stirrups having relatively low strain values. Type I distributions were generally observed when the critical crack formed away from the instrumented stirrups causing little to no increase in recorded stirrup strain.

Type II distributions were observed in cases where very low strain levels were recorded until a finite number of fatigue cycles were applied, and a subsequent sudden increase in strain followed by a fairly gradual increase over the remaining life of the slab. Type II distributions typically represent cases where the load range applied did not initially result in significant diagonal cracking, although cracks eventually formed after a given number of cycles at which point the stirrups began to carry load, with a gradual increase in strain as the cracks grew in width.

Type III distributions are those in which a change in the location of the primary crack caused a redistribution of stresses often evidenced by the reduction in strain in one stirrup and a corresponding increase in another. Type III distributions were observed when secondary cracks became more prominent with additional cycles, eventually becoming wider than initial cracks.

Type IV distributions are those in which all strain values were negligible until a rapid increase just prior to failure. Type IV distributions are similar to Type II, except that cracking was restrained for a larger portion of the slab's fatigue life and is followed by rapid degradation.

Finally Type V distributions are those in which a gradual increase in strain is observed over the complete fatigue life of the slab. Type V distributions occurred when applied load ranges were sufficiently high to cause diagonal cracking and engage the stirrups after the first cycle.

The different stirrup strain distributions highlight the fact that the critical shear section under static loading is not necessarily the same as the critical section under fatigue loading. This is particularly true for the slabs with unanchored stirrups as local slip of individual stirrups resulted in a redistribution of forces to adjacent stirrups, whereas the anchored stirrups tended to show much more gradual changes, if any. Furthermore, although stirrup strains may initially be very small, they can increase rapidly as the concrete grows weaker in tension under the repeated loading.

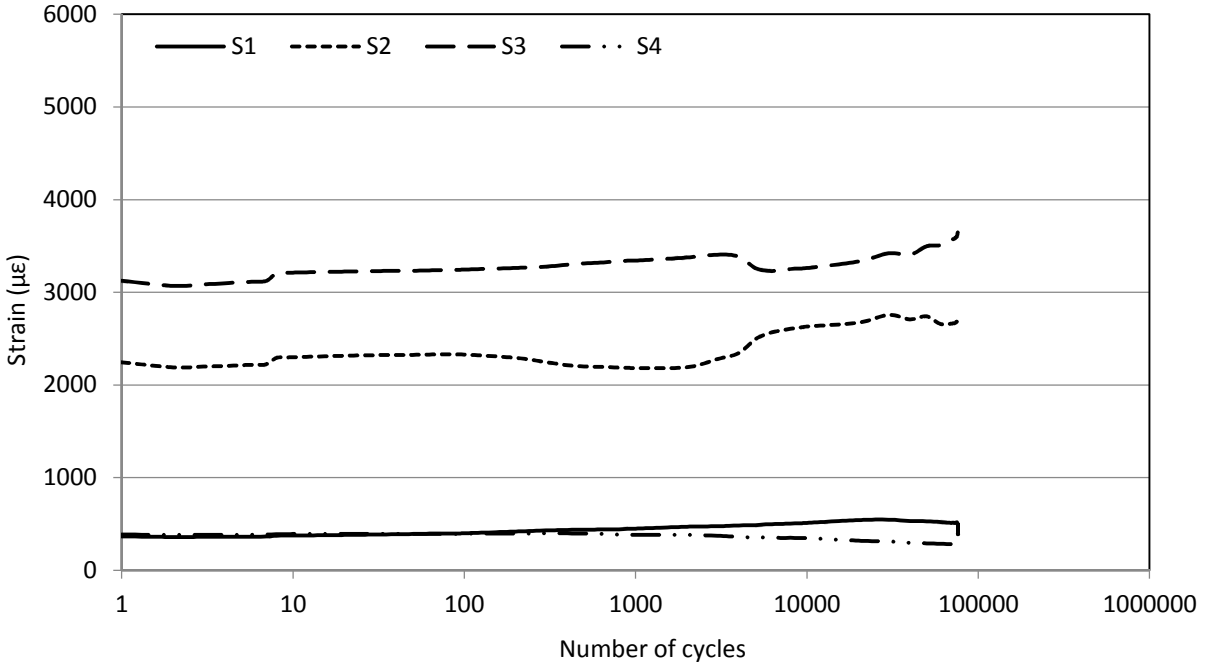

a) Type I (GS-12-F1b)

Figure 4.20 – Typical stirrup strain distributions under cyclic loading

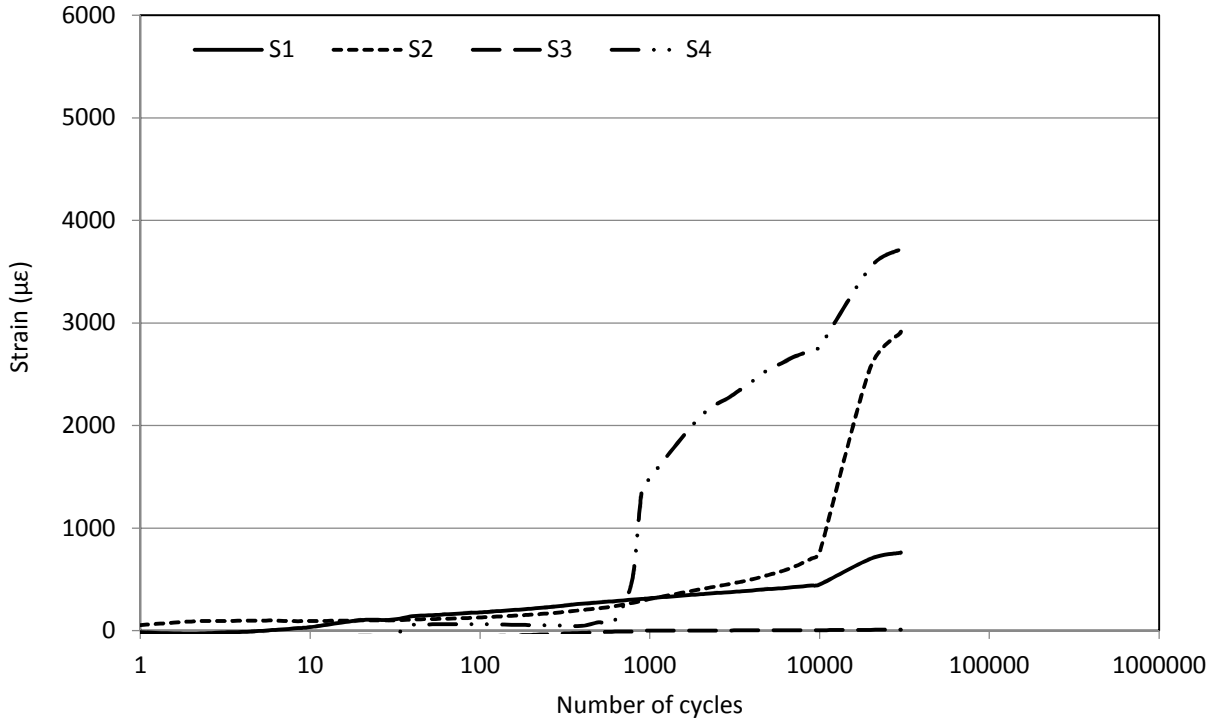

b) Type II (GU-10-F3)

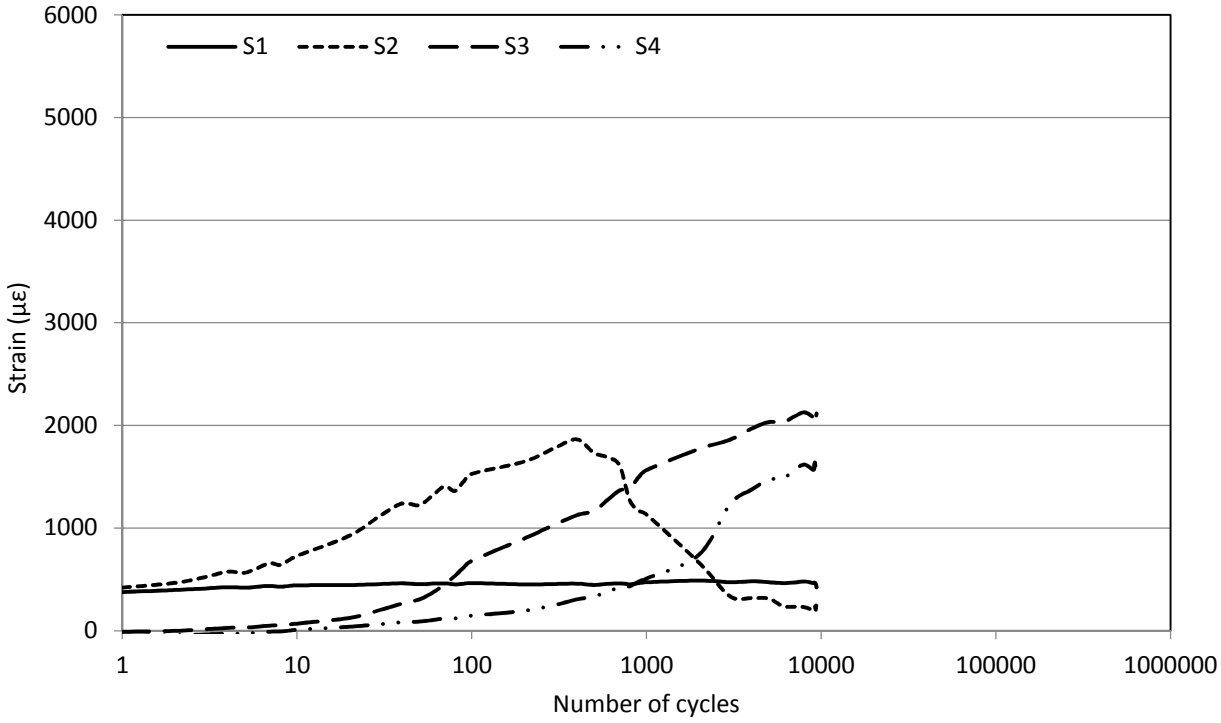

c) Type III (CU-10-F2)

Figure 4.20 – Typical stirrup strain distributions under cyclic loading (continued)

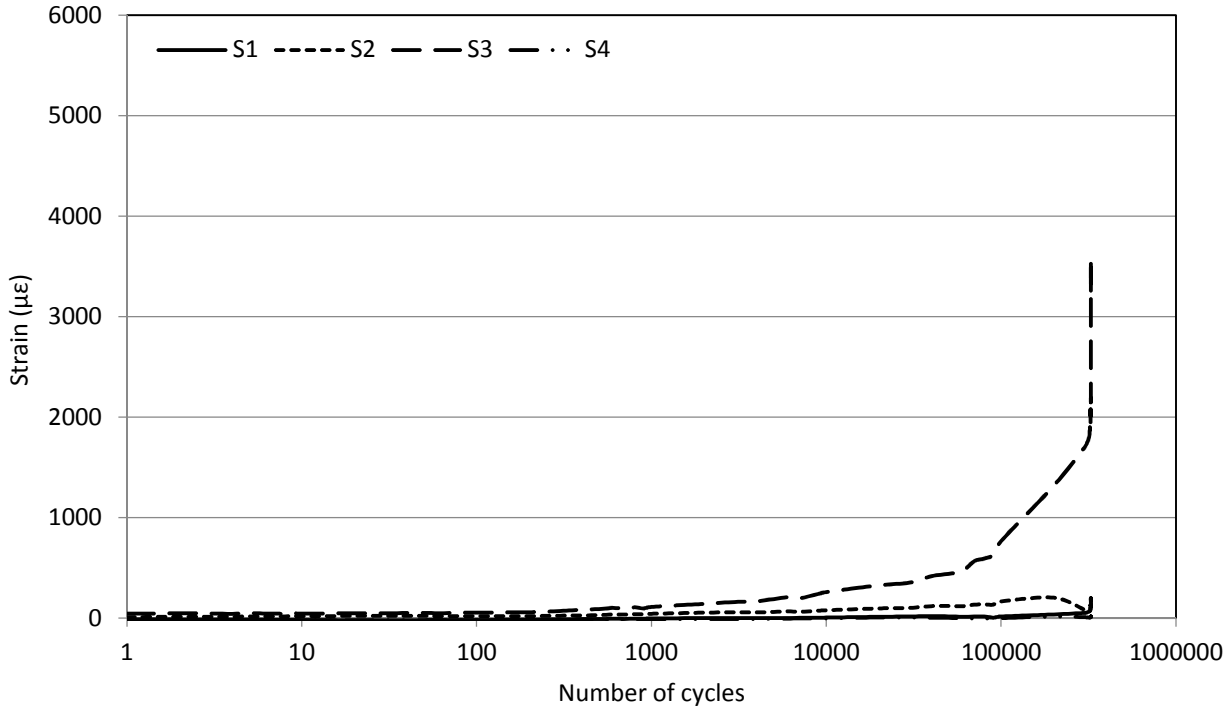

d) Type IV (GC-10-F4)

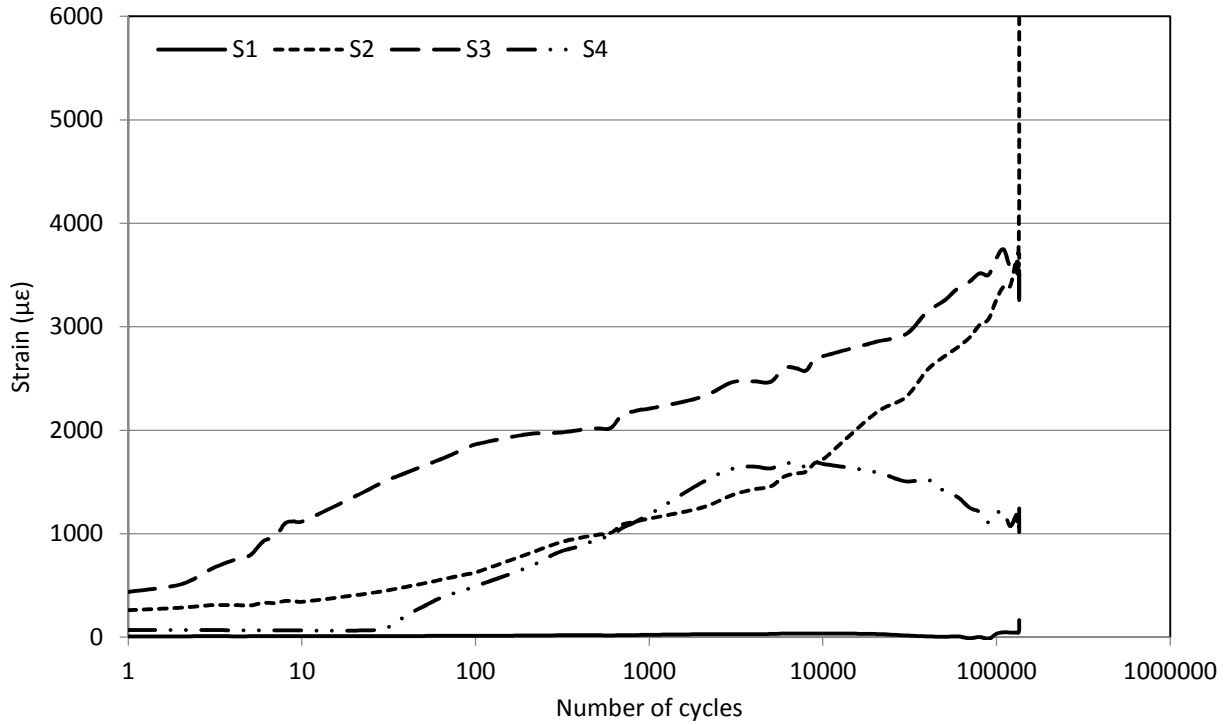

e) Type V (GS-12-F2)

Figure 4.20 - Typical stirrup strain distributions under cyclic loading (continued)

4.4 Phase III – Full-Scale Fatigue Testing

The results from Phase II demonstrated that each of the five reinforcing types considered were effective in resisting shear after the formation of diagonal cracks; the performance of the double-headed anchor bars was superior in terms of ultimate load-carrying capacity and fatigue behaviour compared with the other types considered. The C-shaped stirrups sustained a slightly higher ultimate shear capacity than the double-headed bars under static loading; however, the fatigue lives of series GC-10 were consistently less than for series GS-12. Furthermore, the use of double-headed anchor bars is more viable from a constructability standpoint for slabs than closed or C-shaped stirrups. Meanwhile, the slabs with inverted U-shaped stirrups showed significantly more scatter and consistently shorter fatigue lives than series GS-12; while the performance of the inverted U-shaped stirrups would likely be improved in an actual slab bridge due to the increased cover and confinement provided by adjacent concrete, the added mechanical anchorage of the headed bars provides a more reliable load transfer mechanism with more consistent results.

Based on the Phase II test results, the double-headed anchor bars were selected as the preferred shear reinforcement method for the proposed FRP reinforcement system for slab bridges. In order to validate this system, additional full-scale specimens were constructed and tested under fatigue loading. In the time between the construction of Phase II specimens and the construction of Phase III specimens (except for series PT2, which were constructed earlier), the manufacturer of the CFRP and GFRP bars used for the longitudinal reinforcement in this study developed a similar double-headed bar as that used in Phase II, except that the minimum bar diameter was 16 mm. In order to develop a reinforcement system that can be available

from a single manufacturer, these double-headed bars were adopted for use in Phase III. The mechanical properties of the longitudinal GFRP bars were also improved during this period, such that the properties of the bars used in series G1, G1S and PT2S were slightly different than for the previously constructed slabs. The mechanical properties for these bars are given in Chapter 3.

Sixteen full-scale specimens were subjected to constant amplitude cyclic loading using the same test configuration as used in Phase I tests. The force was applied under load control at a rate of 0.5 to 1.1 Hz, depending on the magnitude of the midspan deflection; the test frequencies used are relatively small and are not expected to affect the results. Eight specimens had the same cross-section and longitudinal reinforcing details as slab G1 with top and bottom GFRP mats and the remaining eight specimens were post-tensioned with two CFRP prestressing tendons similarly to slab PT2 (see Chapter 3). Four non-prestressed and four prestressed slabs were reinforced in shear with double-headed anchor bars spaced at 150 mm, while the remaining slabs were unreinforced in shear. They are referred to herein as series G1, G1S, PT2 and PT2S, with suffixes F1 through F4 for the four slabs in each series.

The first slab tested under repeated loading was specimen PT2-F1, which was subjected to a load range of approximately 60% of the ultimate strength of slab PT2 for 1 million cycles. This was considered to be the runout limit, and the load was subsequently increased to a load range of about 75% of the ultimate static strength until the specimen failed after approximately 260000 cycles. Load ranges for the remaining slabs were chosen to cause failure within one million cycles based on the results of the previous tests; slabs which sustained more than one million cycles were re-tested at a higher load range. Fatigue specimens were considered to

have failed when the slabs were no longer able to reach the maximum load peaks and were beginning to deflect excessively. When the targeted maximum cyclic load could no longer be attained due to the accumulated fatigue damage, the fatigue test was stopped and the specimen was loaded monotonically to failure. In all cases, final failure occurred at a load well below the maximum target load applied during the fatigue test.

Table 4.6 summarizes the results of the fatigue tests for Phase III. In all cases the minimum load was kept constant at 10 kN, while the maximum load was chosen to give the desired load range. The relationship between the applied load range and number of cycles to failure is plotted in the S-N curve shown in Figure 4.21. As expected, the fatigue strengths of the prestressed slabs were significantly higher than the non-prestressed slabs, as the added tendons both increased the shear resistance of the section and reduced the stress in the GFRP reinforcement. Minimal scatter was observed within each series, with a corresponding increase in fatigue life as the load range was decreased.

All but three specimens tested in fatigue in Phase III had a flexural failure mode (Table 4.6); below a critical load range, GFRP rupture became the dominant failure mode even for slabs without shear reinforcement. This can be observed in Figure 4.21 as the steepness of the S-N curves changes from being very flat for shear failures and becomes steeper for failures induced by GFRP rupture. For example, for series PT2, flexural failures occurred at load ranges of 150 kN and lower, while shear failures were observed at load ranges above 150 kN (specimen PT2 also failed in diagonal tension under monotonic load). For this reason, it is more appropriate to approximate the relationship between the applied load range and fatigue life using two trend lines rather than one, as shown in Figure 4.22. Although slab PT2-F1 failed in flexure, shear

failure was imminent as evidenced by the formation of a wide diagonal shear crack. Thus this point can be taken as the transition point from shear to flexural failures for this series.

Table 4.6 - Fatigue test results

Slab	Applied load range (kN)	Applied load range (% ultimate)	Fatigue life (cycles)	Failure mode[a]
G1-F1	80	48	6019	DT
G1-F2	60	36	168445	FR
G1-F3	50	30	481851	FR
G1-F4	70	42	89949	FR
G1S-F1	50	24	480199	FR
G1S-F2	80	38	90213	FR
G1S-F3a	40	19	>1000000	--
G1S-F3b	70	33	131007	FR
G1S-F4	60	28	189403	FR
PT2-F1a	120	58	>1000000	--
PT2-F1b	150	73	257511	FR
PT2-F2	160	78	534	DT
PT2-F3	140	68	686872	FR
PT2-F4	155	75	21084	SC
PT2S-F1	140	57	113205	FR
PT2S-F2	130	53	312561	FR
PT2S-F3	120	49	482663	FR
PT2S-F4	160	65	20408	FR

a – DT = diagonal tension failure, FR = flexural failure by GFRP rupture, SC = shear compression failure

The data for the Phase III specimens which failed by GFRP rupture are plotted in Figure 4.23 according to the stress range induced in the GFRP reinforcement. Since the measured strain in the GFRP bars at midspan depends on the proximity of the nearest crack to the strain gauge, stresses were instead calculated using a cracked-section analysis using design values for mechanical properties. It is evident from Figure 4.23 that the prestressed slabs displayed longer fatigue lives for similar GFRP stress ranges, despite having a similar failure mode by GFRP rupture. While this may be partially attributed to scatter in the fatigue properties of GFRP, it is also likely a result of the mean stress effect (a reduction in fatigue life due to an increase in mean stress). At the minimum load level, cracks in the prestressed slabs were fully closed such

that the stress in the GFRP reinforcement was negligible, even slightly compressive. Conversely, after the first load cycle the GFRP reinforcement in the cracked non-prestressed slabs sustained a stress of approximately 65 MPa at the minimum load level (including the moment due to the self-weight of the slab), thus increasing the mean stress for the same applied load range.

Figure 4.24 shows a typical example of the gradual softening (reduction in stiffness) and creep (plastic deformation due to sustained loads) caused by repeated loading. The slabs were initially loaded and unloaded under monotonic load to determine the initial member response and to observe the concrete cracking. For specimen PT2-F1, the slab was again loaded and unloaded under monotonic load following the initial one million cycles. When the fatigue test was terminated due to an inability of the member to sustain the maximum applied load, the specimens were again loaded gradually to failure. As shown in Figure 4.24, fatigue failure was preceded by large deformations and a significant reduction in stiffness compared with the initial cycle.

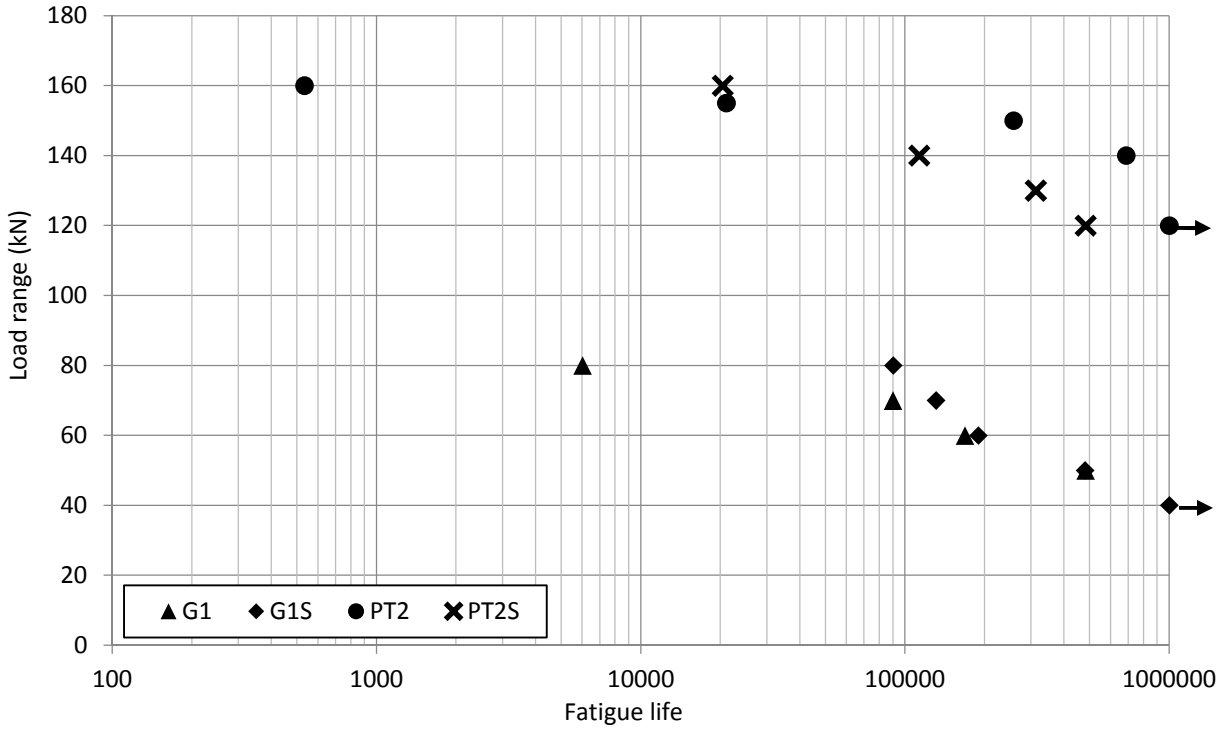

Figure 4.21 - Fatigue life of full-scale GFRP-RC slabs

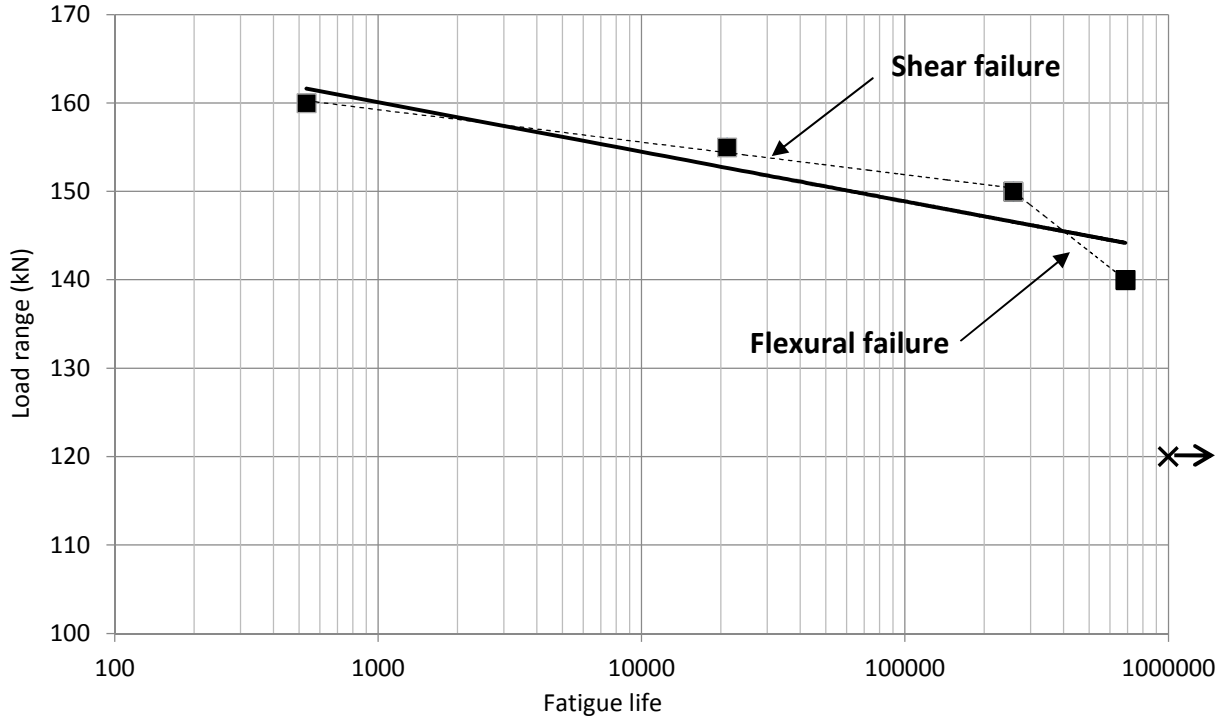

Figure 4.22 - S-N curve for series PT2

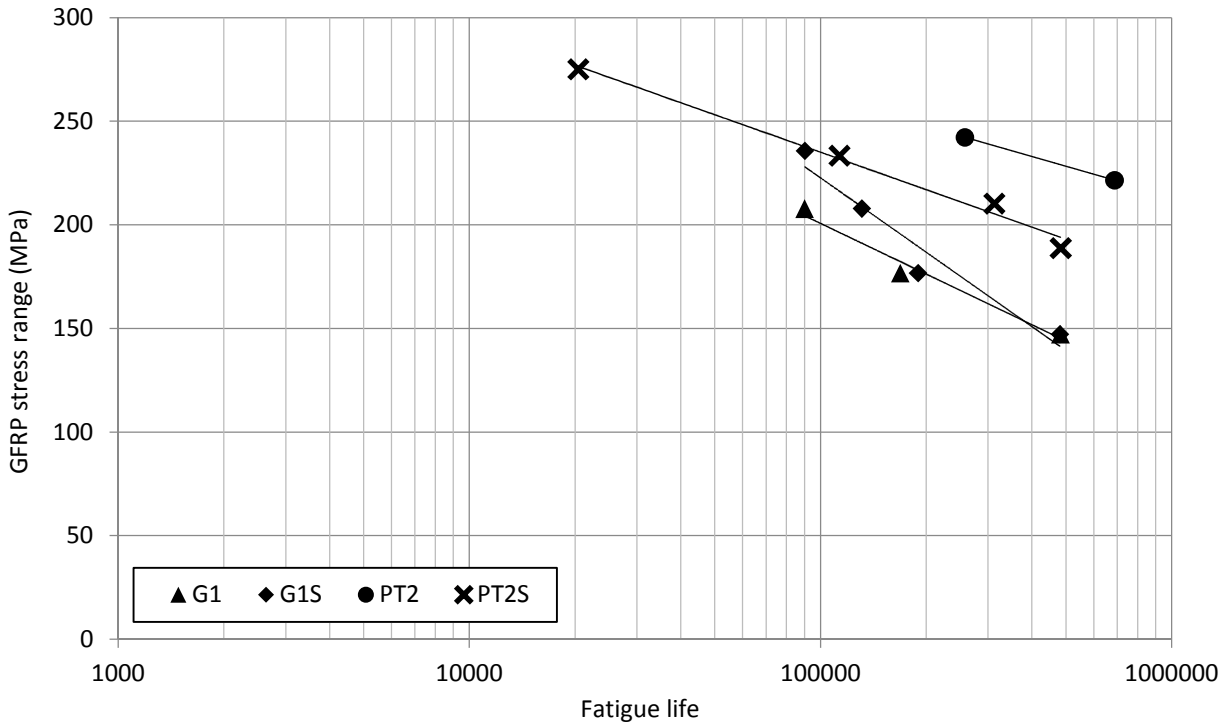

Figure 4.23 - Fatigue lives of GFRP reinforcement in full-scale slab strips

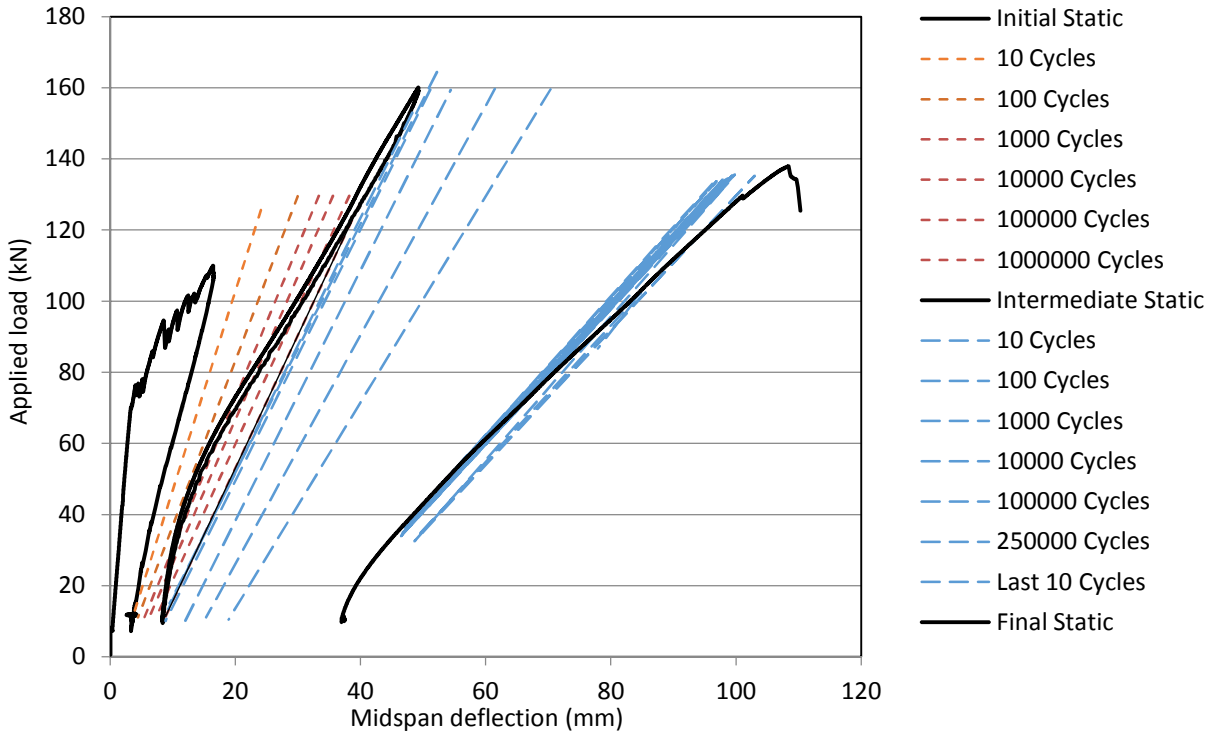

Figure 4.24 - Fatigue softening and creep of specimen PT2-F1

The effects of cyclic loading on midspan deflections, flexural crack widths and maximum stirrup strains are shown in Figures 4.25 to 4.27. For all of the tested slabs, midspan deflections, crack widths and stirrup strains increased gradually with increasing number of cycles until the slabs approached their fatigue life. As the specimens approached failure, the midspan deflections at the peak loads began to increase rapidly. Similar trends were observed for the flexural crack widths for the slabs which failed by GFRP rupture. For the specimens which failed in shear, the flexural cracks did not show similar increases in width, and in some cases a slight reduction in the flexural crack widths was observed just prior to failure as rotations were concentrated at the critical crack location. Stirrup strains in the non-prestressed slabs in series G1S remained fairly constant throughout the duration of the test, while the stirrup strains in series PT2S—which were tested at much higher load ranges—increased gradually throughout each test. In all cases the stirrup strains remained below 2000 με.

4.4.1 Mechanism of Failure

Examples of failed Phase III test specimens are shown in Figure 4.28. Each of the specimens tested under fatigue loading was pre-cracked during the initial static load cycle. The initial cycles showed some reduction in stiffness due to crack propagation followed by a stabilized period of very gradual crack growth, bond degradation and fatigue softening of the concrete in compression. Permanent plastic deformations resulting from cyclic creep, extensive cracking and gradual loss of bond between the reinforcement and the concrete were evidenced by the increase in deflection at the minimum load level. In most cases failure was initiated by rupture of the GFRP reinforcement regardless of whether shear reinforcement was present or not, indicating that high cycle fatigue is governed by the fatigue behaviour of the GFRP

reinforcement. At high load ranges (low cycle fatigue), wide shear cracks developed and propagated towards the load points; for three of the slabs without shear reinforcement, failure eventually occurred due to diagonal tension rupture of the longitudinal reinforcement at the location of the shear crack, or by shear compression at one of the load points.

4.5 Summary

Several observations can be made from the experimental results obtained from this experimental study. From the results of Phase I, it is clear that the proposed reinforcement system has excellent performance characteristics at service loads; prestressed slabs were uncracked at service, displayed minimal deflections and the strains in the GFRP reinforcement were negligible. Ultimate load capacities also exceeded factored design loads and the CHBDC performance deformability factor was satisfactory for all slabs with bonded tendons. The only concern for design engineers may be the brittle shear failure mode which occurred when shear reinforcement was not provided; although collapse of a slab bridge by one-way shear is unlikely due to load sharing from the rest of the slab, additional conservatism is beneficial when applying a new design concept.

For this reason, the slabs in Phase II were constructed to further investigate shear reinforcement types which are better suited for the construction of slab bridges. Twenty-five reduced-length specimens were constructed in five series reinforced with different types of shear reinforcement; the slabs were tested under either monotonic or cyclic loading and were designed to fail in shear to differentiate between the effectiveness of the various shear reinforcement types considered. The use of double-headed shear bars was found to be

practical for constructability while also displaying a significant increase in shear capacity and good resistance to fatigue loading.

In Phase III, the fatigue behaviour of prestressed and non-prestressed full-scale slab strips with and without double-headed shear bars were compared. Regardless of whether or not shear reinforcement was provided, rupture of the GFRP reinforcement governed the high cycle fatigue lives of the slabs; although the non-prestressed slabs did fail within 1 million cycles at load ranges near the CHBDC service moment from the CL-625 design truck (see Chapter 8), the load ranges causing failure in the prestressed slabs were much higher. Furthermore, since the cracking moment of the prestressed slabs is greater than the service moment, it is likely that the slabs would be uncracked for a large part of their service life leading to a further increase in fatigue life, as the stresses in the GFRP would be almost negligible.

Based on the experimental results from this study, the proposed reinforcement system combining prestressed CFRP tendons and non-prestressed GFRP reinforcement has the potential to provide a viable alternative to conventional steel reinforcement for concrete slab bridges, with good performance at serviceability, ultimate and fatigue limit states. Since the fatigue lives of concrete slab bridges at load ranges in the service range are likely to be governed by the GFRP reinforcement once the concrete is cracked, an improved understanding of the fatigue properties of the GFRP is required; this is one of the primary focuses of the ancillary tests described in Chapter 5.

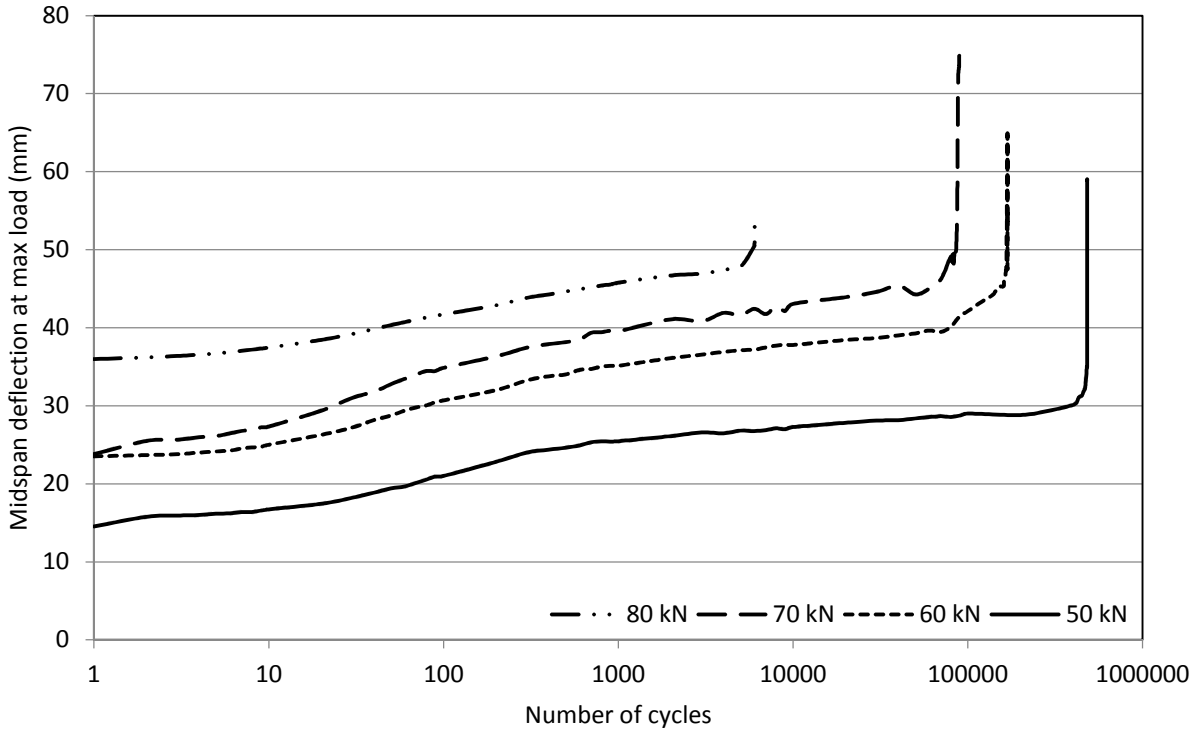

a) G1 series

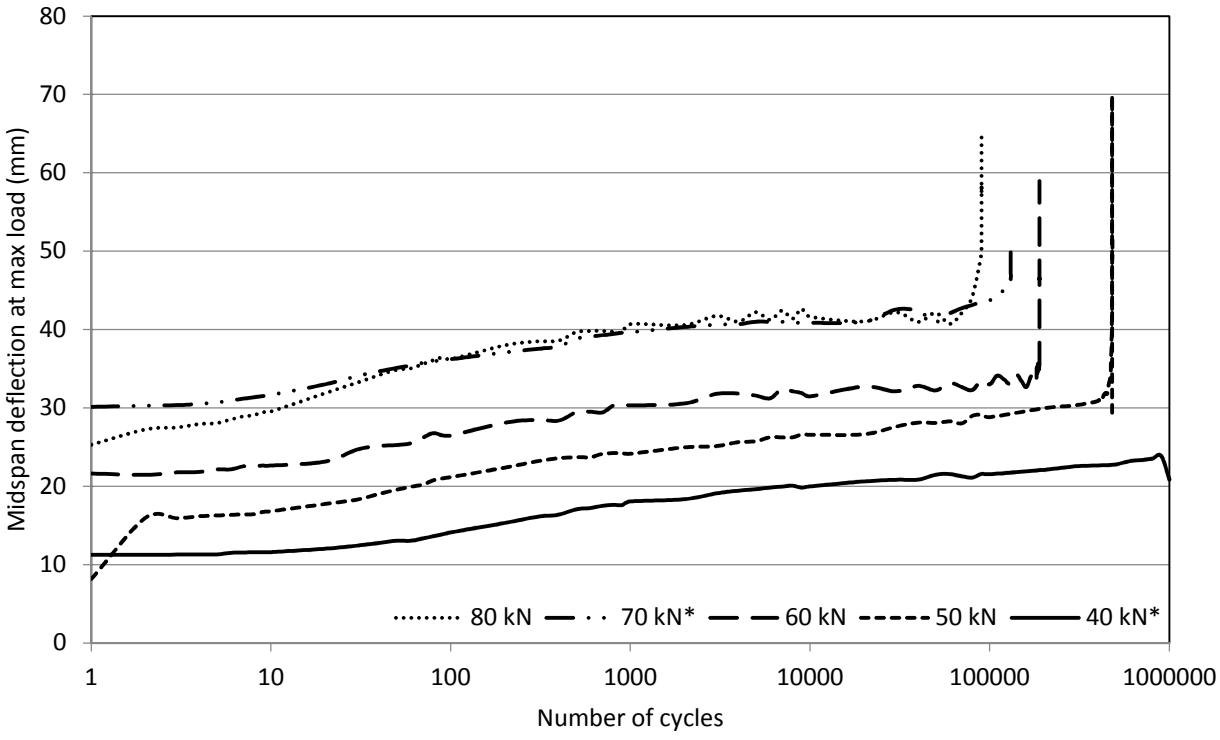

b) G1S series

Figure 4.25 – Effect of number of cycles on midspan deflection

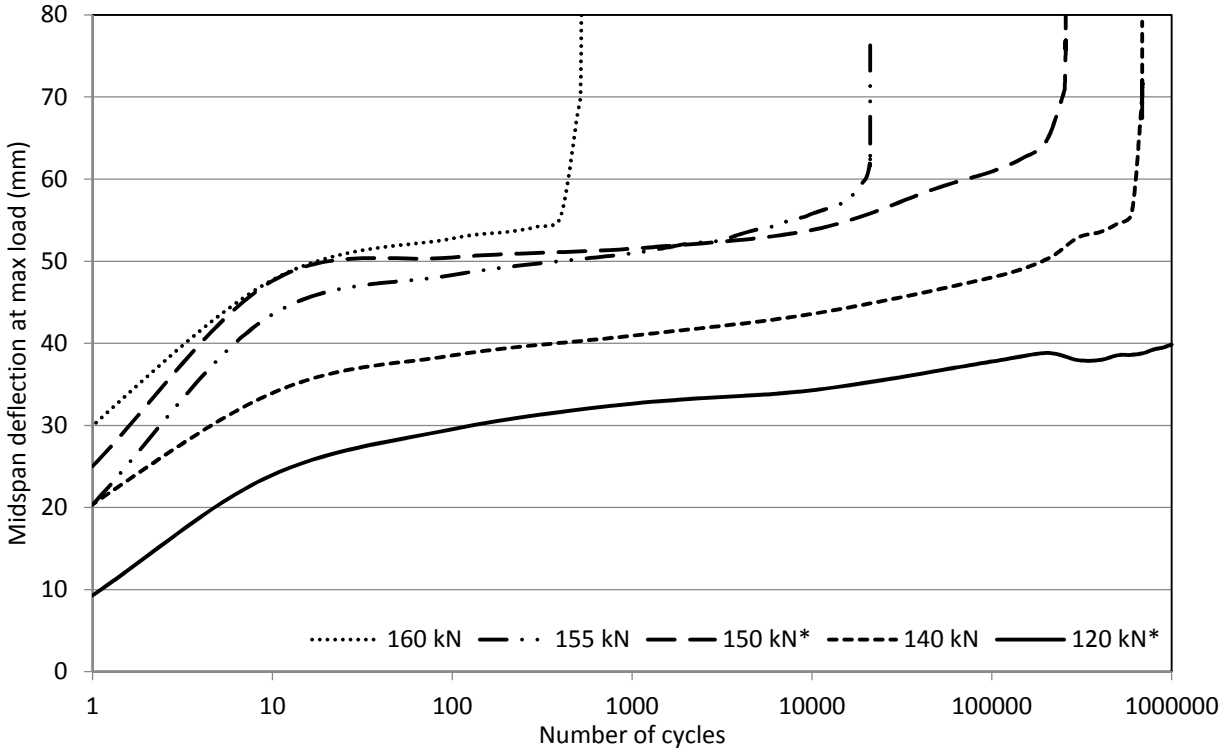

a) PT2 series

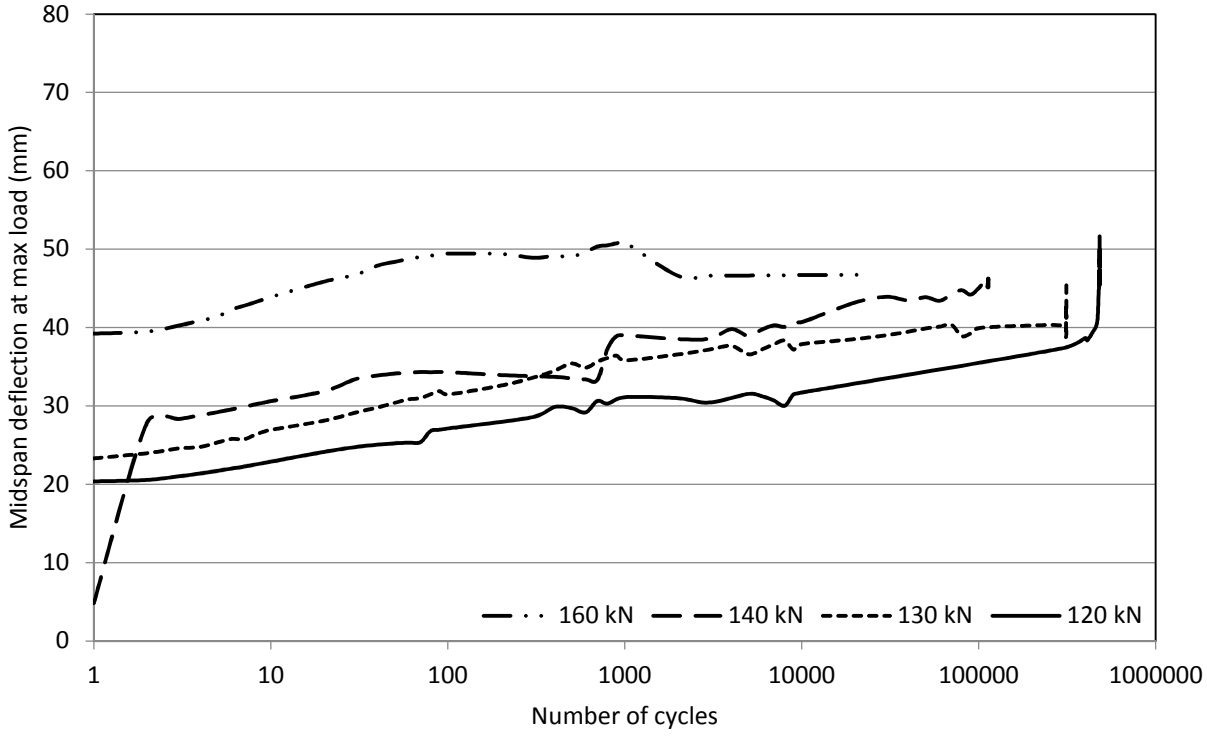

b) PT2S series

Figure 4.25 - Effect of number of cycles on midspan deflection (continued)

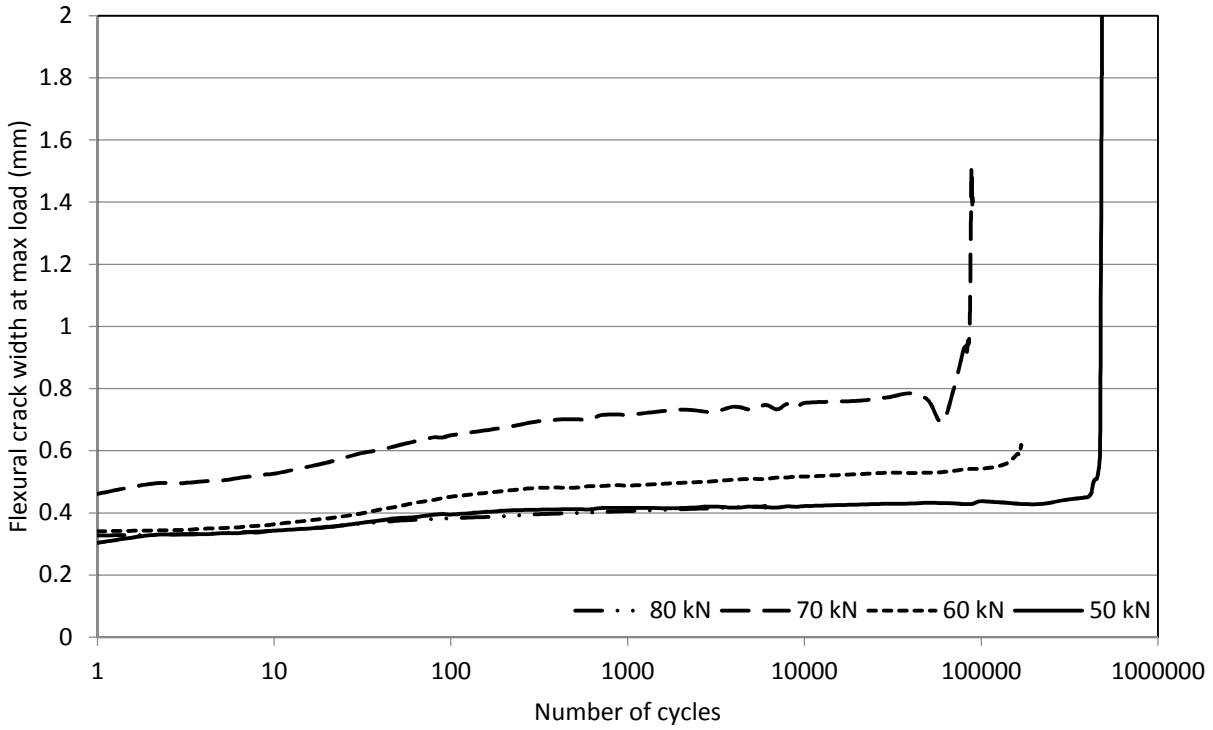

a) G1 series

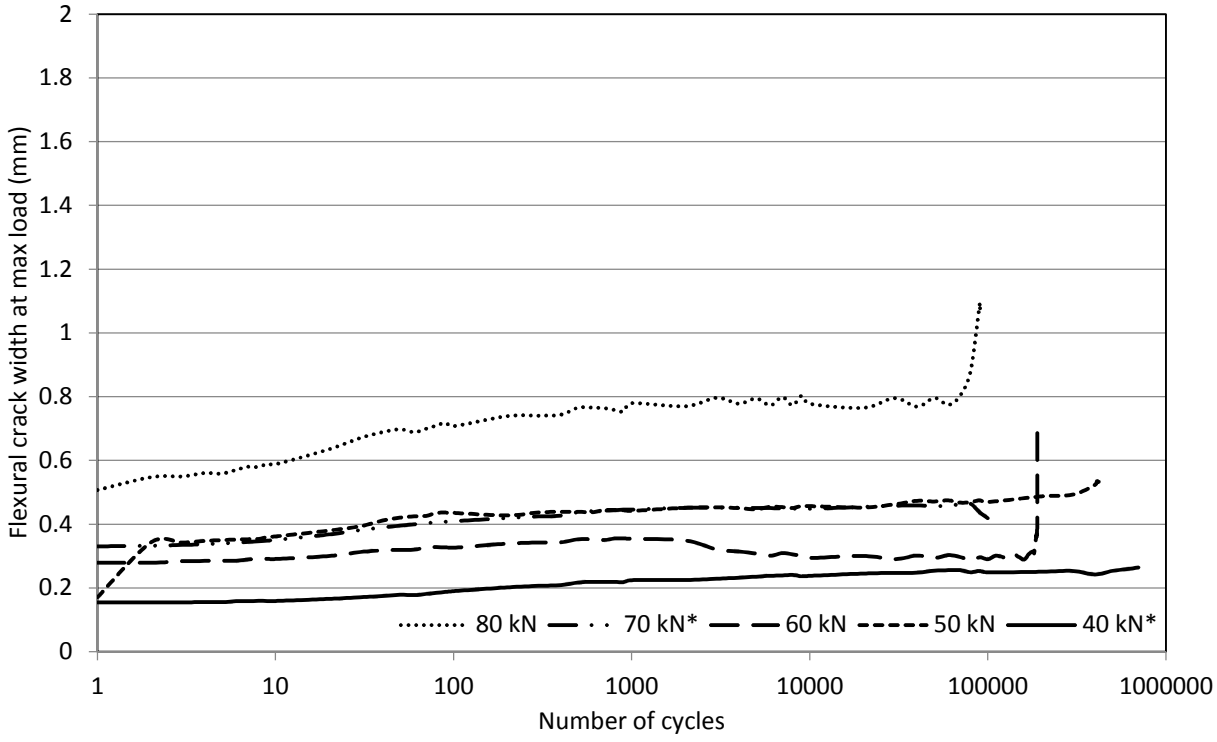

c) G1S series

Figure 4.26 - Effect of number of cycles on flexural crack widths

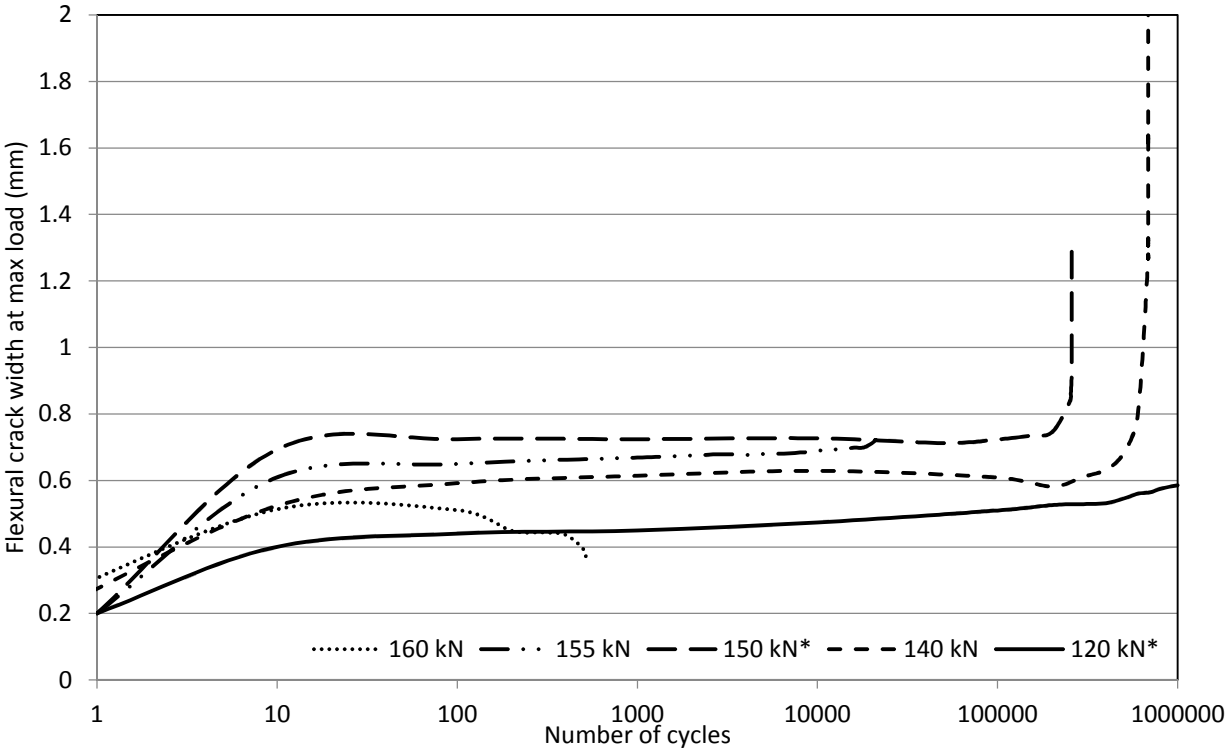

c) PT2 series

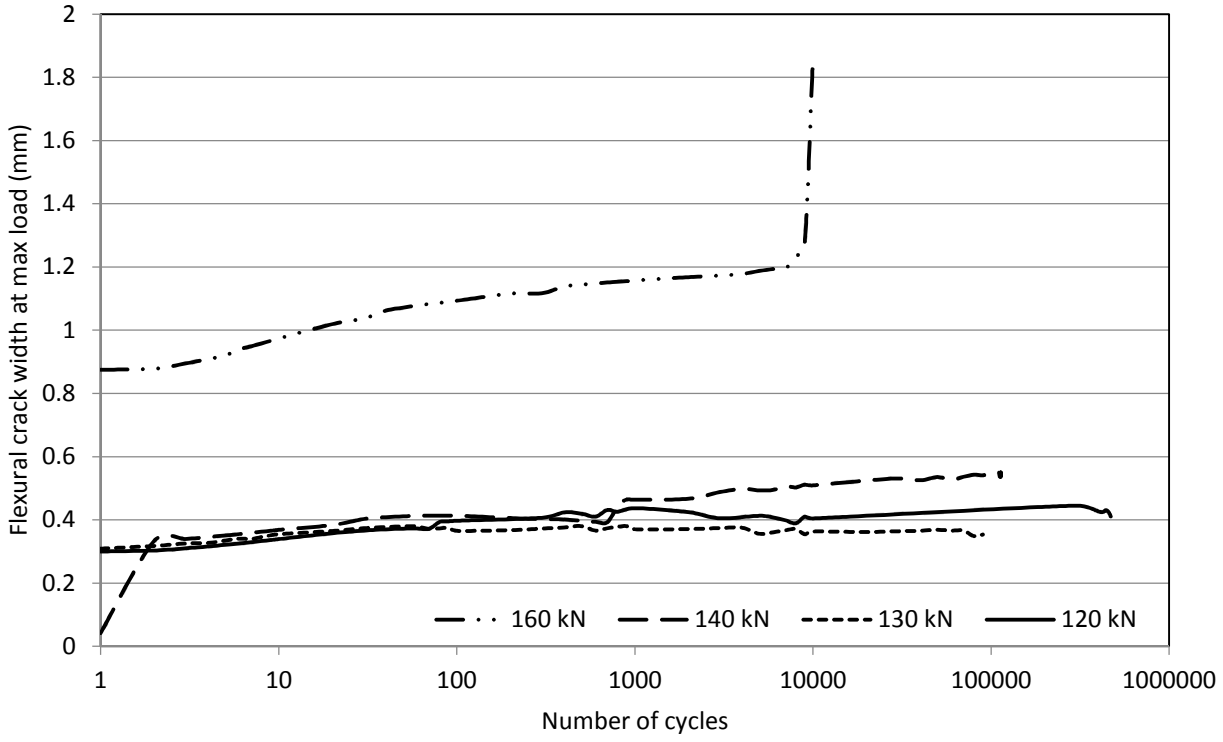

d) PT2S series

Figure 4.26 - Effect of number of cycles on flexural crack widths (continued)

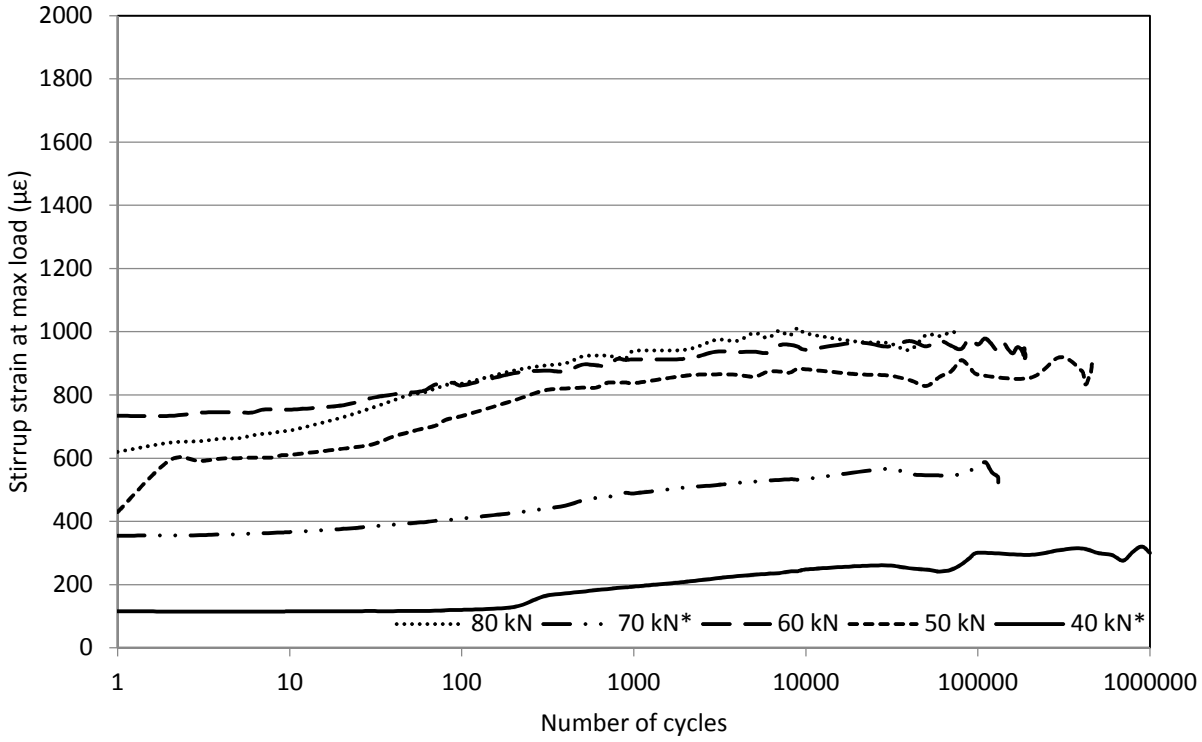

a) G1S series

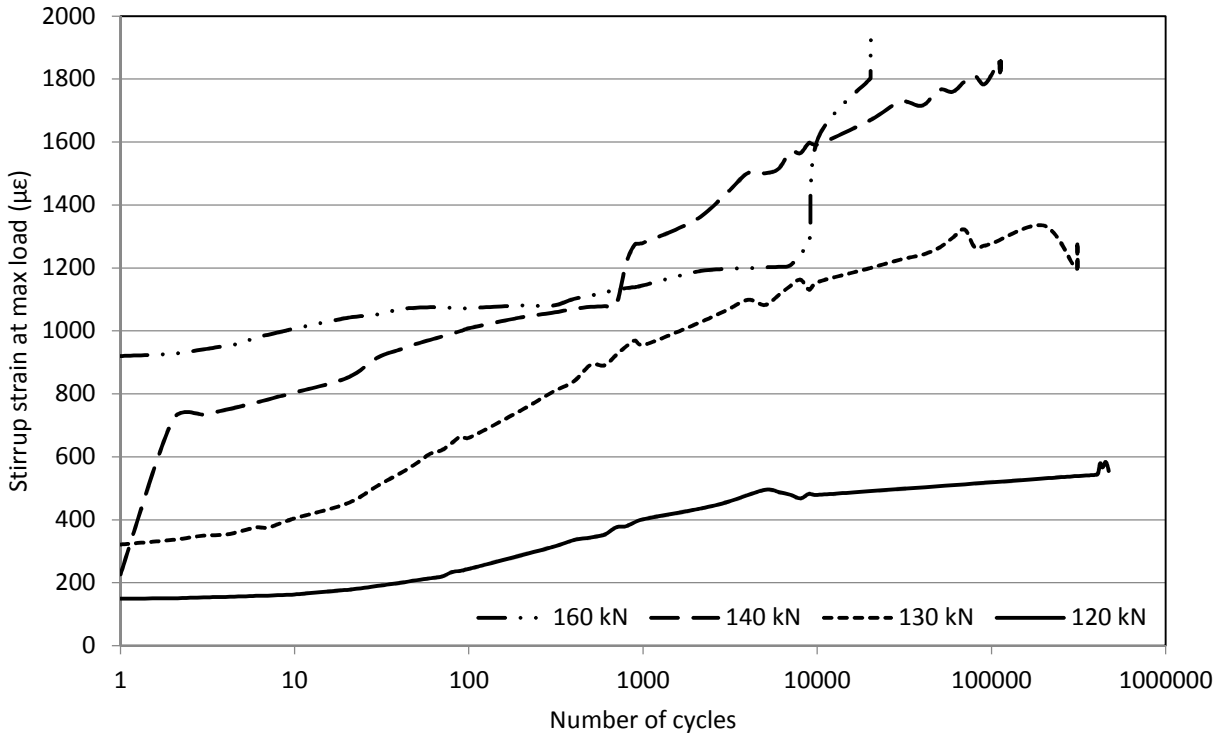

b) PT2S series

Figure 4.27 - Effect of cyclic loading on maximum stirrup strains

Figure 4.28 - Fatigue failure modes: shear (top) and flexure (bottom)

Chapter 5 - Ancillary Testing

5.1 Overview

In addition to the flexural tests conducted on the concrete slab specimens (Chapter 4), a number of ancillary tests were performed to characterize the various materials being used and to contribute towards the calibration of the analytical models discussed in Chapter 7. The mechanical properties of the CFRP and GFRP bars used in this study were determined using standard test methods, where applicable. Fifteen GFRP-RC beam-hinge specimens were also constructed and tested under static and fatigue loading to establish a fatigue life curve for the GFRP reinforcing bars; these results were compared with fatigue tests performed on bare GFRP bars in order to quantify the effect of the surrounding concrete on the fatigue life of the GFRP bars used in this study.

5.2 Mechanical Properties of CFRP Bars

The ultimate tensile capacity of the CFRP bars was determined experimentally using a total of 80 test specimens. 40 bars had a smooth, shiny surface following the pultrusion process while the surface of the remaining 40 bars was sanded down along the length of the bar as is often done prior to the application of a sand coating to enhance the CFRP-concrete bond. A simple test setup was constructed in order to test the bars under direct tension. The length of each bar was 1.2 m, leaving approximately 1 m between the wedge-type anchors used at each end (Figure 5.1). The test method was conducted in accordance with ASTM D7205/D7205M (2011); although the standard recommends the use of a rigid pipe anchor, any type of anchor is permitted as long as

failure of the bar occurs between the anchors and the anchors prevent excessive slip of the bar prior to failure.

Figure 5.1 - CFRP bar with anchors

A 500 kN capacity MTS testing frame with a hydraulic actuator was used to apply the tensile force to the bars. A fixture was mounted to the actuator which consisted of four steel rods and a pair of steel plates to transfer the applied load to the CFRP bar by bearing against the top anchor (Figures 5.2 and 5.3). One of the steel plates had a slot to allow the CFRP bar to be easily inserted into the test setup. A similar slotted steel plate was used at the bottom end of the bar-anchor assembly which was restrained by a pair of steel straps held in place by threaded steel rods fixed to the bottom of the test frame.

Due to the violent nature of failures caused by tendon rupture, several steps were carried out to ensure that the failure was properly contained and to reduce the risk of injury or equipment damage. A box was built around the test setup using plywood panels and a sheet of plexiglass, such that the test could be easily and safely monitored from outside the box. A hinged door was placed on one side to allow easy access to the test setup for installing and removing the test specimens. Lastly, the top anchor was tied down with a rope to prevent it from damaging anything or being damaged as a result of the energy released by rupture of the CFRP bar.

Figure 5.2 - Test fixture and setup

A load cell mounted on the hydraulic actuator connected to a computer controlled data acquisition system was used to monitor and record the applied load. Three specimens were also instrumented with 5 mm electrical resistance strain gauges to measure the strain at ultimate and to determine the elastic moduli of the bars. The diameter of each bar was measured manually using a set of digital callipers.

Prior to anchoring the CFRP bar, the surface of the bar was cleaned using acetone and then the copper sleeve was placed onto the rod. The outer surfaces of the steel wedges and the inner surface of the barrel were lubricated using a graphite spray. The wedge-sleeve-bar assembly was then inserted inside the barrel, after which the wedges were pre-seated into the barrel using a hydraulic seating device to a pressure of 6000 psi (or 54 kN compression force). The

wedge distance after seating was, on average, 15.30 +/-1.46 mm for the unsanded bars and 9.95 +/-1.40 mm for the sanded bars.

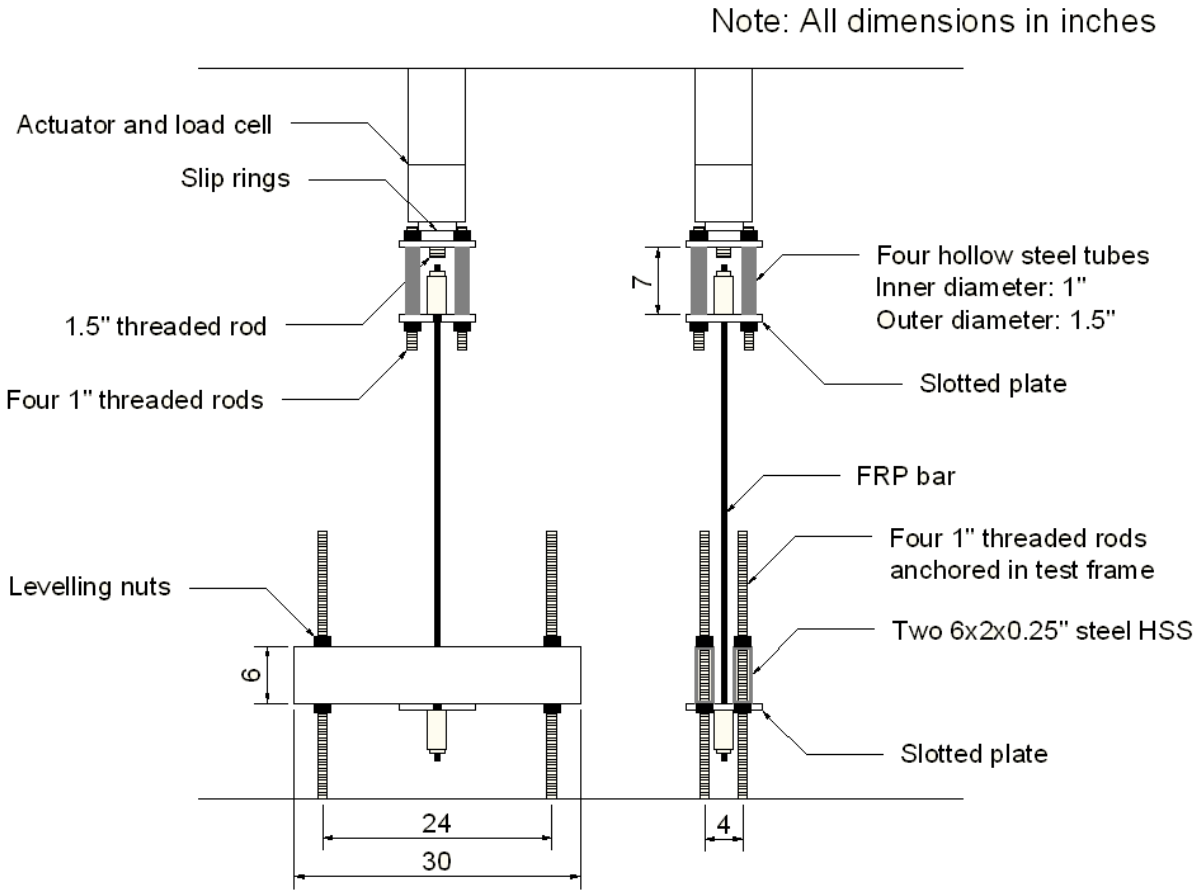

Figure 5.3 - Test setup

After the CFRP bar was in place in the test frame, the actuator was operated manually using a control pod until the bottom anchor and steel plate were bearing snugly against the bottom straps. The load was subsequently applied at a controlled rate of 6 mm/min until failure. Since the total displacement typically included some movement of the wedges within the anchors, rupture of the test specimen generally occurred 4 to 5 minutes after commencing the loading procedure. After failure of each specimen, the fragments were removed prior to installing the next bar. It is worth mentioning that the steel barrel and the wedges were reusable. Only the

copper sleeves were discarded at the end of each test, and new sleeves were used for the next specimen.

A summary of the test results is given in Tables 5.1 and 5.2. Figure 5.4 shows a plot of the applied load at failure versus the average bar diameter. As expected, the bars which had been sanded were slightly smaller in diameter than those which had been left unsanded. However, the ultimate failure loads and corresponding ultimate stresses were generally within the same range irrespective of whether the surface had been sanded or not. While the sanded bars had a slightly lower average failure load than the unsanded specimens, the average ultimate stress was actually higher due to the smaller cross-sectional area. This is attributed to the resin-rich area on the outside of the unsanded bars which does not contribute significantly to load-carrying capacity.

The sanded bars displayed greater scatter in all three categories, as tabulated in Tables 5.1 and 5.2. In particular, a significant increase in scatter can be observed in the bar diameter where the standard deviation of the sanded bars is almost four times that of the unsanded bars. This is indicative of greater variation in the sanding process than the pultrusion process. The increased scatter can be easily observed in Figure 5.4.

Table 5.1 - Summary of test results on unsanded bars

	Minimum	Maximum	Average	Standard deviation
Bar diameter (mm)	12.37	12.54	12.45	0.03
Failure load (kN)	191.3	234.4	211.5	10.0
Ultimate stress (MPa)	1569	1916	1736	82

Table 5.2 - Summary of test results on sanded bars

	Minimum	Maximum	Average	Standard deviation
Bar diameter (mm)	12.13	12.44	12.31	0.11
Failure load (kN)	191.0	245.2	209.3	11.4
Ultimate stress (MPa)	1577	2080	1760	98

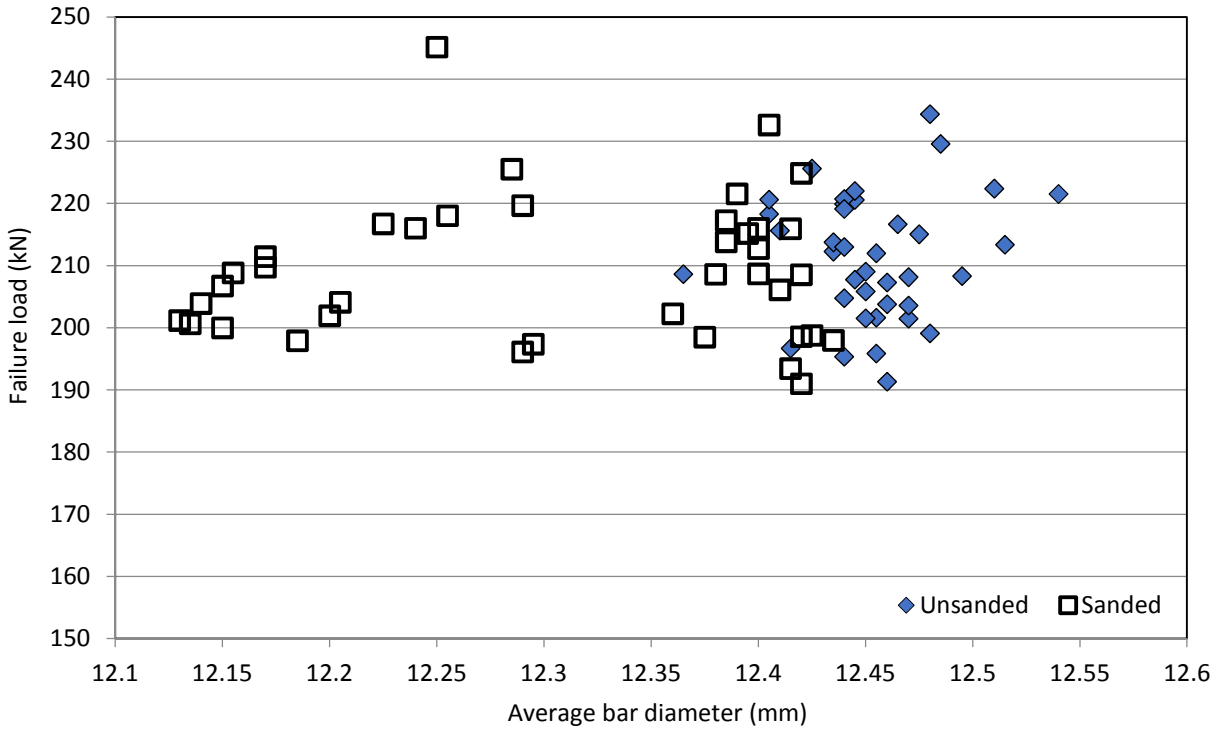

Figure 5.4 - Relationship between failure load and bar diameter

Average ultimate strengths of 1736 MPa and 1760 MPa were obtained for the unsanded and sanded bars, respectively. The strains at failure for the three bars instrumented with strain gauges were 11894, 11990 and 12483 με corresponding to elastic modulus values of 146, 147 and 146 GPa, respectively. These values are in general agreement with the manufacturer's reported values of 1765 MPa ultimate strength and 144 GPa modulus of elasticity; the results

are slightly surprising in that the measured strengths are generally expected to be higher than the guaranteed minimum values provided by the manufacturer. The manufacturer did not report the effective area used to calculate the tensile strength, which may have varied slightly from the measured dimensions used in this study. The test procedure may also have influenced the test results by introducing a slight eccentricity of the tension force, although no signs of premature rupture within the anchors were observed.

The CFRP bar ruptures were violent and brittle. Failures initiated by rupture of individual fibres, scattering bar fragments in all directions. Failure did not initiate at the anchors demonstrating that the anchors used were successful in transferring the load to the bar without damaging the fibres. Examples of failed specimens are shown in Figure 5.5.

Figure 5.5 - CFRP bars after failure

5.3 Mechanical Properties of GFRP Bars

5.3.1 Static Tensile Strength

The mechanical properties of the #5 GFRP bars used as primary passive reinforcement in the concrete slabs were measured by simple uniaxial tension tests. Three 1 m samples of the GFRP bars without the external sand coating were gripped at each end by a modified version of the wedge-type anchor used for CFRP prestressing and tested to failure in a 500 kN capacity hydraulic test frame as shown in Figure 5.6. In order to accommodate the reduced transverse strength of the GFRP bar as well as the larger diameter compared with the #4 CFRP bars, new wedge-type anchors were fabricated having an increased length of 5 inches and an inner diameter of approximately 16 mm. The outer diameter of the barrel was kept constant at 50 mm.

Figure 5.6 - GFRP bar uniaxial tension test

Each bar was instrumented with an electrical resistance strain gauge to measure the elastic modulus of the bar. The load was applied at a rate of 40 kN per minute until failure occurred. The experimental results of these tests are compared with the guaranteed values given by the manufacturer in Table 5.3; both the ultimate tensile strength and elastic modulus values exceeded the guaranteed values.

Table 5.3 - GFRP axial tension test results

GFRP bar	Ultimate stress (MPa)	Elastic modulus (GPa)
1	745	55.7
2	802	56.3
3	805	55.8
Average	784	55.9
Guaranteed	683	48.2

5.3.2 Fatigue Tensile Strength

In order to further investigate the response of the GFRP-RC slabs under cyclic loading, it is beneficial to examine the fatigue behaviour of the individual components of the structure. CFRP is known to have excellent fatigue characteristics, an observation which has been validated by the present study; all of the specimens subjected to repeated loading ultimately exhibited a failure mode which was dominated by rupture of the GFRP reinforcement or diagonal tension shear failure. Furthermore, shear failures were eliminated in the full scale specimens when transverse shear reinforcement in the form of double-headed shear bars was provided; even when no shear reinforcement was provided, fatigue failure was governed by GFRP rupture at lower load levels. Based on these observations, it is reasonable to conclude that the fatigue life of the GFRP reinforcing bars at load ranges corresponding to the service condition due to live truck loads will govern the overall fatigue life of the prestressed slab

bridge, irrespective of whether or not shear reinforcement is provided. Therefore, in order to better predict the fatigue response of GFRP-RC structures, an improved understanding of the fatigue behaviour of the GFRP bars themselves and their interaction with the concrete are needed.

Gripping mechanisms and the presence of concrete surrounding the bar during the fatigue test can have a significant effect on the test results (ACI 440.1R-06). Concrete has an adverse effect on the fatigue behaviour of FRP bars due to its harsh alkaline environment and friction between the FRP bar and the concrete which causes abrasion of the bar surface (Rahman et al. 1996, Adimi et al. 2000). Fatigue failure of an FRP bar embedded in concrete may be initiated at the bar surface inside the concrete in the form of matrix cracks caused by friction with the concrete (Adimi et al. 2000). Friction fretting of the rod surface causing successive destruction of the bar may take place near flexure-induced cracks where bond stresses are high and partial slip occurs (CEB-FIP 2000). Katz (2000) observed significant damage at the surface of FRP bars subjected to cyclic loads embedded in concrete and in some cases the external layer of the bar was completely sheared off. In an effort to quantify the effect of concrete on the behaviour of GFRP bars under cyclic loading, a direct comparison of the fatigue behaviour of bare GFRP bars and GFRP bars in concrete beams is needed; the following is a discussion of the ancillary tests which were conducted in an attempt to address these issues.

5.3.2.1 Bare Bar

No standard test methods are currently available for the fatigue testing of FRP reinforcing bars (although ACI 440.3R-04 recommends the same setup used for the static specimens for fatigue

testing, this has proved to lead to premature rupture due to stress concentrations at the location where the bar is gripped). Difficulties arising from gripping methods have caused numerous problems in previous attempts to study the fatigue behaviour of FRP bars (Braimah 2000). Most axial fatigue tests of composite materials—such as FRP laminates—conducted in the past for non-civil engineering applications have used specially prepared coupons with dog-bone profiles or notched specimens to give a reduced cross-section in the middle of the specimen. Some researchers studying the behaviour of FRP reinforcing bars for civil engineering applications have used large concrete blocks to grip the FRP bars (Adimi et al. 2000). However, limited data is available characterizing the fatigue properties of GFRP reinforcing bars for reinforced concrete applications and there have been no reported studies using a simple, reusable anchorage system capable of reaching the full fatigue life of GFRP reinforcing bars in cyclic tension.

Initial attempts to conduct axial fatigue tests on #5 (16 mm diameter) GFRP bars using a similar test setup as the static tests consistently resulted in premature failure of the bars with fracture initiating within the anchors due to the local stress concentration at the end of the steel wedges. GFRP is very susceptible to transverse pressure, and while the anchors were successful in developing the full static tensile capacity of the bars, cyclic loading quickly led to local fibre failures which, in turn, resulted in failure of the bar. For this reason, GFRP test specimens were carefully machined using a computer numerical control (CNC) machine to give a reduced diameter of 12 mm at the middle of the specimens (Figure 5.7), effectively reducing the critical cross-section by approximately 43%. The cross-section was reduced using a gradual transition with a constant radius over a length of 140 mm to eliminate any stress concentrations arising

from the change in geometry and to allow adequate load transfer between fibres; the ratio of the "notch" radius (1320 mm) to minimum bar diameter (12 mm) was 110, giving a stress concentration factor, K_{tn}, of less than 1.0025 as shown in Figure 5.8 (Pilkey & Pilkey 2008).

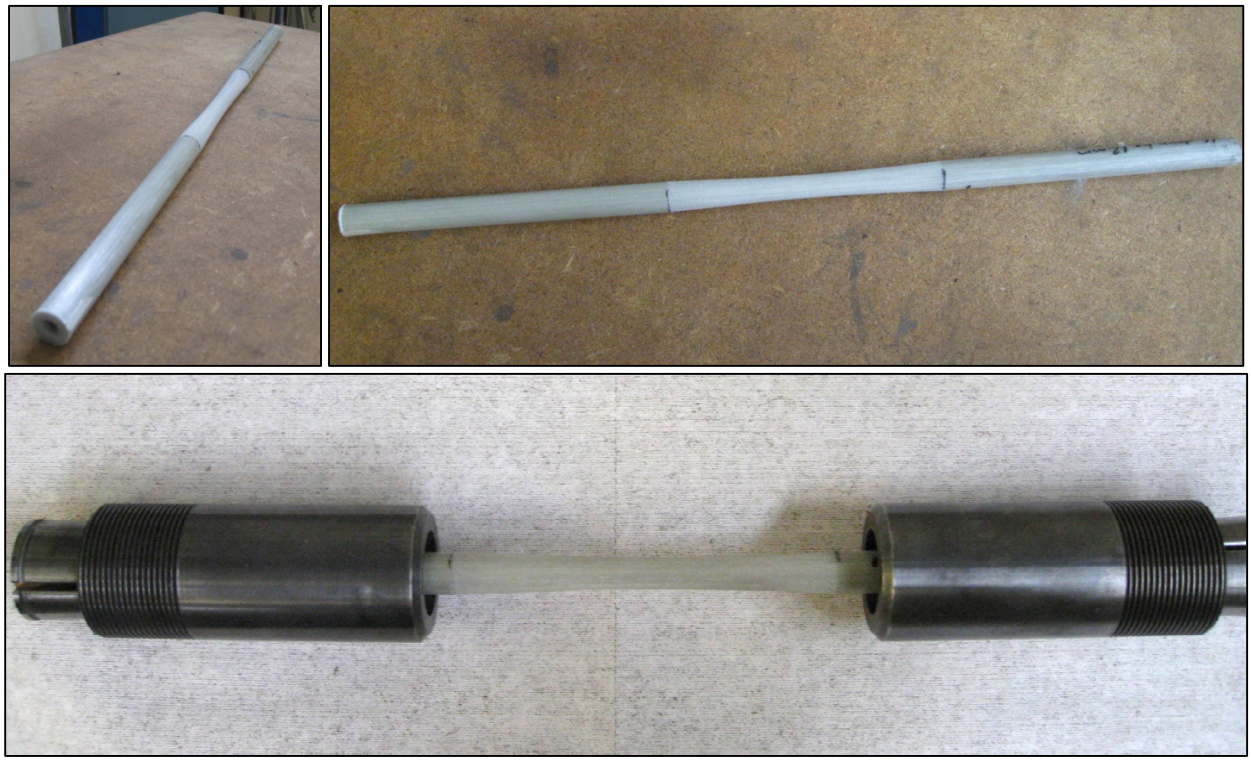

Figure 5.7 - GFRP axial fatigue test specimen

Each specimen had a length of 500 mm and was gripped at each end using the same wedge-type anchors described previously. The test setup was similar to that used for the static tests, with a slotted plate mounted to a hydraulic actuator at the top and another slotted plate anchored to the bottom of the test frame. A protective box was built around the test setup to contain the failure and increase safety. The test setup is shown in Figure 5.9.

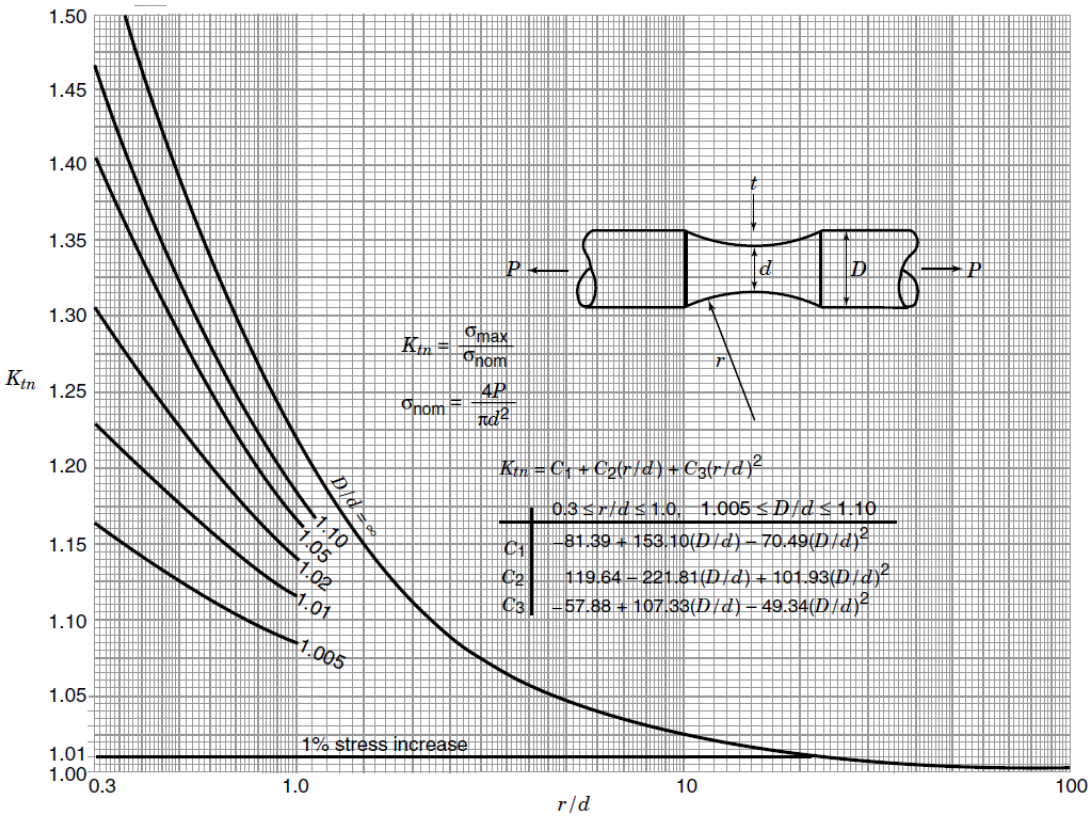

Figure 5.8 – Peterson's stress concentration factors (Pilkey & Pilkey 2008)

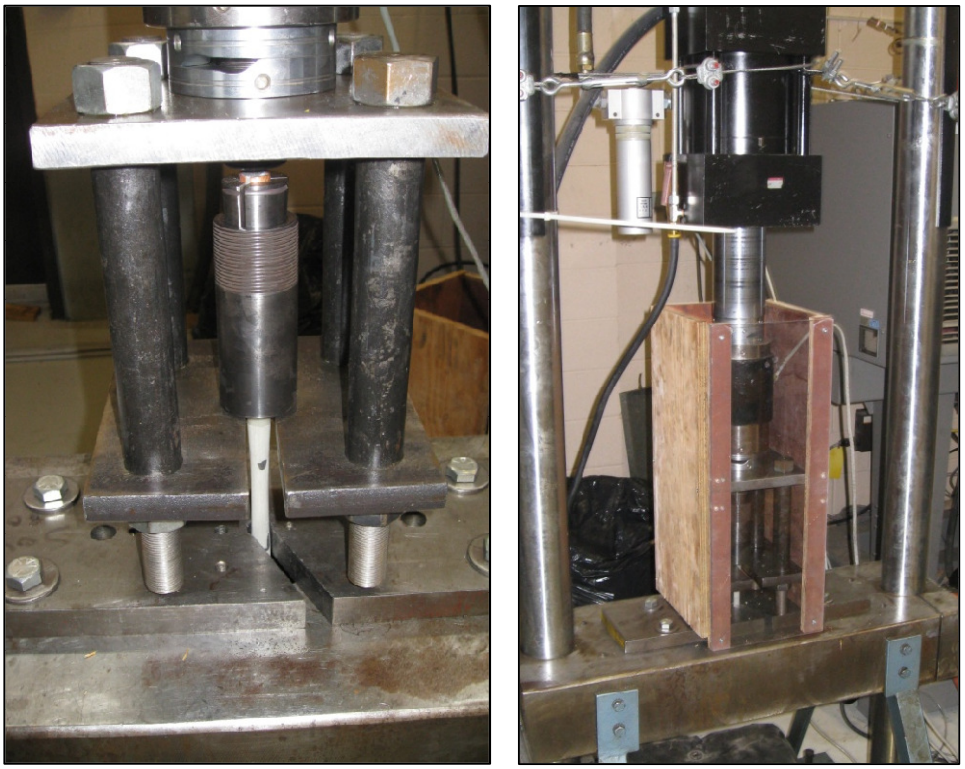

Figure 5.9 - Axial tension fatigue test setup

Even after machining the specimens, the first few fatigue tests resulted in a mixed failure mode which initiated by fracture of several fibres within the critical section, and was followed by rapid propagation of the matrix cracks to one of the anchors. As the cracks propagated to the anchors, some of the fibres were no longer contributing to the load resistance leading to eccentricity within the anchor; this internal bending caused an uneven distribution of transverse pressure leading to shearing of the outer fibres at the anchor-bar interface. The specimens typically ultimately failed by rupture at the tip of the anchor wedges. In order to eliminate this premature failure mode for subsequent tests, the copper sleeves used in the anchors were placed in such a way that a small gap was present at the tip of the wedges between the steel wedges and the GFRP bar as shown in Figure 5.10. This eliminated any stress concentration at the wedge tip and, in turn, eliminated failures within the anchors. All subsequent tests showed no evidence of failure within the anchors; only these results are reported here.

A total of twelve GFRP specimens were tested in fatigue at five different load ranges. The fatigue test results are summarized in Table 5.4. The minimum load level was kept constant at a load corresponding to a stress in the critical section of 30 MPa, similar to that in the beam-hinge specimens (described in the following section). The maximum load level was varied to give stress ranges between 225 MPa and 325 MPa, corresponding to approximately 33% and 48% of the guaranteed ultimate strength of the bars, respectively, to cause failures within 2 million cycles. One specimen survived the full 2 million load cycles and was retested at a higher load range until failure. A data acquisition system was used to record data during the test including applied load, relative displacement between the top and bottom anchor and strain at

the critical section measured using a 5 mm electrical strain gauge affixed at the mid-depth of the specimen. For each test, the specimen was first loaded up to its maximum load level and then unloaded to give the first cycle response and to seat the wedges in the anchor. The fatigue loading was then commenced at a rate of 4 Hz until failure.

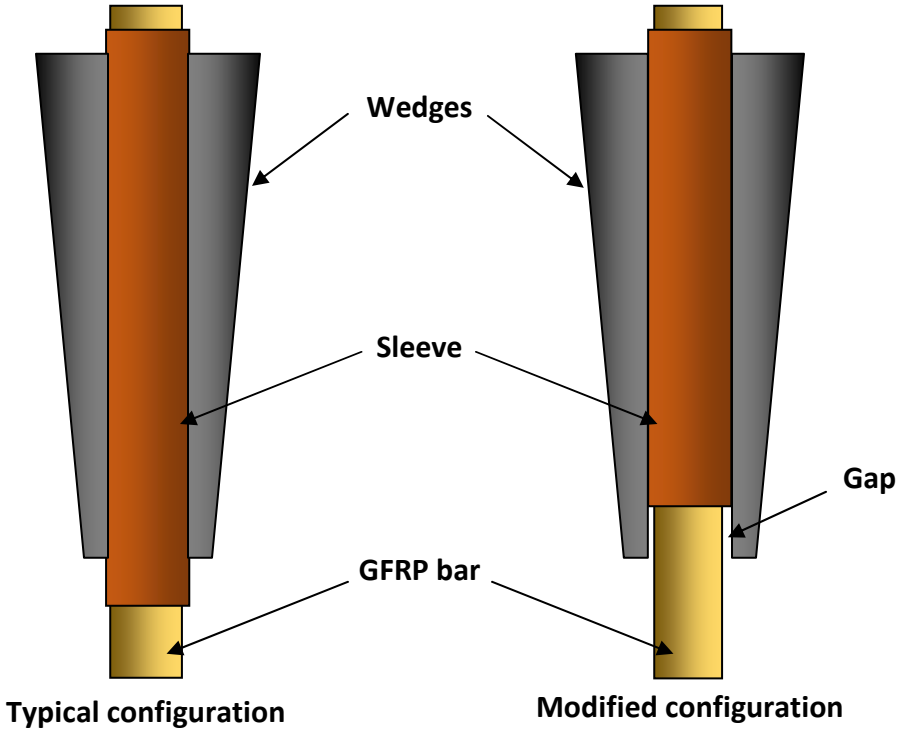

Figure 5.10 - Wedge and sleeve setup for axial fatigue tests

The data recorded during the initial cycle were used to determine the initial elastic modulus of the bar. A typical stress-strain response from an initial load cycle is shown in Figure 5.11. As seen, the elastic modulus values measured from the fatigue specimens were similar to those obtained from the static tests. Measured strains at the maximum load level tended to increase very gradually until just prior to failure when individual fibre ruptures resulted in a sudden increase in the average stress in the cross-section as shown in Figure 5.12.

Table 5.3 - GFRP fatigue test results

Test	Stress range (MPa)	Fatigue life
1	225	>2000000
2	250	550715
3	250	1162199
4	250	1165753
5	275	169532
6	275	449021
7	275	195646
8	300	311504
9	300	120965
10	300	289291
11	325	91538
12	325	121670
13	325	79971

The relative displacement between the two anchors increased substantially in the initial cycle as the wedges seated themselves into the anchor barrel (Figure 5.13). Subsequent load cycles resulted in a very gradual change in the relative displacement until just prior to failure (Figure 5.14). In most cases, the strain gauges did not survive the entire fatigue life of the specimen. However, since the ratio of strain to relative displacement remained approximately constant, it is assumed that after the initial cycle the change in strain, ε, can be approximated by the change in displacement, Δ, as given by Equation 5.1:

Eq. 5.1 $$\frac{\Delta_N}{\Delta_i} \approx \frac{\varepsilon_N}{\varepsilon_i}$$

Where, Δ_N and Δ_i are the relative displacements between the two anchors after N cycles and after the initial cycle, respectively, and ε_N and ε_i are the strains at the critical section after N cycles and after the initial cycle, respectively.

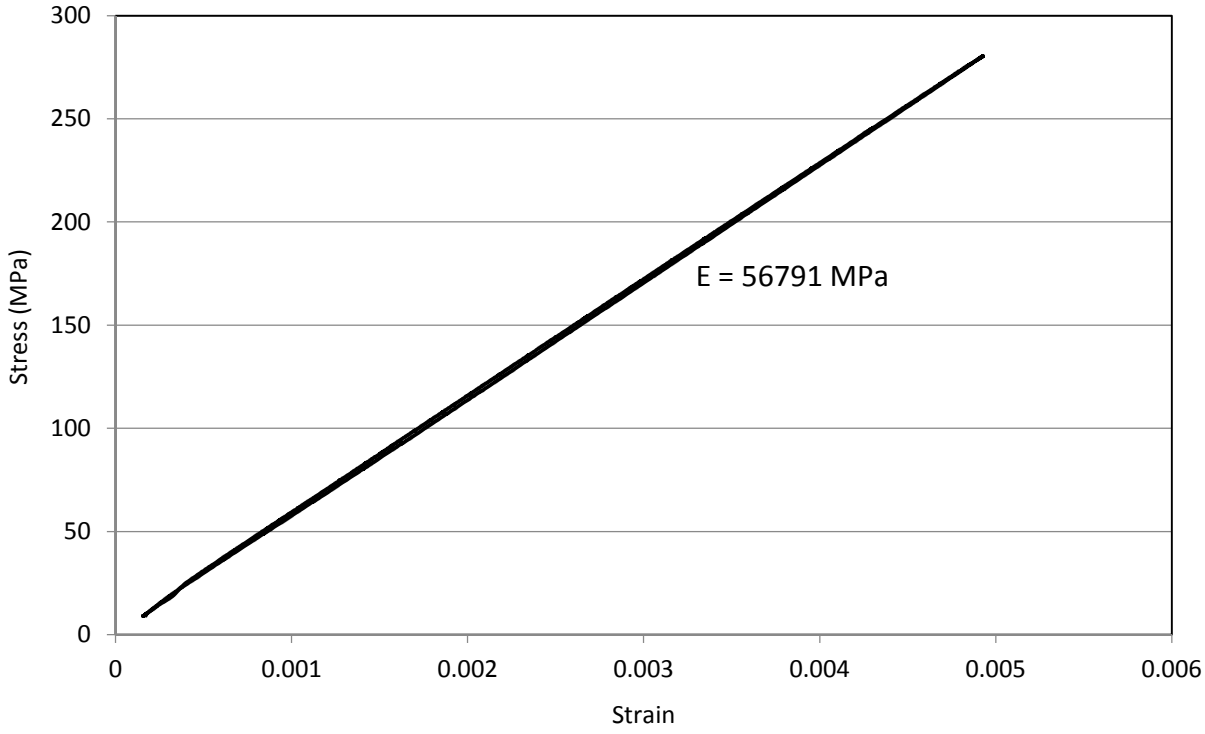

Figure 5.11 - Typical stress-strain curve for axial fatigue specimens

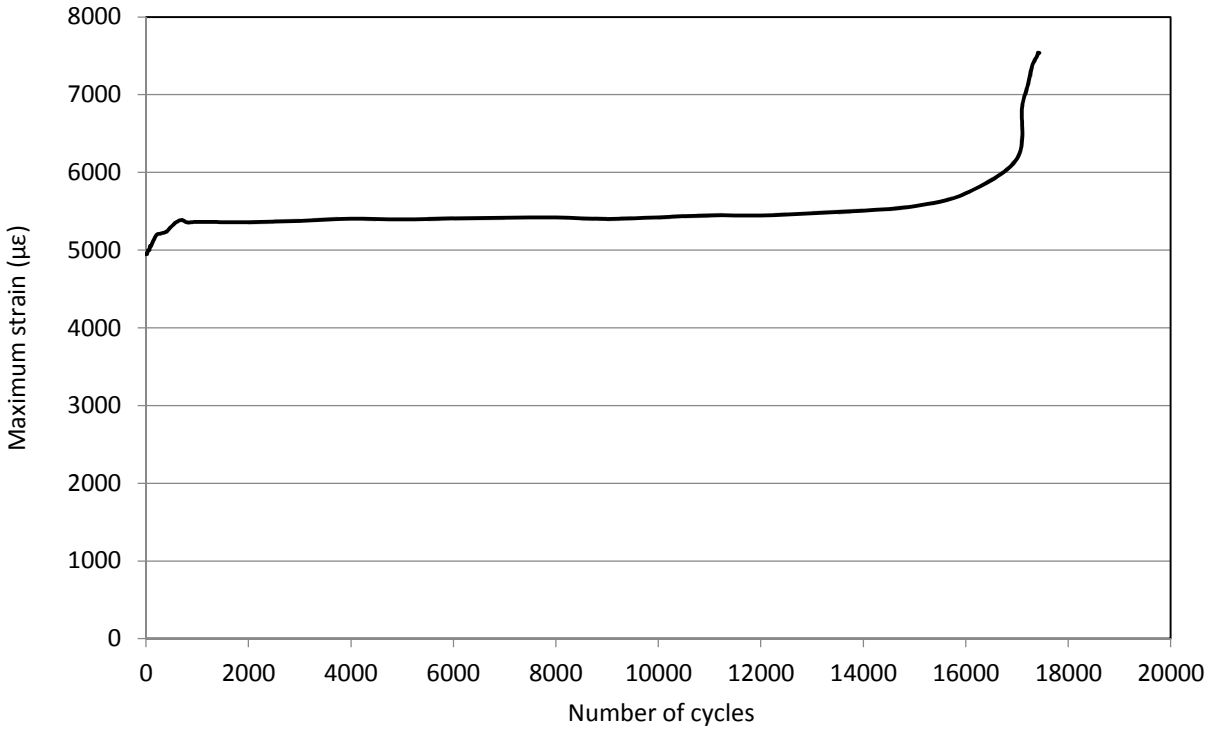

Figure 5.12 - Typical strain variation with repeated loading

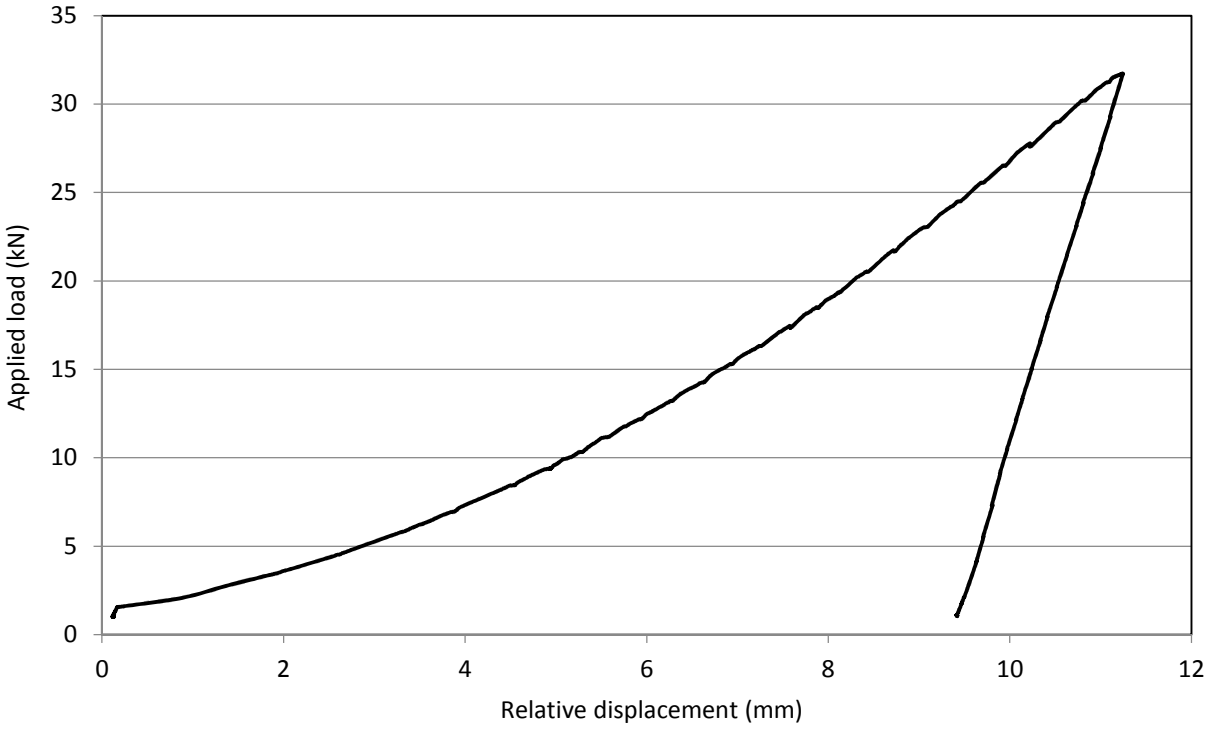

Figure 5.13 - Typical relative displacement between anchors during initial load cycle

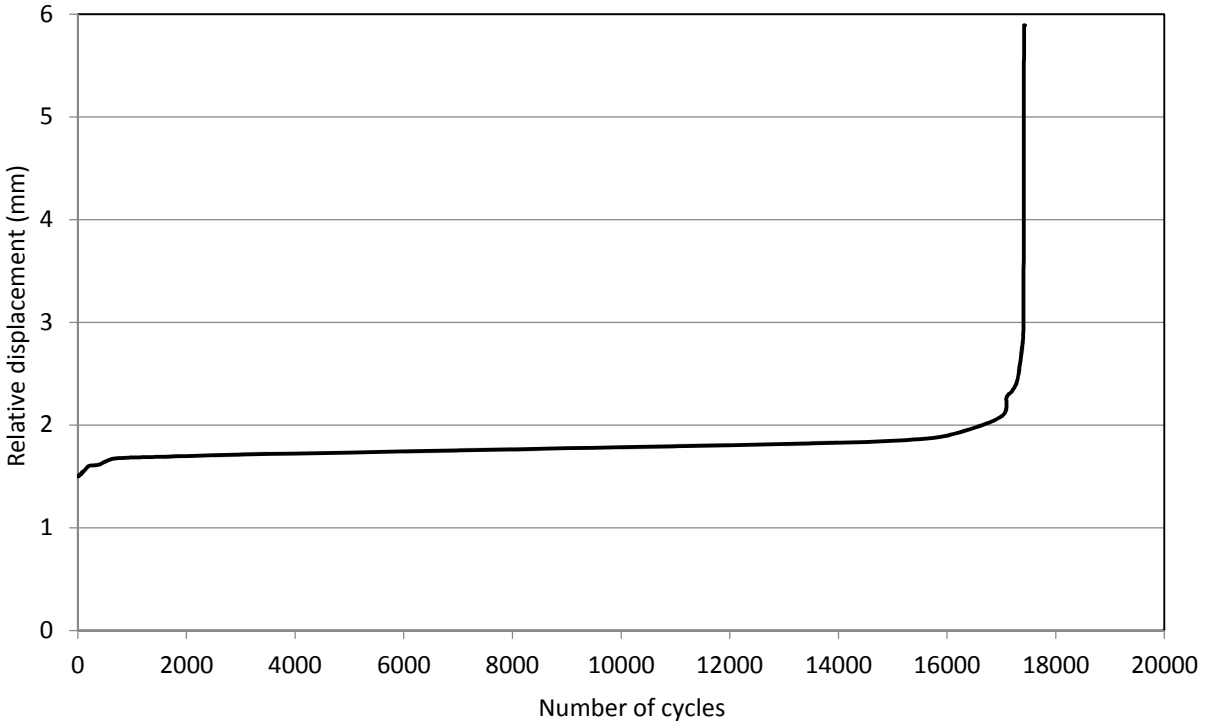

Figure 5.14 - Typical variation in relative displacement between anchors with repeated loading

Failures initiated at the critical section and longitudinal matrix cracks propagated towards the end anchors. Some fractured fibres and longitudinal splits could typically be observed at the mid-life of each of the test specimens, although the bars continued to take a significant number of additional load cycles before failing. Final failure occurred when the remaining intact fibres could no longer sustain the applied load resulting in fracture at the critical section. Examples of the GFRP fatigue failures are shown in Figure 5.15.

5.3.2.2 Beam-Hinge

The fatigue life of GFRP reinforcing bars in concrete beams subjected to cyclic loads at various constant amplitude load ranges was investigated using 15 modified beam-hinge specimens tested to failure under monotonic and fatigue loading. The classical beam-hinge specimen (RILEM 1982) was developed as an alternative to pullout tests to measure the bond between reinforcing bars and concrete in a way that accurately simulated the flexural behaviour of a reinforced concrete beam. The modified beam-hinge specimens had an increased embedment length to ensure that failure occurred by rupture of the GFRP reinforcement rather than bond failure of the bar-concrete interface.

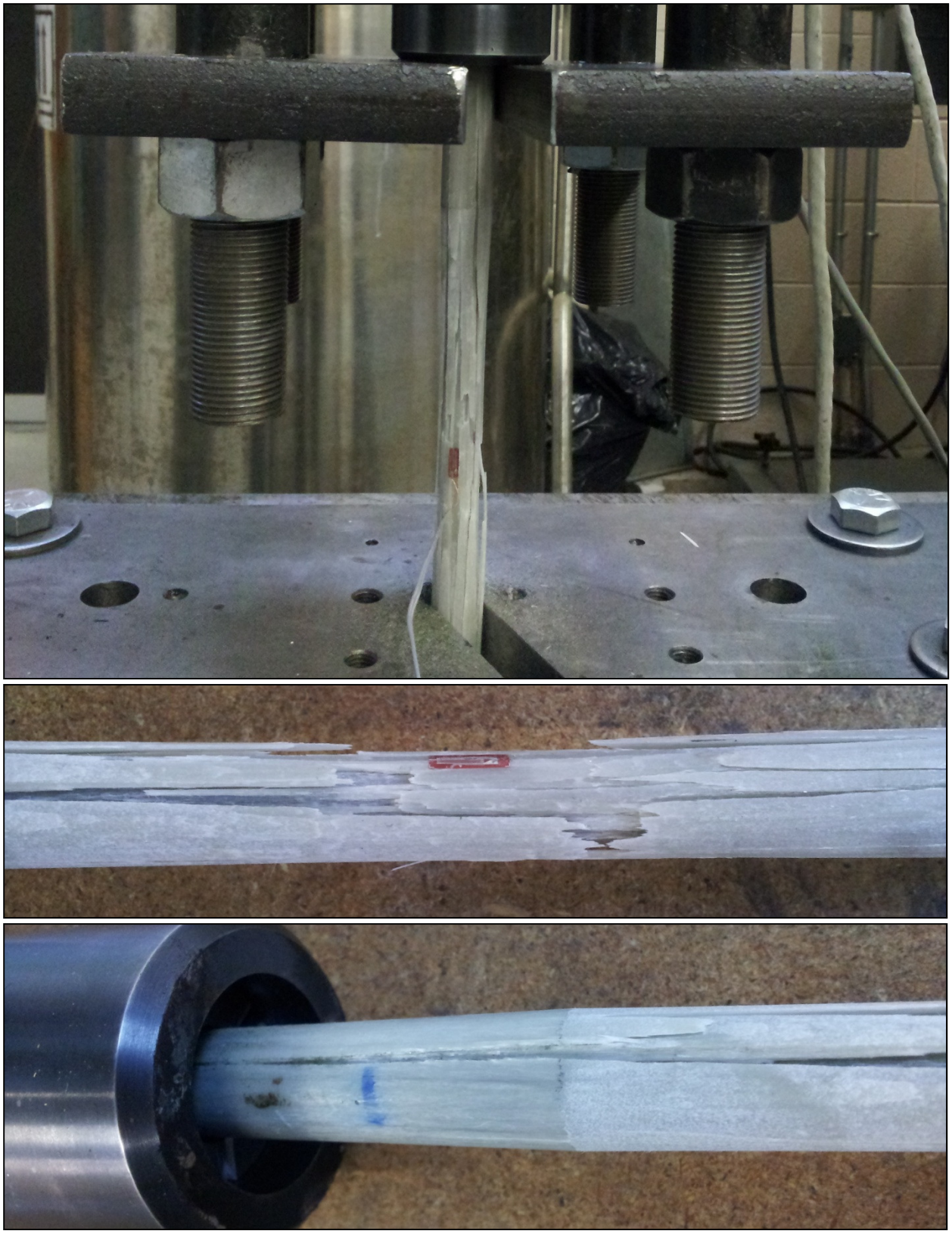

Figure 5.15 - Failure mode of axial tension fatigue tests

The main advantage of conducting bending fatigue tests on concrete beams rather than axial bar tests is that the beams accurately simulate service conditions such as interactions at the reinforcement-concrete interface. Disadvantages include the necessity to make assumptions about the load carrying contribution of the concrete and the accuracy of the placement of the reinforcement (Tilly 1979). The use of a beam-hinge specimen reduces this uncertainty by fixing the length of the moment lever arm. It is generally agreed that beam-hinge tests realistically simulate the stress conditions of reinforced concrete elements subjected to bending (Benmokrane et al. 1996, Bakis et al. 1998). Tilly (1979) observed that bending fatigue tests on steel-reinforced beams could give longer lives than axial bar tests because of the reduced probability of the highest stress concentrations (crack locations) coinciding with the locations of the worst defects in the bar. However, in the case of GFRP reinforcing bars, the effects of friction at the crack location may reduce the fatigue life of the bar by abrasion of the bar surface, effectively reversing this effect.

A total of 15 beam-hinge specimens were constructed, each having a length of 2.6 m and a height and width of 200 mm and 150 mm, respectively, as shown in Figures 5.16 and 5.17. 10M steel stirrups were provided at a spacing of 100 mm in order to preclude shear failure. Each specimen was reinforced with one #5 GFRP bar having a guaranteed ultimate strength and elastic modulus of 683 MPa and 48.2 GPa, respectively. The bars had a sand coating to enhance the bond with the concrete and a nominal cross-sectional area of 197.93 mm^2. The clear cover to the GFRP bar was 30 mm. A hinge was placed at midspan and was comprised of a 4 inch diameter round steel bar bearing against two steel angles cast into the concrete (Figure 5.18). During casting, a piece of foam was used to form the separation between the two individual

beam ends. The purpose of the hinge was to control the length of the internal moment arm and hence the force in the reinforcing bar. The hinge simulates a flexural crack with a known lever arm length in order to control the stress in the bar.

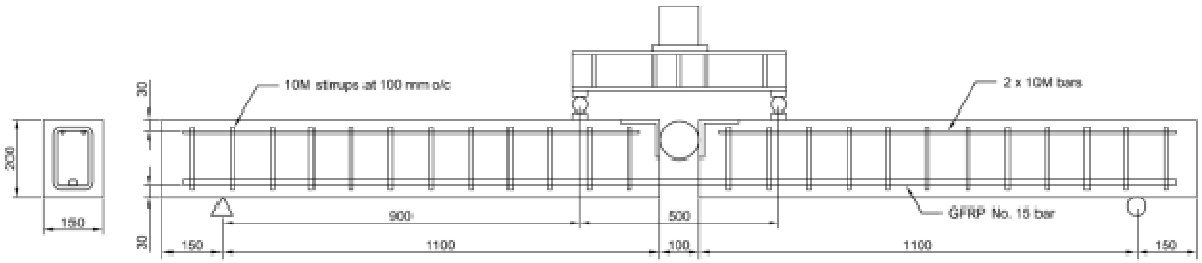

Figure 5.16 - Test setup and specimen geometry

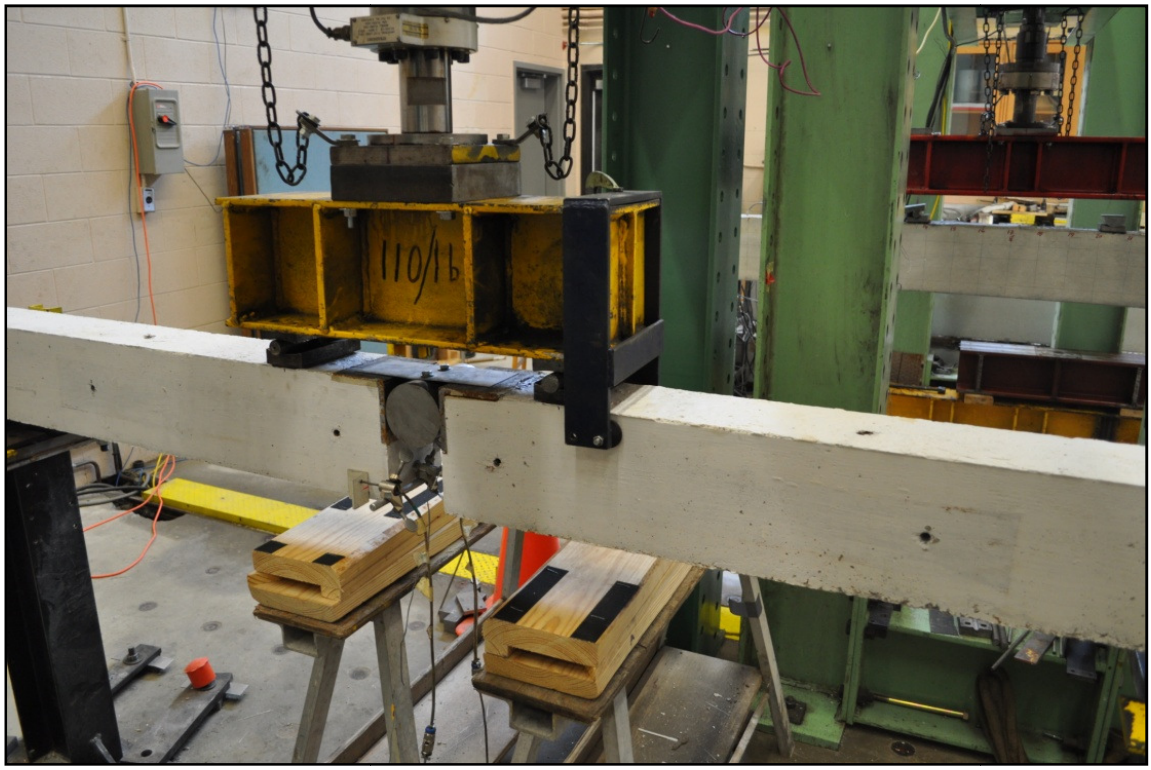

Figure 5.17 - Beam-hinge test specimen in test frame

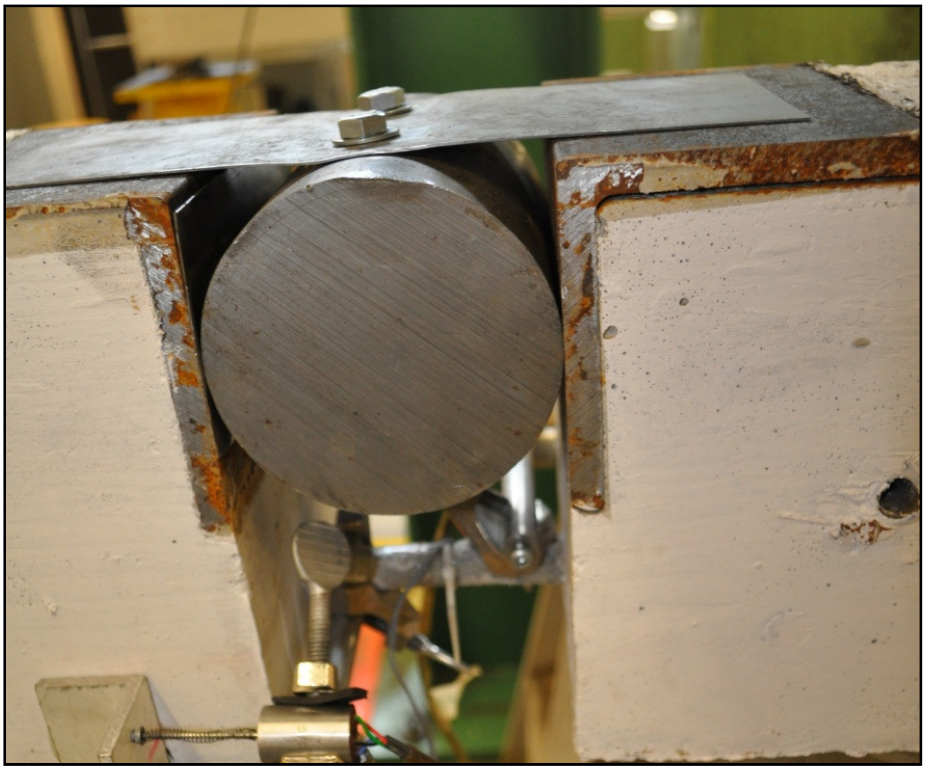

Figure 5.18 - Steel hinge at midspan of beam-hinge specimens

A spreader beam was used to create a constant moment region with a length of 500 mm and shear spans with lengths of 900 mm. Three specimens were tested monotonically to failure at a rate of 1 mm/min. The remaining twelve specimens were subjected to cyclic load ranges between 20% and 55% of the average ultimate static capacity. Cyclic loads were applied at frequencies ranging from 0.2 Hz to 1.0 Hz, depending on the range of deflections caused by the applied loads. Minimum loads were kept constant at 1.5 kN while the maximum load was varied to produce the desired load range. Strain gauges were used to monitor the strain in the GFRP bar at midspan and short stroke LVDTs were used to measure the relative displacement between the GFRP bar and concrete at the hinge location.

The results from the statically loaded beam-hinge specimens are given in Table 5.4; a typical stress-strain curve is given in Figure 5.19. A fully linear-elastic response was observed until just prior to failure, when successive failure of individual fibres preceded ultimate failure. The tensile strength and elastic modulus values obtained from the beam-hinge tests are within 5% of those recorded in bare bar tests; some reduction in capacity is expected resulting from the slight stress gradient induced in the bar due to bending leading to higher-stressed fibres at the bottom of the bar. However, the recorded values were well above the guaranteed values provided by the manufacturer.

Table 5.4 – Monotonic beam-hinge test results

Specimen	Ultimate stress (MPa)	Elastic modulus (GPa)
BH-1	752	51.4
BH-2	708	53.1
BH-3	787	55.5
Average beam-hinge	749	53.3
Average bare bar	784	55.9
Guaranteed	683	48.2

GFRP strain values increased gradually with the application of repeated load cycles until just prior to failure (Figure 5.20). Midspan deflections also increased gradually over the life of each specimen as a result of successive cracking of the concrete, crack widening, vertical crack propagation and breakdown of bond between the reinforcing bar and the concrete; similar trends were observed in the relative displacement between the GFRP bar and the concrete (Figure 5.21). Relative slip values were less than 1 mm at the maximum load when the applied load range was between 20% and 40% of the ultimate static capacity. These slip values are not insignificant, particularly when the load cycles are repeated upwards of one million cycles; this

relative displacement induces abrasion of the bar surface which can initiate fatigue failure mechanisms.

The fatigue results are summarized in Table 5.5, and the S-N curve for the beams representing the relationship between applied cyclic load range and fatigue life is shown in Figure 5.22. The stress ranges given for the GFRP bar reflect the actual measured distance of the moment arm when this value differed slightly from the design value. Tests which reached 1 million cycles were assumed to have reached the runout limit; when this occurred, the load range was increased and a second test was conducted with the same beam. As expected, the effects of the first million cycles on the fatigue life of the beam at an increased load range appear to be negligible. Minimal scatter was observed with the fatigue results, which further validates the use of beam-hinge tests for controlled fatigue experiments. Rupture of the GFRP bars occurred within one million cycles at load ranges as low as 20% of the measured ultimate static capacity; it is clear from these tests that limiting the stresses in GFRP reinforcing bars in concrete structures is imperative when the structure is expected to sustain a large number of load cycles. As shown in Chapter 4, introducing CFRP post-tensioned tendons is an effective way to reduce the induced stresses in passive GFRP reinforcement.

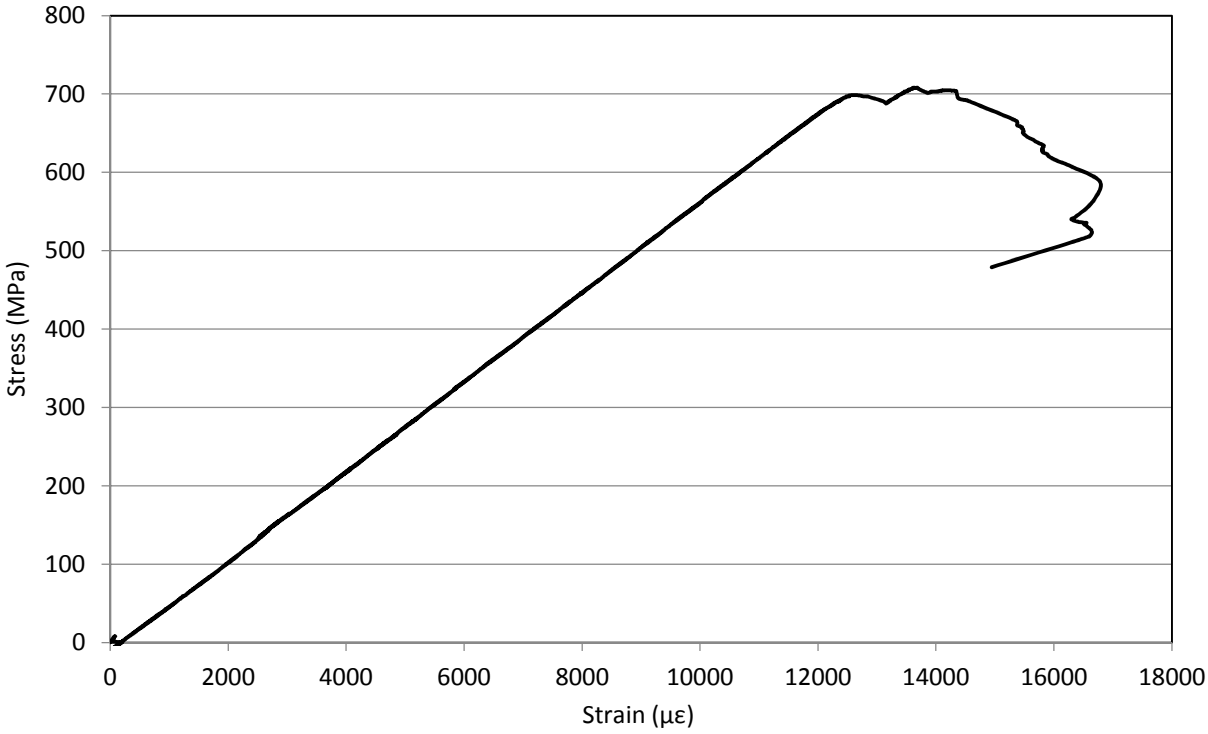

Figure 5.19 – Typical stress-strain response of GFRP bar in beam-hinge specimen

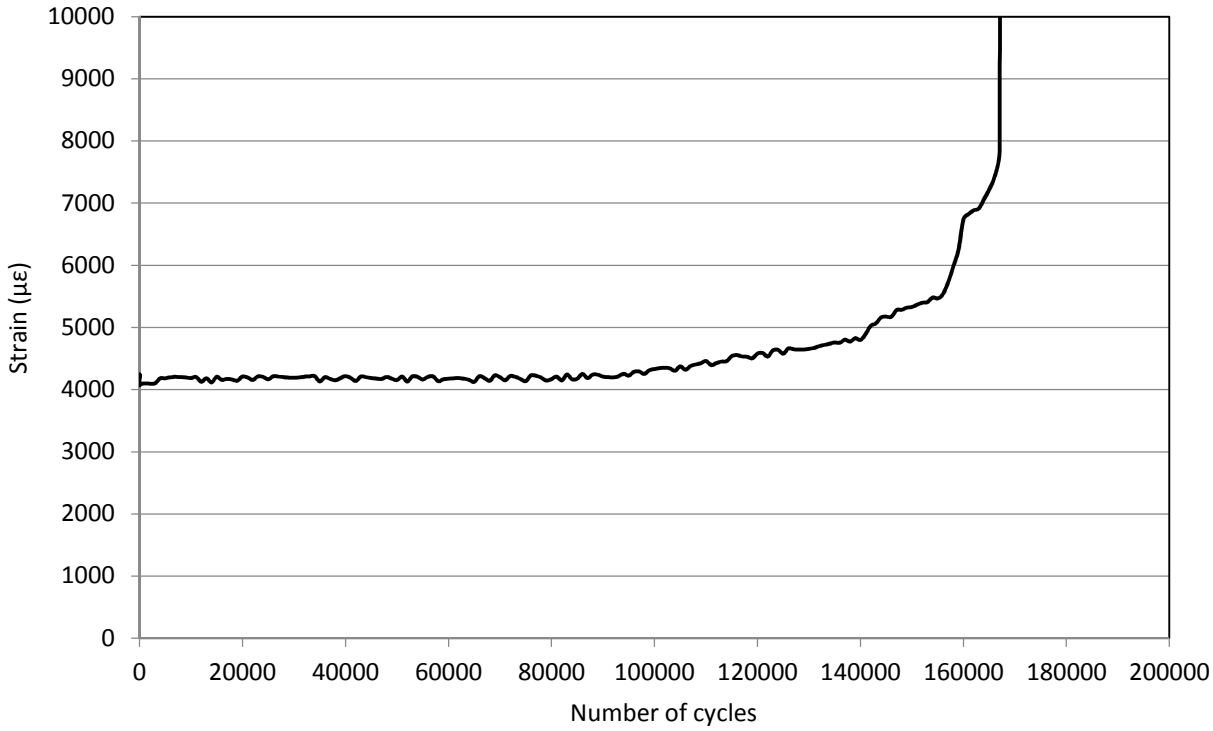

Figure 5.20 – Typical change in GFRP strain at maximum load under cyclic loading

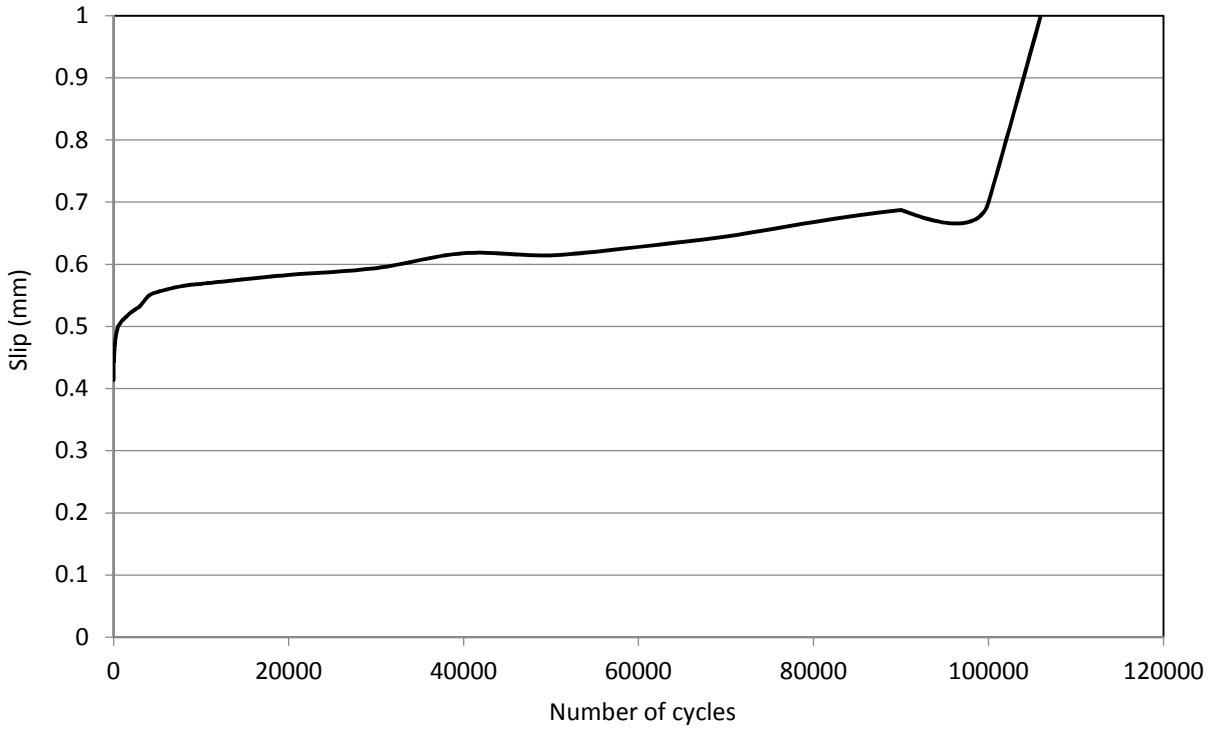

Figure 5.21 – Typical relative displacement between GFRP and concrete under fatigue loading

Table 5.5 - Beam-hinge fatigue data

Specimen	Load range (kN)	GFRP stress range (MPa)	GFRP stress range (% ultimate)	Number of cycles to failure
BH-4	20	406	53.7	2699
BH-5	11	217	28.8	240790
BH-6	10	199	26.3	335445
BH-7a	8	162	21.5	>1000000
BH-7b	15	304	40.3	15214
BH-8	15	299	39.6	12996
BH-9	11	221	29.3	189706
BH-10	8	157	20.7	439376
BH-11a	7.5	150	19.9	>1000000
BH-11b	20	401	53.0	5314
BH-12	13	269	35.5	96388
BH-13	13	254	33.6	98577
BH-14	10	202	26.7	305615
BH-15	15	299	39.6	21413

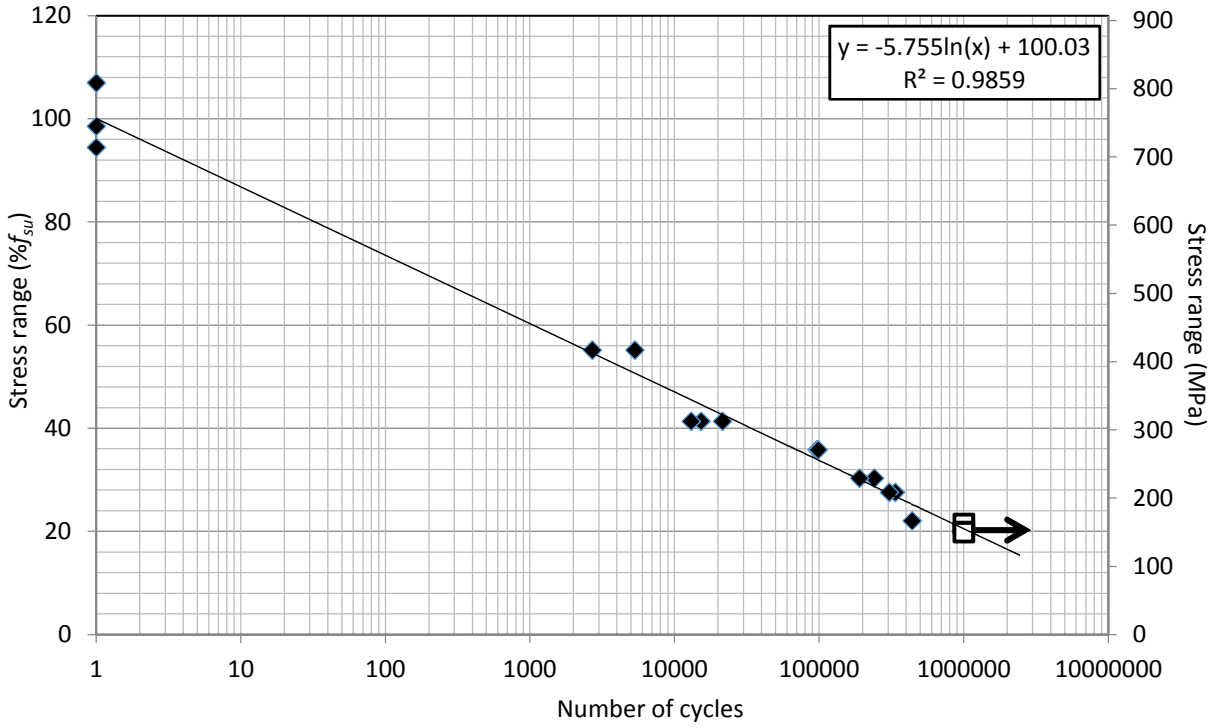

Figure 5.22 - S-N curve for beam-hinge specimens

Each of the beam-hinge specimens failed by rupture of the GFRP reinforcing bar near midspan (Figure 5.23). Fatigue failure typically initiated in the embedded bar just inside one of the free faces of the concrete blocks near the hinge location. The onset of fatigue failure of the GFRP bar was preceded by matrix cracking, interfacial debonding and individual fibre breakage evidenced by portions of the bar sliding relative to each other. This gradual failure mode was accompanied by a significant loss of stiffness resulting in increased strains in the reinforcement as well as increased deflections. Final failure occurred either by tension rupture of the bar or by bending failure of the bar once a sufficient fraction of the fibres had failed (Figure 5.24). Although bending failures are not likely to occur in a reinforced concrete beam due to a short unsupported length of the reinforcement at a crack location, the mechanisms leading to final fatigue failure are also caused by a similar ratio of uniform tension stress and non-uniform

bending stresses. Moreover, bending failures occurred only once a significant number of fibres had already ruptured such that the remaining fibres could no longer carry the equilibrium tension resultant force and would have failed by tension rupture imminently.

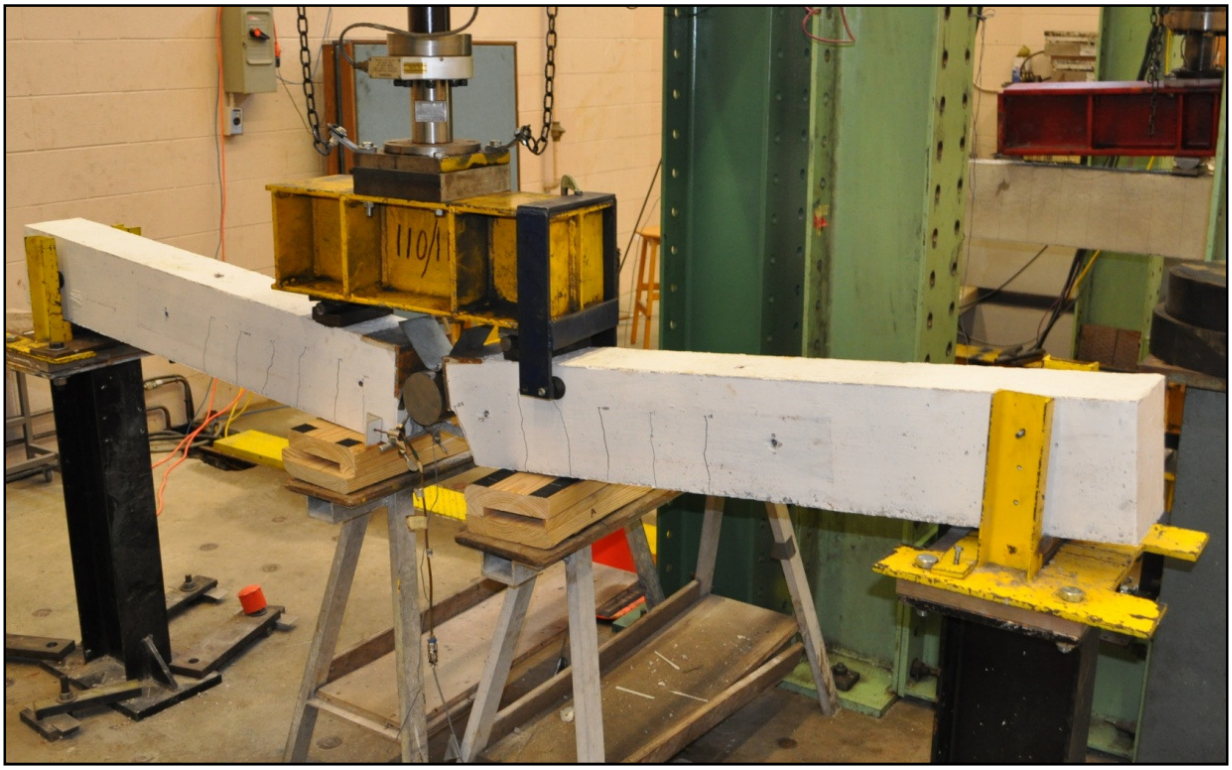

Figure 5.23 - Beam-hinge specimen post-failure

Following failure of the beam-hinge specimens, examination of the GFRP and concrete surfaces just inside the concrete block near the hinge location revealed that in most cases the sand coating had been scraped off of the bar surface and left a white residue on the concrete where the two surfaces had rubbed together (Figure 5.25). This residue was comprised of sand particles as well as resin and fibre particles from the outer layer of the reinforcing bar. The bar itself was scratched and displayed several longitudinal matrix cracks; this provides physical

evidence of the abrasion of the bar surface caused by relative slip between the bar and the concrete.

5.3.3 Summary

The results of the fatigue tests on the GFRP bare bars and beam-hinge specimens are shown together in Figure 5.26. The bare bars consistently displayed longer fatigue lives than the bars encased in concrete. There are several factors which may have contributed to the decrease in the fatigue lives of the GFRP reinforcing bars in the beam-hinge specimens. Firstly, the bare bar specimens were machined so that the outer resin-rich area of the bar was removed, leaving a core which may have had a slightly higher strength than the average strength of the bar; this effect is assumed to be negligible. Secondly, the reinforcement in the beam-hinge specimens was subjected to a stress gradient resulting from the bending of the beam which could adversely affect fatigue life due to the higher stressed fibres at the bottom of the bar. Thirdly, and presumably most importantly, the reinforcing bars in the beam-hinge specimens were subjected to repeated abrasion from the surrounding concrete which wore away the sand coating and damaged the outer fibres of the bar.

Figure 5.24 - Failure of GFRP in beam-hinge specimens
From top left: a) failure initiated at bar-concrete interface, b) longitudinal matrix cracks caused sliding of individual planes of fibres prior to failure, c) broom-type tension failure and d) bending failure following tensile rupture of large portion of cross-section

Figure 5.25 - White residue from the GFRP bar surface remains on the concrete after testing

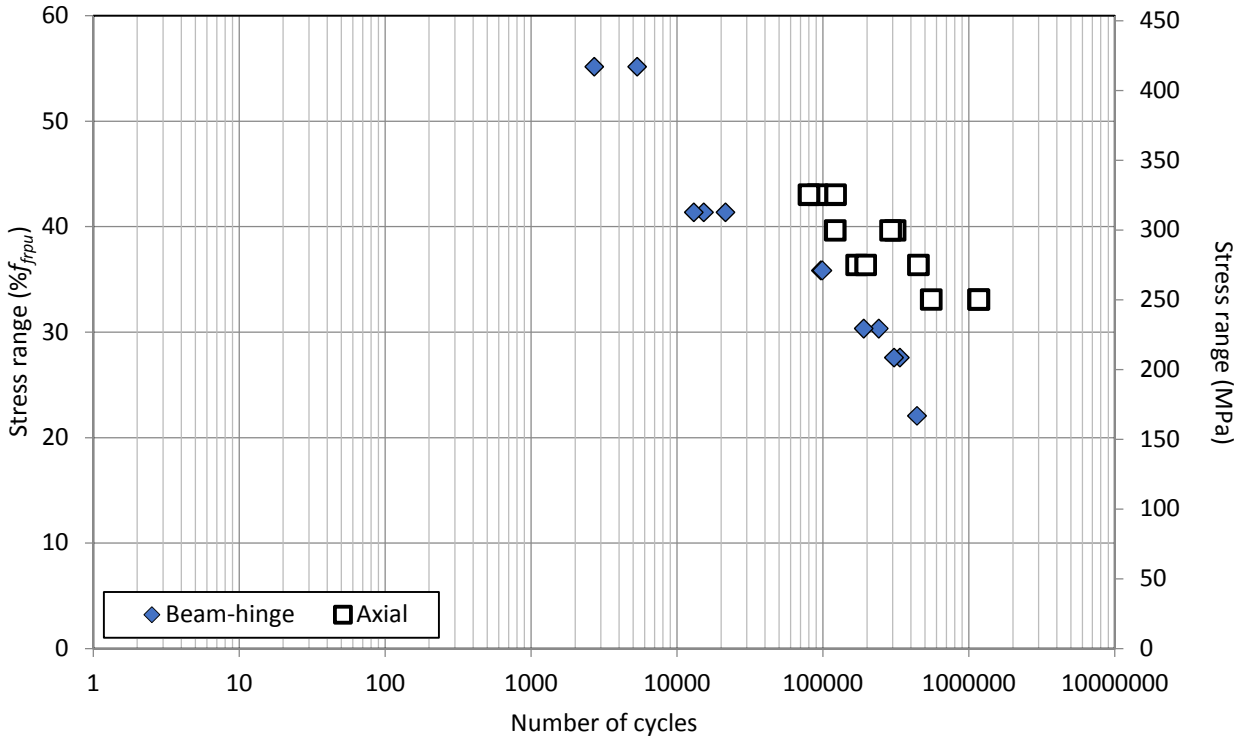

Figure 5.26 - GFRP fatigue results

The results of the beam-hinge specimens are expected to better approximate the fatigue behaviour of real reinforced concrete members compared with the axial bar specimens. However, the test method is more involved and requires more time, labour and resources. In order to characterize the fatigue behaviour of new FRP materials, a simple and easily repeatable test method is needed. Axial tension tests are simpler to perform and the use of reusable anchors is particularly attractive if more than a few tests are to be conducted. Correlation of the ancillary tests to the results of the main study and reinforced concrete structures in general is discussed in the following chapters.

Chapter 6 - Analysis of the Static Behaviour of FRP-RC Slabs

6.1 General

While the search for sustainable infrastructure solutions continues to be a driving force in the impetus to consider alternative building materials and design methods, the implementation of a new design concept is governed by the accuracy with which its structural behaviour can be predicted using relatively simple design models. Industry acceptance can be further facilitated through the use of familiar code equations or very minor modifications, as opposed to the introduction of new and convoluted methodologies. An effort has been made in the following two chapters to use design models found in current North American bridge design codes to predict the behaviour of the post-tensioned FRP-RC slabs described in Chapters 3 and 4. Where these models were found to be inadequate, simple modifications were proposed based on literature review and the experimental results presented in Chapters 4 and 5; in cases where no current code equations are available (such as for fatigue behaviour) simple design methods have been introduced to predict the slab behaviour under fatigue loading (see Chapter 7). Whenever possible, the form of these equations was presented in a similar form as existing design models to maintain familiarity with design practitioners.

6.2 Serviceability Predictions

As previously mentioned, the design of FRP-RC members is often governed by their ability to meet serviceability criteria including deflections, crack widths and allowable stresses. Thus, an accurate prediction of the behaviour of slab bridges reinforced with FRP bars and prestressed

tendons at service loads is essential. A number of design methods have been developed to estimate the serviceability of FRP-RC sections; these are evaluated in the following sections.

6.2.1 Cracking

Prior to cracking, serviceability is generally not a concern as deflections, crack widths and reinforcement stresses are negligible. After cracking, however, the flexural stiffness is greatly reduced and sudden increases in deformation occur. The cracking moment of reinforced concrete sections is given by Equation 6.1, with the modulus of rupture given by Equation 6.2. Since the stiffness of FRP materials is comparable to that of concrete, the CHBDC (CSA 2010) permits the use of gross section properties in place of transformed section properties when calculating the cracking moment. For prestressed members, the cracking moment is given by Equation 6.3:

Eq. 6.1 $$M_{cr} = \frac{f_r I_t}{y_t}$$

Eq. 6.2 $$f_r = 0.60\sqrt{f'_c}$$

Eq. 6.3 $$M_{cr} = \frac{f_r I_t}{y_t} + \frac{P I_t}{A y_t} + Pe$$

Where, M_{cr} is the cracking moment, f_r is the modulus of rupture of the concrete, I_t is the moment of inertia of the section, y_t is the depth to the centroid of the section, P is the effective prestressing force, A is the area of the concrete section, e is the eccentricity of the prestressing tendons, f_r is the modulus of rupture and f'_c is the concrete compressive strength.

The measured cracking moments for the different slabs are compared with predicted values in Table 6.1, accounting for the actual measured concrete compressive strength and prestressing force in each slab. In addition to the applied load, the slabs sustained a maximum self-weight moment at midspan of approximately 10.7 kN·m, assuming a concrete unit weight of 23.5 kN/m^3.

Table 6.1 - Experimental vs. predicted cracking moments

Slab	f'_c (MPa)	Effective prestress (kN)	Experimental cracking moment[a] (kN·m)	Predicted cracking moment (kN·m)	M_{exp}/M_{pred}
S	58.1	--	32.8	41.2	0.80
G1	58.1	--	28.5	41.2	0.69
G1-ST	58.1	--	31.1	41.2	0.75
G2	58.1	--	32.8	41.2	0.80
G2-ST	58.1	--	38.5	41.2	0.93
PT2a	63.8	194.4	39.4	47.8	0.82
PT2	58.1	218.6	62.0	68.5	0.91
PT2-ST	63.8	217.4	55.0	70.3	0.78
PT2-G	59.1	242.4	63.1	71.8	0.88
PT2-S	64.5	244.8	67.9	74.0	0.92
PT2-S45	64.5	246.0	74.8	74.1	1.01
PT2-U	55.7	247.6	63.3	71.6	0.88
PT4	55.7	488.8	80.8	101.4	0.80
PT4-G	59.1	355.8	82.5	85.9	0.96
PT4-U	55.7	482.4	97.2	100.6	0.97
PT4-P	59.1	256.4	71.7	73.6	0.97

a – Includes self-weight

It is clear from Table 6.1 that the cracking moments were consistently over-predicted, with an average ratio of experimental-to-predicted cracking moments of 0.87. According to ACI 237R-07 (ACI Committee 237 2007), the flexural strength of SCC is not expected to be lower than that of conventional concrete with similar mix proportions, and in some cases may be higher. As noted in Chapter 3, the splitting tensile strength of the concrete at the time of testing ranged from $0.45\sqrt{f'_c}$ to $0.57\sqrt{f'_c}$, which is similar to the mean split cylinder strength of $0.53\sqrt{f'_c}$ reported from a large number of studies (MacGregor & Bartlett 2000). Splitting tensile strength is

typically lower than flexural cracking strength; the mean modulus of rupture has been expressed in the literature as $0.69\sqrt{f'_c}$.

High scatter is inherent in the tensile strength of concrete, which may have had an effect on the observed cracking results. Since the flexural cracking strengths were consistently lower than expected, it is likely that another factor was also influencing the results. The discrepancy observed in this case may be a result of high shrinkage strains which, when restrained by flexural reinforcement and the inner concrete core of the slab, develop tensile stresses in the concrete and decrease the moment required to cause cracking (Bischoff 2001, Bischoff & Johnson 2007, Al-Sunna et al. 2012). The specimens were not cured in a humidity controlled environment due to their large size, and hence, likely developed greater shrinkage strains than a moist-cured member.

Shrinkage strains can be estimated from Equation 6.4 (MacGregor & Bartlett 2000). Shrinkage is a function of time, relative humidity and cement content, which is implicitly and empirically accounted for using the concrete compressive strength. Due to the high cement content and low water-cement ratios found in SCC mixes, greater shrinkage may also occur relative to conventional mixes.

Eq. 6.4 $$\varepsilon_{cs} = 1.2\beta_s\beta_{RH}\left[160 + \beta_{sc}\left(9 - \frac{f_{cm}}{f_{cmo}}\right)\right]x10^{-6}$$

Where, ε_{cs} is the axial shrinkage strain, β_s, β_{RH} and β_{sc} are factors to account for the effects of time, relative humidity and cement type, respectively, f_{cm} is related to the concrete compressive strength and f_{cmo} is 10 MPa.

For a concrete compressive strength of 60 MPa, an average relative humidity of 50% and a curing time of 200 days, the shrinkage strain is calculated as 0.000155. Only restrained shrinkage develops tensile stresses; the shrinkage strains are restrained both by the longitudinal reinforcement and the inner concrete core which retains moisture longer. While the restraining effect of the longitudinal reinforcement can be readily calculated based on its relative stiffness compared with the concrete section, the contribution of the concrete core is more difficult to predict; for large specimens, the inner concrete will have a significant effect on the development of external tensile stresses. Typical values for restrained shrinkage are between 0% and 25% of the total shrinkage strain (MacGregor & Bartlett 2000).

The effect of shrinkage can be accounted for in the cracking moment equation by reducing the modulus of rupture by the shrinkage-induced stress, as given by Equations 6.5 and 6.6:

Eq. 6.5 $$f_{r,eff} = 0.6\sqrt{f'_c} - E_c\varepsilon_{sh}$$

Eq. 6.6 $$E_c = \left(3300\sqrt{f'_c} + 6900\right)\left(\frac{\gamma_c}{2300}\right)^{1.5}$$

Where, $f_{r,eff}$ is the effective modulus of rupture, f'_c is the concrete compressive strength, E_c is the elastic modulus of the concrete, γ_c is the unit weight of the concrete (taken as 2350 kg/m^3) and ε_{sh} is the restrained shrinkage strain in the concrete.

Assuming that 20% of the shrinkage strains are restrained, the predicted cracking moments are reduced to the values given in Table 6.2, which give more conservative estimates and better correlation with the experimentally observed values. The actual shrinkage stresses induced will vary between specimens depending on age, curing environment and the contribution of the

inner concrete core. It should also be noted that the CHBDC (CSA 2010) accounts for the effects of restrained shrinkage by reducing the cracking strength of concrete to a value of $0.4\sqrt{f'_c}$; the cracking moments predicted using the CHBDC approach—which tended to be fairly conservative—are also compared in Table 6.2. The conservatism in the CHBDC approach may be justified by the fact that it also accounts for the possibility of greater restraint and thermal strains which can develop in real structures.

Table 6.2 - Experimental vs. predicted cracking moments accounting for shrinkage

Slab	f'_c (MPa)	Effective prestress (kN)	Experimental cracking moment[a] (kN·m)	Predicted cracking moment (kN·m)	M_{exp}/M_{pred}	CHBDC cracking moment (kN·m)	M_{exp}/M_{pred}
S	58.1	--	32.8	31.6	1.04	27.4	1.20
G1	58.1	--	28.5	31.6	0.90	27.4	1.04
G1-ST	58.1	--	31.1	31.6	0.98	27.4	1.14
G2	58.1	--	32.8	31.6	1.04	27.4	1.20
G2-ST	58.1	--	38.5	31.6	1.22	27.4	1.41
PT2a	63.8	194.4	39.4	40.9	0.96	37.8	1.04
PT2	58.1	218.6	62.0	58.9	1.05	54.8	1.13
PT2-ST	63.8	217.4	55.0	61.4	0.90	55.9	0.98
PT2-G	59.1	242.4	63.1	62.3	1.01	58.0	1.09
PT2-S	64.5	244.8	67.9	65.1	1.04	59.5	1.14
PT2-S45	64.5	246.0	74.8	65.3	1.15	59.7	1.25
PT2-U	55.7	247.6	63.3	61.4	1.03	57.8	1.10
PT4	55.7	488.8	80.8	91.6	0.88	88.0	0.92
PT4-G	59.1	355.8	82.5	76.5	1.08	72.2	1.14
PT4-U	55.7	482.4	97.2	90.8	1.07	87.2	1.11
PT4-P	59.1	256.4	71.7	64.1	1.12	59.7	1.20

a – Includes self-weight

6.2.2 Allowable Stress

The CHBDC (CSA 2010) places service stress limits on CFRP and GFRP reinforcement of 65% and 25% of their ultimate strength, respectively. The stress in the FRP reinforcement at service in a singly-reinforced concrete member can be calculated using Equation 6.7:

Eq. 6.7 $$f_{frp} = \frac{M_s}{A_{frp} j d}$$

Where, f_{frp} is the stress in the reinforcement, M_s is the service moment, A_{frp} is the cross-sectional area of the reinforcement and *jd* is the lever arm.

In a beam with more than one layer of reinforcement, the stress in each layer can be computed from the moment equilibrium equation given by Equation 6.8 with the condition that strain compatibility and internal force equilibrium are satisfied:

Eq. 6.8 $$M_s = f_{frp1}A_{frp1}\left(d_{frp1} - \frac{a}{2}\right) + f_{frp2}A_{frp2}(d_{frp2} - \frac{a}{2})$$

Where, f_{frpi}, A_{frpi} and d_{frpi} are the stress, area and depth of reinforcement layer *i*, respectively, and *a* is the depth of the concrete rectangular stress block.

The CHBDC service moment due to live load is taken as 41.6 kN·m (see Chapter 8). The predicted GFRP stresses, accounting for self-weight, are compared to stresses at midspan computed from measured GFRP strains in the non-prestressed slabs for moments ranging from 30 kN·m to 60 kN·m in Figures 6.1 and 6.2. GFRP stresses in the post-tensioned slabs are negligible because the slabs were uncracked at service and are not considered here. It should be noted that the measured strains can vary depending on their proximity to the nearest crack, and are not necessarily the maximum strain developed in the reinforcing bar.

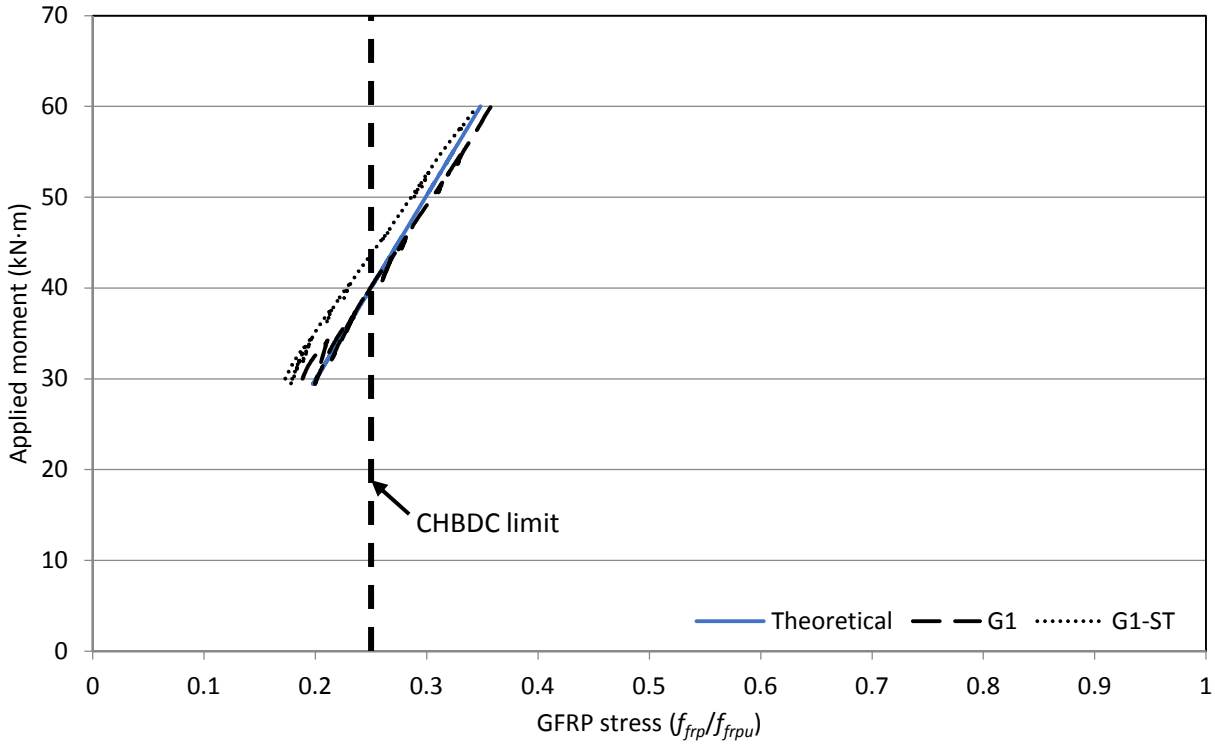

Figure 6.1 - GFRP service stress for G1 and G1-ST

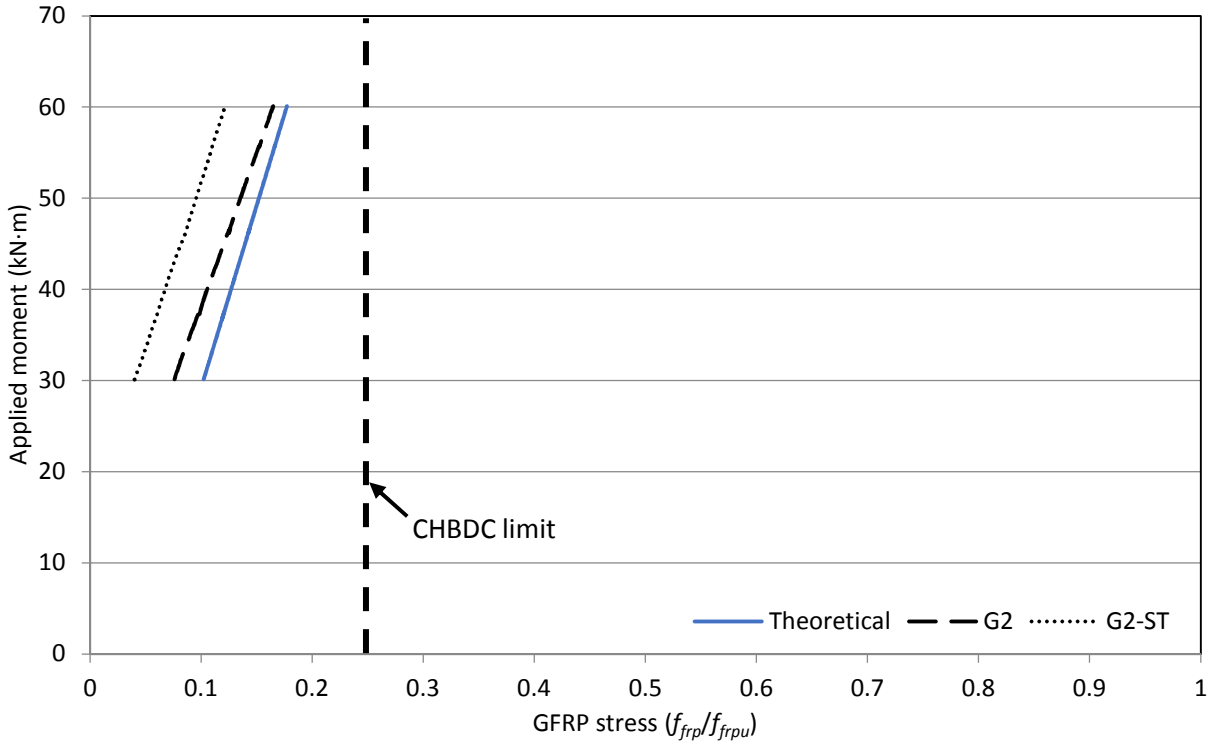

Figure 6.2 - GFRP service stress for G2 and G2-ST

The predicted GFRP service stresses correlate well with the measured strains for slabs G1 and G1-ST. Although the service stresses are slightly over-predicted for slabs G2 and G2-ST, this may be a result of the strain gauges being located away from a flexural crack; in any case, the predicted result is conservative. As seen in Figures 6.1 and 6.2, the GFRP stress in the under-reinforced slabs, G1 and G1-ST, exceed the CHBDC limit of $0.25f_{frpu}$ beyond an applied moment of approximately 40 kN·m, while the over-reinforced slabs, G2 and G2-ST, are well below the service stress limit for the entire range of loads considered.

6.2.3 Crack Width

For many years, crack widths of reinforced concrete members were predicted using the empirically-derived Gergely-Lutz equation for steel bars. Since crack widths are a function of reinforcement stiffness and bond properties, the effect of the type of reinforcement is significant; hence, various modifications to the Gergely-Lutz equation for FRP reinforcing bars have been proposed (Salib & Abdel-Sayed 2004).

Frosch (1999) developed a physically-derived crack width model (Equation 6.9) applicable to any reinforcement type which has been adopted by a number of design codes, including the CHBDC. The model takes into account the stiffness and bond properties of the reinforcement as well as the concrete cover and transverse spacing of the reinforcing bars. The CHBDC proposes that when no detailed information is available, the bond coefficient, k_b, for sand-coated FRP reinforcing bars may be taken as 0.8. ACI 440, on the other hand, proposes a more conservative value of 1.4.

Eq. 6.9 $$w = 2\frac{f_{frp}}{E_{frp}}\frac{h_2}{h_1}k_b\sqrt{d_c^2 + (\frac{s}{2})^2}$$

Where, w is the crack width at the tension face of the member, f_{frp} and E_{frp} are the stress and elastic modulus of the reinforcement, respectively, h_2 and h_1 are the distance from the tension face to the neutral axis and from the centroid of the reinforcement to the neutral axis, respectively, k_b is a coefficient to account for the bond properties of the reinforcement, d_c is the concrete cover to the centroid of the reinforcement, and s is the transverse spacing of the reinforcement.

The predicted and experimentally measured maximum crack widths for the non-prestressed slabs are shown in Figures 6.3 and 6.4. Since the crack widths were measured at the level of the reinforcement, they were multiplied by the ratio h_2/h_1 for comparison with the CHBDC crack width limit of 0.5 mm for aggressive environments. The service range is once again taken as 30 kN·m to 60 kN·m, and the self-weight of the slab is taken into account for the predicted crack widths.

As seen in Figures 6.3 and 6.4, the measured crack widths in the under-reinforced slabs, G1 and G1-ST, exceeded the CHBDC crack width limit for moments greater than approximately 45 kN·m, while the over-reinforced slabs, G2 and G2-ST, were well within the CHBDC limit for all loads within the range considered. A bond coefficient of 1.4 gave highly conservative estimates of crack widths compared with experimental results; in fact, predicted values of crack widths for the under-reinforced slabs exceeded the CHBDC limit for the entire range of loads considered. Conversely, a bond coefficient of 0.8 gave reasonable estimates of crack width for the GFRP-RC slabs, although estimates became slightly unconservative at higher loads.

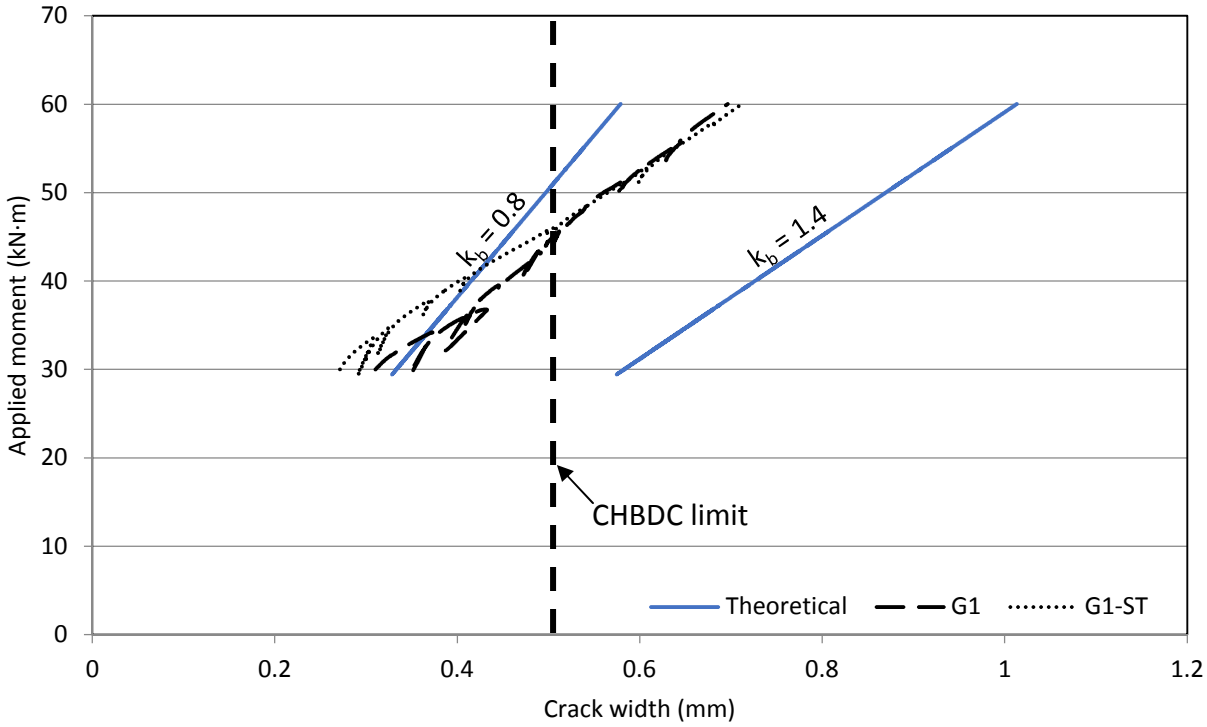

Figure 6.3 - Crack widths for slabs G1 and G1-ST

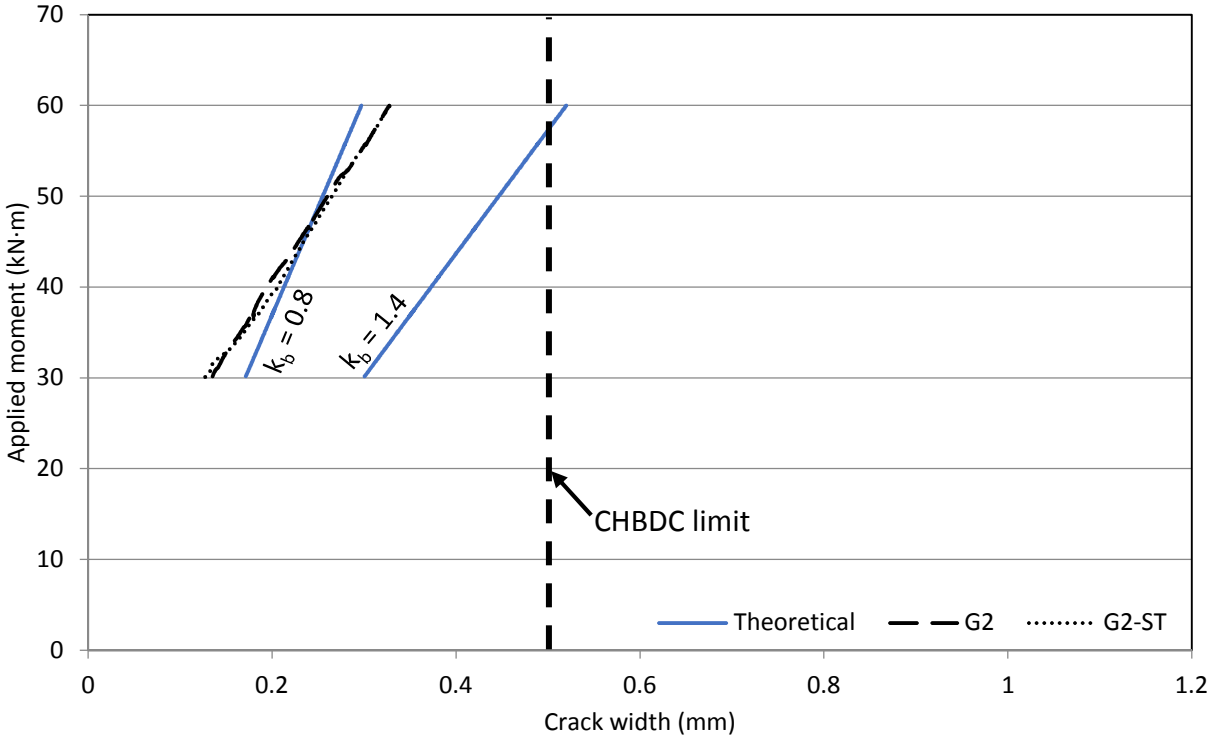

Figure 6.4 - Crack widths for slabs G2 and G2-ST

The actual bond coefficient can be calculated by rearranging the terms in Equation 6.9. By recognizing that for a given cross-section all of the geometric terms and material properties are constant, Equation 6.9 can be rewritten to give Equation 6.10 (McCallum & Newhook 2012):

Eq. 6.10 $$w = Cf_{frp}k_b$$

Where, C is a constant and all other terms are as noted previously.

Thus the normalized crack width, *w/C*, can be plotted against the theoretical stress in the FRP reinforcement to find the bond coefficient, as shown in Figure 6.5. Once again, only the stresses corresponding to applied moments ranging from 30 kN·m to 60 kN·m are considered; to give equal weight to each of the tested slabs, seven data points from each test within the service range were selected corresponding to intervals of 5 kN·m, for a total of 28 data points.

As seen in Figure 6.5, the data points from the two over-reinforced slabs, G2 and G2-ST, and the two under-reinforced slabs, G1 and G1-ST, fit trendlines having similar slopes but different non-zero intercepts. As noted by McCallum & Newhook (2012), the experimentally calibrated value of the bond coefficient, k_b, is not constant but rather depends on the stress level in the reinforcement. A constant value of k_b implies that the crack width equation has a zero intercept, even though cracking occurs only beyond a certain load. As seen in Figures 6.3 and 6.4, the slopes of the lines representing the theoretical crack widths with a bond coefficient of 1.4 are nearly parallel to the experimental curves. Therefore, an approach employing a constant bond coefficient may be more appropriately derived by shifting the predicted values to provide consistent accuracy at all load levels.

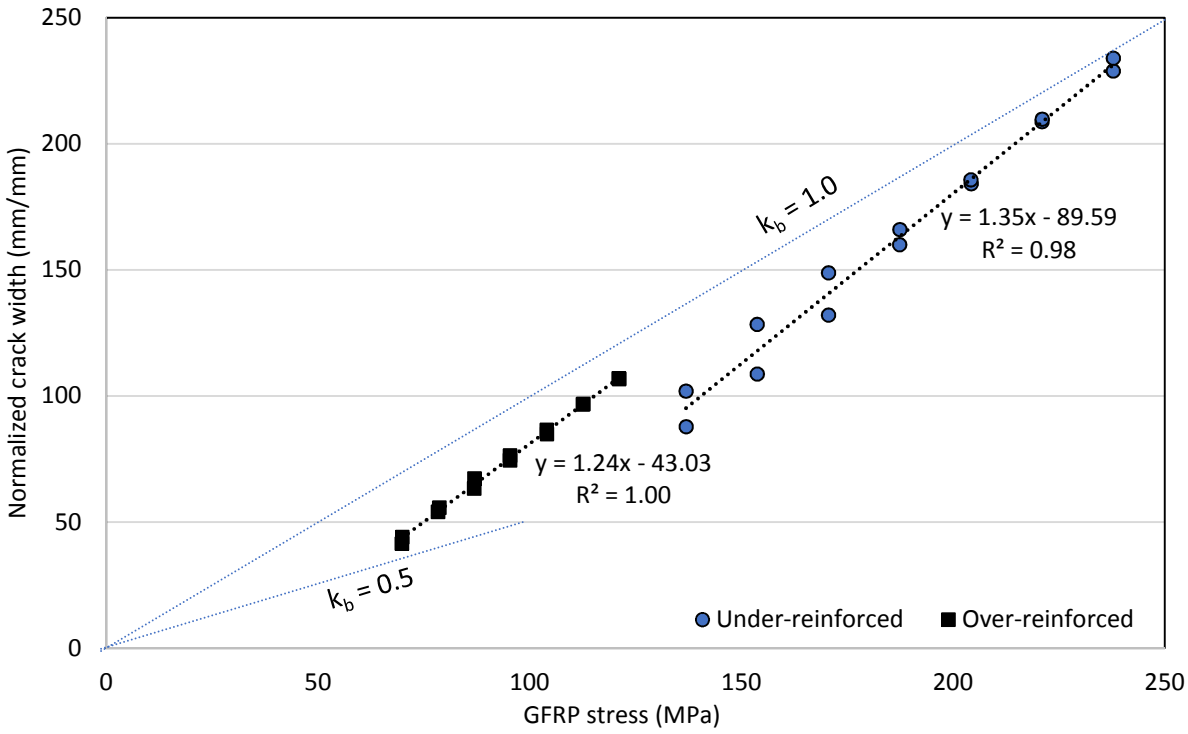

Figure 6.5 - Normalized crack width versus reinforcement stress

The Frosch equation is based on the assumption that the crack width is directly proportional to the reinforcement strain, as given by Equation 6.11. This assumption ignores any tensile strain in the concrete since it is small, as well as tension stiffening between cracks. Though technically conservative, this approach essentially forces a zero-intercept on the crack width equation so that the accuracy of crack width predictions is highly dependent on the load level at which it is calculated compared to that at which the bond coefficient, k_b, was calibrated. It is more accurate to represent the crack width using Equation 6.12 which accounts for the tensile contribution of concrete between cracks:

Eq. 6.11 $$w = \varepsilon_{frp} S_c$$

Eq. 6.12 $$w = (\varepsilon_{frp} - \varepsilon_c) S_c$$

Where, ε_{frp} is the strain in the bottom layer of reinforcement, ε_c is the average strain in the concrete between cracks and S_c is the crack spacing.

The concrete contribution to the tension resultant force, or tension stiffening, is dependent on the bond between the reinforcement and the concrete, and is represented schematically in Figure 6.6. Since the tension stiffening effects of FRP-RC are not well-defined, they are often neglected; however, when it comes to its effect on crack widths, tension stiffening of FRP reinforcement is not insignificant (Aiello et al. 2003).

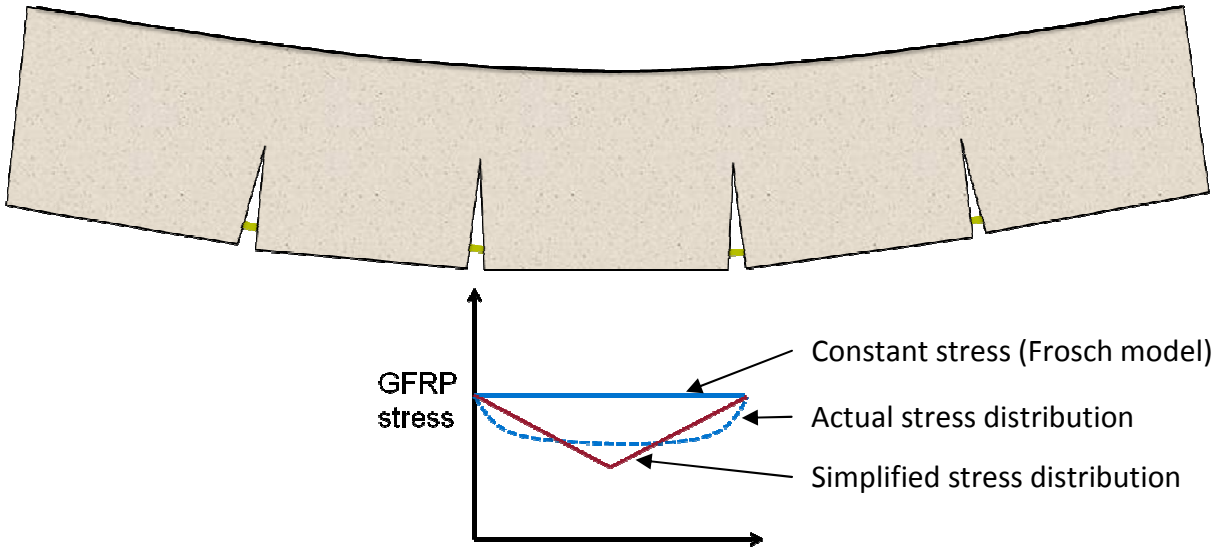

Figure 6.6 - Schematic of tension stiffening between cracks

The exact solution of Equation 6.12 requires the definition of the bond-slip law governing the reinforcement behaviour as well as the simultaneous solution of a system of equations defining the compatibility condition between two points based on the relative slip between the reinforcement and the concrete, the axial equilibrium condition for the reinforcement relating the axial stress to the bond stress, and the equilibrium conditions for sections to ensure equilibrium of forces and moments. For a reinforced concrete member in the crack

stabilization phase, it is impossible to solve these equations in a closed form and complex numerical solutions are needed (Aiello & Ombres 2000). However, approximating the non-linear bond distribution along the reinforcing bar with a uniform distribution of bond stresses gives a small error for short bond lengths and greatly simplifies the analysis (Aiello et al. 2007). Equation 6.13 can be used to describe the mean reinforcement strain in an axially loaded concrete tension member (Aiello et al. 2003):

Eq. 6.13 $$\varepsilon_m = \frac{1}{E_r}\left[\frac{F}{A_r} - \frac{f_{ct}A_{ct}}{2A_r}\right]$$

Where, ε_m is the mean reinforcement strain, E_r and A_r are the elastic modulus and area of the reinforcement, respectively, F is the force in the reinforcement, f_{ct} is the maximum stress in the concrete between cracks and A_{ct} is the effective area of concrete in tension.

The maximum stress that can develop in the concrete between cracks is the tensile strength of the concrete. Due to the stress gradient, the average stress carried by the effective concrete area midway between cracks will be less than the modulus of rupture, $0.6\sqrt{f'_c}$. Considering the tension zone in a reinforced concrete flexural member as analogous to an axially loaded member, the average stress in the effective concrete area midway between cracks is taken here as the direct tensile strength of concrete, $0.4\sqrt{f'_c}$, and A_{ct} as the area of concrete having the same centroid as the primary reinforcement (as recommended by CSA A23.3). The direct tensile strength of concrete is used because it allows for the convenient analogy of a reinforced concrete tension member and is a reasonable approximation of the average concrete stress midway between cracks. Ultimately, the sensitivity of the predicted crack widths to small variations in the assumed tensile strength of the concrete is low.

Equation 6.9 can then be modified to give Equations 6.14 and 6.15; the last term in Equation 6.15 is a constant for a given geometry and concrete strength.

Eq. 6.14 $$w = 2\frac{f_{frpm}}{E_{frp}}\frac{h_2}{h_1}k_b\sqrt{d_c^2 + (\frac{s}{2})^2}$$

Eq. 6.15 $$f_{frpm} = f_{frp} - \frac{0.4\sqrt{f'_c}(2bd_c - A_{frp})}{2A_{frp}}$$

Where, f_{frpm} is the mean stress in the reinforcement between two cracks, f_{frp} is the stress in the FRP reinforcement at a cracked section, d_c is the concrete cover to the centroid of the reinforcement and all other terms are as noted previously.

The proposed modification to the Frosch equation correlated well with the measured crack widths for the under-reinforced slabs (G1 and G1-ST) and gave slightly conservative estimates for the over-reinforced slabs (G2 and G2-ST). It was also consistently accurate for the entire load range considered as shown in Figure 6.7. The bond coefficient, k_b, was taken as 1.3 from Figure 6.5.

The Frosch crack width model may also be used to predict crack widths in prestressed and partially prestressed members by considering the load increase above the decompression moment (Xue & Tan 2012). The decompression moment is used here to refer to the moment at which the stress in the extreme bottom fibre is equal to zero. Since flexural cracking is primarily controlled by the outermost layer of non-prestressed reinforcement, Equation 6.14 can be applied considering only the stress in the bottom layer of the reinforcement (in this case, the passive GFRP reinforcing bars), taking the decompression moment as the point of reference.

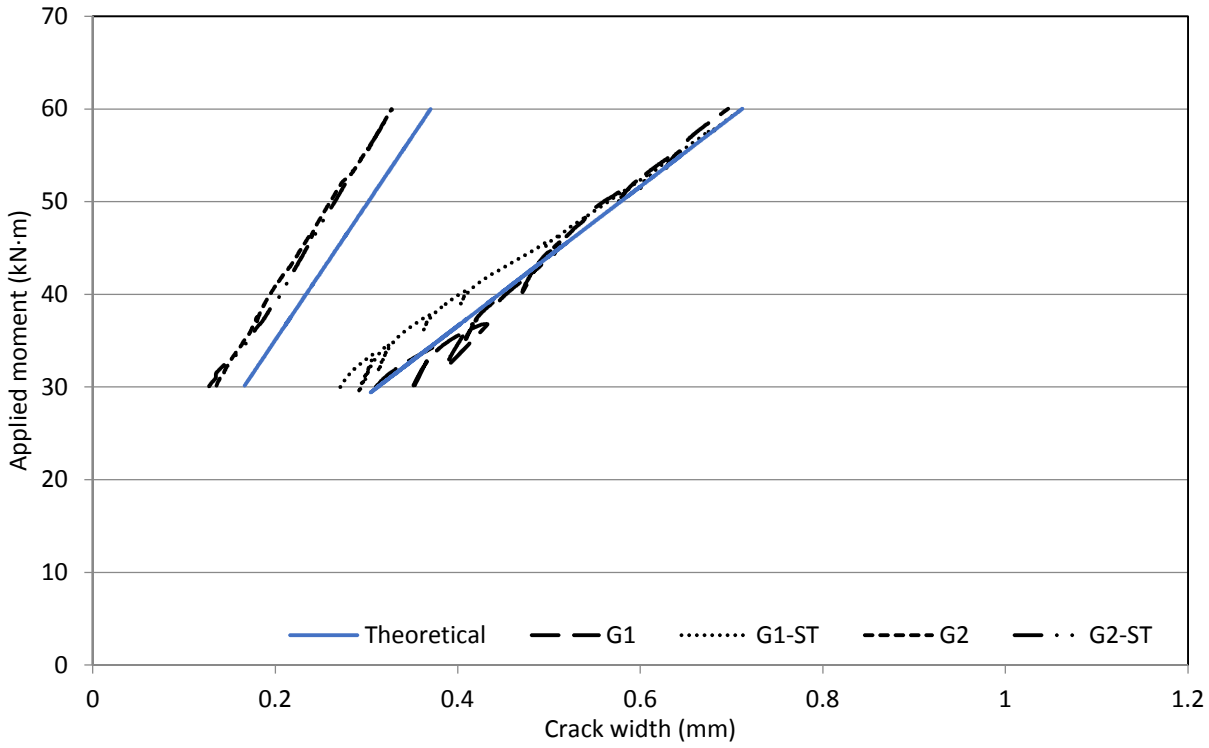

Figure 6.7 - Predicted and experimental crack widths for GFRP-RC slabs

Although the prestressed slabs were uncracked at service, the methodology described above accounting for tension stiffening was used to predict their crack widths after cracking in order to validate its effectiveness for partially prestressed members. Thus, the "service load range" was arbitrarily selected to give stress values in the GFRP reinforcement similar to those considered in the non-prestressed slabs shortly after cracking. For slabs post-tensioned with two CFRP tendons, crack widths were predicted for applied moments ranging from 70 kN·m to 100 kN·m, corresponding to GFRP stresses of approximately 80 MPa to 150 MPa. Meanwhile, for slab PT4, which had four CFRP tendons, crack widths were predicted for applied moments ranging from 110 kN·m to 160 kN·m, corresponding to GFRP stresses of approximately 50 MPa to 140 MPa; since one of the tendons in slab PT4-G was lost prior to testing, it was not included in this analysis.

In order to account for the presence of the CFRP tendons, the axial tension force in the concrete between cracks was assumed to be distributed between the GFRP and CFRP bars according to their respective axial stiffness, as explained by the schematic shown in Figure 6.8. The area of concrete engaged in tension is also expected to increase compared with the non-prestressed slabs due to the vertical distribution of the reinforcement, and the neutral axis depth will also be greater than for the non-prestressed slabs. Consequently, the average stress carried by the effective concrete section will decrease due to the steeper stress gradient; this is accounted for in this simplified analysis by reducing the average concrete tensile stress to $0.3\sqrt{f'_c}$. This value was selected because it represents the average concrete tensile stress for an effective concrete section equal to the total area of the concrete in tension with a stress at the extreme tension fibre equal to the modulus of rupture of the concrete ($0.6\sqrt{f'_c}$). Once again, predicted crack width values are not highly sensitive to small variations in the assumed tensile strength of the concrete.

The mean stress in the GFRP reinforcement is then given by Equations 6.16 and 6.17 and the predicted crack widths are plotted versus GFRP stress in Figures 6.9 and 6.10.

Eq. 6.16 $$f_{frpm} = f_{gfrp} - f_{gfrp,dc} - \frac{(1-\alpha_c)0.3\sqrt{f'_c}(2bd_c - A_{gfrp} - A_{ducts})}{2A_{gfrp}}$$

Eq. 6.17 $$\alpha_c = \frac{E_{cfrp}A_{cfrp}}{E_{gfrp}A_{gfrp} + E_{cfrp}A_{cfrp}}$$

Where, $f_{gfrp,dc}$ is the stress in the GFRP reinforcing bars at the decompression moment (a negative value), A_{ducts} is the area of the post-tensioning ducts, α_c is the axial stiffness ratio of

the CFRP tendons to the combined reinforcement stiffness, and all other terms are as previously noted.

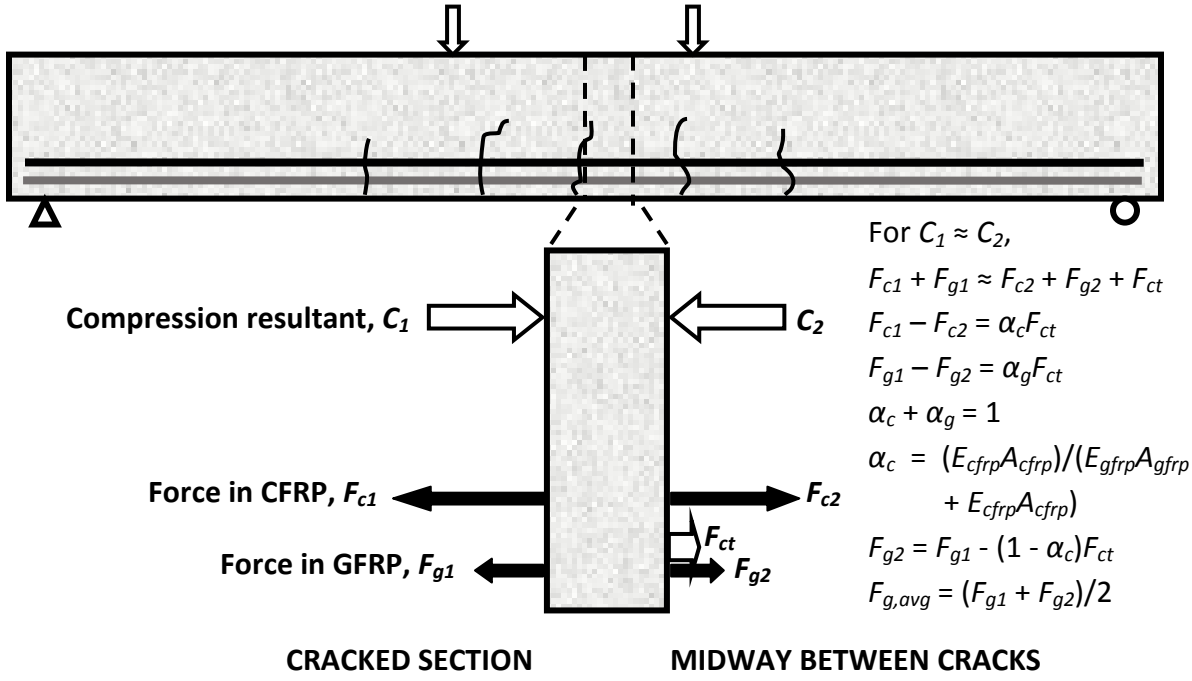

Figure 6.8 - Distribution of concrete tension force for prestressed slabs

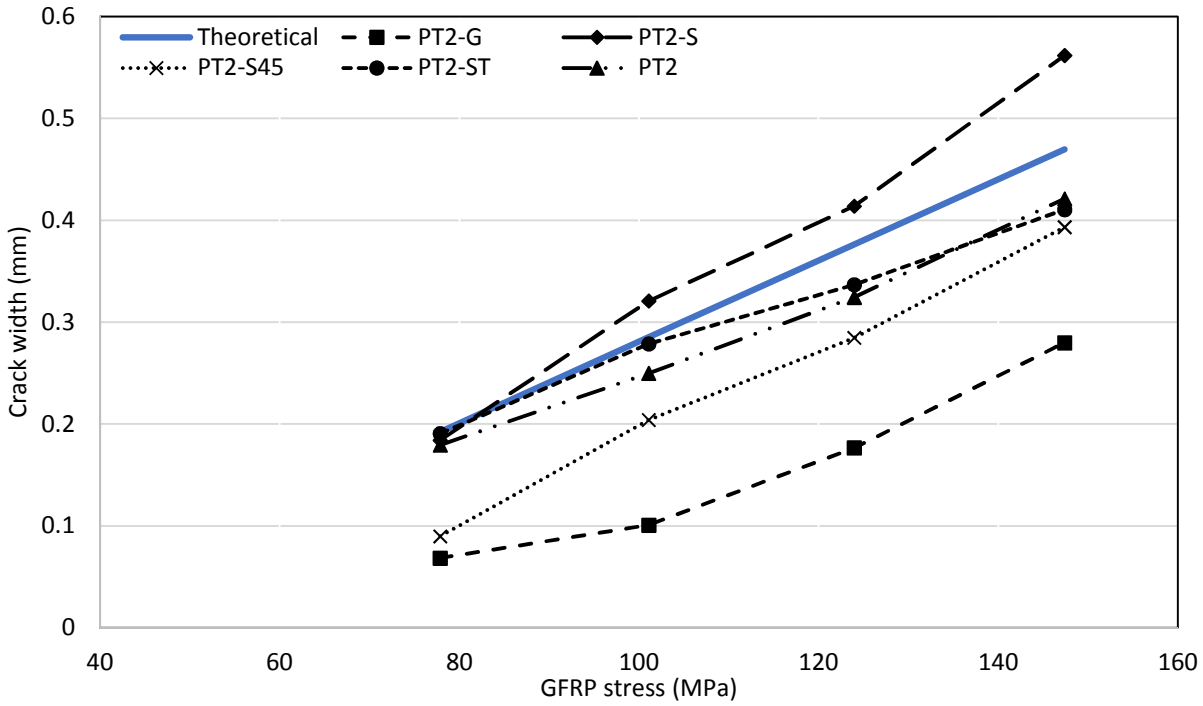

Figure 6.9 - Crack width predictions for slabs with two CFRP tendons

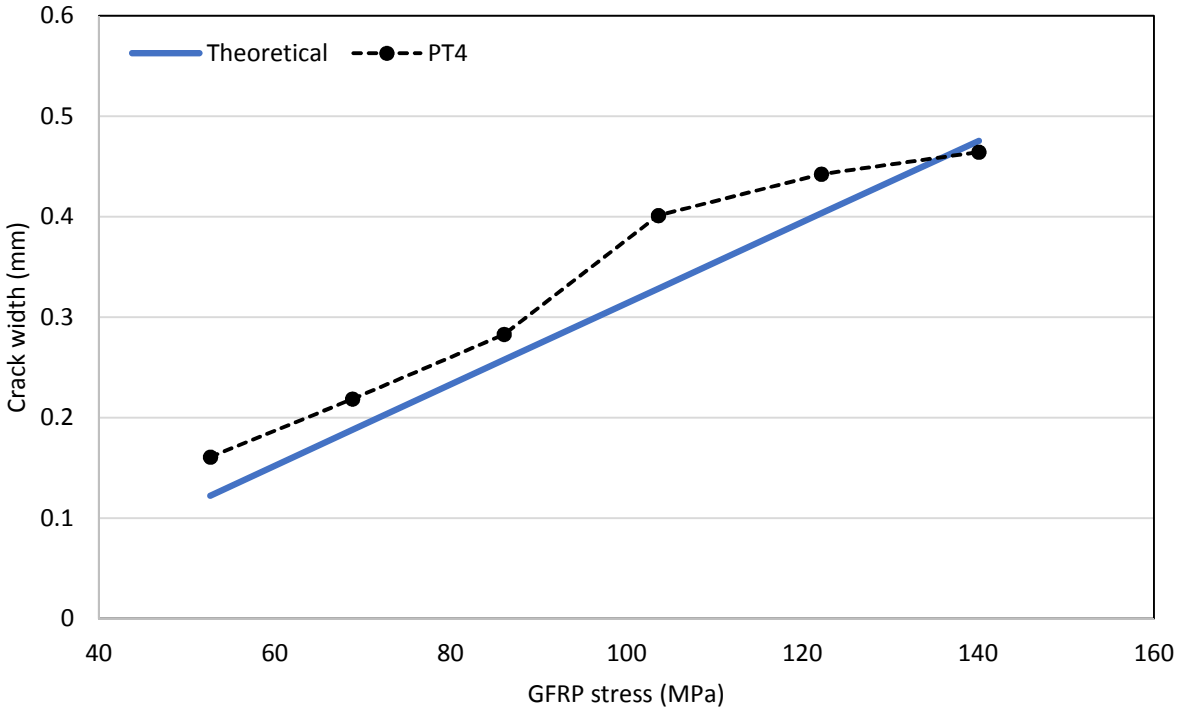

Figure 6.10 - Crack width predictions for slab PT4

The measured crack widths in the slabs with two CFRP tendons showed considerable scatter, but were reasonably predicted with the proposed approach. Crack widths for the slab with four CFRP tendons, PT4, were slightly under-predicted. The level of accuracy was once again fairly consistent for all load levels.

It should be noted that in the method described above, it is assumed that the concrete stress reaches its tensile strength midway between cracks; this is an upper bound estimation since the maximum stress will always be below the actual tensile strength—if the tensile strength of the concrete is reached, a new crack will form midway between the two existing cracks. Therefore it would be more conservative to use a smaller value for the maximum concrete stress for design purposes, such as a value between 0.2 to $0.3\sqrt{f'_c}$, depending on the effective area of concrete in tension (ie. when the depth of the effective area of concrete and/or the depth to

the neutral axis increases, the stress gradient becomes steeper and the average stress value is reduced).

6.2.4 Deflection

There are two common methods of predicting the deflections of a flexural member, namely the curvature approach and the effective moment of inertia approach. The curvature approach is essentially an integration of the curvature along the length of the member using the method of virtual work (Equation 6.18). The curvature at any section of a member is given by Equation 6.19; the midspan deflection of a simply supported member can be approximated by Equation 6.20 (Ghali 1993). A model based on the curvature approach has been proposed by Razaqpur et al. (2000), which assumes that there is an uncracked length, L_g, near the supports and a fully cracked region away from the supports (tension stiffening is neglected); the resulting curvature diagram is illustrated in Figure 6.11. The midspan deflection for a cracked member under four point bending using this approach is given by Equation 6.21:

Eq. 6.18 $$\delta = \int m\psi dx$$

Eq. 6.19 $$\psi = \frac{M}{E_c I}$$

Eq. 6.20 $$\delta = \frac{10\psi_{mid} L^2}{96}$$

Eq. 6.21 $$\delta = \frac{PL^3}{24E_c I_{cr}}\left[3\left(\frac{a}{L}\right) - 4\left(\frac{a}{L}\right)^3 - 8\eta\left(\frac{L_g}{L}\right)^3\right]$$

Where, δ is the deflection at midspan, m and M are the moments at a section due to virtual and real loads, respectively, ψ and ψ_{mid} are the curvature at a section and the curvature at midspan,

respectively, P is the applied load, a and L are the shear span and clear span of the member, respectively, L_g is the length of the uncracked section near the supports, E_c is the modulus of elasticity of the concrete, I_{cr} is the moment of inertia of the cracked section and η is a factor to correct for the higher flexural stiffness of the uncracked region.

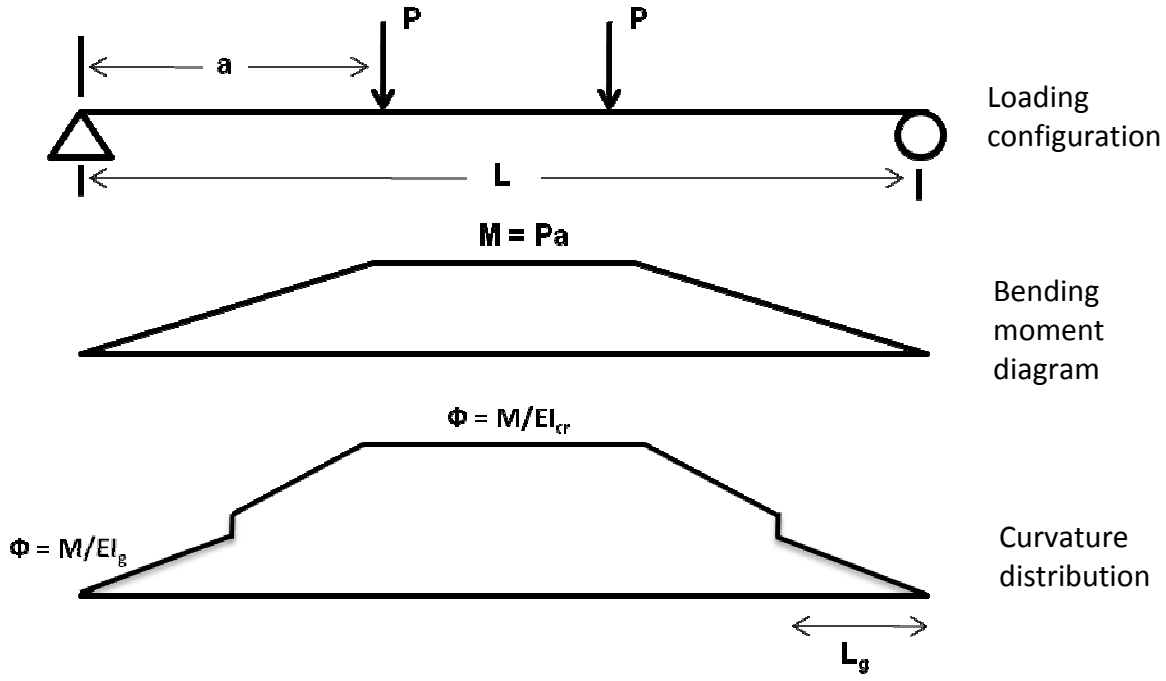

Figure 6.11 - Assumed curvature distribution for Razaqupur et al. (2000) model

Several models exist to calculate the effective moment of inertia of a section, a concept that is used to describe the overall flexural stiffness of a cracked member as a hybrid of fully cracked and uncracked sections. These models provide empirically derived values which lie between the moment of inertia of the fully cracked section and the gross moment of inertia of the uncracked section, depending on the ratio of applied to cracking moment. The CHBDC proposes the use of the Branson model for calculating the effective moment of inertia of a steel-reinforced section as given by Equation 6.22. This model has been shown to

underestimate deflections for FRP-RC members (Bischoff 2007). ACI 440.1R-06 (2006) uses a modified form of the Branson model for FRP-RC members given by Equation 6.23:

Eq. 6.22 $$I_e = I_{cr} + \left(I_g - I_{cr}\right)[\frac{M_{cr}}{M_a}]^3 \leq I_g$$

Eq. 6.23 $$I_e = (\frac{M_{cr}}{M_a})^3 \beta_d I_g + [1 - (\frac{M_{cr}}{M_a})^3] I_{cr} \leq I_g$$

Where, I_e, I_{cr} and I_g are the effective, cracked and gross moments of inertia, respectively, M_{cr} and M_a are the cracking moment and applied moment, respectively, and β_d is a factor to account for the reduced stiffness of FRP.

The procedure for using the Razaqpur et al. (2000) curvature model and the effective moment of inertia approach are straightforward. In either case the first point on the load-deflection curve corresponds to the cracking stage. Using gross or transformed section properties, the deflection of the uncracked section just prior to the onset of first cracking can be determined, giving the first point for the load-deflection curve. The deflection calculation depends on the loading arrangement and is given by Equation 6.24 for the case of four-point bending. The moment of inertia of the concrete section at the location of a crack is calculated using a reduced cross-section depth based on the depth to the neutral axis of $c = kd$, where k is given by Equation 6.25 (ACI 440.4R-04 2004). Several values of the applied moment between the cracking moment and the nominal moment resistance of the section are selected to give additional points on the load-deflection curve using Equation 6.21 or Equations 6.23 and 6.24. The analysis is stopped when the section fails either by reinforcement rupture or concrete crushing.

Eq. 6.24 $$\delta = \frac{PL^3}{6E_cI_e}\left[\frac{3a}{4L} - \left(\frac{a}{L}\right)^3\right]$$

Eq. 6.25 $$k = \frac{\sqrt{\left(n\sum_{i=1}^{m}\rho_i\right)^2 + 2(1-\xi)n\sum_{i=1}^{m}\rho_i\left(\xi + \frac{d_i}{d}(1-\xi)\right)} - n\sum_{i=1}^{m}\rho_i}{1-\xi}$$

Where, *k* is the ratio of the neutral axis depth to the effective depth of the reinforcement, *n* is the modular ratio of the reinforcement to the concrete, ρ_i is the reinforcement ratio of reinforcement at level *i*, ξ is the ratio of effective stress to ultimate strength of the prestressing tendons, and *d* and d_i are the effective depth to the centroid of the reinforcement and depth of reinforcement level *i*, respectively. All other terms are as noted previously.

Abdelrahman & Rizkalla (1999) noted that deflection calculations for partially prestressed members after cracking should also take into account the shift in the effective centroid of the section which changes the eccentricity of the prestressing force. A simple method for calculating the effective centroid was proposed, which is a function of the applied and cracking moments as given by Equations 6.26 and 6.27. The midspan deflection is then given by Equation 6.28. The effective centroid concept was used in conjunction with the effective moment of inertia approach to predict the deflections of the prestressed slabs.

Eq. 6.26 $$y_e = \psi^2 y_g + (1 - \psi^2)y_{cr} \leq y_g$$

Eq. 6.27 $$\psi = \left(\frac{M_{cr} - M_{dc}}{M_s - M_{dc}}\right)$$

Eq. 6.28 $$\Delta = -k_p\frac{P_e(d_p - y_e)L^2}{E_cI_e} + k_s\frac{M_sL^2}{E_cI_e}$$

Where, y_e, y_g and y_{cr} are the effective, gross and cracked section centroids, respectively, ψ is a factor accounting for the load level, M_{cr}, M_{dc} and M_s are the cracking, decompression and applied moments, respectively, Δ is the midspan deflection, k_p and k_s are coefficients to account for the tendon profile and loading configuration, P_e is the effective prestressing force, d_p is the depth to the prestressed tendons, L is the span length, E_c is the modulus of elasticity of the concrete and I_e is the effective moment of inertia.

The curvature distribution along the length of the member can also be obtained using a layer-by-layer strain compatibility analysis, an iterative procedure which divides the section into layers and applies the stress-strain characteristics of the materials within each layer to achieve compatibility between layers. In the case of prestressed members, initial strains in the prestressing tendons and concrete must be considered. This approach is shown schematically in Figure 6.12.

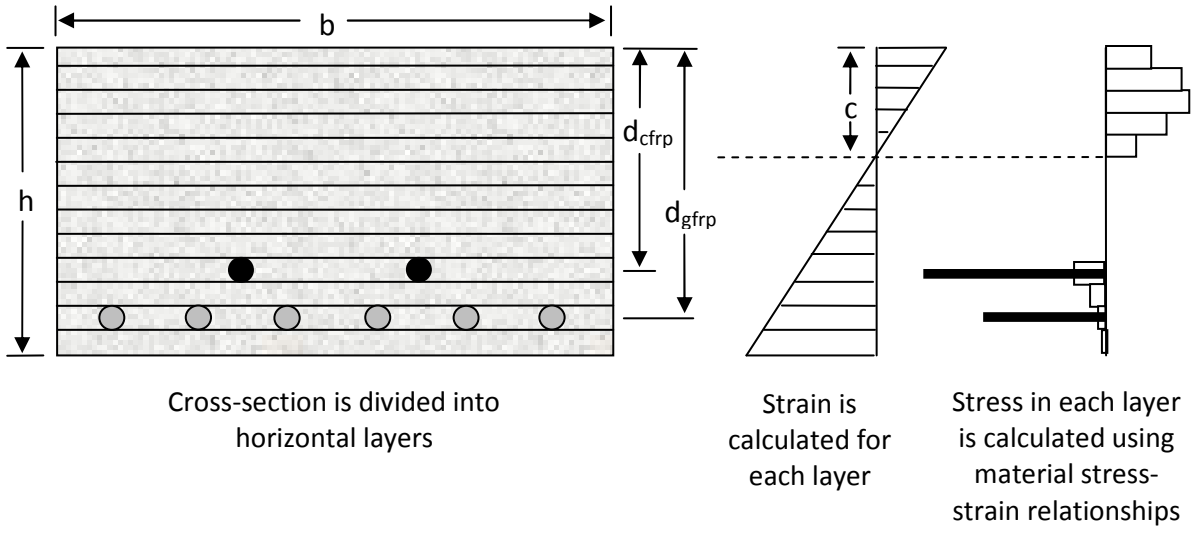

Figure 6.12 - Schematic of layered approach

The layer-by-layer strain compatibility analysis requires an understanding of the stress-strain characteristics of each of the materials involved, namely the reinforcement, concrete in compression and concrete in tension. Assumed stress-strain curves for each of these materials are given in Figure 6.13. FRP materials are modeled as linear elastic to failure, with the stress at a given strain determined by Equation 6.29. The stress-strain curves for concrete are more complex; an approximation for the stress-strain relationship of concrete in compression is the modified Hognestad model given by Equations 6.30 and 6.31. Tension stiffening between cracks can be considered with the use of a smeared crack model for concrete in tension, as given by Equation 6.32 (Collins & Mitchell 1991). Neglecting tension stiffening results in more conservative estimates of deflection. For this study, the effective area of concrete in tension after the onset of cracking was taken as the area of the concrete surrounding the reinforcing bars and having the same centroid, as recommended by CSA A23.3 (2004). For the prestressed slabs, the centroid of the reinforcement was taken as the weighted geometric average of the CFRP and GFRP bars.

Eq. 6.29 $$f_{frp} = E_{frp}\varepsilon_{frp}$$

Eq. 6.30 $$f_c = 0.9f'_c[2\frac{\varepsilon_c}{\varepsilon'_c} - (\frac{\varepsilon_c}{\varepsilon'_c})^2]; \qquad \text{for } \varepsilon_c \leq \varepsilon'_c$$

Eq. 6.31 $$f_c = 0.9f'_c - \left(\frac{0.135f'_c}{0.0038-\varepsilon'_c}\right)(\varepsilon_c - \varepsilon'_c); \qquad \text{for } \varepsilon'_c \leq \varepsilon_c \leq 0.0038$$

Eq. 6.32 $$f_t = \frac{\alpha_1\alpha_2 f_r}{1+\sqrt{500\varepsilon_t}}$$

Where, f_{frp} and ε_{frp} are the stress and strain in the FRP reinforcement, respectively, E_{frp} is the modulus of elasticity of the FRP, f_c and ε_c are the compressive stress and strain in the concrete,

respectively, f'_c is the compressive strength of the concrete, ε'_c is the concrete strain corresponding to the peak stress, f_t is the average tensile stress in the concrete, α_1 and α_2 are coefficients accounting for the bond characteristics of the reinforcement and the loading conditions, respectively, f_r is the modulus of rupture of the concrete and ε_t is the average tensile strain in the concrete.

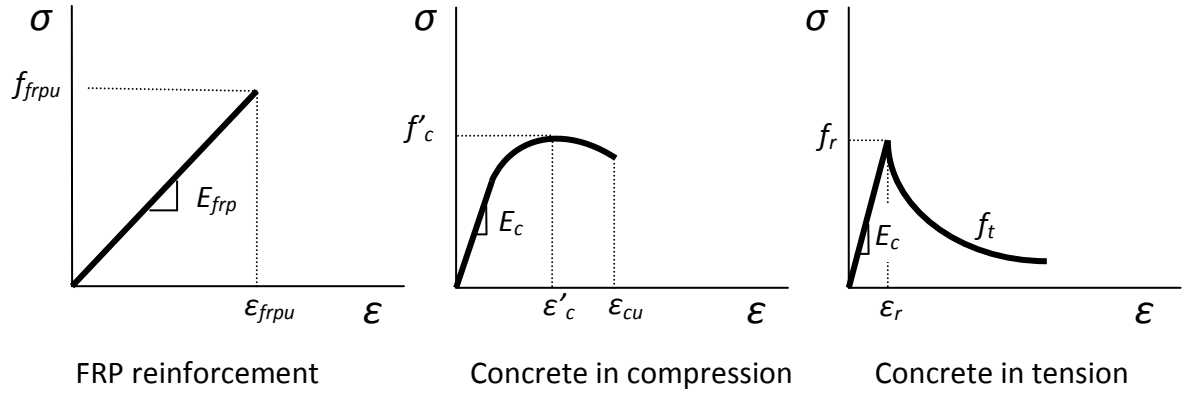

Figure 6.13 - Stress-strain characteristics of FRP reinforcement and concrete (not to scale)

The procedure for predicting the load-deflection response of FRP-reinforced and prestressed members using the layer-by-layer strain compatibility analysis is more complex than either of the previously described approaches and is summarized in Figure 6.14. For a given value of midspan moment, the procedure is repeated for multiple sections along the span and—assuming a linear distribution of curvature between sections—the resulting deflection is calculated using a piece-wise integration as given by Equation 6.33. For this study, curvatures were calculated at 150 mm intervals along the length of the slabs; the resulting curvature distribution is similar in shape to that shown in Figure 6.11, with relatively high curvatures in the cracked region and smaller curvatures in the uncracked region near the supports. Within the cracked region, the predicted curvatures tended to be smaller than those obtained using

the Razaqpur et al. (2000) model, particularly when tension stiffening was included through the smeared crack approach.

Eq. 6.33 $$\delta = \sum m_c \psi_a x$$

Where, m_c is the average moment between sections *i* and *i+1* due to a virtual unit load placed at midspan, ψ_a is the average curvature between sections *i* and *i+1* due to real loads, and *x* is the distance between sections *i* and *i+1*.

Typical plots comparing the predicted load-deflection response of the tested slabs to experimental results are given in Figures 6.15 through 6.18. The contribution of the CFRP tendons to either load resistance or flexural stiffness of the prestressed slabs following rupture is neglected; it is assumed that the tension resultant force after CFRP rupture is taken by the GFRP reinforcing bars only. In reality, the CFRP tendons will likely have some positive effect on the flexural stiffness at sections away from the location of CFRP rupture.

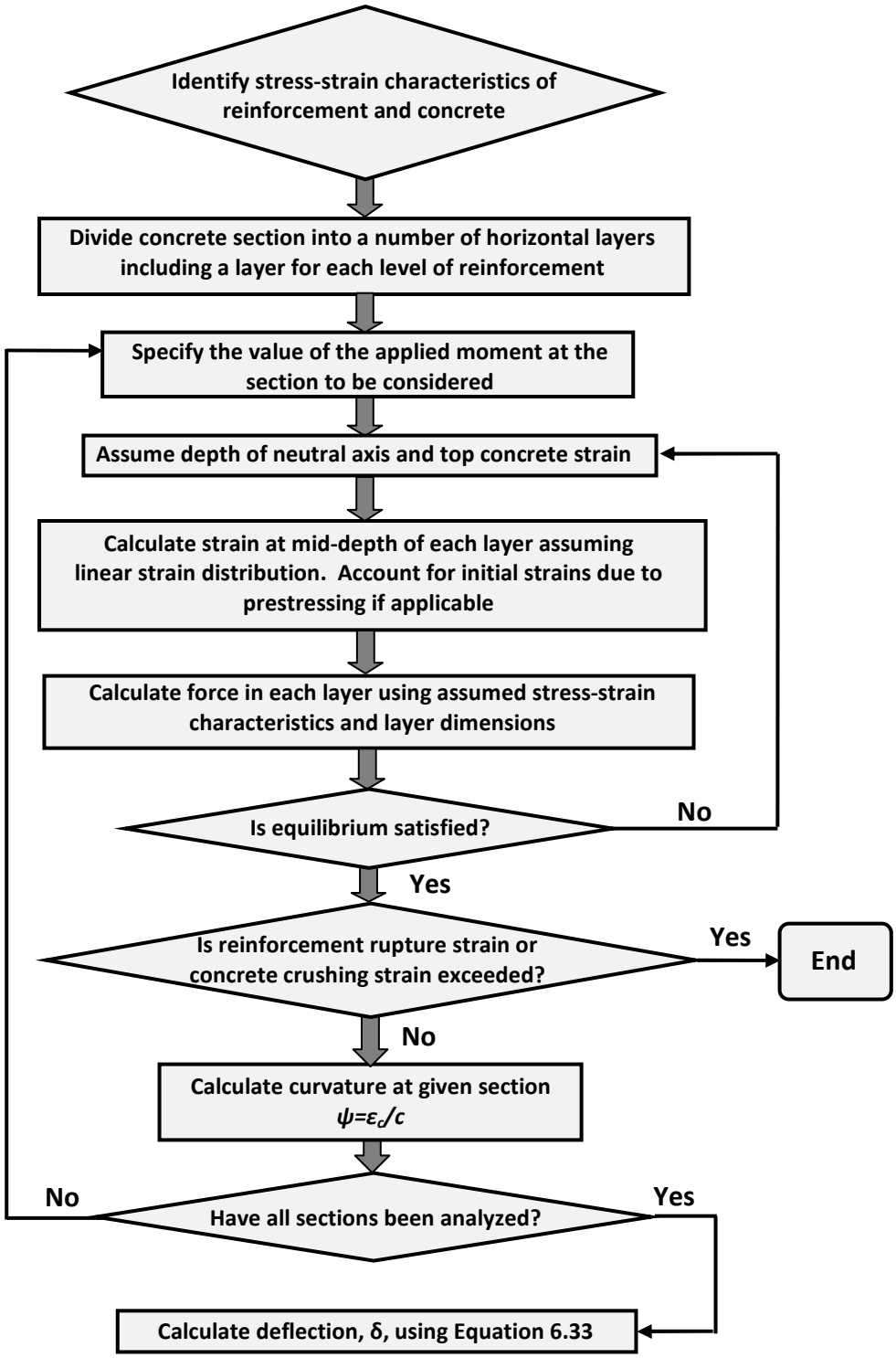

Figure 6.14 - Procedure for determining load-deflection response using the layer-by-layer strain compatibility analysis

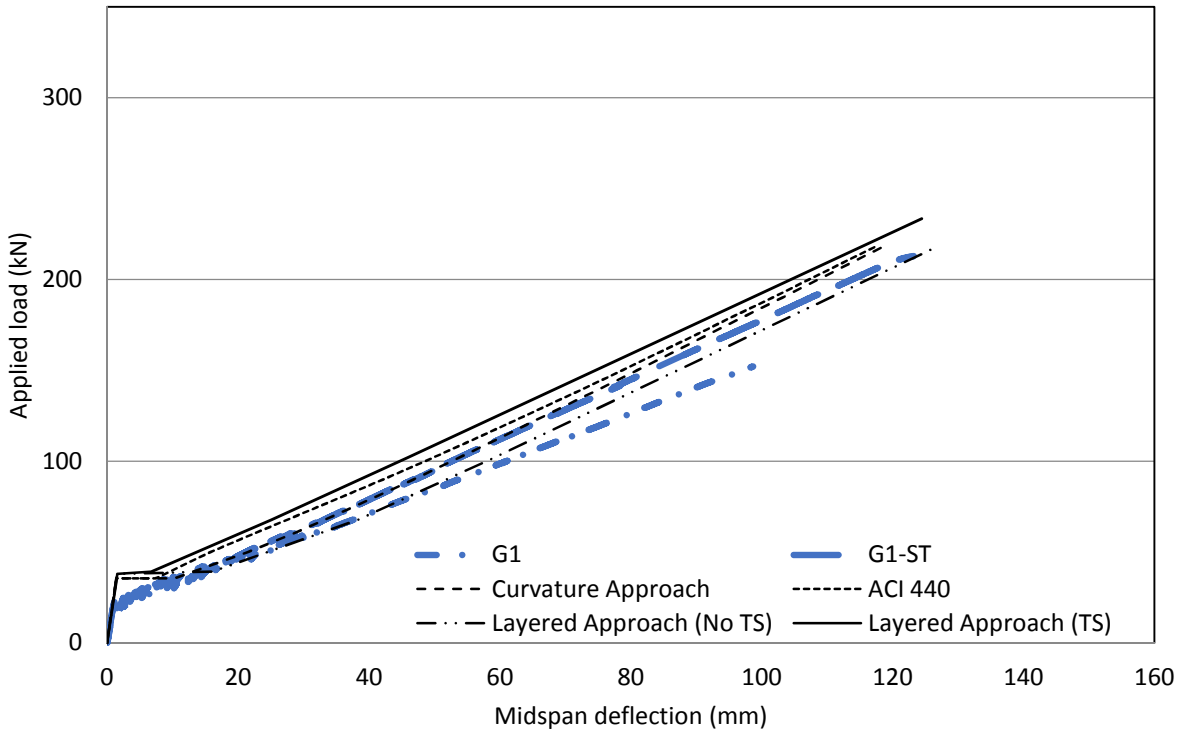

Figure 6.15 - Comparison of experimental and predicted load-deflection response for G1 and G1-ST

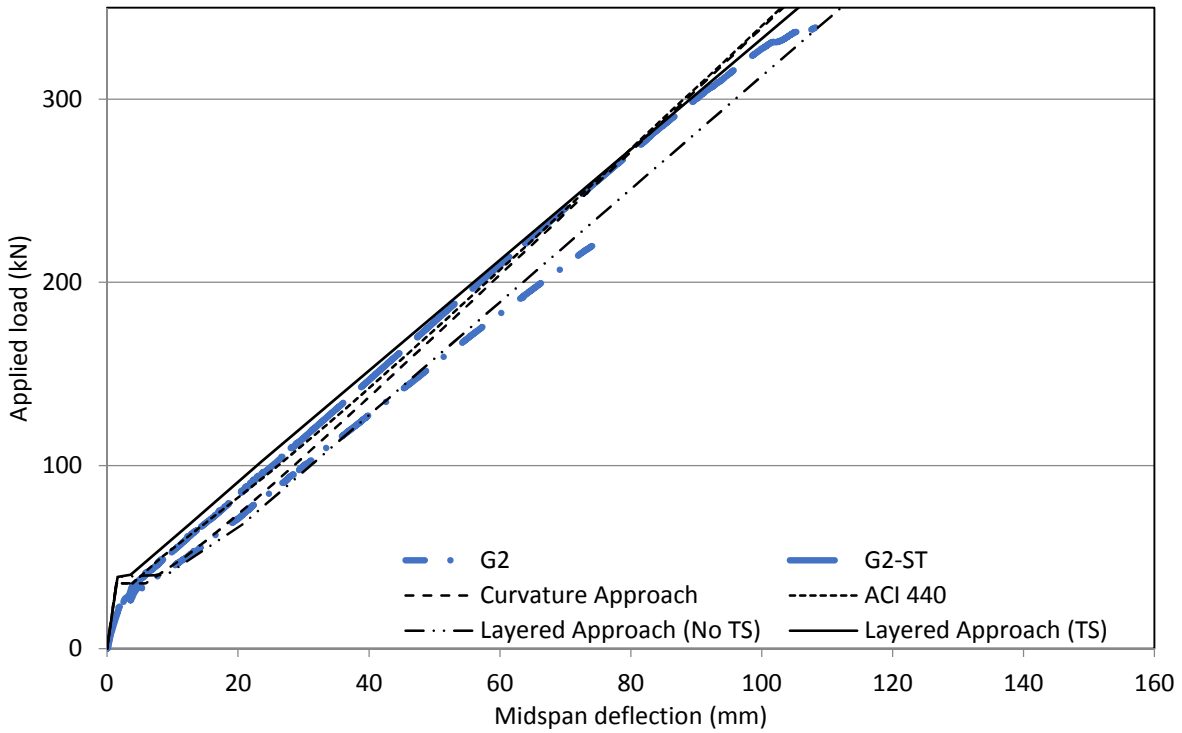

Figure 6.16 - Comparison of experimental and predicted load-deflection response for G2 and G2-ST

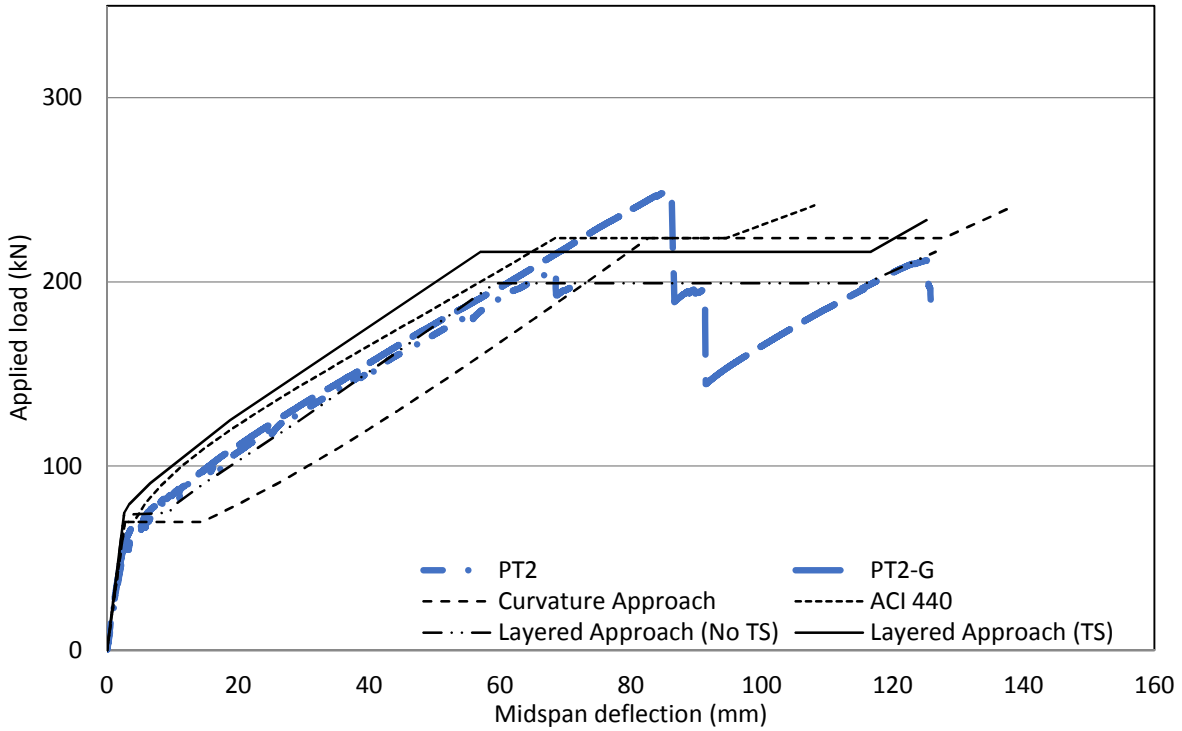

Figure 6.17 - Comparison of experimental and predicted load-deflection response for PT2 and PT2-G

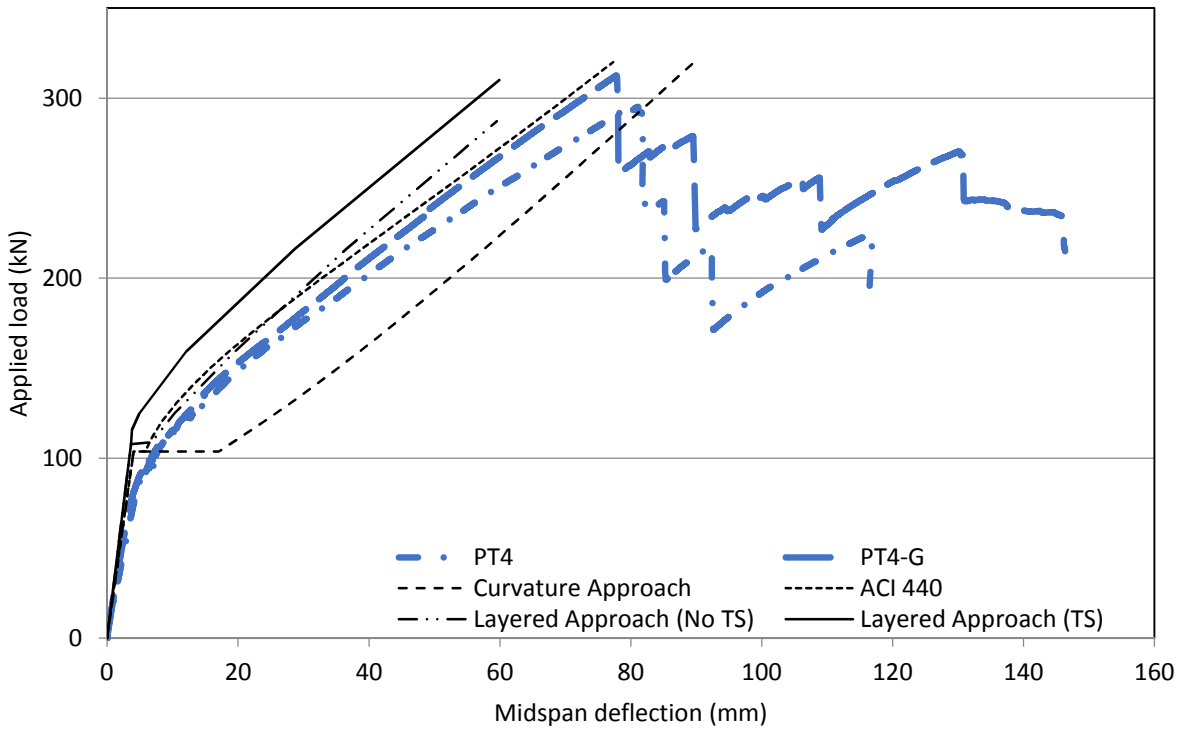

Figure 6.18 - Comparison of experimental and predicted load-deflection response for PT4 and PT4-G

Figures 6.15 to 6.18 show that the deflection models considered above typically overestimated the post-cracking stiffness of the tested slabs, particularly for the models which account for tension stiffening (ACI 440 and the layered approach). Conversely, the layered approach without consideration for tension stiffening overestimated deflections for the non-prestressed slabs with shear reinforcement, and the curvature approach was overconservative for the prestressed slabs after cracking. It should be noted that slab PT4-G suffered the loss of one tendon before testing, and thus it is expected that the stiffness of this slab is lower than predicted.

Two main observations can be made from the predicted load-deflection plots. First, the accuracy of all of the deflection models considered are highly dependent on the accuracy of the estimation of the cracking moment. As previously noted, the experimental cracking moment was consistently below predicted values; as a result, predicted post-cracking deflections are unconservative when tension stiffening is considered. When the experimental cracking moment was used in place of the predicted value, the deflections of slabs with shear reinforcement were predicted with good accuracy (Figures 6.19 to 6.22).

Second, the slabs without shear reinforcement consistently displayed a lower post-cracking stiffness compared with specimens containing shear reinforcement. There are two factors that are likely contributing to the lower stiffness of slabs without shear reinforcement, namely lack of confinement and the presence of additional shear deformations resulting from wider inclined cracks.

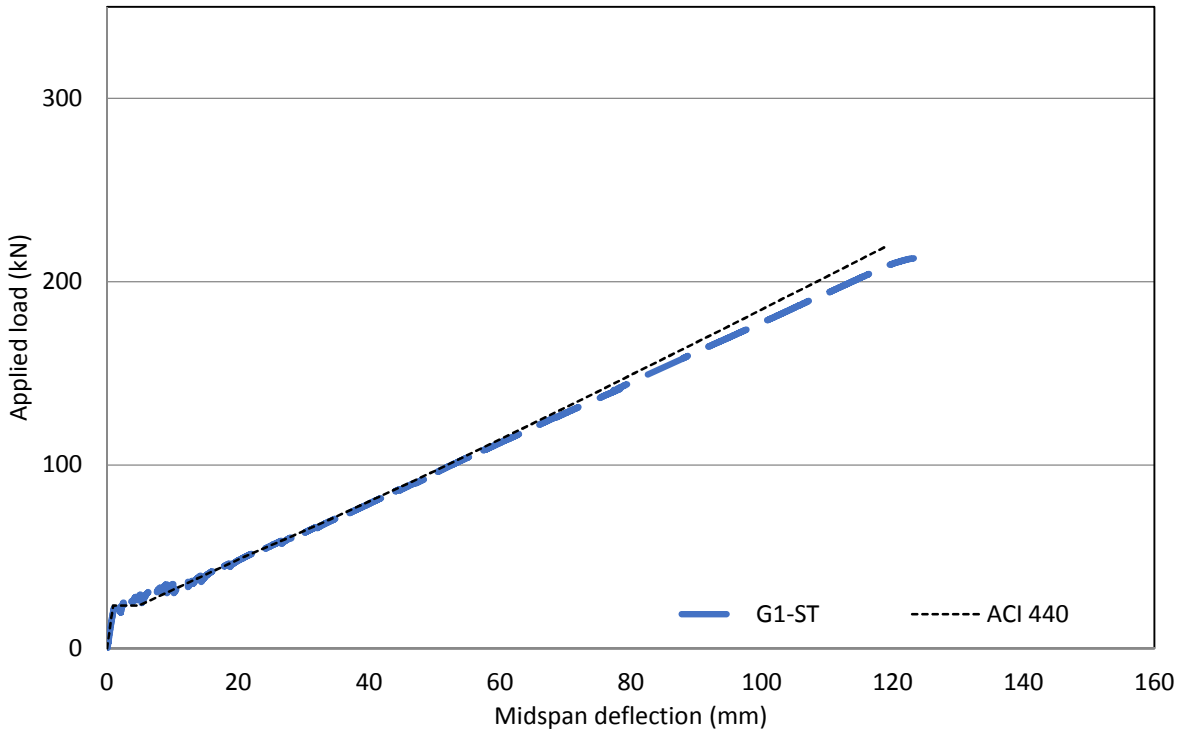

Figure 6.19 - Comparison of experimental and predicted load-deflection response for G1-ST using experimental cracking moment

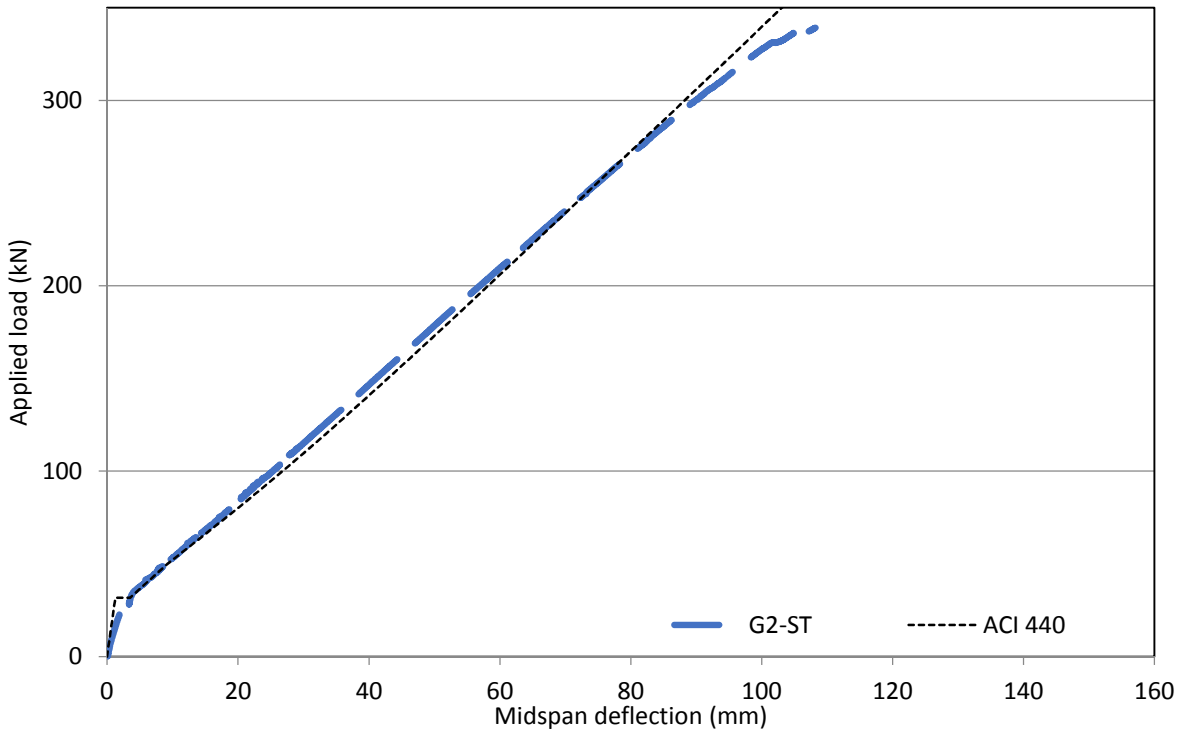

Figure 6.20 - Comparison of experimental and predicted load-deflection response for G2-ST using experimental cracking moment

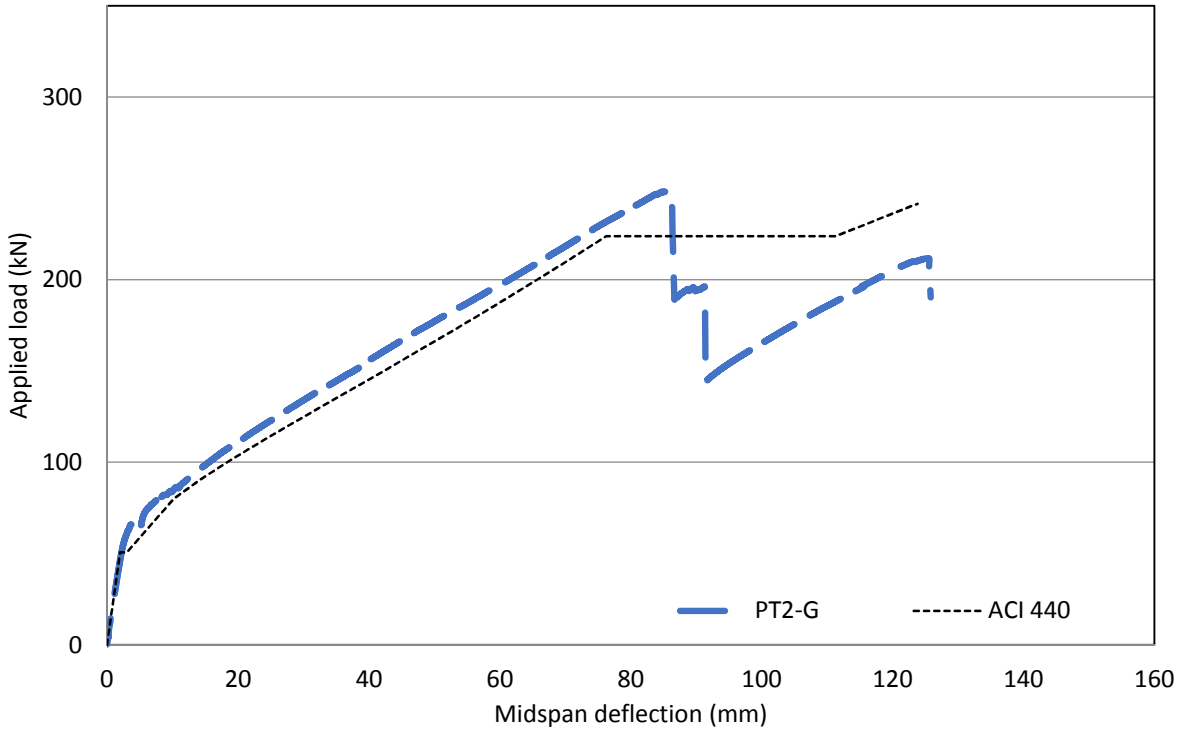

Figure 6.21 - Comparison of experimental and predicted load-deflection response for PT2-G using experimental cracking moment

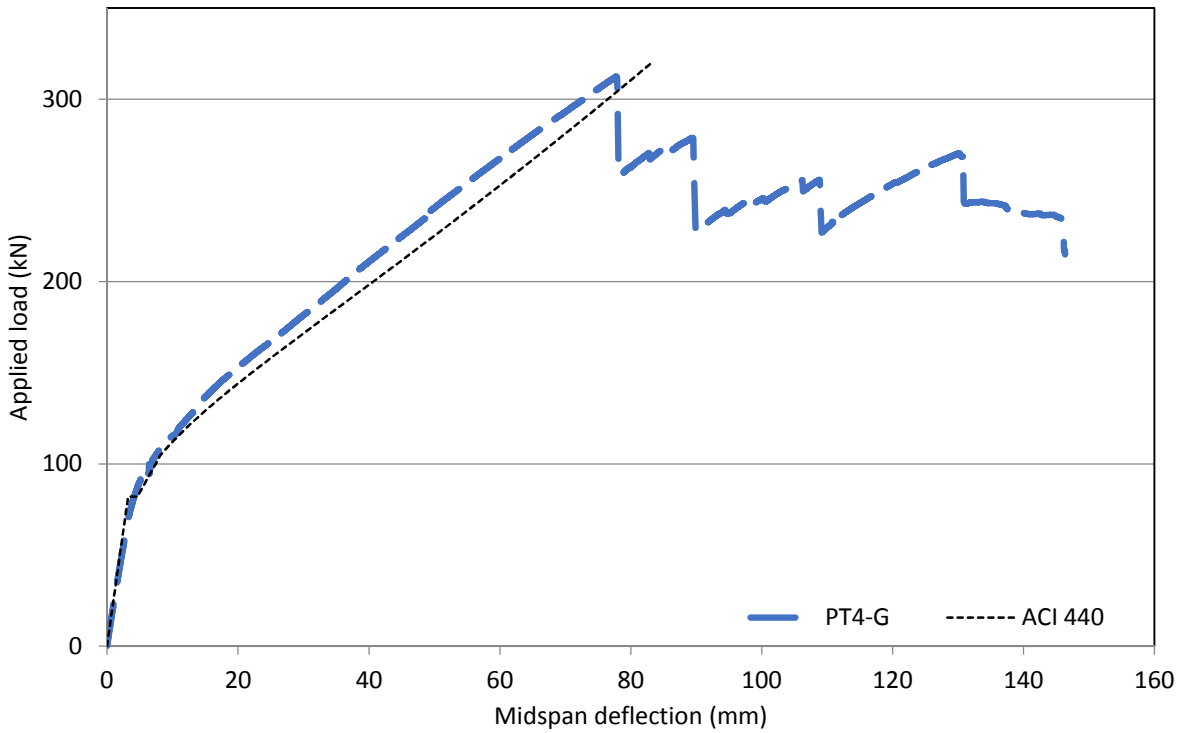

Figure 6.22 - Comparison of experimental and predicted load-deflection response for PT4-G using experimental cracking moment

The additional deformation resulting from unrestrained diagonal cracking, which may be significant in some cases, is neglected by most deflection models (Imjai et al. 2009). Al-Sunna et al. (2012) found that the lower modulus of elasticity of FRP bars compared to steel resulted in additional shear deformation due to rotation around the shear crack tip, a phenomenon which has not been observed for steel-RC beams. Additional deflections in the range of 20% of the total measured deflections at failure were observed. Existing approaches to estimate deflections considering solely their flexural behaviour tend to underestimate overall deformations.

Representing the member stiffness using the cracked moment of inertia should give conservative predictions of flexural deflection. As seen in Figure 6.23, even this upper bound estimate of deflection is exceeded by a considerable amount when no shear reinforcement is provided. From the experimental results of this study, it seems that the shear reinforcement provided was effective in restraining the vertical widening of diagonal shear cracks; however, specimens without shear reinforcement did not have this benefit, and hence, their deflections were under-predicted.

A simple model adapted from Imjai et al. (2009) is proposed to predict the value of these additional deformations after cracking. The model uses a single fictitious inclined crack having a width equal to the sum of the individual distributed crack widths as a simple way to represent the contribution of shear cracking to the total deflection, given by Equation 6.34 and shown in Figure 6.24. It is assumed here that three idealized straight inclined cracks are formed on either side of the constant moment region which contribute to the shear deformation (Figure 6.25);

this assumption is conservative at loads which are just slightly higher than the cracking load, as it is unlikely that cracks will appear away from the maximum moment location. Since the cracks are initially very narrow, the error introduced is small. As the load increases, new cracks form within the shear span and contribute to the total displacement. The horizontal width of each crack is assumed to be proportional to the maximum flexural crack width, calculated using Equation 6.14. Assuming an average crack spacing equal to one half of the depth of the slab, the additional shear deformation due to rigid body movement for a symmetrically loaded beam is given by Equation 6.35. The angle of the crack, θ, is taken as 45° for the non-prestressed slabs and 30° for the prestressed slabs. The assumptions regarding the number of inclined cracks and the crack inclination may not apply to all loading configurations; however, these assumptions are expected to be conservative for shorter spans (where less cracks are likely to form at a given moment) whereas for longer spans the ratio of moment-to-shear increases and shear deformation may comprise a smaller portion of the total displacement.

Eq. 6.34 $$\delta_s = (\frac{w_s \sin\theta}{y})(\frac{L/2}{1+I_1/I_2})$$

Eq. 6.35 $$\delta_s = (\frac{w_c \sin^2\theta}{y})(3a - 3d_v - 1.5h)$$

Where, δ_s is the additional shear deformation due to unrestrained shear cracking, w_s and w_c are the inclined width of the fictitious shear crack and the maximum flexural crack width, respectively, L is the span of the member, I_1 and I_2 are the horizontal distances from the fictitious crack tip to each support, θ is the angle of the idealized inclined crack, y is the height of the crack, a is the length of the shear span, h is the height of the section and d_v is the effective shear depth of the section.

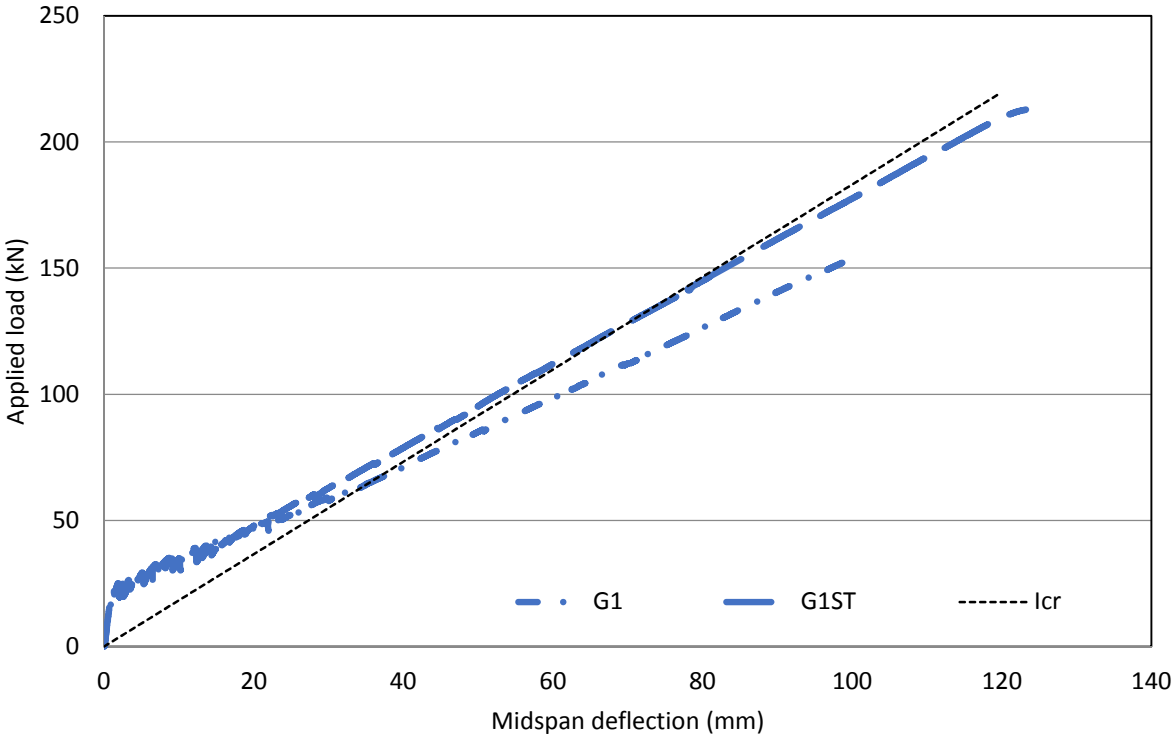

Figure 6.23 - Load-deflection response compared with fully cracked moment of inertia

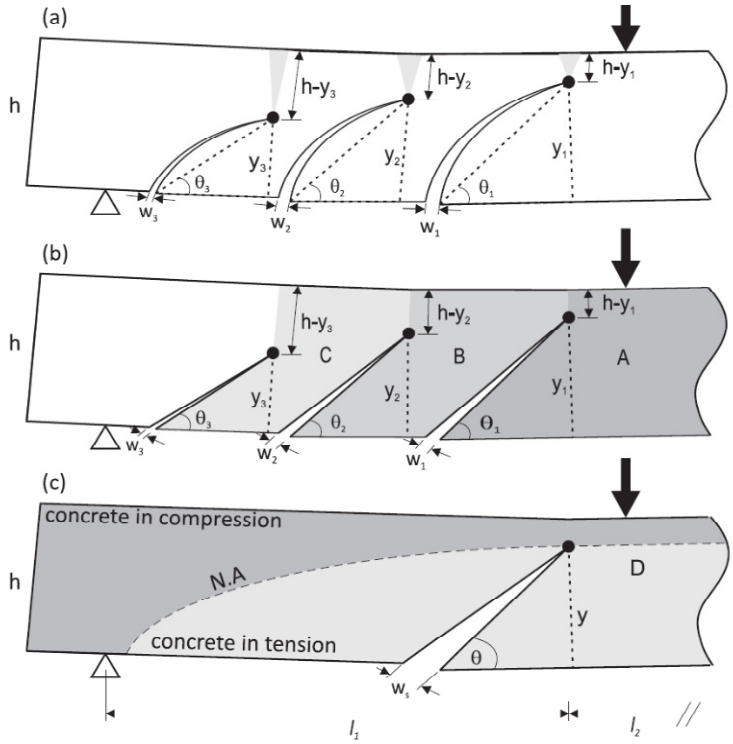

Figure 6.24 - Shear crack deformation model (Imjai et al. 2009)

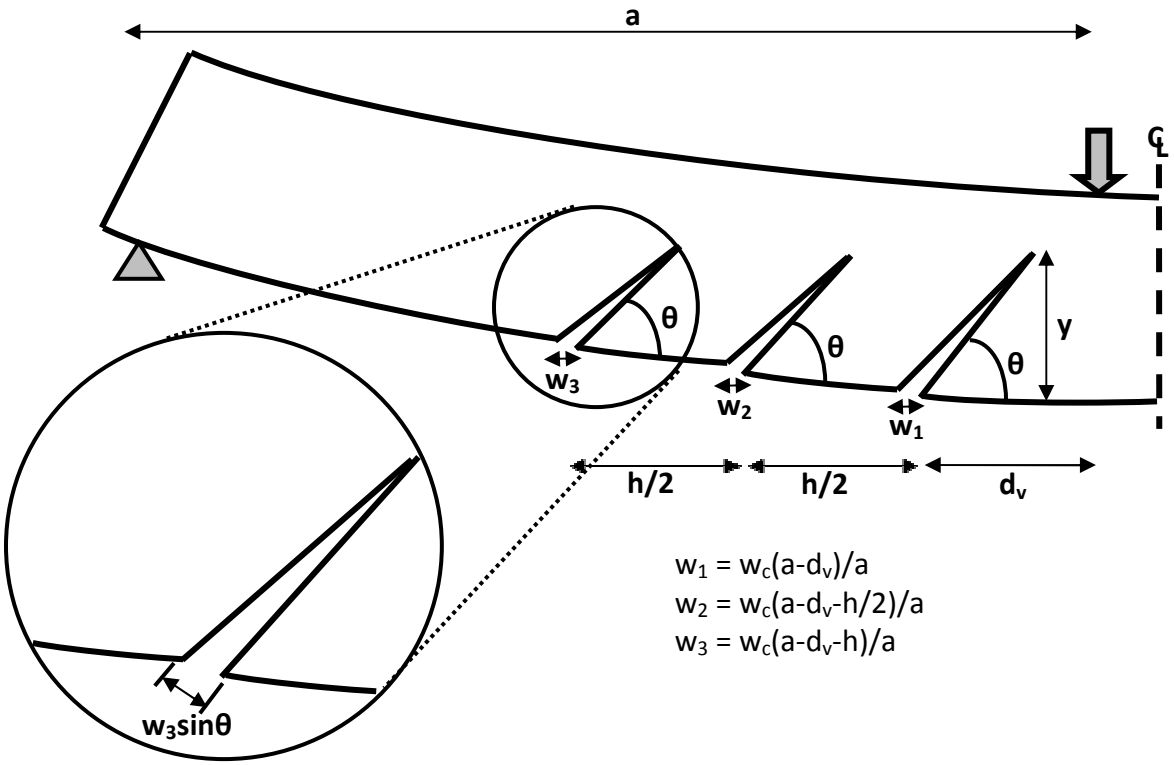

Figure 6.25 – Modified shear crack deformation model

The deflection calculated by Equation 6.35 was added to the flexural deflection predicted using the ACI 440 model (using the experimental cracking moment) to estimate the total deflection of the slabs without shear reinforcement. As seen in Figures 6.26 to 6.29, the predicted deflections correlated well with the experimental results, although the post-cracking deflections of slab PT4 were slightly over-estimated.

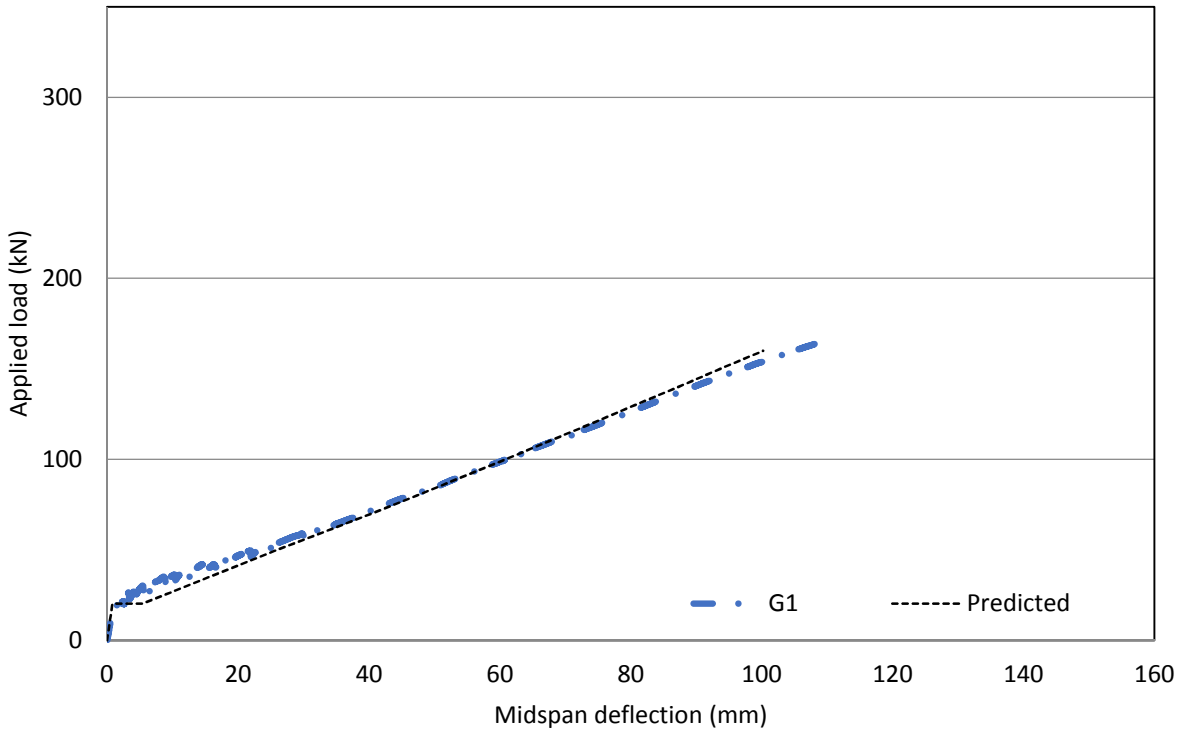

Figure 6.26 - Load-deflection prediction for slab G1

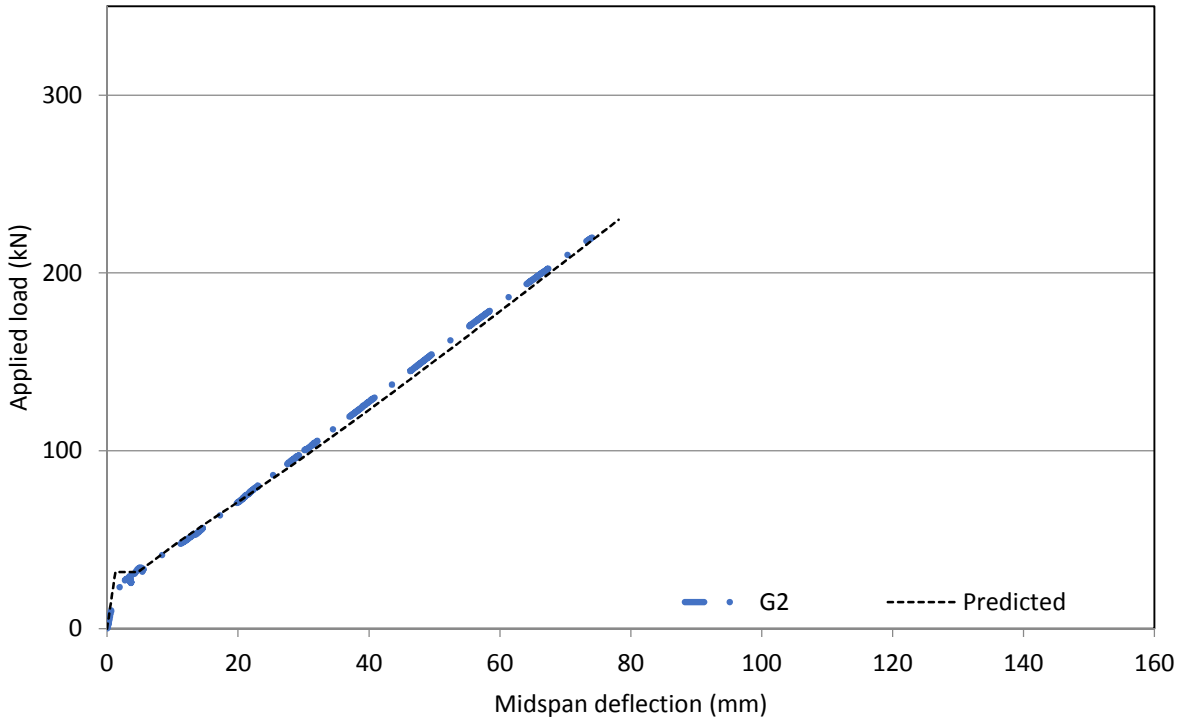

Figure 6.27 – Load-deflection prediction for slab G2

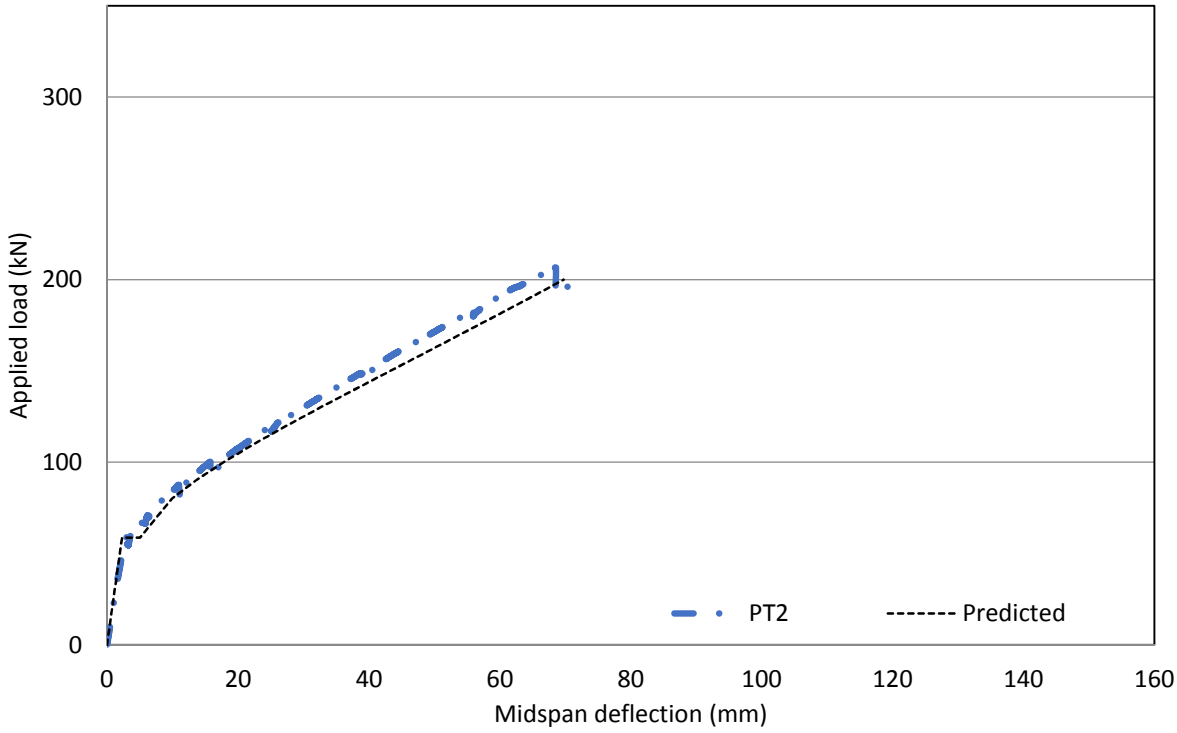

Figure 6.28 – Load-deflection prediction for slab PT2

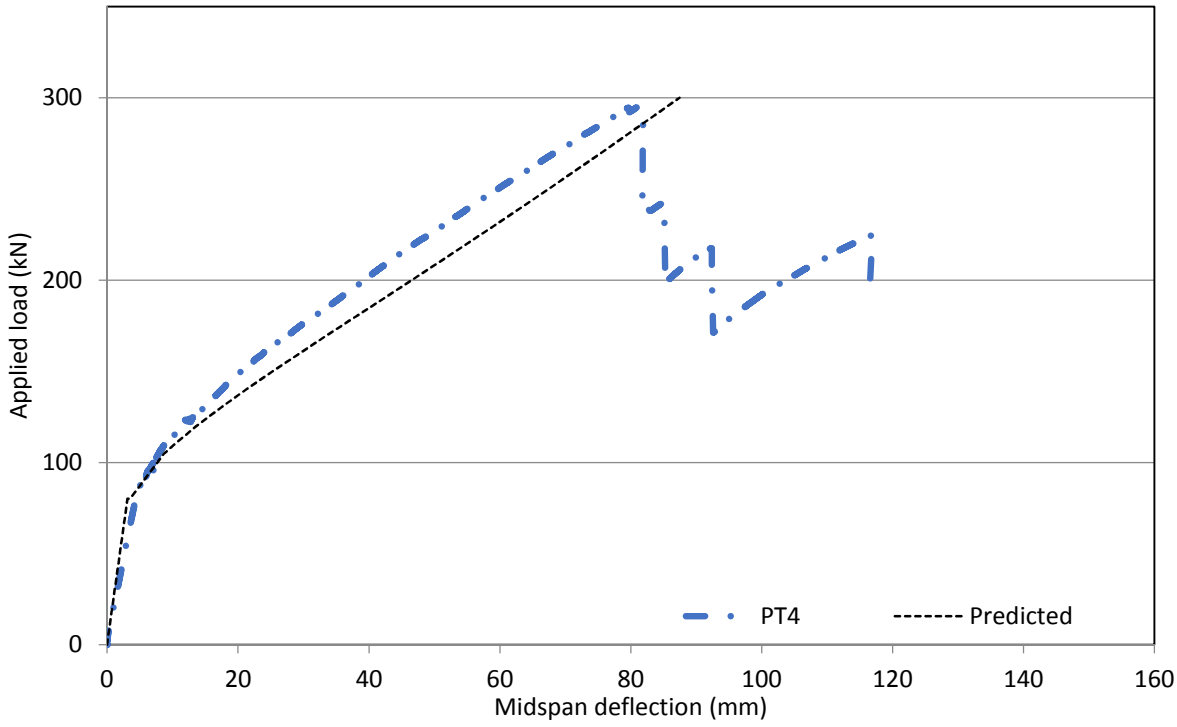

Figure 6.29 - Load-deflection prediction for slab PT4

6.3 Ultimate Predictions

Once the serviceability criteria have been satisfied, designs must be checked for the ultimate limit state. Both the factored flexural capacity and shear resistance of the section must exceed the factored load effects to ensure an adequate margin of safety for design. In the following sections, all resistance factors have been taken as unity for comparison with the experimental results. Factored loads according to the CHBDC are given in Chapter 8.

6.3.1 Flexure

Flexural design of FRP-RC members can be achieved using the straight-forward concept of strain compatibility assuming that plane sections remain plane. To determine the mode of failure, the reinforcement ratio is compared to the balanced reinforcement ratio, as discussed in Chapter 2. The moment capacity of a flexural member is given by Equation 6.36 based on the equilibrium condition given by Equation 6.37:

Eq. 6.36 $$M_r = T_1\left(d_1 - \frac{\beta_1 c}{2}\right) + T_2\left(d_2 - \frac{\beta_1 c}{2}\right)$$

Eq. 6.37 $$T_1 + T_2 = C$$

Where, M_r is the moment resistance of the section, T_1 and T_2 are the resultant tension forces in reinforcement layers 1 and 2, respectively, d_1 and d_2 are the depth to reinforcement layer 1 and 2, respectively, β_1 is the ratio of the depth of the equivalent concrete stress block to the depth of the neutral axis, c is the depth to the neutral axis and C is the resultant compression force in the concrete.

Tendon stresses at ultimate in unbonded prestressing tendons can be approximated with the use of a strain reduction coefficient, Ω_u, as given by Equation 6.38. This is based on the work of Naaman et al. (2002) and Alkhairi (1991), where the average strain in the tendon is related to an equivalent strain in a bonded tendon at the critical section calculated using strain compatibility. For two-point or uniform loading conditions, the strain reduction coefficient at ultimate is given by Equation 6.39, based on a regression analysis on test data from 143 beams prestressed with steel tendons. Alkhairi (1991) recalibrated the coefficient with additional conservatism for design purposes, as given in Equation 6.40:

Eq. 6.38 $$f_p = f_{pe} + \Omega_u E_p \varepsilon_{cu} (\frac{d_p}{c_u} - 1)$$

Eq. 6.39 $$\Omega_u = \frac{5.4}{(\frac{L}{d_p})}$$

Eq. 6.40 $$\Omega_u = \frac{3.0}{(\frac{L}{d_p})}$$

Where, f_p and f_{pe} are the equivalent stress in the prestressing tendon and the effective prestress, respectively, Ω_u is the strain reduction coefficient at ultimate, E_p is the modulus of elasticity of the prestressing tendon, ε_{cu} is the concrete crushing strain, d_p is the depth of the prestressing tendons, c_u is the depth of the neutral axis at ultimate and L is the span length.

Both slabs with unbonded tendons, PT2-U and PT4-U, suffered premature rupture of their prestressing tendons at lower loads than expected. Based on the methodology given above, slab PT2-U had an expected flexural capacity governed by GFRP rupture of 306.2 kN with CFRP stresses at ultimate of 81% of the guaranteed ultimate tensile strength (GUTS) using Equations

6.37 and 6.38. Similarly, slab PT4-U had an expected ultimate flexural capacity governed by concrete crushing at 335.7 kN with CFRP stresses of 76% of GUTS. In reality, the first tendon rupture occurred at loads of 126 kN and 203 kN for slabs PT2-U and PT4-U, respectively; in both cases, average CFRP stresses based on measured strain readings corresponded to only 68% of GUTS. This discrepancy highlights a safety concern with unbonded FRP tendons, as discussed in Chapter 4.

Table 6.3 gives the experimental and predicted ultimate moment resistance of each of the slabs displaying a flexural mode of failure. Experimental values given include the midspan moment due to the self-weight of the concrete members (10.7 kN·m). Resistance factors were taken as unity and the compressive strength of the top level of GFRP reinforcement was neglected. It should be noted that the CFRP tendons in the slabs containing two post-tensioned tendons were expected to rupture at a lower applied moment than that causing rupture of the GFRP bars. Hence, some residual capacity was expected with a sudden decrease in stiffness but an identical failure load as the non-prestressed slab G1-ST; however, since the peak load obtained experimentally corresponds to rupture of the CFRP tendons, the theoretical moment causing CFRP rupture is listed in Table 6.3 rather than the ultimate predicted moment corresponding to GFRP rupture.

In general, the predicted values for flexural resistance correlated reasonably well with experimental results, with a tendency to be slightly conservative. As noted in Chapter 5, the measured tensile strengths of the CFRP tendons were approximately equal to the design values; the conservatism observed here may be due to the stiffness of the GFRP reinforcement exceeding the reported values such that a lesser proportion of the tensile resultant force was

actually resisted by the CFRP tendons than predicted using design values. Conversely, the moment resistance of slab PT4-U was over-predicted; as previously mentioned, the premature rupture of the CFRP tendons due to friction within the post-tensioning duct resulted in lower than expected load capacities for the slabs with unbonded tendons.

Table 6.3 - Comparison of theoretical and experimental moment resistance

Slab	Predicted moment capacity (kN·m)	Experimental moment capacity (kN·m)	M_{exp}/M_{pred}
S	121.9[a]	157.2	1.29
G1-ST	202.2	196.9	0.97
G2-ST	319.8	307.4	0.96
PT2-ST	192.5	260.2	1.35
PT2-G	184.1	229.0	1.24
PT2-S	184.1	227.4	1.24
PT2-S45	184.1	217.7	1.18
PT4	270.3	269.0	1.00
PT4-G	227.7[b]	284.1	1.25
PT4-U	280.2[b]	222.2	0.79

a – Assumes linear elastic-perfectly plastic behaviour
b - Calculated for three CFRP tendons

6.3.2 Shear

The two most commonly used shear resistance models for FRP-RC bridges in North America are based on the simplified modified compression field theory (MCFT) (Bentz et al. 2006) and the empirically-derived Tureyen & Frosch model (Tureyen & Frosch 2003). The CHBDC has adopted the simplified MCFT model given by Equation 6.41 while ACI 440.1R-06 and the AASHTO LRFD bridge design code have adopted the latter model, as given by Equation 6.42:

Eq. 6.41 $$V_c = 2.5\beta f_{cr} b_v d_{long}$$

Eq. 6.42 $$V_c = 0.42\sqrt{f'_c} b_w c$$

Where, V_c is the concrete contribution to shear resistance, β is a factor to account for the shear strength of cracked concrete, f_{cr} is the tensile strength of concrete, b_v and b_w are the width of

the concrete member, d_{long} is the effective shear depth of the section and c is the depth to the neutral axis.

Table 6.4 lists the predicted and actual shear capacities for the slabs which ultimately failed in shear.

Table 6.4 - Predicted vs. experimental shear resistance

Slab	V_{exp} (kN)	CHBDC		Tureyen & Frosch	
		V_{pred} (kN)	V_{exp}/V_{pred}	V_{pred} (kN)	V_{exp}/V_{pred}
G1	83.1	79.7	1.04	67.4	1.23
G2	109.9	85.2	1.29	92.6	1.19
PT2a	86.3	81.1	1.06	83.1	1.04
PT2	103.2	93.5	1.10	94.2	1.10
PT2-U[a]	91.0	79.7	1.14	81.9	1.11
PT4-P	127.5	106.6	1.20	94.9	1.34

a – Calculated for 1 tendon

Both models gave reasonable estimates of shear capacity which were found to be conservative in all cases. The simplified MCFT gave an average experimental-to-predicted ratio of 1.14, while the Tureyen & Frosch model yielded an experimental-to-predicted ratio of 1.17.

None of the full-scale slabs containing shear reinforcement failed in shear. To assess the contribution of the various shear reinforcement types considered, the failure loads of the reduced-length slabs tested in Phase II can be compared with analytical predictions.

The capacity of FRP stirrups is given in the CHBDC as the smaller of Equations 6.43 and 6.44. The contribution to shear resistance provided by vertical FRP stirrups is given by Equation 6.45:

Eq. 6.43 $$\sigma_v = \frac{\left(0.05\frac{r}{d_s}+0.3\right)f_{FRPbend}}{1.5}$$

Eq. 6.44 $$\sigma_v = E_{vFRP}\varepsilon_v = 0.004E_{vFRP}$$

Eq. 6.45 $$V_{frp} = \frac{A_v \sigma_v d_{long} cot\theta}{s}$$

Where, σ_v is the stress developed in the stirrups, r is the radius of the stirrup bend, d_s is the stirrup diameter, $f_{FRPbend}$ is the ultimate tensile strength of the FRP stirrup, E_{vFRP} is the modulus of elasticity of the FRP stirrup, ε_v is the effective strain of the stirrup, A_v is the cross-sectional area of each stirrup, d_{long} is the effective shear depth of the section, θ is the angle of the shear crack and s is the stirrup spacing.

The contribution to load capacity of shear reinforcement without hooked or headed anchorages at each end is dependent on the bond developed along the embedded length of the bar. The embedded length of each bar depends on the depth at which it intercepts a shear crack; the average embedment length is assumed to be half the height of each stirrup. Assuming a uniform bond distribution along the embedded length of the stirrup, the average effective stress developed in the unanchored stirrups is taken as the lesser of Equations 6.44 and 6.46. The development length of FRP bars is given in the CHBDC by Equation 6.47:

Eq. 6.46 $$\sigma_v = \frac{\ell_e}{\ell_d} f_{FRPu}$$

Eq. 6.47 $$\ell_d = 0.45 \frac{k_1 k_4}{[d_{cs} + K_{tr} \frac{E_{FRP}}{E_s}]} \left[\frac{f_{FRPu}}{f_{cr}}\right] A$$

Where, ℓ_e and ℓ_d are the embedment length and development length of the unanchored stirrup, respectively, k_1 and k_4 are coefficients accounting for the bar location and bond, respectively, d_{cs} is the concrete cover to the centroid of the bar being developed, K_{tr} is a factor accounting for the presence of transverse reinforcement, E_{FRP} and E_s are the elastic modulus of

the FRP bar and steel, respectively, f_{cr} is the tensile strength of concrete, A is the area of the reinforcing bar and f_{frpu} is the tensile capacity of the stirrup.

The predicted and experimental shear resistance of each of the monotonically tested slabs in Phase II is given in Table 6.5. The concrete contribution to shear resistance was calculated using the simplified MCFT approach as detailed above.

Table 6.5 - Predicted and experimental shear capacities of shear-reinforced slabs

Slab	Experimental shear capacity (kN)	Predicted shear capacity (kN)	V_{exp}/V_{pred}
GU-10	404	311	1.30
GU-12	400	342	1.17
CU-10	398	372	1.07
GC-10	484	311	1.56
GS-12	475	358	1.33

The shear capacities of both slabs with anchored shear reinforcement, GC-10 and GS-12, were conservatively predicted. In both cases, the effective stress developed in the FRP shear reinforcement significantly exceeded the design values. For slabs with unanchored shear reinforcement, the accuracy of the predictions varied but were conservative in all cases. The level of conservatism decreased as the diameter of the GFRP stirrups was increased from 10 mm to 12 mm (slab GU-12 vs. slab GU-10). This may be as a result of the reduced cover-to-bar diameter ratio which prevented the stirrups from reaching the same effective stress prior to bond failure. In a real slab bridge, where the stirrup confinement would be significantly enhanced by the adjacent concrete, the efficiency of the stirrup may be higher. Similarly, the capacity of the slab with the 10 mm CFRP stirrups (slab CU-10) was well-predicted, but the estimated strength was less conservative than for the other shear-reinforced slabs. As noted in Chapter 4, although the unanchored stirrups did contribute significantly to the ultimate shear

capacity of the concrete slabs, their efficiency is dependent on the height at which they intercept the shear crack and the confinement provided by the concrete. The use of anchor heads results in an increase in the contribution of the FRP shear reinforcement and is less dependent on the crack geometry.

6.4 Summary

Various analytical models were used to predict the behaviour of the GFRP-RC slabs at the serviceability and ultimate limit states. Lower cracking moments were observed compared with predicted values, which is likely a result of restrained shrinkage stresses. When these lower cracking moments were taken into account, the load-deflection responses of the slabs were well-predicted using the straightforward effective moment of inertia approach proposed by ACI 440.1R-06 for members containing shear reinforcement. When no shear reinforcement was provided, additional deflections caused by rigid body rotation about the inclined shear cracks resulted in unconservative estimates of the midspan deflection using conventional methods; a model was adapted from Imjai et al. (2009) capable of estimating these additional deformations with reasonable accuracy.

Crack widths were also predicted using the Frosch (1999) model, although the accuracy of the predictions varied with the stress level in the GFRP reinforcement. In particular, the bond coefficient of 1.4 proposed by ACI 440.1R-06 was found to be overly conservative, while the value of 0.8 suggested by the CHBDC was unconservative for high stress levels. A modification was proposed to account for the contribution of the concrete between cracks which gave

consistently accurate predictions for all stress levels in the service range. The bond coefficient was experimentally determined to be 1.3 for the modified Frosch equation.

The flexural capacities of the GFRP-RC slabs were reasonably well-predicted using a conventional strain compatibility approach. However, slabs with unbonded tendons suffered premature rupture of the CFRP tendons at stresses of only 68% of ultimate which is likely due to friction induced at the tendon-duct interface. It is therefore recommended to only use fully bonded tendons unless some kind of frictionless sheathing is used to protect the bar.

Both the MCFT and Tureyen & Frosch (2002) equations gave good estimates of the shear capacities of slabs without shear reinforcement. Shear strengths were also conservatively predicted for the slabs containing transverse shear reinforcement, even when the stirrups were unanchored at one end.

Chapter 7 - Fatigue Analysis of FRP-RC Slabs

7.1 General

Cyclic loading affects both the strength and stiffness of reinforced concrete members and therefore the static behaviour predicted by the models presented in Chapter 6 may not accurately represent the structural behaviour observed throughout its service life. To date, no significant research efforts have been conducted to predict the effect of repeated loads on the serviceability and ultimate performance of FRP-RC or PC flexural members, in part due to the difficulty involved in characterizing the fatigue behaviour of FRP reinforcing bars through experimental testing. An attempt is made here to bridge this gap using relatively simple models to predict the effect of fatigue on flexural deflections and crack widths, as well as the fatigue life of flexural members with and without transverse shear reinforcement.

7.2 Effective Fatigue Stress Factor

The fatigue data corresponding to the test specimens which failed by tensile rupture of the GFRP reinforcement—whether they were bare axial bars, beam-hinge specimens or slabs—are shown in Figure 7.1. Two notable observations can be made by comparing the results of each test type and loading condition: firstly, the significant decrease in fatigue life for the beam-hinge specimens compared with the axial bar specimens, and secondly, the change in slope between the prestressed and non-prestressed slab specimens. The first observation is attributed to fretting fatigue of the GFRP bar due to abrasion with the surrounding concrete; the local stress concentration at the flexural crack face as well as the abrasion induced at the bar-concrete interface reduced the observed fatigue lives of the GFRP reinforcing bars by

approximately an order of magnitude. The second observation is likely a function of the change in mean stress between the GFRP bars in the prestressed and non-prestressed slabs; at the minimum applied load level the GFRP stress in the prestressed slabs was essentially zero, whereas the non-prestressed slabs had a minimum stress level of approximately 65 MPa, including the self-weight of the slab. The change in mean stress may result in a shift in the S-N curve—as is commonly observed for various types of materials—as well as a change in slope due to its effect on crack opening and bond-slip, thus affecting the fretting mechanism.

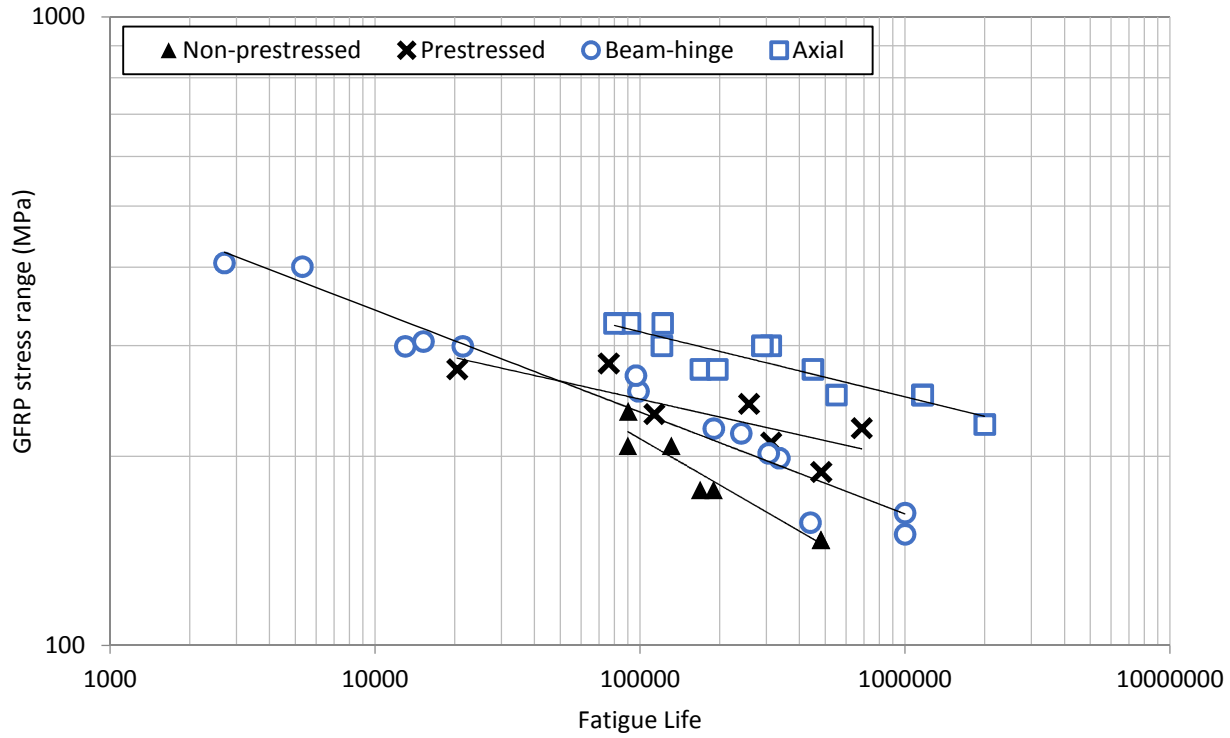

Figure 7.1 - Combined fatigue data

The fatigue design of structural elements with geometric discontinuities is generally accommodated with the use of a stress concentration factor, K_t, to relate the peak stress induced from the change in geometry to the nominal stress calculated using the nominal

section properties. A similar concept is employed here to account for the effect of concrete on the fatigue behaviour of the GFRP bars as given by Equation 7.1:

Eq. 7.1 $$\sigma_e = K_{te}\sigma_n$$

Where, σ_e is the effective stress range for fatigue calculations, K_{te} is the effective fatigue stress factor accounting for the presence of concrete and σ_n is the nominal stress range in the GFRP bar calculated using elastic cracked section analysis.

The effect of the mean stress on the fatigue life of GFRP bars in concrete can be accounted for by considering the change in the stress ratio, *R*, which is given by Equation 7.2. Figure 7.2 shows the change in the stress ratio for different values of minimum stress; while the GFRP stress ratio is zero for all load ranges for the prestressed slabs (σ_{min} = 0 MPa), the stress ratio increases at low load ranges for the non-prestressed slabs (σ_{min} = 65 MPa) and beam-hinge specimens (σ_{min} = 30 MPa). Thus, multiplying the effective stress range by a factor of *(1 + R)* will shift the data from the non-prestressed slabs upward, especially at low load ranges, to match the data from the prestressed slabs; the resulting proposed equation describing all of the GFRP fatigue data is then given by Equation 7.3.

Eq. 7.2 $$R = \sigma_{min}/\sigma_{max}$$

Eq. 7.3 $$K_{te}\sigma_n(1 + R) = AN^B$$

Where, *R* is the stress ratio, σ_{min} is the minimum applied stress, σ_{max} is the maximum applied stress, and all other terms are as noted previously.

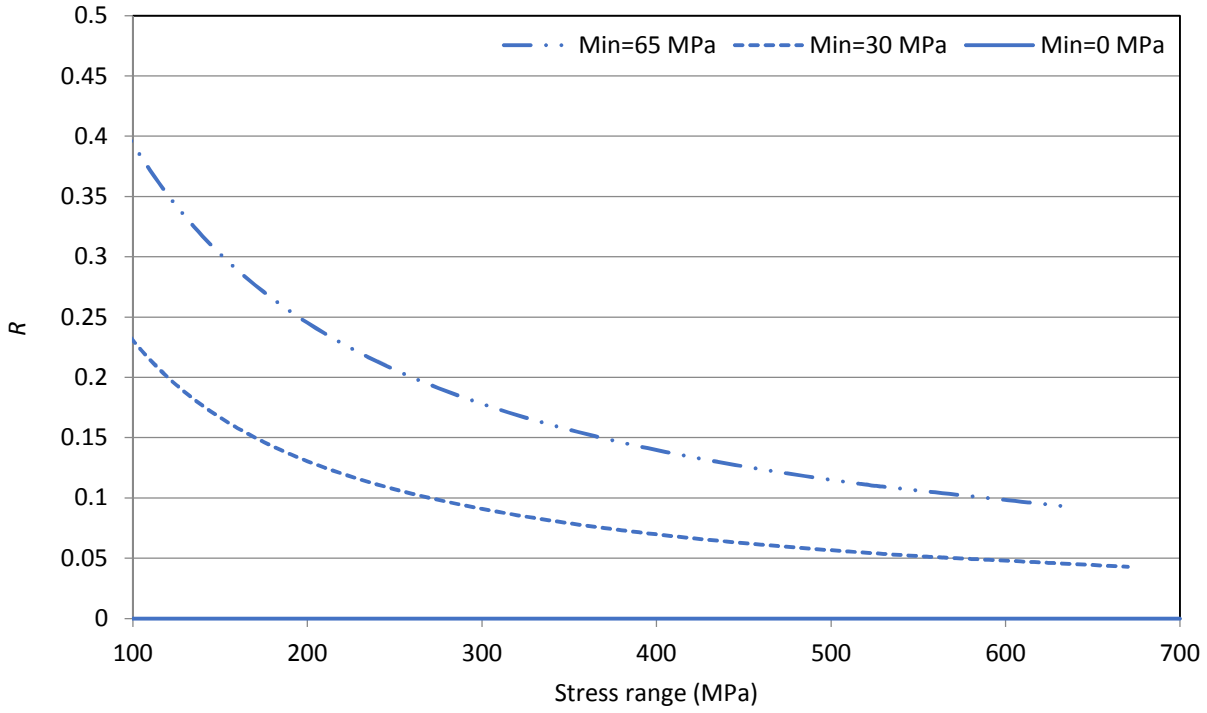

Figure 7.2 - Variation in stress ratio for constant minimum stress level

The effective fatigue stress factor for the materials and reinforcement configuration used in this study was obtained by comparing the fatigue results of the axial bar tests and beam-hinge tests described in Chapter 5. The stress concentration factor for the axial bar tests was taken as unity while the effective fatigue stress factor for the beam-hinge tests was optimized through a least squares regression analysis used to fit a power law function to the fatigue data, with the fatigue life taken as the dependent variable (Figure 7.3); this procedure resulted in a value of K_{te} given by Equation 7.4 and the regression line given by Equation 7.5. The modified data set is shown in Figure 7.4.

Eq. 7.4 $$K_{te} = 1.529 - 0.000671\sigma_n \geq 1.0$$

Eq. 7.5 $$K_{te}\sigma_n(1+R) = 1632N^{-0.132}$$

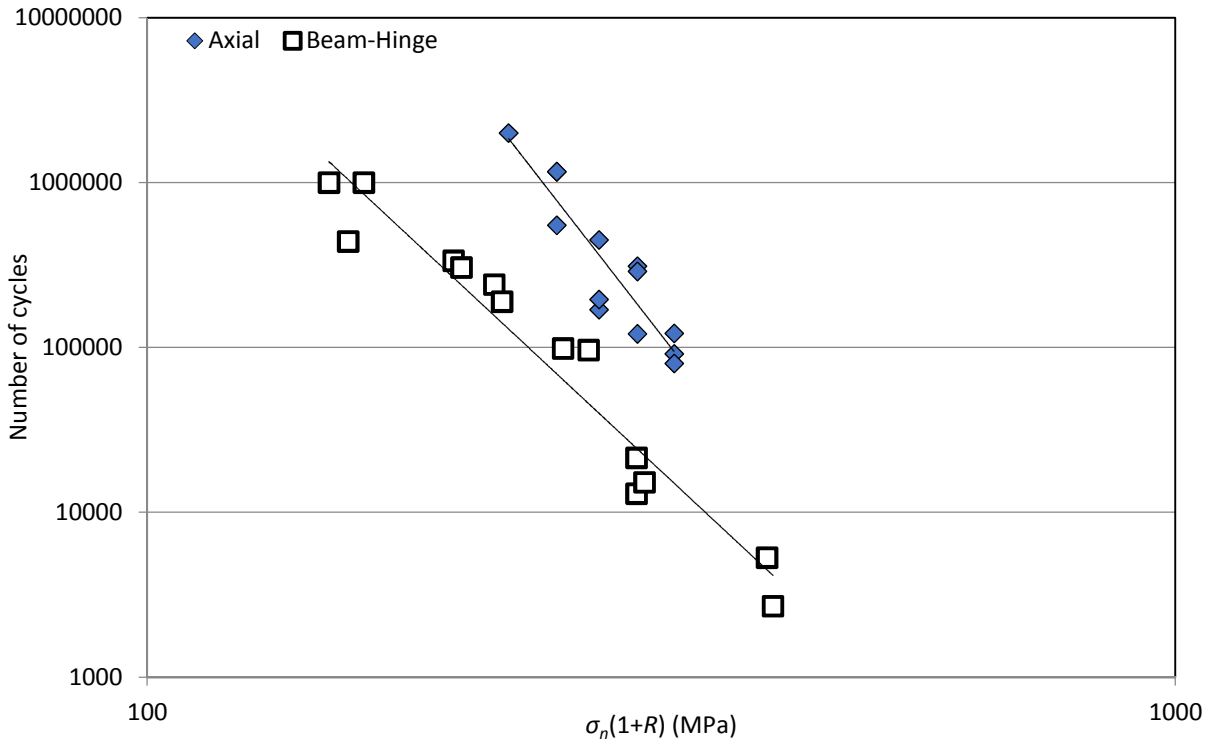

Figure 7.3 – Fatigue life data

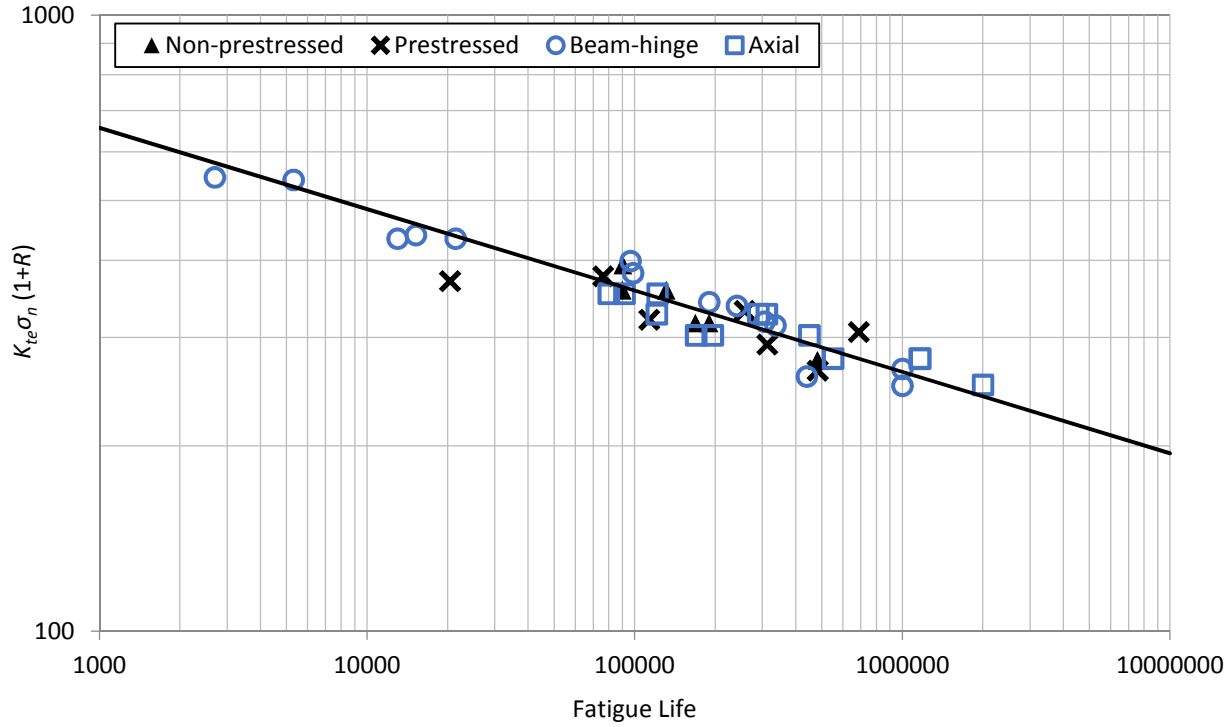

Figure 7.4 – Fatigue life data using effective stress range

The effective fatigue stress factor is dependent on the applied stress level since it is a function of the abrasion caused by bond-slip of the reinforcement. As the applied stress range approaches the static strength of the GFRP bar, the effective fatigue stress factor approaches a value of 1.0.

7.3 Deflection Predictions

The cyclic deflections for the FRP-RC slabs were predicted using the ACI 440 effective moment of inertia equation with some modifications to account for the change in stiffness of the concrete and reinforcement. Balaguru & Shah (1982) presented a framework for calculating the cyclic deflections and crack widths of steel-RC flexural members accounting for the cyclic creep of concrete in compression and the reduction in concrete tensile strength caused by repeated loading. These changes in the concrete properties were used to modify the Branson equation for the effective moment of inertia of a member under cyclic loading as given by Equations 7.6 to 7.10:

Eq. 7.6 $$\varepsilon_c = 129\sigma_m t^{1/3} + 17.8\sigma_m \Delta N^{1/3}$$

Eq. 7.7 $$f_{r,N} = f_r\left(1 - \frac{logN}{10.954}\right)$$

Eq. 7.8 $$E_N = \frac{\sigma_{max}}{\frac{\sigma_{max}}{E_o} + \varepsilon_c}$$

Eq. 7.9 $$M_{cr,N} = \frac{I_g f_{r,N}}{y_t}$$

Eq. 7.10 $$I_{e,N} = I_{cr,N} + \left(\frac{M_{cr,N}}{M_a}\right)^3 (I_g - I_{cr,N})$$

Where, ε_c is the cyclic creep strain in the concrete, σ_m and Δ are the mean compressive stress and stress range in the concrete expressed as a fraction of the compressive strength, respectively, t is the time under cyclic loading in hours, f_r and $f_{r,N}$ are the modulus of rupture values for the concrete under static and cyclic loads, respectively, E_o and E_N are the modulus of elasticity values for the concrete under static and cyclic loads, respectively, σ_{max} is the maximum compressive stress in the concrete, $M_{cr,N}$ is the cyclic cracking moment of the concrete, $I_{cr,N}$ is the cracking moment of inertia calculated using E_N, $I_{e,N}$ is the effective moment of inertia under cyclic loading and all other terms are as previously noted in Chapter 6.

The model described above assumed that for medium and high-cycle fatigue loading the steel reinforcing bars were cyclically stable. As seen in Chapter 5, the stiffness of the GFRP reinforcing bars decreases gradually under fatigue loading; hence, this model was adapted for FRP-RC members by considering the change in stiffness of the FRP reinforcement with repeated loading.

Brondsted et al. (1997) proposed a model considering the stiffness degradation of FRP composites as a manifestation of fatigue damage which has been modified here to account for the presence of concrete as given by Equation 7.11, with the fatigue modulus given by Equation 7.12:

Eq. 7.11 $$\frac{d(\frac{E}{E_1})}{dN} = -K(\frac{\sigma_e(1+R)}{E_o})^n$$

Eq. 7.12 $$E_f = E_o[1 - KN(\frac{\sigma_e(1+R)}{E_o})^n]$$

Where, $d(E/E_1)/dN$ is the rate of stiffness degradation, σ_e is the applied effective stress range, K and n are constants and all other terms are as previously noted.

This model assumes that the rate of stiffness degradation is a constant for a given stress range, neglecting the initial rapid change in stiffness at the beginning of the fatigue life of the specimen. The model was calibrated using the experimental results described in Chapter 5; calibration involves taking the slope of the stiffness degradation curve within the linear range for each specimen (Figures 7.5 and 7.6) and plotting the data points versus the ratio $\sigma_e(1+R)/E_o$, as shown in Figure 7.7. Since the strain gauges did not survive the full fatigue life for most of the specimens in this study, the stiffness degradation was measured using the change in the relative displacement between the anchors (axial tests) or midspan deflection (beam-hinge tests). This is an acceptable assumption because after the initial seating of the wedges in the bare bar tests and stabilization of the crack pattern in the beam-hinge tests, the ratio of strain-to-total deformation was approximately constant as evidenced by the experimental results shown in Figures 7.8 and 7.9. Thus, the error introduced by this approximation is small.

The cyclic deflections of the Phase III slabs were then predicted using the model framework proposed by Balaguru & Shah (1982) accounting for the change in GFRP stiffness using the Brondsted residual stiffness model. The calibrated equation for the GFRP stiffness degradation is given by Equation 7.13. It is assumed that the CFRP tendons are not susceptible to stiffness degradation due to their excellent fatigue properties. A flow chart of the model framework is shown in Figure 7.10.

Eq. 7.13 $$E_f = E_o[1 - 4.837x10^{13}N(\frac{\sigma_e(1+R)}{E_o})^{8.915}]$$

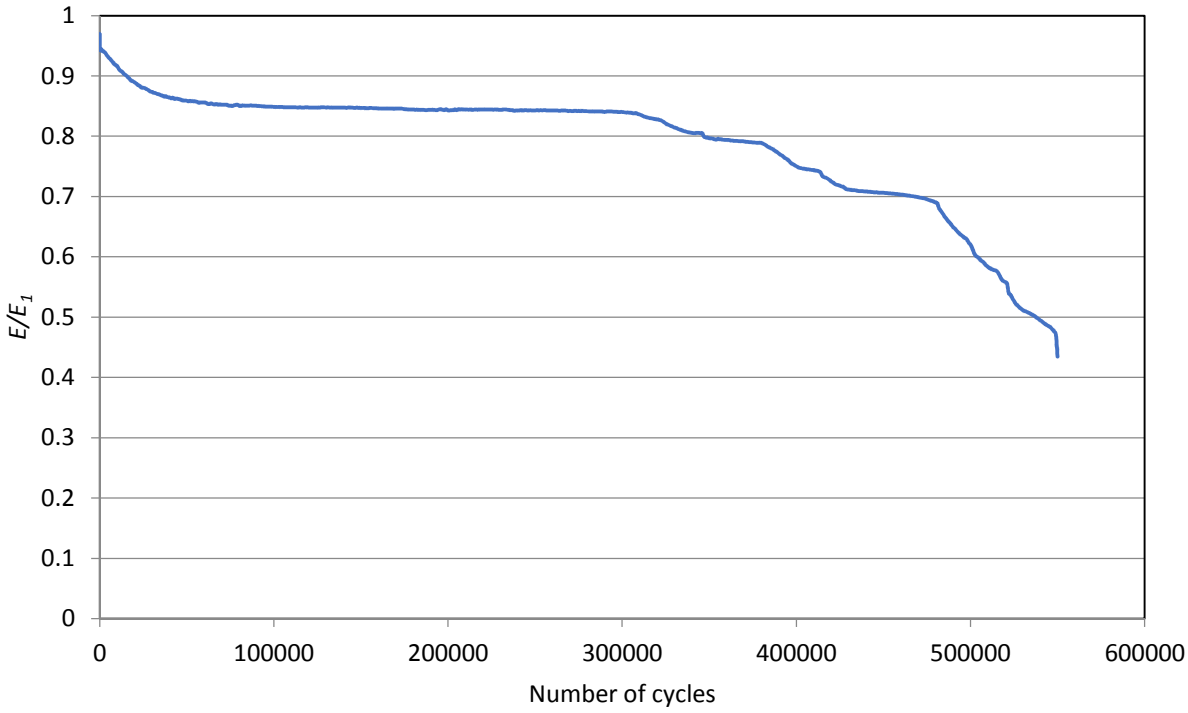

Figure 7.5 - Typical stiffness degradation curve

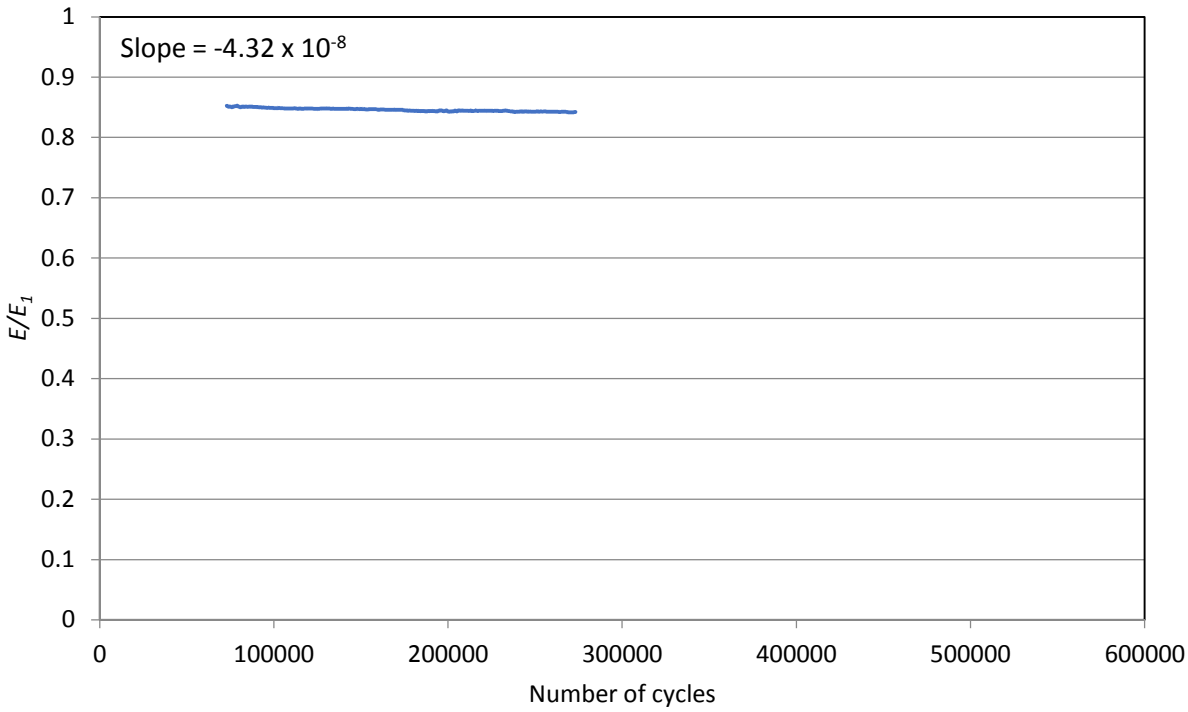

Figure 7.6 - Linear portion of typical stiffness degradation curve

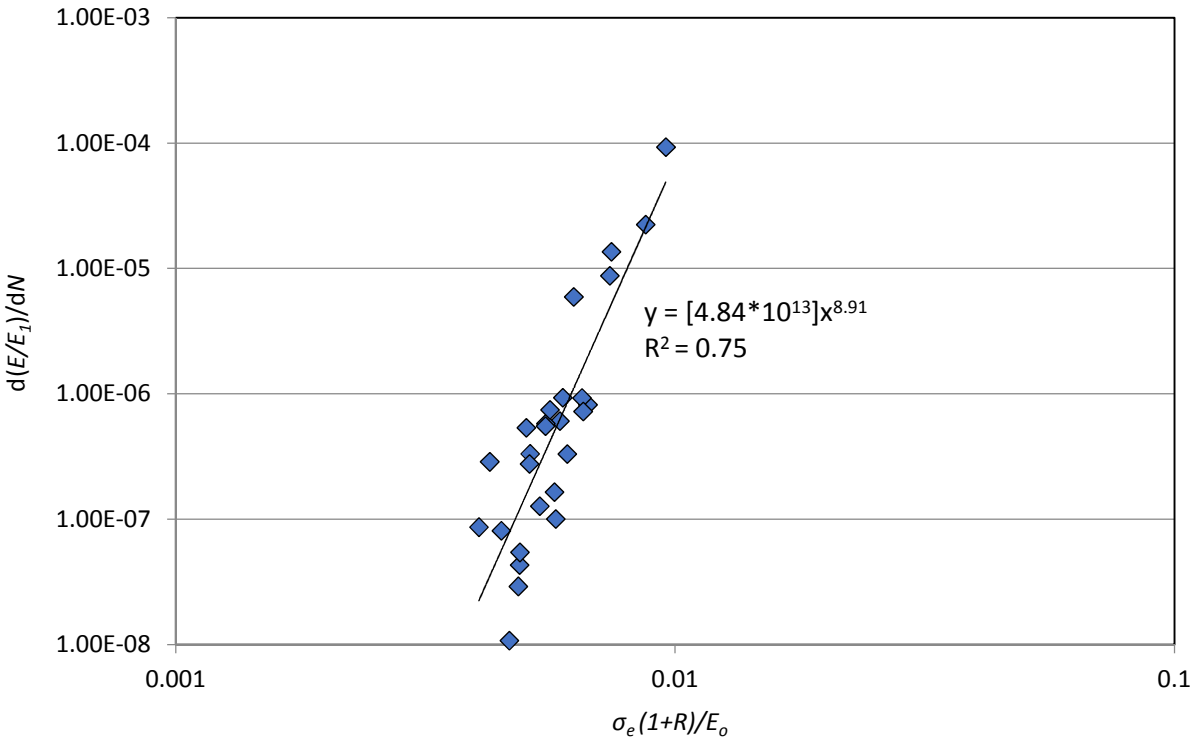

Figure 7.7 - Calibration of Brondsted residual stiffness model

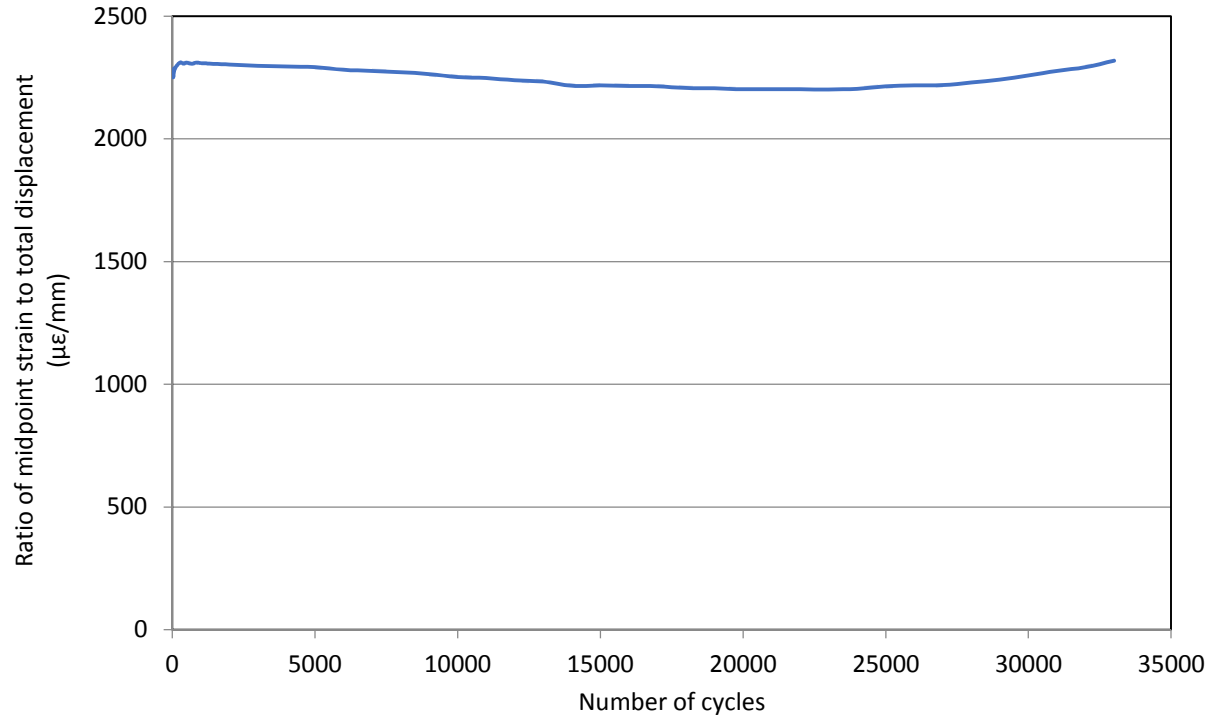

Figure 7.8 - Typical strain-displacement response for axial tension tests

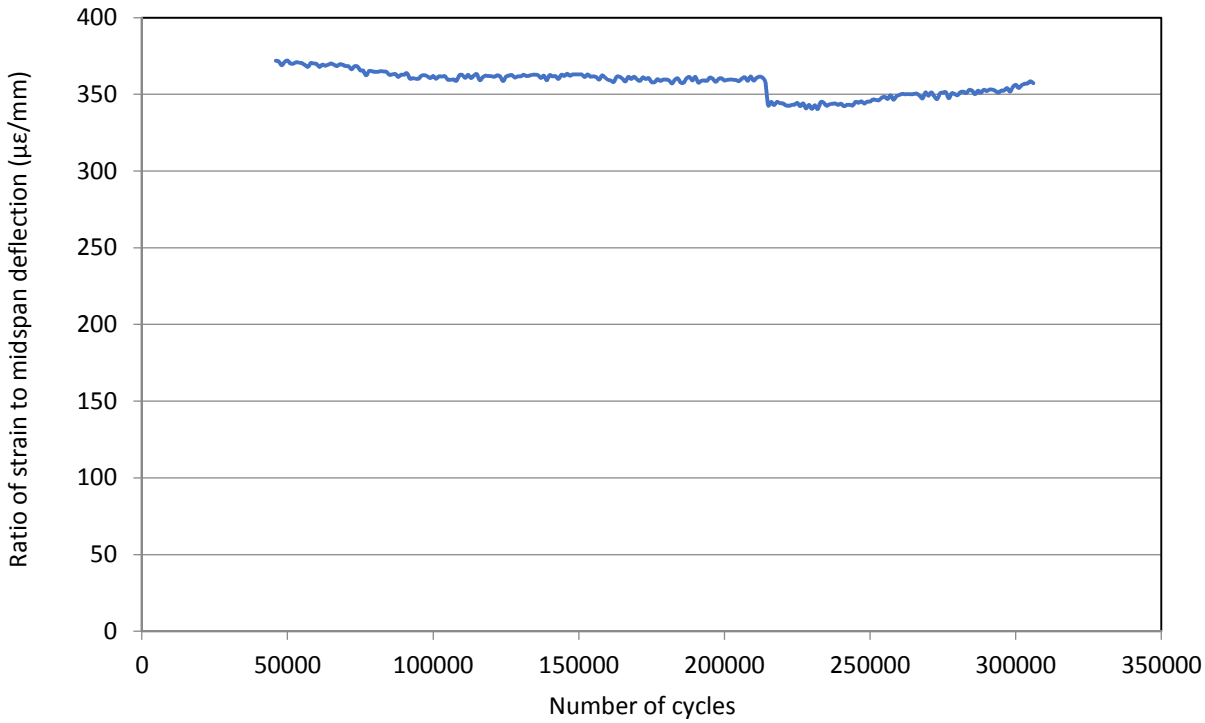

Figure 7.9 - Typical strain-deflection response for beam-hinge tests

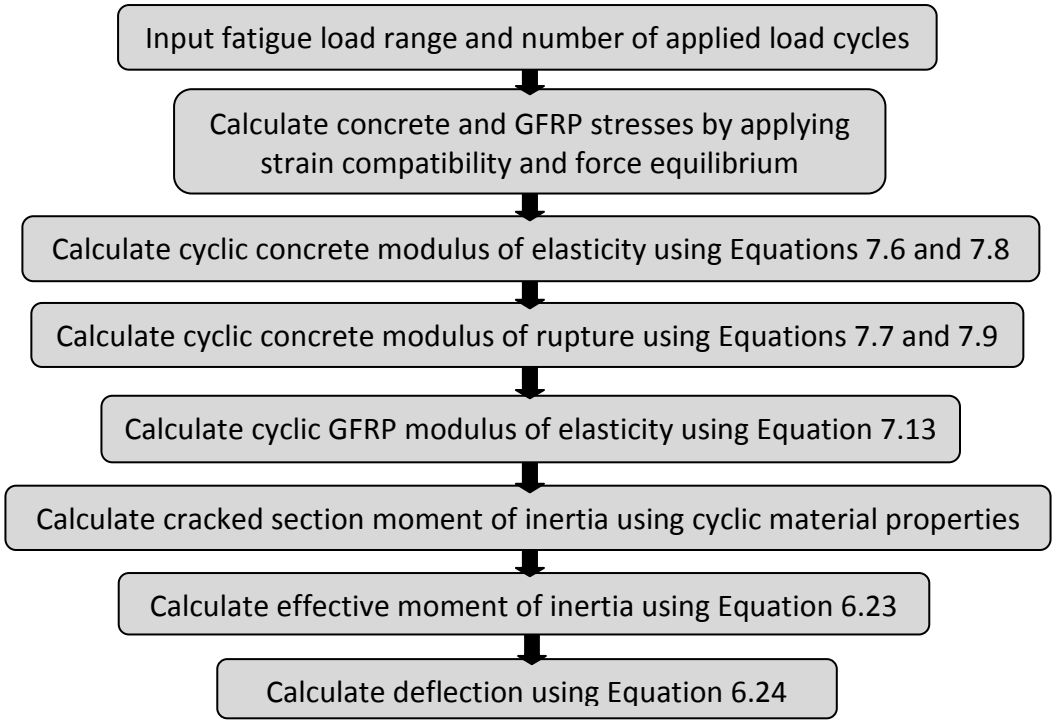

Figure 7.10 - Flow chart for cyclic deflection calculations

The deflections were calculated using the ACI 440 effective moment of inertia equation (see Chapter 6) using the cyclic material properties of the concrete and GFRP reinforcing bars. The actual measured concrete compressive strength values obtained from cylinder tests were used in the calculation of the cyclic modulus of elasticity of the concrete. For the calculation of the cyclic creep in the concrete, a frequency of 1 Hz was assumed for all cases; the error introduced from this assumption is small. For specimens which reached runout and were retested at a higher load range, the initial elastic modulus values of the concrete and FRP were taken as the fatigue modulus values after the initial 1 million cycles for the deflection estimations of the subsequent load cycles.

The predicted responses are compared with measured deflections for the Phase III slabs in Figures 7.11 to 7.14. In general, the predicted deflections were in good agreement with the measured deflections, particularly after the behaviour stabilized after about 1000 cycles, and tended to be slightly conservative.

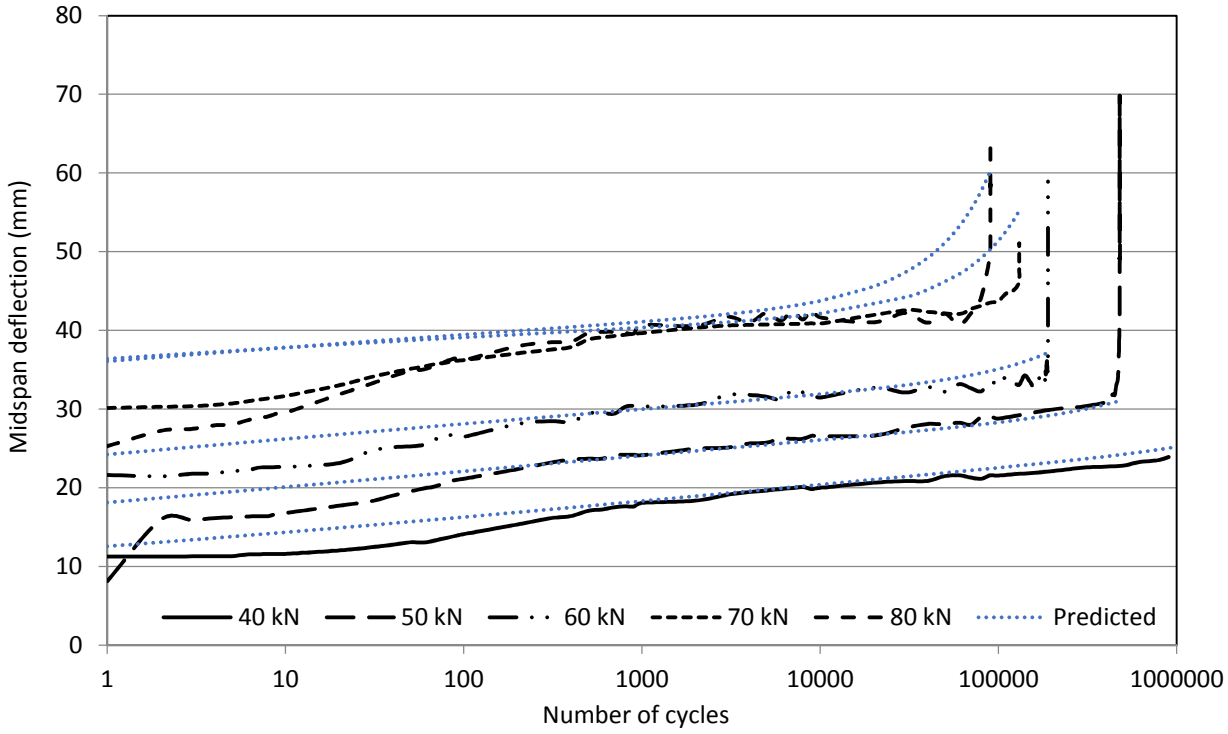

Figure 7.11 - Cyclic deflections predicted using Brondsted model (series G1S)

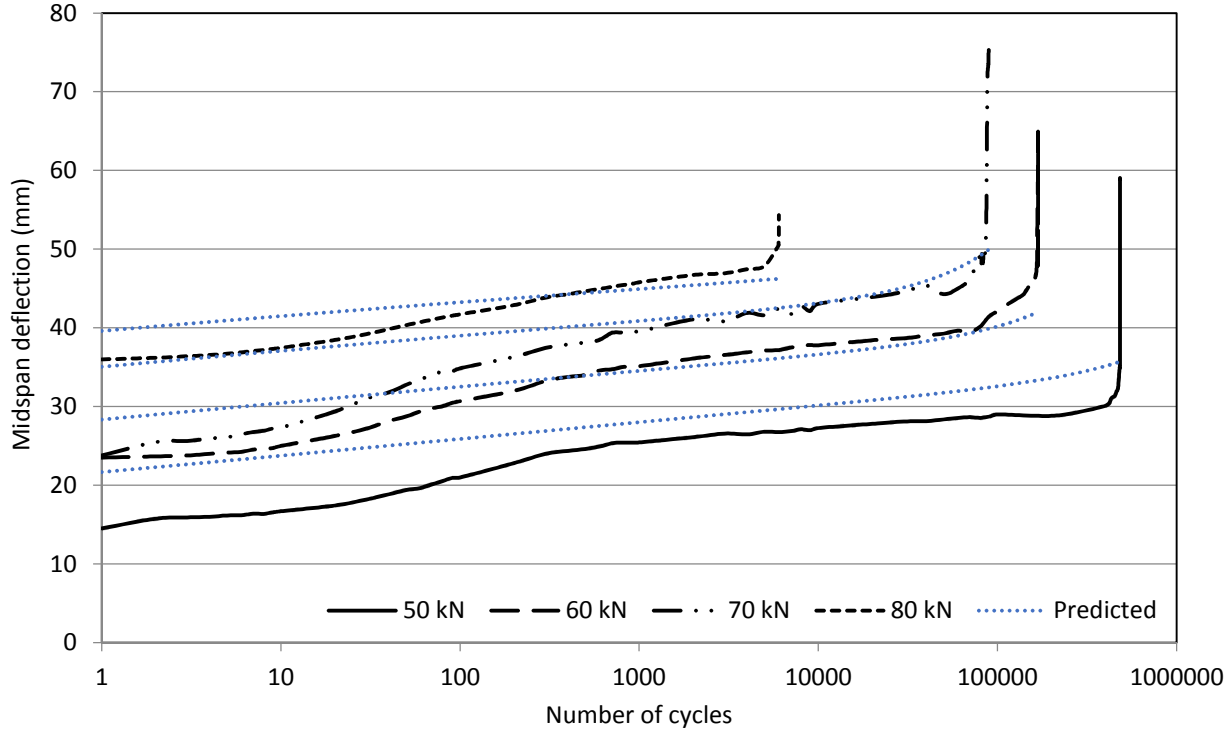

Figure 7.12 - Cyclic deflections for series G1

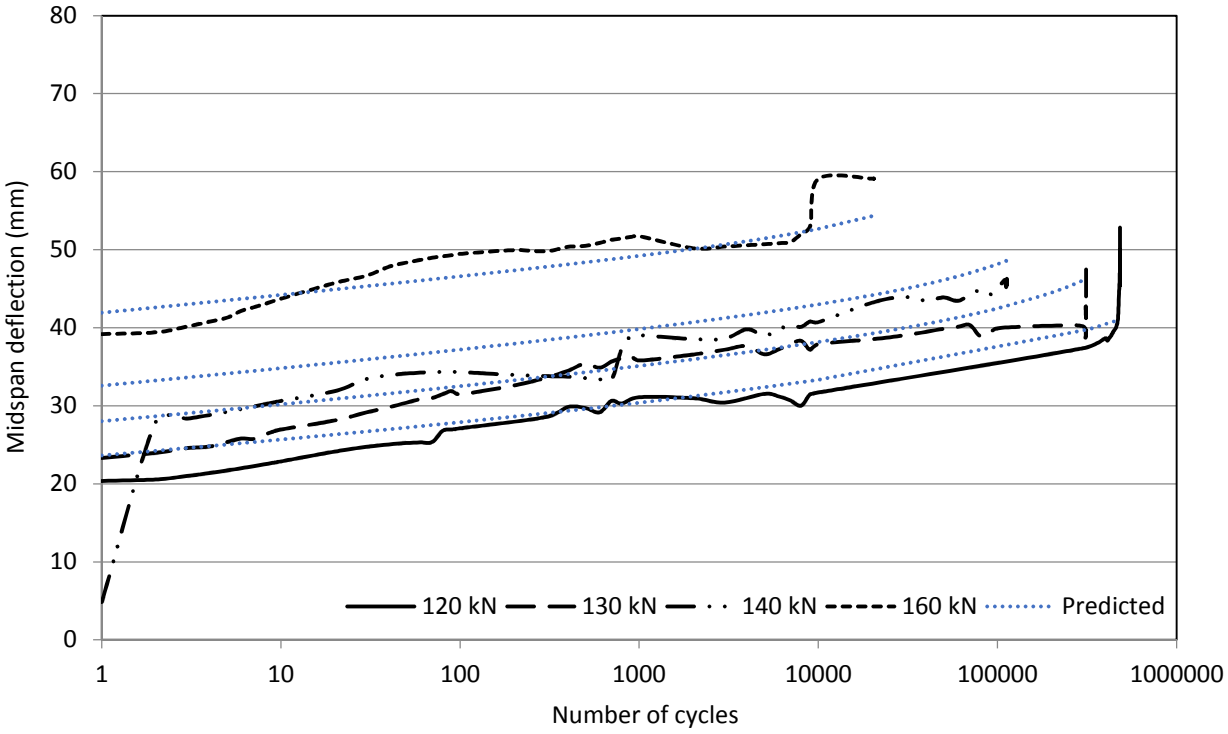

Figure 7.13 - Cyclic deflections for series PT2S

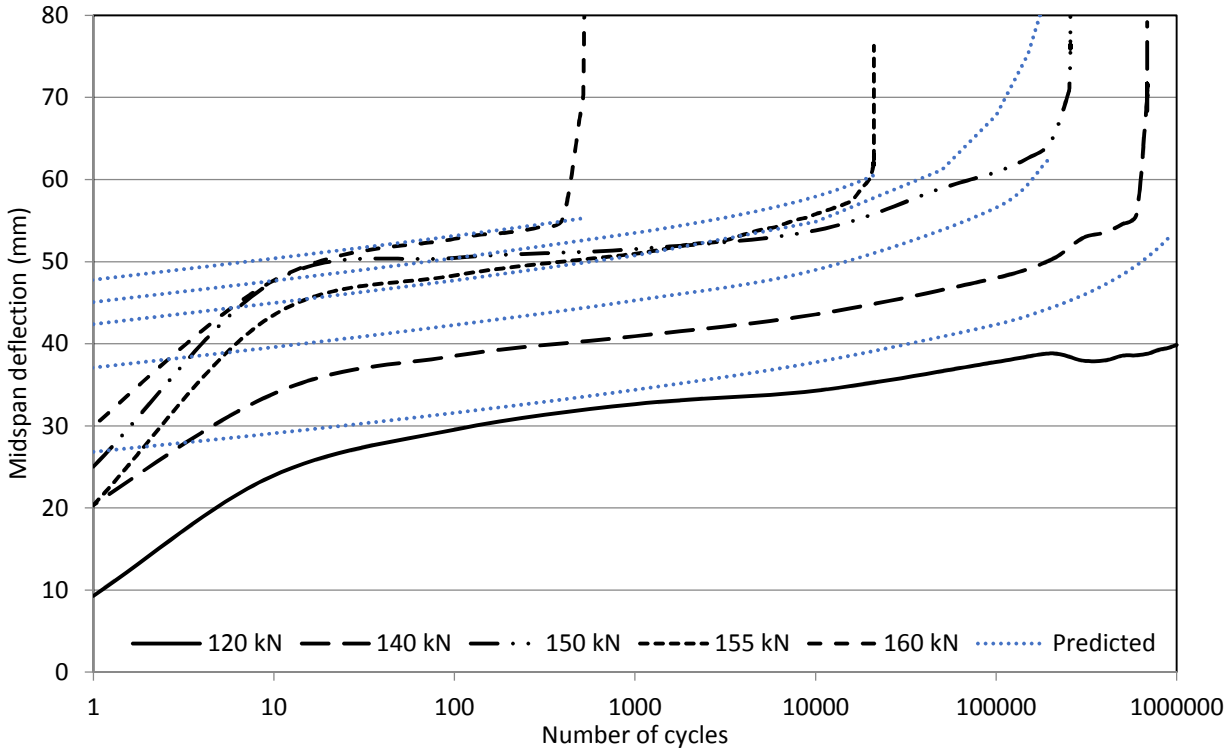

Figure 7.14 - Cyclic deflections for series PT2

7.4 Crack Width Predictions

The proposed methodology for calculating the cyclic crack widths is similar to that used for predicting deflections. In Chapter 6, a crack width model was proposed which accounted for both the stress in the GFRP bar at a crack location and the contribution of the concrete between cracks. In order to account for the effects of cyclic loading, the proposed model is modified here to account for the change in stiffness of the GFRP bars as well as the reduction in tensile strength of the concrete, as given by Equations 7.14 to 7.16 for both non-prestressed and prestressed slabs:

Eq. 7.14 $$w_N = 2\frac{f_{frp,N}}{E_{frp,N}}\frac{h_{2,N}}{h_{1,N}}k_b\sqrt{d_c^2 + (\frac{s}{2})^2}$$

Eq. 7.15 $$f_{frp,N} = f_{frp} - \frac{0.4\sqrt{f'_c}(2bd_c - A_{frp})}{2A_{frp}}(1 - \frac{logN}{10.594})$$

Eq. 7.16 $$f_{frp,N} = f_{frp} - f_{gfrp,dc} - \frac{(1-\alpha_c)0.3\sqrt{f'_c}(2bd_c - A_{frp} - A_{ducts})}{2A_{frp}}(1 - \frac{logN}{10.594})$$

Where, w_N is the cyclic crack width, $f_{frp,N}$ is the average stress in the GFRP reinforcement, $E_{frp,N}$ is the fatigue modulus of the GFRP reinforcement calculated using Equation 7.13, $h_{2,N}/h_{1,N}$ is the ratio of the distance between the neutral axis and the extreme tension face of the member and the distance between the neutral axis and the reinforcement, k_b is the bond coefficient, d_c is the concrete cover, s is the spacing of the reinforcement, f_{frp} is the stress in the GFRP reinforcement at the crack, $f_{gfrp,dc}$ is the stress in the GFRP reinforcing bars at the decompression moment, f'_c is the concrete compressive strength, b is the width of the member, A_{ducts} is the area of the post-

tensioning ducts, A_{frp} is the area of GFRP reinforcement, α_c is the axial stiffness ratio of the CFRP tendons to the combined reinforcement stiffness and N is the number of applied load cycles.

For comparison with the experimental results, which were measured at the level of the reinforcement, the ratio $h_{2,N}/h_{1,N}$ was taken as unity. The proposed model was used to predict the crack widths for the Phase III slabs as shown in Figures 7.15 to 7.18. The predicted values tended to be slightly conservative in all cases, with the exception of the slab tested at a load range of 160 kN in series PT2S (Figure 7.17); since the measured crack widths for this slab were significantly greater than the slab tested at the same load range in series PT2, it is suspected that this unconservative result is an anomaly.

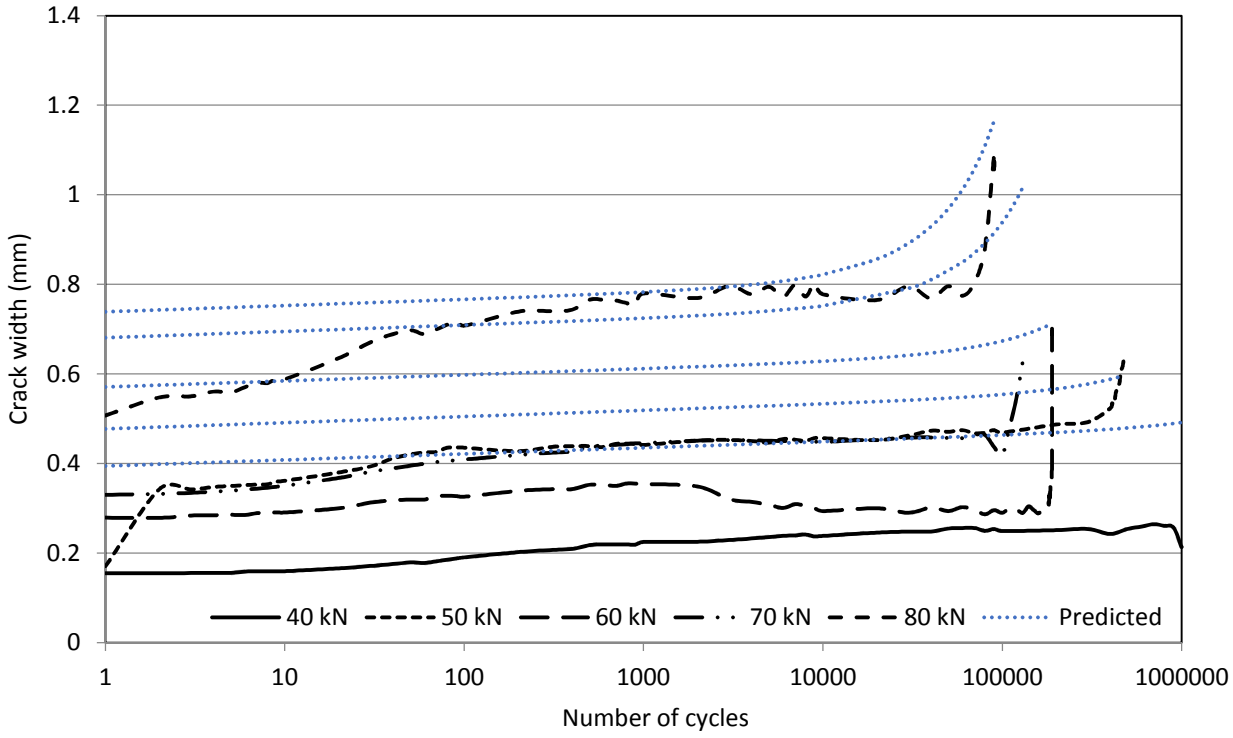

Figure 7.15 - Cyclic crack widths for series G1S

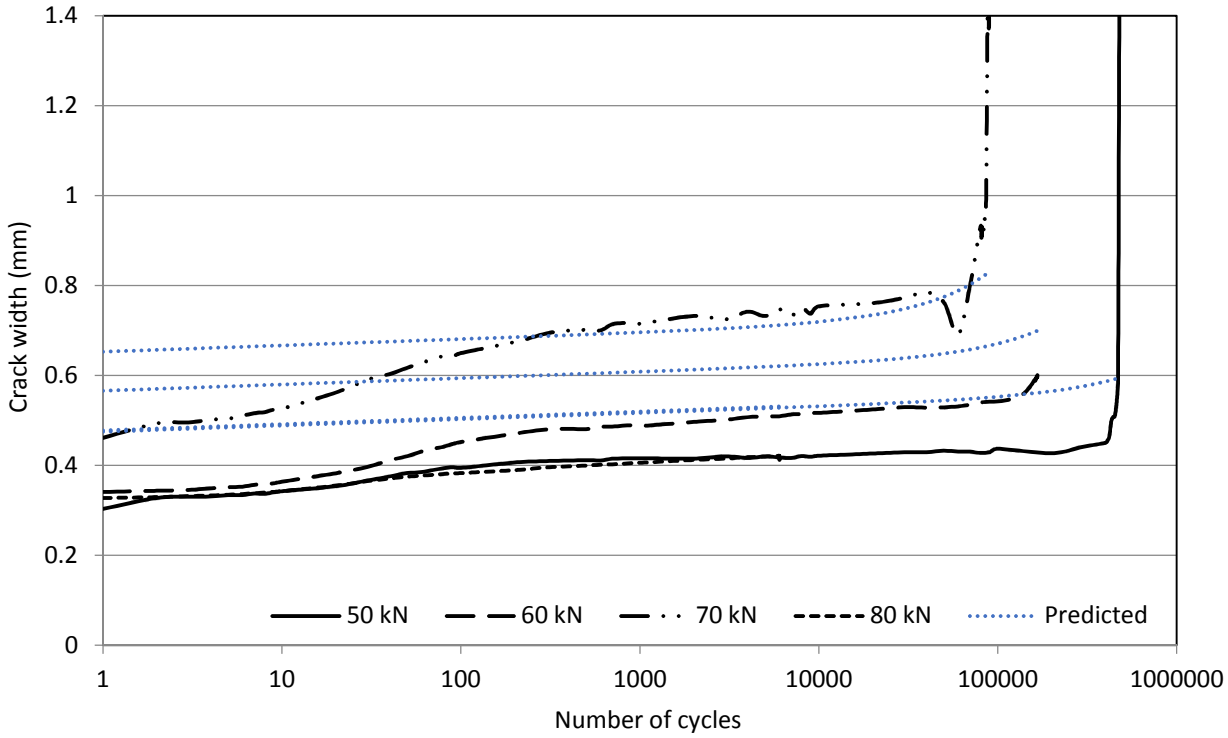

Figure 7.16 - Cyclic crack widths for series G1

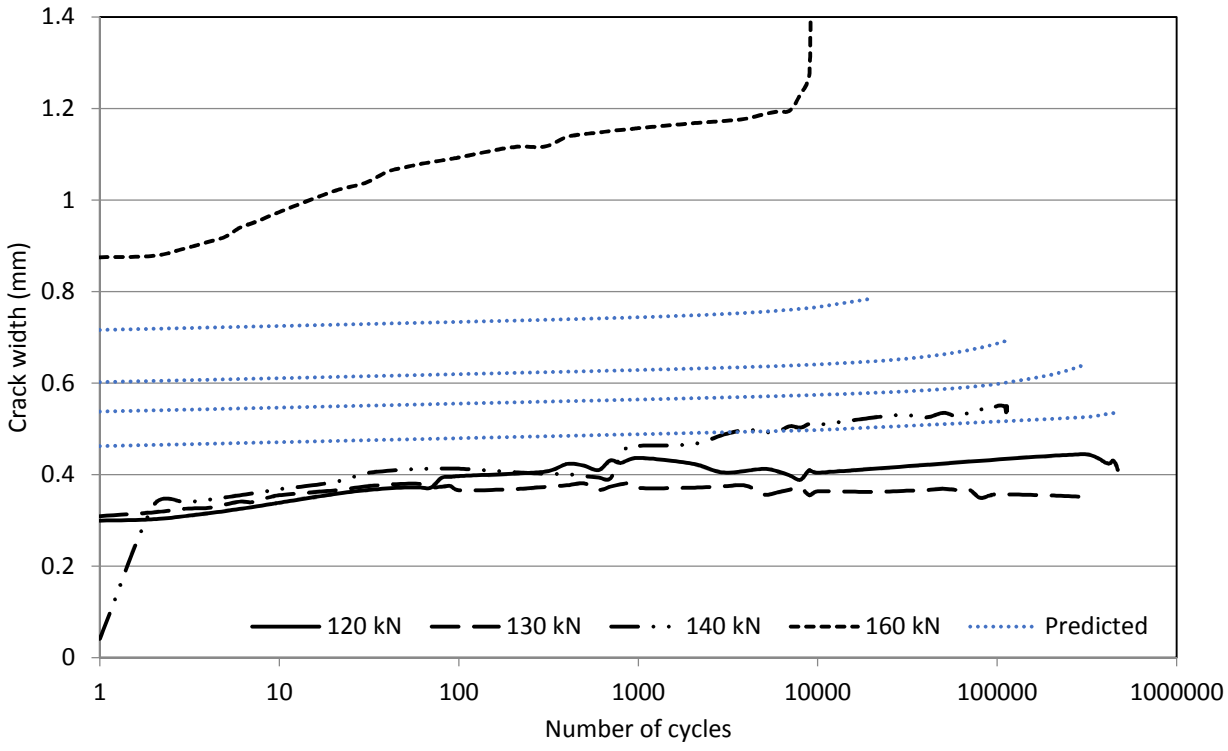

Figure 7.17 - Cyclic crack widths for series PT2S

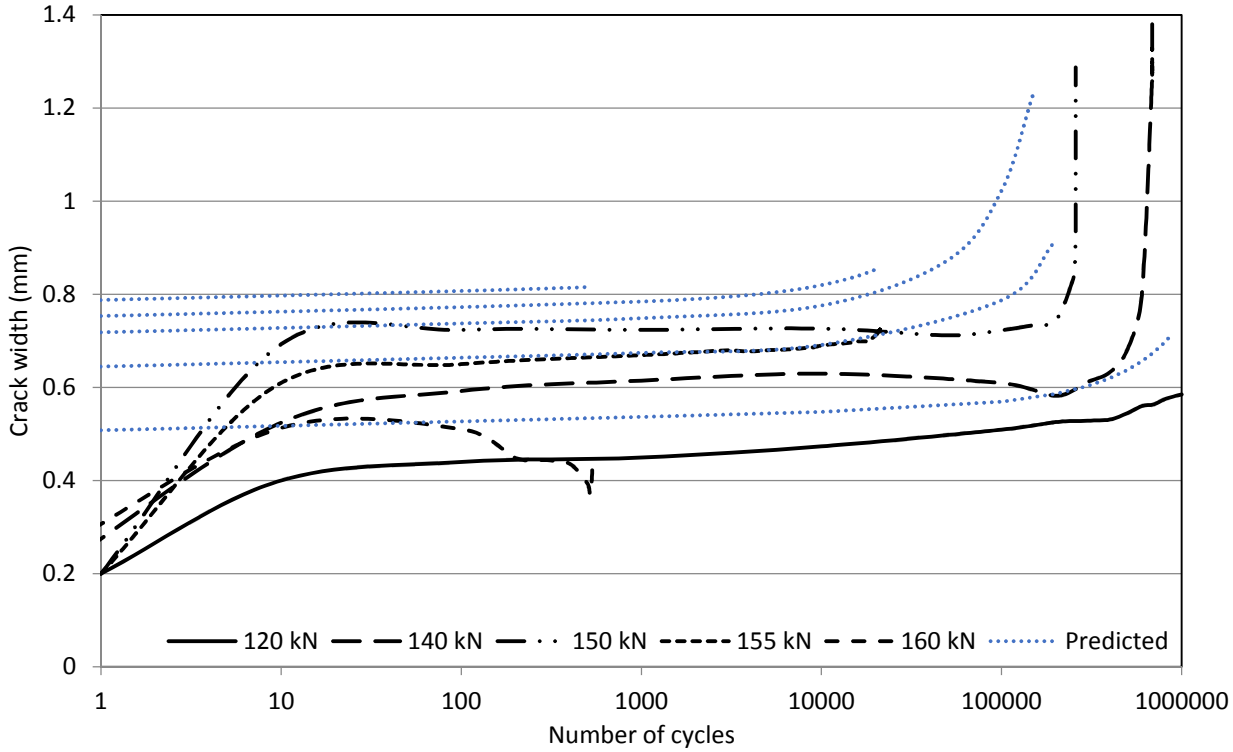

Figure 7.18 - Cyclic crack widths for series PT2

7.5 Shear Fatigue

Teng et al. (2000) proposed a method of predicting the fatigue shear strength of deep beams with steel reinforcement in which the fatigue strength of the concrete in tension was represented by Equation 7.17:

Eq. 7.17 $$\sigma_r = (1 - \beta log N)(1 - \frac{f_{min}}{f_t})f_t$$

Where, σ_r is the fatigue stress range in the concrete, β is a material constant, f_{min} is the minimum stress level, f_t is the strength of the concrete in tension and N is the number of applied load cycles.

Teng et al. (2000) also suggested that the ratio f_{min}/f_t could be taken to be the same as V_{min}/V_u, where V_{min} and V_u are the minimum applied shear force and ultimate shear capacity,

respectively. Various values of β have been proposed by different researchers; as previously noted, Balaguru & Shah (1982) used a value of β equal to 1/10.954 (see Equation 7.7).

To predict the concrete contribution to shear strength under fatigue loading, it is proposed to modify the modified compression field theory (MCFT) equation to account for the reduction in concrete tensile strength using Equation 7.18. The resulting shear equation is then given by Equation 7.19:

Eq. 7.18 $$f_{cr,N} = f_{cr}(1 - \frac{logN}{10.954})(1 - \frac{V_{min}}{V_u})$$

Eq. 7.19 $$V_{c,N} = 2.5\beta_N f_{cr,N} b_v d_{long}$$

Where, $V_{c,N}$ is the concrete contribution to shear capacity under fatigue loading, β_N is a coefficient calculated using the shear and moment values at the critical section corresponding to the maximum applied fatigue load, $f_{cr,N}$ is the fatigue tensile strength of the concrete and all other terms are as noted previously.

As with the MCFT equation for statically loaded members, Equation 7.19 can be solved using an iterative procedure to either solve for the fatigue shear strength for a given fatigue life, or conversely the fatigue life can be estimated by setting $V_{c,N}$ equal to the maximum applied shear force. Equation 7.19 was used to predict the shear strengths of the slabs in series G1 and PT2, which did not contain any shear reinforcement, as shown in Figures 7.19 and 7.20. Fatigue shear capacities were calculated using the actual measured concrete strength obtained from cylinder tests.

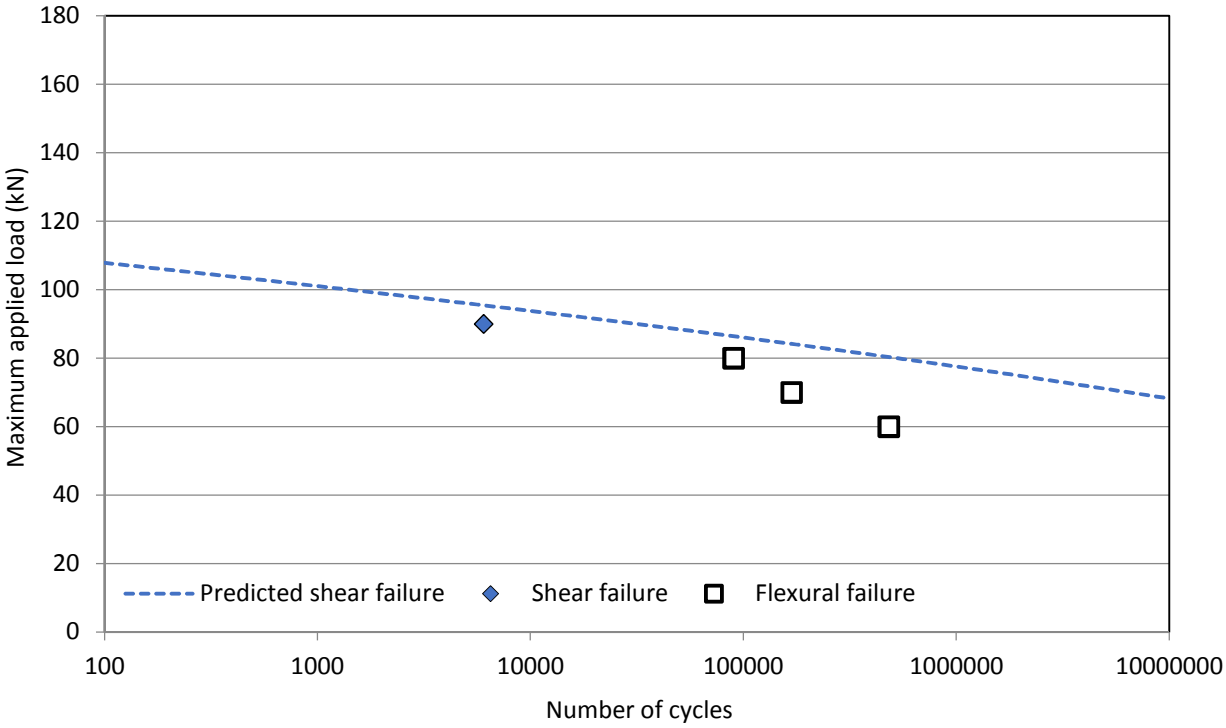

Figure 7.19 - Predicted shear fatigue lives for series G1

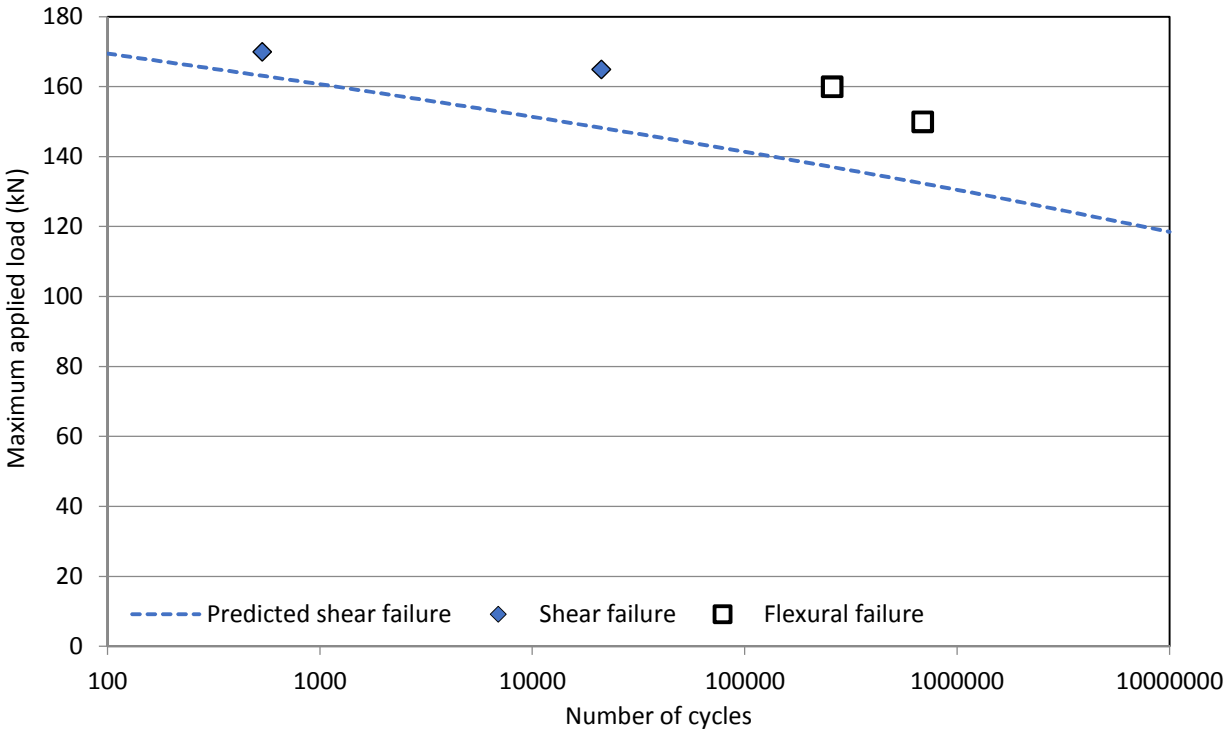

Figure 7.20 - Predicted shear fatigue lives for series PT2

Due to the limited number of fatigue shear failures observed in the slabs without shear reinforcement, it is difficult to assess the accuracy of the proposed model. The predicted values for the non-prestressed slabs in series G1 were slightly unconservative compared with the actual fatigue life of the one slab which failed in shear. Conversely, for the prestressed series PT2, the predicted values were conservative in all cases. Further testing is needed before drawing any major conclusions from the limited data presented here. However, since the S-N curve for shear failures appears to be fairly flat, it is expected that the conservatism of the proposed model increases with increasing fatigue life, such that for high cycle fatigue (which is of primary concern for bridges) the model will be consistently conservative. This observation should be validated with additional tests.

The proposed model was also used to predict the fatigue lives of the slabs with shear reinforcement tested in Phase II, as shown in Figures 7.21 to 7.25. The contribution of the shear reinforcement was calculated in the same way as for the static shear capacity, except that the angle θ was calculated using the applied shear and moment values caused by the predicted fatigue load at the critical section.

The proposed method gave conservative estimates of shear fatigue life for all of the slabs except for those in series GU-12 and CU-10. The unconservative estimates in this case are a result of the breakdown in bond between the unanchored stirrups and the concrete. For slabs with anchored shear reinforcement, the proposed method gave conservative estimates of shear fatigue life in all cases.

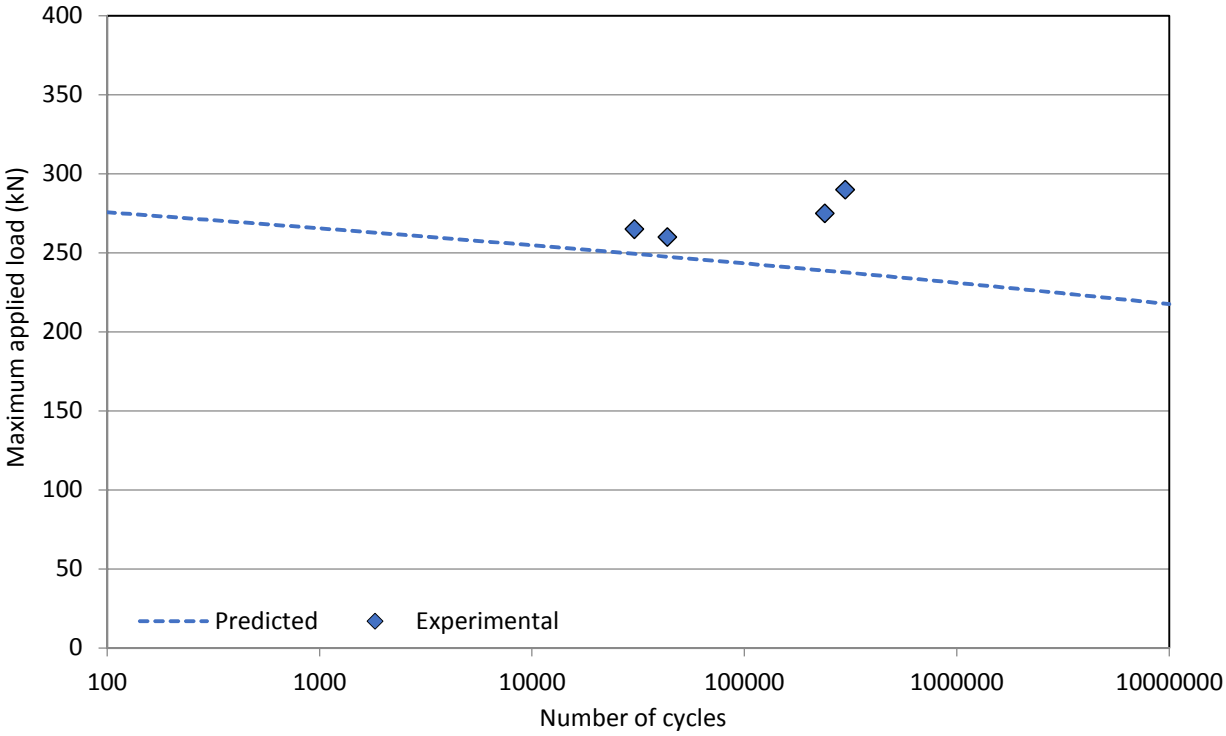

Figure 7.21 - Predicted shear fatigue lives for series GU-10

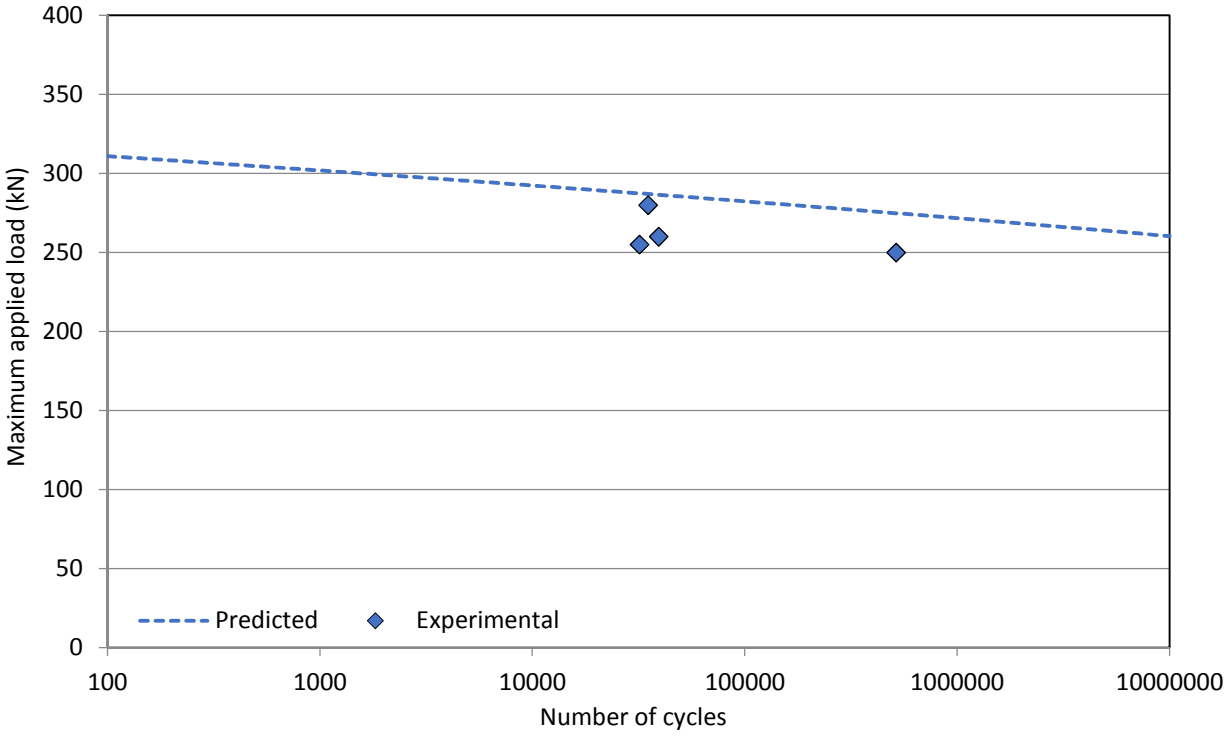

Figure 7.22 – Predicted shear fatigue lives for series GU-12

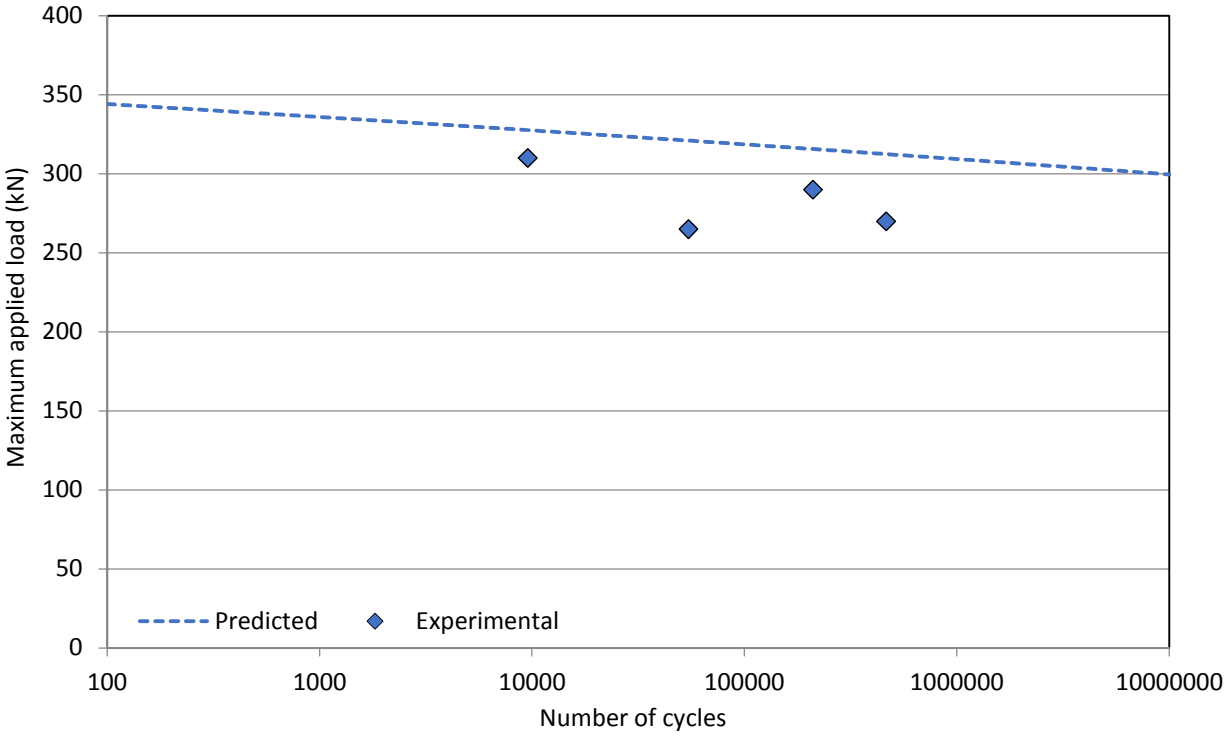

Figure 7.23 - Predicted shear fatigue lives for series CU-10

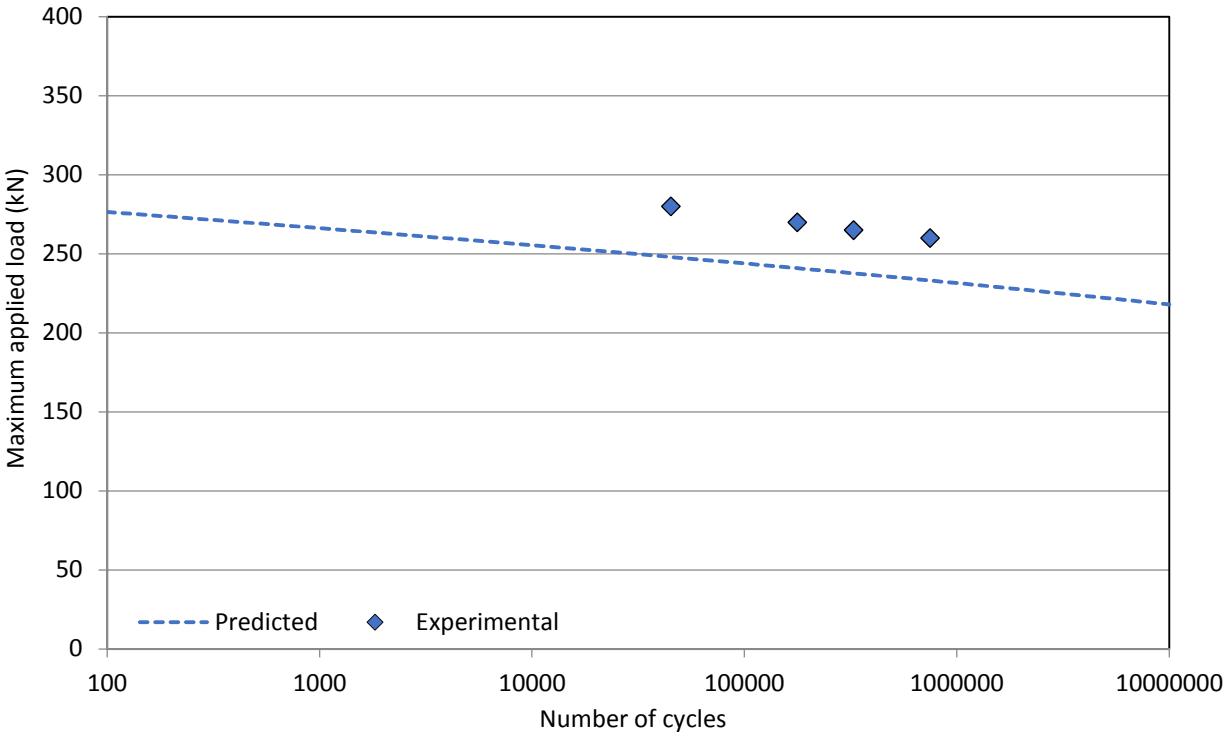

Figure 7.24 - Predicted shear fatigue lives for series GC-10

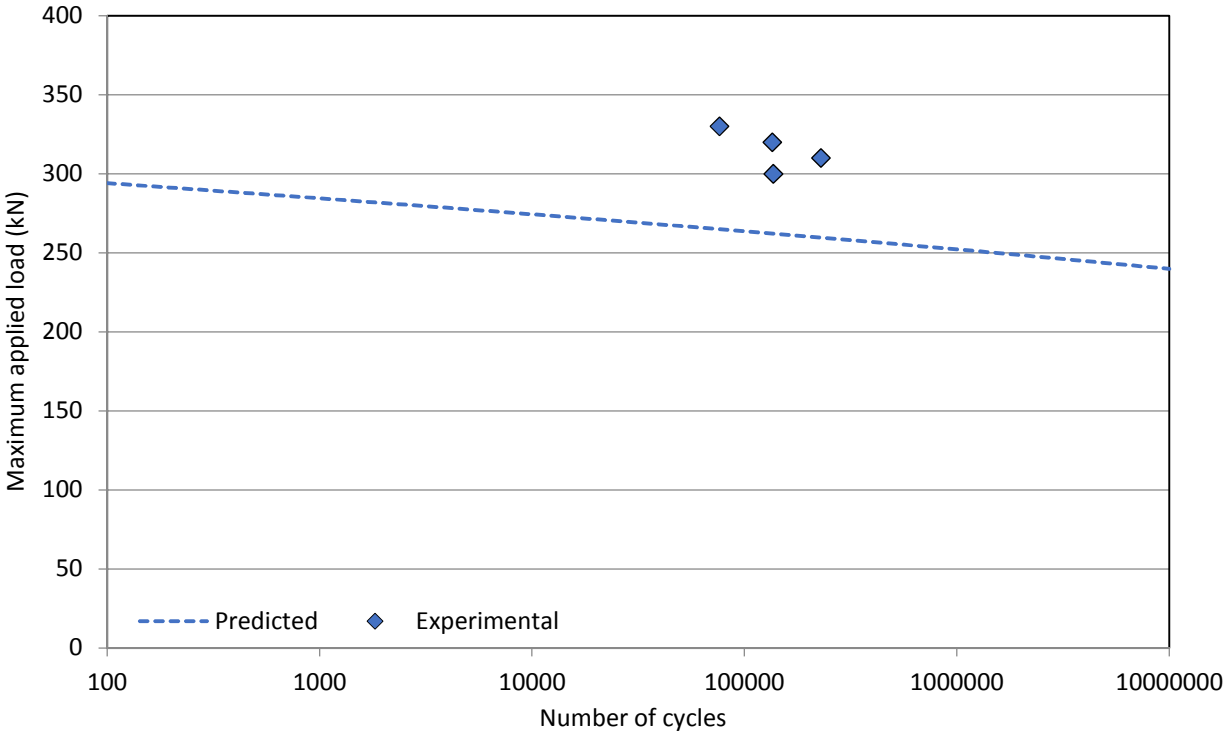

Figure 7.25 - Predicted shear fatigue lives for series GS-12

7.6 Flexural Fatigue

All of the observed flexural fatigue failures were governed by GFRP rupture. Thus, the fatigue lives of GFRP-RC flexural members in general can be predicted by calibrating various fatigue models proposed in the literature using the experimental results obtained in this study governed by the tensile fatigue of the GFRP reinforcement. Two approaches for predicting the fatigue lives of FRP composites are considered here, namely probabilistic methods and residual stiffness models, which are discussed in the following sections.

7.6.1 Probabilistic Methods

Vassilopoulos & Keller (2011) outlined several common methods for the statistical analysis of fatigue data. The simplest method involves assuming a normal distribution of the fatigue life at

each stress level for a given reliability level and coefficient of variation (COV). Assuming a COV of 15% and a confidence interval of 95%, the characteristic values representing the expected scatter band of the cycles to failure for a given stress level are given by Equation 7.20:

Eq. 7.20 $$R_{ki} = \overline{N}_i[1 \pm 0.15(1.645 + \frac{1.645}{\sqrt{m_i}})]$$

Where, R_{ki} is the characteristic value of the fatigue life, $\overline{N}_i$ is the average value of the fatigue life and m_i is the number of specimens at a given stress level.

Alternatively, if a normal distribution is assumed, a linear regression analysis of the logarithm of the fatigue data using a least squares approach—with the fatigue life as the dependent variable—can be easily performed to describe the scatter in the data, with 95% of the data expected to lie within two standard deviations of the mean.

On the other hand, ASTM E739 (2011) suggests the use of a log-normal distribution of the fatigue data and outlines a procedure for calculating the maximum likelihood estimators for the fatigue distribution. The confidence band for the fatigue data can be calculated using Equation 7.21; it should be noted however that the ASTM method is not suitable for extrapolation outside of the region of experimental data.

Eq. 7.21 $$logN = \hat{A} + \hat{B}log\sigma \pm \sqrt{2F_p}\hat{\mu}[\frac{1}{n} + \frac{(log\sigma - \overline{log\sigma})^2}{\sum(log\sigma_i - \overline{log\sigma})^2}]^{1/2}$$

Where, N is the normalized fatigue life, σ is the applied stress range, $\overline{log\sigma}$ is the average of the logarithm of the applied stress ranges, $\hat{A}$ and $\hat{B}$ are the maximum likelihood estimators for the lognormal distribution, F_p is a coefficient depending on the reliability level, $\hat{\mu}$ is the variance and n is the total number of specimens.

Each of the previously described statistical models was calibrated using the combined fatigue data from the various types of tests conducted. The predicted scatter bands are plotted with the experimental fatigue data in Figure 7.26. While each of these simple statistical approaches reasonably described most of the data, both the simplified method and the least squares approach excluded more than 5% of the data. Although it is simple to use, these results suggest that the normal distribution is not well-suited for the given data set. The ASTM method described the full data set well, although it produced an unreasonably wide scatter band at high or low load levels.

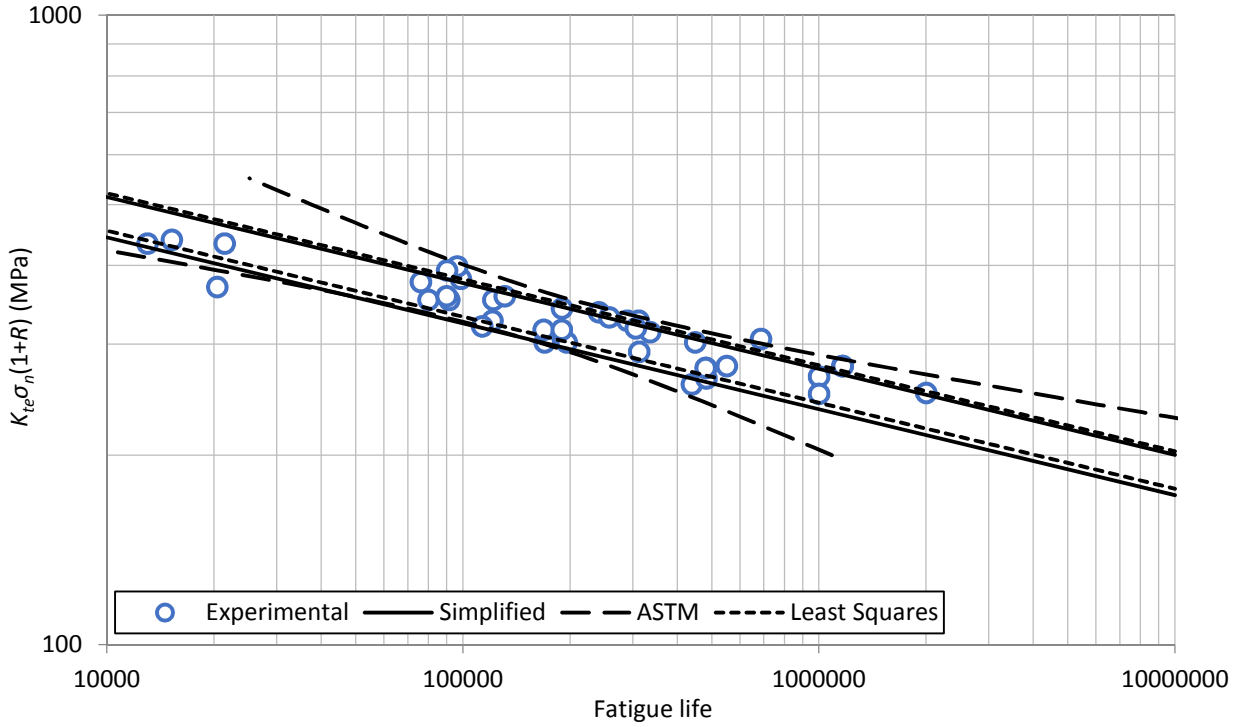

Figure 7.26 – Fatigue life distributions

Sendeckyj (1979) proposed a method for combining the results from static tests and fatigue tests by applying the strength-life equal rank (SLER) assumption, meaning that the strongest specimen will also have the longest fatigue life. The fatigue data is first converted to an

equivalent static strength (Equation 7.22) and is then fitted with a two parameter Weibull distribution (Equation 7.23) to simultaneously determine the fatigue model parameters and the distribution parameters describing the static strength. The model parameters are obtained through an iterative process which is assumed to be optimized by maximizing the Weibull shape parameter. The S-N curve for any reliability level can then be plotted using Equations 7.24 and 7.25:

Eq. 7.22 $$\sigma_e = \sigma_r[1 - C + CN]^S$$

Eq. 7.23 $$P(\sigma_e) = \exp\left[-\left(\frac{\sigma_e}{\beta}\right)^{\alpha}\right]$$

Eq. 7.24 $$\sigma_r = \beta\{[-ln(P(N))]^{1/\alpha}\}[(N - A)C]^{-S}$$

Eq. 7.25 $$A = -\frac{1-C}{C}$$

Where, σ_e is the equivalent static strength of the bar, σ_r is the applied stress range, *C*, *S* and *A* are model parameters and all other terms are as previously noted.

The Sendeckyj model was calibrated using the experimental fatigue data set with the maximum likelihood estimation method. Through an iterative process, the parameters *S*, *C*, α and β were found to be 0.13, 0.0041, 19.4 and 777.4, respectively. The resulting S-N scatter band is plotted for a 5% and 95% reliability in Figure 7.27. The model was capable of giving good predictions for both the static and fatigue data; the Sendeckyj model flattens out at high stress levels, which is in agreement with reported experimental results of fatigue tests on various composite materials. This is indicative of a change in the fatigue failure mechanisms in the low cycle range compared to the high cycle range. Low cycle fatigue of FRP is dominated by the tensile strength

distribution of individual fibres and is characterized by a relatively flat S-N relationship. Failure occurs when a sufficient number of fibre breaks occur in proximity to one another to cause the remaining fibres in the cross-section to rupture. On the other hand, high cycle fatigue results in the breakdown of the matrix between fibres which limits the load-sharing ability of the composite and longitudinal matrix cracks propagate between different cross-sections with ruptured fibres. This results in an increased rate of fatigue damage accumulation and resultantly, the S-N curve is steeper compared with the low cycle region.

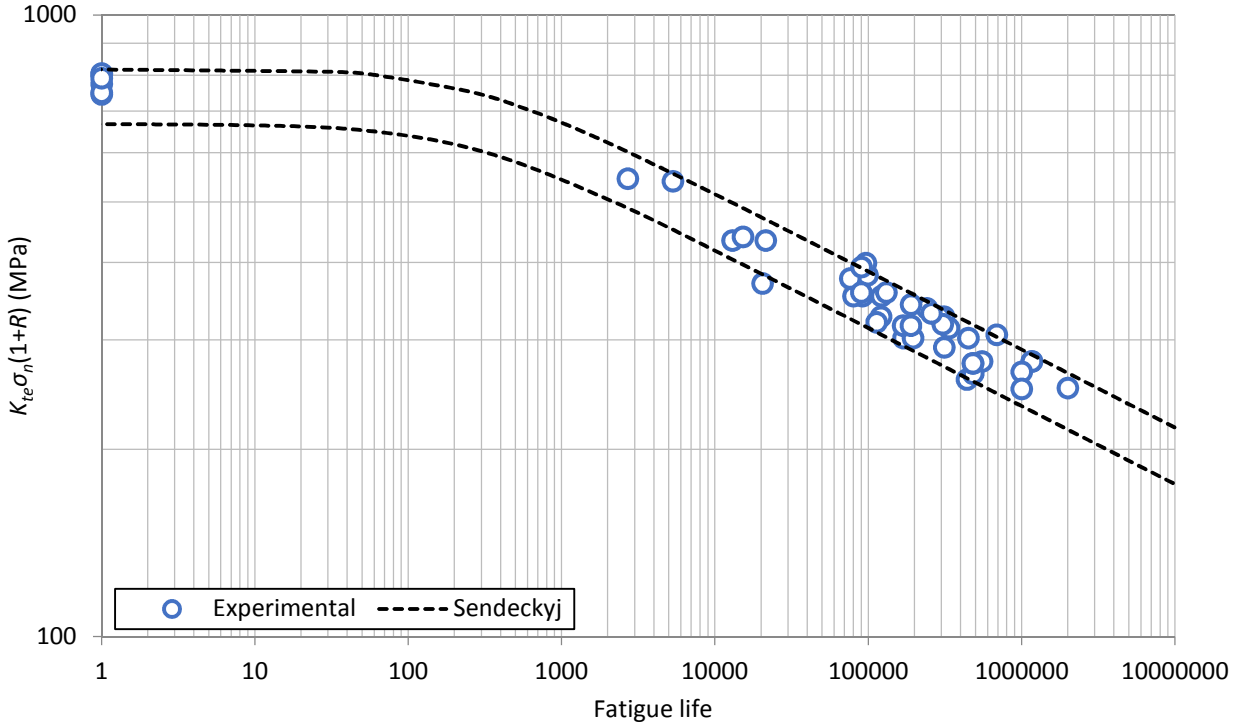

Figure 7.27 - Fatigue life predictions using Sendeckyj wear-out model

7.6.2 Residual Stiffness Models

One of the main advantages of residual stiffness models compared with other approaches is the ability to assess the remaining life of a structure through non-destructive testing (such as using sensors to monitor the change in stiffness of a bridge). As previously noted, the Brondsted et

al. (1997) residual stiffness model gave good estimates of the change in GFRP stiffness for deflection and crack width predictions. This model was used to generate a family of curves for different values of stiffness degradation as shown in Figure 7.28. A stiffness degradation of 10% gives reasonable predictions of the observed fatigue lives of the GFRP-RC slabs; for a more conservative estimate a stiffness degradation of 3% or 5% can be used. It should be noted that this represents the stiffness change following stabilization and does not include the rapid change in stiffness in the initial load cycles.

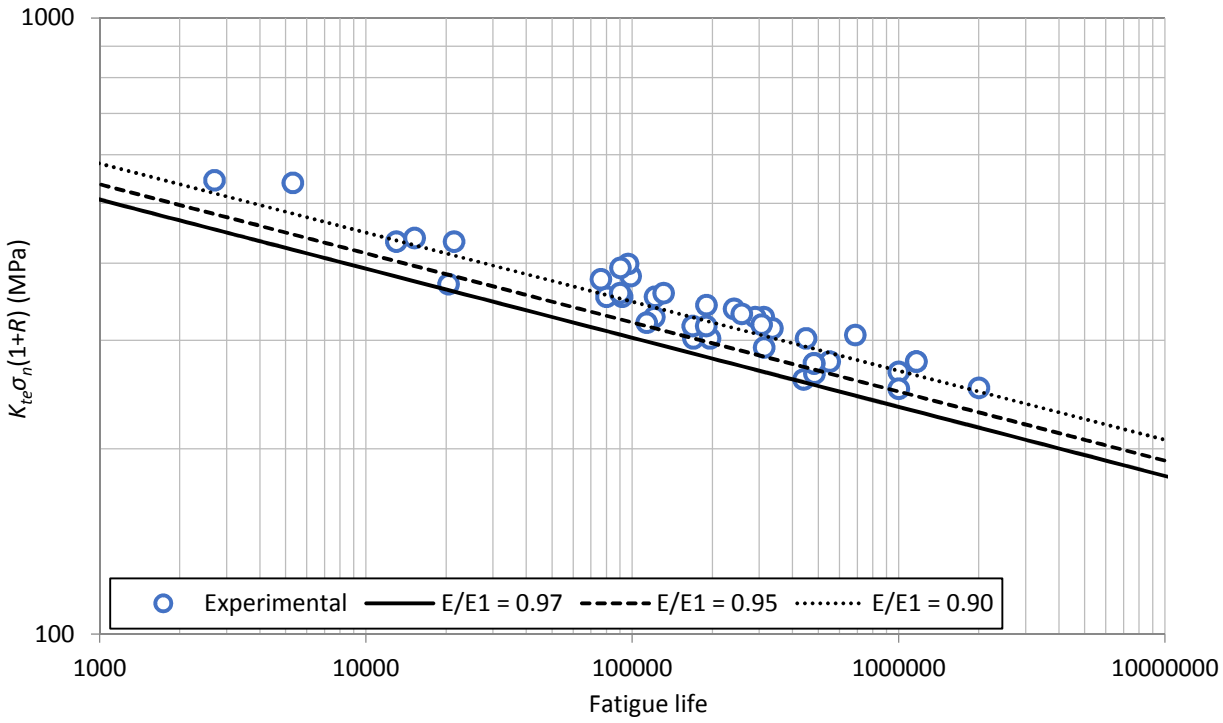

Figure 7.28 - Fatigue curves using Brondsted residual stiffness model

7.7 Summary

A number of fatigue models have been evaluated to predict the effect of repeated loads on the serviceability and ultimate performance of GFRP-RC members with and without prestressed CFRP tendons. The models were calibrated using experimental results obtained from the

ancillary tests described in Chapter 5. An effective fatigue stress factor, K_{te}, which is a function of the applied stress, was used to quantify the detrimental effect of the concrete on the fatigue life of GFRP bars. The mean stress was found to have a noticeable effect on the fatigue life of the GFRP bars and may have influenced the fretting behaviour caused by abrasion between the reinforcing bar and the concrete. Modifying the applied stress range by a factor of (1 + R) was found to be an effective way of accounting for the mean stress effect.

The Brondsted et al. (1997) residual stiffness model used within the framework proposed by Balaguru & Shah (1982) for calculating the deflections and crack widths of reinforced concrete members subjected to fatigue loading yielded reasonable predictions of the observed behaviour throughout the fatigue lives of the prestressed and non-prestressed slabs at various load levels.

The shear fatigue lives of the prestressed slabs without shear reinforcement were conservatively predicted using a modified form of the MCFT equation accounting for the reduction in concrete tensile strength due to fatigue loading. Although the predicted life of the non-prestressed slab which failed in shear was slightly over-predicted, there were an insufficient number of data points to draw any major conclusions. For slabs with shear reinforcement, the proposed model also gave conservative predictions in all cases when the shear reinforcement was adequately anchored.

Various statistical models were used to describe the flexural fatigue behaviour of the GFRP-RC slabs. Both the simplified method (Vassilopoulos & Keller 2011) and a linear regression using a least squares approach assumed the data to be normally distributed, and were found to

reasonably describe most of the fatigue data although the actual scatter was greater than predicted. The ASTM method (2011), which assumes a log-normal distribution, described the data well but produced unreasonably wide scatter bands at both high and low stress ranges. On the other hand, the Sendeckyj (1982) model was able to predict both the fatigue and static data with good accuracy by making use of the SLER assumption and fitting the data with a Weibull distribution; however the process is slightly more involved than the other statistical methods.

Applying a residual stiffness approach to predict the flexural fatigue lives of the GFRP-RC slabs using the Brondsted et al. (1997) model correlated well with the experimental data; the level of conservatism depends on the value of stiffness degradation selected, with a stiffness degradation value of 3% giving conservative estimates for the entire data set.

Chapter 8 - Evaluation Based on the CHBDC and AASHTO LRFD Bridge Design Codes

8.1 Overview

Bridges in North America are typically designed according to the provisions of either the Canadian Highway Bridge Design Code (CHBDC) (CSA 2010a) or the American Association of State Highway and Transportation Officials (AASHTO) Load and Resistance Factor Design (LRFD) Bridge Design Specifications (AASHTO 2010). The CHBDC allows for the use of FRP materials as both prestressed and primary reinforcement, while the design of GFRP-RC bridge decks including slab-type bridges is addressed in the AASHTO LRFD Bridge Design Guide Specifications for GFRP-Reinforced Concrete Bridge Decks and Traffic Railings (AASHTO 2009). Simple design checks of an FRP-RC slab bridge using both major North American bridge design codes are presented in this chapter.

The examples presented in this chapter constitute design checks for a given bridge structure using design loads and procedures from the CHBDC and AASHTO LRFD design codes, and do not represent the full design process in which the slab depth and required reinforcement are determined for a given span and loading conditions. For more detailed design guidelines for FRP-RC members, the reader is referred to the design manuals produced by ISIS Canada (2007, 2008).

8.2 Bridge Details

For this design example, a simply supported short span slab bridge having a clear span of 4.5 m and two lanes of traffic with a total deck width of 8 m is considered, as shown in Figure 8.1. The bridge is not skewed and has a deck thickness of 300 mm. The added weight as well as the increase in stiffness provided by barrier walls is neglected. However the bridge is assumed to have a thin wearing surface applied with a uniform weight of 1.2 kPa.

ISIS Canada (2007) recommends a maximum span-to-depth ratio of approximately 15 for simply-supported FRP-RC slabs in order to minimize deflections and crack widths (in comparison, steel-RC slabs have a maximum recommended span-to-depth ratio of 20). While greater span-to-depth ratios can be achieved with the introduction of additional prestressing tendons, the benefits of having a shallower section must be weighed against the increase in prestressing costs. If the recommended span-to-depth ratio is unreasonable for a given bridge crossing, the designer has the option of adding CFRP prestressing tendons as necessary to reduce deflections and crack widths at service.

It should be noted that while the span length used in these examples is not unreasonable for short-span bridge crossings, typical span lengths for slab bridges can range from approximately 3 to 16 m (Azizinamini et al. 1994). For longer spans, the factored moments will increase; the designer has the option of increasing the slab depth, increasing the reinforcement ratio of the non-prestressed reinforcement and/or increasing the amount of prestressing provided. In such cases, the proposed design methodology is as follows: first, determine the slab depth based on the ISIS design recommendation of $L/15$ (provided that the chosen depth is permitted by

clearance and weight considerations); second, design the amount of non-prestressed reinforcement to meet the required moment resistance; and third, provide the required amount of prestressed CFRP tendons to meet deflection, crack width and fatigue limits. If possible, the slab should be designed in such a way that if the CFRP tendons were to rupture, the load would be redistributed to the GFRP bars without collapsing, resulting in a progressive failure mode with ample warning prior to failure.

For these examples, the concrete is assumed to have a specified design strength of 60 MPa, and is reinforced in the primary longitudinal direction by #5 GFRP bars at a spacing of 100 mm on centre with a clear cover of 30 mm. The GFRP bars have a modulus of elasticity and ultimate strength of 48.2 GPa and 683 MPa, respectively. The bridge is also longitudinally post-tensioned using #4 CFRP tendons spaced at 300 mm on centre at an effective depth of 225 mm. The CFRP tendons have a modulus of elasticity and ultimate strength of 144 GPa and 1765 MPa, respectively. The tendons are prestressed to an effective stress of $0.55f_{frpu}$. Long term prestressing losses are neglected. #4 GFRP reinforcing bars are used as temperature and shrinkage reinforcement forming a top mat with a spacing of 150 mm in each orthogonal direction, as well as running transversely along the bottom of the slab at 150 mm on centre. Double-headed GFRP anchor bars as shear reinforcement are placed throughout the slab at a spacing of 150 mm in the longitudinal direction and 600 mm in the transverse direction (Figure 8.2).

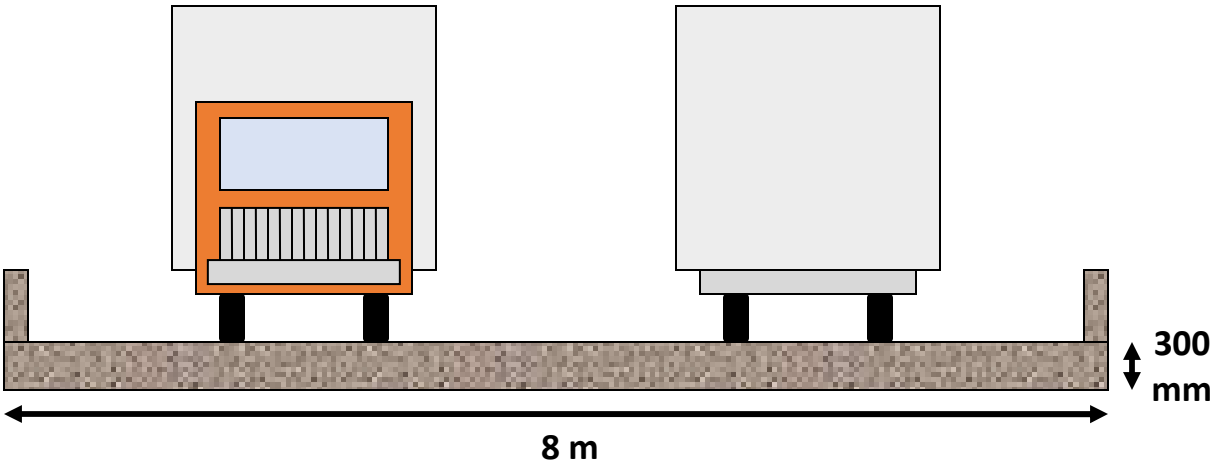

Cross-section

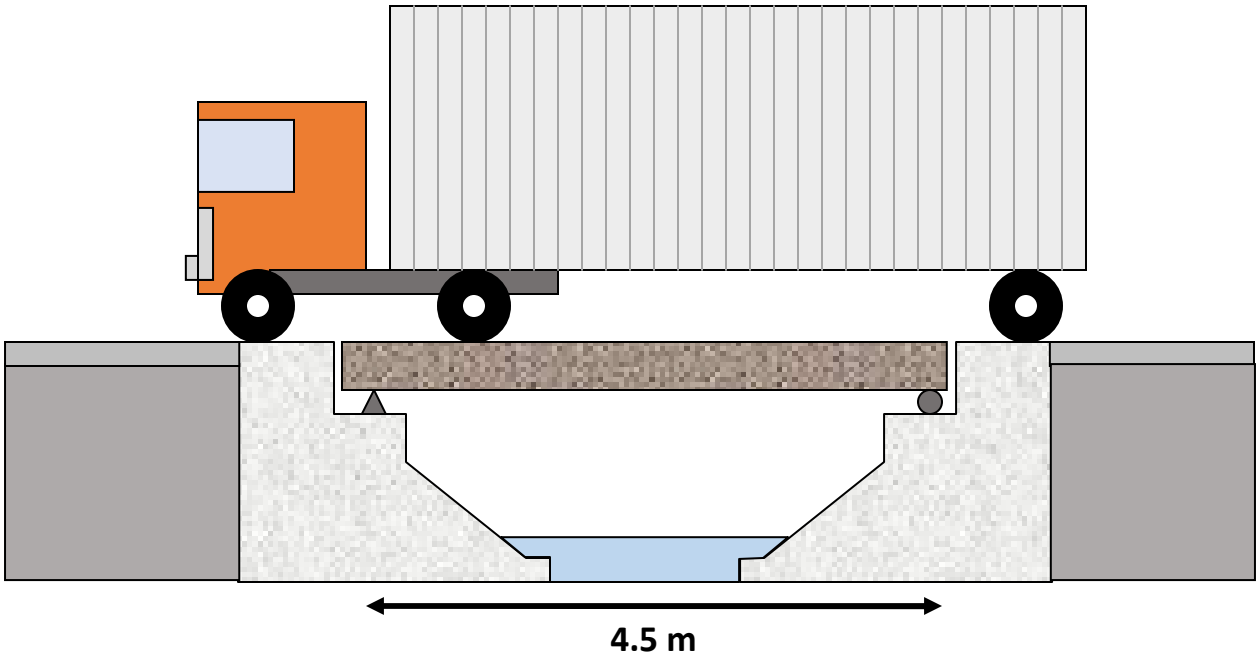

Elevation

Figure 8.1 - Bridge geometry

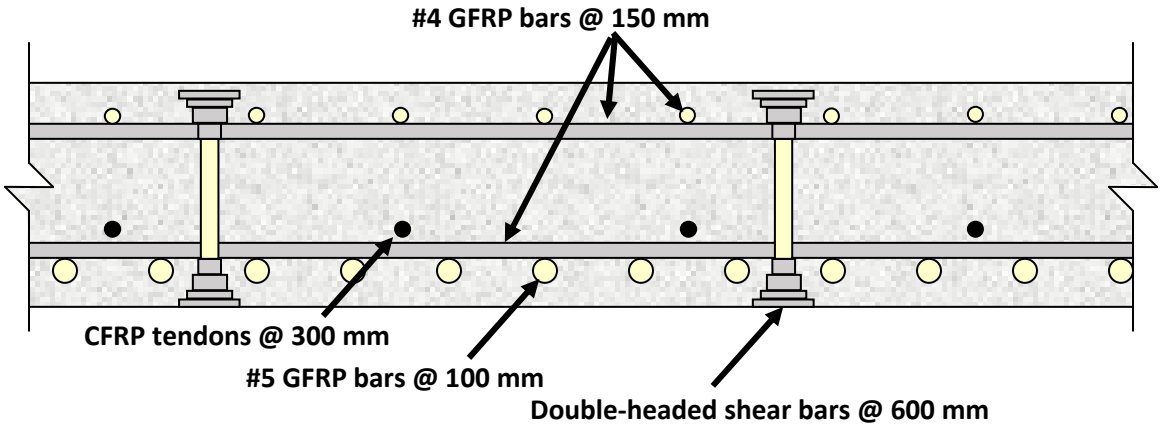

Transverse cross-section

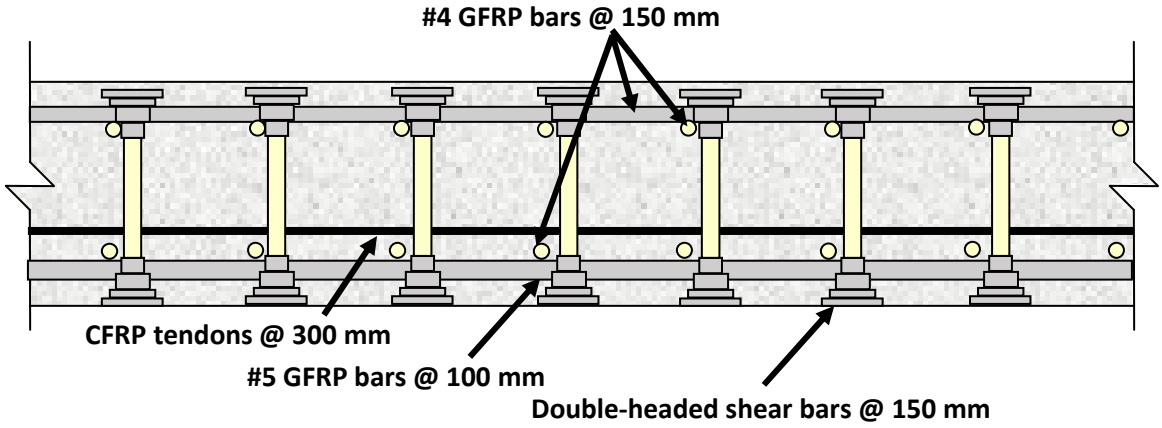

Longitudinal cross-section

Figure 8.2 - Reinforcing details

8.3 Canadian Highway Bridge Design Code

For convenience, applicable equations from the CHBDC are summarized briefly below. The details provided in this section are limited to avoid regurgitation of the code itself which is readily available; the reader is encouraged to refer to Sections 3.8 and 5.7 of the CHBDC (CSA 2010a) and Commentary (CSA 2010b) for additional information. All notations are as defined in previous chapters, and at the beginning of this thesis. It should also be noted that the

allowable concrete stresses at transfer are easily met, although the calculations are not reproduced here.

Design live loads are approximated by a design truck (Figure 8.3) and/or design lane loads. For short span bridges, the design is typically governed by the CL-625 tandem axles, each with a weight of 125 kN at a spacing of 1.2 m. The dynamic effects of the moving wheel loads are accounted for in design by increasing the axle loads by a dynamic load allowance (DLA) factor. In this case the DLA is taken as 0.3.

The CHBDC provisions include simplified methods of analysis for the transverse distribution of loads on bridge decks using the concept of design lanes. The average moment per unit width is multiplied by an amplification factor, F_m, to account for the transverse variation in maximum longitudinal moment intensity as given by Equations 8.1 through 8.3 for slab bridges (referred to as Type A in the CHBDC). A similar approach is used for factored shear forces, given by Equations 8.4 to 8.6:

Eq. 8.1 $$m = F_m m_{avg}$$

Eq. 8.2 $$F_m = \frac{B}{F[1+\frac{\mu C_f}{100}]} \geq 1.05$$

Eq. 8.3 $$m_{avg} = \frac{nM_T R_L}{B_e}$$

Eq. 8.4 $$v = F_v v_{avg}$$

Eq. 8.5 $$F_v = \frac{B}{F} \geq 1.05$$

Eq. 8.8 $$v_{avg} = \frac{nV_T R_L}{B_e}$$

Where, m and m_{avg} are the maximum and average longitudinal moments per metre of width due to live loads, respectively, B and B_e are the overall and effective width of the bridge, respectively, F and C_f are a width dimension characterizing load distribution and corresponding correction factor, respectively, taken from tables in the CHBDC (reproduced in part in Tables 8.1 to 8.4), μ is a lane width modification factor, n is the number of design lanes on the bridge, M_T and V_T are the maximum longitudinal moment and shear for one lane width of truck or lane loading including dynamic load allowance, respectively, R_L is a modification factor for multi-lane loading, v and v_{avg} are the maximum and average longitudinal vertical shear per metre of width due to live loads, respectively, and F_v is an amplification factor to account for the transverse variation in maximum longitudinal vertical shear intensity.

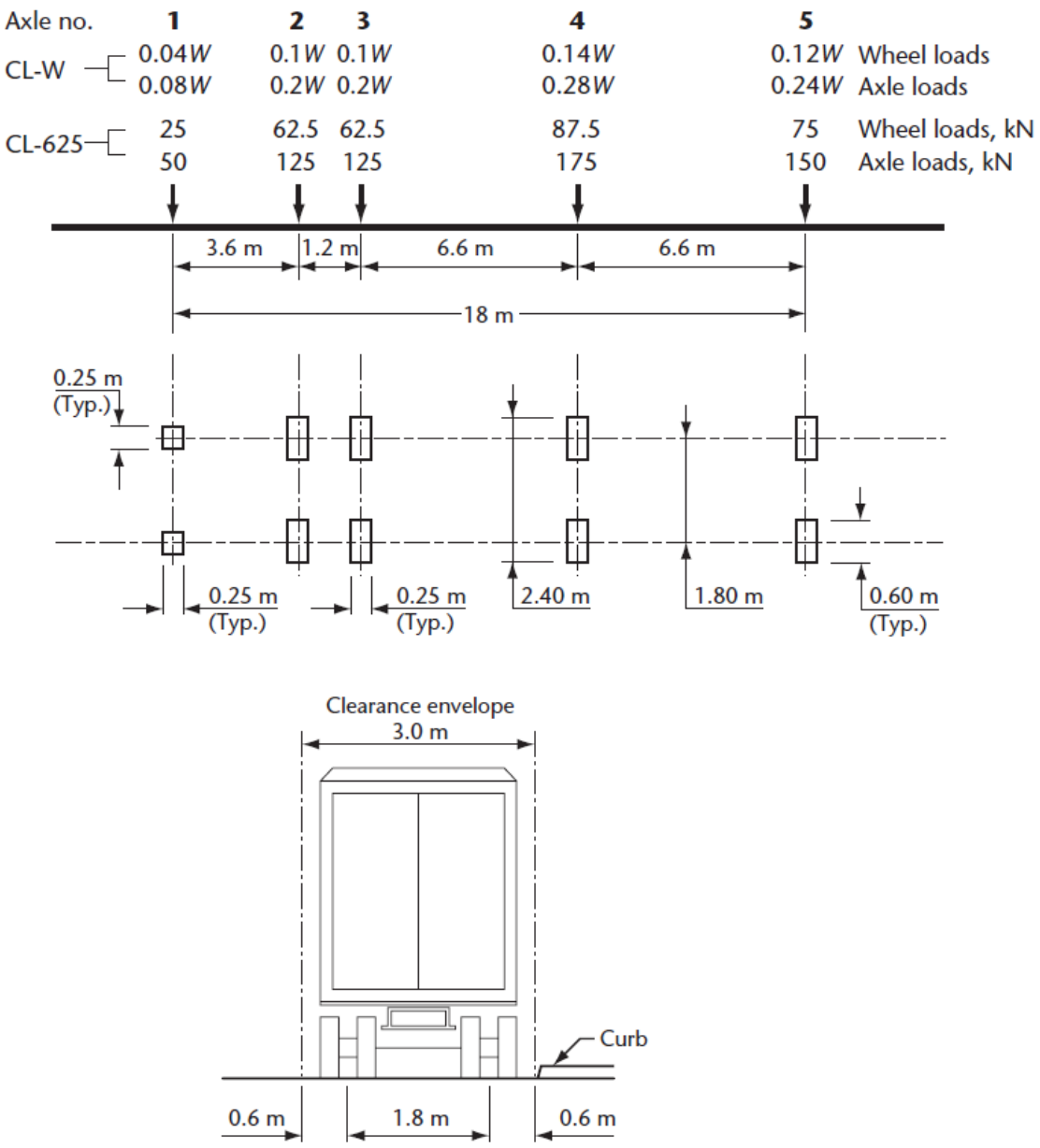

Figure 8.3 - CL-625 CHBDC design truck (CSA 2010a)

Table 8.1 - *F* and C_f factors for longitudinal bending moments (CSA 2010a)

Bridge type (see Clause 5.1)	Highway class (see Clause 1.4.2.2) and applicability	No. of design lanes	Portion	*F*, m: 3 m < *L* ≤ 10 m	*F*, m: *L* > 10 m	C_f, %
Type A or B	A or B (for design of new bridges or evaluation)	1	External	3.80 + 0.04*L*	4.20	16 – (36/*L*)
			Internal	4.00 + 0.04*L*	4.40	16 – (36/*L*)
		2	External	7.10	7.10	20 – (40/*L*)
			Internal	7.60 – (6/*L*)	7.30 – (3/*L*)	20 – (40/*L*)
		3	External	7.90 + 0.21*L*	10.80 – (8/*L*)	16 – (30/*L*)
			Internal	5.90 + 0.41*L*	10.80 – (8/*L*)	16 – (30/*L*)
		4	External	10.10 + 0.26*L*	14.30 – (16/*L*)	16 – (30/*L*)
			Internal	7.40 + 0.56*L*	14.00 – (10/*L*)	16 – (30/*L*)

Table 8.2 - *F* and C_f factors for longitudinal bending moments for fatigue limit state (CSA 2010a)

Bridge type (see Clause 5.1)	No. of design lanes	Portion	*F*, m: 3 m < *L* ≤ 10 m	*F*, m: *L* > 10 m	C_f, %
Type A or B	1	External	3.80 + 0.04*L*	4.20	16 – (36/*L*)
		Internal	4.00 + 0.04*L*	4.40	16 – (36/*L*)
	2	External	3.60 + 0.26*L*	7.00 – (8/*L*)	16 – (36/*L*)
		Internal	3.20 + 0.30*L*	6.40 – (2/*L*)	16 – (36/*L*)
	3	External	3.30 + 0.30*L*	9.60 – (33/*L*)	16 – (36/*L*)
		Internal	3.00 + 0.40*L*	9.80 – (29/*L*)	12 – (36/*L*)
	4 or more	External	3.40 + 0.30*L*	12.00 – (56/*L*)	10 – (30/*L*)
		Internal	3.00 + 0.44*L*	12.00 – (46/*L*)	10 – (30/*L*)

Table 8.3 - *F* factor for shear (CSA 2010a)

Bridge type (see Clause 5.1)	Number of design lanes and class of highway: 1	2	3		4
	All classes	All classes	Class A or B	Class C or D	Class A or B
Type A	2.60 + 0.45$\sqrt{L}$	4.20 + 0.66$\sqrt{L}$	5.60 + 1.05$\sqrt{L}$	5.20 + 0.97$\sqrt{L}$	6.50 + 1.44$\sqrt{L}$

Table 8.4 - *F* factor for shear for fatigue limit state (CSA 2010a)

Bridge type (see Clause 5.1)	Number of design lanes: 1	2	3	4
Type A	2.60 + 0.45$\sqrt{L}$	3.20 + 0.13*L*	3.20 + 0.16*L*	3.60 + 0.14*L*

Placing the tandem axles of the CHBDC CL-625 design truck at the midspan of a 4.5 m span bridge gives a factored live load moment of 455.8 kN·m including the dynamic load allowance per design lane (Equation 8.9). Although maximum live load moments can be obtained by slightly offsetting the tandem axles from the midspan location, the total moment including dead load remains highest and deformations tend to be largest at midspan. Assuming two loaded lanes, each having a width of 4 m, the maximum moment per metre width is 117.8 kN·m/m (Equations 8.10 through 8.15):

Eq. 8.9 $$M_T = 1.7(1 + 0.3)(125)(1.65) = 455.8\ kN \cdot m$$

Eq. 8.10 $$m_{avg} = \frac{2(455.8)(0.9)}{8} = 102.56\ kN \cdot m/m$$

Eq. 8.11 $$\mu = \frac{W_e - 3.3}{0.6} = \frac{4 - 3.3}{0.6} = 1.17 > 1\ \therefore \mu = 1$$

Eq. 8.12 $$F = 7.60 - \frac{6}{L} = 7.60 - \frac{6}{4.5} = 6.27$$

Eq. 8.13 $$C_f = 20 - \frac{40}{L} = 20 - \frac{40}{4.5} = 11.11$$

Eq. 8.14 $$F_m = \frac{8}{6.27(1 + \frac{11.11}{100})} = 1.15 > 1.05\ \therefore OK$$

Eq. 8.15 $$m = 1.15(102.56) = 117.8\ kN \cdot m/m$$

The CHBDC service moment is taken as the unfactored design moment, given by Equations 8.16 and 8.17:

Eq. 8.16 $$M_s = \frac{M_T}{1.7} = \frac{455.8}{1.7} = 268.1\ kN \cdot m$$

Eq. 8.17 $$m_s = \frac{m}{1.7} = \frac{117.8}{1.7} = 69.3\ kN \cdot m/m$$

At the fatigue limit state, only one truck with dynamic load allowance is considered. Following a similar procedure as above with the factors *F* and C_f taken from Table 8.2 gives a moment per metre width of 54.6 kN·m.

The concrete is assumed to be cast-in-place with a unit weight of 24 kN/m^3 and have a wearing surface applying a superimposed dead load of 1.2 kPa. The dead load is assumed to be uniform across the width of the bridge, such that the maximum unfactored and factored dead load moments for a 1 m wide strip are given by Equations 8.18 and 8.19:

Eq. 8.18 $$m_{ds} = \frac{wL^2}{8} = \frac{(24*1*0.3+1.2*1)4.5^2}{8} = 21.3\ kN \cdot m/m$$

Eq. 8.19 $$m_d = \frac{(1.20*24*1*0.3+1.50*1.2*1)4.5^2}{8} = 26.4\ kN \cdot m/m$$

In the case of shear force, maximum effects are obtained when the tandem axles are placed near one of the supports. The shear force due to dead loads near the supports is an additional 15.9 kN per metre width. The maximum factored shear using a similar procedure as above is demonstrated in Equations 8.20 to 8.24:

Eq. 8.20 $$V_T = 1.7(1 + 0.3)\left[125 + 125\left(\frac{3.3}{4.5}\right)\right] = 478.8\ kN$$

Eq. 8.21 $$v_{avg} = \frac{2(478.8)(0.9)}{8} = 107.7\ kN/m$$

Eq. 8.22 $$F = 4.20 + 0.66\sqrt{L} = 4.20 + 0.66\sqrt{4.5} = 5.60$$

Eq. 8.23 $$F_v = \frac{B}{F} = \frac{8}{5.60} = 1.43 > 1.05 \therefore OK$$

Eq. 8.24 $$v = 1.43(107.7) = 153.9\ kN/m$$

The CHBDC design loads are compared with experimental results in Chapter 4. For comparison purposes, the maximum live load moments per metre width of the bridge were multiplied by a factor of 0.6 to give the maximum applied moment and shear in a 600 mm wide slab strip—such as the specimens tested in this study—as shown in Equations 8.25 to 8.27:

Eq. 8.25 $$0.6m = 0.6(117.8) = 70.7\ kN \cdot m$$

Eq. 8.26 $$0.6m_s = 0.6(69.3) = 41.6\ kN \cdot m$$

Eq. 8.27 $$0.6v = 0.6(153.9) = 92.3\ kN$$

The serviceability limits given in the CHBDC include a crack width limit of 0.5 mm in aggressive environments, as well as allowable service stress limits in the GFRP and CFRP of $0.25f_{frpu}$ and $0.65f_{frpu}$, respectively. The expected cracking moment of the slab is given by Equation 8.28:

Eq. 8.28 $$M_{cr} = \frac{f_r I_t}{y_t} + \frac{PI_t}{Ay_t} + Pe$$

$$M_{cr} = \frac{0.6\sqrt{60}(1000)(300^3)}{12(150)} + \frac{0.55(1765)(122.7)\left(\frac{1000}{300}\right)(1000)(300^3)}{12(1000)(300)(150)} + 0.55(1765)(122.7)\left(\frac{1000}{300}\right)(75)$$

$$= 119.3\ kN \cdot m/m$$

Since the total maximum expected service moment is significantly less than the cracking moment, serviceability is not expected to govern the design. Despite this, it is possible that an overload event or fatigue results in the formation of cracks, or that the cracking strength is lower than the predicted strength. For partially prestressed members, the tensile stress in the concrete may exceed the cracking strength; therefore, the expected reinforcement stresses at the service moment for a cracked section are given by solving Equations 8.29 to 8.32:

Eq. 8.29 $$M_s = f_{gfrp}A_{gfrp}\left(d_{gfrp} + \frac{a}{2}\right) + f_{cfrp}A_{cfrp}(d_{cfrp} + \frac{a}{2})$$

Equation 8.29 can be solved using a spreadsheet by setting $M_s = m_s + m_{ds}$ = 69.3 + 21.3 = 90.6 kN·m, and satisfying strain compatibility and equilibrium conditions given by Equations 8.30 to 8.32:

Eq. 8.30 $$\varepsilon_{gfrp} = \varepsilon_c(\frac{d_{gfrp}-c}{c})$$

Eq. 8.31 $$\varepsilon_{cfrp} = \varepsilon_c\left(\frac{d_{cfrp}-c}{c}\right) + \varepsilon_{pe}$$

Eq. 8.32 $$f_{gfrp}A_{gfrp} + f_{cfrp}A_{cfrp} = \alpha\beta f'_c bc$$

Solving, the stress in the GFRP and CFRP bars in a cracked section at the service load are found to be approximately 19 MPa and 1031 MPa, respectively, or 3% and 58% of their respective ultimate capacities, and are thus well below allowable limits. Since the moment at the fatigue limit state is lower than that used for calculating serviceability conditions, by inspection the magnitude of the GFRP stresses due to fatigue loading is not a concern.

The maximum crack width at the bottom face of the slab is given by Equation 8.33:

Eq. 8.33 $$w = 2\frac{f_{frp}}{E_{frp}}\frac{h_2}{h_1}k_b\sqrt{d_c^2 + (\frac{s}{2})^2} = 2\left(\frac{19}{48200}\right)\left(\frac{300-102.4}{262-102.4}\right)(0.8)\sqrt{38^2 + (\frac{100}{2})^2}$$

$$w = 0.05\ mm \ll 0.5\ mm\ \therefore OK$$

Hence, the slab meets both the CHBDC serviceability and fatigue requirements.

The shear resistance of the slab according to the CHBDC is determined according to the modified compression field theory as given by Equations 8.34 to 8.36. For design, the initial values of M_f and V_f can be taken as the factored moment and shear at the critical section near the support. At the critical section for shear, under the given loading case with the tandem axles at the support location, the factored moment is negligible; to be conservative, it is taken here as $V_f d_v$. The stress in the prestressing tendons when the surrounding concrete stress is zero, f_{po}, is taken conservatively as the effective prestress level of $0.55f_{frpu}$.

Eq. 8.34 $$\varepsilon_x = \frac{\frac{M_f}{d_v}+V_f-V_{p,frp}+0.5N_f-A_{frp}f_{po}}{2(E_sA_s+E_{frp}A_{frp})} = \frac{2(169.8x10^3)-\left(\frac{1000}{300}\right)(122.7)(0.55)(1765)}{2[(48200)(198)\left(\frac{1000}{100}\right)+(144000)(122.7)\left(\frac{1000}{300}\right)]}$$

$$\varepsilon_x \cong 0$$

Eq. 8.35 $$\beta = \left(\frac{0.4}{1+1500\varepsilon_x}\right)\left(\frac{1300}{1000+s_{ze}}\right) = 0.4\left(\frac{1300}{1000+300}\right) = 0.4$$

Eq. 8.36 $$V_c = 2.5\beta\phi_c f_{cr} b_v d_{long} = 2.5(0.4)(0.75)\left(0.4\sqrt{60}\right)(1000)(0.9)(262)$$

$$V_c = 547.9\ kN/m \gg V_f = 169.8\ kN/m\ \therefore OK$$

The procedure is repeated in an iterative procedure by changing the value of V_f in Equation 8.34 until $V_c = V_f$. This is easily accomplished using a spreadsheet, giving ε_x = 0.0008, β = 0.18 and V_c = 326.1 kN/m. Based on this result, the shear capacity of the slab bridge is adequate even

without the addition of the double-headed shear bars. Considering instead the case when the tandem axles are applied at the midspan of the member such that the maximum moment and shear are both located beneath one of the axles, M_f and V_f in Equation 8.34 are taken as 144.2 kN·m and 88.9 kN, respectively, and using a similar iterative process, V_c is equal to 149.6 kN/m, which is still much greater than the critical factored shear force at that location. The designer may therefore decide that the added shear reinforcement in the form of shear bars is not necessary, given the large margin of safety. Alternatively, given the conservatism present in both the serviceability and shear resistance, the spacing of the prestressing tendons might be increased to reduce costs.

For shorter spans, shallower sections or lower prestressing levels, the shear capacity of the slab itself may be insufficient. Therefore, the predicted contribution of the shear bars is calculated here to provide guidance for such cases; should the shear bars be used in the design, their contribution to shear resistance can be calculated using Equations 8.37 to 8.39:

Eq. 8.37 $$\sigma_v = 0.004E_{vFRP} = 0.004(62600) = 250.4\ MPa$$

Eq. 8.38 $$\theta = 29 + 7000\varepsilon_x = 34.6°$$

Eq. 8.39 $$V_{frp} = \frac{\phi_{frp}A_v\sigma_v d_{long}cot\theta}{s} = \frac{0.55(198)\left(\frac{1000}{600}\right)(250.4)(0.9)(262)cot34.6°}{150}$$

$$V_{frp} = 103.6\ kN/m$$

The minimum area of shear reinforcement per metre width is given by Equation 8.40:

Eq. 8.40 $$A_{v,min} = 0.06\sqrt{f'_c}\frac{b_w s}{\sigma_v} = 0.06\sqrt{60}\frac{(1000)(150)}{250.4} = 278.4\ mm^2$$

The total area of shear reinforcement per metre width provided in the given design is 330 mm^2 (Figure 8.2), thus meeting code requirements.

For the calculation of ultimate flexural capacity, a quick check shows that failure is expected to initiate by rupture of the prestressed CFRP tendons. Thus, the strain in the CFRP can be set equal to the rupture strain, ε_{cfrpu}, and simultaneously solving Equations 8.41 through 8.44 yields the factored moment resistance per metre width:

Eq. 8.41 $$\varepsilon_{gfrp} = (\varepsilon_{cfrpu} - \varepsilon_{pe})(\frac{d_{gfrp}-c}{d_{cfrp}-c})$$

Eq. 8.42 $$\varepsilon_c = (\varepsilon_{cfrpu} - \varepsilon_{pe})\left(\frac{c}{d_{cfrp}-c}\right)$$

Eq. 8.43 $$\Phi_{gfrp} f_{gfrp} A_{gfrp} + \Phi_{cfrp} f_{cfrp} A_{cfrp} = \Phi_c \alpha_1 \beta_1 f'_c bc$$

Eq. 8.44 $$M_r = \Phi_{gfrp} f_{gfrp} A_{gfrp}(d_{gfrp} - \frac{\beta_1 c}{2}) + \Phi_{cfrp} f_{cfrp} A_{cfrp}(d_{cfrp} - \frac{\beta_1 c}{2})$$

Solving these equations with a spreadsheet, M_r is found to be 206.8 kN·m/m, which exceeds the total factored moment of 144.2 kN·m/m. The capacity of the slab following rupture of the CFRP tendons can be found by repeating the calculations above setting $A_{cfrp} = 0$ and $\varepsilon_{gfrp} = \varepsilon_{gfrpu}$. Doing so gives a predicted residual capacity of 187.1 kN·m/m, which is still greater than the factored load, thus providing additional safety.

The overall performance factor included in the CHBDC to design for deformability is given by Equation 8.45:

Eq. 8.45 $$J = \frac{M_{ult}\psi_{ult}}{M_c \psi_c} \geq 4.0$$

The factored moment resistance was determined above to be 206.8 kN·m/m; setting the resistance factors to unity, the unfactored ultimate moment is 306.8 kN·m/m. The moment corresponding to the service condition, M_c, was calculated in a similar manner by setting the maximum concrete compressive strain, ε_c, equal to 0.001, giving a service moment of 123.7 kN·m/m. The curvatures at ultimate and at service were calculated using Equation 8.46 as 3.17×10^{-5} and 1.79×10^{-5}, respectively:

Eq. 8.46 $$\psi = \frac{\varepsilon_c}{c}$$

Applying this methodology gives J = 4.40 at the point when the CFRP tendons rupture, thus satisfying deformability requirements. As previously mentioned, following CFRP rupture the GFRP reinforcing bars continue to contribute to load resistance. Accounting for the additional deformation permitted by the GFRP reinforcement after CFRP rupture, M_{ult} and ψ_{ult} become 338 kN·m/m and 6.28×10^{-5}, respectively, and the overall performance factor becomes 9.58.

8.4 AASHTO LRFD Bridge Design Code

The AASHTO LRFD specifications also propose that design live loads be approximated by a design truck or design tandem (pair of axles) and design lane loads. The tandem loads typically govern the design of short spans due to their small axle spacing (1.2 m). For slab bridges not exceeding 4600 mm, the design lane load is not considered.

AASHTO allows the use of simplified methods of analysis for the transverse distribution of loads on slab bridges. An equivalent strip method is implemented where each strip is treated as a beam for analysis. The width of each strip depends on the bridge type and dimensions. For

positive moment calculations of bridge decks and slab bridges having a span less than 15 ft (4.6 m), the equivalent strip width in inches is given by Equation 8.47. Slab-type bridges spanning lengths greater than 15 ft have equivalent strip widths given by Equations 8.48 and 8.49 for one or more than one lane loaded, respectively.

Eq. 8.47 $$E = 26.0 + 6.6S$$

Eq. 8.48 $$E = 10.0 + 5.0\sqrt{L_1 W_1}$$

Eq. 8.49 $$E = 84.0 + 1.44\sqrt{L_1 W_1} \leq \frac{12.0W}{N_L}$$

Where, *E* is the width of the equivalent strip in inches, *S* is the distance between supports in feet, L_1 and W_1 are the modified span length and width of the bridge, respectively, *W* is the bridge width and N_L is the number of design lanes.

The total maximum design moments are obtained by placing the AASHTO LRFD HL-93 design tandem at the midspan of the bridge. Using a similar methodology as outlined for the CHBDC, with the exception that the live load factor is taken as 1.75 rather than 1.7 and the design tandem is a pair of 110 kN axles, the factored live load moment per equivalent slab strip—including a dynamic load allowance of 0.33 and a multiple presence factor of 1.2—is found to be 506.9 kN·m (Equation 8.50). For a span of 14.76 ft (4500 mm) the equivalent strip width is 123.4 inches, or 3.1 m. The factored live load moment per metre width is then given by Equation 8.51:

Eq. 8.50 $$M_L = 1.75(1.2)(110)(1.65)(1 + 0.33) = 506.9\ kN \cdot m$$

Eq. 8.51 $$m = \frac{M_L}{E} = \frac{506.9}{3.1} = 163.5\ kN \cdot m/m$$

For serviceability limit states the AASHTO LRFD allows the use of unfactored design loads, although the dynamic load allowance should still be considered. This reduces live load design moments per metre width to 93.4 kN·m. The total service moment per metre width is 114.7 kN·m. The factored dead load moment per metre width at midspan is given by Equation 8.52:

Eq. 8.52 $$m_d = \frac{(1.25*24*1*0.3+1.50*1.2*1)4.5^2}{8} = 27.3\ kN \cdot m$$

Maximum applied shear values can be determined in a similar manner to the design moments except that the tandem axles should be placed adjacent to one of the supports to produce maximum force effects. Using this methodology, maximum factored shear values were calculated as 145.3 kN per metre width.

In the same way that was described for the CHBDC, the reinforcement stresses at service are found to be 50.7 MPa and 1102.1 MPa for the GFRP and CFRP, respectively, corresponding to 7.4% and 62.4% of ultimate. The AASHTO LRFD specification for GFRP-RC bridge decks does not explicitly limit FRP service stresses, but rather imposes creep rupture requirements which are assumed to be satisfied when the stress range in the GFRP reinforcement resulting from fatigue loading satisfies the requirements of Equations 8.53. The design tensile strength of GFRP bars, f_{fd}, is also reduced to account for the service environment; for concrete exposed to earth and weather, f_{fd} is taken as $0.7f_{frpu}$:

Eq. 8.53 $$f_{fs} \leq 0.2f_{fd} = 0.2(0.7)(683) = 95.6\ MPa$$

Fatigue loads are taken as 75% of the unfactored live load. Thus, by inspection, the GFRP stress requirement is satisfied for the present example.

AASHTO LRFD limits crack widths to 0.02 in (0.5 mm) for concrete decks reinforced with GFRP. Crack widths are calculated in a similar way as for the CHBDC, except that the bond coefficient, k_b, is taken as 1.4. The predicted crack widths are thus given by Equation 8.54:

Eq. 8.54 $$w = 2\frac{50.7}{48200}\left(\frac{300-75.4}{262-75.4}\right)(1.4)\sqrt{38^2+\left(\frac{100}{2}\right)^2} = 0.2\,mm \ll 0.5\,mm \;\therefore OK$$

AASHTO LRFD also imposes deflection limits for concrete decks of *L*/800 for decks with no pedestrian traffic, *L*/1000 for decks with limited pedestrian traffic and *L*/1200 for decks with significant pedestrian traffic, corresponding to 5.6 mm, 4.5 mm and 3.8 mm, respectively. The deflections of FRP-RC or PC members are calculated using a modified form of the Branson model given by Equation 8.55 with the term β_d to account for the reduced stiffness of FRP reinforcement, as given by Equation 8.56:

Eq. 8.55 $$I_e = (\frac{M_{cr}}{M_a})^3\beta_d I_g + [1-(\frac{M_{cr}}{M_a})^3]I_{cr} \leq I_g$$

Eq. 8.56 $$\beta_d = \frac{1}{5}\frac{\rho_f}{\rho_{fb}} \leq 1.0$$

In this case, the applied service moment is less than the predicted cracking moment, so that the effective moment is taken as the gross moment of inertia of the uncracked section. For live load deflection calculations, AASHTO LRFD uses the maximum of the design truck or 25% of the design truck plus the lane load. In this case, the heaviest axle of the design truck (145 kN)

placed at the midspan of the member governs, giving a moment per metre width of 84.0 kN·m. For a single point load, the maximum deflection is given by Equation 8.57:

Eq. 8.57 $$\delta = \frac{ML^2}{12E_cI_g} = \frac{84x10^6(4500^2)(12)}{12(4500\sqrt{60})(1000)(300^3)} = 1.81\,mm < 3.8\,mm \;\therefore OK$$

With respect to the ultimate limit state, the methodology is slightly different than that used in the CHBDC as resistance factors are applied to the nominal resistance rather than using individual material resistance factors. Therefore the factored moment resistance, M_r, is taken as ϕM_n, where M_n is the nominal moment resistance. For under-reinforced sections, ϕ = 0.55. The determination of the concrete rectangular stress block is also slightly different as it is assumed to have a width of $0.85f'_c$ and a depth of $a = \beta_1 c$, where β_1 is taken as 0.65 for f'_c greater than 55 MPa. For under-reinforced sections, the depth to the neutral axis, c, is conservatively taken as the depth to the neutral axis for a balanced failure, c_b, (which is larger than the actual value of c) as given by Equation 8.58:

Eq. 8.58 $$c_b = \left(\frac{\varepsilon_{cu}}{\varepsilon_{cu}+\varepsilon_{fd}}\right)d = \left(\frac{0.003}{0.003+0.7(\frac{683}{48200})}\right)262 = 60.8\,mm$$

Since flexural failure for the given slab bridge is governed by CFRP rupture, it is more appropriate—and more conservative—to consider the balanced condition when concrete crushes simultaneously with rupture of the CFRP tendons. Thus, c_b can be taken as 79.3 mm as shown by Equation 8.59:

Eq. 8.59 $$c_b = \left(\frac{\varepsilon_{cu}}{\varepsilon_{cu}+\varepsilon_{cfrpu}-\varepsilon_{pe}}\right)d = \left(\frac{0.003}{0.003+0.45(\frac{1765}{144000})}\right)225 = 79.3\,mm$$

The nominal moment resistance per metre width of the slab is then obtained using Equation 8.60:

Eq. 8.60 $$M_n = T_{gfrp}\left(262 - \frac{0.65(79.3)}{2}\right) + T_{cfrp}(225 - \frac{0.65(79.3)}{2})$$

Applying strain compatibility and internal force equilibrium conditions, the system of equations can be solved to give M_n = 293.1 kN·m. The factored moment resistance is taken as 0.55M_n = 161.2 kN·m, which is close to the total factored moment of 163.5 kN·m. The moment resistance post-CFRP rupture is actually slightly higher as the load is redistributed to the GFRP reinforcement; considering a section without any CFRP tendons and taking the actual depth of the neutral axis, *c*, at failure, the factored moment resistance becomes 185.0 kN·m, which is greater than the factored design moment.

For shear resistance, $V_r = \phi V_n$, where ϕ = 0.75. The concrete contribution to nominal shear resistance is calculated using the Tureyen and Frosch model (2003) given for SI units by Equation 8.61:

Eq. 8.61 $$V_c = 0.42\sqrt{f'_c}\,bc$$

The depth to neutral axis, *c*, is taken here as *kd* where *k* is given by Equation 8.62 for prestressed members:

Eq. 8.62 $$k = \frac{\sqrt{\left(n\sum_{i=1}^{m}\rho_i\right)^2 + 2(1-\xi)n\sum_{i=1}^{m}\rho_i\left(\xi + \frac{d_i}{d}(1-\xi)\right)} - n\sum_{i=1}^{m}\rho_i}{1-\xi}$$

Alternatively, the depth to neutral axis can be calculated for a cracked elastic section by applying conditions of strain compatibility and force equilibrium for a given moment. Since the

moment near the supports is small, the section is not likely to be cracked. To be conservative, a section near the midspan can be selected to calculate *c* for the maximum factored moment of 163.5 kN·m; doing so gives *c* = 59.4 mm. The nominal shear resistance is then given by Equation 8.63:

Eq. 8.63 $$V_c = 0.42\sqrt{60}(1000)(59.4)(\tfrac{1}{1000}) = 193.2\ kN/m$$

The factored concrete contribution to shear resistance is taken as $0.75V_c$ = 144.9 kN/m. This is less than the factored shear force; hence, shear reinforcement is required. The contribution of the double-headed shear bars to nominal shear resistance is given by Equation 8.64:

Eq. 8.64 $$V_f = \frac{A_{fv} f_{fv} d}{s} = \frac{(198)\left(\frac{1000}{600}\right)(0.004)(62600)(262)(\frac{1}{1000})}{150} = 144.3\ kN/m$$

The total nominal shear resistance per metre width, V_n, is taken as the sum of V_c and V_f, or 337.5 kN, giving a total factored shear resistance of 253.1 kN, which is greater than the factored shear force of 145.3 kN; thus the design is adequate for shear. As a final check, the minimum area of shear reinforcement is given by Equation 8.65:

Eq. 8.65 $$A_{fv,min} = 0.05\frac{bs}{f_{fv}} = 0.05\left(\frac{1000(150)}{0.004(62600)}\right) = 30.0\ mm^2 < 330\ mm^2\ \therefore OK$$

The AASHTO LRFD specifications do not currently contain any provisions for the deformability of FRP-RC structures.

8.5 Summary

The design examples above illustrate that the proposed reinforcement system can be implemented to meet all requirements at serviceability, ultimate and fatigue limit states. The

same reinforcement configuration would allow for considerably longer spans than that considered here without exceeding serviceability conditions. Similarly, factored moment and shear resistances easily surpassed factored loads from the CHBDC CL-625 design truck. The factored design based on the AASHTO LRFD specifications is more conservative due to a severe load resistance factor of 0.55 for under-reinforced sections in conjunction with higher factored loads.

Neither the CHBDC nor the AASHTO LRFD explicitly addresses fatigue design for FRP-reinforced elements, although it is implied that by limiting the GFRP stresses at service, the long term performance of the bridge is expected to be satisfactory. The experimental results of this study showed that failure of the GFRP reinforcing bars could occur within one million cycles at stress ranges as low as 20% of the measured static capacity; it is recommended that the fatigue of FRP reinforcement be addressed in more detail in future editions of the design codes. The addition of prestressed CFRP tendons significantly reduces the stresses in the GFRP reinforcement at service; based on the low stresses induced in the GFRP even after cracking, flexural fatigue is not a concern for this bridge. Since the factored shear resistance is much greater than the factored shear force, shear fatigue is also not expected to govern design, especially with the addition of the double-headed shear bars. Based on the structure requirements, the design could be further optimized by increasing the spacing of the prestressing tendons and shear bars, or reducing the concrete compressive strength to lower costs. This is particularly true for the design according to the CHBDC; for the AASHTO LRFD design, reducing the prestressing force in the tendons can be used to increase the moment resistance due to the additional strain capacity in the CFRP tendons.

The CHBDC design loads at service and ultimate limit states are compared with the experimental results of the 600 mm wide slabs in Chapter 4, while the ability of the code equations to accurately predict the behaviour of the slabs is discussed in Chapter 6. Although the AASHTO design moments are slightly greater than those based on the CHBDC, the behaviour of the post-tensioned FRP-RC slab strips meet design criteria at service loads and ultimate conditions.

The CHBDC design example showed that the ultimate deformability of the slabs provides adequate warning prior to failure and even displays significant additional deformation post-CFRP rupture due to load redistribution to the GFRP reinforcing bars. On the other hand, AASHTO LRFD has no deformability provisions at this time. Therefore, the design example shown here demonstrates the simplicity and viability of the proposed structural system.

Chapter 9 - Conclusions and Recommendations

9.1 Conclusions

A total of fifty-seven SCC slab bridge strips were constructed and tested up to failure under either monotonic or fatigue loading to evaluate their performance at serviceability, ultimate and fatigue limit states. The experimental results were analyzed to determine the effect of reinforcement type, reinforcement ratio, prestressing level, bond between post-tensioning tendons and concrete and various types of shear reinforcement on the overall behaviour of slab bridges. A summary of the conclusions that can be drawn from the experimental and analytical program is given below:

- The GFRP-RC slabs displayed higher strength compared with the control slab reinforced with conventional normal-strength steel reinforcement bars with a similar reinforcement ratio, although non-prestressed slabs displayed larger deflections and crack widths at service. This is a result of the different mechanical properties of GFRP reinforcement, which have a much higher strength but lower stiffness compared with steel rebar.
- Post-tensioning the GFRP-RC slabs with CFRP tendons significantly improved their serviceability and ultimate performance. The prestressing action increased the cracking loads so that most of the prestressed slabs were uncracked at service, and the added stiffness of the CFRP tendons increased the post-cracking stiffness of the slabs. As a result, significant reductions in midspan deflections at service were observed with an

increasing number of tendons and prestressing force. The prestressed slabs easily met the CHBDC serviceability limits for crack width and strain in the GFRP reinforcement.

- Although FRP reinforcements possess linear elastic properties to failure, post-peak deformation was observed in the prestressed slabs which failed in flexure. This was a result of the rupture of individual CFRP tendons with some residual capacity provided by the non-prestressed GFRP reinforcement. Rupture of the CFRP tendons led to a redistribution of the applied loads although the slab did not fail until the ultimate strain of the GFRP bars was reached, or the loss of prestressing force eventually resulted in a shear failure.
- Sufficient prestressing force changed the mode of failure from brittle shear to flexural failure by CFRP rupture for the slabs which were unreinforced in shear. The compressive force introduced by the prestressed tendons increased the ability of the cracked concrete to resist shear stresses by aggregate interlock and reduced the width and depth of the inclined cracks.
- Unbonded post-tensioned CFRP tendons suffered premature rupture at stresses as low as 68% of ultimate due to local stress concentrations and friction induced at the tendon-duct interface. Bonded tendons surpassed their reported strengths in all cases.
- All of the GFRP-RC slabs met the deformability requirements set out by the CHBDC regardless of mode of failure, with the exception of specimen PT2-U which suffered a premature tendon rupture. Slab PT2a, which had a reduced depth, had the highest deformability out of all the FRP-reinforced slabs.

- All of the shear reinforcement types used in the given test program were effective in increasing the shear capacity of the section to induce a flexural failure mode in the full-scale slabs. For the reduced-length slabs, which were designed to fail in shear, all of the shear reinforcement types contributed to an increased shear resistance although shear reinforcements with anchorage displayed the highest shear capacities.
- The fatigue lives of slabs with unanchored stirrups showed considerably more scatter than those with anchored shear reinforcement as a result of variability in the tensile fatigue strength of concrete which affects the bond strength of the FRP stirrup. Shear bars with double-headed anchorages presented the best combination of constructability and structural performance.
- Full-scale slabs without shear reinforcement subjected to fatigue loading tended to exhibit shear failures at high load levels and flexural failures governed by GFRP rupture at lower load levels. When shear reinforcement was provided, the fatigue lives of the slabs were governed by GFRP rupture in all cases.
- Gradual increases in midspan deflection and maximum crack widths were observed in the slabs subjected to fatigue loading until just prior to failure when a rapid loss of stiffness was observed. This is normally observed in fatigue tests and is the result of the accumulation of fatigue damage in both the concrete and reinforcement.
- Through a series of ancillary tests, the fatigue lives of GFRP reinforcing bars with sand coating were found to be significantly and adversely affected by the presence of concrete due to abrasion at the bar-concrete interface. Fatigue lives of GFRP bars in beam-hinge tests tended to be approximately a full order of magnitude shorter than

those of bare bars tested in uniaxial tension. GFRP bars in concrete failed within one million cycles at load ranges as low as 20% of the ultimate static capacity of the bars.

- The cracking moments in the concrete slabs were consistently lower than expected, which is likely due to relatively large internally-restrained shrinkage stresses. The magnitude of the restrained shrinkage stresses depends on the contribution of the concrete core, which is more significant for large members; based on the observed cracking moments, the restrained shrinkage was found to be approximately 20% of the predicted total shrinkage assuming a relative humidity of 50%. The reduced concrete cracking strength used by the CHBDC gave generally conservative predictions of the cracking moments.
- A slight modification to the physically-derived Frosch (1999) equation for estimating crack widths was proposed to account for the contribution of concrete between cracks. While neglecting this contribution is technically conservative, the accuracy of the crack width predictions varies with respect to the stress level of the reinforcement relative to that at which the bond coefficient was calibrated and can result in unconservative or overly conservative predictions.
- The load-deflection models considered in this study tended to underestimate deflections for the GFRP-RC slabs after cracking, which is likely a result of overestimating the cracking moment of the test specimens. When the lower cracking moments were taken into account, reasonable estimates of deflection were obtained for all load levels for slabs containing shear reinforcement.

- Slabs without shear reinforcement displayed additional deformation due to unrestrained inclined cracking and a reduction in confinement of the concrete section. A simple model adapted from Imjai et al. (2009) was proposed which gave good estimates of this additional deformation for slabs without shear reinforcement.
- Flexural and shear capacities were predicted with a reasonably good correlation with experimental results. Predicted shear capacities of slabs with anchored shear reinforcement were overconservative due to the strain limits currently in place for FRP stirrups.
- Using a model framework proposed by Balaguru & Shah (1982) in conjunction with the Brondsted et al. (1997) residual stiffness model for GFRP reinforcing bars, the cyclic load-deflection and crack width responses were predicted with reasonable accuracy, and tended to be conservative.
- Modification of the MCFT shear equation to account for the tensile strength reduction in concrete caused by fatigue loading gave conservative estimates of the shear fatigue lives of prestressed slabs without shear reinforcement, although it was slightly unconservative for the one non-prestressed slab which had a shear fatigue failure mode. Due to the limited number of specimens which failed in shear fatigue, no major conclusions can be drawn regarding the accuracy of this method.
- Applying the same modification to the MCFT equation for shear-reinforced members gave conservative estimates of the shear fatigue lives in all cases for members with anchored shear reinforcement.

- Various statistical and residual stiffness fatigue models were calibrated using the results of the fatigue tests on GFRP bars to predict the flexural fatigue lives of the GFRP-RC slabs. Simple methods assuming normally-distributed fatigue data were straightforward to apply and gave reasonable correlation with the fatigue data, although they did not accurately describe the observed scatter. The ASTM (2011) method described the data well, although unreasonably wide scatter bands were produced for both high and low load levels.
- The Sendeckyj (1979) model was slightly more involved, but through an iterative process it gave good predictions of both the static and fatigue data.
- The Brondsted et al. (1997) residual stiffness model was used to predict the fatigue lives of the GFRP-RC slabs, with the level of conservatism depending on the choice of stiffness degradation taken as a failure criterion. The use of a 3% stiffness degradation value gave conservative estimates in all cases.
- An evaluation of the proposed reinforcement system according to the provisions of the CHBDC and AASHTO LRFD bridge design codes demonstrated the feasibility of incorporating the proposed FRP reinforcement system in the design of slab bridges.

9.2 Design Recommendations

The design of FRP-RC slab bridges with post-tensioned tendons has been shown in Chapter 8 to be fairly straightforward. While the reinforcement configuration will vary depending on the bridge geometry and loading, a few general design recommendations should be considered:

- An initial value for the slab depth can be selected using the recommended span-to-depth ratio of 15, provided that clearance and support conditions permit. Longer span-to-depth ratios can be achieved with an increase in the total prestressing force applied.
- Design the passive GFRP reinforcement to meet the required moment resistance based on the factored design loads. After the strength conditions have been satisfied, prestressed CFRP tendons can be added to meet the design requirements at the service load.
- Include a sufficient number of prestressed tendons to limit GFRP stresses, deflections and crack widths to meet serviceability criteria. This will depend on the span length and support conditions of the slab. The expected fatigue stress range in the GFRP reinforcement should be evaluated using the Sendeckyj (1981) model for a desired reliability and compared with the expected number of load cycles in the service life of the bridge. If the concrete is expected to be cracked at the service load, deflections and crack widths should be predicted using the methods proposed in this thesis; the required prestressing force and number of tendons can be determined through an iterative process until all serviceability and fatigue criteria are satisfied.
- Whenever possible, design for a progressive failure mode so that CFRP rupture does not result in total structural collapse but instead results in a redistribution of load to the passive GFRP reinforcement. This can be achieved by choosing an effective prestress level that limits the remaining strain capacity in the CFRP tendons such that the tendons rupture at a load exceeding the factored design moment but less than the moment

resistance provided by the passive reinforcement only. Doing so will ensure that ample visual warning is provided prior to catastrophic failure.

- Use only fully-bonded tendons unless a frictionless system has been experimentally validated.
- If necessary, provide shear reinforcement in the form of double-headed shear bars to prevent a brittle shear failure mode.

9.3 Recommendations for Future Work

A number of parameters were outside the scope of the present work, although they would provide a deeper understanding of some of the observations made in this study. It is recommended that the following be considered for future work:

- An experimental investigation on the effect of mean stress on the fatigue behaviour of GFRP reinforcing bars both in and out of concrete.
- A study considering the fatigue behaviour of different types and diameters of FRP reinforcing bars.
- A study investigating the effect of FRP surface treatment and concrete compressive strength and confinement on the fatigue behaviour of FRP bars in concrete.
- An experimental and analytical program focusing on the shear fatigue behaviour of FRP-RC members.
- An investigation on the effect of variable amplitude loading on the damage accumulation in FRP reinforcing bars.

References

AASHTO 2009. *AASHTO LRFD Bridge Design Guide Specifications for GFRP-Reinforced Concrete Bridge Decks and Traffic Railings*. American Association of State Highway and Transportation Officials, Washington, DC.

Abdelrahman, A. A. and Rizkalla, S. H. 1997. *Serviceability of Concrete Beams Prestressed by Carbon-Fiber-Reinforced-Plastic Bars*. ACI Structural Journal. Vol. 94, No. 4: pp. 447-457.

Abdelrahman, A.A. and Rizkalla, S.H. 1999. *Deflection Control of Concrete Beams Pretensioned by CFRP Reinforcements.* Journal of Composites for Construction, Vol. 3, No. 2: pp. 55-62.

Abdelrahman, A. A., Tadros, G. and Rizkalla, S. H. 1995. *Test Model for the First Canadian Smart Highway Bridge*. ACI Structural Journal. Vol. 92, No. 4: pp. 451-458.

Achillides, Z. And Pilakoutas, K. 2004. *Bond Behavior of Fiber Reinforced Polymer Bars under Direct Pullout Conditions.* Journal of Composites for Construction, Vol. 8, No. 2: pp. 173-181.

ACI Committee 215 1997. *ACI 215R-74: Considerations for Design of Concrete Structures Subjected to Fatigue Loading.* American Concrete Institute, Detroit, Michigan.

ACI Committee 237 2007. *ACI 237R-07: Self-Consolidating Concrete*. American Concrete Institute, Detroit, Michigan.

ACI Committee 318 2008. *ACI 318-08: Building Code Requirements for Structural Concrete*. American Concrete Institute, Detroit, Michigan.

ACI Committee 408 2005. *ACI 408.2R-92: Bond Under Cyclic Loads*. American Concrete Institute, Detroit, Michigan.

ACI Committee 440 2004. *ACI 440.4R-04: Prestressing Concrete Structures with FRP Tendons*. American Concrete Institute, Detroit, Michigan.

ACI Committee 440 2006. *ACI 440.1R-06: Guide for the Design and Construction of Structural Concrete Reinforced with FRP Bars*. American Concrete Institute, Detroit, Michigan.

ACI Committee 440 2007. *ACI 440R-07: Report on Fiber-Reinforced Polymer (FRP) Reinforcement for Concrete Structures.* American Concrete Institute, Detroit, Michigan.

Adimi, R., Benmokrane, B. and Rahman, H. 1997. *Fatigue Behaviour of GFRP Bars Embedded in Concrete.* Proceedings of The Annual Conference of the Canadian Society for Civil Engineering, Sherbrooke, Quebec, May 27-30, pp. 121-130.

Adimi, M.R., Rahman, A.H., and Benmokrane, B. 2000. *New Method for Testing Fiber-Reinforced Polymer Rods under Fatigue.* Journal of Composites for Construction, Vol. 4, No. 4: pp. 206-213.

Ahmed, E. A., El-Salakawy, E., Benmokrane, B. and Goulet, S. 2008. *Performance Evaluation of CFRP Stirrups as Shear Reinforcement for Concrete Beams*, CSCE 2008 Annual Conference, CSCE, Quebec, Canada, June 10-13.

Aiello, M.A. and Ombres, L. 2000. *Cracking Analysis of FRP-Reinforced Concrete Flexural Members.* Mechanics of Composite Materials, Vol. 36. No. 5: pp. 389-394.

Aiello, M.A., Leone, M. and Ombres, L. 2003. *Modeling of the Behavior of Concrete Tension Members Reinforced with FRP Rods.* Mechanics of Composite Materials. Vol. 39, No. 4: pp. 431-444.

Aiello, M.A., Leone, M. and Pecce, M. 2007. *Bond Performances of FRP Rebars-Reinforced Concrete.* Journal of Materials in Civil Engineering, Vol. 19, No. 3: pp. 205-213.

Alam, M.S. and Hussein, A. 2011. *Experimental Investigation on the Effect of Longitudinal Reinforcement on Shear Strength of Fibre Reinforced Polymer Reinforced Concrete Beams.* Canadian Journal of Civil Engineering. Vol. 38: pp. 243-251.

Alkhairi, F.M. 1991. *On the Behavior of Concrete Beams Prestressed with Unbonded Internal and External Tendons.* PhD Thesis, University of Michigan, Ann Arbor, Michigan, 415 p.

Alkhrdaji, T., Wideman, M., Belarbi, A. and Nanni, A. 2001. *Shear Strength of GFRP RC Beams and Slabs*, Composites in Construction, Porto, Portugal, October 10-12, Vol. 1: pp. 409-414.

Al-Mayah, A., Soudki, K. and Plumtree, A. 2006. *Development and Assessment of a New CFRP Rod-Anchor System for Prestressed Concrete*. Applied Composite Materials. Vol. 13, No. 5: pp. 321-334.

Al-Mayah, A., Soudki, K. and Plumtree, A. 2007. *Novel Anchor System for CFRP Rod: Finite-Element and Mathematical Models*. Journal of Composites for Construction. Vol. 11, No. 5: pp. 469-476.

Al-Sunna, R., Pilakoutas, K., Hajirasouliha, I. and Guadagnini, M. 2012. *Deflection behaviour of FRP Reinforced Concrete Beams and Slabs: An Experimental Investigation.* Composites: Part B. Vol. 43: pp. 2125-2134.Composites: Part B. Vol. 43: pp. 2125-2134.

Amato, L. R. 2009. *CFRP Tendons for the repair of post-tensioned, unbonded concrete buildings*. M.Sc. Thesis, Department of Civil Engineering, Queen's University, Kingston, Ontario, 149 p.

ASCE-ACI Committee 445 1998. *Recent Approaches to Shear Design of Structural Concrete*. Journal of Structural Engineering. Vol. 124, No. 12: pp. 1375-1417.

ASTM C39/C39M-12a 2012. *Standard Test Method for Compressive Strength of Cylindrical Concrete Specimens.* ASTM International.

ASTM C496/496M-11 2011. *Standard Test Method for Splitting Tensile Strength of Cylindrical Concrete Specimens.* ASTM International.

ASTM C939-10 2010. *Standard Test Method for Flow of Grout for Preplaced-Aggregate Concrete (Flow Cone Method).* ASTM International.

ASTM C942-10 2010. *Standard Test Method for Compressive Strength of Grouts for Preplaced-Aggregate Concrete in the Laboratory.* ASTM International.

ASTM E739-10 2010. *Standard Practice for Statistical Analysis of Linear or Linearized Stress-Life (S-N) and Strain-Life (ε-N) Fatigue Data.* ASTM International.

Award, M.E. and Hilsdorf, H.K. 1974. *Strength and Deformation Characteristics of Plain Concrete Subjected to High Repeated and Sustained Loads.* ACI SP-41, pp. 1-14.

Azizinamini, A., Boothby, T. E., Shekar, Y. and Barnhill, G. 1994. *Old Concrete Bridges. I: Experimental Investigation*. Journal of Structural Engineering. Vol. 120, No. 11: pp. 3284-3304.

Bakis, C.E., Al-Dulaijan, S.U., Nanni, A., Boothby, T.E. and Al-Zahrani, M.M. 1998. *Effect of Cyclic Loading on Bond Behavior of GFRP Rods Embedded in Concrete.* Journal of Composites Technology & Research. Vol. 20, No. 1: pp. 29-37.

Balaguru, P. And Shah, S.P. 1982. *A Method for Predicting Crack Widths and Deflections for Fatigue Loading.* ACI SP-75, pp. 153-175.

Balazs, G.L. 1991. *Fatigue of Bond.* ACI Materials Journal, Vol. 88, No. 6: pp. 620-629.

Balazs, G.L. 1993. *Cracking Analysis Based on Slip and Bond Stresses.* ACI Materials Journal, Vol. 90, No. 4: pp. 340-348.

Benmokrane, B., Tighiouart, B. and Chaallal, O. 1996. *Bond Strength and Load Distribution of Composited GFRP Reinforcing Bars in Concrete.* ACI Materials Journal, Vol. 93, No. 3: pp. 246-252.

Bentz, E. C., Vecchio, F. J. and Collins, M. P. 2006. *Simplified Modified Compression Field Theory for Calculating Shear Strength of Reinforced Concrete Elements*. ACI Structural Journal. Vol. 103, No. 4: pp. 614-624.

Bischoff, P.H. 2001. *Effects of Shrinkage on Tension Stiffening and Cracking in Reinforced Concrete.* Canadian Journal of Civil Engineering. Vol. 28: pp. 363-374.

Bischoff, P.H. 2005. *Reevaluation of Deflection Prediction for Concrete Beams Reinforced with Steel and Fiber Reinforced Polymer Bars.* Journal of Structural Engineering, Vol. 131, No. 5: pp. 752-767.

Bischoff, P.H. 2007. *Deflection Calculation of FRP Reinforced Concrete Beams Based on Modifications to the Existing Branson Equation.* Journal of Composites for Construction, Vol. 11, No. 1: pp. 4-14.

Bischoff, P.H. 2007. *Rational Model for Calculating Deflection of Reinforced Concrete Beams and Slabs.* Canadian Journal of Civil Engineering, Vol. 34: pp. 992-1002.

Bischoff, P.H. and Johnson, R.D. 2010. *Effect of Shrinkage on Short-Term Deflection of Reinforced Concrete Beams and Slabs.* ACI SP-246: pp. 167-180.

Boel, V., Helincks, P., Desnerck, P. and De Schutter, G. 2010. *Bond Behaviour and Shear Capacity of Self-Compacting Concrete*. Proceedings of SCC2010: Design, Production and Placement of Self-Consolidating Concrete, Montreal, Canada, September 26-29, pp. 343-353.

Braimah, A. 2000. *Long-Term and Fatigue Behaviour of Carbon Fibre Reinforced Polymer Prestressed Concrete Beams*. Ph.D. Thesis, Department of Civil Engineering, Queen's University, Kingston, Ontario, 312 p.

Braimah, A., Green, M. F. and Campbell, T. I. 2006. *Fatigue Behaviour of Concrete Beams Post-Tensioned with Unbonded Carbon Fibre Reinforced Polymer Tendons*. Canadian Journal of Civil Engineering. Vol. 33, pp. 1140-1155.

Brondsted, P., Lilholt, H. and Anderson, S.I. 1997. *Fatigue Damage Prediction by Measurements of the Stiffness Degradation in Polymer Matrix Composites.* Proceedings of the International Conference on Fatigue of Composites Eight International Spring Meeting, Paris, June 3-5.

Brouwers, H. J. H. and Radix, H. J. 2005. *Self-Compacting Concrete: Theoretical and Experimental Study*. Cement and Concrete Research. Vol. 35, pp. 2116-2136.

Burgoyne, C. J. 1993. *Should FRP be Bonded to Concrete?* Fiber-Reinforced-Plastic Reinforcement for Concrete Structures, American Concrete Institute, Vancouver, Canada, March 28-31, pp. 347-366.

CAN/CSA A23.3-04 2010. *Design of Concrete Structures*, Canadian Standards Association, 258 p.

CAN/CSA S6-06 2006. *Canadian Highway Bridge Design Code*, Canadian Standards Association, 800 p.

CAN/CSA S6-10 2010. *Canadian Highway Bridge Design Code*, Canadian Standards Association, 800 p.

CAN/CSA S807-10 2010. *Specification for fibre-reinforced polymers*, Canadian Standards Association, 44 p.

Carlson, R.L. and Kardomateas, G.A. 1996. *An Introduction to Fatigue in Metals and Composites.* Chapman & Hall, London, United Kingdom, 287 p.

CEB-FIP 2000. *Bond of Reinforcement in Concrete*. International Federation for Structural Concrete, Lausanne, Switzerland. 433 p.

Chan, Y., Chen, Y. and Liu, Y. 2003. *Effect of Consolidation on Bond of Reinforcement in Concrete of Different Workabilities*. ACI Materials Journal, Vol. 100, No. 4: pp. 294-301.

Chang, T.S. and Kesler, C.E. 1958. *Static and Fatigue Strength in Shear of Beams with Tensile Reinforcement.* Journal of the American Concrete Institute, Vol. 29, No. 12: pp. 1033-1057.

Chi, Z., Chou, T., Shen, G. 1984. *Determination of Single Fibre Strength Distribution from Fibre Bundle Testings.* Journal of Materials Science. Vol 19: pp. 3319-3324.

Chou, P.C., and Croman, R. (1978). *Residual Strength in Fatigue Based on the Strength-Life Equal Rank Assumption.* Journal of Composite Materials. Vol. 12: pp. 177-194.

Collepardi, M., Borsoi, A., Collepardi, S. and Troli, R. 2005. *Strength, Shrinkage and Creep of SCC and Flowing Concrete.* Proceedings of the 4th International RILEM Symposium on Self-Compacting Concrete, Chicago, Illinois, USA, Vol. 2: pp. 911-919.

Collins, M.P. and Mitchell, D. 1991. *Prestressed Concrete Structures.* Prentice Hall, Englewood Cliffs, NJ, USA.

Cosenza, E., Manfredi, G. and Realfonzo, R. 1997. *Behavior and Modeling of Bond of FRP Rebars to Concrete.* Journal of Composites for Construction, Vol. 1, No. 2: pp. 40-51.

Curtis, P.T. 1989. *The Fatigue Behaviour of Fibrous Composite Materials.* Journal of Strain Analysis. Vol. 24, No. 4: pp. 235-244.

Curtis, P.T. 1991. *Tensile Fatigue Mechanisms in Unidirectional Polymer Matrix Composite Materials.* International Journal of Fatigue, Vol. 13, No. 5: pp. 377-382.

Daoud, A., Lorraine, M. and Laborderie, C. 2003. *Anchorage and Cracking Behaviour of Self-Compacting Concrete.* Proceedings of the 3rd International Symposium on Self-Compacting Concrete, Reykjavik, Iceland, August 17-20, 2003, pp. 692-702.

Davalos, J.F., Chen, Y. And Ray, I. 2008. *Effect of FRP Bar Degradation on Interface Bond with High Strength Concrete.* Cement and Concrete Composites, Vol. 30: pp. 722-730.

De Almeida Filho, F.M., De Nardin, S. and De Cresce El Debs, A.L.H. 2005. *Evaluation of the Bond Strength of Self-Compacting Concrete in Pull-Out Tests.* Proceedings of the 4th International RILEM Symposium on Self-Compacting Concrete, Chicago, Illinois, USA, Vol. 2: pp. 953-958.

Demers, C.E. 1998a. *Fatigue Strength Degradation of E-glass FRP Composites and Carbon FRP Composites.* Construction and Building Materials. Vol. 12: pp. 311-318.

Demers, C.E. 1998b. *Tension-Tension Axial Fatigue of E-Glass Fiber-Reinforced Polymeric Composites: Tensile Fatigue Modulus*. Construction and Building Materials. Vol. 12, No. 1: pp. 51-58.

Desnerck, P., De Schutter, G. and Taerwe, L. 2009. *Shear Friction of Reinforced Self-Compacting Concrete Members.* Proceedings of the 10th International Conference on Recent Advances in Concrete Technology and Sustainability Issues, Sevilla, Spain, December 10-16, pp. 133-143.

Dew-Hughes, D. And Way, J.L. 1973. *Fatigue of Fibre-Reinforced Plastics: A Review.* Composites, pp. 167-173.

Dittenber, D.B. and Hota, G.V.S. 2010. *Evaluation of a Life Prediction Model and Environmental Effects of Fatigue for Glass Fibre Composite Materials.* Structural Engineering International. Vol. 4: pp. 379-384.

Dolan, C.W. and Burke, C.R. 1996. *Flexural Strength and Design of FRP Prestressed Beams.* Proceedings of the 2nd International Conference on Advanced Composite Materials in Bridges and Structures, Montreal, Canada, August 11-14, pp. 383-390.

Domone, P.L. 2006. *Self-Compacting Concrete: An analysis of 11 years of case studies*. Cement & Concrete Composites. Vol. 28: pp. 197-208.

Domone, P. L. 2007. *A Review of the Hardened Mechanical Properties of Self-Compacting Concrete*. Cement and Concrete Composites. Vol. 29, No. 1: pp. 1-12.

Dyer, K.P. and Isaac, D.H. 1998. *Fatigue Behaviour of Continuous Glass Fibre Reinforced Composites.* Composites. Vol. 29: pp. 725-733.

Ehsani, M. R., Saadatmanesh, H. and Tao, S. 1993. *Bond of GFRP Rebars to Ordinary Strength Concrete*, Fiber-Reinforced-Plastic Reinforcement for Concrete Structures, American Concrete Institute, Vancouver, Canada, March 28-31, pp. 333-345.

Ehsani, M. R., Saadatmanesh, H. and Tao, S. 1995. *Bond of Hooked Glass Fiber Reinforced Plastic (GFRP) Reinforcing Bars to Concrete*. ACI Structural Journal. Vol. 92, No. 4: pp. 391-400.

El-Gamal, S. and Benmokrane, B. 2009. *Design of Concrete Bridge Deck Slabs Using Different Types of GFRP Bars.* Proceedings of the 9th International Conference on Fibre-Reinforced Polymer Reinforced Concrete Structures, Sydney, Australia, July 13-15.

El-Ragaby, A., El-Salakawy, E. and Benmokrane, B. 2007. *Fatigue Analysis of Concrete Bridge Deck Slabs Reinforced with E-glass/Vinyl Ester FRP Reinforcing Bars.* Composites: Part B, No. 38: pp. 703-711.

El-Ragaby, A., El-Salakawy, E. and Benmokrane, B. 2007. *Fatigue Life Evaluation of Concrete Bridge Deck Slabs Reinforced with Glass FRP Composite Bars.* Journal of Composites for Construction, Vol. 11, No. 3: pp. 258-268.

Elrefai, A., West, J. S. and Soudki, K. 2007. *Performance of CFRP Tendon–Anchor Assembly Under Fatigue Loading*. Composite Structures. Vol. 80, pp. 352-360.

El-Salakawy, E. and Benmokrane, B. 2004. *Serviceability of Concrete Bridge Deck Slabs Reinforced with Fiber-Reinforced Polymer Composite Bars*. ACI Structural Journal. Vol. 101, No. 5: pp. 727-736.

El-Sayed, A. K., El-Salakawy, E. and Benmokrane, B. 2005. *Shear Strength of One-Way Concrete Slabs Reinforced with Fiber-Reinforced Polymer Composite Bars*. Journal of Composites for Construction. Vol. 9, No. 2: pp. 147-157.

El-Sayed, A. K., El-Salakawy, E. and Benmokrane, B. 2006. *Shear Strength of FRP-Reinforced Concrete Beams without Transverse Reinforcement*. ACI Structural Journal. Vol. 103, No. 2: pp. 235-243.

El-Sayed, A. K., El-Salakawy, E. and Benmokrane, B. 2007. *Mechanical and Structural Characterization of New Carbon FRP Stirrups for Concrete Members*. Journal of Composites for Construction. Vol. 11, No. 4: pp. 352-362.

Fam, A. Z., Rizkalla, S. H. and Tadros, G. S. 1997. *Behavior of CFRP for Prestressing and Shear Reinforcements of Concrete Highway Bridges*. ACI Structural Journal. Vol. 94, No. 1: pp. 77-88.

Fico, R., Galati, N., Prota, A. and Nanni, A. 2005. *Design and Construction of a Bridge Deck Using Mild and Post-Tensioned FRP Bars.* ACI SP-230: pp. 1121-1138.

Fico, R., Galati, N., Prota, A. and Nanni, A. 2006. *Southview Bridge Rehabilitation in Rolla, Missouri*, Center for Infrastructure Engineering Studies University Transportation Center Program, University of Missouri-Rolla, Rolla, Missouri, USA, 190 p.

Fico, R., Prota, A. and Manfredi, G. 2008. *Calibration of Bond Coefficient for Deflection Control of FRP RC Members.* Proceedings of the 4th International Conference on FRP Composites in Civil Engineering, Zurich, Switzerland, July 22-24.

Frederick, G.R. 1997. *Experimental and analytical investigation of load distribution in concrete slab bridges*, Spring Conference, Society for Experimental Mechanics, Bellevue, Washington, USA.

Frosch, R.J. 1999. *Another Look at Cracking and Crack Control in Reinforced Concrete.* ACI Structural Journal. Vol. 96, No. 3: pp. 437-442.

Galati, N., Boschetto, G., Rizzo, A., Nanni, A. and Parretti, R. 2004. *Pre-Construction Investigation for the Rehabilitation of a Bridge using Internal FRP Technology*, 4th International Conference on Advanced Composite Materials in Bridges and Structures, Calgary, Alberta, July 20-23.

Ghali, A. 1993. *Deflection of Reinforced Concrete Members: A Critical Review*. ACI Structural Journal. Vol. 90, No. 4: pp. 364-373.

Girgis, A. F. M. and Tuan, C. Y. 2005. *Bond Strength and Transfer Length of Pretensioned Bridge Girders Cast with Self-Consolidating Concrete*. PCI Journal. Vol. 50, No. 6: pp. 72-87.

Goel, S., Singh, S.P. and Singh, P. 2012. *Fatigue Analysis of Plain and Fiber-Reinforced Self-Consolidating Concrete.* ACI Materials Journal. Vol. 109, No. 5: pp. 573-582.

Grace, N.F., Jensen, E.A., Eamon, C.D. and Shi, X. 2012. *Life-Cycle Cost Analysis of Carbon Fiber-Reinforced Polymer Reinforced Concrete Bridges.* ACI Structural Journal. Vol. 109, No. 5: pp. 697-704.

Grace, N. F. and Sayed, G. A. 1998. *Ductility of Prestressed Bridges using CFRP Strands*. Concrete International. No. 6: pp. 25-30.

Grace, N. F. and Singh, S. B. 2003. *Design Approach for Carbon Fiber-Reinforced Polymer Prestressed Concrete Bridge Beams*. ACI Structural Journal. Vol. 100, No. 3: pp. 365-376.

Hawkins, N.M. 1972. *Fatigue Characteristics in Bond and Shear of Reinforced Concrete Beams.* ACI SP-41: Abeles Symposium on Fatigue of Concrete, pp. 203-236.

Heffernan, P.J. and Erki, M.A. 2004. *Fatigue Behavior of Reinforced Concrete Beams Strengthened with Carbon Fiber Reinforced Plastic Laminates.* Journal of Composites for Construction. Vol. 8, No. 2: pp. 312-140.

Higgins, C., Farrow, W.C., Nicholas, B.S. and Potisuk, T. 2006. *High-Cycle Fatigue of Diagonally Cracked Reinforced Concrete Bridge Girders: Field Tests.* Journal of Bridge Engineering, Vol. 11, No. 6: pp. 699-706.

Higgins, C., Lee, A., Potisuk, T. And Forrest, R.W.B. 2007. *High-Cycle Fatigue of Diagonally Cracked RC Bridge Girders: Laboratory Tests.* Journal of Bridge Engineering, Vol. 12, No. 2: pp. 226-236.

Hordijk, D.A. and Reinhardt, H.W. 1993. *Numerical and Experimental Investigation into the Fatigue Behavior of Plain Concrete.* SEM VII International Congress on Experimental Mechanics, Las Vegas, Nevada, June 8-11, pp. 278-285.

Hoult, N. A., Sherwood, E. G., Bentz, E. C. and Collins, M. P. 2008. *Does the use of FRP Reinforcement Change the One-Way Shear Behavior of Reinforced Concrete Slabs?* Journal of Composites for Construction. Vol. 12, No. 2: pp. 125-133.

Hsu, T.T.C. 1981. *Fatigue of Plain Concrete.* ACI Journal. Vol. 78: pp. 292-304.

Hughes Brothers 2011. *Aslan 200 Carbon Fibre Reinforced Polymer (CFRP) Bar Product Data Sheet*, www.aslanfrp.com.

Hughes Brothers 2011. *Aslan 100 Glass Fibre Reinforced Polymer (GFRP) Rebar Product Data Sheet*, www.aslanfrp.com.

Hull, D. 1994. *Matrix-Dominated Properties of Polymer Matrix Composite Materials.* Materials Science and Engineering. Vol. 184: pp. 173-183.

Hwang, W. and Han, K.S. 1986. *Fatigue of Composites-Fatigue Modulus Concept and Life Prediction*. Journal of Composite Materials. Vol. 20: pp. 154-165.

Hwang, S., Khayat, K.H. and Bonneau, O. 2006. *Performance-Based Specifications of Self-Consolidating Concrete Used in Structural Applications.* ACI Materials Journal. Vol. 103, No. 2: pp. 121-129.

Imjai, T., Guadagnini, M. and Pilakoutas, K. 2009. *Estimation of Shear Crack Induced Deformations of FRP RC Beams.* Proceedings of the 9th International Conference on Fiber-Reinforced Polymers for Reinforced Concrete Structures, Sydney, Australia, July 13-15.

Ishihara, K., Obara, T., Sato, Y., Ueda, T. and Kakuta, Y. 1997. *Evaluation of Ultimate Strength of FRP Rods at Bent-Up Portion*, Non-Metallic (FRP) Reinforcement for Concrete Structures, October, Vol. 2: pp. 27-34.

ISIS Canada 2007. *Design Manual No. 3 – Reinforcing Concrete Structures with Fibre Reinforced Polymers*, Winnipeg, Manitoba, Canada.

ISIS Canada 2008. *Design Manual No. 5 - Prestressing Concrete Structures with Fibre-Reinforced Polymers*, Winnipeg, Manitoba, Canada.

Johnson, D.T.C. and Sheikh, S.A. 2012. *Performance of Bent Stirrup and Headed GFRP Bars in Concrete Structures.* Proceedings of the 6th International Conference on Advanced Composite Materials in Bridges and Structures, Kingston, Ontario, May 22-25.

Katz, A. 1998. *Effect of Helical Wrapping on Fatigue Resistance of GFRP.* Journal of Composites for Construction. Vol. 2, No. 3: pp. 121-125.

Katz, A. 2000. *Bond to Concrete of FRP Rebars After Cyclic Loading.* Journal of Composites for Construction. Vol. 4, No. 3: pp. 137-144.

Kato, T. and Hayashida, N. 1993. *Flexural Characteristics of Prestressed Concrete Beams with CFRP Tendons*, Fiber-Reinforced-Plastic Reinforcement for Concrete Structures, American Concrete Institute, Vancouver, Canada, March 28-31, pp. 419-440.

Khayat, K. H. 1999. *Workability, Testing and Performance of Self-Consolidating Concrete*. ACI Materials Journal. Vol. 96, No. 3: pp. 346-344.

Khayat, K. H. and Mitchell, D. 2009. *Self-Consolidating Concrete for Precast, Prestressed Concrete Bridge Elements*. National Cooperative Highway Research Program Report 628, 99p.

Kim, H.C. and Ebert, L.J. 1978. *Axial Fatigue Failure Sequence and Mechanisms in Unidirectional Fiberglas Composites.* Journal of Composite Materials. Vol. 12: pp. 139-152.

Kim, H.C. and Ebert, L.J. 1979. *Fatigue Life-Limiting Parameters in Fibreglass Composites.* Journal of Materials Science. Vol. 14: pp. 2616-2624.

Kim, Y.H., Trejo, D. And Hueste, M.B.D. 2012. *Bond Performance in Self-Consolidating Concrete Pretensioned Bridge Girders.* ACI Structural Journal. Vol. 109, No. 6: pp. 755-765.

Kim, H.S. and Zhang. J. 2001. *Fatigue Damage and Life Prediction of Glass/Vinyl Ester Composites.* Journal of Reinforced Plastics and Composites. Vol. 20, No. 10: pp. 834-848.

Kobraei, M., Jumaat, M.Z. and Shafigh, P. 2011. *An Experimental Study on Shear Reinforcement in RC Beams Using CFRP-Bars.* Scientific Research and Essays. Vol. 6, No. 16: pp. 3447-3460.

Kong, F., Robins, P.J., Kirby, D.P. and Short, D.R. 1972. *Deep Beams with Inclined Web Reinforcement*. ACI Journal, Vol. 69, No. 3: pp. 172-178.

Konur, O. And Matthews, F.L. 1989. *Effect of the Properties of the Constituents on the Fatigue Performance of Composites: A Review.* Composites. Vol. 20, No. 4: pp. 317-328.

Kordina, K., Hegger, J. and Teutsch, M. *Shear Strength of Prestressed Concrete Beams with Unbonded Tendons.* ACI Structural Journal. Vol. 86, No. 2: pp. 143-149.

KPM Industries 2011. *PT Grout Specification Sheet*. King Packaged Materials Company.

Kreger, M.E., Bachman, P.M. and Breen, J.E. 1989. *An Exploratory Study of Shear Fatigue Behavior of Prestressed Concrete Girders.* PCI Journal, No. 4: pp. 104-125.

Lee, J., Yi, C. And Cheong, Y. 2009. *Experimental Study on the FRP-Concrete Bond Behavior Under Repeated Loadings.* Mechanics of Composite Materials. Vol. 45, No. 6: pp. 609-618.

Lees, J. M. and Burgoyne, C. J. 1999. *Experimental Study of Influence of Bond on Flexural Behavior of Concrete Beams Pretensioned with Aramid Fiber Reinforced Plastics*. ACI Structural Journal. Vol. 96, No. 3: pp. 377-386.

Lin, C. And Chen, J. 2012. *Shear Behavior of Self-Consolidating Concrete Beams.* ACI Structural Journal. Vol. 109, No. 3: pp. 307-315.

Liu, Y. And Mahadevan, S. 2010. *Probabilistic Fatigue Life Prediction of Composite Materials.* In Fatigue Life Prediction of Composites and Composite Structures, Edited by Vassiloupolos, A.P., Woodhead Publishing Limited, Cambridge, United Kingdom, pp. 220-248.

Lovegrove, J.M. and El Din, S. 1982. *Deflection and Cracking of Reinforced Concrete Under Repeated Loading and Fatigue.* ACI SP-75: pp. 133-152.

Lubell, A. A., Bentz, E. C. and Collins, M. P. 2009. *Influence of Longitudinal Reinforcement on One-Way Shear in Slabs and Wide Beams*. Journal of Structural Engineering. Vol. 135, No. 1: pp. 78-87.

Mabsout, M., Tarhini, K., Jabakhanji, R. and Awwad, E. 2004. *Wheel Load Distribution in Simply Supported Concrete Slab Bridges*. Journal of Bridge Engineering. Vol. 9, No. 2: pp. 147-155.

MacGregor, J.G. and Bartlett, F.M. 2000. *Reinforced Concrete Mechanics and Design*. First Canadian Edition, Prentice Hall Canada Inc., Toronto, Ontario, 1042 p.

Maissen, A. and De Smet, C. A. M. 1995. *Comparison of Concrete Beams Prestressed with Carbon Fibre Reinforced Plastic and Steel Strands*, Second International RILEM Symposium, Ghent, Belgium, August 23-25, pp. 430-439.

Mallick, P.K. 2011. *Testing the Fatigue Strength of Fibers Used in Fiber-Reinforced Composites Using Fiber Bundle Tests.* In Creep and Fatigue in Polymer Matrix Composites, Edited by Guedes, R.M., Woodhead Publishing Limited, Cambridge, United Kingdom, pp. 409-423.

Mandell, J.F. 1982. *Fatigue Behavior of Fiber-Resin Composites.* In Developments in Reinforced Plasstics, Volume 2. Applied Science Publishers, London, pp. 67-107.

Maruyama, T., Honma, M. and Okamura, H. 1993. *Experimental Study on Tensile Strength of Bent Portion of FRP Rods*, Fiber-Reinforced-Plastic Reinforcement for Concrete Structures, American Concrete Institute, Vancouver, Canada, March 28-31, pp. 163-176.

McCallum, B.E.C. and Newhook, J.P. 2012. *Evaluation of the Bond Dependent Coefficient and Parameters Which Influence Crack Width in GFRP Reinforced Concrete.* Proceedings of the 6th International Conference on Advanced Composite Materials in Bridges and Structures, Kingston, Ontario, May 22-25.

Michaluk, C. R., Rizkalla, S. H., Tadros, G. and Benmokrane, B. 1998. *Flexural Behavior of One-Way Concrete Slabs Reinforced by Fiber Reinforced Plastic Reinforcements*. ACI Structural Journal. Vol. 95, No. 3: pp. 353-365.

Mohamed, H.M. and Benmokrane, B. 2012. *Pullout Capacity Behaviour of FRP-Headed Rebars.* Proceedings of the 5th International Conference on Composites in Civil Engineering, Rome, Italy, June 13-15.

Morphy, R., Shehata, E. and Rizkalla, S. H. 1997. *Bent Effect on Strength of CFRP Stirrups*, Third International Symposium on Non-Metallic (FRP) Reinforcement for Concrete Structures, Sapporo, Japan, October 14-16, pp. 19-26.

Naaman, A.E. 1982. *Fatigue in Partially Prestressed Concrete Beams.* ACI SP-75, Fatigue of Concrete Structures, pp. 25-46.

Naaman, A. E. and Alkhairi, F. M. 1991. *Stress at Ultimate in Unbonded Post-Tensioning Tendons: Part 1 - Evaluation of the State-of-the-Art*. ACI Structural Journal. Vol. 88, No. 5: pp. 641-651.

Naaman, A. E. and Alkhairi, F. M. 1991. *Stress at Ultimate in Unbonded Post-Tensioning Tendons: Part 2 - Proposed Methodology*. ACI Structural Journal. Vol. 88, No. 6: pp. 683-692.

Naaman, A. E., Burns, N., French, C., Gamble, W. L. and Mattock, A. H. 2002. *Stresses in Unbonded Prestressing Tendons at Ultimate: Recommendation*. ACI Structural Journal. Vol. 99, No. 4: pp. 518-529.

Newaz, G.M. 1985. *Influence of Matrix Material on Flexural Fatigue Performance of Unidirectional Composites.* Composites Science and Technology. Vol. 24: pp. 199-214.

Nijssen, R.P.L. 2006. *Fatigue Life Prediction and Strength Degradation of Wind Turbine Rotor Blade Composites.* Delft University, Netherlands, 267 p.

Nijssen, R.P.L 2010. *Phenomenological Fatigue Analysis and Life Modelling.* In Fatigue Life Prediction of Composites and Composite Structures, Edited by Vassilopoulos, A.P. Woodhead Publishing Limited, Cambridge, United Kingdom, pp. 47-78.

Noël, M. and Soudki, K. 2010. *Effect of Harping on the Tensile Capacity of Carbon Fibre-Reinforced Polymer Tendons.* Proceedings of the 2nd International Structures Specialty Conference, Canadian Society for Civil Engineering, Winnipeg, Manitoba, June 9-12.

NSERC 2010. *Bridging the Gap – Composites Extend Infrastructure Life.* http://www.nserc-crsng.gc.ca/Media-Media/ImpactStory-ArticlesPercutant_eng.asp?ID=1047.

Oh, B.H. 1986. *Fatigue Analysis of Plain Concrete in Flexure.* Journal of Structural Engineering. Vol. 112, No. 2: pp. 273-288.

Okelo, R. and Yuan, R.L. 2005. *Bond Strength of Fiber Reinforced Polymer Rebars in Normal Strength Concrete.* Journal of Composites for Construction. Vol. 9, No. 3: pp. 203-213.

Park, S. Y. and Naaman, A. E. 1999. *Shear Behavior of Concrete Beams Prestressed with FRP Tendons*. PCI Journal. pp. 74-85.

Park, S. Y. and Naaman, A. E. 1999. *Dowel Behavior of Tensioned Fiber Reinforced Polymer (FRP) Tendons*. ACI Structural Journal. Vol. 96, No. 5: pp. 799-807.

Pilkey, W.D. and Pilkey, D.F. 2008. *Peterson's Stress Concentration Factors (3rd edition).* John Wiley & Sons. Online version available at: http://www.knovel.com/web/portal/browse/display?_EXT_KNOVEL_DISPLAY_bookid=2436&VerticalID=0

Post, N.L., Lesko, J.J. and Case, S.W. 2010. *Residual Strength Fatigue Theories for Composite Materials.* In Fatigue Life Prediction of Composites and Composite Structures, Edited by Vassiloupolos, A.P. Woodhead Publishing Limited, Cambridge, United Kingdom, pp. 79-101.

Post-Tensioning Institute, 2003. *Specification for Grouting of Post-Tensioned Structures.* 62 p.

Pultrall 2007. *Technical Data Sheet for Straight Carbon V-Rod*, www.pultrall.com.

Pultrall 2011. *V-Rod LM (40 GPa) Datasheet*, www.trancels-pultrall.com.

Pultrall 2011. *V-Rod Std (50 GPa) Datasheet*, www.trancels-pultrall.com.

Pultrall 2011. *V-Rod HM (60 GPa) Datasheet*, www.trancels-pultrall.com.

Rahman, A.H., Adimi, M.R. and Benmokrane, B. 1996. *Fatigue Behaviour of FRP Reinforcements Encased in Concrete.* Proceedings of the 2nd International Conference on Advanced Composite Materials in Bridges and Structures, Montreal, Quebec, August 11-14, pp. 691-698.

Raju, N.K. 1969. *Prediction of the Fatigue Life of Plain Concrete in Compression.* Building Science. Vol. 4: pp. 99-102.

Ranasinghe, K., Mutsuyoshi, H. and Ashraf, M. 2002. *Effect of Bond on Shear Behavior of RC and PC Beams: Experiments and FEM Analysis*. Transactions of the Japan Concrete Institute. Vol. 23, pp. 407-412.

Razaqpur, A.G., Svecova, D. and Cheung, M.S. 2000. *Rational Method for Calculating Deflection of Fiber-Reinforced Polymer Reinforced Beams.* ACI Structural Journal, Vol. 97, No. 1: pp. 175-185.

Regan, P.E. and Kennedy Reid, I.L. 2004. *Shear Strength of RC Beams with Defective Stirrup Anchorages.* Magazine of Concrete Research. Vol. 56, No. 3: pp. 159-166.

Reifsnider, K.L. 1991. *Damage and Damage Mechanics.* In Fatigue of Composite Materials, Edited by Reifsnider, K.L., Elsevier Science Publishing Company, New York, United States, pp. 11-78.

RILEM 1982. *RC5 – Bond Test for Reinforcement Steel. 1. Beam Test.*

Rteil, A., Soudki, K. and Topper, T. 2011. *Mechanics of Bond Under Repeated Loading.* Construction and Building Materials. Vol. 25: pp. 2822-2827.

Saadatmanesh, H. and Tannous, F.E. 1999. *Relaxation, Creep, and Fatigue Behavior of Carbon Fiber Reinforced Plastic Tendons.* ACI Materials Journal, Vol. 96, No. 2: pp. 143-155.

Salib, S.R. and Abdel-Sayed, G. 2004. *Prediction of Crack Width for Fiber-Reinforced Polymer-Reinforced Concrete Beams.* ACI Structural Journal. Vol. 101, No. 4: pp. 532-536.

Saqan, E. I. and Frosch, R. J. 2009. *Influence of Flexural Reinforcement on Shear Strength of Prestressed Concrete Beams*. ACI Structural Journal. Vol. 106, No. 1: pp. 60-68.

Saraf, V. 1998. *Evaluation of Existing RC Slab Bridges*. Journal of Performance of Constructed Facilities. Vol. 12, No. 1: pp. 20-24.

Schiessl, A. and Zilch, K. 2001. *The Effect of the Modified Composition of SCC on Shear and Bond Behaviour*, Proceedings of the Second International Symposium on Self-Compacting Concrete, Tokyo, Japan, RILEM Publications S.A.R.L., pp. 501-506.

Schindler, A.K., Barnes, R.W., Roberts, J.B. and Rodriguez, S. 2007. *Properties of Self-Consolidating Concrete for Prestressed Members.* ACI Materials Journal. Vol. 104, No. 1: pp. 53-61.

Sendeckyj, G.P. 1981. *Fitting Models to Composite Materials Fatigue Data.* ASTM STP 734, pp. 245-260.

Sendeckyj, G.P. 1991. *Life Prediction for Resin-Matrix Composite Materials.* In Fatigue of Composite Materials, Edited by Reifsnider, K.L., Elsevier Science Publishing Company, New York, United States, pp. 431-484.

Shah, S.P. 1984. *Predictions of Cumulative Damage for Concrete and Reinforced Concrete.* Materiaux et Constructions. Vol. 17, No. 97: pp. 65-68.

Shehata, E., Morphy, R. and Rizkalla, S. H. 2000. *Fibre Reinforced Polymer Shear Reinforcement for Concrete Members: Behaviour and Design Guidelines*. Canadian Journal of Civil Engineering. Vol. 27, pp. 859-872.

Schoeck Canada 2011. *Technical Information Schoeck ComBAR*, www.schoeck.ca.

Sonebi, M., Grunewald, S. and Walraven, J. 2007. *Filling Ability and Passing Ability of Self-Consolidating Concrete*. ACI Materials Journal. Vol. 104, No. 2: pp. 162-170.

Sonebi, M., Tamimi, A. K. and Bartos, P. J. M. 2003. *Performance and Cracking Behavior of Reinforced Beams Cast with Self-Consolidating Concrete*. ACI Materials Journal. Vol. 100, No. 6: pp. 492-500.

Sooriyaarachchi, H., Pilakoutas, K. and Byars, E. 2005. *Tension Stiffening Behavior of GFRP-Reinforced Concrete.* ACI SP-230, pp. 975-990.

Tabsh, S.W. 1995. *Structural Safety of Post-Tensioned Concrete Slab Bridges with Unbonded Tendons.* ACI Structural Journal. Vol. 92, No. 4: pp. 1-7.

Talreja, R. 1981. *Estimation of Weibull Parameters for Composite Material Strength and Fatigue Life Data.* ASTM STP 723, pp. 291-311.

Talreja, R. 1981. *Fatiuge of Composite Materials: Damage Mechanisms and Fatigue-Life Diagrams.* Proceedings of the Royal Society of London. Series A, Mathematical and Physical Sciences. Vol. 378, No. 1775: pp. 461-475.

Talreja, R. 1991. *Statistical Considerations.* In Fatigue of Composite Materials, Edited by Reifsnider, K.L., Elsevier Science Publishing Company, New York, United States, pp. 485-501.

Talreja, R. 1999. *Damage Mechanics and Fatigue Life Assessment of Composite Materials.* International Journal of Damage Mechanics. Vol. 8: pp. 339-354.

Tan, K.H., Tang, C.Y. and Tong, K. 2004. *Magazine of Concrete Research.* Vol. 56, No. 8: pp. 443-452.

Tastani, S.P., Pantazopoulou, S.J. and Karvounis, P. 2005. *Local Bond-Slip Characteristics of G-FRP Bars.* ACI SP-230, pp. 1481-1496.

Teng, S., Ma, W. and Wang, F. 2000. *Shear Strength of Concrete Deep Beams under Fatigue Loading.* ACI Structural Journal, Vol. 97, No. 4: pp. 572-580.

Tilly, G.P. 1979. *Fatigue of Steel Reinforcement Bars in Concrete: A Review.* Fatigue of Engineering Materials and Structures. Vol. 2: pp. 251-268.

Turcry, P., Loukili, A., Haidar, K., Pijaudier-Cabot, G. and Belarbi, A. 2006. *Cracking Tendency of Self-Compacting Concrete Subjected to Restrained Shrinkage: Experimental Study and Modeling.* Journal of Materials in Civil Engineering. Vol. 18, No. 1: pp. 46-54.

Tureyen, A. K. and Frosch, R. J. 2002. *Shear Tests of FRP-Reinforced Concrete Beams without Stirrups*. ACI Structural Journal. Vol. 99, No. 4: pp. 427-434.

Tureyen, A. K. and Frosch, R. J. 2003. *Concrete Shear Strength: Another Perspective*. ACI Structural Journal. Vol. 100, No. 5: pp. 609-615.

Ueda, T. And Okamura, H. 1983. *Behavior in Shear of Reinforced Concrete Beams Under Fatigue Loading.* Journal of the Faculty of Engineering, The University of Tokyo. Vol. 37, No. 1: pp. 17-48.

Van Paepegem, W. 2010. *Fatigue Damage Modelling of Composite Materials with the Phenomenological Residual Stiffness Approach.* In Fatigue Life Prediction of Composites and

Composite Structures, Edited by Vassiloupolos, A.P. Woodhead Publishing Limited, Cambridge, United Kingdom, pp. 102-138.

Van Paepegem, W. and Degrieck, J. 2002. *Coupled Residual Stiffness and Strength Model for Fatigue of Fibre-Reinforced Composite Materials.* Composites Science and Technology. Vol. 62: pp. 687-696.

Van Paepegem, W. and Degrieck, J. 2002. *A New Coupled Approach of Residual Stiffness and Strength For Fatigue of Fibre-Reinforced Composites.* International Journal of Fatigue. Vol. 24: pp. 747-762.

Varney, J.C., Brown, M.D., Bayrak, O. and Poston, R.W. 2011. *Effect of Stirrup Anchorage on Shear Strength of Reinforced Concrete Beams.* ACI Structural Journal. Vol. 108, No. 4: pp. 469-478.

Vassilopoulos, A.P. and Keller, T. 2011. *Fatigue of Fiber-Reinforced Composites.* Engineering Materials and Processes, Springer-Verlag London Limited, 238 p.

Vecchio, F. J. and Collins, M. P. 1986. *The Modified Compression-Field Theory for Reinforced Concrete Elements Subjected to Shear*. ACI Structural Journal. Vol. 83, No. 2: pp. 219-231.

Wegian, F. M. and Abdalla, H. A. 2005. *Shear Capacity of Concrete Beams Reinforced with Fiber Reinforced Polymers*. Composite Structures. Vol. 71, pp. 130-138.

Whitney, J.M. 1981. *Fatigue Characterization of Composite Materials.* ASTM STP 723, pp. 133-151.

Whitworth, H.A. 1998. *A Stiffness Degradation Model for Composite Laminates Under Fatigue Loading.* Composite Structures. Vol. 40, No. 2: pp. 95-101.

Wolf, T. S. and Frosch, R. J. 2007. *Shear Design of Prestressed Concrete: A Unified Approach*. Journal of Structural Engineering. Vol. 133, No. 11: pp. 1512-1519.

Yang, K., Chung, H. and Ashour, A.F. 2007. *Influence of Inclined Web Reinforcement on Reinforced Concrete Deep Beams with Openings*. ACI Structural Journal, Vol. 104, No. 5: pp. 580-589.

Yao, W.X. and Himmel, N. 2000. *A New Cumulative Fatigue Damage Model for Fibre-Reinforced Plastics.* Composites Science and Technology. Vol. 60: pp. 59-64.

Yonekura, A., Tazawa, E. and Nakayama, H. 1993. *Flexural and Shear Behavior of Prestressed Concrete Beams using FRP Rods as Prestressing Tendons*, Fiber-Reinforced-Plastic Reinforcement for Concrete Structures, American Concrete Institute, Vancouver, Canada, March 28-31, pp. 525-548.

Yost, J. R., Gross, S. P. and Dinehart, D. W. 2001. *Shear Strength of Normal Strength Concrete Beams Reinforced With Deformed GFRP Bars*. Journal of Composites for Construction. Vol. 5, No. 4: pp. 268-275.

Xue, W. and Tan, Y. 2012. *Cracking Behavior and Crack Width Predictions of Concrete Beams Prestressed with Bonded FRP Tendons.* Proceedings of the 6th International Conference on Composites in Civil Engineering, Rome, Italy, June 13-15.

Zhou, Y. And Mallick, P.K. 2004. *Fatigue Strength Characterization of E-Glass Fibers Using Fiber Bundle Test.* Journal of Composite Materials. Vol. 38, No. 22: pp. 2025-2035.

Zhu, W., Sonebi, M. and Bartos, P.J.M. 2004. *Bond and Interfacial Properties of Reinforcement in Self-Compacting Concrete.* Materials and Structures, Volume 37, No. 5: pp. 442-448.

Zielinski, Z.A. and Rigotti, M. 1995. *Tests on Shear Capacity of Reinforced Concrete.* Journal of Structural Engineering, No. 11: pp. 1660-1666.

Appendix A – Load-Crack Width Response of Phase I Slabs

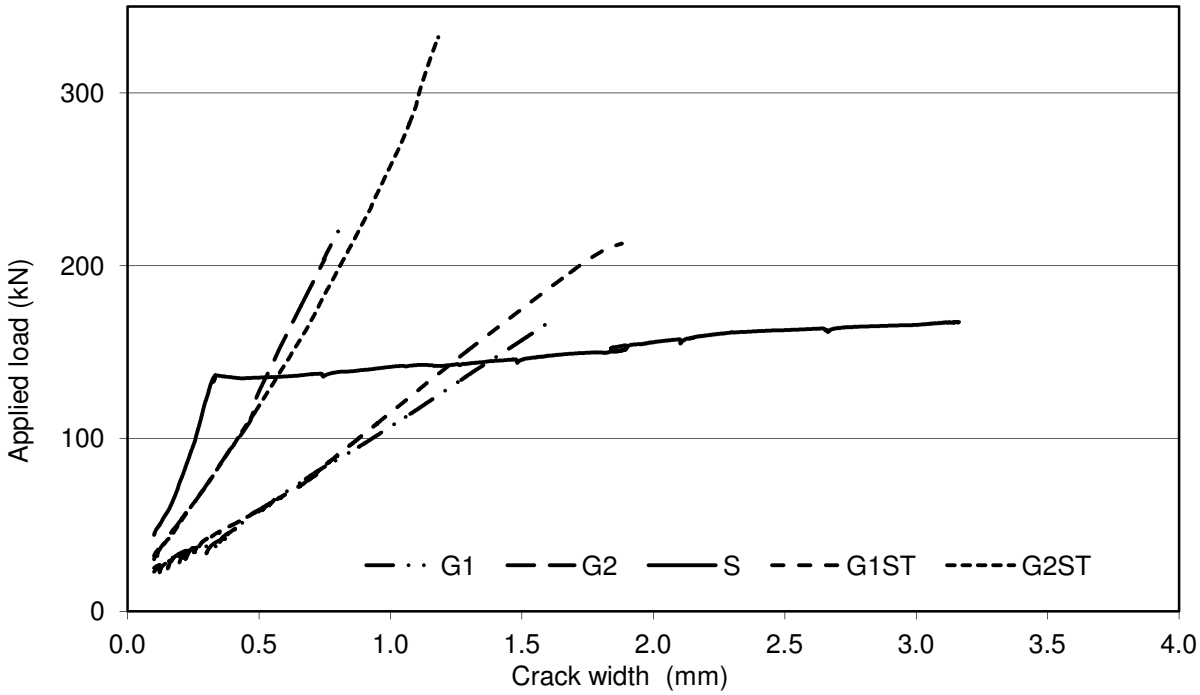

a) Effect of reinforcement type and ratio

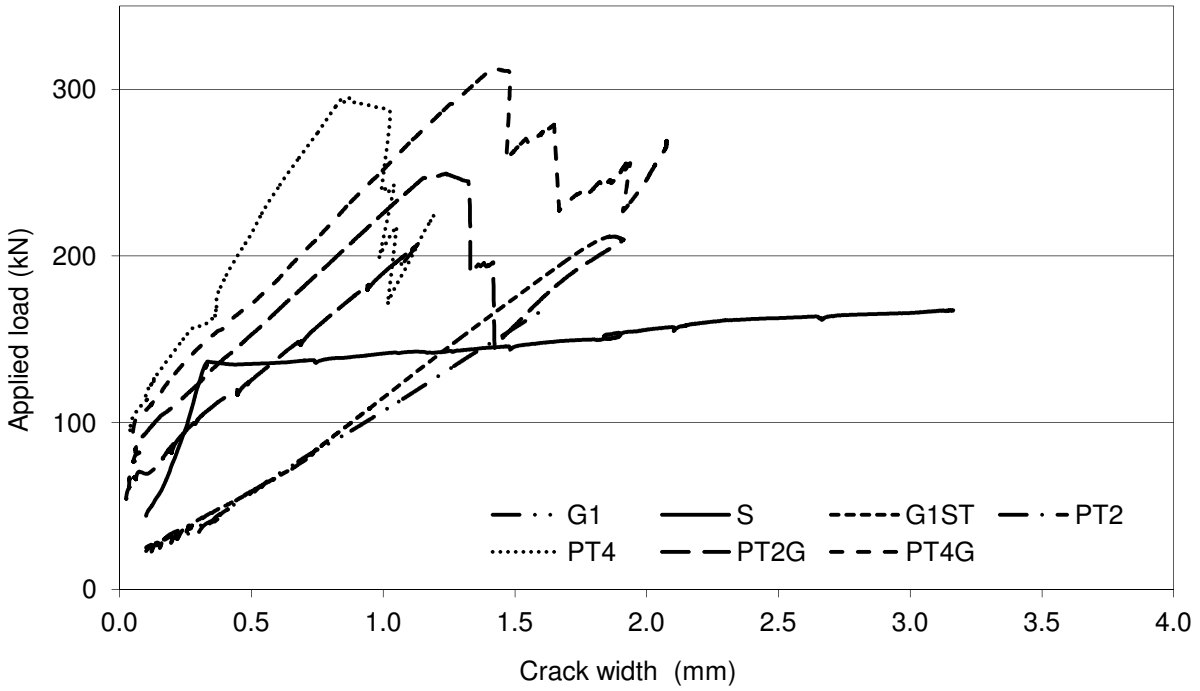

b) Effect of prestressing – 0, 2 or 4 post-tensioned tendons

Figure A.1 – Load-crack width response

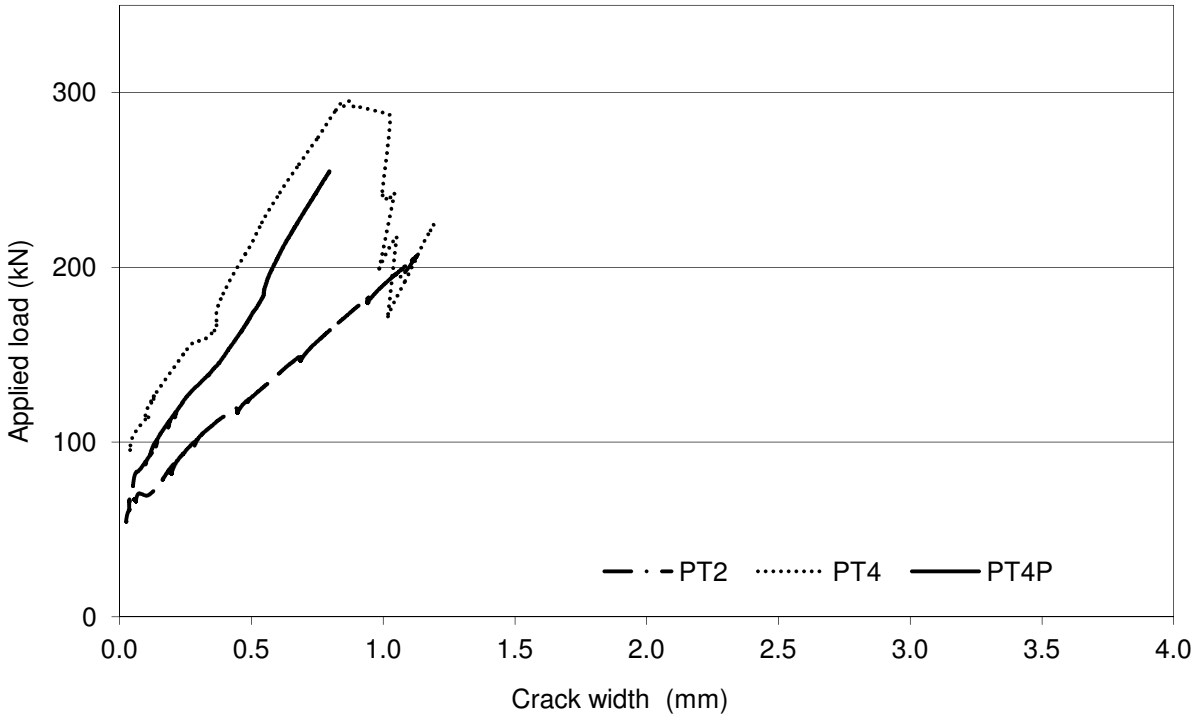

c) Effect of prestressing – 2 or 4 post-tensioned tendons with 30% or 55% prestress

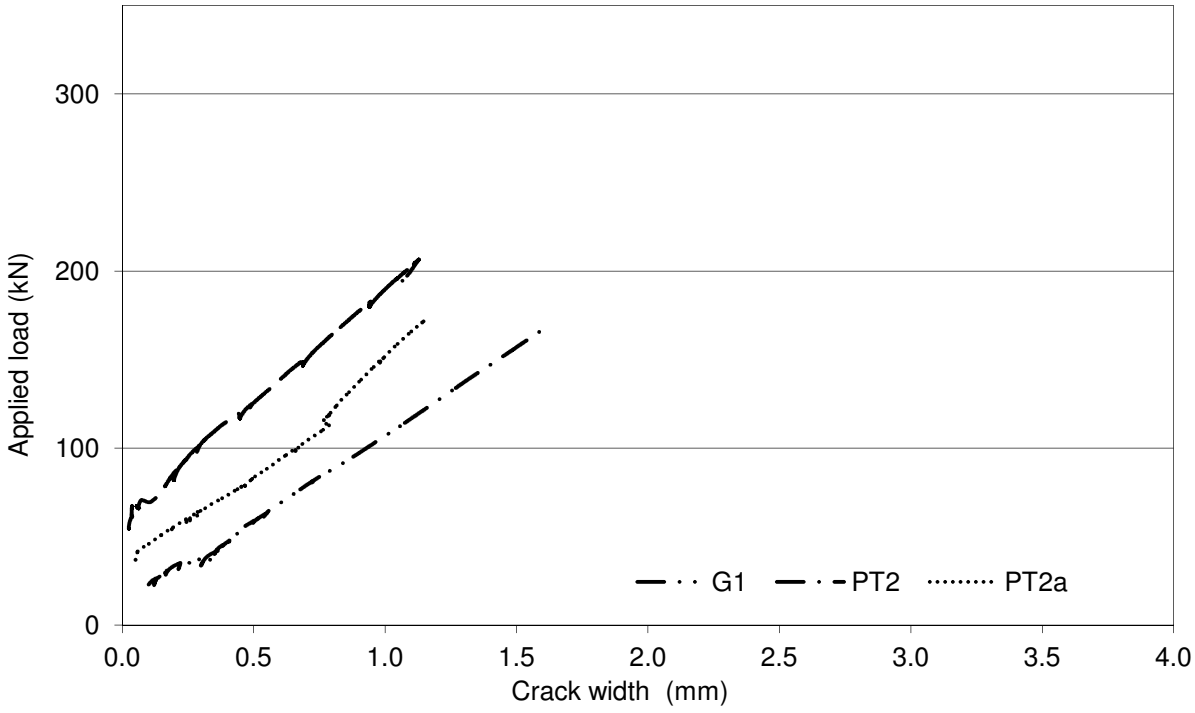

d) Effect of cross-section depth

Figure A.1 – Load-crack width response (continued)

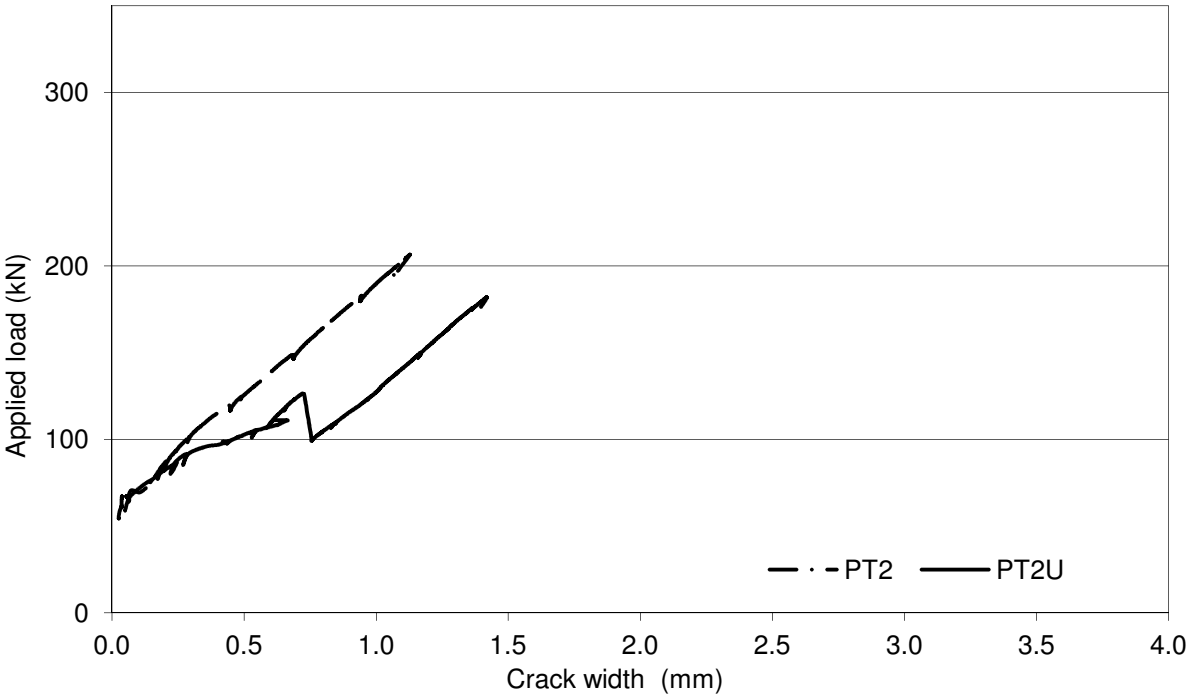

e) Bonded vs. unbonded – 2 post-tensioned tendons

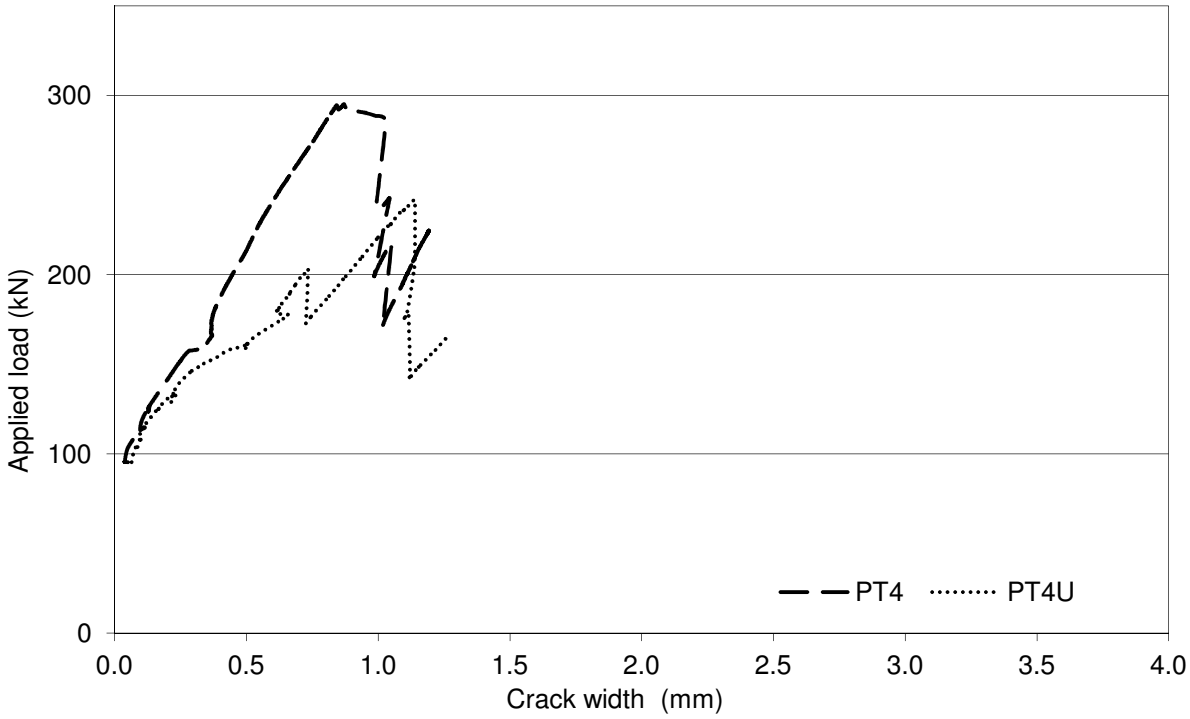

f) Bonded vs. unbonded – 4 post-tensioned tendons

Figure A.1 – Load-crack width response (continued)

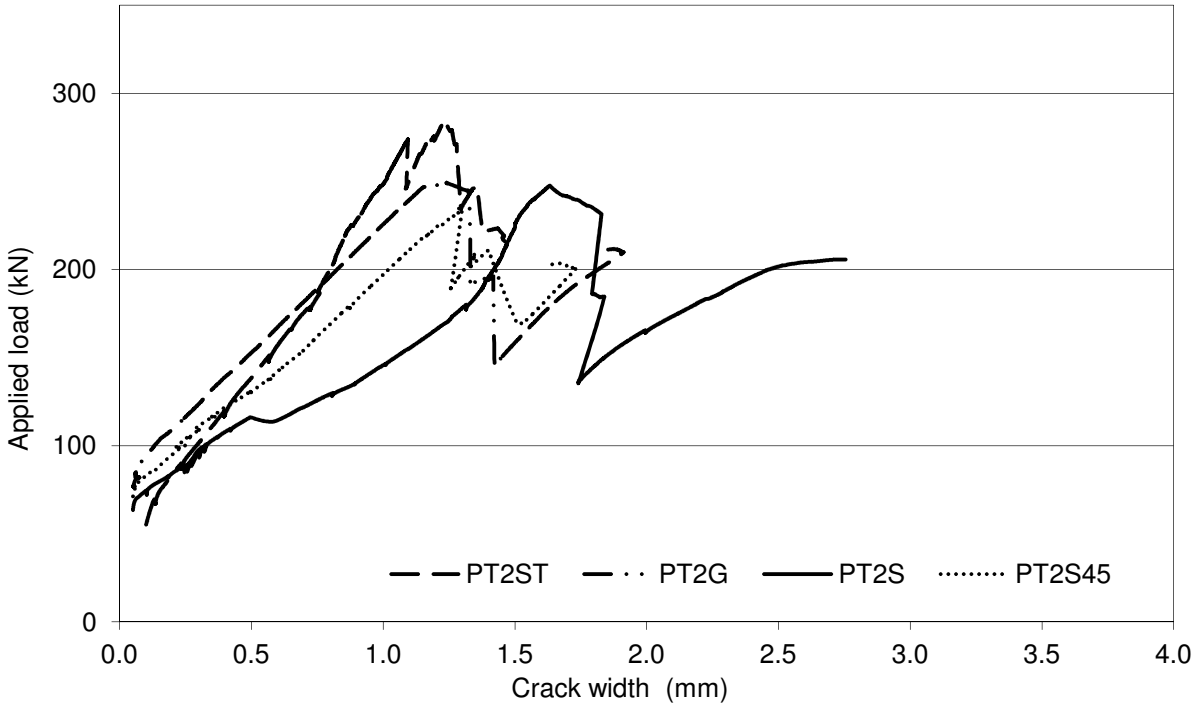

g) Shear-reinforced prestressed slabs

Figure A.1 - Load-crack width response (continued)

Appendix B – Load-Strain Response of Phase I Slabs

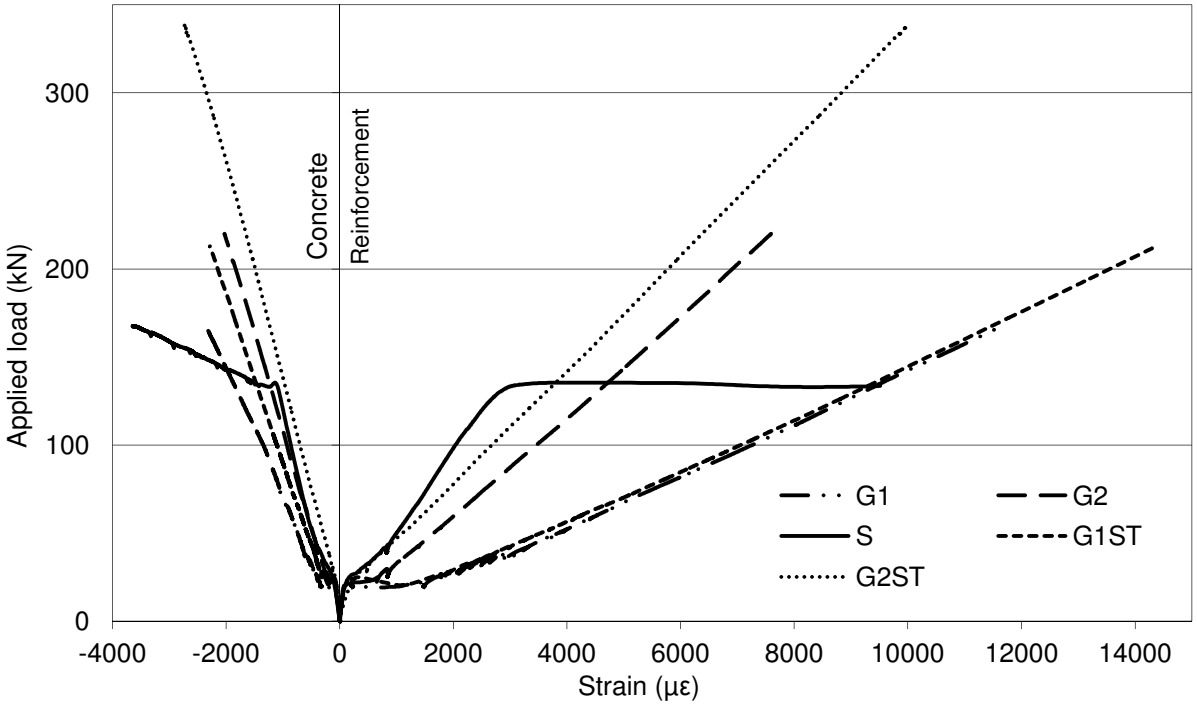

a) Effect of reinforcement type and ratio

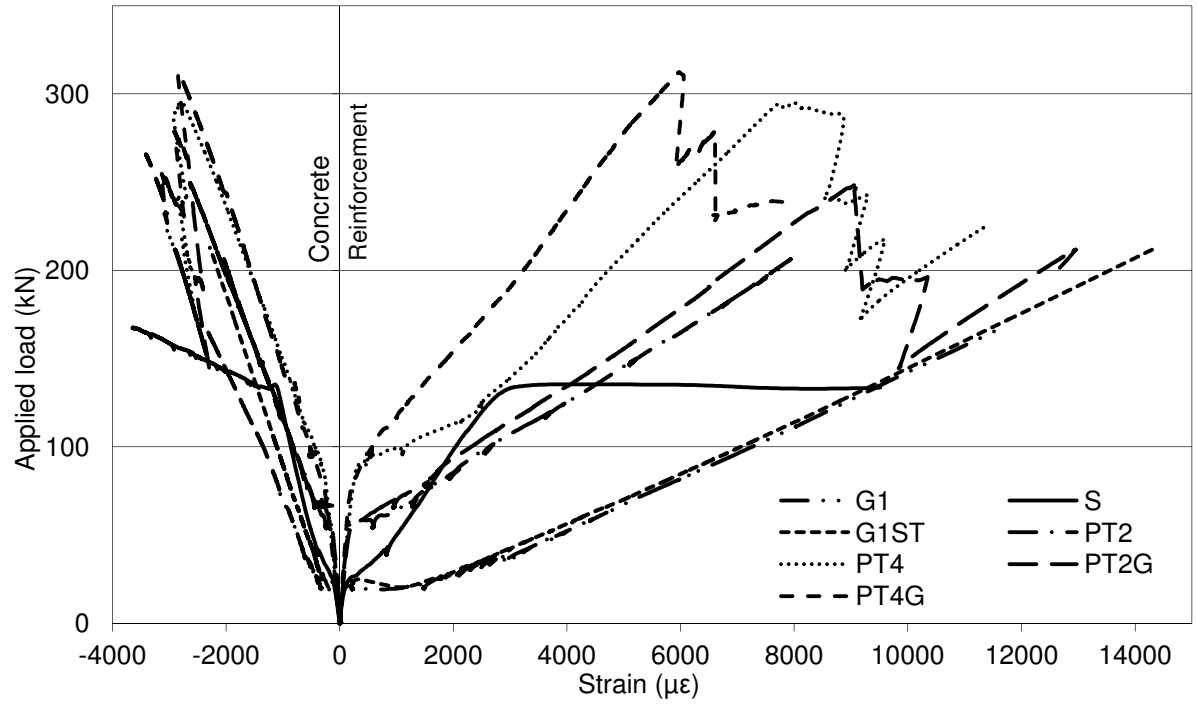

b) Effect of prestressing – 0, 2 or 4 post-tensioned tendons

Figure B.1 – Load-strain response

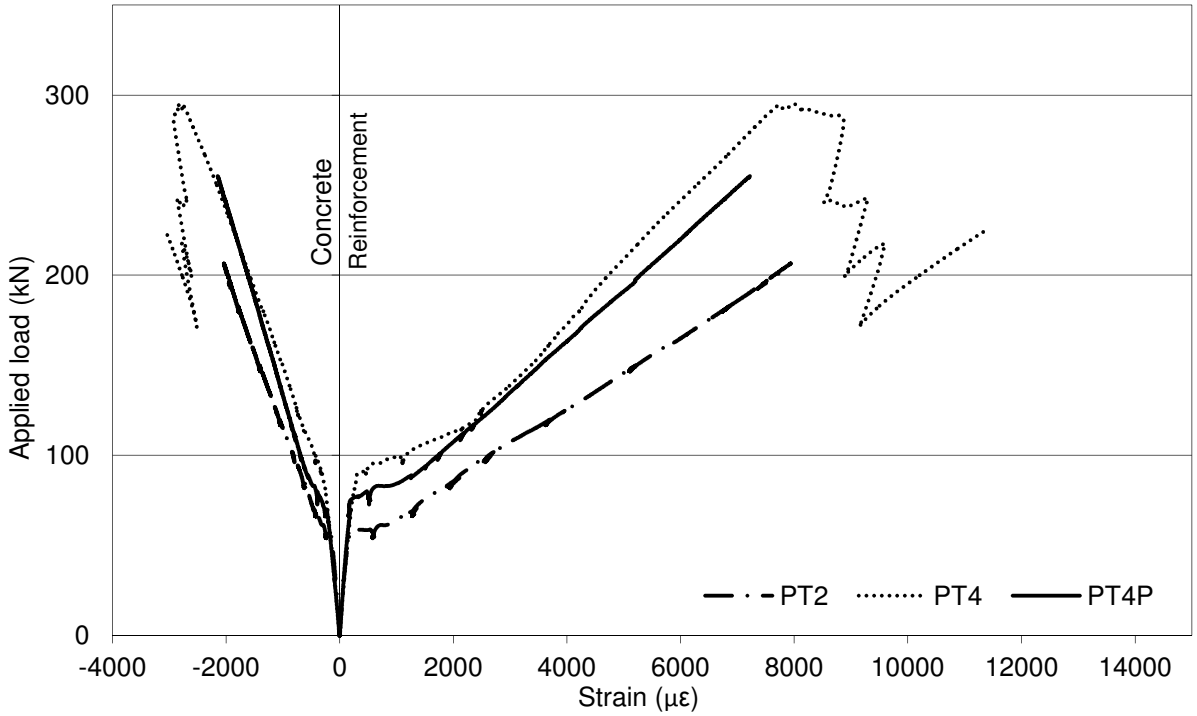

c) Effect of prestressing – 2 or 4 post-tensioned tendons with 30% or 55% prestress

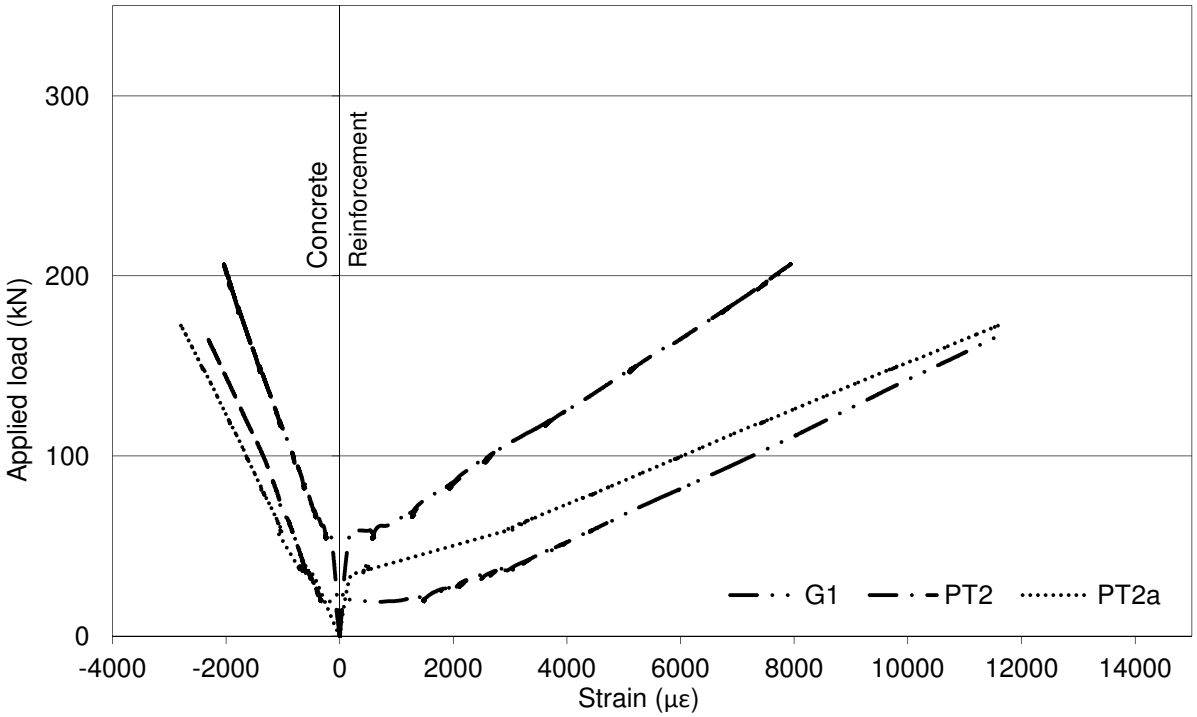

d) Effect of cross-section depth

Figure B.1 – Load-strain response (continued)

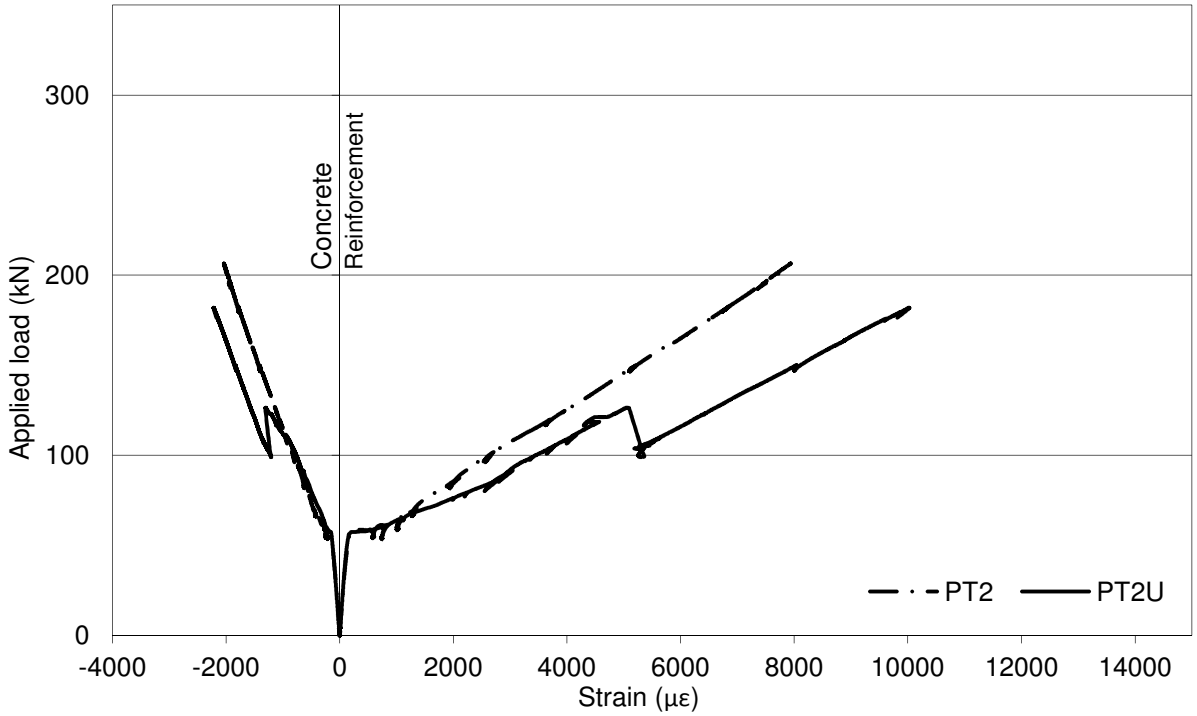

e) Bonded vs. unbonded – 2 post-tensioned tendons

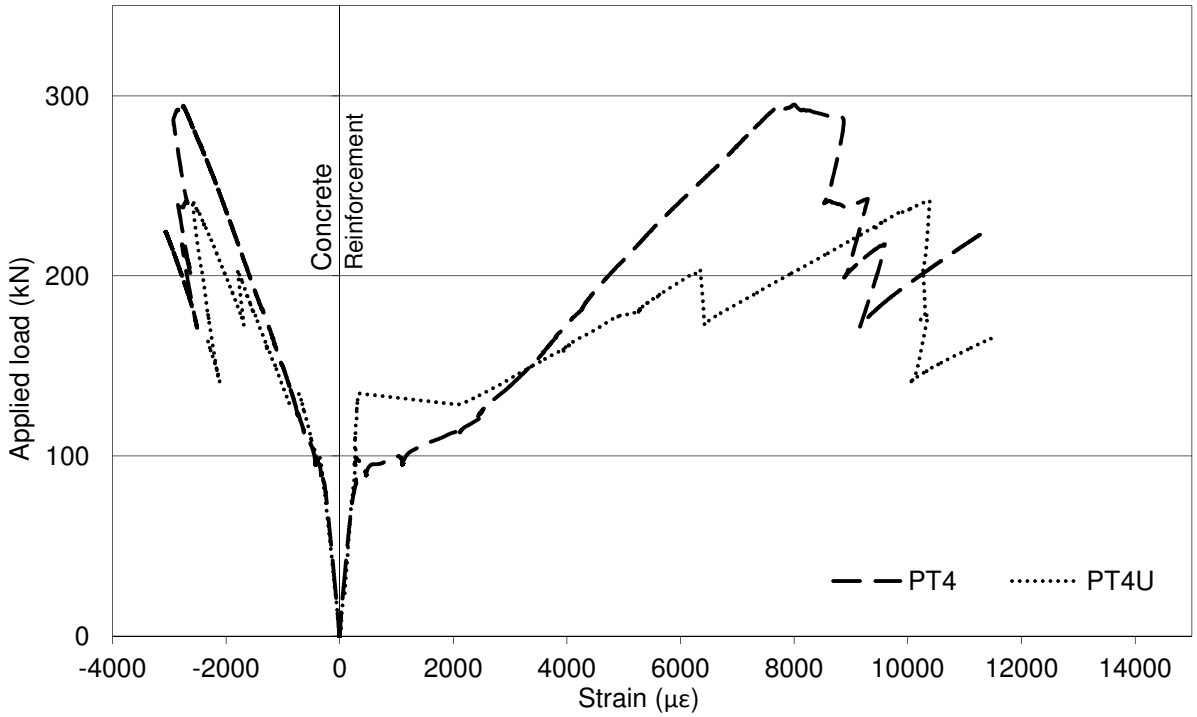

f) Bonded vs. unbonded – 4 post-tensioned tendons

Figure B.1 – Load-strain response (continued)

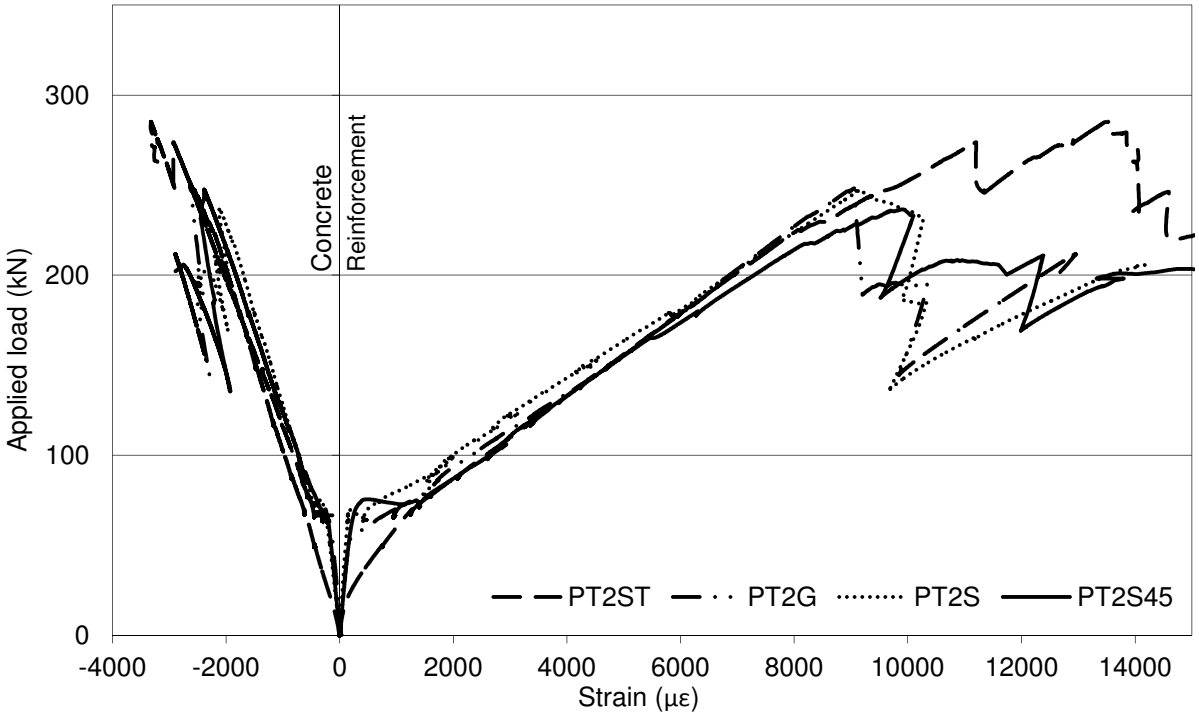

g) Shear-reinforced prestressed slabs

Figure B.1 - Load-strain response (continued)